Modelling Random Wave Boundary Layers

Thesis submitted in accordance with the requirements of the University of Liverpool for the degree of Doctor in Philosophy

by

John M. Harris

August 1997

Declaration

I hereby declare that no portion of the work referred to in this thesis has been submitted in support of an application for another degree or qualification of this or any other university or institution of learning.

Acknowledgements

I wish to thank my supervisor Professor B.A. O'Connor for his guidance, advice, patience and support throughout this work. I also wish to thank Drs. L. Kaczmarek and R. Ostrowski of the IBW PAN, Gdansk, Poland, for providing me with some of the random wave data as well as for the many useful discussions. I wish to acknowledge the support of The British Council and The Polish Academy of Sciences for enabling the links with IBW PAN. I would also like to thank Dr. B.M. Sumer of ISVA, Denmark, for providing me with some of the oscillating water tunnel data along with Dr. J.J. Williams of the Proudman Oceanographic Laboratory, for providing me with the random field data collected as part of the CSTAB project. I would like to thank Dr. A.W. Lewis of University College, Cork, for providing financial support and for Dr. E. Hitching for some useful discussions. I also wish to acknowledge the financial support provided under the European Communities, MAST programme. Finally, I wish to thank my parents, without whose love and support this thesis would not have been possible and to whom I dedicate this work.

Abstract

The thesis describes the development of one- and two-equation turbulence models for the simulation of random wave boundary layers. The models make use of the transport equations for the turbulent kinetic energy, k, and the isotropic dissipation rate, ε. In addition, a moveable bed model has been developed which enables the variation in the bed roughness to be simulated as a time-series within the boundary layer models.

The model equations are solved at a point through the vertical (1DV) using the semi-implicit Crank-Nicolson finite difference scheme. The method has the advantage of being unconditionally stable and offers higher-order accuracy. Further, in order to allow for the calculation of the large velocity gradients close to the wall (seabed), a logarithmic grid transform has been introduced in the vertical space direction.

The boundary layer models were first run using monochromatic waves. Results from these initial runs were compared with Lamb's analytical solution for laminar flow and then with laboratory data for fully turbulent flow (Jonsson and Carlsen 1976; and Jensen *et al.* 1989) and for transitional rough turbulent flow (McDowell 1983; Savell 1986). Results for the transitional rough turbulent flow regime were compared with a standard high-Reynolds number k-ε model and a two-layer k-ε model. Application of the high-Reynolds number k-ε model leads to poor results since the assumption of a fully turbulent flow regime has not been reached. However, the two-layer model shows excellent agreement with the velocity measurements and good agreement with the laboratory results overall.

From the results with a monochromatic wave it was decided to adapt only the two-equation k-ε model initially to run with random waves. The choice of model was made on the basis of computational efficiency. The random wave boundary layer model has been compared with

the random wave experiments of Ostrowski (1993). As part of these tests, measurements of the bed shear stress were performed using a shear plate device.

In addition to the laboratory data of Ostrowski (1993), the random wave boundary layer model has been tested against field measurements (Williams 1996). These measurements were undertaken as part of an European Community funded project, CSTAB.

Reasonable agreement between the model results and both the laboratory and field measurements was obtained. However, the approach used to compare the field measurements to the model predictions has been shown to be questionable.

Significantly, the random wave boundary layer model has demonstrated that turbulent kinetic energy can be carried over from one half period to the next. This has important implications for sediment transport calculations. Further, previously suggested approaches which assume that for random waves each wave can be treated individually as a monochromatic wave, for example Smith (1977), are clearly incorrect.

The moveable bed model has been developed using laboratory results for both monochromatic and irregular waves. The assumption that a ripple can be treated as an increased roughness length, such as 4 x the ripple height, has been shown to be invalid for a 1DV, one- or two-equation turbulence model and without modifying the models leads to underprediction in the energy dissipation factor. It has been hypothesized that the underprediction is due to vortex shedding off the ripples. A new coefficient, C_{vor}, has been proposed that adjusts the dissipation term in the turbulent kinetic energy transport equation, compensating for the vortex action. Lack of suitable experimental data has prevented a full description of C_{vor} being determined.

It has been demonstrated that the proposed moveable bed for random waves is capable of enabling the ripple geometry to be determined as a continuous time-series.

Table of Contents

		Page No.
Acknowledgements		i
Abstract		ii
Table of Contents		iv
Notation		ix
Chapter 1	**Introduction**	1
Chapter 2	**The Hydrodynamic Equations**	
2.1	Introduction	11
2.2	The flow field in the turbulent boundary layer	11
2.3	Hydrodynamic boundary conditions	17
2.3.1	Introduction	17
2.3.2	Sinusoidal waves	18
2.3.3	Sinusoidal waves and current	18
2.4	Conclusions	20
Chapter 3	**Literature Review**	
3.1	Introduction	21
3.2	The wave boundary layer	22
3.3	Laminar flow	24
3.4	Boundary layer modelling	25
3.5	Eddy viscosity modelling	27
3.6	Turbulence models	37
3.6.1	Zero-equation models	38
3.6.2	One-equation models	39
3.6.3	Two-equation models	41
3.6.4	Algebraic stress (Reynolds stress) models	42
3.6.5	Direct numerical simulation (DNS) models	45
3.7	Modelling random sea boundary layers	46
3.8	Conclusions	47

Chapter 4 Theory

4.1 Introduction 51
4.2 Introduction to turbulence modelling 51
4.3 The k-ε model 54

4.3.1 Introduction 54
4.3.2 The exact k-equation 54
4.3.3 The modelled k-equation 55
4.3.4 The exact ε-equation 56
4.3.5 The modelled ε-equation 58
4.3.6 Turbulence model constants 59
4.3.7 Low-Reynolds number k-ε model 61
4.3.8 Two-layer model 62

4.4 The k model 64
4.5 Boundary conditions 65
4.6 Random seas 65
4.7 Wave spectra 69

4.7.1 Introduction 69
4.7.2 The Pierson-Moskowitz (P-M) spectrum 70
4.7.3 The JONSWAP spectrum 71
4.7.4 Double-peaked spectra 71
4.7.5 Multi-directional seas 73

4.7.5.1 The directional spreading function 74

4.7.6 The effect of currents on wave spectra 76

4.7.6.1 Equilibrium range constraint 78

4.8 Conclusions 79

Chapter 5 Numerical Scheme and Convergence

5.1 Introduction 86
5.2 Vertical grid transformation 86
5.3 Numerical scheme 87
5.4 Numerical stability and convergence 88
5.5 Conclusions 90

Chapter 6 Results: Part I

6.1 Introduction 95
6.2 Monochromatic waves without current 95

6.2.1	Jonsson and Carlsen (1976)	95
6.2.2	Jensen *et al.* (1989)	99
6.2.3	Model results for test 12, Jensen *et al.* (1989)	101
6.2.4	Model results for test 13, Jensen *et al.* (1989)	103
6.3	Conclusions	107
Chapter 7	**Results: Part II**	
7.1	Manchester Experiments	136
7.2	Test 52: Waves alone	137
7.3	Test 59: Combined waves and current	139
7.4	Conclusions	141
Chapter 8	**Results: Part III**	
8.1	Random waves without current	154
8.1.1	Introduction	154
8.1.2	Gdansk flume experiments	154
8.1.3	The numerical model	155
8.2	Results	156
8.2.1	Test 1	156
8.2.2	Test 2	158
8.2.3	Test 3	159
8.2.4	Comparison between k-ε model and a time-invariant eddy viscosity model	160
8.3	Turbulent kinetic energy under random waves	160
8.4	Spectral approach to generating time-series	161
8.5	Conclusions	162
Chapter 9	**Results: Part IV**	
9.1	Multi-directional seas	184
9.1.1	Introduction	184
9.1.2	Background	184
9.2	Field data	185
9.3	Model results	186
9.4	Conclusions	192

Chapter 10 Moveable Bed Model

10.1 Moveable bed roughness 202
10.2 Friction factor under oscillatory waves over a fixed horizontal bed 203

10.2.1 Introduction 203
10.2.2 Friction factor formulae 204
10.2.3 Energy dissipation factor 207

10.3 Energy dissipation over fixed ripples 208
10.4 Energy dissipation over a moveable bed 210
10.5 Moveable bed models 217
10.6 The proposed model 221
10.7 Conclusions 224

Chapter 11 Conclusions and Recommendations

11.1 Introduction 244
11.2 Overview of present work 244
11.3 Recommendations for future work 250

References 252

Appendix A Derivation of The Exact k-Equation 272

Appendix B Derivation of The Exact ε-Equation 275

Appendix C Vertical Grid Transformation and Model Discretization

C.1 Vertical grid transformation 278

C.1.1 Introduction 278
C.1.2 Vertical space transform 279

C.2 Discretized model equations 280

C.2.1 Introduction 280
C.2.2 The discretized momentum equation 281
C.2.3 The discretized turbulent kinetic energy equation 284
C.2.4 The discretized isotropic dissipation rate equation 286

Appendix D Numerical Stability and Convergence

D.1 Introduction 288
D.2 Numerical convergence 289
D.3 Conclusions 291

Appendix E Tables of Results for Numerical Models 318

Appendix F Tables of Results for Moveable Bed Model 345

Appendix G Publications Related to Present Work 355

Notation

a	=	Near-bed orbital amplitude
a_2	=	Amplitude of second harmonic of turbulent eddy viscosity
$c_{\varepsilon 1}$	=	Turbulence model constant
$c_{\varepsilon 2}$	=	Turbulence model constant
c_μ	=	Turbulence model constant
c_2	=	Factor on length scale
d_{50}	=	Mean grain diameter
e	=	Exponential (1) = 2.71828.....
e	=	Energy density
f_e	=	Energy dissipation factor
f_w	=	Wave friction factor
f_μ	=	Multiplying function in low-Reynolds number k-ε model
f_1	=	Multiplying function in low-Reynolds number k-ε model
f_2	=	Multiplying function in low-Reynolds number k-ε model
g_i	=	Gravitational vector ($g_x = 0$; $g_y = 0$; $g_z = -g$; where g is the acceleration due to gravity)
i	=	$\sqrt{-1}$
k	=	Turbulent kinetic energy $\left(= \left(\overline{u_i' u_i'}\right)/2\right)$
k	=	Wave number $(= 2\pi/L)$
k_n	=	Wave number of the nth component
k_s	=	Nikuradse equivalent roughness
l	=	Mixing length
l_ε	=	Length scale
l_μ	=	Length scale

p	=	Hydrodynamic pressure
u_B	=	Modified shear velocity
u_d	=	Defect velocity $(u_d = u_0 - u)$
u_i	=	Instantaneous velocity tensor at position (x_i, t)
$\overline{u}_i$	=	Turbulence mean velocity
u_i	=	Fluctuating turbulent velocity component
$\tilde{u}_i$	=	Wave-induced velocity component
u_0	=	Free stream velocity
u_∞	=	Velocity amplitude
u_*	=	Shear velocity
u_{*b}	=	Bed shear velocity
$u_{*B,max}$	=	Maximum bed shear velocity
u_{*C}	=	Current related bed shear velocity
s	=	Specific gravity
s_{ij}	=	Rate of strain
t	=	Time
x	=	Horizontal co-ordinate
y	=	Horizontal co-ordinate
z	=	Vertical co-ordinate
z^+	=	Dimensionless wall distance $(= u_{*b} z / \nu_L)$
z_0	=	Vertical level at which the velocity is assumed zero $(= k_s/30)$
z_{top}	=	Upper limit of computational domain
A	=	Constant (=0.0081) in Pierson-Moskowitz spectrum
A_t	=	Turbulence model constant
A_{C1}	=	Turbulence model constant
A_μ	=	Turbulence model constant
A^*	=	Turbulence model parameter
B	=	Constant (= 0.74) in Pierson-Moskowitz spectrum
C_D	=	Drag coefficient

C_{gr} = Relative group velocity

C_{g0} = Group velocity in zero current region

C_L = Lift coefficient

C_m = Added mass coefficient

C_l = Turbulence model constant

C_a = Absolute, or apparent, wave celerity

C_r = Relative wave celerity

C_{vor} = Vortex coefficient

D = Flow depth

D_B = Constant (Brevik 1981)

D_E = Energy dissipation

$\overline{E}$ = Wave energy density

$\overline{E}_0$ = Wave energy density in zero current region

F = Wave generation fetch

$G_{ER}(\theta)$ = Spreading function within the equilibrium range

H = Wave height

$H_0^{(1)}$ = Hankel function of the first kind, zeroth order

$H_1^{(1)}$ = Hankel function of the first kind, first order

H_{rms} = Root-mean-square wave height

H_S = Significant wave height

I = Slope of energy line

K = Free parameter

L_{oa} = Deep water wave length for stationary observer

L_{or} = Deep water wave length for moving frame of reference

Re = Real part of a complex number

Re = Amplitude Reynolds number $\left(= u_0 a/\nu_L\right)$

R_k = Turbulence Reynolds number $\left(= \sqrt{k}z/\nu_L\right)$

R_t = Turbulence Reynolds number $\left(= k^2/(\nu_L \varepsilon)\right)$

$S_\eta(\omega_n)$ = Spectral density of the surface elevation

$S_\eta(\omega_n, U)$	=	Spectral density of the surface elevation in current region
T	=	Wave period or turbulent averaging period
T_a	=	Absolute, or apparent, wave period
T_B	=	Constant (Brevik 1981)
T_r	=	Relative wave period
T_z	=	Zero crossing period
U	=	Current velocity
$U_{19.5}$	=	Wind speed at 19.5 m above mean sea level
α	=	Angle between wave crests and current direction
α_ω	=	Turbulence model constant
β	=	Inverse of the Stokes length $\left(=\sqrt{\omega/2\nu_L}\right)$
β_e	=	Turbulence model constant
β_ω	=	Turbulence model constant
γ	=	Turbulence model constant (Section 3.6.3)
γ	=	Peak enhancement factor in JONSWAP spectrum (Section 4.7.3)
δ	=	Boundary layer thickness
δ_J	=	Boundary layer thickness as defined by Jonsson
δ_K	=	Boundary layer thickness as defined by Kajiura
δ_S	=	Boundary layer thickness as defined by Sleath
$\delta_{0.01}$	=	Boundary layer thickness defined as when the velocity defect has reached 1% of the free stream amplitude
δ_i	=	Thickness of inner layer
δ_{ij}	=	Kronecker delta ($\delta_{ij} = 1$ if $i = j$, otherwise $\delta_{ij} = 0$)
δ_n	=	Random phase angle (values between 0 and 2π)
ε	=	Isotropic dissipation rate
ζ	=	Dimensionless parameter
η	=	Surface elevation
η	=	Transformed space co-ordinate (Chapter 5)
η_n	=	Function of z
θ	=	Shields parameter

θ_C	=	Critical Shields parameter
κ	=	Von Karman constant
μ	=	Dynamic viscosity
ν_L	=	Kinematic (molecular) viscosity
ν_0	=	Shape function
ν_t	=	Turbulent eddy viscosity
ξ	=	Stream function
ρ	=	Fluid density
σ_ε	=	Turbulence model constant
σ_{ij}	=	Instantaneous stress tensor at position (x_i, t)
σ_k	=	Turbulence model constant
σ_η	=	Standard deviation of η, the surface elevation
σ_η^2	=	Variance of η, the surface elevation
σ_ω	=	Turbulence model constant
τ_b	=	Bed shear stress
τ_C	=	Current related shear stress
φ_n	=	Function of z
ψ	=	Mobility number
ω	=	Angular frequency of oscillation
ω_a	=	Absolute, or apparent, angular wave frequency
ω_r	=	Relative, or intrinsic, angular wave frequency
ω_S	=	Vorticity density
Δ	=	Upper point of overlap layer
Δ	=	Ripple height (Chapter 10)
$\bar{}$		Overbar denotes the Reynolds' time-average
$\sim$		Tilde denotes a phase-average in relation to the wave period

Sub-scripts:

b	=	Bed
c	=	Current
m	=	Maximum
w	=	Waves
S	=	Swell
W	=	Wind

Abbreviations:

ABS	Acoustic backscatter (probe)
CSTAB	Circulation and Sediment Transport Around Banks
DNV	Det Norske Veritas
ECM	Electromagnetic Current Meter
IBW PAN	Institute of Hydroengineering, Polish Academy of Sciences, 80-953 Gdansk.
ISVA	Institute of Hydrodynamics and Hydraulic Engineering, Technical University of Denmark, DK - 2800 Lyngby.
LDA	Laser-Doppler Anemometer
LDV	Laser-Doppler Velocimeter
P-M	Pierson-Moskowitz
STABLE	Sediment Transport And Boundary Layer Equipment
SWOP	Stereo Wave Observation Project
GWK	Großer Wellenkanal

Chapter 1
Introduction

The investigation of wave and wave and current boundary layers is of importance in a large number of areas in coastal and offshore engineering. Within the coastal region the hydrodynamics and associated sediment transport are essential in any attempt to understand changes in coastal morphology, erosion around structures and longshore and cross-shore sediment transport. In particular, flow inside the seabed boundary layer is a significant factor in wave attenuation, sediment transport and bedform formation as well as in areas such as the transport of pollutants.

Interest in the seabed boundary layer has arisen due to its dynamic characteristics. The region is an interface allowing exchanges of particles, chemicals and organisms with the water column above. The seabed boundary layer provides an area for turbulent mixing and frictional dissipation.

Boundary layer flows can be extremely complex. For example, water motion on the continental shelf is driven by various mechanisms such as tides, wind, sea surface slope, density differences and atmospheric pressure gradients. The importance of each driving mechanism will vary depending on location. Tidal flows dominate much of the seas around Britain.

Tidal flows in shelf seas are affected by friction at the seabed. In deep water, the boundary layer where these frictional forces act is generally relatively thin, whilst in shallow water, the boundary layer may occupy the whole depth and dominate the tidal dynamics. A similar behaviour is also observed with steady and meteorologically induced currents (Soulsby 1983).

The scale difference between the thickness of tidal / current boundary layers and, say, wind wave boundary layers can be easily demonstrated. Nielsen (1985) relates the boundary layer thickness, δ, to the period of the flow, T and the turbulent eddy viscosity, ν_t , such that:-

$$\delta \propto \sqrt{T\nu_t} \qquad \textbf{(1.1)}$$

Assuming the eddy viscosity to be constant, then for a semi-diurnal tide ($T \approx 12.42$ hours) and wind waves of period 6 seconds, the tidal boundary layer will be approximately 86 times thicker than for the waves. Grant and Madsen (1986) suggest that the wave boundary layer is typically of 3 - 30 cm in thickness depending on wave conditions, though it is possible for the upper limit to be greater and of the order of 50 cm.

Therefore, following on from this, it is clear that for a combined wave-current flow two distinct boundary layer scales exist. Firstly, in the immediate vicinity of the bed, the wave boundary layer develops with contributions to the turbulence from both the waves and current. The height to which the wave-induced turbulence can diffuse acts as the vertical limit to this layer. Above this region is a layer where the turbulence is due to the current alone.

Lundgren (1973) was one of the first researchers to investigate the mechanism of wave-current interaction. Lundgren developed a simple model for a current in waves, however, non-linear interaction was ignored. The first models to account for non-linear wave-current interaction are those of Smith (1977) and Grant (1977) (see also Grant and Madsen 1979).

In the 1970's and early 1980's there was a rapid expansion in the offshore oil and gas industries. With it came a need for greater understanding of how structures would respond to hydrodynamic forces. In particular, there was a need to protect piles and platform legs as well as pipelines from scour.

For example, exposed seabed pipelines in shallow or intermediate water depths are also subject to the hydrodynamic forces in the wave or combined wave-current boundary layer. It is the fluid motion in this region that is the major mechanism which governs sediment transport and hence scour. Deigaard *et al.* (1985) reviewed bed boundary layer models with a view to investigating marine pipeline stability. They took the combined wave-current flow

field as being the most general case to which pipelines would be exposed. It had previously been shown that the lift (C_L) and drag (C_D) coefficients attain greater values in waves than in currents alone (e.g. Sarapkaya and Rajabi 1979).

Investigation of wave and combined wave-current boundary layers has been undertaken on three fronts, direct measurements in the field, laboratory experiments and from a theoretical approach using both analytical and computer (numerical) models of varying complexity.

Measurements in the wave boundary layer are difficult to take in the field. Not only can the environment be extremely hostile to equipment, leading to possible loss, but for the measuring devices to survive in such an environment they tend to be quite bulky, which is a problem because of the wave boundary layer thickness being relatively small. To date, there is a lack of such data and this is a major obstacle which will need to be overcome if a full understanding of boundary layer processes is to be attained. Only Myrhaug *et al.* (1992) and Soulsby and Humphrey (1990) have made field measurements of flow velocities below 15 cm from the bed. Myrhaug *et al.* deployed a tripod in the North Sea equipped with acoustic current meters with the lowest measurement point at 10 cm from the bed. However, the data is limited in that it was recorded at a frequency of 1 Hz, excluding turbulence from the data. Soulsby and Humphrey also had a measurement point at 10 cm above the bed. Chriss and Caldwell (1982) performed measurements of flow velocities with their lowest point 15 cm from the bed. Unfortunately, most data sets have measurement points at 20 cm or more from the seabed: Drake and Cacchione (1985; 1986); Lambrakos (1985), Lambrakos *et al.* (1988); Madsen *et al.* (1993); Gross *et al.* (1994); Williams (1996).

With typical wave boundary layer thickness' of between 10 cm and 50 cm most of the data sets contain no or at best one measurement point within this region. Therefore, to be able to relate their data to the wave boundary layer many researchers have fallen back on modelling techniques. There is, therefore, a need to try and ensure that any model applied to aid such deficiencies in field data collection are able to provide sufficiently accurate simulations if their output is to be of use.

Recently Agrawal and Aubrey (1992) used a laser Doppler velocimeter (LDV) in the field to take measurements in the trough, lee and crest of a bed ripple in 2.5 m of water. It is the application of such measurement techniques in the field that will eventually help to provide a greater number of measurement points within the wave boundary layer. However, for now, researchers will have to rely on the use of models to aid their interpretation of the real world.

Whilst laboratory experiments may be seen as a way of obtaining more detailed information on processes such as turbulence in the wave boundary layer, it was not until the development of equipment such as the oscillating wave tunnel (Lundgren and Sørensen 1959) that it was possible to reproduce the conditions found at prototype scale. The oscillating water tunnel developed by Lundgren and Sørensen consisted of two vertical risers connected by a horizontal tunnel. The water was oscillated by air pressure. Since the original oscillating water tunnel was built at ISVA, Denmark, several other institutions have acquired similar tunnels, (see King *et al.* 1985).

As there is no free surface in an oscillating tunnel no waves are formed. Therefore, the flow field is unable to fully reproduce wave motion because there are no vertical oscillatory velocities. Further, such facilities are unable to reproduce phenomenon such as turbulence due to wave breaking.

However, with the development of large scale facilities such as the Delta flume in the Netherlands, SUPERTANK in the USA and the GWK in Germany, it is now possible to carry out experiments at prototype scale. Whilst field data should be seen as the ideal, the difficulties of measuring in the field as well as the lack of control on external conditions (such as sea state and wind action) makes the use of prototype scale facilities very attractive.

The first detailed set of measurements in the turbulent wave boundary layer were those of Jonsson (1963). Jonsson used a micro-propeller meter to measure the velocity over a bed covered in triangular roughness elements used to simulate ripples. Further tests were reported in Jonsson and Carlsen (1976) (see Chapter 6 for further details). More recently, the work of Jensen *et al.* (1989) stands out for its quality and breadth, investigating oscillatory wave boundary layers for a range of Reynolds numbers for both smooth and rough beds.

Of the earliest laboratory studies to investigate the combined wave-current boundary layer, the most detailed are those due to Bakker and Van Doorn (1979) and Kemp and Simons (1982; 1983).

To date very few experiments have been performed to investigate the hydrodynamics of random wave and combined wave-current boundary layers. To this author's knowledge the first detailed investigation of such flows was due to O'Connor *et al.* (1988), who reported on a series of experiments performed at The University of Manchester. However, although the report highlights a comprehensive set of experiments no results were shown. More recently Ostrowski (1993) performed a series of tests using a shear plate to measure the bed shear stress under random waves (See Chapter 8). Unfortunately, the data is limited in that the lowest velocity measurement point is 13 mm above the bed. Simons *et al.* (1995) also describe experiments with a shear plate to investigate bottom shear stress under random waves with an imposed current.

The lack of data on such flows leaves many uncertainties as to how the flow field behaves under irregular waves. For example, Smith (1977) assumes that for irregular waves each wave can be treated individually as a monochromatic wave. However, if the turbulent kinetic energy were to persist into the next half wave period such an assumption would be flawed.

Modelling presently provides the link between the field and laboratory. As models have become more sophisticated so too has their ability to provide more detailed answers. Early modelling techniques were analytic in form due to the level of computer technology at the time. Kajiura (1968) developed a three-layer time-invariant eddy viscosity model yielding an ordinary differential equation which could be solved analytically. This was the first of this type of model based on Boussinesq's viscosity assumption.

As computers became more powerful and more accessible so boundary layer modelling techniques became more complex. Bakker (1975) adopted a mixing length closure, rewriting the linear flow equation in terms of a dimensionless shear velocity. Johns (1977) presented a one-equation k-model which included the horizontal advective term introduced through the

use of a pseudo-spectral method. However, prior to Johns (1977), Vager and Kagan (1969; 1971) had used a one-equation k-model to study the boundary layer of tidal flows.

Smith and Takhar (1977) describe the use of mean Reynolds stress and mean turbulence energy closure models for the prediction of oscillatory flow in open channels. Smith and Takhar applied three models which required the solution of some or all of the differential equations governing the dominant Reynolds shear stress, the turbulent kinetic energy, k and the isotropic dissipation rate, ε. Smith and Takhar concluded that a one-equation k-model was a sufficient order of closure for the solution of environmental problems.

Sheng (1985) applied a Reynolds stress model to the turbulent wave boundary layer. Such models remove the need to use the Boussinesq eddy viscosity hypothesis. However, Sheng failed to make a detailed investigation of the wave boundary layer. Brørs and Eidsvik (1994) compared the results from a Reynolds stress model with the oscillatory boundary layer data of Jensen *et al.* (1989). In addition, they included a sediment transport module in the model, the results of which they compared with the laboratory data of Ribberink and Al-Salem (1992). Brørs and Eidsvik concluded that a k-ε model provided results for stratified sediment-laden flows that were not that different than those predicted by the Reynolds stress model. Therefore, the k-ε model was a sufficient level of closure for modelling such flows.

The most sophisticated model used to study oscillatory flow is that of Spalart and Baldwin (1987). Spalart and Baldwin modelled oscillatory flow over a smooth wall using direct simulation techniques, that is, solving the full three-dimensional Navier-Stokes equations using a spectral method. However, due to computer resources, their results were limited to a maximum Reynolds number of $Re = 5 \times 10^5$.

As present knowledge stands, modelling provides an essential link between the reality of the field and the ideal of the laboratory. Through the use of models it is possible to aid in the interpretation of data, in particular field data where the measurement points might be limited. Additionally, such data helps to validate the numerical model. Within the European Community MAST I research programme, researchers at the University of Liverpool's

Department of Civil Engineering developed a boundary layer model that could simulate wave and combined wave-current boundary layers under random sea states O'Connor *et al.* (1993).

The boundary layer modelling work developed under MAST I was further refined in a second project CSTAB (O'Connor 1996) which was part of the MAST II programme O'Connor *et al.* (1994). Part of the CSTAB project involved the deployment of STABLE (see Humphrey 1987) an autonomous boundary layer tripod supporting a suite of sensors. With the use of the data collected by STABLE the performance of the boundary layer model, which used a simple mixing-length closure, was tested further. In addition, results from the model helped in the interpretation of some of the measurements made by STABLE. As part of the results from STABLE, it was found that wave groups exerted a 'pumping' action on the bed sediments and hence on sediment transport concentrations. It was unclear though as to what the exact mechanism in the boundary layer was causing this effect. One possibility was that there was a carry over of turbulence from one half wave period to another. However, whilst the mixing length model showed that it could predict the flow field and shear stress adequately, it was unable to provide any insight into the turbulence structure. Therefore, to investigate such phenomenon, a higher order model would be required.

In addition to the effect of wave groups on the turbulence structure within the wave boundary layer it has also been suggested (O'Connor 1996) that the time-varying bed roughness might also enhance the pumping action of the waves. Clearly any influence of one wave on the next makes it difficult to justify the operation of models of suspended sediment transport (Davies and Li 1997) with an equivalent mono-frequency wave.

The present research, therefore, chose to look at higher order eddy viscosity models based on one- and two-equation closures to investigate random wave and wave-current boundary layers. Initial work involved comparing the models against existing laboratory data in order to ascertain whether there was a clear advantage over using a particular level of closure. Smith and Takhar (1977) stated that for environmental problems a one-equation k-model was a sufficient level of closure. Also, Brørs and Eidsvik (1994) suggested that a two-equation k-ε model was adequate for prediction of sediment laden flows.

In addition, a moveable bed module would be added to the boundary layer model to enable the bed roughness to vary with time in order to determine the effect on the turbulence structure within the boundary layer as well as comparing this model with existing theories for moveable bed roughness under random waves (e.g. Madsen *et al.* 1991).

The proposed work is organized as follows:-

Chapter 2 describes the pertinent hydrodynamic equations for the present problem.

Chapter 3 presents a state-of-the-art review of wave and wave/current boundary layer modelling. The aim of the review is to provide a context in which the present modelling work may be viewed and describes the various methods available for modelling wave and wave/current boundary layers. In addition, the relative novelty of modelling the random sea boundary layer directly rather than employing a representative monochromatic wave is highlighted.

Chapter 4 describes the theoretical background for the methods employed in modelling monochromatic as well as random wave boundary layers. A description of the equations involved in the various models is provided together with the boundary conditions applied within the numerical schemes. A detailed description of the transport equations involved in modelling turbulence enables the reader to gain a better understanding as to why such models do not always provide 'perfect' answers. Use of appendices allows greater detail to be provided for the interested reader (Appendices A and B).

Chapter 5 presents a brief overview of the numerical scheme employed in the model together with a summary of the results of stability and convergence tests carried out. Further details are provided in Appendices C and D.

Chapters 6 to 10 describe the results from the present work. In Chapters 6 and 7 the initial model development is compared with established laboratory data for monochromatic waves.

Chapter 6 compares the performance of various levels of eddy viscosity model applied to the prototype scale data of Jonsson and Carlsen (1976) and Jensen *et al.* (1989). A comparison of three different models; mixing length, k, and k-ε models is shown. Using these results it is intended to select the most appropriate model with which to simulate random wave boundary layers based on accuracy and efficiency.

Chapter 7 compares results from some of the data collected at the University of Manchester (McDowell 1983; Savell 1986) with two numerical models; a high-Reynolds number k-ε model and a two-layer k-ε model. Both experimental tests chosen for comparison (Tests 52 and 59) were conducted in a small wave flume (see Chapter 7). The scale of the measurements places the flow in the transitional stage of development. Test 52 (waves alone) indicates the importance of choosing the appropriate model to match the physics, whilst test 59 (waves and imposed current) shows that the addition of a current enhances the turbulence development of the flow.

Chapter 8 describes the results of the random wave boundary layer model as tested against laboratory data from IBW PAN, Gdansk, Poland.

Chapter 9 shows the results of the random model run for field data gathered by STABLE during the CSTAB project. The model has been modified to allow for multi-directional waves.

Chapter 10 describes results from the investigation into moveable bed roughness and its application in the random wave boundary layer model. Initial work focuses on flow over ripples and in particular fixed bed experiments of Bagnold (1946) and Sleath (1985) and the moveable bed experiments of Carstens *et al.* (1969), Lofquist (1986), Rosengaus (1987) and Mathisen (1989). The measured energy dissipation factors over ripples obtained during the experiments are compared with output from the boundary layer model using a modified equivalent roughness based on 4 x the ripple height. Development of a moveable bed model for random waves is shown and comparison is made with other existing models.

Chapter 11 draws together the key results from each chapter enabling conclusions about the numerical models and wave boundary layers to be made. Recommendations for further research are also presented.

Appendices provide additional details on the work conducted, in particular some of the model results (Appendix E) as well as experimental data from the ripple tests (Appendix F).

Chapter 2

The Hydrodynamic Equations

2.1 Introduction

Chapter 2, introduces the hydrodynamic equations which form part of the theory used in the present work. The necessary equations are derived from the Navier-Stokes equations and for brevity, the initial formulation uses tensor notation.

2.2 The flow field in the turbulent boundary layer

The equations of motion for an incompressible fluid can be written in tensor form:

$$\frac{\partial u_i}{\partial t} + u_j \frac{\partial u_i}{\partial x_j} = \frac{1}{\rho} \frac{\partial}{\partial x_j} \sigma_{ij} + g_i \qquad (2.1)$$

$$\frac{\partial u_i}{\partial x_i} = 0 \qquad (2.2)$$

where u_i is the instantaneous velocity at position (x_i, t) and represents the Cartesian velocities u, v, w in the x, y and z planes respectively. Eq. (2.2) is the fluid mass continuity equation. The other various quantities can be defined as:-

σ_{ij} = the instantaneous stress tensor at position (x_i, t).

g_i = the gravitational vector ($g_x = 0$; $g_y = 0$; $g_z = -g$; where g is the acceleration due to gravity).

If the fluid is Newtonian, that is, elements of the stress tensor and the deformation tensor are related through linear relationships then,

$$\sigma_{ij} = -p\delta_{ij} + 2\mu s_{ij} \qquad (2.3)$$

where:-

δ_{ij} = the Kronecker delta and is further defined as $\delta_{ij} = 1$ if $i = j$ otherwise $\delta_{ij} = 0$.

p = the hydrodynamic pressure.

μ = the dynamic viscosity

s_{ij} = the rate of strain

The rate of strain s_{ij} is defined as

$$s_{ij} = \frac{1}{2}\left(\frac{\partial u_i}{\partial x_j} + \frac{\partial u_j}{\partial x_i}\right) \tag{2.4}$$

Substituting Eqs. (2.3) and (2.4) into Eq. (2.1) and using the mass continuity equation produces the equation:-

$$\frac{\partial u_i}{\partial t} + u_j \frac{\partial u_i}{\partial x_j} = -\frac{1}{\rho}\frac{\partial p}{\partial x_i} + \frac{\partial}{\partial x_j}\left(\nu_L \frac{\partial u_i}{\partial x_j}\right) + g_i \tag{2.5}$$

where ν_L is the kinematic (or molecular) viscosity $(\nu_L = \mu/\rho)$; ρ is the fluid density.

Using Reynolds' method of relating the instantaneous local velocities to the turbulence-mean $(\bar{u}_i)$ and fluctuating (u_i') values (see Reynolds 1894) that is:-

$$u_i = \bar{u}_i + u_i' \tag{2.6}$$

Eq. (2.5) becomes:-

$$\begin{aligned}\frac{\partial}{\partial t}(\bar{u}_i + u_i') + (\bar{u}_j + u_j')\frac{\partial}{\partial x_j}(\bar{u}_i + u_i') = -\frac{1}{\rho}\frac{\partial}{\partial x_i}(\bar{p}_i + p_i') \\ + \frac{\partial}{\partial x_j}\left(\nu_L \frac{\partial}{\partial x_j}(\bar{u}_i + u_i')\right) + g_i\end{aligned} \tag{2.7}$$

However, by definition the time-average of u_i' is zero such that:-

$$\overline{u_i'} = \lim_{T\to\infty}\frac{1}{T}\int_{t_0}^{t_0+T}(u_i - \bar{u}_i)dt \equiv 0 \tag{2.8}$$

where T is a turbulent averaging period which is long compared to the frequency of oscillation of the turbulence.

Therefore time-averaging Eq. (2.7) gives

$$\frac{\partial \bar{u}_i}{\partial t} + \bar{u}_j \frac{\partial \bar{u}_i}{\partial x_j} = -\frac{1}{\rho}\frac{\partial \bar{p}_i}{\partial x_i} + \frac{\partial\left(-\overline{u_i'u_j'}\right)}{\partial x_j} + \frac{\partial}{\partial x_j}\left(\nu_L \frac{\partial \bar{u}_i}{\partial x_j}\right) + g_i \tag{2.9}$$

where the overbar, $\bar{}$ indicates a time-average over the time-scale T.

For combined wave-current flow, it has become more common practice to describe the instantaneous local velocity by the inclusion of a third component. Therefore,

$$u_i = \bar{u}_i + u_i' + \tilde{u}_i \tag{2.10}$$

where $\bar{u}_i$ and u_i' are defined as previously and $\tilde{u}_i$ represents the wave-induced flow. It is usual to assume that these three terms all operate on different time-scales and are not mutually related. $\bar{u}_i$ is taken as operating on the largest time-scale and u_i' the smallest, whilst the orbital wave motion $\tilde{u}_i$ is assumed to operate on a time-scale large enough to allow turbulent fluctuations to die out. This latter point is not valid since the turbulent properties vary at a much greater time-scale than the orbital wave motion. However, as present knowledge stands, the exact nature of the correlation between the wave and turbulent parts is not clearly understood and as a consequence they are assumed to be uncorrelated. Therefore,

$$\lim_{T\to\infty}\frac{1}{T}\int_{t_0}^{t_0+T} u_i dt = \bar{u}_i \tag{2.11}$$

$$\lim_{T\to\infty}\frac{1}{T}\int_{t_0}^{t_0+T} u_i' dt = \overline{u_i'} = 0 \tag{2.12}$$

$$\lim_{T\to\infty}\frac{1}{T}\int_{t_0}^{t_0+T} \tilde{u}_i dt = \overline{\tilde{u}_i} = 0 \tag{2.13}$$

and following from this, the cross-products of the three terms are assumed to be zero.

Further, the periodic component represented by the tilde is described as the phase-average over N periods minus the time-average:-

$$\tilde{u}_i(z,t) = \frac{1}{N}\sum_{n=1}^{N} u_i(z,t+nT) - \bar{u}_i(z) \tag{2.14}$$

It is therefore possible to derive similar equations to that of Eq. (2.9) by introducing Eq. (2.10) into Eq. (2.5). Thus:-

$$\begin{aligned}\frac{\partial}{\partial t}(\bar{u}_i + u_i' + \tilde{u}_i) + (\bar{u}_j + u_j' + \tilde{u}_j)\frac{\partial}{\partial x_j}(\bar{u}_i + u_i' + \tilde{u}_i) = -\frac{1}{\rho}\frac{\partial}{\partial x_i}(\bar{p}_i + p_i' + \tilde{p}_i) \\ + \frac{\partial}{\partial x_j}\left(\nu_L \frac{\partial}{\partial x_j}(\bar{u}_i + u_i' + \tilde{u}_i)\right) + g_i\end{aligned} \tag{2.15}$$

Time-averaging Eq. (2.15) leads to the following equation:-

$$\frac{\partial \overline{u}_i}{\partial t} + \overline{u}_j \frac{\partial \overline{u}_i}{\partial x_j} + \overline{u'_j \frac{\partial u'_i}{\partial x_j}} + \overline{\tilde{u}_j \frac{\partial \tilde{u}_i}{\partial x_j}} = -\frac{1}{\rho}\frac{\partial \overline{p}_i}{\partial x_i} + \frac{\partial}{\partial x_j}\left(\nu_L \frac{\partial \overline{u}_i}{\partial x_j}\right) + g_i \qquad \textbf{(2.16)}$$

If Eq. (2.15) is phase-averaged then the following equation results:-

$$\frac{\partial \overline{u}_i}{\partial t} + \frac{\partial \tilde{u}_i}{\partial t} + \overline{u}_j \frac{\partial \overline{u}_i}{\partial x_j} + \overline{u}_j \frac{\partial \tilde{u}_i}{\partial x_j} + \overline{u'_j \frac{\partial u'_i}{\partial x_j}} + \overline{\tilde{u}_j \frac{\partial \overline{u}_i}{\partial x_j}} + \overline{\tilde{u}_j \frac{\partial \tilde{u}_i}{\partial x_j}} = -\frac{1}{\rho}\frac{\partial \overline{p}_i}{\partial x_i} - \frac{1}{\rho}\frac{\partial \tilde{p}_i}{\partial x_i} + \frac{\partial}{\partial x_j}\left\{\nu_L\left(\frac{\partial \overline{u}_i}{\partial x_j} + \frac{\partial \tilde{u}_i}{\partial x_j}\right)\right\} + g_i \qquad \textbf{(2.17)}$$

Eq. (2.17) represents the momentum equation for phase-averaged flow for combined waves and currents. From this equation it is possible to derive an equation for periodic flow with no applied current.

Assuming the steady component, $\overline{u}_i$ to be varying only very slowly in time, then $\partial \overline{u}_i / \partial t$ can be neglected. Therefore, Eq. (2.17) can be written as

$$\frac{\partial \tilde{u}_i}{\partial t} + \overline{u}_j \frac{\partial \overline{u}_i}{\partial x_j} + \overline{u}_j \frac{\partial \tilde{u}_i}{\partial x_j} + \overline{u'_j \frac{\partial u'_i}{\partial x_j}} + \overline{\tilde{u}_j \frac{\partial \overline{u}_i}{\partial x_j}} + \overline{\tilde{u}_j \frac{\partial \tilde{u}_i}{\partial x_j}} = -\frac{1}{\rho}\frac{\partial \overline{p}_i}{\partial x_i} - \frac{1}{\rho}\frac{\partial \tilde{p}_i}{\partial x_i} + \frac{\partial}{\partial x_j}\left\{\nu_L\left(\frac{\partial \overline{u}_i}{\partial x_j} + \frac{\partial \tilde{u}_i}{\partial x_j}\right)\right\} + g_i \qquad \textbf{(2.18)}$$

respectively.

For the case when the steady component, $\overline{u}_i = \partial \overline{u}_i / \partial x_j = 0$, that is, there is no imposed current, Eq. (2.18) becomes:-

$$\frac{\partial \tilde{u}_i}{\partial t} + \overline{u'_j \frac{\partial u'_i}{\partial x_j}} + \overline{\tilde{u}_j \frac{\partial \tilde{u}_i}{\partial x_j}} = -\frac{1}{\rho}\frac{\partial \tilde{p}_i}{\partial x_i} + \frac{\partial}{\partial x_j}\left(\nu_L \frac{\partial \tilde{u}_i}{\partial x_j}\right) + g_i \qquad \textbf{(2.19)}$$

Comparing Eq. (2.20) with Eq. (2.9) reveals that for the case of waves alone Eq. (2.19) and Eq. (2.9) are of a similar form.

Substituting Eq. (2.10) into Eq. (2.2) leads to the equation:-

$$\frac{\partial u_i}{\partial x_i} = \frac{\partial}{\partial x_i}\left(\overline{u}_i + u'_i + \tilde{u}_i\right) = \frac{\partial \overline{u}_i}{\partial x_i} + \frac{\partial u'_i}{\partial x_i} + \frac{\partial \tilde{u}_i}{\partial x_i} = 0 \qquad \textbf{(2.20)}$$

In Eqs. (2.9) and (2.19) the terms including the turbulent velocity fluctuation components are known as the 'Reynolds stresses'. These stresses provide a description for the exchange of momentum between different elements of the fluid due to turbulent fluctuations. They are also the source of the problem in any attempt to solve the Navier-Stokes equations for turbulent flow. Exact solution requires a vast time and space resolution which is only just becoming feasible with the super-computers of today.

Boussinesq (1877) introduced an eddy viscosity concept such that the turbulent stresses are assumed to be proportional to the gradients in the mean velocity field:-

$$\overline{u_i' u_j'} = \frac{2}{3} k \delta_{ij} - \nu_t \left(\frac{\partial \overline{u}_i}{\partial x_j} + \frac{\partial \overline{u}_j}{\partial x_i} \right) \qquad \textbf{(2.21)}$$

where ν_t = turbulent eddy viscosity; k = the turbulent kinetic energy and is defined by the equation:-

$$k = \frac{1}{2} \overline{u_i' u_i'} \qquad \textbf{(2.22)}$$

and all other terms are defined as previously.

Models which use Boussinesq's hypothesis are collectively known as eddy viscosity models. Based on Eq. (2.21) it is possible to substitute for the Reynolds stresses in Eq. (2.19) leading to the equation:-

$$\frac{\partial \tilde{u}_i}{\partial t} + \tilde{u}_j \frac{\partial \tilde{u}_i}{\partial x_j} = -\frac{1}{\rho} \frac{\partial \tilde{p}_i}{\partial x_i} + \frac{\partial}{\partial x_j} \left\{ (\nu_t + \nu_L) \frac{\partial \tilde{u}_i}{\partial x_j} \right\} + g_i \qquad \textbf{(2.23)}$$

From Eq. (2.23) it is now possible to write the flow equations (the x- and z-directions) for a two-dimensional turbulent shear boundary.

$$\frac{\partial \tilde{u}}{\partial t} + \tilde{u} \frac{\partial \tilde{u}}{\partial x} + \tilde{w} \frac{\partial \tilde{u}}{\partial z} = -\frac{1}{\rho} \frac{\partial \tilde{p}}{\partial x} + \frac{\partial}{\partial x} \left\{ (\nu_t + \nu_L) \frac{\partial \tilde{u}}{\partial x} \right\} + \frac{\partial}{\partial z} \left\{ (\nu_t + \nu_L) \frac{\partial \tilde{u}}{\partial z} \right\} \qquad \textbf{(2.24)}$$

$$\frac{\partial \tilde{w}}{\partial t} + \tilde{u} \frac{\partial \tilde{w}}{\partial x} + \tilde{w} \frac{\partial \tilde{w}}{\partial z} = -\frac{1}{\rho} \frac{\partial \tilde{p}}{\partial z} + \frac{\partial}{\partial x} \left\{ (\nu_t + \nu_L) \frac{\partial \tilde{w}}{\partial x} \right\} + \frac{\partial}{\partial z} \left\{ (\nu_t + \nu_L) \frac{\partial \tilde{w}}{\partial z} \right\} - g \qquad \textbf{(2.25)}$$

Consider now the equation of motion for the horizontal component only. For a thin boundary layer, the flow inside the boundary layer is normally assumed as being horizontal in which case:-

$$\tilde{w} \approx 0$$

Further, assuming the gradient of $\tilde{u}$ in the z-direction is much greater than that in the x-direction then the following term may be neglected.

$$\frac{\partial}{\partial x}\left\{(\nu_t + \nu_L)\frac{\partial \tilde{u}}{\partial x}\right\}$$

Eq. (2.24), therefore, reduces to:-

$$\frac{\partial \tilde{u}}{\partial t} + \tilde{u}\frac{\partial \tilde{u}}{\partial x} = -\frac{1}{\rho}\frac{\partial \tilde{p}}{\partial x} + \frac{\partial}{\partial z}\left\{(\nu_t + \nu_L)\frac{\partial \tilde{u}}{\partial z}\right\} \qquad \textbf{(2.26)}$$

This is still not an easy equation to solve due to the non-linear convective acceleration term $\tilde{u}\partial\tilde{u}/\partial x$. If the flow is considered to be horizontally uniform then generally it is considered acceptable to omit this term. In order to obtain horizontal uniformity, the free stream velocity, u_0 must be uniform. Secondly, any non-uniformities due to the bed roughness elements should be restricted to a layer which is much thinner than the boundary layer itself.

The final simplification in solving Eq. (2.26) is replacing the pressure term. Assuming that the wave boundary layer is thin and that the flow outside the boundary layer is irrotational (that is the shear stress is zero) the pressure distribution in the boundary layer can be considered as hydrostatic. Therefore, outside the boundary layer the following equation holds:-

$$\frac{\partial u_0}{\partial t} = -\frac{1}{\rho}\frac{\partial \tilde{p}}{\partial x} \qquad \textbf{(2.27)}$$

which follows from Eq. (2.26) when applied at the top of the wave boundary layer.

Therefore, Eq. (2.26) can be written as:-

$$\frac{\partial \tilde{u}}{\partial t} = \frac{\partial u_0}{\partial t} + \frac{\partial}{\partial z}\left\{(\nu_t + \nu_L)\frac{\partial \tilde{u}}{\partial z}\right\} \qquad \textbf{(2.28)}$$

2.3 Hydrodynamic boundary conditions

2.3.1 Introduction

In steady boundary layer flow the characteristics of the boundary layer are dependent on boundary roughness. In unsteady flows the effect that a hydraulically rough or smooth bed

has on the boundary layer has been less well studied. In oscillatory wave boundary layer flow most research has concentrated on flow over rough beds (see Chapter 3). However, Hino *et al.* (1983) performed experiments to measure the velocity and turbulence profiles in smooth and transitionally rough turbulent oscillating flow in a wind tunnel. More recently, Sumer *et al.* (1987) and Jensen *et al.* (1989) describe results from extensive experiments in the oscillating wave tunnel at ISVA. These provided measurements of the velocity and turbulence structure in smooth, transitionally rough and rough turbulent oscillatory boundary layers.

Whilst much modelling work has been presented for oscillatory wave boundary layers over rough beds, very little work has been performed for the smooth bed case. The earliest attempt to model oscillatory flow over a smooth bed is probably that of Kajiura (1968). Fredsøe (1984) presented results for flow over a smooth bed using the integral momentum approach. Justesen (1988a) showed results from a one equation model of an investigation of a developing oscillatory wave boundary layer over a smooth bed. Recently, Wiberg (1995) has examined flow over a smooth bed using a simple eddy viscosity model. However, in the present work, modelling has been restricted to the rough bed case.

In order to be able to model wave boundary layer flows it is necessary to specify boundary conditions for both the bed and the upper computational domain. For a non-porous bed it is normal to apply a no-slip boundary condition in the hydrodynamic equations. However, for the surface boundary condition the specification can be slightly more complex. In wave boundary layer flows many modellers choose the top of the wave boundary layer as their upper computational domain. However, in tidal flows the boundary layer normally extends to the surface in coastal waters.

2.3.2 Sinusoidal waves

For the case where the free stream velocity, u_0 is assumed to be sinusoidal, then the velocity is given by the equation:

$$u_0 = u_\infty \sin(\omega t) \qquad \textbf{(2.29)}$$

where u_∞ is the velocity amplitude and ω is the angular frequency of oscillation. Further, $\omega = 2\pi/T$ where T is the wave period.

To enable solution of the hydrodynamic equations it is necessary to specify boundary conditions. For the flow equations a no-slip boundary condition is applied at the bed. At the upper edge of the computational domain the velocity gradient is set to zero. Therefore:-

$$\tilde{u}(z_0, t) = 0 \qquad \text{at } z = z_0 \tag{2.30}$$

$$\frac{\partial \tilde{u}}{\partial z}(z_{top}, t) = 0 \qquad \text{at } z = z_{top} \tag{2.31}$$

where z_0 is defined as the vertical level at which point the velocity is assumed to be zero and can be expressed as:

$$z_0 = \frac{k_S}{30} \tag{2.32}$$

where k_S is the Nikuradse roughness. z_{top} is the upper limit of the computational domain and has generally been taken to be at the water surface, D.

2.3.3 Sinusoidal waves and current

To enable the model to represent the combined wave-current boundary layer, it is necessary to return to Eq. (2.17).

$$\frac{\partial \bar{u}_i}{\partial t} + \frac{\partial \tilde{u}_i}{\partial t} + \bar{u}_j \frac{\partial \bar{u}_i}{\partial x_j} + \bar{u}_j \frac{\partial \tilde{u}_i}{\partial x_j} + \overset{\sim}{u'_j} \frac{\partial \overset{\sim}{u'_i}}{\partial x_j} + \tilde{u}_j \frac{\partial \bar{u}_i}{\partial x_j} + \tilde{u}_j \frac{\partial \tilde{u}_i}{\partial x_j} = -\frac{1}{\rho}\frac{\partial \bar{p}_i}{\partial x_i} - \frac{1}{\rho}\frac{\partial \tilde{p}_i}{\partial x_i} + \frac{\partial}{\partial x_j}\left\{\nu_L\left(\frac{\partial \bar{u}_i}{\partial x_j} + \frac{\partial \tilde{u}_i}{\partial x_j}\right)\right\} + g_i \tag{2.17}$$

Based on similar assumptions to those used for the case of waves alone, Eq. (2.17) reduces to the equation:-

$$\frac{\partial \tilde{u}_i}{\partial t} + \bar{u}_j \frac{\partial \bar{u}_i}{\partial x_j} + \tilde{u}_j \frac{\partial \tilde{u}_i}{\partial x_j} = -\frac{1}{\rho}\frac{\partial \bar{p}_i}{\partial x_i} - \frac{1}{\rho}\frac{\partial \tilde{p}_i}{\partial x_i} + \frac{\partial}{\partial x_j}\left\{(\nu_t + \nu_L)\left(\frac{\partial \bar{u}_i}{\partial x_j} + \frac{\partial \tilde{u}_i}{\partial x_j}\right)\right\} + g_i \tag{2.33}$$

which for combined wave-current flow in the x-direction leads to the equation:-

$$\frac{\partial \tilde{u}}{\partial t} = -\frac{1}{\rho}\frac{\partial \bar{p}}{\partial x} - \frac{1}{\rho}\frac{\partial \tilde{p}}{\partial x} + \frac{\partial}{\partial z}\left\{(\nu_t + \nu_L)\left(\frac{\partial \bar{u}}{\partial z} + \frac{\partial \tilde{u}}{\partial z}\right)\right\} \tag{2.34}$$

The pressure gradient due to the wave motion is determined as previously:

$$-\frac{1}{\rho}\left(\frac{\partial \tilde{p}}{\partial x}\right) = \frac{\partial u_0}{\partial t} \tag{2.35}$$

and

$$u_0 = u_\infty \sin(\omega t)$$

The pressure gradient due to the mean current is determined from steady flow where the shear stress distribution is taken as being triangular in shape such that:-

$$\frac{\tau_C}{\rho} = u_{*C}^2\left(1 - \frac{z}{D}\right) \tag{2.36}$$

where D is the flow depth; τ_C is the current related shear stress and u_{*C} is the current related bed shear velocity. The sub-script c corresponds to the current. Therefore,

$$\frac{1}{\rho}\left(\frac{\partial \bar{p}}{\partial x}\right)D = -g\,I\,D \tag{2.37}$$

where I is the slope of the energy line and g is the gravitational constant.

Averaged over a wave period, the pressure gradient due to waves $(\partial \tilde{p}/\partial x)$ goes to zero which leaves only the pressure term due to the current. However, since the mean flow gradient must be known prior to solution, the mean current velocity can only be solved for via an iterative process.

Justesen (1988a) uses the iterative process as proposed by Deigaard *et al.* (1986). This requires assuming an initial value for the mean current profile. After one wave period, the shear stresses are averaged over the period and the deviation $\Delta\bar{\tau}(z)$ from the required distribution determined such that

$$\Delta\bar{\tau}(z) = \tau_C - \int_0^{2\pi} \tau(z,\omega t)\,d\omega t \tag{2.38}$$

The velocity profile is then adjusted using the following correction, $\Delta\bar{u}(z)$

$$\Delta\bar{u}(z) = \int \frac{\Delta\bar{\tau}(z)}{\bar{\nu}_t(z)}\,dz \tag{2.39}$$

where $\Delta\bar{u}(z)$ is the velocity correction and $\bar{\nu}_t(z)$ is the mean turbulent eddy viscosity over one wave period. The iteration is continued until the required convergence is reached.

Justesen (1988a) proposes a correction to the length scale used in the one-equation model on the grounds that beyond a certain distance from the boundary, the presence of that boundary is no longer affecting the turbulence. The modified length scale is given as:

$$l = \begin{cases} c_2 z & \text{for } z \le \dfrac{0.07D}{c_2} \\ 0.07D & \text{for } z > \dfrac{0.07D}{c_2} \end{cases} \qquad \textbf{(2.40)}$$

and

$$c_2 = \kappa \sqrt[4]{c_\mu} \qquad \textbf{(2.41)}$$

where κ is the von Karman constant (≈ 0.4) and c_μ is a turbulence model constant (see Chapter 4).

Davies *et al.* (1988) apply the current as a horizontally uniform motion in the direction of the applied current (Davies *et al.* allow for a current at an angle to the waves). The current is initially generated as a tidal input in the model which generates an oscillatory pressure gradient. Once the initial transient motion has ceased then the pressure gradient is replaced by a constant pressure gradient and the solution is run until a steady state is reached.

Development of boundary conditions for the hydrodynamic equations for random waves and combined random waves and current will not be developed in this Chapter. Such theory will be left until Chapter 4.

2.4 Conclusions

The development of the hydrodynamic equations has been given and the equation of motion in the x-z plane has been developed and reduced to one which can be solved relatively easily. The boundary conditions have been introduced for this equation for both the case of waves alone and also that of co-linear waves and current. Development of the boundary conditions for the random case are presented elsewhere (see Chapter 4).

Chapter 3
Literature Review

3.1 Introduction

The seabed boundary layer is important for many reasons. To adequately describe such phenomenon as wave energy loss, sediment transport, transport of pollutants and bedform formation requires knowledge of the boundary layer flow field. Over the last three decades various theoretical models have been proposed. Until very recently, all these models have been written to describe a pure sinusoidal wave boundary layer or that under a non-linear wave. The first model to describe a truly random wave and wave-current boundary layer was described in O'Connor *et al.* (1993). This model was based on a mixing length assumption, and whilst the closure method used might have it detractors, the results show the model to give reasonable answers, O'Connor *et al.* (1993), O'Connor *et al.* (1994).

The inability of a mixing length model to describe more than the basic physics of boundary layer flow is an inherent problem. To provide a more 'physically' accurate model requires greater computational power, the level of which is dependent on the type of model used. The complexity of the numerical model can be increased by the addition of equations to the solution: k - models; k - ε and k - *l* models; Reynolds stress models; and direct simulation of the Navier-Stokes equations. Because of computational implications, such as memory and time, it would be currently unrealistic to attempt to describe a random boundary layer using the latter two approaches.

Since, generally, the aim in coastal hydrodynamic models is to provide a flow description to assist in the calculation of sediment transport, the ability of the flow model to adequately describe the hydrodynamics is essential. In real seas, modellers have, until recently, tended to drive models with representative values rather than simulate a random sea, due to the added complexities involved, for example Ockenden and Soulsby (1994). However, workers in the field (e.g. Williams (1996)) have shown that the effects of wave groups on sediment

entrainment is significant. Wave groups have a pumping action such that the wave-period-mean sediment concentrations increase with the passage of each group so that the effect of groups cannot be ignored. Also, whilst a parameterization of the effect of wave groups may be incorporated into a monochromatic boundary layer model by using a higher than average wave condition, it is impossible for such a model to directly account for the non-linearity and random nature of a real sea. In addition, the effect of waves and currents on bedform size and hence bed roughness has always been treated as a fixed quantity in such models, and under a pure sinusoidal wave this is a reasonable assumption. However, in reality the size of bedforms varies in time due to the flow field and in turn this affects the hydrodynamics. Studies have shown that random waves create ripples that are less steep and of shorter length and height than those generated under monochromatic waves (e.g. Nielsen 1981). Madsen *et al.* (1991) suggested that the rounded nature of ripple crests found under random waves was due to the larger waves shaving off the sharp ripple crests.

It is the intention of this work to provide a better description of the random wave and wave-current flow field via the use of one- and two-equation models. In addition, the effects of varying the bed roughness are to be studied in an attempt to provide a better description of a random wave and combined wave-current boundary layer.

3.2 The wave boundary layer

It is perhaps useful to look briefly at the bed boundary layer formed close to a solid bed. Researchers have shown for wave motion over a horizontal bed that the particle motion close to that bed oscillates horizontally, for example see Svendsen and Jonsson (1976). The bed boundary layer is created by the fluid adhering to the boundary causing a layer to develop having vorticity and shear stresses. The thickness of this wave boundary layer has been defined differently by researchers.

Jonsson (1967):
Jonsson defined the top of the boundary layer as the minimum elevation where u(z,t) equals the free stream velocity $u_0(t)$ when the latter is a maximum (see Figure 3.1). This corresponds to the equation:-

$$\delta_J = \frac{\pi}{2}\sqrt{\frac{2\nu_L}{\omega}} \tag{3.1}$$

where ω is the wave angular velocity and is defined by:

$$\omega = \frac{2\pi}{T} \tag{3.2}$$

Where T is the wave period and ν_L is the kinematic viscosity.

Kajiura (1968):

Kajiura defined the top of the boundary layer via the use of a displacement thickness defined as:-

$$\delta_K = \frac{1}{a\omega}\left\{\int_0^\infty (u_0 - u)dz\right\}_{max} \tag{3.3}$$

a is the water particle amplitude just outside the boundary layer, see Figure 3.1.

Sleath (1987):

Sleath's definition for the top of the boundary layer is defined as the position where the amplitude of the velocity defect has dropped to 5% of the velocity amplitude u_∞.

$$\delta_S = \sqrt{\frac{2\nu_L}{\omega}} \tag{3.4}$$

The boundary layer thickness represents the transitional area between zero velocity at the wall (non-porous bed) and the free-stream velocity. In time, the thickness of the layer will grow influencing a larger part of the flow field. Nielsen (1992) suggests that the practical limit for measuring boundary layer structures is where the velocity defect has reached one percent of the free stream amplitude, $\delta_{0.01}$. The relationship of $\delta_{0.01}$ to the other expressions for boundary layer thickness defined above is shown in Figure 3.1.

In wave motion, the particles in the area of the bed move in the direction of oscillatory motion until the maximum particle velocity is achieved and deceleration of the fluid particles starts. At this stage the particles closest to the bed begin to move in the reverse direction to the main outer flow which has not stopped its motion yet. This effect is called separation of the boundary layer and is the point at which a new boundary layer will begin to develop.

This effect is very important in any attempt to accurately model the boundary layer. The cause of this deceleration of particles outside the boundary layer is due to an adverse pressure gradient, in other words, an increasing pressure gradient acting in the direction of the particle motion within the boundary. This will happen twice every wave period in pure oscillatory flow, ensuring that, for short period waves (high frequency), the boundary layer remains thin compared to the water depth.

In the absence of wave breaking, this enables simple wave theory based on irrotational flow to be used. Therefore, from the above it is clear that the flow within the boundary layer does not always follow the 'law of the wall' (logarithmic layer) for at least part of the cycle. It has been argued (Shima 1993) that a model applicable up to the wall itself is required to properly predict this flow.

3.3 Laminar flow

In the real world, the steady currents within the sea are virtually always turbulent. However, it has been shown that if steady currents are small then wave-induced flows may be laminar for a range of conditions. Stokes (1851) presented a solution for an infinite flat bed oscillating in still water. This work was later extended by Lamb (1932) who obtained a first approximation for waves over a flat bed.

$$u = u_\infty\left(\cos(\omega t) - e^{-\beta z}\cos(\omega t - \beta z)\right) \tag{3.5}$$

where β is a height scale given by the equation:

$$\beta = \sqrt{\frac{\omega}{2\nu_L}} \tag{3.6}$$

(see also Eq. (3.4)) and; T is the wave period. In addition, the shear stress distribution is given by:

$$\frac{\tau}{\rho} = \sqrt{2}\nu_L\beta u_\infty e^{-\beta z}\sin\left(\omega t - \beta z + \frac{\pi}{4}\right) \tag{3.7}$$

Numerous researchers have measured laminar profiles in the laboratory and have found excellent agreement with Eq. (3.5), see Figure 3.2.

3.4 Boundary layer modelling

Amongst the earliest theoretical works those of Jonsson (1963; 1967) and Kajiura (1964) are key works. Kajiura (1964) attempted to produce a theoretical approach to predicting the frictional coefficient for fully developed turbulent oscillatory flow over rough and smooth beds under long waves (seiches/tsunamis). In such a case the boundary layer occupies a significant part of the water depth. This work was later extended in an attempt to provide a description of the oscillatory turbulent boundary layer for wind waves, Kajiura (1968).

Jonsson (1963; 1967) suggested using the integrated momentum equation to obtain an expression with which to evaluate the friction factor. Jonsson assumed a logarithmic velocity profile to extend to the free stream velocity. For rough turbulent flow Jonsson obtained the semi-empirical relationship:-

$$\frac{1}{4\sqrt{f_w}} + \log_{10}\frac{1}{4\sqrt{f_w}} = -0.08 + \log_{10}\frac{a}{k_s} \qquad \frac{a}{k_s} > 1.57 \qquad \textbf{(3.8)}$$

Kamphuis (1975) suggested a slightly different empirical relationship:-

$$\frac{1}{4\sqrt{f_w}} + \log_{10}\frac{1}{4\sqrt{f_w}} = -0.35 + \frac{4}{3}\log_{10}\frac{a}{k_s} \qquad \frac{a}{k_s} > 1.57 \qquad \textbf{(3.9)}$$

For further comparison of wave friction factors see Chapter 10.

The following sections are intended to provide a state-of-the-art review of wave boundary layer modelling techniques in order to provide a context for the present work. Whilst the list of papers is intended to be as comprehensive as possible, it is not exhaustive. Many of the models have been written with the intention of describing sediment transport effects within wave and wave/current boundary layers. However, it is not intended to discuss detailed sediment transport aspects in the present work.

Before discussing the modelling schemes for turbulent wave boundary layers in detail, it is perhaps useful to mention the work of Bijker (1967) and Lundgren (1973) who are some of the first researchers to address the topic of wave-current interaction.

Bijker's model is primarily based on two main assumptions. Firstly, that the combined velocity field is formed by the linear superposition of the velocities due to the individual wave and current components. Secondly, the instantaneous bed shear stress can be calculated from the velocity field derived from steady flow equations.

Bijker introduces a dimensionless constant p ($p = \sqrt{2}/\ln(33\delta/k)$, where k = bed roughness ; δ = boundary layer thickness) which is derived from a logarithmic turbulent boundary layer assumption. The bed shear stress for the combined case is found by integrating the instantaneous bed shear stress over the wave period. Bijker's model allows for waves and current to interact at any angle.

However, the assumptions made by Bijker are questionable. The thickness of the wave boundary layer is not constant and, therefore, neither is p constant. The vector addition of the wave and current fields introduces inconsistencies between the mean velocity and mean shear stress gradients. Finally, the logarithmic assumption is not valid for all the phases of the wave motion.

Swart (1977) attempted to address the problem of the varying boundary layer thickness using Jonsson's definition for the thickness. However, Swart failed to fit this modified equation against the data used by Bijker to calibrate his model. Savell (1986) argues that since p was used as a calibration factor, it possibly compensated for the incorrect assumption. Savell contends that using Swart's equation with Bijker's experimental results leads to an average error of 100% in the enhanced shear stress.

Lundgren (1973) proposed a model for the mean velocity and eddy viscosity distributions in a combined wave-current flow. The combined eddy viscosity is taken to be the vector sum of the individual eddy viscosities for the steady and wave flow fields. Initially the current velocity component is unknown, since it is defined by the shear stress.

The current viscosity is represented by a mixing length expression while that for the waves is curve fitted from the experimental data of Jonsson (1963) and Carlsen (cited in Lundgren

1973). The total eddy viscosity is then calculated from the vector sum of the individual components.

The mean velocity profile is obtained by integrating the velocity gradient from the theoretical bed level to the top of the boundary layer. Since the eddy viscosity is increased within the wave boundary layer the velocity above this layer is reduced, however, the gradient remains the same as for the steady flow case.

Finally, the paper of Grant and Madsen (1979) deserves a mention since Grant and Madsen were the first to point out the influence of waves on a steady current above the wave boundary layer and the apparent increase in bed roughness felt by the current. However, Fredsøe (1984) suggests that this could also have been deduced from Lundgren (1973).

3.5 Eddy viscosity modelling

Kajiura (1968) introduced a three-layer, time-invariant eddy viscosity model for oscillatory turbulent flow for both a smooth and rough bed. The three layers consisted of an inner layer, overlap layer and outer layer (see Eq. 3.12 and Figure 3.3).

The inner layer is often referred to as the viscous or laminar sublayer for smooth beds. In this layer the viscous stresses are dominant. For rough beds this layer is less clearly defined since the region still exists but is located between the bed roughness elements or ripples.

The overlap layer is so called because it is the area of overlap between the wall and 'defect' layer. The defect layer being the region where the velocity defect is unaffected by viscosity.

The outer layer (sometimes called the 'wake' region) is the area of the defect layer unaffected by the wall layer.

Within the solution procedure, Kajiura assumed continuity between the overlap and outer layer in both the shear velocity, u_* and velocity, u, whilst only assuming continuity in the turbulent eddy viscosity, ν_t . However, although the model is conceptually quite simple, the

analytical calculations are not so straight forward. Using the linearized equation of motion, Kajiura assumed that the relationship between shear stress and velocity is given by:

$$\frac{\partial}{\partial t}(u - u_0) = \frac{\partial}{\partial z}\left(\frac{\tau}{\rho}\right) \tag{3.10}$$

$$\nu_t \frac{\partial u}{\partial z} = \frac{\tau}{\rho} \tag{3.11}$$

Ignoring Kajiura's solution for smooth beds, Kajiura's three-layer model for rough turbulent flow assumed the following eddy viscosity distribution:

$$\begin{array}{ll} \text{Inner layer} & \\ \text{Overlap layer} & \overline{\nu_t} = \begin{cases} 0.185\kappa u_{*_{B,max}} k_s & \text{for } 0 \le z \le k_s/2 \\ \kappa u_{*_{B,max}} z & \text{for } k_s/2 < z \le \Delta \\ \kappa u_{*_{B,max}} \Delta & \text{for } z > \Delta \end{cases} \\ \text{Outer layer} & \end{array} \tag{3.12}$$

and Δ = the upper point of the overlap layer.

Kajiura (1968) suggested that the overlap layer would disappear if the condition

$$\frac{a}{k_s} < 30 \tag{3.13}$$

was satisfied. However, Horikawa and Watanabe (1968) suggested that Kajiura's results were more closely fitted if the following condition was used:-

$$\frac{a}{k_s} < 115 \tag{3.14}$$

Kajiura's model is also able to describe the phase difference, φ, between the bed shear stress and the free-stream velocity. However, the model makes no allowance for the variation of the boundary layer thickness with time. Jonsson (1978a; 1980) shows good comparison between Kajiura's model and his experimental results.

Brevik (1981) introduced a simplified model based on that of Kajiura (1968). Brevik proposed a two-layer model omitting the inner part of the boundary layer description and extending the overlap layer down to the $z = z_0$ (see Figure 3.4). Brevik assumed that the physics were such that the overlap layer existed and proposed the following eddy viscosity relations:

$$\begin{array}{ll} \text{Overlap layer} & \overline{\nu_t} = \kappa u_{*max} z \qquad z_0 \le z \le \Delta \\ \text{Outer layer} & \overline{\nu_t} = \kappa u_{*max} \Delta \qquad z > \Delta \end{array} \tag{3.15}$$

The solution of Brevik's model is similar to that of Kajiura (1968). It is analytical in nature and involves the concept of a defect velocity as introduced by Jonsson (1978a) which is defined as:

$$u_d = u_0 - u \tag{3.16}$$

Assuming the effects of molecular viscosity to be negligible, the linearized equation of motion can be written as:-

$$\frac{\partial u_d}{\partial t} = \frac{\partial}{\partial z}\left(\nu_t \frac{\partial u_d}{\partial z}\right) \tag{3.17}$$

Brevik (1981) introduced complex notation by allowing the free stream velocity to be expressed as:-

$$u_0 = u_\infty \exp(i\omega t) \tag{3.18}$$

Therefore the mean and defect velocities become:-

$$u = u_{b_\infty} e^{i\omega t} \tag{3.19}$$

$$u_d = u_{db_\infty} e^{i\omega t} \tag{3.20}$$

Where $i = \sqrt{-1}$. The solution to the physics is provided by the real part. Equation (3.17) can now be written as:-

$$\frac{d}{dz}\left(\bar{\nu}_t \frac{du_d}{dz}\right) - i\omega u_d = 0 \tag{3.21}$$

In turn, this equation reduces to a standard differential equation for Kelvin functions of zeroth order in the overlap layer, such that:-

$$u_d = u_0 D_B\left[A(\mathrm{ber}\xi + i\mathrm{bei}\xi) + B(\mathrm{ker}\,\xi + i\mathrm{kei}\xi)\right] \tag{3.22}$$

Where D_B is a constant and ξ is a non-dimensional variable defined as (see also Brevik 1981):-

$$\xi = \left(4\omega \frac{z}{\kappa u_{*max}}\right)^{\frac{1}{2}} \tag{3.23}$$

In the outer layer equation (3.22) becomes

$$u_d = -u_0 T_B D^{-1} \exp\left[-(1+i)\beta(z-\Delta)\right] \tag{3.24}$$

Where T_B is another constant which is generally complex in nature. Solution of these equations requires the determination of boundary conditions and to match equations (3.22) and (3.24) at the interface. The thickness of the overlap layer has to be determined before the problem is solved finally.

Brevik (1981) noted that whilst there appeared to be no experimental evidence against extending the overlap layer down to $z = z_0$, there was some uncertainty about where the upper limit of this layer should be. Using two definitions for Δ, Brevik investigated the sensitivity of the model. Firstly, Δ was chosen as (Jonsson 1963; 1978a; 1980):-

$$\Delta = \frac{1}{2}\delta \qquad \textbf{(3.25)}$$

where δ = the boundary layer thickness and is given by Eq. (3.1) and secondly the definition of Δ as given by Kajiura (1968) was used:-

$$\Delta = 0.05\left(\frac{1}{2}f_w\right)^{\frac{1}{2}}a \qquad \textbf{(3.26)}$$

where f_w = wave friction factor. The results indicated that the velocity profile was relatively insensitive to the choice of Δ. However, the phase of the velocity was best predicted by Jonsson's simple relationship.

Various authors have produced similar models of this type with a time-invariant eddy viscosity distribution. The ability of these models to provide reasonable agreement with both field and laboratory data could be considered somewhat surprising given the assumptions made in many of these works. Further, whilst models of this type are capable of predicting the velocity and shear stress distributions relatively well, at least for maximum values (see Wiberg 1995), such models are totally incapable of providing a detailed description of the variation of the turbulent properties of the flow. Since the eddy viscosity is a function of these turbulent properties then such simple models are unable to represent the detailed physics.

The assumption that the eddy viscosity is independent of time has been shown to be incorrect experimentally by several investigators (for example Horikawa and Watanabe 1968; Sleath 1987). Research has, however, shown that, at least for certain heights, the eddy viscosity is linear in form (compare with Eq. 3.12). Sleath (1987) found that whilst this latter point

corresponded to his experimental results, the value of the constant of proportionality (the von Karman constant, κ) was significantly different from accepted values (κ, ≈ 0.1, as opposed to the normally accepted value of κ, ≈ 0.4). In addition, Sleath (1987) found that the eddy viscosity went negative near the bed, though little work on this aspect appears to have been studied by other researchers (Figure 3.5).

Hunt and Maxey (1978) have shown that under certain circumstances it is theoretically possible for the viscosity to go negative. They showed that for rapid changes in the flow, the concept of an eddy viscosity defined by $\nu_t = \tau/(\partial\bar{u}/\partial z)$ is incorrect in principle, one reason being that τ is not zero when $\partial\bar{u}/\partial z$ is zero. It is unclear though what are the implications or physical meaning of a negative viscosity. However, maybe the outcome of any theoretical reasoning is dependent on what is taken as your initial starting point, in this case the eddy viscosity concept. The theoretical approach used within this work is unable to operate with negative values of eddy viscosity.

Despite technical advances in experimental measuring techniques there is still much that is not understood about boundary layer dynamics. In addition, the ability to make velocity measurements in the field within the first 10 cm of the bed is still far from being routine, see Agrawal and Aubrey (1992). It is, therefore, necessary to try and model the wave and wave/current boundary layer as accurately as possible so as to enable interpretation of near-bed measurements as well as providing invaluable data with which to test models.

Sleath (1991a) presents an eddy viscosity model for combined wave-current flows over rough beds. Sleath assumes that the eddy viscosity is given by:

$$\nu_t = \nu_{t_c} + \nu_{t_w} \tag{3.27}$$

and that that eddy viscosity for current alone and waves alone are given by:-

$$\nu_{t_c} = \kappa \bar{u}_* z \tag{3.28}$$

$$\nu_{t_w} = \nu' l \tag{3.29}$$

respectively. It might be reasonable to add the two eddy viscosities if the turbulence produced by the oscillatory flow and steady flow are statistically independent. Sleath suggests that

whilst there exists a fluctuation in turbulence intensity over a wave cycle, the time-mean turbulence intensity may remain little changed. Sleath justifies this assumption on the basis of laboratory experiments (Sleath 1991b).

In calculating the mixing length, l for the periodic eddy viscosity component, Sleath assumes a value of 0.1 for the von Karman constant, κ. Sleath bases his choice of κ on previous experiments (Sleath 1987; 1990) which indicated that rather than taking the normally accepted value for κ (≈ 0.4) for steady flows, in oscillatory flows a value of 0.1 - 0.2 should be adopted. These lower values were obtained when Sleath tried to obtain agreement with his measured data (Sleath 1987; 1990).

Sleath (1991a) uses a solution method similar to that of Grant and Madsen (1979). Sleath's approach avoids the division of the boundary layer into one for waves and one for currents, avoiding any assumption as to what height this occurs at. The model makes use of oscillatory flow measurements for the eddy viscosity near the bed. However, the model is limited in its application. The paper is short on results on which to make a full assessment of its merits.

Wiberg (1995) describes the use of an eddy viscosity model based on that proposed by Smith (1977), to investigate smooth, transitional and rough turbulent boundary layers under waves. In addition, a comparison is made with a time-invariant and a time-variant form of the model. Whilst overall, both forms of the eddy viscosity model give reasonable agreement with the data used (Jonsson and Carlsen 1976; Jensen *et al.* 1989), Wiberg (1995) concludes that the time-invariant form does not adequately describe the wave boundary layer through the wave period. However, good agreement with the velocity and shear stress distribution at maximum velocity is obtained with the simple model.

In addition to Wiberg (1995), the use of time-variant eddy viscosity models has been proposed by Trowbridge and Madsen (1984a; b) and Davies (1986a). Further, the use of the integral momentum equation has also been proposed by Patel (1981) and Fredsøe (1984).

Trowbridge and Madsen (1984a) proposed a time-variant eddy viscosity model based on the time-invariant form as given by authors such as Kajiura (1968), Brevik (1981) and Myrhaug (1982). Trowbridge and Madsen suggested the following temporal variation for the viscosity:

$$\nu_t = \nu_0 \mathrm{Re}\left(1 + a_2 e^{i2\omega t}\right) \tag{3.30}$$

and

$$\nu_0 = \kappa \bar{u}_* \begin{cases} z & z_0 \le z \le \delta_i \\ \delta_i & z > \delta_i \end{cases} \tag{3.31}$$

The shape function, ν_0, is averaged over the wave period. The value of δ_i,the thickness of the inner layer, is assumed to be:

$$\delta_i = \frac{\kappa \bar{u}_*}{6\omega} \tag{3.32}$$

Re represents the real part and a_2 is a complex constant representing the amplitude of the second harmonic and is given by:

$$a_2 = \overline{2e^{-i2\omega t}|u_*|} \tag{3.33}$$

Using this description for the eddy viscosity and the linearized equation of motion, Trowbridge and Madsen (1984a) produce an analytical solution to the problem. Results are shown for the mean components only and this makes evaluation of the improved model difficult. Trowbridge and Madsen (1984a) report that the time-variant eddy viscosity model suggest that the temporal variation is not significant for reproducing the first harmonic. However, their results indicate that higher harmonics are present in the velocity and shear stress distribution and in a linear model this feature can only be represented by the use of an eddy viscosity that varies with time. As in all of the above models, Trowbridge and Madsen (1984a) assume that the boundary layer thickness is constant in time, but this has clearly been shown not to be the case (for example see Sleath 1987; Jensen *et al.* 1989).

In a second paper, Trowbridge and Madsen (1984b) include second order effects into their model. The effect of wave-induced mass transport on the turbulent wave boundary layer was studied. The results show that a time-variant eddy viscosity has an important effect on the mass transport. Also, Trowbridge and Madsen (1984b) showed that for relatively long waves, reversal of the mass transport took place.

An earlier paper by Lavelle and Mofjeld (1983) also addressed the question of time-varying viscosity. Their approach was similar to that of Trowbridge and Madsen (1984a). They assumed the viscosity to be given by the equations:-

$$\nu_t = \kappa |u_B(t)| z \quad z_0 \le z \le \delta \tag{3.34}$$

$$\delta \nu_t = \kappa |u_B(t)| \delta \quad z > \delta \tag{3.35}$$

where δ is the matching height and u_B is a modified shear velocity and are defined by the equations:-

$$\delta = \frac{|\bar{u}_B|^2}{\omega u_0} \tag{3.36}$$

$$|u_B(t)| = \left\{ u_*^2(t) + c^2 u_*^2\left(t + \frac{T}{4}\right) \right\}^{\frac{1}{2}} \tag{3.37}$$

and c is given an arbitrary value of 0.2.

Lavelle and Mofjeld (1983) conclude that time-varying viscosities introduce higher harmonics of the fundamental velocity signal which can be important for certain phases of the flow, as was found by Trowbridge and Madsen (1984a) . Further, there was an indication that neglecting time variations in viscosity could lead to an under-estimation of maximum bed shear stress and distortion of the flow profile close to flow reversal.

Takhar and Thomas (1991) investigated turbulent mass transport and wave attenuation in Stokes waves using numerical methods to solve first and second order turbulent boundary layer equations. They noted that the eddy viscosity should possess time dependence if such flows are to be modelled correctly. Any attempt to model the behaviour of turbulent mass transport using a time-invariant eddy viscosity would fail to capture the fundamental mechanism. Takhar and Thomas concluded that the simplest model of turbulence with the requisite properties to predict turbulent mass transport is the mixing length model.

Davies (1986a) has also addressed the question of time-varying viscosity. The model chosen by Davies uses the following eddy viscosity description:

$$\nu_t(z,t) = \frac{1}{2}\kappa u_{*_m}\left(\frac{2}{1+K}\right)\{1 + K\sin(2\omega t)\} \tag{3.38}$$

where K is a free parameter in the range $0 \leq K \leq 1$. The linearized flow equation is solved in the form:-

$$u = u_0 - \sum_{n=1}^{N} \left\{ \varphi_n(z)\sin(n\omega t) + \eta_n(z)\cos(n\omega t) \right\} \qquad \textbf{(3.39)}$$

where φ_n and η_n are functions of z. Whilst approximate analytical solutions are shown for N = 2 and N = 3, solution by computer is required.

Davies illustrates the influence of the time-varying viscosity in the paper through the parameter, K. K= 0 represents a time-invariant solution, whilst K = 1 gives a sinusoidal eddy viscosity distribution with a minimum of zero twice every period. Based on a more sophisticated turbulence model Davies suggests that 0.5 should be the approximate value for K.

Fredsøe (1984) assumed that the velocity profile in the wave boundary layer was logarithmic.

$$\frac{u}{u_*} = \frac{1}{\kappa}\ln\left(\frac{30z}{k_s}\right) \qquad \textbf{(3.40)}$$

Fredsøe also assumed that for each half period the flow field could be considered to start from rest. Integrating the momentum equation, Eq. (3.41) was obtained:-

$$\frac{\tau_b}{\rho} = \int_{k_s/30}^{\delta + k_s/30} \frac{\partial}{\partial t}(u_0 - u)dz \qquad \textbf{(3.41)}$$

using the upper limit in the integral as $\delta + k_s/30$ rather than δ since $\delta = 0$ for $t = 0$.

Fredsøe (1984) chose the upper boundary condition as :

$$z = \delta + \frac{k_s}{30} \quad : \quad u = u_0 \qquad \textbf{(3.42)}$$

Substituting into Eq.(3.40) gives

$$\delta = \frac{k_s}{30}\left(e^{\zeta} - 1\right) \qquad \textbf{(3.43)}$$

where

$$\zeta = \frac{\kappa u}{u_*} \qquad \textbf{(3.44)}$$

After a little manipulation, Fredsøe (1984) obtains the following differential equation for the variation of non-dimensional velocity with phase:-

$$\frac{d\zeta}{d(\omega t)} = \beta \frac{\sin(\omega t)}{e^{\zeta}(\zeta - 1) + 1} - \frac{\zeta\left(e^{\zeta} - \zeta - 1\right)}{e^{\zeta}(\zeta - 1) + 1} \frac{1}{u_0} \frac{du_0}{d(\omega t)} \tag{3.45}$$

where

$$\beta = 30\kappa^2 \frac{a}{k_s} \tag{3.46}$$

Equation (3.45) must be solved numerically. Fredsøe's approach predicts the phase lead of the bed shear stress over the free stream velocity, an effect that the previous time-invariant eddy viscosity models fail to predict. The phase lead is a result of the small thickness of the boundary layer allowing the pressure gradient to penetrate undisturbed through the boundary layer down to the bed. The bed shear stress has a maximum at an angle, φ, before the free stream velocity reaches a maximum. In a laminar boundary layer $\varphi = 45°$. The results also show good agreement with the wave friction factor results of Jonsson and Carlsen (1976) and Kamphuis (1975) for values of a/k_s greater than about 30. However, the failure of the model for values of a/k_s less than 30 is perhaps to be expected since the logarithmic layer assumption must be questionable in this range.

Fredsøe (1984) also provides solution for the smooth wall case as well as for a wave/current boundary layer.

Finally, within these class of simple models the papers of Tanaka (1989) and Supharatid *et al.* (1993) require a mention. Tanaka proposed an extension to a simple time-invariant eddy viscosity model in order to represent non-linear wave motion via the stream function, as suggested by Dean (1965). The eddy viscosity was represented by:

$$\nu_t = \kappa u_{*_{cw}} z \tag{3.47}$$

and

$$\psi = -\frac{u_\infty}{k} \mathrm{Re}\left[\left\{\sinh k(z - z_0) + \frac{ik\xi}{2c} \frac{H_1^{(1)}(\xi)}{H_0^{(1)}}\right\} e^{i(kx - \omega t)}\right] \tag{3.48}$$

where $H_0^{(1)}$ is the Hankel function of the first kind, zeroth order and $H_1^{(1)}$ is the Hankel function of the first kind, first order.

$$c = \frac{\omega}{\kappa u_{*_{cw}}} \tag{3.49}$$

and

$$\xi = 2e^{\pi i/4} \tag{3.50}$$

Tanaka's manipulation results in the representation of the stream function as:-

$$\begin{aligned}\psi(x,z) &= \frac{L}{T}z - \frac{u_{*_c}^2}{\kappa u_{*_{cw}}} z\left\{\ln\left(\frac{z}{z_0}\right) - 1\right\} \\ &+ \sum_{n=1}^{N} \sinh\{nk(z-z_0)\}\{X(n)\cos(nkx) + Y(n)\sin(nkx)\} \\ &+ \mathrm{Re}\left[\sum_{n=1}^{N} \frac{ik\xi_n}{2c} \frac{H_1^{(1)}(\xi_n)}{H_0^{(1)}(\xi_{n0})}\{X(n) - iY(n)\}\exp(inkx)\right]\end{aligned} \tag{3.51}$$

Tanaka's analysis is only for rough fully turbulent flow. Comparison is made with the laboratory data of van Doorn (1981) and Nadaoka *et al.* (1982). Reasonable agreement is obtained for the results presented. Tanaka concludes that for velocity prediction in the surf zone, Dean's wave (stream function) theory provided better results over other wave theories.

Supharatid *et al.* (1993) extended the analysis of Tanaka (1989) to include currents. Supharatid *et al.* modified the current profile and formulated their model with the stream function formulated in terms of a truncated Fourier series. Their results show reasonable agreement with data except in the velocity 'overshoot' region. However, as Supharatid *et al.* point out their time-invariant eddy viscosity assumption is not valid.

3.6 Turbulence models

The use of higher order models to study turbulent flows has generally been led by the aerospace and mechanical engineering disciplines. In coastal engineering the application of such models has always followed from these developments.

3.6.1 Zero-equation models

Bakker (1975) was the first to use a mixing length closure model in the context of modelling turbulent wave boundary layers. Following from the approach of Prandtl (1925), the shear stress in the boundary layer is assumed to be given by the equation:-

$$\frac{\tau}{\rho} = l^2 \frac{\partial u}{\partial z}\left|\frac{\partial u}{\partial z}\right| \tag{3.52}$$

where

$$l = \kappa z \tag{3.53}$$

and l is a mixing length. Therefore the shear velocity is defined as:-

$$u_* = \kappa z \frac{\partial u}{\partial z} \tag{3.54}$$

The linearized equation of motion can be written as:

$$\frac{\partial u_d}{\partial t} = \frac{\partial}{\partial z}\left(\kappa^2 z^2 \frac{\partial u_d}{\partial z}\left|\frac{\partial u_d}{\partial z}\right|\right) \tag{3.55}$$

using Jonsson's definition of a defect velocity (see Eq. 3.16). Further, using the substitution, $\tau = \rho p^2$ gives:-

$$\frac{\partial p}{\partial t} = \kappa z \frac{\partial^2 (p|p|)}{\partial z^2} \tag{3.56}$$

Bakker (1975) introduces a non-dimensionalized form of this equation before solving using a finite difference scheme, ($p_* = p/\hat{p}_b$) where $\hat{p}_b$ is the maximum bed shear stress. Since the model solves for p_*, a distribution for this must first be prescribed. Bakker assumes a sinusoidal variation at the bed. In a later paper, Bakker and van Doorn (1979), the bed boundary condition was modified by the inclusion of harmonics up to the third order.

Wong (1984) used Bakker's (1975) approach but solved the equation using a simpler explicit finite difference method. The numerical results were compared with laboratory data from the University of Manchester studies (Savell 1986; O'Connor *et al.* 1988; Taplin 1989) and that of Jonsson and Carlsen (1976). The comparison with the Manchester flume experiments showed the model to provide only a first order fit even when second and third harmonic effects were included. However, when the model was compared with data for wave and current conditions a better fit was found. This would indicate that, to a certain extent, the

presence of a current acts to suppress non-linear effects in the wave field. In a later modified model, Solomou (1987) used a different numerical scheme based on a variable grid spacing over the flow depth, to investigate the influence of artificial viscosity on Bakker's results. The results suggested that numerical viscosity was of secondary importance.

Johns (1975) proposed a mixing length model which was valid from the bed to the free surface. Unlike Bakker (1975), Johns (1975) solved for the velocity. Unfortunately the paper is short on results and as such any model evaluation is difficult to make.

Vongvisessomjai (1984) also proposed a mixing length model solved using the velocity distribution. Vongvisessomjai investigated the difference between the boundary layer parameters for an oscillating bed (e.g. Bagnold 1946) compared with an oscillating fluid. The results showed that whilst the velocity profiles for the different cases were the same, values for the boundary layer thickness, the shear stress and the friction factor were larger for the oscillating flow. The differences are due to the difference in turbulence production. Vincent (1959) was probably the first to recognize the difference between the results from oscillating the fluid and oscillating the bed. Nielsen (1992) also notes the distortion of the inertia/pressure forces on sediment particles on oscillating beds.

Van Kesteren and Bakker (1985) proposed a mixing length model which could deal with a 'three-dimensional' bed boundary layer for waves and current. The model is not truly three-dimensional in that it is still solving at a point in space (i.e. one-dimensional), however, it allows for waves and current interacting at an angle with each other.

3.6.2 One-equation models

The one-equation k model has been used to study the boundary layer of tidal flows by Vager and Kagan (1969; 1971); Smith and Takhar (1977); Johns (1977) and wave and wave/current boundary layers by King *et al.* (1985); Davies (1986b; 1991); Davies *et al.* (1988); Trowbridge *et al.* (1987); Justesen (1988a; 1988b; 1990; 1991); Davies and Jones (1987);

Johns (1977) describes the use of a one-equation model which retained the advective terms in the equations. This enabled the modelling of second-order effects such as wave-induced mass transport. A pseudo-spectral method enabled the advective terms to be calculated. Unfortunately the paper only provides results for the mass transport effects.

King *et al.* (1985), Davies (1986b) and later Davies *et al.* (1988) use a one-equation k-model to describe the boundary layer for both waves and tidal conditions. In Davies *et al.* (1988) the model is extended to include waves and currents.

King *et al.* (1985) use two different descriptions for the mixing length term. The first is the method proposed by Vager and Kagan (1969) which is time dependent and the second is the simple expression derived from steady flow which allows the length-scale to increase linearly away from the wall.

The work of Trowbridge *et al.* (1987) deserves special mention since they incorporate second-order effects into their one-equation k-model. They use a simplification based on the assumption of periodicity in space and time together with the continuity equation to enable the vertical velocity to be calculated. Trowbridge *et al.* found that the steady second-order velocity field only became established after a few hundred wave periods. They also concluded from their results that both first- and second-order advection and diffusion of turbulent kinetic energy played only a minor part in determining the averaged velocity field.

Davies (1991) investigated transient effects in wave-current boundary layer flows using a one-equation k-model. The investigation studied the effect of superimposing waves on a co-linear current and also the case when waves are removed from a combined wave-current flow. Davies found that in both cases immediate changes to the near-bed period-averaged velocity, turbulent kinetic energy and shear stress distributions occurred. These changes gradually extended upwards through the water column to the surface as the flow attempted to reach a new equilibrium. In addition the time-scale required for such adjustments depended not only on the physical parameter settings but on whether the mass flux was held constant or the pressure gradient was held constant. The time-scale was shorter for the former case. Davies

suggests that such conditions would be relevant for a wave-current field at a coastal site should they alter suddenly due to refraction effects or tidal elevation variations.

3.6.3 Two-equation models

Two-equation k-ε models are probably the most widely used turbulence models for boundary layer study. Over the last ten years, various authors have presented papers for both high- and low-Reynolds number models. Smith and Takhar (1977) applied three different mean turbulence energy models to oscillatory flow in open channels, one of which was a high-Reynolds number k-ε model. Cousteix *et al.* (1979); Hagatun and Eidsvik (1986); Justesen (1988a; 1988b; 1990; 1991) Celik and Rodi (1985); Sato (1987); and Utnes (1988) have all applied high-Reynolds number k-ε models to the turbulent wave boundary layer. Utnes (1988) used a finite element scheme in his solution. Papers detailing the use of low-Reynolds number k-ε models have been presented by Aydin and Shuto (1988); Asano *et al.* (1988); Tanaka and Sana (1994).

In addition to the k-ε model, two-equation models of the k-*l* type have been proposed, based on the earlier work of Lewellen (1977). Models of this type have been used by Bocar-Karakiewicz *et al.* (1990) Huynh Thanh and Temperville (1991a; 1991b); Chapalain and Bocar-Karakiewicz (1992).

Of the high-Reynolds number k-ε model studies, the work of Hagatun and Eidsvik (1986) and that of Justesen (1988a; 1988b; 1990; 1991) stand out. The theory behind such eddy viscosity models can be found in Chapter 4.

Sato *et al.* (1985) and Sato (1987) applied a two-equation k-ε model to flow over ripples. Sato (1987) describes the taking of a comprehensive set of measurements above symmetric and asymmetric ripples using hot-film and laser anemometer techniques. Both references use these results to compare with the model predictions with reasonable agreement with the velocity distributions.

It is worth mentioning a slightly different two-equation model based on that proposed by Saffman (1970; 1974). Saffman proposed that the turbulence components responsible for mixing and momentum transfer could be expressed through an energy density, e and a vorticity density, ω_S and are described through the equations:-

$$\frac{\partial \omega_S^2}{\partial t} + \bar{u}_i \frac{\partial \omega_S^2}{\partial x_i} = \alpha_\omega \omega_S^2 \left\{ \left(\frac{\partial \bar{u}_i}{\partial x_j} \right)^2 \right\}^{\frac{1}{2}} - \beta_\omega \omega_S^3 + \frac{\partial}{\partial x_j} \left(\sigma_\omega \nu_t \frac{\partial \omega_S^2}{\partial x_j} \right) \qquad \textbf{(3.57)}$$

$$\frac{\partial e}{\partial t} + \bar{u}_i \frac{\partial e}{\partial x_i} = \alpha_e e \left\{ 2 \left[\frac{1}{2} \left(\frac{\partial \bar{u}_i}{\partial x_j} + \frac{\partial \bar{u}_j}{\partial x_i} \right) \right]^2 \right\}^{\frac{1}{2}} - \beta_e e\omega + \frac{\partial}{\partial x_j} \left(\sigma_e \nu_t \frac{\partial e}{\partial x_j} \right) \qquad \textbf{(3.58)}$$

and where α_ω, β_ω, σ_ω, α_e, β_e, σ_e are assumed to be universal constants. Further, the turbulent eddy viscosity, ν_t is given by the equation:-

$$\nu_t = \frac{\gamma e}{\omega} \qquad \textbf{(3.59)}$$

where γ is another universal constant.

Jacobs (1984) used Saffman's approach to study mass transport in a turbulent wave boundary layer and Blondeaux (1987) employed Saffman's turbulence model to investigate the turbulent bed boundary layer due to gravity waves. It is not clear whether such an approach has any advantage over, say, the k-ε scheme.

3.6.4 Algebraic stress (Reynolds stress) models

All the models reviewed so far use the Boussinesq hypothesis relating the turbulent stresses to the mean strain. Reynolds stress models (also referred to as second-order closure schemes) model the production terms and body force terms that influence the Reynolds stresses exactly. This allows the Reynolds stress model to correctly account for effects induced by additional mean flow strains introduced for example in swirling flows or buoyancy driven flows. However, correctly modelling the pressure and dissipation terms is not straight forward.

In some cases up to 28 transport equations have been proposed in Reynolds stress models which include higher order correlations (see Rodi 1980). Whilst such models undoubtedly

have much to offer where the transport of stresses and fluxes is essential to the solution and where such terms cannot be approximated, they are computationally expensive. For many situations a much simpler turbulence model will provide results not that different from the Reynolds stress approach.

Some of the earliest attempts to use Reynolds stress models in coastal engineering problems were presented by Sheng (1985; 1987). More recently Shima (1993) and Brørs and Eidsvik (1994) have described the use of such second-moment closures to model oscillatory wave boundary layers.

Sheng (1985) first proposed a Reynolds stress model for modelling turbulent wave and wave-current boundary layers. Sheng described the problem through the use of seven equations. Comparison was made with the data of Jonsson and Carlsen (1976). However, it is not clear whether these results are any more superior than those obtained with a one or two equation model. Sheng also ran the model for a cnoidal wave in an attempt to provide a better description of a boundary layer in a real sea.

In a later paper, Sheng (1987) discussed the application of a Reynolds stress model to a broader range of problems. Sheng attempted to show that the Boussinesq eddy viscosity assumption was an inadequate basis for studying turbulent boundary layers by comparing the results of the Reynolds stress model with the eddy viscosity values calculated from Jonsson and Carlsen's (1976) laboratory data. Like many other experimental results for eddy viscosity (for example see Sleath 1987) the experimental data is often scattered and sometimes negative, and as such has no physical meaning. Because Reynolds stress models remove the need for the Boussinesq eddy viscosity assumption by modelling the second-order turbulent correlations in terms of transport equations they are seen as being of higher accuracy than the models discussed up to now. However, these transport equations cannot be solved directly and empirical approximations are introduced in order to allow solution. Therefore, because of these introduced simplifications the superiority of such methods over more simple models is less clear.

Sheng (1985; 1987) fails to properly present any comparison of the Reynolds stress model with any turbulence measurements. This makes judgement of Sheng's approach difficult, since it must be on these quantities that the model's performance is assessed.

Shima (1993) uses an extension of the high-Reynolds number closure of Gibson and Launder (1978) to assess the performance of the Reynolds stress model when applied to free surface boundary layers with a periodic pressure gradient. Whilst Gibson and Launder took the coefficients of the redistribution terms to be constants, Shima makes the coefficients dependent on the two invariants of the anisotropic stress tensor (see Shima 1993 for further details).

Shima compares his model with the direct numerical simulation data for an oscillating boundary layer of Spalart and Baldwin (1987) (see below). Shima argues that as the logarithmic law of the wall assumption does not hold true for all of the flow cycle, a model which is applicable up to the wall itself is required to predict such flows. The adapted model is valid up to the wall. Shima (1993) shows that the extended high-Reynolds number closure model, which is valid to the wall, is capable of reproducing the complex behaviour of the oscillatory flow well.

Brørs and Eidsvik (1994) present a standard dynamic Reynolds stress model based on the model of Gibson and Launder (1978) and which includes a sediment transport module. Brørs and Eidsvik compare the model against the high-Reynolds-number oscillating tunnel data of Jensen *et al.* (1989). They show results for tests 12 and 13 of Jensen *et al.* (see Chapter 6). However, whilst the model reproduces the flow physics well, it is less clear how superior these results are to, say, those predicted by a k-ε turbulence model.

Brørs and Eidsvik test their sediment module against data from Ribberink and Al-Salem (1992). Their results show reasonable agreement considering they perform no model adjustment. The measured and calculated phase lag between the low level sediment concentration and the free steam velocity is clearly different. Comparison of results from the Reynolds stress model sediment module against those predicted by a sediment module

attached to k-ε model (Hagatun and Eidsvik 1986) imply that the k-ε model predicts sediment transport in oscillatory flows as well as the Reynolds stress model.

Lewis *et al.* (1996) presented a comparison of laboratory measurements for flow over vortex ripples against a range of numerical models from different research institutes; two k-ε models, a k-*l* model, a Reynolds stress model and a discrete vortex model (the latter type of model is not discussed in the present work). Only limited details are given in the paper on the model formulations.

Lewis *et al.* found that from time-series comparisons, the Reynolds stress model predicted the phases of the Reynolds stresses most accurately whilst one of the k-ε models provided the best description of the magnitude of the stresses. Clearly from this it can be surmised that the formulation of a numerical model is important, otherwise one would expect that both k-ε models would be equally better at predicting the magnitudes of the stresses.

3.6.5 Direct numerical simulation (DNS) models

Spalart and Baldwin (1987) solved the time-dependent, three-dimensional, incompressible Navier-Stokes equations using a numerical method which is fully spectral in space and second-order-accurate in time. The numerical technique is described in detail by Spalart (1986). The time integration uses a low-storage Runge-Kutta scheme (Wray 1987) for the transport term and the Crank-Nicolson scheme for the Stokes terms. Such solution methods are termed direct numerical simulation (DNS). Spalart and Baldwin present results for oscillatory flow over a flat plate conducting direct numerical simulations for Reynolds numbers up to 5×10^5.

In addition, Spalart and Baldwin applied a high-Reynolds number k-ε model to the oscillatory flow case but with their first grid point at $z \geq 2\sqrt{2\nu_L/\omega}$. Boundary conditions for u, k and ε at $z = 2\sqrt{2\nu_L/\omega}$ were taken from the direct simulations. Their results showed very good agreement with the direct numerical simulations. By adjusting one of the standard constants in the k-ε model (see Chapter 4), $c_\mu = 0.085$ rather than the normally accepted value of 0.09

agreement was further improved. The results also suggested that a lower value of σ_k (0.8 instead of 1.0) should be used, though such a change had much less of an effect on the results. Excluding the wall region, Spalart and Baldwin have shown that a simple high-Reynolds number k-ε model is quite capable of accurately predicting oscillatory wave boundary layer flows.

3.7 Modelling random sea boundary layers

All of the previous models reviewed were written to model linear mono-frequency or mildly non-linear mono-frequency waves. The first work which truly tackled the modelling of random sea boundary layers is that of O'Connor *et al.* (1993). This model uses a mixing length closure scheme so that the eddy viscosity varies in time and space. Model results were compared with data from the North Sea (See also O'Connor *et al.* (1994)).

The early work of investigating random bed boundary layers involved the development of two mixing length models, one of which used an approach similar to Bakker (1975) driving the model using the shear velocity, the other used the free stream velocity as a boundary condition. The former approach made the development of a random model more complicated with extra computational steps and assumptions. Results for the random zero-equation model (based on the free stream velocity approach) are presented in O'Connor *et al.* (1993; 1994). Results were shown for a multi-directional sea state and show the influence of wave groups on the hydrodynamics. In particular, that the effect of wave groups has a tendency to produce lower values of actual seabed roughness than methods based on significant wave height and peak period.

More recently, Kaczmarek and Ostrowski (1995) presented results from a random two-layer time-invariant eddy viscosity model. In addition, their approach involves the use of Fredsøe's momentum integral equation to determine the representative shear velocity and the boundary layer thickness. Kaczmarek and Ostrowski compare their model results with random time-series obtained from the laboratory data of Ostrowski (1993) (see Chapter 8 for further details). Their approach of driving the eddy viscosity model is identical to the method used by O'Connor *et al.* (1993; 1994).

Whilst the results of O'Connor *et al.* (1993; 1994) and Kaczmarek and Ostrowski (1995) compare favourably with field and laboratory data respectively, such models are incapable of providing details of turbulence properties as highlighted previously. In an attempt to improve the representation and understanding of the physics of random bed boundary layers, the present author has developed one- and two-equation turbulence models.

3.8 Conclusions

It is clear from having reviewed the literature that there are a large variety of models available for which to study the turbulent wave boundary layer. Surprisingly, even with the advances in computational power many researchers choose to use very simple time-invariant eddy viscosity models. Whilst these models undoubtedly give reasonable results for maximum velocity and shear stress, many of the assumptions on which these schemes are based are questionable or incorrect. Takhar and Thomas (1991) noted that if turbulent mass transport effects are to be modelled correctly, the eddy viscosity should possess time dependence, otherwise, using a time-invariant eddy viscosity will fail to capture the fundamental mechanism of such flows. Takhar and Thomas concluded that the simplest model of turbulence with the correct properties to predict turbulent mass transport effects is the mixing length model. However, there is an optimum level of simulation based on the results obtained and the work required to obtain a solution to a given problem.

To be able to simulate a real sea and to attempt to understand the complex processes involved requires a level of modelling which is sufficient to adequately describe the physics. This must at least involve the prediction of turbulence if the model is to eventually be used to model sediment transport since turbulence is an essential part of sediment transport events on the continental shelf (Gross *et al.* 1994). From a modelling approach, Smith and Takhar (1977) describe the use of mean Reynolds stress and mean turbulence energy closure models for the prediction of oscillatory flow in open channels. Smith and Takhar concluded that a one-equation k-model was a sufficient order of closure for the solution of environmental problems.

Assumptions used in some models have been shown to be incorrect. For example, the experimental results of Sleath (1987) and Jensen *et al.* (1989), have shown that the eddy viscosity varies with time. In addition Jensen *et al.* (1989) have shown experimentally that the logarithmic law of the wall is not valid at all phases of the wave cycle.

Whilst second-order closure models provide the ability to model the individual stress terms, not only are the computational costs prohibitive, the level of sophistication has yet to be clearly justified. The importance of highly advanced numerical models serves to provide a control level for the less complex schemes so that any failings in these more simple models can be identified and quantified. Spalart and Baldwin (1987) used their direct numerical simulation data to assess the capability of a simple high-Reynolds number k-ε model in predicting oscillatory wave boundary layer flows. Spalart and Baldwin showed that, excluding the wall region, the oscillating boundary layer was well reproduced by a k-ε model.

In addition to Spalart and Baldwin (1987), Brørs and Eidsvik (1994) showed that a k-ε model predicted sediment transport in oscillatory flows as well as a more sophisticated Reynolds stress closure model.

Clearly, in attempting to improve any description of the flow in random wave boundary layers over that of existing models (e.g. O'Connor *et al.* 1993) the following points should be considered.

- Smith and Takhar (1977) concluded that a one-equation k model is the lowest order of model closure necessary for the prediction of environmental problems.

- Choice of model formulation is important and influences the performance of the model in accurately reproducing the flow physics.

- A two-equation k-ε model is capable of accurately reproducing oscillatory wave boundary layer flows, excluding the near-wall region, and has been shown to provide a similar level of accuracy in predicting sediment transport as that of a Reynolds stress model.

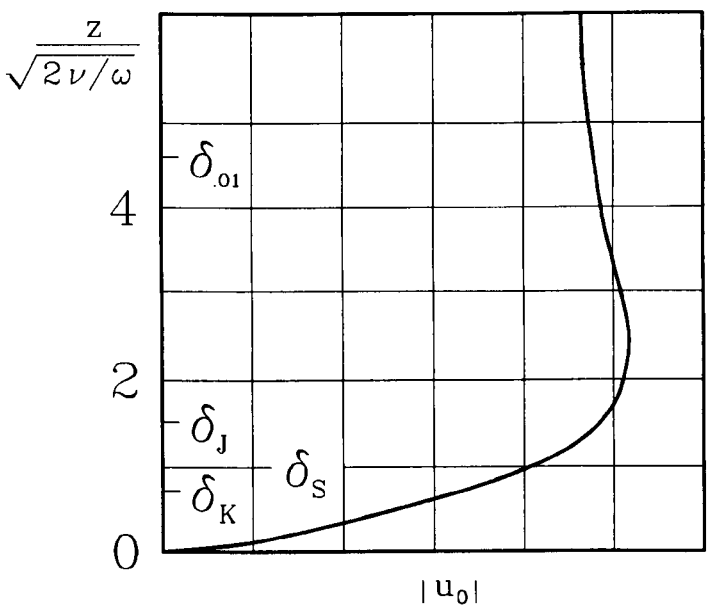

Figure 3.1: Sketch showing relationship between different definitions for wave boundary layer thickness. δ_K ,δ_J and δ_S represent Kajiura's, Jonsson's and Sleath's definitions, respectively. (*After Nielsen 1992*).

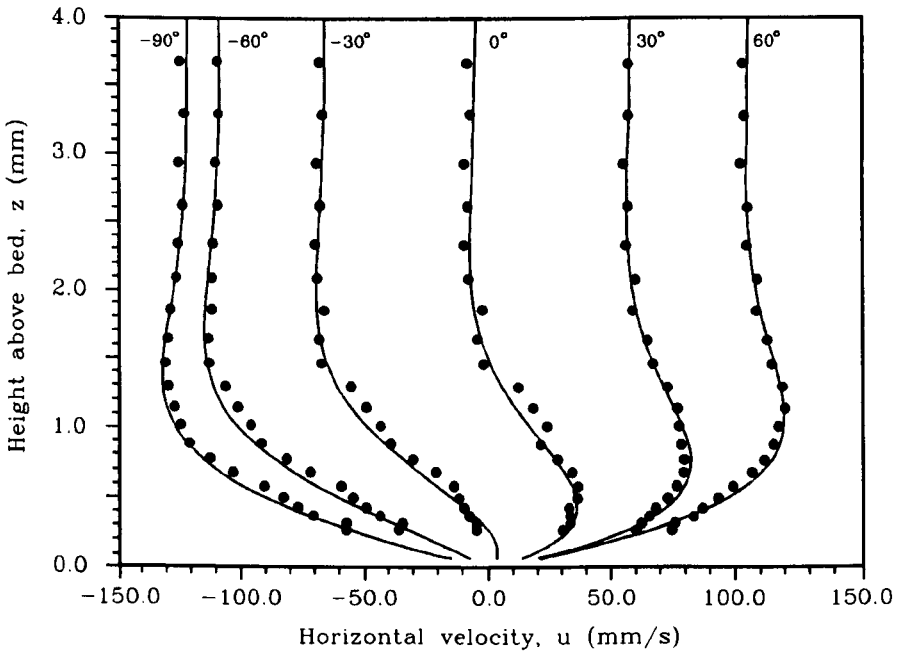

Figure 3.2: Instantaneous velocity profiles for laminar waves, Manchester Experiments. • Experiment (Test 30); —— Analytical solution for laminar flow, Lamb (1932). (*After Savell 1986*).

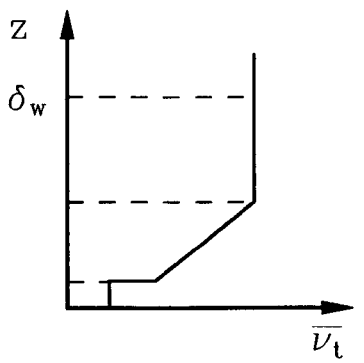

Figure 3.3: Schematic showing Kajiura's mean eddy viscosity distribution.

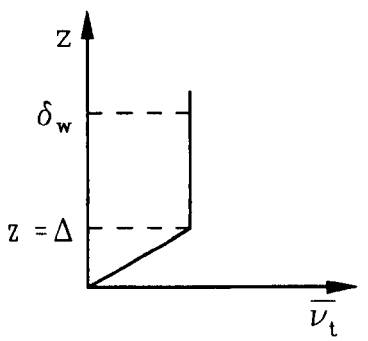

Figure 3.4: Schematic showing Brevik's mean eddy viscosity distribution.

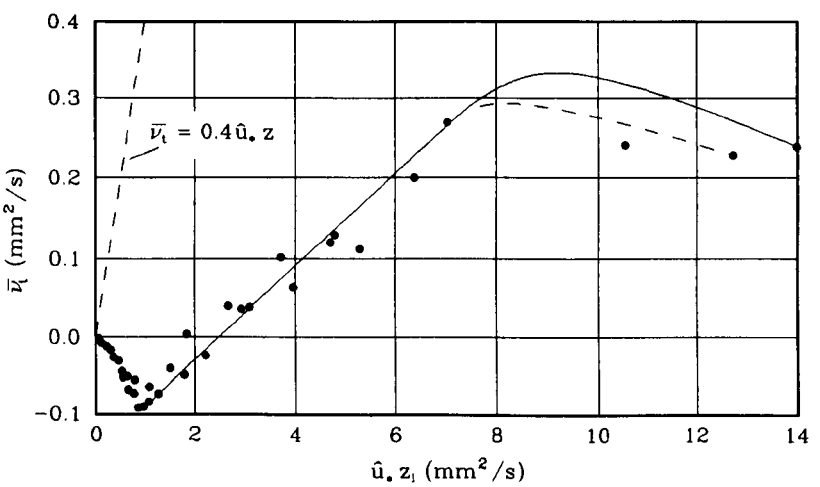

Figure 3.5: Variation of time-mean eddy viscosity with height (*After Sleath 1987*).

Chapter 4
Theory

4.1 Introduction

Chapter 2, showed the development of the hydrodynamic equations which form a major part of the present work. In Chapter 3 a state-of-the-art review of wave boundary layer modelling was given. From this it was concluded that in order to model coastal seabed boundary layers for waves and the combined wave-current case a one-equation turbulence model is the lowest model closure that should be used if such flows are to be modelled sufficiently accurately (Smith and Takhar 1977). In the present chapter the theory behind the closure schemes used in the present work will be introduced. Further, one- and two-equation turbulence models will be discussed in more detail since they form an important part of this investigation.

It is not the intention of the author to provide a detailed insight into all of the theoretical techniques used. Not only would such a task be outside the scope of this present work, but any attempt would fail to adequately address the questions which still require resolving with some of the methods. An example of this would be the simulation of directional seas. Numerous methods have been proposed (see Huang *et al.* 1990), however, progress has been slow compared to the work done on describing one-dimensional spectra because of limited observational methods.

4.2 Introduction to turbulence modelling

In Chapter 3, a review of existing boundary layer models applied to the coastal zone was undertaken with a view to providing a context in which to place the present work. However, in addition to that review it is worth a more detailed look at the general background to turbulence modelling and, in particular, modelling turbulent flows using k- and ε- transport equations.

In the early 1980's, a competition was held at Stanford University to evaluate the various turbulence models used for calculating complex turbulent flows, Kline *et al.* (1981). In total, 67 different methods were used and their numerical results compared with experimental data. One of the conclusions of those evaluating the tests was that the satisfactory performance of the models was quite limited and that further study and refinement was required.

At the Stanford conference, the k-ε model was one of the most extensively used methods. Generally such models are run with empirical wall functions, by which surface boundary conditions are transferred to points in the fluid which are at some distance from the boundaries. However, those evaluating the models also pointed out that in many situations, the use of wall functions is not well established and that methods which allowed calculations to continue right to the wall were superior to the use of wall functions, Kline *et al.* (1981).

Jones and Launder (1972;1973) were the first to extend the high-Reynolds number version of the k-ε model to form what is known as a low-Reynolds number model, which allows calculations right up to a solid wall. Since then, numerous forms of low-Reynolds number k-ε model have been proposed but will not be listed here (see Patel *et al.* 1985; Shih and Mansour 1990). Of note is the modified k-ε model of Lam and Bremhorst (1981). However, even these versions of the k-ε model have been shown to fail to adequately predict the effects of an adverse pressure gradient, Rodi and Scheuerer (1986).

The inability to properly predict the effects of an adverse pressure gradient on shear flows not only by simple mixing-length models but especially two-equation and Reynolds stress equation models, employing a transport equation for a characteristic length-scale, was a worrying result of the 1980-81 Stanford conference. The numerical calculations predicted the flow to be still attached when experiments were showing that separation had occurred. Rodi and Scheuerer (1986) point out that the reason for these poor predictions is due to the length-scale determined by the ε-equation rising more steeply near the wall than is the case for a zero pressure gradient. Experimental data suggests that the length-scale gradient is virtually independent of the pressure gradient for a wide range of values. For this reason, one-equation models which use an empirical length-scale provide much better predictions for adverse pressure gradient boundary layers than does the k-ε model.

The oscillatory boundary layer experiments of Jensen *et al.* (1989) suggest that even for relatively high Reynolds numbers ($Re = 6 \times 10^6$) the logarithmic layer does not exist for all of the flow cycle (see also Jensen (1989)). The experiments of Hino *et al.* (1983) also show similar results. Jensen *et al.* (1989) show that the logarithmic layer exists for longer as the Reynolds number increases. However, even for fully developed turbulent flow over a rough wall Jensen *et al.* show that the logarithmic layer is not always present.

More recently, researchers have proposed two-layer turbulence models (see Rodi (1991)). This approach involves using k-ε or Reynolds-stress-equation models within the turbulent part of the flow field whilst close to the wall where viscous effects are greatest, a simpler one-equation model is employed. Previously, because of the steep gradients often present in the near-wall layer, the numerical resolution required was beyond available computer resources. Wall functions were used to relate the velocity and turbulence transport terms at the first grid point above the wall using the assumption of a logarithmic velocity distribution and the local equilibrium of the turbulence, that is, production = dissipation. However, such assumptions are not always valid, particularly in separated flows. Low-Reynolds-number models were developed to enable the k-ε model to remain valid in the near-wall region by replacing some of the model constants with viscosity dependent functions. However, even these models require quite high numerical resolution close to the wall mainly due to the steep gradient of the dissipation term, ε.

To overcome the problem of numerical grid resolution close to the wall and increase the robustness of the method, the use of a simpler model involving a length-scale prescription has been proposed, for example Iacovides and Launder (1987); Chen and Patel (1988; 1989). The use of such models has almost been exclusively confined to the mechanical and aerospace disciplines, although recently Utnes and Eidsvik (1995) used a two-layer turbulence model to investigate oscillatory flow over two-dimensional ripples. More recently, the present author has investigated their use for modelling wave boundary layers under monochromatic and random waves, Harris and O'Connor (1997).

4.3 The k-ε model

4.3.1 Introduction

The k-ε two-equation model derives both the velocity and length scales using two local turbulence quantities. The distribution of these quantities is obtained through the solution of two transport equations. Almost all two-equation models derived to date use the turbulent kinetic energy, k as one of the transported turbulence variables. The length scale equation does not necessarily require that the length scale itself is the dependent variable (see Rodi 1980) and can be selected as almost any turbulence quantity with the form $k^m l^n$ since k is known from solving the k-equation. Chou (1945); Davidov (1961); Harlow and Nakayama (1967) and Jones and Launder (1972) suggested an equation for the isotropic dissipation rate ε, where $\varepsilon \propto k^{3/2}/l$. However, other approaches have been proposed involving an equation for kl, an equation for the frequency $k^{1/2}/l$ and an equation for a turbulence vorticity k/l^2 (see Rodi 1980).

The k-ε approach has become the more popular method used since all the other approaches require the inclusion of a near-wall correction term which is not required in the ε-equation. Further, the dissipation equation is relatively easily obtained and also the ε term appears in the kinetic energy equation. Generally, most development with this level of turbulence model has been in steady flows. However, Chapter 3 reviewed work undertaken in unsteady flows with higher level models, for example Johns (1977), Sheng (1985), Justesen (1988a).

4.3.2 The exact k-equation

The exact transport equation for the turbulent kinetic energy, k, is given by the following expression (see Appendix A):

$$\frac{Dk}{Dt} = P_k + T_k + \Pi_k + D_k - \varepsilon \qquad \textbf{(4.1a)}$$

where D/Dt represents a total differential and is given by the equation:-

$$\frac{D}{Dt} = \frac{\partial}{\partial t} + u_i \frac{\partial}{\partial x_i} \qquad \textbf{(4.1b)}$$

the individual terms are defined as:

Rate of production:

$$P_k = -\overline{u_i' u_j'} \frac{\partial \overline{u}_i}{\partial x_j} \tag{4.2}$$

Rate of turbulence transport:

$$T_k = -\frac{1}{2} \frac{\partial}{\partial x_j} \left(\overline{u_i' u_i' u_j'} \right) \tag{4.3}$$

Rate of pressure diffusion:

$$\Pi_k = -\frac{1}{\rho} \frac{\partial}{\partial x_i} \left(\overline{u_i' p_i'} \right) \tag{4.4}$$

Rate of viscous diffusion:

$$D_k = \frac{\partial}{\partial x_j} \nu_t \frac{\partial k}{\partial x_j} \tag{4.5}$$

Rate of dissipation:

$$\varepsilon = \nu_t \overline{\frac{\partial u_i'}{\partial x_j} \frac{\partial u_i'}{\partial x_j}} \tag{4.6}$$

As Hinze (1975) pointed out, Eq. (4.6) only represents dissipation in homogeneous turbulence. Mansour *et al.* (1987) produced a figure (see Figure 4.1) showing the magnitude of the various terms based on the results of Kim *et al.* (1987). The viscous term D_k becomes significant in the buffer layer and laminar sub-layer. Very near the wall, the viscous diffusion balances the dissipation ε. In the fully turbulent region the only terms that matter are the production and dissipation. However, in the buffer layer and viscous sub-layer all terms except the pressure diffusion are required to be modelled correctly.

4.3.3 The modelled k-equation

The turbulent transport and pressure diffusion terms can be combined assuming that the diffusion of k is isotropic, that is, that the diffusion occurs equally in all directions. Therefore,

$$T_k + \Pi_k = \frac{\partial}{\partial x_j} \frac{\nu_t}{\sigma_k} \frac{\partial k}{\partial x_j} \tag{4.7}$$

where σ_k is a model constant (see Section 4.3.6).

Also, through consistency with Boussinesq's (1877) hypothesis (Eq. 2.21) which assumes that the turbulent stresses are related to the mean strain, P_k can be written as:-

$$P_k = \nu_t \left(\frac{\partial \overline{u}_i}{\partial x_j} + \frac{\partial \overline{u}_j}{\partial x_i} \right) \frac{\partial \overline{u}_i}{\partial x_j} \tag{4.8}$$

Combining Eqs. (4.5), (4.6) and (4.8) gives:-

$$\frac{Dk}{Dt} = \frac{\partial}{\partial x_j} \frac{\nu_t}{\sigma_k} \frac{\partial k}{\partial x_j} + \frac{\partial}{\partial x_j} \nu_L \frac{\partial k}{\partial x_j} + \nu_t \left(\frac{\partial \overline{u}_i}{\partial x_j} + \frac{\partial \overline{u}_j}{\partial x_i} \right) \frac{\partial \overline{u}_i}{\partial x_j} - \varepsilon \tag{4.9}$$

$$\frac{Dk}{Dt} = \frac{\partial}{\partial x_j} \left[\left(\nu_L + \frac{\nu_t}{\sigma_k} \right) \frac{\partial k}{\partial x_j} \right] + \nu_t \left(\frac{\partial \overline{u}_i}{\partial x_j} + \frac{\partial \overline{u}_j}{\partial x_i} \right) \frac{\partial \overline{u}_i}{\partial x_j} - \varepsilon \tag{4.10}$$

The resulting Eq. (4.10) becomes the modelled equation for k. Since deriving this equation did not require any significant assumptions it is expected that the equation should be adequate for modelling the kinetic energy distribution in both the fully turbulent and near wall regions.

4.3.4 The exact ε-equation

The exact transport equation for the isotropic dissipation rate, ε, is given by the following expression (see Appendix B):

$$\frac{D\varepsilon}{Dt} = P_\varepsilon^1 + P_\varepsilon^2 + P_\varepsilon^3 + P_\varepsilon^4 + T_\varepsilon + \Pi_\varepsilon + D_\varepsilon - \gamma \tag{4.11}$$

where the individual terms are defined as:

Rate of production by mean velocity gradient:

$$P_\varepsilon^1 = -2\nu_t \overline{\frac{\partial u_i' \partial u_j'}{\partial x_m \partial x_m}} \frac{\partial \overline{u}_i}{\partial x_j} \tag{4.12}$$

Rate of mixed production:

$$P_\varepsilon^2 = -2\nu_t \overline{\frac{\partial u_j' \partial u_i'}{\partial x_j \partial x_m}} \frac{\partial \overline{u}_j}{\partial x_m} \tag{4.13}$$

Rate of gradient production:

$$P_\varepsilon^3 = -2\nu_t \overline{u_j' \frac{\partial u_i'}{\partial x_m}} \frac{\partial^2 \overline{u}_i}{\partial x_j \partial x_m} \tag{4.14}$$

Rate of turbulent production:

$$P_\varepsilon^4 = -2\nu_t \overline{\frac{\partial u_i'}{\partial x_j}\frac{\partial u_i'}{\partial x_m}\frac{\partial u_j'}{\partial x_m}} \tag{4.15}$$

Rate of turbulent transport:

$$T_\varepsilon = -\nu_t \overline{u_j' \frac{\partial}{\partial x_j}\frac{\partial u_i'}{\partial x_m}\frac{\partial u_i'}{\partial x_m}} \tag{4.16}$$

Rate of pressure transport:

$$\Pi_\varepsilon = -\frac{2\nu_t}{\rho}\frac{\partial}{\partial x_i}\overline{\frac{\partial p_i'}{\partial x_m}\frac{\partial u_i'}{\partial x_m}} \tag{4.17}$$

Rate of viscous transport:

$$D_\varepsilon = \frac{\partial}{\partial x_j}\nu_t\frac{\partial \varepsilon}{\partial x_j} \tag{4.18}$$

Rate of dissipation:

$$\gamma = 2\nu_t^2\overline{\left(\frac{\partial^2 u_i'}{\partial x_j \partial x_m}\right)^2} \tag{4.19}$$

Kim *et al.* (1987) produced the magnitude of these terms from direct simulation.

In the fully turbulent region P_ε^4 and γ dominate and approximately balance each other (see Figure 4.2). The terms Π_ε, T_ε and P_ε^3 are all negligible throughout compared to the other terms. The dissipation term γ is significant in all regions and is non-zero at the wall. The viscous diffusion term D_ε is significant very close to the wall and is the main term balancing the dissipation γ. Also, P_ε^1, P_ε^2 and P_ε^4 are significant in the near wall region ($z^+ < 30$), where z^+ is defined as:-

$$z^+ = \frac{u_{*b} z}{\nu_L} \tag{4.20a}$$

where ν_L is the kinematic viscosity and u_{*b} is the bed shear velocity and is defined as:

$$u_{*b} = \sqrt{\frac{\tau_b}{\rho}} \tag{4.20b}$$

where τ_b is the bed shear stress and ρ is the fluid density.

4.3.5 The modelled ε-equation

The ε-equation has many terms involving higher order correlations that require to be modelled if the Two Equation Model is to achieve closure.

The terms $\Pi_\varepsilon + T_\varepsilon$ are combined and modelled as

$$\Pi_\varepsilon + T_\varepsilon = \frac{\nu_t}{\sigma_\varepsilon}\frac{\partial \varepsilon}{\partial x_k} \qquad (4.21)$$

where σ_ε is a model constant (see Section 4.3.6).

This is not altogether satisfactory as direct simulation results show (Figure 4.3 after Mansour *et al.* 1987). The model does not agree well with the data below $z^+ < 40$ and does not have the correct asymptotic behaviour at the wall. However, the contribution of this term to the overall balance is very small and the discrepancies are of little significance.

Through dimensional arguments, Mansour *et al.* (1987), P_ε^3, can be shown to be much smaller than the other production terms and is therefore neglected. Again by dimensional arguments the remaining terms can be represented as (see Mansour *et al.* 1987):-

$$P_\varepsilon^1 + P_\varepsilon^2 + P_\varepsilon^4 - \gamma = c_{\varepsilon 1}\frac{P_k \varepsilon}{k} - c_{\varepsilon 2}\frac{\varepsilon^2}{k} \qquad (4.22)$$

Where $c_{\varepsilon 1}$ and $c_{\varepsilon 2}$ are turbulence model constants (see section 4.3.6).

The interpretation of this dimensional argument is somewhat divided amongst modellers. Kim *et al.* (1987) interpret the first term on the right hand side as representing P_ε^1 and P_ε^2 and the second term as the sum P_ε^4 and γ. However, their direct simulation, whilst showing reasonable agreement in the fully turbulent region ($z^+ > 30$) is quite poor close to the wall.

Alternatively, it has been suggested that at high Reynolds numbers the dissipation scale eddies are isotropic and hence the terms P_ε^1 and P_ε^2 are zero. Therefore the terms of the right hand side of Eq. (4.21) represent the balance between P_ε^4 and γ. However, since either

interpretation leads to the same model form the debate as to which approach is correct is somewhat academic.

Therefore the modelled ε-equation becomes

$$\frac{D\varepsilon}{Dt} = \frac{\partial}{\partial x_j}\left[\left(\nu_L + \frac{\nu_t}{\sigma_\varepsilon}\right)\frac{\partial \varepsilon}{\partial x_j}\right] + \frac{c_{\varepsilon 1}\nu_t}{k}\varepsilon\left(\frac{\partial \overline{u}_i}{\partial x_j} + \frac{\partial \overline{u}_j}{\partial x_i}\right)\frac{\partial \overline{u}_i}{\partial x_j} - c_{\varepsilon 2}\frac{\varepsilon^2}{k} \qquad \textbf{(4.23)}$$

This is the high-Reynolds number form of the ε-equation.

4.3.6 Turbulence model constants

The standard values of the constants used in the k and k-ε models as recommended by Launder and Spalding (1974) are given in Table 4.1.

c_μ	σ_k	σ_ε	$c_{\varepsilon 1}$	$c_{\varepsilon 2}$
0.09	1.0	1.3	1.44	1.92

Table 4.1: Values of standard constants in k and k-ε models.

The empirical constants in the standard k-ε model were determined as follows (see Rodi 1980);

In the decay of turbulence, k behind a fixed grid, $c_{\varepsilon 2}$ is the only constant appearing in the k and ε transport equations (Eqs. 4.1 and 4.11). Therefore, $c_{\varepsilon 2}$ can be determined directly from the measured decay rate behind the grid and was found to be in the range 1.8 - 20.

The constant c_μ appears in both the one- and two-equation models. For local equilibrium shear layers, production = dissipation (Eq. 4.2 = Eq. 4.6). The turbulent eddy viscosity, ν_t is described by the equation:-

$$\nu_t = c_\mu \frac{k^2}{\varepsilon} \qquad \textbf{(4.24)}$$

Combining Eq. (4.24) with Eq. (4.1) (see Rodi 1980) yields:-

$$c_\mu = \left(\frac{\overline{uw}}{k}\right)^2 \qquad (4.25)$$

Measurements in these flows yielded $\overline{uw}/k \approx 0.3$ thus $c_\mu = 0.09$.

In near-wall regions a logarithmic velocity profile exists, the production is approximately equal to the dissipation and the convection of dissipation is negligible. Therefore the ε-transport equation reduces to:-

$$c_{\varepsilon 1} = c_{\varepsilon 2} - \frac{\kappa^2}{\sigma_\varepsilon \sqrt{c_\mu}} \qquad (4.26)$$

Once the values of the other constants have been determined, then the value of $c_{\varepsilon 1}$ can be found.

The diffusion constants σ_k and σ_ε were assumed to be close to unity and they, along with $c_{\varepsilon 2}$, were tuned using computer optimization. For further details see Rodi (1980).

The above constants were established under steady flow conditions. However, there is no reason to believe that the same set of constants should be applicable for all complex turbulent flows.

Spalart and Baldwin (1987) applied a high-Reynolds number k-ε model to oscillatory flow case but with their first grid point at $z \geq 2\sqrt{2\nu_L/\omega}$. Using direct numerical simulation data for u, k and ε at $z \geq 2\sqrt{2\nu_L/\omega}$ Spalart and Baldwin found that by adjusting c_μ to 0.085 rather than the normally accepted value of 0.09 agreement was further improved. The results also indicated that a lower value of σ_k (0.8 instead of 1.0) should be used.

Justesen (1988a) also carried out a sensitivity study for the constants used in the k-ε model although the method chosen was not intended to provide optimized values for the particular problem of turbulent wave boundary layers.

Justesen used the following values of the constants in his study:

Constant	c_μ	σ_k	σ_ε	$c_{\varepsilon 1}$	$c_{\varepsilon 2}$
High value	0.10	1.1	1.5	1.50	2.05
Standard value	0.08	1.0	1.3	1.44	1.92
Low value	0.06	0.9	1.1	1.38	1.79

Table 4.2: Values of model constants used in Justesen's (1988) sensitivity study.

Justesen concluded that although a change in the model constants leads to a response in the results, the standard values are a good choice for the wave boundary layer. (see Justesen 1988a for further details.

In the present work the values for the model constants have been taken as follows:

c_μ	σ_k	σ_ε	$c_{\varepsilon 1}$	$c_{\varepsilon 2}$
0.085	0.8	1.3	1.44	1.92

Table 4.3: Values of model constants used in the present work.

4.3.7 Low-Reynolds number k-ε model

The low-Reynolds number model of Lam and Bremhorst (1981) uses the standard k equation but a modified expression for the dissipation rate.

$$\frac{D\varepsilon}{Dt} = \frac{\partial}{\partial x_j}\left[\left(\nu_L + \frac{\nu_t}{\sigma_\varepsilon}\right)\frac{\partial \varepsilon}{\partial x_j}\right] + \frac{c_{\varepsilon 1} f_1 \nu_t}{k}\varepsilon\left(\frac{\partial \overline{u}_i}{\partial x_j} + \frac{\partial \overline{u}_j}{\partial x_i}\right)\frac{\partial \overline{u}_i}{\partial x_j} - c_{\varepsilon 2} f_2 \frac{\varepsilon^2}{k} \qquad (4.27)$$

and the turbulent eddy viscosity, ν_t is given by the equation:

$$\nu_t = \frac{c_\mu f_\mu k^2}{\varepsilon} \qquad (4.28)$$

where c_μ is a model constant and f_μ is a function used as a multiplier in the turbulent eddy viscosity relationship to mimic the direct effect of molecular viscosity on the shear stress.

$$f_\mu = \left(1 - e^{-A_\mu R_k}\right)^2 \left(1 + \frac{A_t}{R_t}\right) \tag{4.29}$$

$$f_1 = 1 + \left(\frac{A_{C1}}{f_\mu}\right)^3 \tag{4.30}$$

$$f_2 = 1 - e^{-R_t^2} \tag{4.31}$$

Where A_t, A_{C1}, A_μ are constants equal to 20.5, 0.05 and 0.0165 respectively; R_k is the turbulence Reynolds number defined as $= \sqrt{k}z/\nu_L$ and R_t is the turbulence Reynolds number defined as $= k^2/(\nu_L \varepsilon)$ and ν_L is the kinematic (molecular) viscosity.

There are many different proposed forms for low-Reynolds number models, for example see Patel *et al.* (1985), however, the Lam and Bremhorst model has been shown (see Patel *et al.* 1985) to be one of the better formulations for steady flow conditions and this form of low Reynolds number model was adapted for wave boundary layer flows. Whilst such a formulation is inappropriate for fully developed turbulent flow, in laminar and transitional boundary layers such models may well be of use. Tanaka and Sana (1994) compared several low-Reynolds number models to the experimental wave boundary layer data of Jensen *et al.* (1989) for a smooth bed. Tanaka and Sana found that the original Jones and Launder (1972) model gave the best results when compared with experimental data for transitional flow. However, Rodi (1991) has shown that by using the standard k-ε model in that part of the flow away from the wall and using a one-equation model to simulate the viscosity-affected near-wall region a more computationally efficient and robust model can be created. Further, such hybrid models have in many instances either been as good as or have out-performed both high- and low-Reynolds k-ε models.

4.3.8 Two-layer model

The two-layer model employed in the present work uses a standard high-Reynolds number k-ε model to describe the flow away from the wall. The viscosity-affected near-wall region is

modelled using a one-equation k-model with the turbulent eddy-viscosity and the dissipation rate ε determined by the following equations (see Rodi 1991):

$$\nu_t = c_\mu \sqrt{k} l_\mu \tag{4.32}$$

$$\varepsilon = \frac{k^{3/2}}{l_\varepsilon} \tag{4.33}$$

The length scales l_μ and l_ε behave in the same manner in the log-law region, where they vary linearly. However, very close to the wall, they both deviate from the linear distribution and this deviation is different for the two functions. The damping of the eddy viscosity very close to the wall is brought about by the use of an exponential function (see Eq. 4.34).

$$l_\mu = C_l z\left(1 - \exp\left(-\frac{R_k}{A_\mu}\frac{25}{A^*}\right)\right) \tag{4.34}$$

Where C_l and A_μ are constants and C_l is defined as:-

$$C_l = \kappa c_\mu^{-3/4} \tag{4.35}$$

and c_μ is a constant defined as previously (see Section 4.3.6) and κ is the von Karman constant. A_μ is given a value of 50.5 (after Rodi 1991). However, other researchers have employed different values: Chen and Patel (1988; 1989) use a value of 70.0 and Iacovides and Launder (1990) a value of 62.5. R_k is the turbulence Reynolds number and is defined as $= \sqrt{k} z/\nu_L$. A^* is a parameter that is kept constant in the present model ($A^* = 25$), but which Fujisawa *et al.* (1990) allow to vary (see Rodi 1991).

Rodi (1991) points out that the damping of the turbulent eddy-viscosity caused by the exponential function in Eq. (4.34) is not actually a viscous effect, but is due to the near-wall reduction of the normal fluctuations $\overline{w'^2}$ caused by a pressure-strain mechanism.

The other length scale term is given by the equation:

$$l_\varepsilon = \frac{C_l z}{\left(1 + \frac{5.3}{R_k}\right)} \tag{4.36}$$

Eq. (4.36) was proposed by Norris (1975).

More recently Rodi *et al.* (1993) presented a new one-equation model based on the suggestion by Durbin (1991) that in near-wall shear layers, the normal fluctuations $\left(\overline{w'^2}\right)^{1/2}$ may be a better velocity scale than $k^{1/2}$ and that no damping functions may be required using this approach. However, this suggestion has not been developed further during the present work.

4.4 The k model

In addition to the k-ε model, a one-equation k model has also been used in the present work. The transport equation employed is identical to Eq. (4.10) with the dissipation term being described by the equation:-

$$\varepsilon = \frac{c_\mu k^{1.5}}{l} \tag{4.37}$$

The mixing length, l, has been described by both a time-dependent expression (Vager and Kagan 1969) and a simple time-independent expression.

Vager and Kagan (1969) suggested the following expression:

$$l = -\kappa \frac{\sqrt{k}}{l} \left\{ \frac{\partial}{\partial z} \left(\frac{\sqrt{k}}{l} \right) \right\}^{-1} \tag{4.38}$$

This equation can be integrated to give the following

$$l = \kappa \sqrt{k} \left\{ \int_{z_0}^{z} k^{-0.5} dz + z_0 k_0^{-0.5} \right\} \tag{4.39}$$

where κ is the von Karman constant; z_0 is defined as the vertical level at which point the velocity is assumed to be zero (see Eq. 2.35); and k_0 is the value of turbulent kinetic energy at z_0. Eq. (4.39) is an expression which is more easily applied than Eq. (4.38).

The time-independent mixing-length expression used is a simple linear assumption

$$l = \kappa z \tag{4.40}$$

4.5 Boundary conditions

For monochromatic waves:

The boundary conditions for the k-equation are taken as:

$$k(z_0,t) = \frac{1}{\sqrt{c_\mu}} \nu_t \left| \frac{\partial \bar{u}}{\partial z} \right| \qquad \textbf{(4.41a)}$$

$$\frac{\partial k}{\partial z}(z_{top},t) = 0 \qquad \textbf{(4.41b)}$$

where z_0 and z_{top} are defined as previously (see Chapter 2).

The bed condition for the k equation is derived from steady rough turbulent boundary layer information. Unlike a smooth bed, the turbulent velocity fluctuations do not disappear at a hydraulically rough bed. The upper boundary condition assumes that the gradient of the turbulent kinetic energy is zero. In the case of the two-layer model, the lower boundary condition for the turbulent kinetic energy transport equation is usually given as:

$$k(z_0,t) = \frac{\partial k}{\partial z}(z_0,t) = 0 \qquad \textbf{(4.41c)}$$

The boundary conditions for the ε equation follow from Rodi (1980).

$$\varepsilon(z_0,t) = (c_\mu)^{3/4} \frac{k^{3/2}}{\kappa z} \qquad \textbf{(4.42a)}$$

$$\frac{\partial \varepsilon}{\partial z}(z_{top},t) = 0 \qquad \textbf{(4.42b)}$$

In a two-layer model the lower boundary condition becomes:

$$\varepsilon(z_0,t) = \nu_L \left(\frac{\partial^2 k}{\partial z^2} \right) \qquad \textbf{(4.42c)}$$

4.6 Random seas

In a real sea the elevation of the water surface (measured from mean-water-level, mwl) is a random process with waves travelling in many different directions. However, whilst the generation of upper boundary conditions is more complex the underlying principles are the

same as for monochromatic waves. It is necessary to treat the problem statistically and it is useful to review statistical wave theory before writing the equation for the upper boundary condition. The following is based on Tickell (1985).

However, before reviewing the statistical approach it is important to outline all the methods available for arriving at boundary conditions for the numerical models. The spectral approach is based on using an actual measured spectrum or generating a spectrum using the techniques described below. Alternatively, it is possible to drive the model using a Fourier transformation of an actual velocity time-series. This enables the free stream velocity time-series to be reproduced exactly and also permits the boundary layer models to be run for real situations.

For a narrow-banded process it is possible to approximate η, the surface elevation, as the sum of a large number of linear regular waves all propagating in the x-direction such that:-

$$\eta(x,t) = \sum_{n+1}^{N} a_n \cos(k_n x - \omega_n t + \delta_n) \qquad \textbf{(4.43)}$$

Where:- a_n = the amplitude of the nth component
ω_n = the frequency of the nth component
k_n = the wave number of the nth component

The angles δ_n (with n = 1 to N) allow for arbitrary phase relationships between the various components. If the random independent variables are drawn from a uniform distribution between 0 and 2π , then the probability density function (pdf), $p(\delta)$ is given by:-

$$p(\delta) = \frac{1}{2\pi} \qquad \textbf{(4.44)}$$

Assuming that the process is Gaussian (an assumption which is valid for a large number of components), then the probability density of η is given by the equation:-

$$p(\eta) = \frac{\exp\left[-\eta^2/2\sigma_\eta^2\right]}{\sqrt{2\pi}\sigma_\eta} \qquad \textbf{(4.45)}$$

where σ_η is the standard deviation and σ_η^2 is the variance of η, respectively. In addition, the mean of η is zero (see Figure 4.4).

Considering the n^{th} component and taking δ_n and x to be fixed, enables the variance of the component to be calculated as:-

$$\overline{\sigma_n^2} = \frac{1}{T_n}\int_0^{T_n} a_n^2 \cos^2(-\omega_n t)dt = \frac{a_n^2}{2} \qquad \textbf{(4.46)}$$

Since the phase angles, δ_n are independent of the various components then

$$\sigma_\eta^2 = \sum_{n=1}^{N} \frac{a_n^2}{2} \qquad \textbf{(4.47)}$$

The wave spectrum can now be defined as the distribution of surface-elevation variance with frequency. If the total frequency range is divided into N intervals each of width $\Delta\omega$, and defining the spectral density, $S_\eta(\omega)$, such that the variance associated with the band centred on the frequency ω_n is $S_\eta(\omega_n)\Delta\omega$, then it follows that:-

$$S_\eta(\omega_n)\Delta\omega = \frac{a_n^2}{2} \qquad \textbf{(4.48)}$$

For a real sea, the number of component waves is considerable, ensuring that N approaches infinity. Further, combining equations (4.47) and (4.48) gives:-

$$\sigma_\eta^2 = \int_0^\infty S_\eta(\omega_n)d\omega \qquad \textbf{(4.49)}$$

However, from Eq. (4.45) if $\eta(x,t)$ is a Gaussian process it can be shown that the wave heights follow a Rayleigh distribution and:

$$p(H) = \frac{H}{4\sigma_\eta^2}\exp\left[-\frac{H^2}{8\sigma_\eta^2}\right] \qquad \textbf{(4.50)}$$

where H is the wave height.

From Eq. (4.50) it is possible to express the root-mean-square (rms) wave height by the equation:-

$$H_{rms} = \left[\int_0^\infty H^2 p(H)dH\right]^{\frac{1}{2}} = 2\sqrt{2}\sigma_\eta \qquad \textbf{(4.51)}$$

Therefore, the variance of η, σ_η^2 can be expressed as:-

$$\sigma_\eta^2 = \frac{H_{rms}^2}{8} \qquad \textbf{(4.52)}$$

Returning to Eq. (4.43) and substituting for a_n enables the simulation of water elevations in a random sea, provided the form of the spectrum can be defined.

$$\eta(x,t) = \sum_{n=1}^{N} \left(2S_\eta(\omega_n)\Delta\omega\right)^{0.5} \cos(k_n x - \omega_n t + \delta_n) \tag{4.53}$$

At a point (x = 0) equation (3.75) reduces to:

$$\eta(t) = \sum_{n=1}^{N} \left(2S_\eta(\omega_n)\Delta\omega\right)^{0.5} \cos(-\omega_n t + \delta_n) \tag{4.54}$$

Eq. (4.54) can be further simplified as follows:-

From the surface spectrum the co-cumulative spectrum can be calculated by integrating the area under the former (see Figure 4.6). Dividing the vertical axis $\int S_\eta(\omega)d\omega$ into elements of equal energy leads to (see Figure 4.6):-

$$\begin{aligned} \text{Area} \Rightarrow & \int_{\omega_{LC}}^{\omega_n} S_\eta(\omega)d\omega - \int_{\omega_{LC}}^{\omega_{n-1}} S_\eta(\omega)d\omega \\ & = \frac{1}{N}\int_{\omega_{LC}}^{\omega_{UC}} S_\eta(\omega)d\omega = \frac{\sigma_\eta^2}{N} \end{aligned} \tag{4.55}$$

Where subscripts LC and UC are the lower and upper cut-off values of the spectrum and σ_η^2 is the variance of η.

$$\therefore \sum_{n=1}^{N} \frac{a_n^2}{2} = \sum_{n=1}^{N} \frac{\sigma_\eta^2}{N} \tag{4.56}$$

However, to avoid periodicity in the simulated time-series σ_η^2/N is made constant. The periodicity will occur because if the range of ω is, say, 0 to ω_C, where ω_C is the upper limit of the surface spectrum, then $\Delta\omega = \omega_C/N$ will give ω_n values which will cause the repetition of $\eta(t)$ within a finite period. However, if a_n is chosen to be a constant and equal to $2\sigma_\eta^2/N$, the corresponding ω_n values will be spaced at non-linear intervals (see Figure 4.6) and thus the cyclic behaviour of $\eta(t)$ will be eliminated (Borgman 1969).

$$\eta(t) = \sqrt{\frac{2\sigma_\eta^2}{N}} \sum_{n=1}^{N} \cos(-\omega_n t + \delta_n) \tag{4.57}$$

To simulate a velocity time-series from the surface spectrum, the horizontal velocity component of a water particle located a distance z below mean-sea-level in water of depth D is given by linear wave theory as:-

$$u(t) = \sum_{n=1}^{N} a_n \left(\frac{\omega_n \cosh k_n (z+D)}{\sinh k_n D} \right) \cos(-\omega_n t + \delta_n) \qquad \textbf{(4.58)}$$

However, assuming the boundary layer to be very small compared to the depth then z = -D, therefore:

$$u_0(t) = \sqrt{\frac{2\sigma_\eta^2}{N}} \sum_{n=1}^{N} \left(\frac{\omega_n}{\sinh k_n D} \right) \cos(-\omega_n t + \delta_n) \qquad \textbf{(4.59)}$$

substituting for a_n as well.

Equation (4.59) therefore provides the random driver in the boundary layer model and forms the upper velocity boundary condition. The other boundary conditions remain unchanged. The final choice to be made is what type of spectrum to apply to drive the model.

4.7 Wave spectra

4.7.1 Introduction

The type of spectra used to describe random waves can take many forms (see Huang *et al.* (1990)). Two of the most commonly applied methods are those proposed by Pierson and Moskowitz (1964) and Hasselmann *et al.* (1973; 1976). The Pierson-Moskowitz (P-M) spectrum is based on extensive field data and is designed to represent a fully developed sea state. In reality, only a small percentage of observed spectra fulfil this proposed form (≈10%) indicating that fully developed sea states are perhaps not that easily achieved.

The work of Hasselmann *et al.* (1973; 1976) was based on an extensive field experiment, the **J**oint **N**orth **S**ea **W**ave **P**roject, and has commonly become known as the JONSWAP spectrum. This spectrum is a general form of the P-M spectrum allowing for a developing sea while the original form of the spectrum was dependent on the wind speed and fetch.

However, whilst the above spectral formulations can be used to represent single peaked spectra, they are unable to describe spectra that exhibit two peaks. The so-called double-peaked spectrum arises when both swell and wind seas are present simultaneously or when a changing wind direction creates a developing wave system. Guedes Soares (1984) proposed a four-parameter representation of such spectra based on a JONSWAP approach. Guedes Soares compared the theoretical formulation with data from the North Atlantic and North Sea, showing a good fit.

Through the use of the above spectral formulations it is therefore possible to describe the majority of sea states encountered on the continental shelf. In addition, by using the techniques described below it is possible to provide appropriate upper boundary conditions for the model. However, whilst the methods chosen appear to be able to adequately represent developing and fully developed seas as well as seas of a double-peaked nature, they are not the only methods available. A full review of spectral representation is outside the scope of the present work but a good general review is provided by Huang *et al.* (1990).

4.7.2 The Pierson-Moskowitz (P-M) spectrum

The Pierson-Moskowitz spectrum is defined by the equation:-

$$S_\eta(\omega) = \frac{Ag^2}{\omega^5}\exp\left[\frac{-B\omega_0^4}{\omega^4}\right] \qquad \textbf{(4.60)}$$

Where A and B are constants and are equal to 0.0081 and 0.74 respectively; g is the acceleration due to gravity and ω is the wave angular frequency. In addition, ω_0 , is defined by

$$\omega_0 = \frac{g}{U_{19.5}} \qquad \textbf{(4.61)}$$

where $U_{19.5}$ is the wind speed at 19.5m above mean sea level.

If it is required to express the P-M spectrum in terms of significant wave height, H_S and zero crossing period, T_Z then paramaterized versions of the formulation exist. One such formulation is the Det Norske Veritas (DNV) spectrum defined as:-

$$S_\eta(\omega) = \frac{H_S^2 T_Z}{8\pi^2}\left[\frac{T_Z\omega}{2\pi}\right]^{-5} \exp\left[-\frac{1}{\pi}\left(\frac{T_Z\omega}{2\pi}\right)^{-4}\right] \tag{4.62}$$

A typical P-M spectrum as generated by the model formulation is shown in Figure 4.7.

4.7.3 The JONSWAP spectrum

The JONSWAP spectrum has the form:

$$S_\eta(\omega) = \frac{2\pi\alpha g^2}{\omega^5}\exp\left\{-1.25\left(\frac{\omega_p}{\omega}\right)^4\right\}\gamma^q \tag{4.63}$$

Where

$$\alpha = 0.076\left(\frac{gF}{U_{10}^2}\right)^{-0.22} \tag{4.64}$$

$$q = \exp\left[-\frac{(\omega-\omega_p)^2}{2\sigma^2\omega_p^2}\right] \tag{4.65}$$

and

$$\sigma = \begin{cases} 0.07 & \omega \le \omega_p \\ 0.09 & \omega > \omega_p \end{cases} \tag{4.66}$$

$$\gamma = 3.3$$

where F is the wave generation fetch.

The value of 3.3 for the peak enhancement factor, γ, is an averaged value derived by Hasselmann *et al.* (1973). However, Hasselmann *et al.* found a range of values for γ between 1 and 6. Figure 4.8 shows an example of a JONSWAP spectrum

4.7.4 Double-peaked spectra

Guedes Soares (1984) proposed a four parameter representation for a double-peaked spectrum based on a two-parameter description of a JONSWAP spectrum. Guedes Soares chose to model both the wind and swell seas using two JONSWAP spectra. The wind sea is in a developing state which makes such a choice appropriate, however, the choice to use a

JONSWAP spectrum for a swell sea was based on the narrowness of such sea spectra. Once the shape of the two spectral components has been defined, a double-peaked spectrum is totally described by knowing the ratios of the peak frequencies and spectral peaks. The spectrum is therefore defined as:

$$S_\eta(\omega) = S_{\eta S}(\omega) + S_{\eta W}(\omega) \qquad \textbf{(4.67)}$$

Where $S_{\eta S}(\omega)$ and $S_{\eta W}(\omega)$ are the swell and wind sea components respectively.

Also, the moments of the sea spectrum must be equal to the sum of the moments of the individual components. Hence,

$$M_0 = M_{0S} + M_{0W} \qquad \textbf{(4.68a)}$$

$$M_1 = M_{1S} + M_{1W} \qquad \textbf{(4.68b)}$$

Where M_0 and M_1 are the zeroth and first moments of the wave spectrum; M_{0S} and M_{0W} are the zeroth moments of the swell and wind components of the double peak spectrum; and M_{1S} and M_{1W} are the first moments of the swell and wind components of the double peak spectrum. Further, the moment of a spectrum is given by the equation:-

$$M_{i_k} = \int_0^\infty \omega^i S_k(\omega) d\omega \qquad \textbf{(4.69)}$$

which defines the ith moment of spectrum k.

In turn, it is possible to relate these quantities to the significant wave height, H_S , and the zero-crossing period, T_Z.

$$H_S = 4\sqrt{M_0} \qquad \textbf{(4.70)}$$

$$T_Z = \frac{1}{2\pi}\frac{M_0}{M_1} \qquad \textbf{(4.71a)}$$

normally T_Z, is defined by the equation:-

$$T_Z = 2\pi\sqrt{\frac{M_0}{M_2}} \qquad \textbf{(4.71b)}$$

However, in the present work Eq. (4.71a) is applied, as suggested by Guedes Soares (1984).

Using these expressions and substituting into Eqs. (4.68a) and (4.68b) gives the following equations:

$$H_{SW} = H_S \sqrt{\frac{1}{\left(1 + H_R^2\right)}} \tag{4.72}$$

$$H_{SS} = H_S \sqrt{\frac{H_R^2}{\left(1 + H_R^2\right)}} \tag{4.73}$$

$$T_{ZW} = \left(\frac{1 + \left(H_R^2 / T_R \right)}{1 + H_R^2} \right) T_Z \tag{4.74}$$

$$T_{ZS} = \left(\frac{T_R + H_R^2}{1 + H_R^2} \right) T_Z \tag{4.75}$$

where H_R and T_R are defined as:-

$$H_R = \frac{H_{SS}}{H_{SW}} \tag{4.76}$$

$$T_R = \frac{T_{ZS}}{T_{ZW}} \tag{4.77}$$

Figure 4.9 shows a typical double-peaked spectrum as generated by the model.

4.7.5 Multi-directional seas

It is not sufficient to describe sea waves from their frequency spectra alone. To do so would describe so-called long-crested waves, waves having straight parallel crest lines when viewed from above. However, from the patterns of wave crests in most seas, it is clear that they consist of many component waves propagating in various directions, so-called short-crested seas.

Researchers have therefore introduced the concept of directional spectra allowing the description of superimposed directional components. The directional spectrum enables not just the representation of wave energy in the frequency domain, but also in direction and generally takes the form:

$$S(\omega,\theta) = S(\omega)G(\omega,\theta) \tag{4.78}$$

where $S(\omega,\theta)$ is the directional wave spectrum ; $S(\omega)$ is the frequency spectrum; $G(\omega,\theta)$ is a directional spreading function and θ is the wave direction.

The spreading function $G(\omega,\theta)$ represents the directional distribution of wave energy and has been shown to vary with frequency. It is a dimensionless function, normalized as :

$$\int_{-\pi}^{\pi} G(\omega,\theta)d\theta = 1 \qquad \textbf{(4.79)}$$

4.7.5.1 The directional spreading function

The difficulty in making reliable field measurements has hindered the understanding of how the directional energy of sea waves is distributed. Various expressions to represent the spreading function have been proposed and Huang *et al.* (1990) present a comprehensive review of existing methods.

The earliest model of the form of the directional spectrum was suggested by Arthur (1949). This idea was taken up by Pierson *et al.* (1955) who developed a cosine-squared directional spreading function which is independent of frequency and takes the form:-

$$G(\omega,\theta) = \frac{2}{\pi}\cos^2\theta \qquad \textbf{(4.80)}$$

The directional spectral analysis of sea surface contours obtained using stereophotogrammetry in the SWOP project (Stereo Wave Observation Project) resulted in Cote *et al.* (1960) proposing a spreading function of the following form:-

$$G(\omega,\theta) = \frac{1}{\pi}\left\{1+\left(0.50+0.82\exp\left[-\frac{1}{2}\left(\frac{\omega}{\omega_o}\right)^4\right]\right)\cos 2\theta + 0.32\exp\left[-\frac{1}{2}\left(\frac{\omega}{\omega_o}\right)^4\right]\cos 4\theta\right\} \quad \text{for } |\theta| \le \frac{\pi}{2} \qquad \textbf{(4.81)}$$

$$G(\omega,\theta) = 0 \quad \text{for } |\theta| > \frac{\pi}{2} \qquad \textbf{(4.82)}$$

Where $\omega = 2\pi f$ and $f = 1/T$; $\omega_o = g/U_{5.0}$ and $U_{5.0}$ is the wind speed at 5.0 m above the sea surface.

It has been suggested (see Huang *et al.* 1990) that the form of these two proposed distributions for the directional spreading function are unrealistic since they give equal directional divergence to all wave components. Huang *et al.* (1990) point out that the short waves in a wind wave field have greater directional diversity than the main energy-containing components.

Mitsuyasu *et al.* (1975) proposed the following expression based on detailed field measurements with a cloverleaf buoy (see also Cartwright and Smith 1964) as well as with other available field data.

$$G(\omega,\theta) = G_0 \cos^{2s}\left(\frac{\theta}{2}\right) \tag{4.83}$$

The function, G_0, was introduced to satisfy the condition given by Eq. (4.79). G_0 is given by the equation:

$$G_0 = \left\{ \int_{\theta_{min}}^{\theta_{max}} \cos^{2s}\left(\frac{\theta}{2}\right) d\theta \right\}^{-1} \qquad \text{(All about } \bar{\theta} = 0\text{)} \tag{4.84}$$

where s is a parameter related to the frequency and represents the degree of directional energy concentration and θ_{min} and θ_{max} represent the range of directional spread (typically $\pi/2$ to $-\pi/2$). The parameter, s , has a peak value close to the frequency of the spectral peak. In the original paper Mitsuyasu *et al.* relate s to the wind speed.

$$s = \begin{cases} s_{max}\left(\omega/\omega_p\right)^5 & \left(\omega \le \omega_p\right) \\ s_{max}\left(\omega/\omega_p\right)^{-2.5} & \left(\omega > \omega_p\right) \end{cases} \tag{4.85}$$

where ω_p is the angular frequency at the spectral peak and s_{max} is defined by the equation:-

$$s_{max} = 11.5\left(\frac{\omega_p U_{10}}{g}\right)^{-2.5} \tag{4.86}$$

Because of limited field data, the directional distribution function is not considered fully validated. However, Goda *et al.* (1979) suggested the following values for s_{max}.

$$s_{max} = \begin{cases} 10 & \text{(wind waves)} \\ 25 & \text{(swell with short decay distance)} \\ 75 & \text{(swell with long decay distance)} \end{cases} \tag{4.87}$$

It is the Mitsuyasu *et al.* (1975) approach for representing a directional spreading function that has been used in the present study. However, whilst other similar expressions exist, without better theoretical guidance for defining the angular spreading function use of any more elaborate scheme is unwarranted (see Huang *et al.* 1990). Without more detailed field data and a greater understanding of air-sea interaction processes, further advancement on developing improved spectral forms for directional seas will be slow.

4.7.6 The effect of currents on wave spectra

In order to describe the effect of a current on random waves it is useful to consider briefly the effects of a current on a regular wave train. However, the following is not intended to provide a full description of those effects and the reader should consult more detailed texts such as Hedges (1981; 1987), Hedges *et al.* (1985), Hedges *et al.* (1993) and Jonsson (1978b; 1990).

Consider a train of regular waves travelling on a current, U which is constant with depth. The current is travelling at an angle, α, to the wave crests and is positive if the component along the wave orthogonal is in the direction of wave propagation (see Figure 4.10).

To an observer who is stationary, the waves appear to be moving with celerity C_a and there is a current velocity $U\sin\alpha$ in the direction of wave propagation (Figure 4.11). However, to an observer who is moving with the wave orthogonal at velocity $U\sin\alpha$ apparently the waves have celerity C_r and there is no current. Therefore,

$$C_r = C_a - U\sin\alpha \qquad \textbf{(4.88)}$$

The waves pass the stationary observer with period T_a

$$C_a = \frac{L}{T_a} \qquad \textbf{(4.89)}$$

and to the moving observer with period T_r

$$C_r = \frac{L}{T_r} \qquad \textbf{(4.90)}$$

From Eq. (4.88) the following expression can be obtained by multiplying through by the wave number, k $(= 2\pi/L)$ where L is the wavelength.

$$\omega_r = \omega_a - kU\sin\alpha \qquad \textbf{(4.91)}$$

Where $\omega_r = 2\pi/T_r$ is the angular frequency in the moving frame of reference and $\omega_a = 2\pi/T_a$ is the apparent wave angular frequency as seen by the stationary observer.

Substituting for C_a and C_r in Eq. (4.88) leads to the expression:

$$\frac{1}{T_r} = \frac{1}{T_a}\left(1 - \frac{T_a U \sin\alpha}{L}\right) \tag{4.92}$$

In deep water, the wavelengths become L_{or} and L_{oa} for the moving frame of reference and the stationary observer, respectively.

where

$$L_{or} = \frac{gT_r^2}{2\pi} \tag{4.93}$$

and

$$L_{oa} = \frac{gT_a^2}{2\pi} \tag{4.94}$$

The interactions of currents with random waves are more complex than with regular waves. Huang *et al.* (1972) were the first to describe the changes in wave spectra due to currents. However, their formulation ignored the increased level of wave breaking observed when an opposing current is met.

The wave energy density, $\overline{E}$ is given by:-

$$\overline{E} = \frac{1}{8}\rho g H^2 \tag{4.95}$$

where H is the wave height and ρ and g are the fluid density and acceleration due to gravity, respectively.

Bretherton and Garrett (1969) and Bretherton (1971) showed that the conservation of wave action, defined as $\overline{E}/\omega_r$, is governed by the equation:

$$\frac{\partial}{\partial t}\left(\frac{\overline{E}}{\omega_r}\right) + \frac{\partial}{\partial x}\left\{\left(U + C_{gr}\right)\frac{\overline{E}}{\omega_r}\right\} + \frac{\partial}{\partial y}\left\{\left(U + C_{gr}\right)\frac{\overline{E}}{\omega_r}\right\} = 0 \tag{4.96}$$

where C_{gr} is the relative wave group velocity.

In steady state Eq. (4.96) reduces to:-

$$\frac{\partial}{\partial x}\left\{\left(U+C_{gr}\right)\frac{\overline{E}}{\omega_r}\right\}=0 \tag{4.97}$$

Considering one wave component in both a zero current region and a region where a steady current exists then:-

$$\frac{\overline{E}_0 C_{g0}}{\omega_a}=\frac{\overline{E}\left(U+C_{gr}\right)}{\omega_r} \tag{4.98}$$

where subscript '0' represents a quantity existing in the zero current area. Eq. (4.98) can be arranged as:-

$$\overline{E}=C_{g0}\frac{\omega_r}{\omega_a}\frac{1}{\left(U+C_{gr}\right)}\overline{E}_0 \tag{4.99}$$

Considering the spectral density of the surface elevation in a fixed frame of reference in the current area, $S_\eta(\omega_a,U)$ and noting that ω_a is the same in both regions then:-

$$S_\eta(\omega_a,U)d\omega_a=C_{g0}\frac{\omega_r}{\omega_a}\frac{1}{\left(U+C_{gr}\right)}S_\eta(\omega_a)d\omega_a \tag{4.100}$$

$$\therefore\quad S_\eta(\omega_a,U)=C_{g0}\frac{\omega_r}{\omega_a}\frac{1}{\left(U+C_{gr}\right)}S_\eta(\omega_a) \tag{4.101}$$

where

$$C_{g0}=\frac{1}{2}\left(1+\frac{2k_0D}{\sinh 2k_0D}\right)\frac{\omega_a}{k_0} \tag{4.102}$$

and

$$C_{gr}=\frac{1}{2}\left(1+\frac{2kD}{\sinh 2kD}\right)\frac{\omega_r}{k} \tag{4.103}$$

Therefore the spectral density for the surface wave in the current region, $S_\eta(\omega_a,U)$, is related to the value in the quiescent area, $S_\eta(\omega_a)$, through the expression (see Hedges *et al.* 1979):

$$\frac{S_\eta(\omega_a,U)}{S_\eta(\omega_a)}=\frac{\omega_r\left[1+\dfrac{2k_0D}{\sinh 2k_0D}\right]}{2k_0\left[U+\left(1+\dfrac{2kD}{\sinh 2kD}\right)\dfrac{\omega_r}{2k}\right]} \tag{4.104}$$

4.7.6.1 Equilibrium range constraint

Wave growth at a particular frequency and direction cannot continue indefinitely since wave breaking must occur, regardless of whether the spectrum is propagating in a current dominated area or not. There exists a range of frequencies, the equilibrium range, beyond which the spectrum becomes saturated. Phillips (1958) suggested an approach for calculating the equilibrium range spectrum for waves alone. Hedges *et al.* (1993) have suggested an expression which is valid for both long- and short-crested seas encountering a current flowing in or directly against the predominant wave direction. The expression can also be applied to waves propagating on still water.

Hedges *et al.* (1993) proposed

$$S_\eta(\omega_a,\theta,U) = \frac{B^* k^{-3}}{C'_{ga}} G_{ER}(\theta) \qquad \textbf{(4.105)}$$

Where, $G_{ER}(\theta)$ is a spreading function which describes the angular distribution of wave component energy within the equilibrium range; B^* is a non-dimensional constant and C'_{ga} is defined as:

$$C'_{ga} = U\sin\alpha + C_{gr} \qquad \textbf{(4.106)}$$

and C_{gr} is the magnitude of the relative group velocity and is defined by the expression:

$$C_{gr} = \frac{\omega_r}{2k}\left[1 + \frac{2kD}{\sinh 2kD}\right] \qquad \textbf{(4.107)}$$

For long-crested waves, $G_{ER}(\theta)$ is omitted from Eq. (4.105). Kitaigordskii *et al.* (1975) discuss possible forms for the function , $G_{ER}(\theta)$, however, there is a scarcity of information. Hedges *et al.* (1993) propose the following form for $G_{ER}(\theta)$:-

$$G_{ER}(\theta) = \frac{1}{\sigma^2_{\eta WA}} \int_0^\infty S_{\eta WA}(\omega_a,\theta,U)\,d\omega_a \qquad \textbf{(4.108)}$$

where $S_{\eta WA}(\omega_a,\theta,U)$ is the spectral density based on the assumption that wave action is conserved and $\sigma^2_{\eta WA}$ is the associated total variance of surface elevation. These results are valid for a general water depth.

4.8 Conclusions

The present chapter has described briefly the theory behind a number of different topics, the combination of which are required in order that a random wave boundary layer can be modelled. The turbulence transport equations employed in the hydrodynamic model have been outlined along with the necessary boundary conditions and values for any empirical constants used. Detailed discussion of many of the topics, in particular, the description of directional seas is outside the scope of the present work.

The turbulence closure schemes described are of varying complexity and all contain a number of simplifying assumptions. The simplest scheme described is the one-equation k closure. The most complex scheme is the two-layer k-ε closure, where the turbulence away from the near-wall is modelled with a standard high-Reynolds number approach, whilst in the near-wall region a one-equation model is used. To this author's knowledge, use of such models in investigating wave boundary layers is unique, although Utnes and Eidsvik (1995) have investigated oscillatory flow over ripples using a similar approach.

The description of most sea states encountered on the continental shelf has been enabled using the methods described in Section 4.7. This includes allowance for the effects of currents on wave spectra and representation of a directional sea.

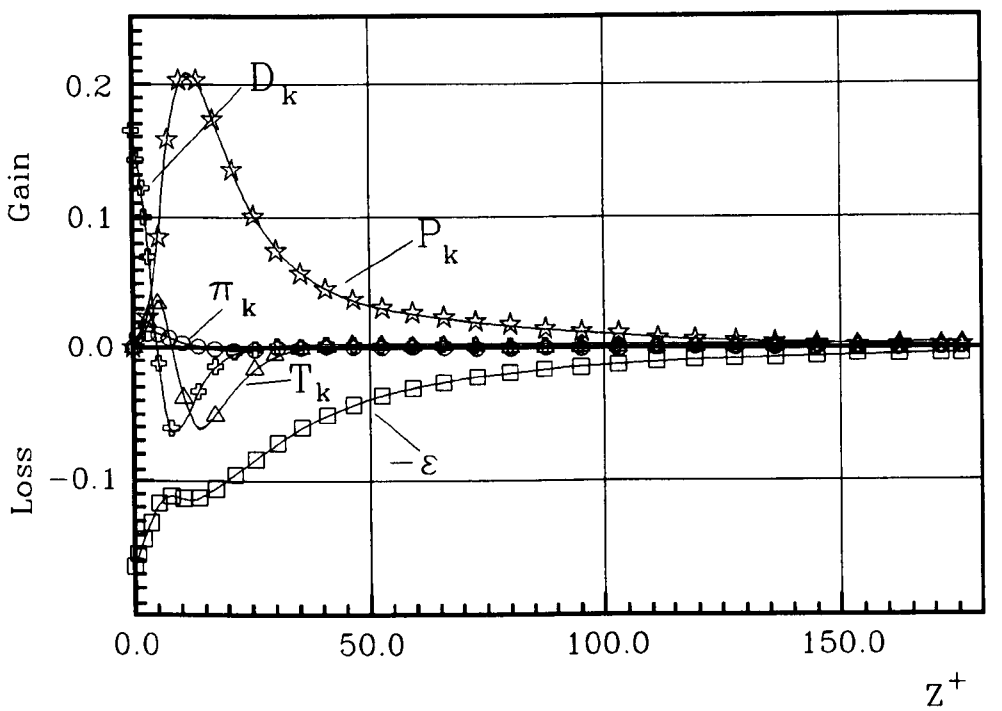

Figure 4.1: Terms in the exact equation of the turbulence kinetic energy, k for dimensionless height. (*After Mansour et al. 1987*).

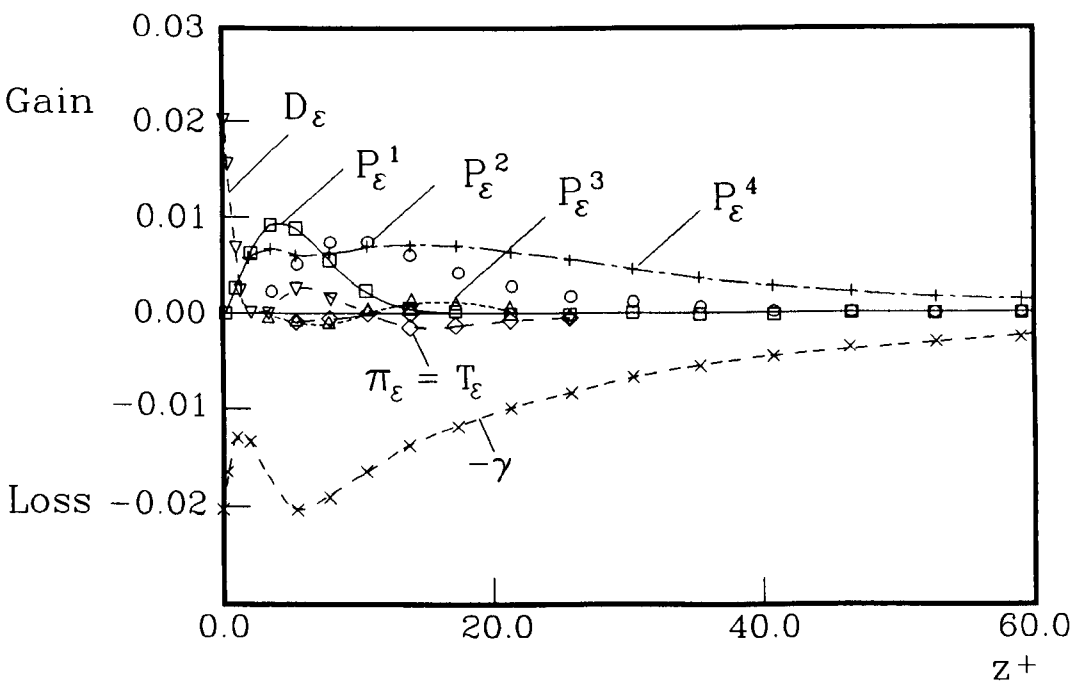

Figure 4.2: Terms in the exact equation of the dissipation rate, ε for dimensionless height (*After Mansour et al. 1987*).

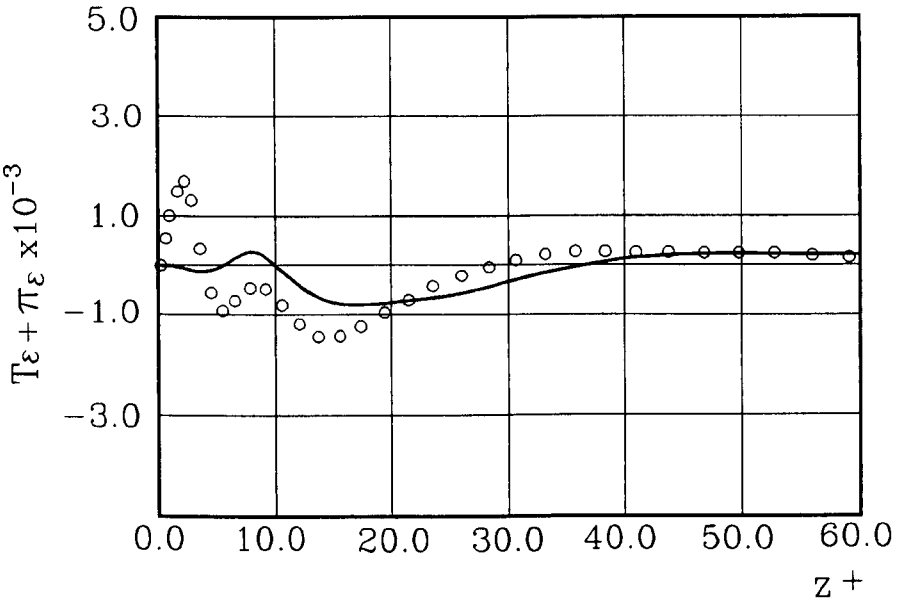

Figure 4.3: Plot showing a comparison of the turbulent transport rate of ε, for model of Mansour *et al.* against laboratory data. (*After Mansour et al. 1987*).

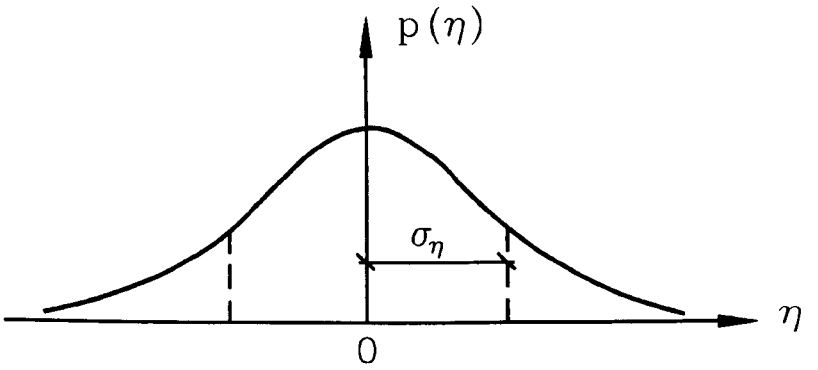

Figure 4.4: Figure showing the probability density of η.

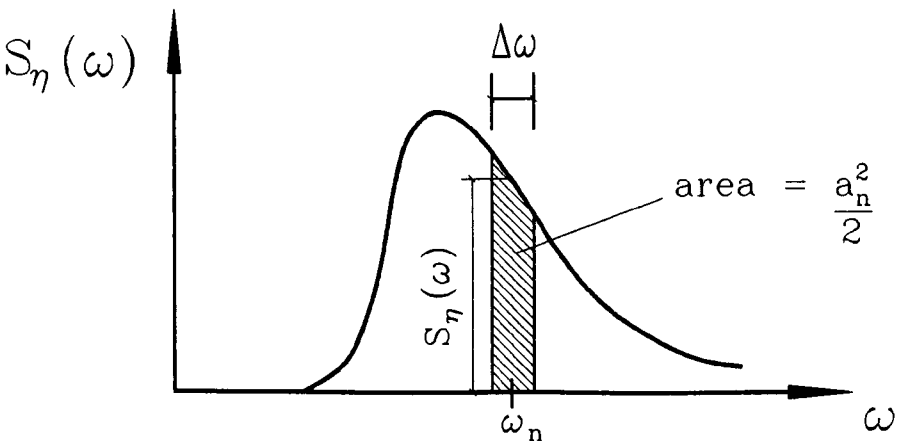

Figure 4.5: Figure showing the definition of the spectral density.

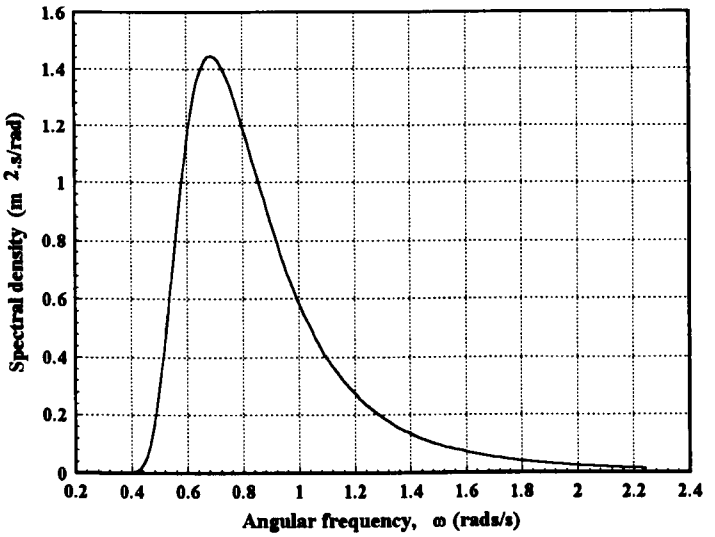

(a)

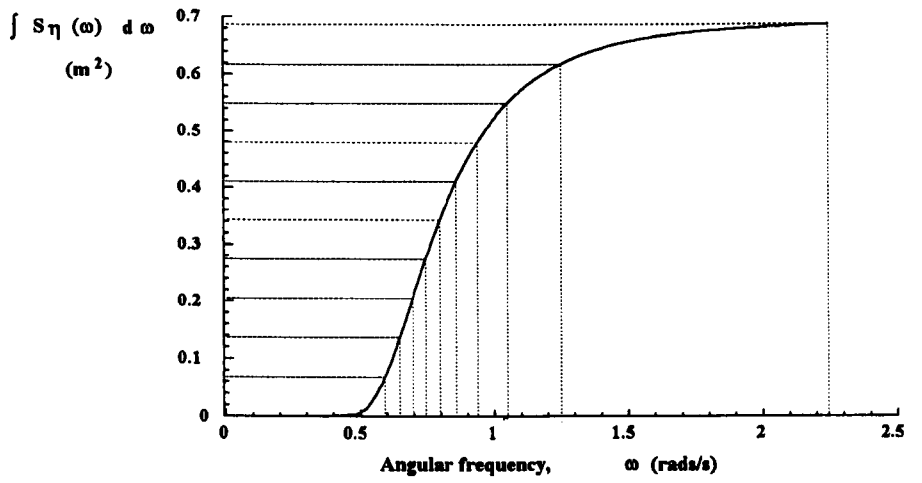

(b)

Figure 4.6 Figure showing the development of the co-cumulative spectrum (b) from the surface spectrum (a). The dashed lines show the division of the co-cumulative spectrum into segments of equal energy and hence unequal angular frequency components.

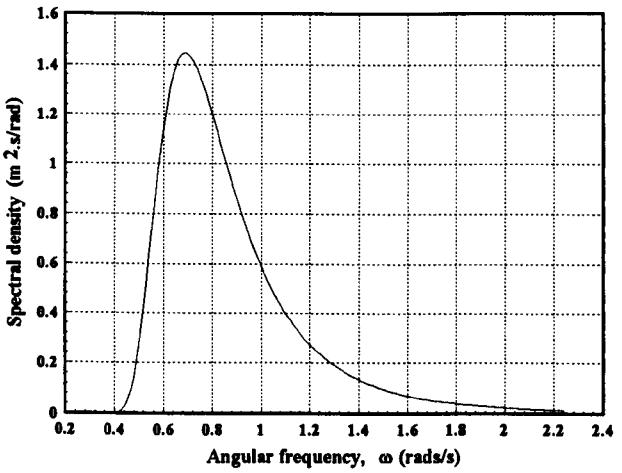

Figure 4.7: Pierson-Moskowitz spectrum.

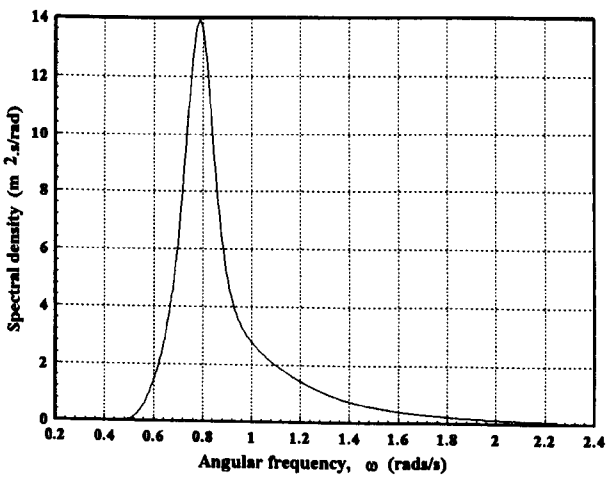

Figure 4.8: JONSWAP spectrum.

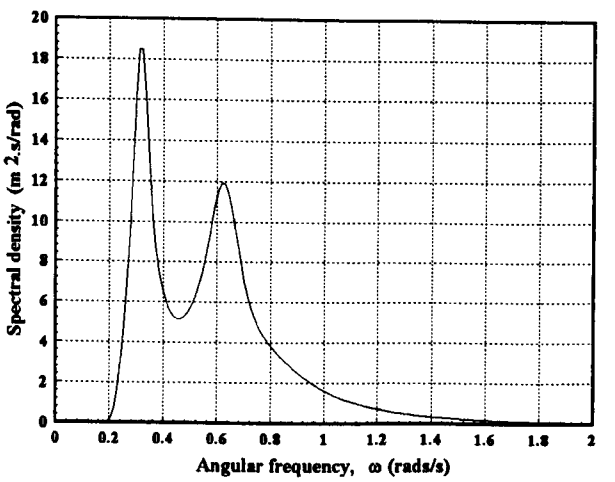

Figure 4.9: Double-peaked spectrum.

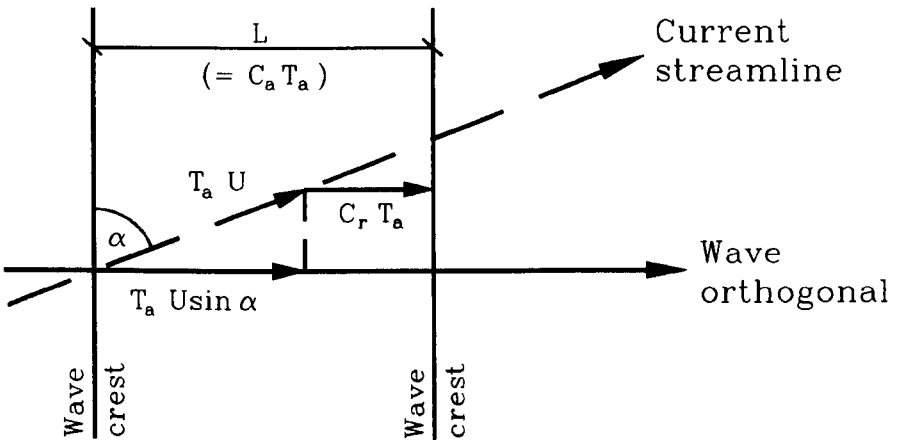

Figure 4.10: Sketch showing the wave and current directions. (*After Hedges 1987*).

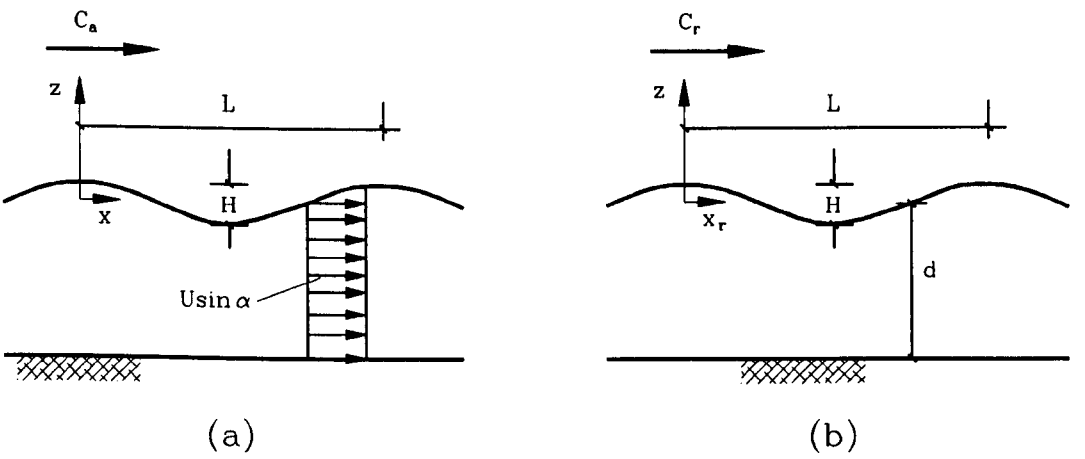

Figure 4.11: Sketch showing : (a) waves in a stationary frame of reference containing wave orthogonal; (b) waves in a moving frame of reference containing wave orthogonal. (*After Hedges 1987*).

Chapter 5
Numerical Scheme and Convergence

5.1 Introduction

The equations described in the previous chapters (Chapters 2 and 4) cannot be solved analytically and require numerical solution. There are two main methods for solving partial differential equations; finite-difference and finite-element methods. The present work will concentrate only on numerical solution using finite-difference methods.

The problem statement cannot be considered complete until the boundary and initial conditions have been specified. The boundary conditions for the equations of motion and turbulence transport have already been described in Chapters 2 and 4. In addition, because of the large velocity gradients present close to the seabed in wave and wave-current boundary layers, a logarithmic straining of the vertical co-ordinate, z, has been introduced to enable the near-bed velocities to be calculated without causing excessive numerical instability.

The accuracy of the numerical schemes introduced has been tested against the analytical solution of laminar flow presented by Lamb (1932). The results of these tests are presented and discussed.

5.2 Vertical grid transformation

It is necessary, when using turbulence models to model boundary layer flows, to ensure that there are a sufficient number of calculation points within the boundary layer. This requires that the calculation volume is divided into a large number of points, or a split grid is applied or a varying grid is applied. The first approach is all but impractical except for laboratory scale and even this could involve hundreds of grid points. The second method will result in numerical diffusion, the severity of which is dependent on the scale of the two grids applied.

The final approach allows for a grid which will be of a fine scale within the boundary layer and which will gradually become more coarse with distance from the bed.

The present work employs a logarithmic grid transform in the vertical such that real space, z is described by the equation:-

$$z = \left(\frac{D}{z_0}\right)^{\eta} z_0 \qquad \textbf{(5.1)}$$

Where D is the water depth; z_0 is the roughness height and η is transformed space in the vertical. A schematic showing the variable grid as represented in real space is given in Figure 5.1.

Within the numerical scheme the logarithmic grid transform is implemented through the replacement of $\partial/\partial z$ and $\partial^2/\partial z^2$ such that:-

$$\frac{\partial}{\partial z} = R\frac{\partial}{\partial \eta} \qquad \text{where} \quad R = \frac{C}{z} \qquad \textbf{(5.2)}$$

and

$$C = \frac{1}{\ln\left(\frac{D}{z_0}\right)} \qquad \textbf{(5.3)}$$

and

$$\frac{\partial^2}{\partial z^2} = R^2\left(-\frac{1}{C}\frac{\partial}{\partial \eta} + \frac{\partial^2}{\partial \eta^2}\right) \qquad \textbf{(5.4)}$$

For further details see Appendix C.

5.3 Numerical scheme

The solution of fluid flow problems through the use of numerical methods has become more general as digital computers have developed. The present problem requires the solution of non-linear partial differential equations for which the methodology is less well established. It is usual that a comparison is made with its linear counterpart when attempting to solve a non-

linear equation. In particular, the equations involved in the present work are of the parabolic type with a corresponding linear expression of the form:

$$\frac{\partial \tilde{u}}{\partial t} = \frac{\partial}{\partial z}\left(\nu_L \frac{\partial \tilde{u}}{\partial z}\right) \tag{5.5}$$

Various numerical methods exist for solving this equation. However, only finite difference methods are considered here. Within finite difference methods exist two sub-groups, explicit and implicit methods. For further details see Appendix C.

The numerical scheme used within the present work is the well known Crank-Nicolson semi-implicit method (Crank and Nicolson 1947). The scheme has the advantage of being unconditionally stable and offers higher-order accuracy (see also Abbott and Basco 1989).

The discretization of the equations is explained in Appendix C and will not be considered further in this chapter. However, Figure 5.2 shows a schematic of the semi-implicit Crank-Nicolson method as applied to the transformed space with an equal vertical grid spacing of $\Delta\eta$.

5.4 Numerical stability and convergence

The non-linear equations used to describe the physics require numerical solution and this requires the introduction of an 'approximation technique'. The finite difference method has been chosen here for solving the partial differential equations and whilst such methods generally provide solutions which are as accurate as required such methods do contain truncation errors. Therefore, it is important to assess the performance of the numerical scheme employed to ensure that it is efficient and also that it is as accurate as the problem warrants.

Stokes (1851) presented a solution for an infinite flat bed oscillating in still water. Lamb (1932) extended this work obtaining a first approximation for waves over a flat bed. The equations for Lamb's solution are shown in Chapter 3 (Eqs. 3.5 - 3.7), see also Appendix D.

In order to test the accuracy of the numerical scheme as well as the convergence of the k and k-ε models solution for varying densities of points in the vertical grid, a comparison between Lamb's analytical equations was undertaken. Results for a phase angle of zero are shown in Figures 5.3 - 5.4.

Figures 5.3a and 5.4a show a comparison of Lamb's analytical solution for velocity against the k-ε and k models, respectively. In both model solutions for grid densities of 40 and 60 points in the vertical excellent agreement with Lamb is seen. Appendix D shows tabulated values of depth-averaged results for the 3 different grid densities along with Lamb's analytical solution for both velocity and shear stress (τ/ρ). The percentage errors for the depth-averaged values as calculated by the models against Lamb's solution have the following ranges:

Velocity:

k-ε (60):	0.214% - 0.868%	k (60):	0.214% - 0.868%
k-ε (40):	0.586% - 1.479%	k (40):	0.586% - 1.479%
k-ε (20):	0.365% - 3.507%	k (20):	0.365% - 3.507%

Shear stress, τ/ρ:

k-ε (60):	0.775% - 14.247%	k (60):	0.580% - 10.335%
k-ε (40):	1.775% - 31.154%	k (40):	1.335% - 22.370%
k-ε (20):	5.348% - 87.487%	k (20):	3.580% - 52.460%

Figures 5.3b and 5.4b show the results of the comparison with the analytical shear wave solution against those for the k and k-ε models for the same phase angle. Overall, the model results for grid densities of 40 and 60 points in the vertical show excellent agreement with Lamb. However, for the phases of 150° and 330° the percentage error between the results from k and k-ε models and Lamb's solution increases significantly over the other phases through the wave period (≈ 5 - 6 times). This larger error occurs during flow reversal (see Appendix D) and as such the depth-averaging does not provide a sufficiently accurate assessment of the models performance during these phases and the use of such a method is

questionable. In order that a better assessment can be made, the root-mean-square deviation for all the results was calculated such that:

$$\sigma_{rms} = \sqrt{\frac{\sum(x - \bar{x})^2}{N}} \qquad \textbf{(5.6)}$$

This removed the bias created during flow reversal and provided the following error ranges:-
Velocity:

k-ε (60):	0.093% - 0.997%	k (60):	0.093% - 0.997%
k-ε (40):	0.088% - 2.076%	k (40):	0.088% - 2.076%
k-ε (20):	0.517% - 5.221%	k (20):	0.517% - 5.221%

Shear stress, τ/ρ:

k-ε (60):	0.099% - 1.378%	k (60):	0.020% - 0.700%
k-ε (40):	0.274% - 3.047%	k (40):	0.003% - 1.523%
k-ε (20):	1.373% - 9.589%	k (20):	0.207% - 3.585%

For grid densities of 40 and 60 the maximum percentage error from both velocity and shear stress results is of the order of only 3%. For the lowest grid density of 20, the maximum error is less than 10%. Overall, the k model provides better results for the shear stress calculations than does the k-ε model, whilst the velocity results show a negligible difference.

Interestingly, for both the velocity and shear stress results, the lowest grid density of 20 points shows excellent agreement with the analytical solution of Lamb close to the bed (approximately 2 mm). This is probably due to the varying space transform used in the model. The transform ensures a sufficiently fine grid spacing close to the wall and only when the space step increases at some point away from the bed does the vertical grid density become important. Clearly, this will only be true up to a minimum number of vertical points. Appendix D contains the detailed results of the comparison of the models with Lamb's analytical solution.

5.5 Conclusions

From the comparison of the model results against the analytical solution of Lamb (1932) it can be concluded that the numerical finite difference schemes (including the vertical grid transformation) are performing well. The accuracy of the numerical schemes and their application to the non-linear equations used to model the wave boundary layer have been verified.

The tests carried out using varying grid densities have shown that whilst, overall, the lowest grid density of 20 points through the vertical fails to fully reproduce the analytical solution, close to the wall the results are reasonable due to the vertical grid straining applied in the numerical models. For grid densities of between 40 to 60 points the velocity results show a maximum percentage error (calculated from root-mean-square deviations) of about 2% of the analytical solution. Similar results from the shear stress solutions show a maximum error of about 3%. Use of depth-averaging to provide an assessment of model performance is misleading due to flow reversal leading to unrepresentative percentages being generated.

The k model appears to out-perform the k-ε model based on the results of the shear stress calculations. However, the k-ε model is computationally more efficient despite the extra turbulence transport equation due to the summation required in calculating the time-dependent mixing length term in the k model.

It has been demonstrated that for typical model runs where grid densities of between 40 and 60 points are applied, the computational scheme is sufficient to ensure numerical errors are minimal. For further details, see Appendices C and D.

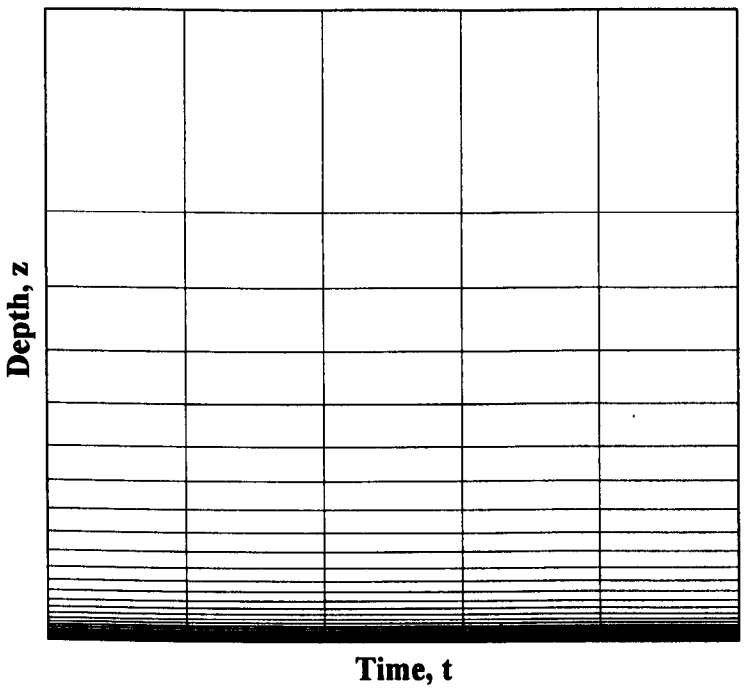

Figure 5.1: Schematic showing the variable grid as represented in real space.

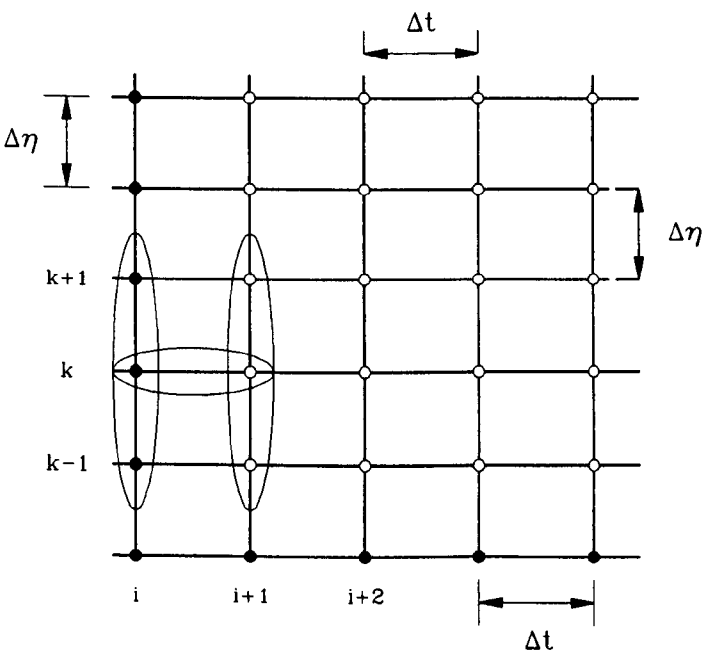

Figure 5.2: Schematic showing the Crank-Nicolson semi-implicit scheme.

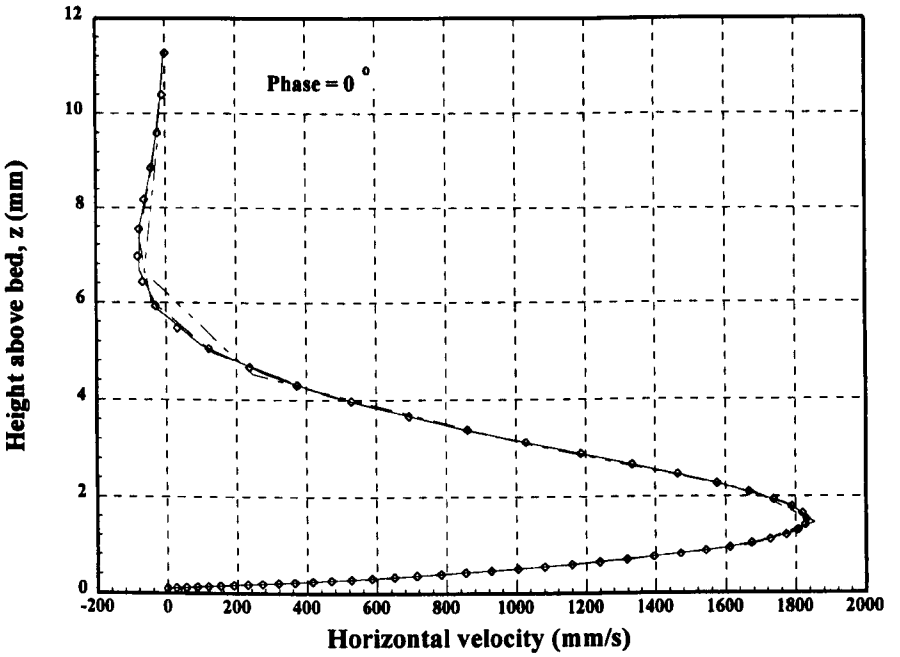

(a)

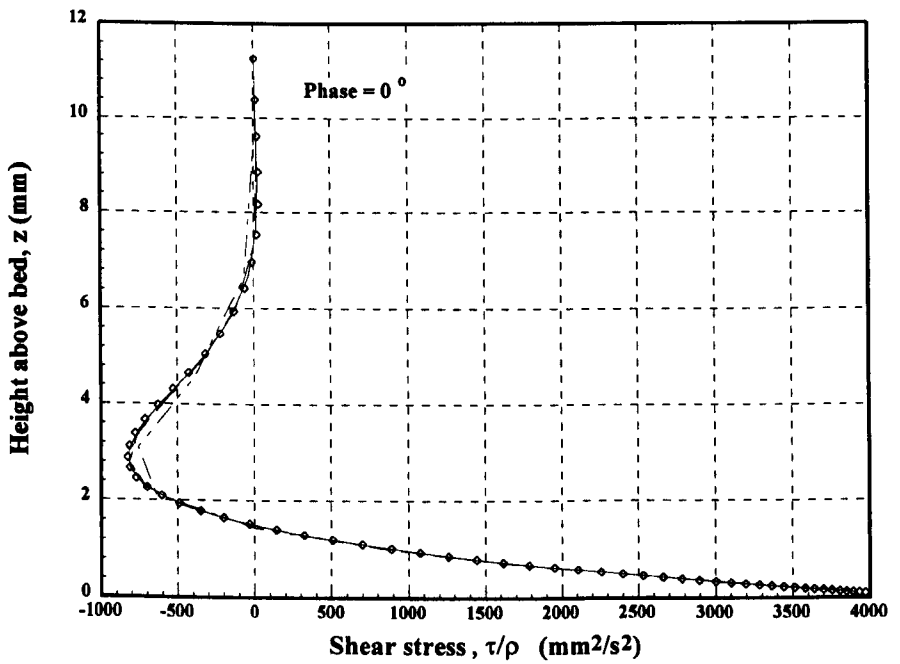

(b)

Figure 5.3: Comparison of Lamb's analytical solution against results from the k-ε model for different numbers of vertcial nodes: ◊ Lamb; — k-ε model (60 nodes); – – – k-ε model (40 nodes); — – – — k-ε model (20 nodes).

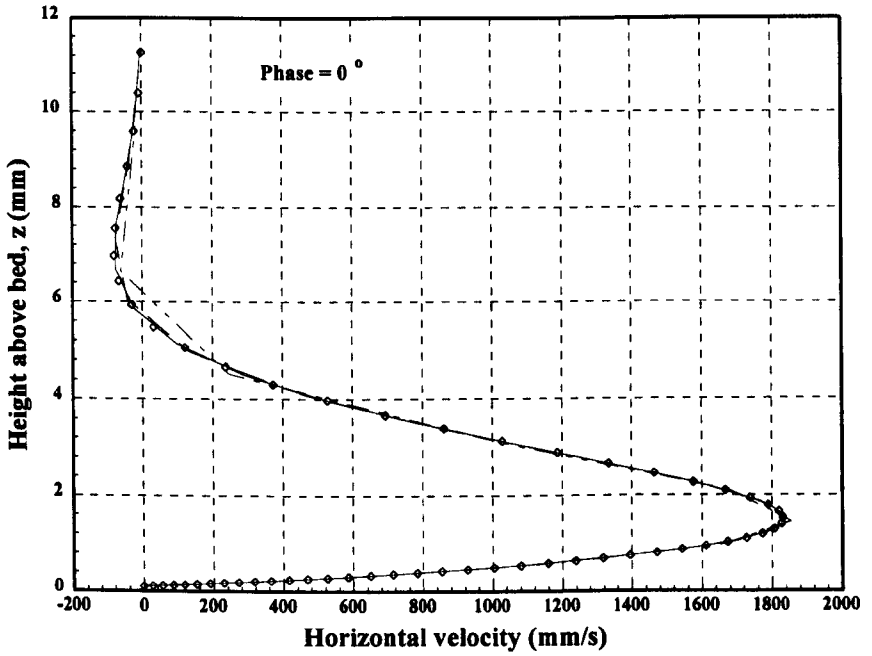

(a)

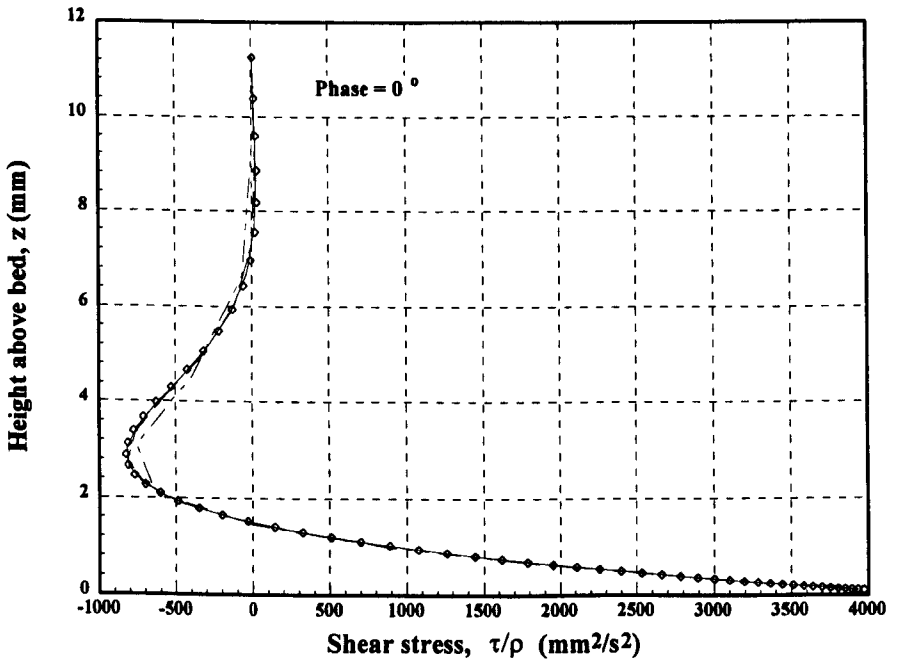

(b)

Figure 5.4: Comparison of Lamb's analytical solution against results from the k model for different numbers of vertcial nodes: ◊ Lamb; — k model (60 nodes); - - - k model (40 nodes); — - - — k model (20 nodes).

Chapter 6
Results: Part I

6.1 Introduction

This chapter presents the results from the first of the model tests against laboratory data for monochromatic waves. All the tests were carried out at ISVA, Denmark in the large oscillating tunnel. As such these tests are of prototype scale since the tunnel is able to generate conditions similar to those experienced in the field though at small scale.

6.2 Monochromatic waves without current

6.2.1 Jonsson and Carlsen (1976)

The first detailed investigation of the turbulent wave boundary layer was performed by Jonsson (1963), see Chapter 3. Jonsson (1963) presented results for a single test, Test No. 1, and later in Jonsson and Carlsen (1976) these same results were presented alongside the results of a second test, Test No. 2. Test No. 2 is generally considered to be less reliable than Test No. 1, see Jonsson and Carlsen (1976), and the value of the roughness parameter in this test was not determined correctly, see Jonsson (1980). Therefore, for these reasons Test No. 2 has not been used for comparison purposes. The experimental parameters used in the first test are shown in Table 6.1.

The measurements were performed in the oscillating water tunnel at ISVA (then the Coastal Engineering Laboratory). The tunnel has been described in detail by Lundgren and Sørensen (1959), but briefly, it is a large U-shaped tube, consisting of two vertical risers at each end of a horizontal tunnel. The working section is 10 m in length, 0.3 m high and 0.4 m wide. The top and sides of this section are made of plexi-glass and the natural resonance of the tunnel is about 9.5 secs. The water is forced to oscillate by pneumatic machinery (see Figure 6.1a). The velocities were measured using a 5 mm micro-propeller, Jonsson (1965). In the experiments

Jonsson and Carlsen used two-dimensional triangular roughness elements to simulate ripples, Figure 6.1b.

Wave period, T (s)	8.39
Free stream amplitude, a (mm)	2850
Mean free stream velocity amplitude, u_∞ (mm/s)	2110
Nikuradse sand roughness, k_S (mm)	23.0
Height of roughness above theoretical bed level (mm)	2.5
Amplitude Reynolds number, Re	6.01×10^6
Amplitude to roughness ratio, a/k_S	124

$\nu_L = 1.00 \times 10^{-2}$ cm^2 / s

Table 6.1: Jonsson and Carlsen (1976) main parameters for Test No. 1.

The results of the tests show that the velocity signal in the wave tunnel was not perfectly sinusoidal and this led to the velocity fields being unsymmetric for the two half periods. To compensate for this the numerical model has been driven using the following scheme:

$$\bar{u}_0(z,\omega t) = 0.5\left(\bar{u}_\infty \sin(\omega t) - \bar{u}_\infty \sin(\omega t + \pi)\right) \qquad \textbf{(6.1)}$$

Differentiating Eq. (6.1) with respect to t provides an expression which enables the input values for the pressure term in the horizontal momentum equation to be determined and provides the upper boundary condition for the equation. All other boundary conditions are as given in Chapters 2 and 4. The values of the model constants used in the present work are also given in Chapter 4, Section 4.3.6.

Results from the one-equation k-model (time dependent mixing length) show good agreement with the velocity measurements for Test No. 1, see Figure 6.2. The k-model has been run with two different turbulent eddy viscosity descriptions. The first uses the mixing length description suggested by Vager and Kagan (1969) and is time dependent (see Eq. 4.39). The second expression for mixing length is a simple time independent expression (see Eq. 4.40). The time dependent description shows a better fit than that for the more simple expression. Figure 6.2 shows a comparison of the two k-models against the velocity data of Jonsson and Carlsen, test 1. Clearly using the time dependent expression for mixing length suggested by

Vager and Kagan provides better agreement with the laboratory data. This implies that the specification of the mixing length is of some importance when considering the performance of a one-equation model. Therefore, the choice of mixing length specification will affect the accuracy of such models and should be considered with care. However, it should also be noted that the expression of Vager and Kagan (1969) requires more computational time than the simple linear expression since it involves a summation.

Figure 6.3 shows a comparison of the high-Reynolds number k-ε model with the velocity data of Jonsson and Carlsen, test 1. The model clearly gives very good agreement with the laboratory measurements. Figure 6.4 compares three different models against the same data. The three model types shown are a zero-equation mixing length model (approach of Bakker 1975; Eq. 3.56), the k-model (time dependent mixing length; Eqs. 4.10, 4.37 and 4.39) and the high Reynolds number k-ε model, Eqs. (4.10), (4.23) and (4.24). Overall, the worst fit is given by the zero-equation mixing length model. The k-ε model shows a better fit to the laboratory data in the 'overshoot' region over both the mixing length and k-equation models. All models show a reasonable fit close to the wall, however, the k-model appears to provide the best fit close to the wall. There is an obvious advantage of using the k and k-ε models over the basic mixing length model, however, it is more difficult to chose between the k and k-ε models.

Using root-mean-square deviations of the depth-average velocities obtained from the numerical models and comparing them to those of the experimental data, a percentage error was calculated. For the phases through the wave period shown in Figures 6.2 - 6.4 the following range of errors was obtained (see also Table 6.4):-

l:	25.835% - 48.602%
k:	10.105% - 30.681%
k-ε:	6.666% - 35.733%

Whilst such methods enable error values to be assigned to the particular models, they are determined on the basis that the experimental data are correct and ignore errors which occur in the measurement process. Therefore, the percentage errors should be seen as a guide rather than a true indicator of the models performance. The k and k-ε models appear to provide a

similar level of accuracy based on the root-mean-square deviation. See Table 6.4 for further details.

Eliminating the zero-equation mixing length model from further discussion, the one- and two-equation turbulence models have been studied further. To this end, the shear stress values calculated by Jonsson and Carlsen provide an additional check.

Jonsson and Carlsen (1976) suggested two methods for calculating the shear stress distribution. The first method involved integrating the equation of motion to obtain the shear stress.

$$\frac{\tau}{\rho} = \int_{z_1}^{z_2} \frac{\partial}{\partial t}(u_0 - u)dz \qquad \textbf{(6.2)}$$

where $z_1 = z_0$, the vertical level at which point the velocity is assumed to be zero; z_2 is a level at which $\tau = 0$ and u_0 is the free stream velocity.

Jonsson and Carlsen (1976) integrated over the depth of the oscillating tunnel, but Sumer *et al.* (1987) have pointed out that the limit could be at any depth where $\tau = 0$, that is where $\partial u/\partial z = 0$.

The second method suggested by Jonsson and Carlsen (1976), is to fit the velocities to a logarithmic velocity distribution. However, both methods are quite sensitive and show quite large deviations between values except at the maximum bed shear velocity (see Figure 6.7). Regarding the sensitivity of such methods, the accuracy of the integral method is dependent on the accuracy of the measured velocities. The logarithmic velocity distribution is affected by the close links between the theoretical bed level, the bed roughness and the shear stress. The difficulty is deciding the height which should be taken as the bed level for calculation purposes, since the logarithmic velocity distribution could exist for a wide range of bed levels.

The results from the numerical simulation tend to underpredict the values of shear stress calculated by Jonsson and Carlsen (1976), Figures 6.5 - 6.7. Hagatun and Eidsvik (1986) and

Justesen (1988a) also found the experimental values to be generally higher than those predicted by theory. However, despite numerous studies into this effect, no explanation has been found. Justesen (1988a) suggested that a possible cause is due to the flow structure in the vicinity of the two-dimensional roughness elements used by Jonsson and Carlsen (1976) not conforming to the idea of a Nikuradse equivalent roughness as would be valid for a three-dimensional sand grain covered bed. This point is worth further consideration and will be returned to later in the present Chapter.

A comparison between the present models and those of Hagatun and Eidsvik (1986) and Justesen (1988a) has not been possible since none of the authors provide values for their model results in their papers.

Figures 6.5 - 6.7 show a comparison of the shear stress data of Jonsson and Carlsen (test 1) with the results for the k and k-ε models. It is difficult to decide which gives a better a fit to the laboratory data since neither model fit the data well. However, on the basis of the root-mean-square deviations (Table 6.5) the k-model shows the best agreement with the experimental values.

6.2.2 Jensen *et al.* (1989)

The most recent and, arguably, the most detailed published study of turbulence in oscillatory boundary layers is that performed at ISVA, Denmark. The early results of this work were published by Sumer *et al.* (1986;1987). Jensen (1989) and Jensen *et al.* (1989) describe the experiments in detail.

The experimental programme covered a wide range of a/k_s values for both hydraulically smooth and rough beds. The experiments compliment the earlier smooth wall tests of Hino *et al.* (1983) performed in a wind tunnel, as well as the rough bed tests of Sleath (1987) carried out in an oscillating water tunnel.

Jensen *et al.* (1989) describe 15 tests in total which were undertaken in the oscillating water tunnel at ISVA. Tests 1 - 11 were all performed over a smooth bed, whilst tests 12 - 15 were

carried out over a rough bed. All the tests were for monochromatic waves with no added current. The rough-wall experiments were further divided into two sets; tests 12 and 13 were performed with a roughness height of k = 0.35 mm and tests 14 and 15, a roughness height of k = 1.5 mm. The k and k-ε models have been run against tests 12 and 13.

Test No.	Period, T (s)	u_∞ (m/s)	a (m)	Re = au_∞/ν_L	a/k_s
12	9.72	1.02	1.58	1.6×10^6	1880
13	9.72	2.00	3.10	6.0×10^6	3700

$\nu_L = 1.14 \times 10^{-2}$ cm^2 / s

Table 6.2: Experimental parameters for Tests 12 and 13 Jensen *et al.* (1989).

For tests 12 and 13 the rough bed was achieved by gluing a sheet of sandpaper onto the bed. As mentioned above the roughness height for these tests was k = 0.35 mm. Jensen *et al.* (1989) calculated the density of the sand to be 80 grains / cm^2 . The resulting Nikuradse equivalent roughness was found to be k_s = 0.84 mm. The velocity measurements were made using both a one-component and two-component laser Doppler anemometer (LDA) system. The basic test parameters for the two tests are shown in Table 6.2.

Jensen *et al.* (1989) found that in their rough bed experiments, the flow did not feel the effect of the roughness until ωt had reached a value of approximately 15° and for test 12, the flow did not respond to the roughness until $\omega t \approx 45°$. This indicates that for a certain part of the flow fully turbulent conditions do not apply. This raises the question as to the validity of many turbulence models which assume fully turbulent conditions at all stages of the flow. The implication is that in order to accurately model the hydrodynamics of such flows, it requires a model which is valid all the way to the wall and is able to take account of such laminar effects.

6.2.3 Model results for test 12, Jensen *et al.* (1989)

Between the two tests of Jensen *et al.* presented here, test 12 has the lower amplitude Reynolds number (1.6×10^6). The flow is still considered to be fully turbulent in nature. Figures 6.8a and 6.8b show a comparison of the numerical models against the experimental velocity data of Jensen *et al.*. Profiles are shown at 15° intervals, from 0° to 165°. Laboratory data was not made available for the full wave cycle, however, the data enables the effect of flow reversal to be seen. Both the k-ε and the time-dependent k-model show excellent agreement with the velocity data. The k-model tends to underpredict the overshoot as was seen with the data of Jonsson and Carlsen (1976).

The percentage errors of the root-mean-square deviation of the depth-average velocities from the experimental data were calculated for the 12 phases through the wave cycle shown in Figure 6.8 (see Table 6.6). The results show an average error for all the phases of 4.24% and 3.42% for the k-ε and k models, respectively. The smallest percentage error is 0.172% calculated by the k-ε model.

A visual comparison of the shear stress results from the two models would appear to show reasonable agreement with the laboratory data (Figure 6.9). The k-ε model has a tendency to overpredict the overshoot, with the k-model showing better overall agreement. However, results from the root-mean-square deviation calculations for the various phases are less encouraging, with average errors of 79.37% and 52.27% for the k-ε and k models, respectively.

As mentioned previously, in Section 6.2.1, the percentage errors assume the measurements to be correct. Clearly this is not possible, no matter how carefully the experiments are undertaken. In addition, the Reynolds stress values are calculated on the basis of two measured values u′ and w′ which are in themselves subject to errors. Jensen *et al.* (1989) calculated the mean values of their measured quantities using ensemble averaging. The total number of periods sampled was 80 in tests 12 and 13. Sleath (1987) found no significant improvement in the reliability of the statistics for record lengths greater than about 50 cycles. Jensen *et al.* observed similar findings. It is suggested that, whilst the percentage errors

provide a guide to the relative performance of each model, they are not a true indicator of the accuracy of the models.

Figure 6.10 shows a comparison of the bed shear stress measurements and those calculated by the k-ε model. The agreement is best between $\omega t = 45° - 150°$. Values for the bed shear stress over the whole wave period were not provided so it is not possible to observe the total fit. The free stream velocity profile is shown alongside that of the shear velocity. It is possible to observe the phase lead of the shear velocity over the free stream velocity. For test 12 the phase lead is 14° which is much lower than that for the laminar case (45°). This decrease in the phase lead is to be expected, since in turbulent flow, the near-wall velocities are not reduced as much as in the laminar case because of the vertical exchange of momentum by the eddies.

Jensen *et al.* (1989) measured the turbulent components in the x and z directions but not in the cross-stream direction (y). This means that some assumptions have to be made if the turbulent kinetic energy is to be calculated. The kinetic energy is given by the equation:

$$k = \frac{1}{2}\left(\overline{u'}^2 + \overline{v'}^2 + \overline{w'}^2\right) \qquad \textbf{(6.3a)}$$

$$k' = \frac{1}{2}\left(\overline{u'}^2 + \overline{v'}^2\right) \qquad \textbf{(6.3b)}$$

Flow	Relative values of Reynolds stress components			k / k′
	$\overline{u'}^2$	$\overline{v'}^2$	$\overline{w'}^2$	
Boundary layer:				
Inner layer	0.61	0.28	0.10	1.42
Outer layer	0.45	0.33	0.22	1.47
Plane jet	0.42	0.29	0.30	1.40
Plane wake	0.42	0.26	0.32	1.35
Homogenous isotropic turbulence	0.33	0.33	0.33	1.50

Table 6.3: Relative values of Reynolds stress components for a range of flows. After Townsend (1976).

Jensen *et al.* only measured u′ and w′ therefore, it is necessary to try and relate these to Eq. (6.3). Townsend (1976) quotes the relative values for the Reynolds stress components for different types of shear flow (see Table 6.3). Based on these measurements it is possible to estimate a value for k based on only the two stress components.

The range of values for k/k' shown in Table 6.3 indicate a factor of between 1.3 and 1.5 in order to correct for the missing Reynolds stress component. Justesen (1988) assumes a value of 1.5.

Figure 6.11 shows the comparison of the turbulent kinetic energy measurements of Jensen *et al.* test 12 against the k and k-ε model. The experimental data is shown for two k/k' ratios. The first ratio assumes that there is no turbulent component in the y-direction (that is a factor of 1) and the second is based on a factor of 1.3. Whilst, overall, both models provide a reasonable fit to the data it could be argued from the profiles that the k-model fits the test data best. This can be confirmed from the root-mean-square deviation calculations shown in Table 6.8. A better fit is observed for a factor of 1.3.

The laboratory data shows a decrease in the turbulent kinetic energy close to the bed and this reduction is observed in the corresponding numerical results, though not perfectly. On a visual inspection of the model results of Justesen (1988a) and Chapalain and Boczar-Karakiewicz (1992) this reduction appears to be not so well reproduced suggesting that the present model formulation provides a better description of the physics. Unfortunately, any real qualitative comparison between the models of Justesen and Chapalain and Boczar-Karakiewicz and those used in the current work is not possible since the former authors provide no numerical output with which to compare. The reason for the improved fit is most likely due to the logarithmic depth transform applied in the model allowing a finer grid to be applied at the wall than in the models of Justesen and Chapalain and Boczar-Karakiewicz.

6.2.4 Model results for test 13, Jensen *et al.* (1989)

The results of a comparison of the experimental velocity profiles for test 13, against the numerical models again show a reasonable fit (Figure 6.12). The performance of the k-ε

model over that of the k-model has been assessed as before using root-mean-square deviations, see Table 6.9. The deviation from the experimental results is greater than for test 12. The mean error for the phases shown are 15.92% and 13.17% for the k-ε and k models, respectively. Whilst the k-ε model tends to predict the extent of the velocity overshoot better than the k model, for some phases both models fail to predict the true extent of the velocity overshoot. Whether this discrepancy in the velocity results is due to some experimental failing, for example boundary layer development being curtailed by the oscillating tunnel's cross-section, a feature seen in the experimental results of Jonsson and Carlsen (1976), is unclear.

A comparison of results for the shear stress (Figure 6.13) show better agreement with the models than was seen for test 12 of Jensen *et al.* The experimental results show the shear stress to decrease close to the bed for many of the phases shown and this feature is well reproduced in the models. The k-ε model shows good agreement with the data for most phases whilst the k-model tends to underpredict the extent of the overshoot in the profiles. During part of the decelerating phase of the flow, $\omega t = 135° - 165°$, both of the models underpredict the extent of the overshoot (see Figures 6.13j - 6.13l). Results from the root-mean-square deviation calculations confirm the visual inspection with mean errors of 11.32% and 16.30% for the k-ε and k models, respectively (see Table 6.10).

Figure 6.14 shows a comparison of the bed shear stress calculated by the k- and k-ε models against the measured values. Since a non-smoothed version of the laboratory data is used there is much fluctuation (see Figure 6.14). However, during the first half of the wave period, the measured bed shear stress appears to be significantly higher than that predicted by the models. Whether this is due to experimental errors in the LDA measurements, such as signal loss due to reflection from the bed is uncertain.

Figure 6.14 also shows the results from a modified turbulence k-model which has been run with the inclusion of molecular viscosity. In theory, since the flow is fully developed it is expected that the effect on the bed shear stress will be negligible. However, when the results are plotted on the same graph a clear difference can be seen. Since Jonsson and Carlsen's test 1 is of a similar amplitude Reynolds number to test 13 of Jensen *et al.* (6.01×10^6 and $6.0 \times$

10^6 respectively) it was decided to investigate whether the same effect would be observed by including molecular viscosity in the k-model run for test 1 of Jonsson and Carlsen. Interestingly, the inclusion of molecular viscosity in the model had no discernible effect on the calculated shear velocity values, as theory would suggest for fully turbulent flow. Since both experiments were performed in the oscillating water tunnel at ISVA the only significant difference in the tests is the measurement technique and the bed roughness used. Jonsson and Carlsen used triangular roughness elements whilst Jensen *et al.* used sandpaper glued to the bed of the tunnel. Intuitively, it would seem most reasonable to assume that the difference in shear velocity is due primarily to the difference in bed roughness rather than due to experimental error. Obviously, the triangular roughness elements provide more turbulence than the sandpaper due to vortex shedding. The underprediction of the shear stress in Jonsson and Carlsen could, therefore, be as Justesen (1988a) suggested, that is, the triangular roughness elements deform the flow structure such that the Nikuradse roughness assumption is invalidated.

However, the other important point that should be made is that the flow structure in Jensen *et al.* test 13 is fully developed turbulent and yet molecular viscosity appears to still be significant. Does this indicate a failing in the theory surrounding fully developed turbulent wave boundary layers? Jonsson and Carlsen calculated their shear stress from their velocity measurements based on the integral momentum equation, Eq. (6.2). In Jensen *et al.* the shear stress is calculated from the Reynolds stress components as measured by the laser system. Whilst generally, laser measurements are seen as being more accurate than intrusive measurement techniques, such as the use of a propeller meter, errors when measuring close to the bed can be significant. Certainly, close to the bed reflection from the sand grains can cause significant signal disruption when using a laser and the measurement volume of the laser beams (typically 0.3 mm in diameter and 1.0 mm long) limits how close to the bed measurements can be undertaken. Therefore, a possible source of error is in the measurement technique. Jensen *et al.* (1989) report a high drop-out rate in the laser measurements in the near-wall region (z = 1 - 2 mm) for their smooth bed experiments due to reflection from the bed. Jensen *et al.* found that this was improved in the rough bed experiments, but they do not discuss to what extent.

Jensen *et al.* (1989) found that for smooth-turbulent flow the logarithmic layer comes into existence some time after flow reversal and grows in size as the flow progresses. The larger the Reynolds number the earlier the logarithmic layer is established. A similar effect was observed for fully turbulent flow. Therefore, for part of the flow the logarithmic layer will not exist because the boundary layer thickness is too small to support it. Hence, it could reasonably be expected that even for high-Reynolds number flows, the effect of kinematic viscosity should be included at some phases of the flow. Ultimately, there must be a Reynolds number beyond which the flow is fully turbulent at all phases through the cycle and hence the kinematic viscosity has a negligible effect as appears to happen in Jonsson and Carlsen's Test 1.

The problem with this explanation is that the solution including the effect of kinematic viscosity could be expected to deviate little from the measured values for a significant part of the cycle since the turbulent component should be considerably greater. Clearly, from Figure 6.14 this is not the case. Secondly the measured bed shear stress is not symmetric, with greater shear being generated in the first half period than in the second. It is not clear why this should be so, since the free stream velocity profile shows symmetry. It has, therefore, not been possible to conclude why the inclusion of kinematic viscosity in the model solution has such a significant effect in test 13 of Jensen *et al.* when for a similar test (Jonsson and Carlsen test 1) shows the inclusion of the kinematic viscosity to be negligible.

The measured shear values from the laser only include the Reynolds stress component. Maybe, the assumption of fully turbulent flow which would suggest that the total shear is given wholly by the turbulent component is incorrect and the viscous component is still significant. The total stress would then be given as:

$$\tau_{total} = \tau_{viscous} + \tau_{turbulent} \qquad \textbf{(6.4)}$$

Comparison of the measured turbulent kinetic energy data against the results from the one- and two-equation turbulence models is shown in Figure 6.15. As for test 12, results are shown against experimental data for factors of 1 and 1.3. Results of root-mean-square deviation calculations show the results to be reasonable for most phases of the flow (see Table 6.11) though for the phases 15° to 75° the errors are much greater than for the other phases shown.

Generally, the measurements show better agreement against the models with a factor of 1.3, though at 75° both models show a lower error with a factor of 1 used as a multiplier. It is conceivable that during the wave cycle, the factor varies between a small range of values, say 1 to 1.5, however, this has not been investigated further. The reduction of the kinetic energy in the near-wall region is again reproduced.

6.3 Conclusions

The one-equation k model (time-variant version) and the high-Reynolds number k-ε model have been compared against the prototype scale oscillating water tunnel data of Jonsson and Carlsen (1976) and Jensen *et al.* (1989). Both models show good agreement, overall, with the data. In addition to testing the performance of these two models, a comparison has also been made with a mixing length model and also a k model run using a time-invariant mixing length description (see Eqs. 4.39 and 4.40). Both the k and k-ε models out-performed the mixing length model with differences of nearly 20% (see Table 6.4).

The results of using different descriptions for the mixing length in the k model revealed the importance of choosing the mixing length expression carefully. The time-variant description (Eq. 4.39) showed a better representation of the physics than did the simple time-invariant description (Eq. 4.40). However, the mixing length expression of Vager and Kagan (1969) (Eq. 4.39) leads to a computationally slower model due to the summations required for the mixing length expression. The effect of the summation makes the one-equation k-model computationally slower than the two-equation k-ε model. Ultimately, this had an overriding effect on which model was chosen to develop for random wave modelling. This does also make the point of what criteria should be used when deciding on a model. Both the accuracy and the efficiency are important but it might be necessary to compromise, particularly when the difference in accuracy is not sufficient to warrant the greater computational cost.

Results of the model runs against the shear stress data of Jensen *et al.* (1989) suggest that possibly even for flows considered to be fully turbulent (amplitude Reynolds number, $Re = 6.0 \times 10^6$) kinematic (molecular) viscosity may still have some influence during certain phases through the wave cycle. Unfortunately, whilst the model is able to work at the

molecular level (smallest grid spacing at laboratory scale Δz = 0.0071 mm) experimental techniques are still not able to measure at this scale.

The use of root-mean-square deviations to test model performance provided a method by which to quantify results. Such methods are only as reliable as the measurements against which the models output is being compared. It is clear that despite every effort to limit errors within an experiment, errors will be present. Such statistical techniques can only provide a guide to the relative performance of the models. The accuracy of the models' output is much harder to quantify and the errors shown in Tables 6.4 - 6.11 should not be seen as absolute.

Model	Percentage Error, %					
	30°	60°	270°	300°	330°	360°
k-ε	35.733	20.428	24.154	20.450	13.274	6.666
k	30.681	12.543	20.267	18.926	15.609	10.105
l	48.602	26.248	32.191	31.259	28.976	25.835

Table 6.4: Percentage error of root-mean-square (rms) deviation of depth average velocities from the experimental results of Jonsson and Carlsen (1976), test 1. Results are shown for different phases through the wave period and for the different models.

Model	Percentage Error, %					
	30°	60°	270°	300°	330°	360°
k-ε	45.814	25.091	15.687	32.075	29.188	27.901
k	28.832	15.426	16.096	14.519	8.113	30.811

Table 6.5: Percentage error of root-mean-square (rms) deviation of depth-average shear stresses, τ/ρ, from the experimental results of Jonsson and Carlsen (1976), test 1. Results are shown for different phases through the wave period for the k and k-ε models.

Model	Percentage Error, %											
	0°	15°	30°	45°	60°	75°	90°	105°	120°	135°	150°	165°
k-ε	5.041	0.172	1.158	1.540	3.884	3.985	1.569	0.587	2.964	6.357	10.730	12.885
k	0.705	7.125	2.281	4.307	1.625	2.177	0.200	1.378	2.916	4.941	6.769	6.641

Table 6.6: Percentage error of root-mean-square deviation of depth-average velocities from the experimental data of Jensen *et al.* (1989), test 12. Results are shown for different phases through the wave period for the k and k-ε models.

Model	Percentage Error, %											
	0°	15°	30°	45°	60°	75°	90°	105°	120°	135°	150°	165°
k-ε	19.994	165.421	120.149	93.688	82.476	78.771	74.503	75.899	86.285	80.218	49.699	25.368
k	38.910	125.981	95.396	71.268	59.085	52.989	45.899	42.717	45.477	35.497	13.312	0.678

Table 6.7: Percentage error of root-mean-square deviation of depth-average shear stresses, τ/ρ, from the experimental data of Jensen *et al.* (1989), test 12. Results are shown for different phases through the wave period for the k and k-ε models.

Model	Percentage Error, %											
	0°	15°	30°	45°	60°	75°	90°	105°	120°	135°	150°	165°
k-ε (1.0)	127.072	163.943	227.210	233.751	172.275	148.002	145.429	140.206	134.002	127.396	123.600	102.990
k (1.0)	87.682	96.971	165.453	179.171	127.781	104.983	98.612	88.390	75.747	62.845	58.869	55.565
k-ε (1.3)	74.692	103.081	151.665	156.761	109.441	90.760	88.795	84.774	79.987	74.920	71.982	56.154
k (1.3)	44.388	51.552	104.166	114.771	75.215	57.670	52.781	44.916	35.179	25.266	22.194	19.672

Table 6.8: Percentage error of root-mean-square deviation of depth-average turbulent kinetic energy, k, from the experimental data of Jensen *et al.* (1989), test 12. Results are shown for different phases through the wave period for the k and k-ε models as well as for multiplication factors of 1.0 and 1.3 applied to the measured values (see Section 6.3.3).

Model	Percentage Error, %											
	0°	15°	30°	45°	60°	75°	90°	105°	120°	135°	150°	165°
k-ε	17.138	23.808	13.853	20.335	18.612	14.690	12.313	9.401	3.440	6.171	18.044	33.218
k	14.646	20.504	9.418	15.708	14.015	10.039	7.763	5.059	0.606	9.596	19.673	30.968

Table 6.9: Percentage error of root-mean-square deviation of depth-average velocities from the experimental data of Jensen *et al.* (1989), test 13. Results are shown for different phases through the wave period for the k and k-ε models.

Model	Percentage Error, %											
	0°	15°	30°	45°	60°	75°	90°	105°	120°	135°	150°	165°
k-ε	2.947	34.095	28.245	21.886	10.365	3.287	1.194	6.635	15.441	1.917	9.623	0.165
k	10.486	40.544	39.530	30.534	15.255	4.651	1.228	0.835	0.810	16.566	25.435	10.680

Table 6.10: Percentage error of root-mean-square deviation of depth-average shear stresses, τ/ρ, from the experimental data of Jensen *et al.* (1989), test 13. Results are shown for different phases through the wave period for the k and k-ε models.

Model	Percentage Error, %											
	0°	15°	30°	45°	60°	75°	90°	105°	120°	135°	150°	165°
k-ε (1.0)	34.905	213.483	750.427	289.776	120.913	62.862	58.021	67.481	79.233	68.051	50.169	57.171
k (1.0)	5.345	165.848	628.924	231.070	84.388	67.909	28.517	31.090	32.591	16.389	4.589	22.825
k-ε (1.3)	3.776	141.137	554.135	199.824	69.934	71.432	21.554	28.831	37.872	29.273	15.515	20.900
k (1.3)	18.963	104.495	460.676	154.666	41.838	75.314	1.141	0.839	1.994	10.468	19.546	5.520

Table 6.11: Percentage error of root-mean-square deviation of depth-average turbulent kinetic energy, k, from the experimental data of Jensen *et al.* (1989), test 13. Results are shown for different phases through the wave period for the k and k-ε models as well as for multiplication factors of 1.0 and 1.3 applied to the measured values (see Section 6.3.3).

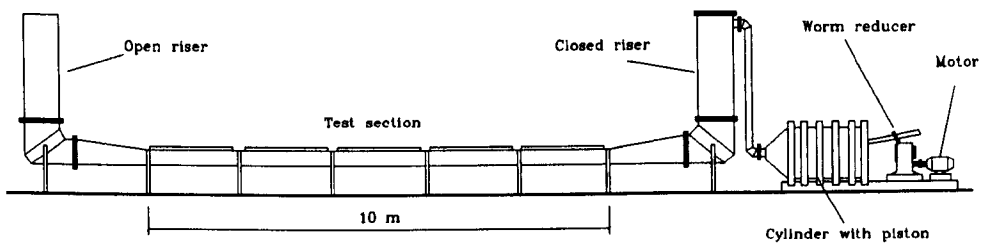

Figure 6.1a: ISVA's oscillating water tunnel. *(After Lundgren and Sorensen 1956).*

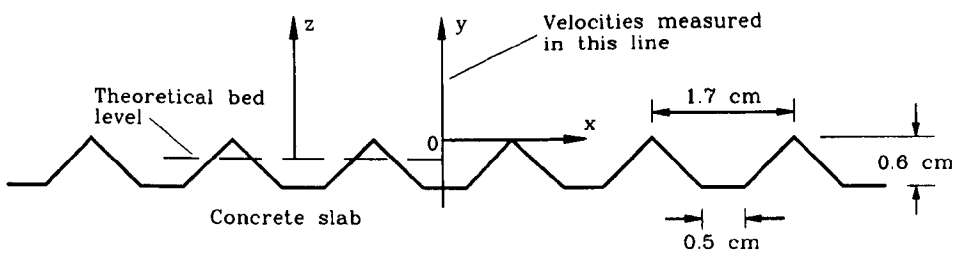

Figure 6.1b: Bed configuration for test 1, Jonsson and Carlsen (1976). Sketch shows dimensions of the triangular roughness elements.

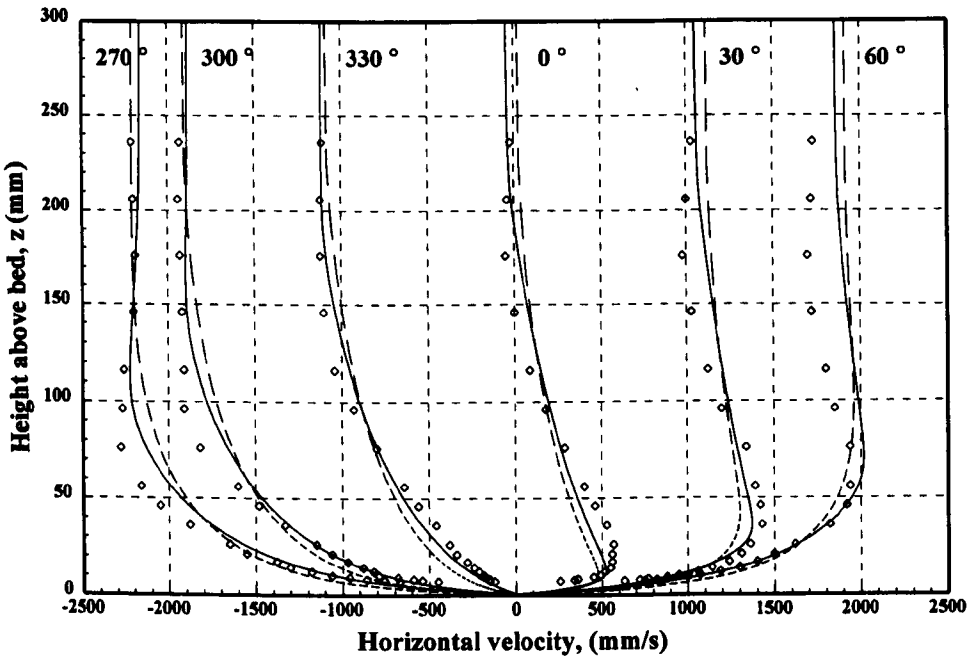

Figure 6.2: Comparison of one-equation k-models against the laboratory data of Jonsson and Carlsen (1976): ◊ test 1 Jonsson and Carlsen; —— k-model, time-dependent expression; — — k-model, time-independent expression.

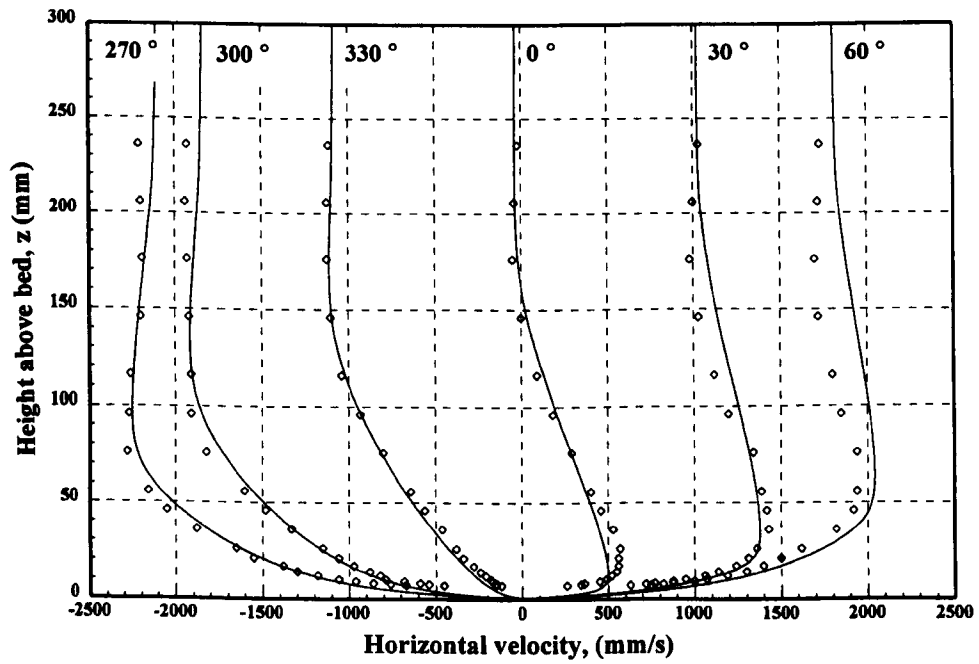

Figure 6.3: Comparison of two-equation k-ε model against the laboratory data of Jonsson and Carlsen (1976): ◊ test 1 Jonsson and Carlsen; ——k-ε model.

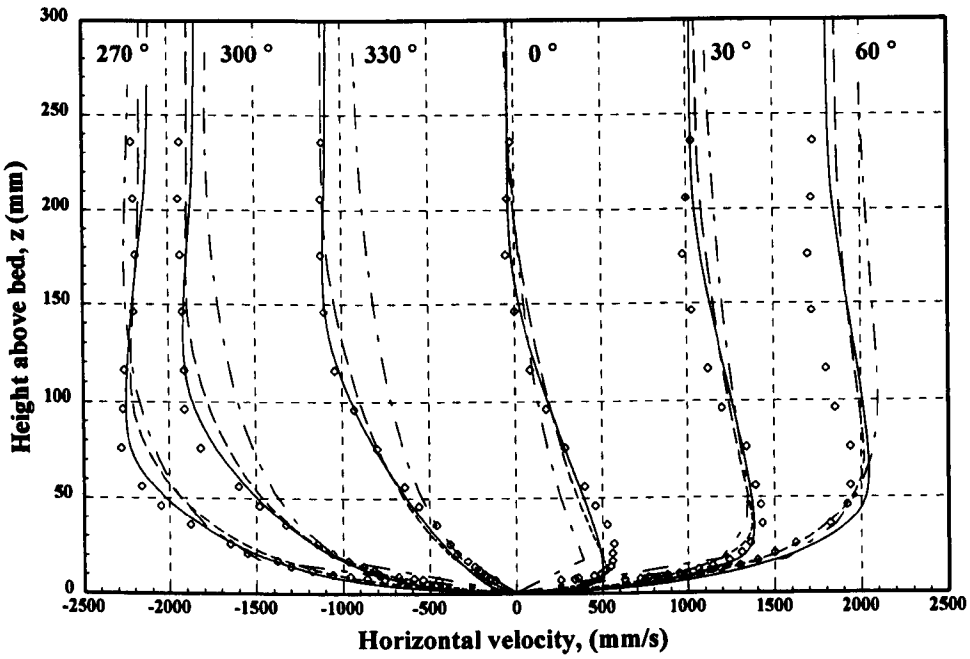

Figure 6.4: Comparison of k-ε, k and mixing length models against the laboratory data of Jonsson and Carlsen (1976): ◊ test 1 Jonsson and Carlsen; —— k-ε model; — — k-model; — – — mixing length model.

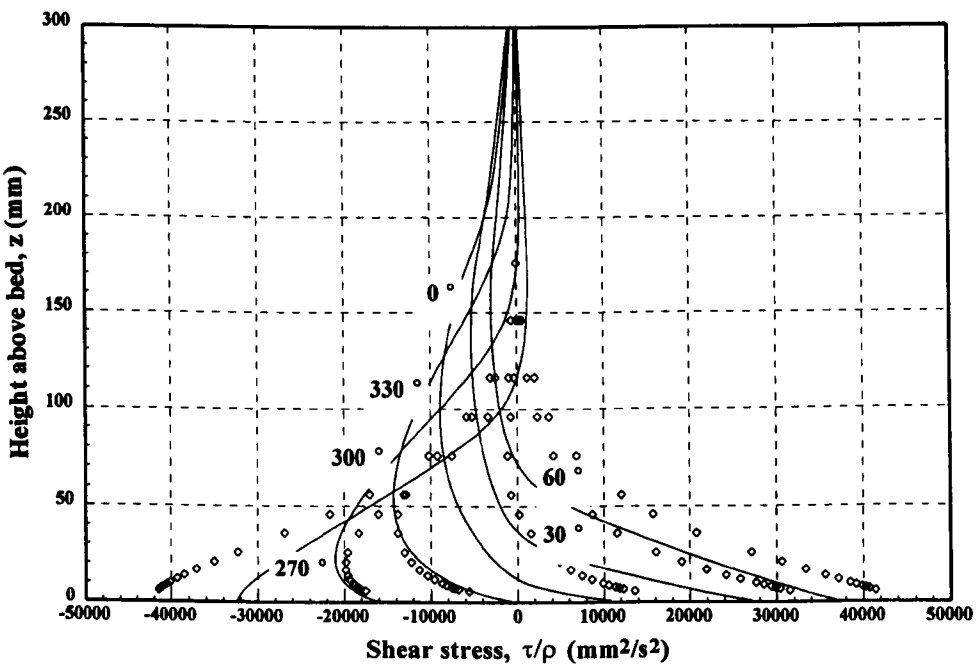

Figure 6.5: Comparison of shear stress results from time-dependent k-model (——) against laboratory data of Jonsson and Carlsen (1976), test 1 (◊).

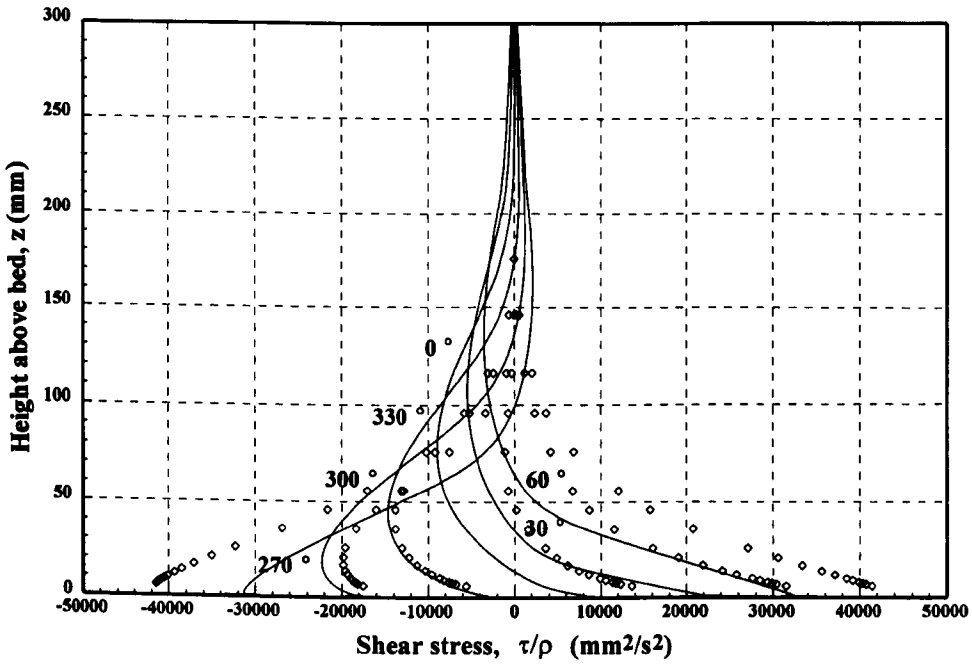

Figure 6.6: Comparison of shear stress results from k-ε model (——) against laboratory data of Jonsson and Carlsen (1976), test 1 (◊).

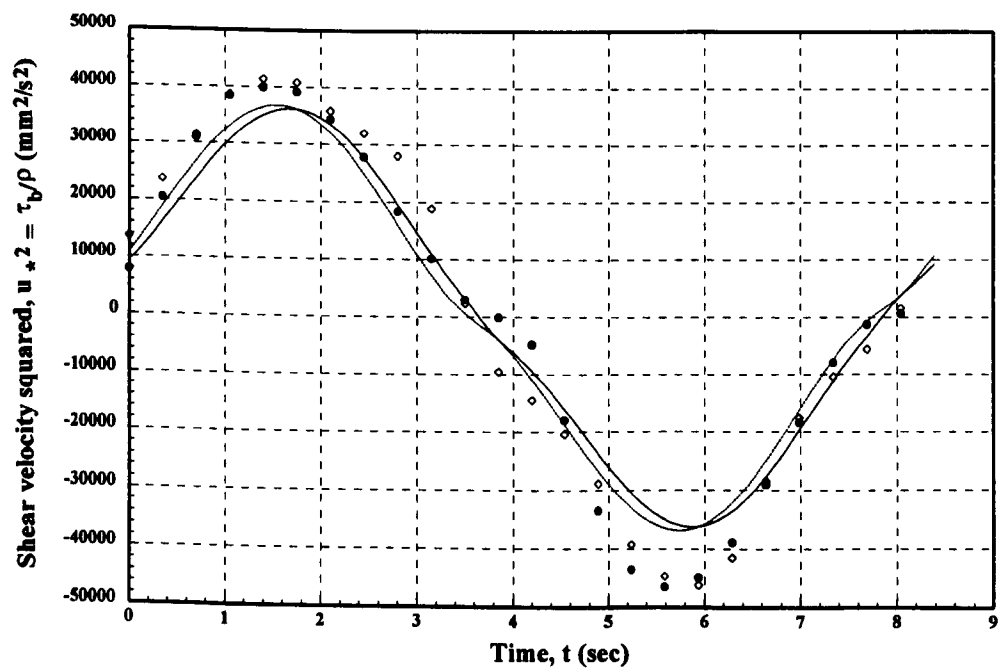

Figure 6.7: Comparison of shear velocity results from k-ε model and time-dependent k-model against laboratory data of Jonsson and Carlsen (1976): —— k-ε model; — — k-model; Jonsson and Carlsen, test 1, ◊ (momentum integral method), • (logarithmic velocity profile method).

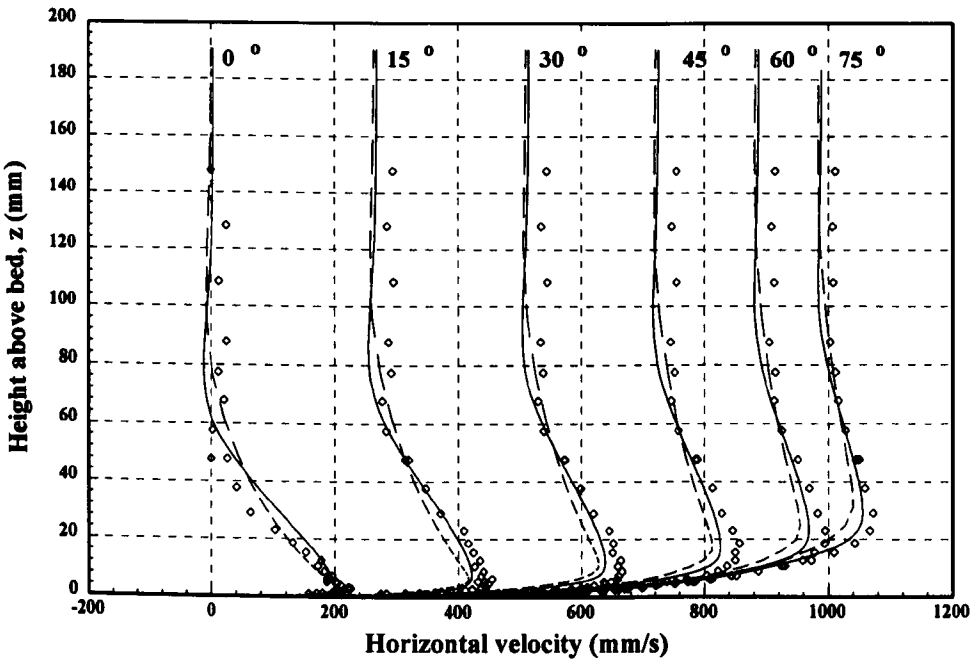

Figure 6.8a: Comparison of k-ε model and time-dependent k-model against laboratory data of Jensen *et al.* (1989): ◊ test 12, Jensen *et al*; — k-ε model; – – k-model.

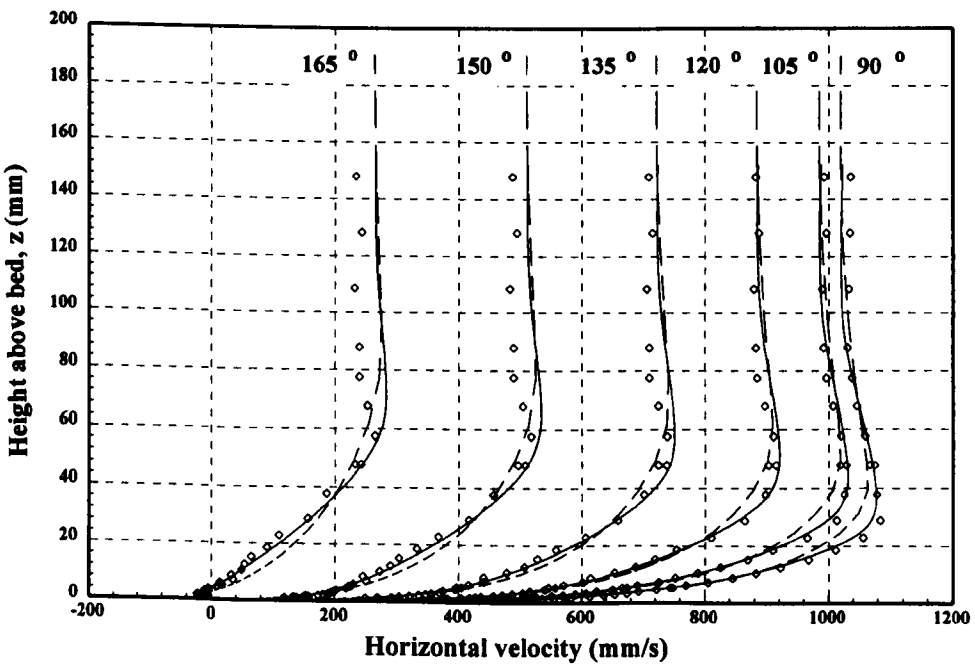

Figure 6.8b: Comparison of k-ε model and time-dependent k-model against laboratory data of Jensen *et al.* (1989): ◊ test 12, Jensen *et al*; — k-ε model; – – k-model.

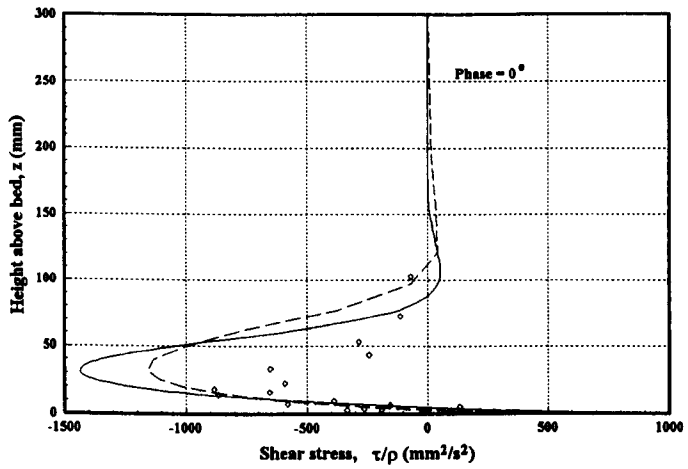

(a)

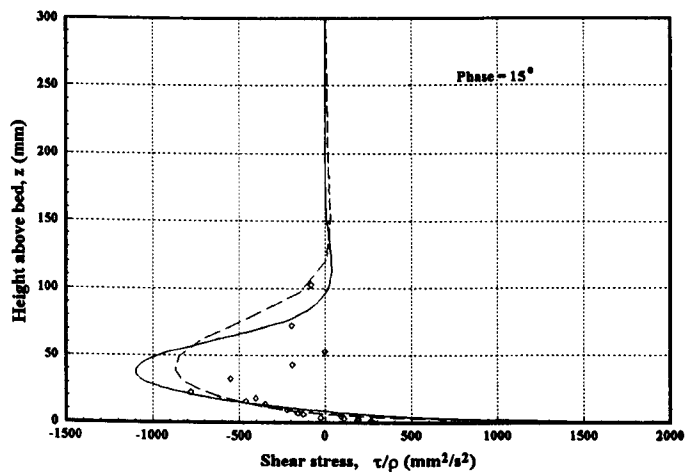

(b)

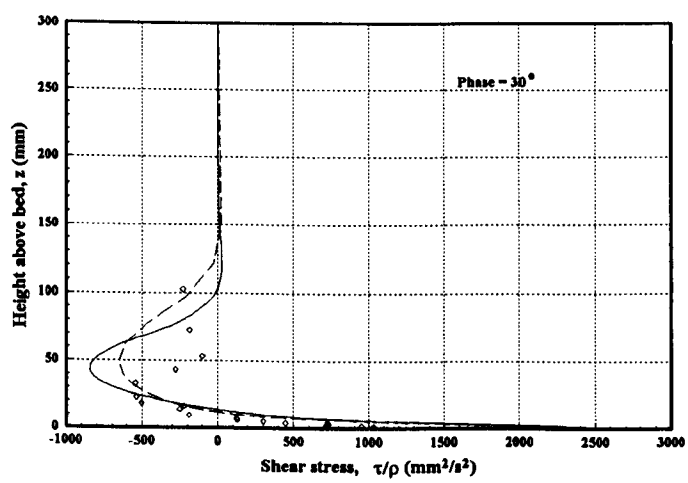

(c)

Figure 6.9: Comparison of shear stress values from k-ε model and time-dependent k-model against laboratory data of Jensen *et al.* (1989): ◊ test 12, Jensen *et al.*; —— k-ε model; — — k-model.

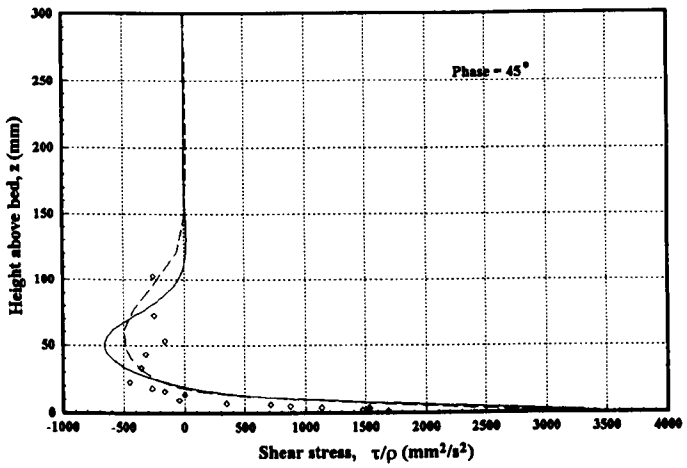

(d)

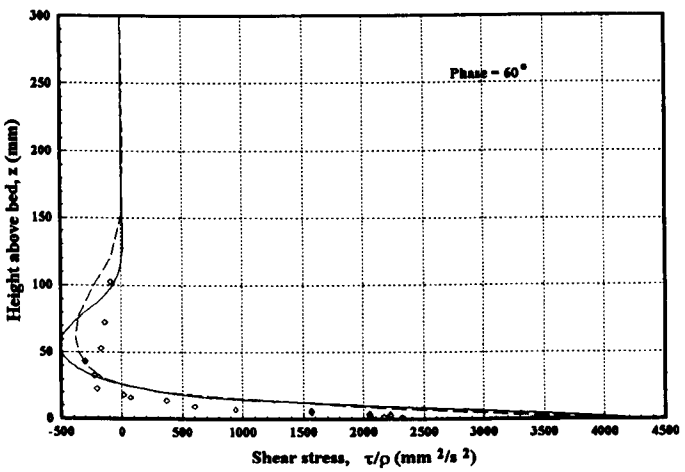

(e)

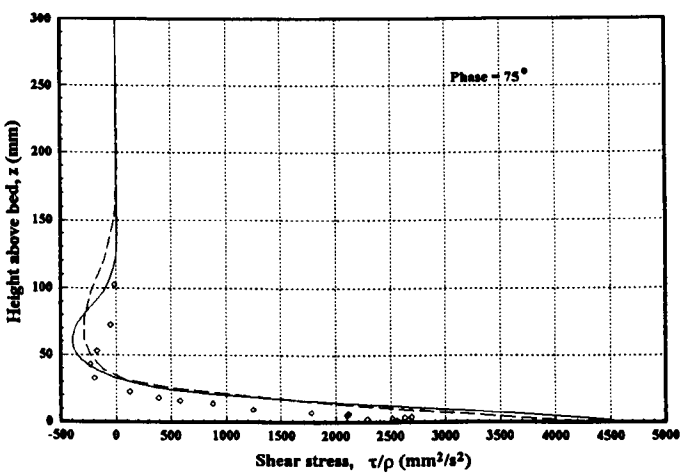

(f)

Figure 6.9(Cont.): Comparison of shear stress values from k-ε model and time-dependent k-model against laboratory data of Jensen *et al.* (1989): ◊ test 12, Jensen *et al.*; —— k-ε model; — — k-model.

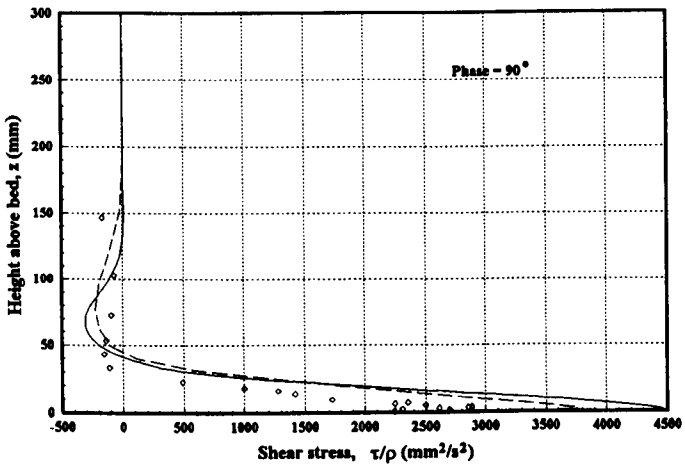

(g)

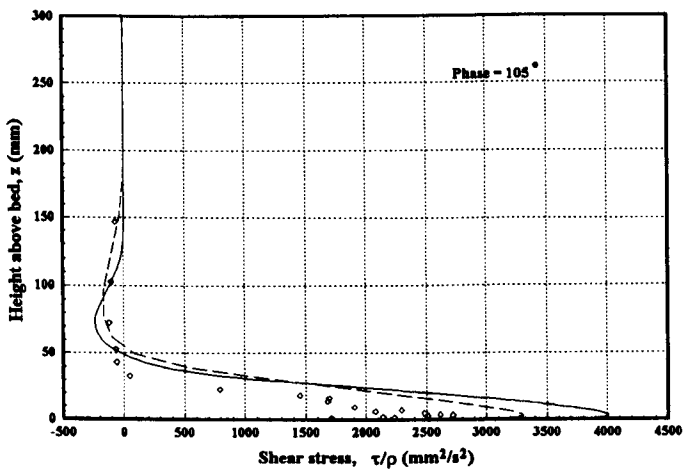

(h)

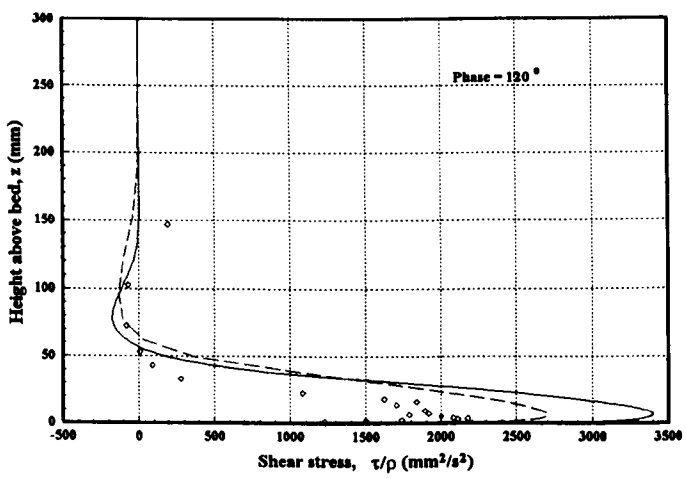

(i)

Figure 6.9(Cont.): Comparison of shear stress values from k-ε model and time-dependent k-model against laboratory data of Jensen *et al.* (1989): ◊ test 12, Jensen *et al.*; —— k-ε model; — — k-model.

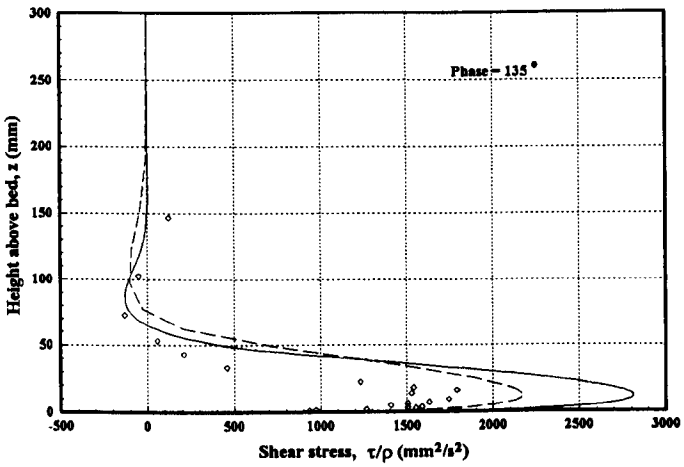

(j)

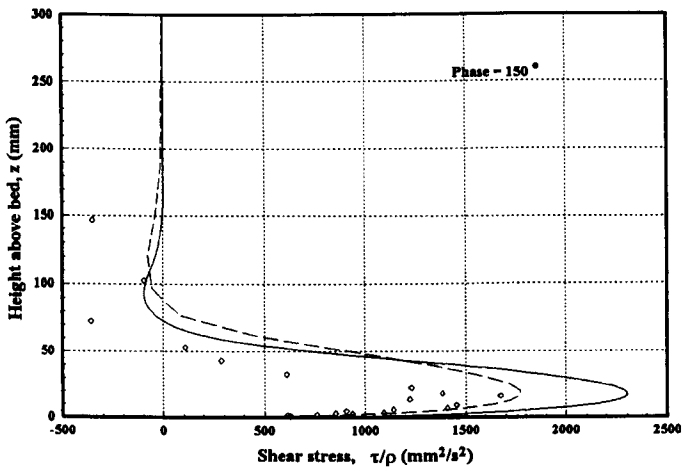

(k)

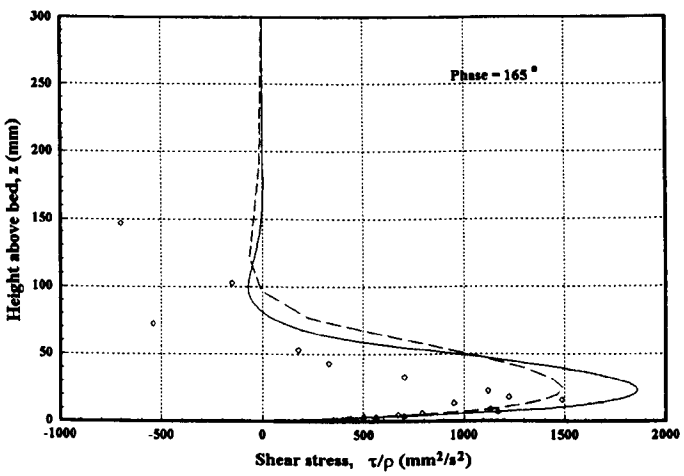

(l)

Figure 6.9(Cont.): Comparison of shear stress values from k-ε model and time-dependent k-model against laboratory data of Jensen *et al.* (1989): ◊ test 12, Jensen *et al.*; —— k-ε model; — — k-model.

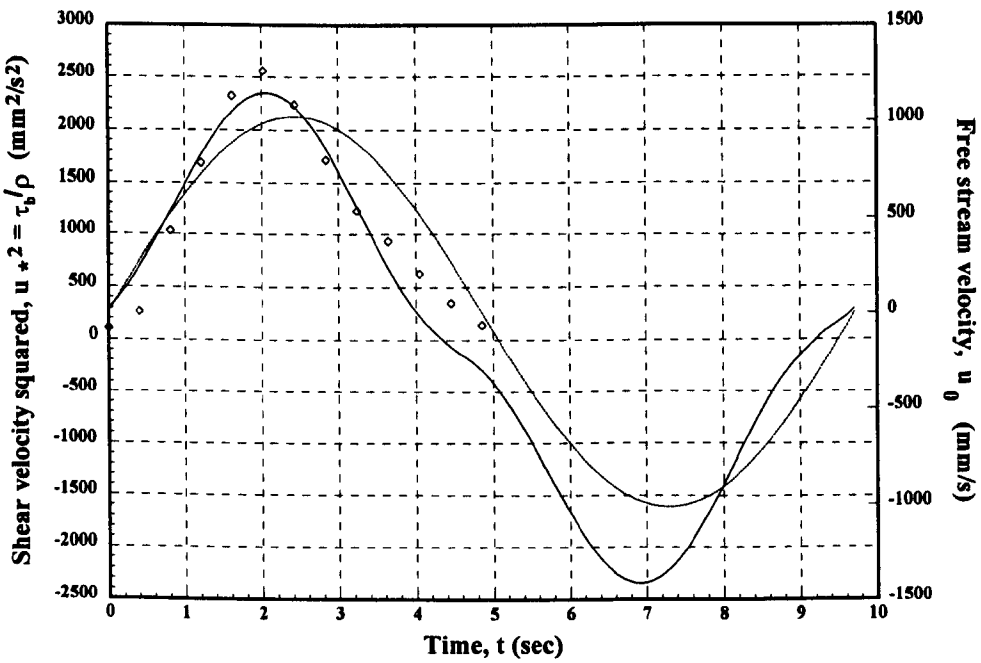

Figure 6.10: Comparison of bed shear stress (—) and freestream velocity (– – –) from k-ε model. ◊ shear velocity data, test 12, Jensen *et al* (1989).

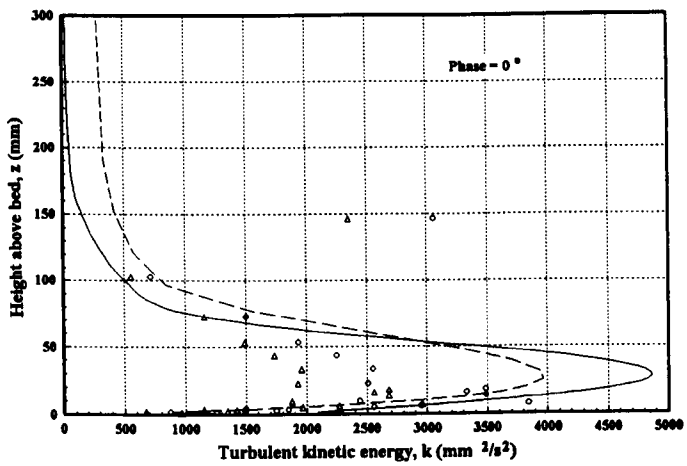

(a)

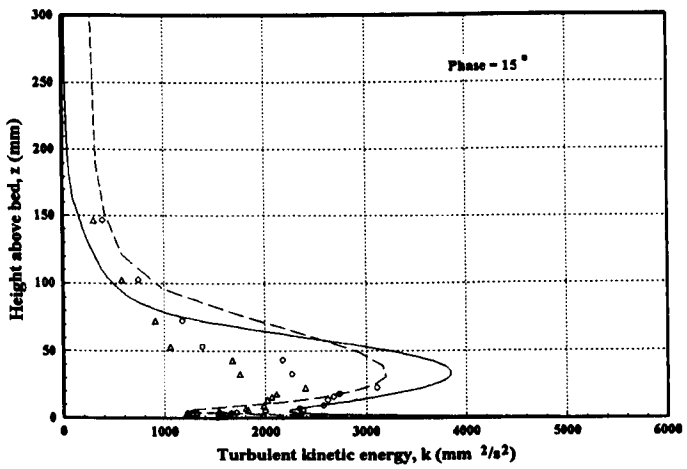

(b)

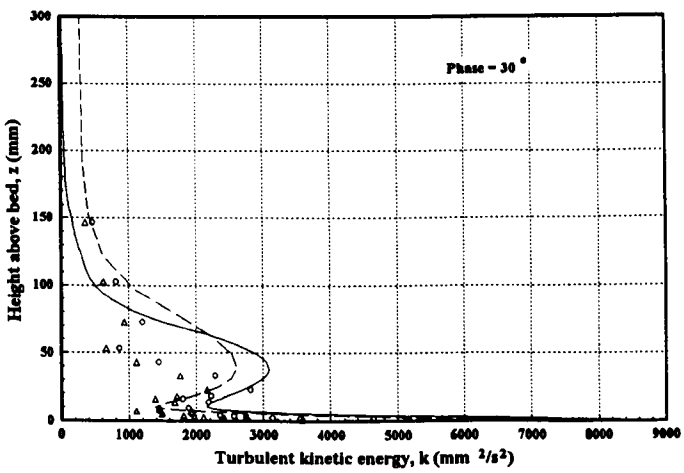

(c)

Figure 6.11: Comparison of turbulent kinetic energy (k) values from k-ε model and time-dependent k-model against laboratory data of Jensen *et al.* (1989): O (x 1.3) Δ (x 1.0) test 12, Jensen *et al.*; —— k-ε model; — — k-model.

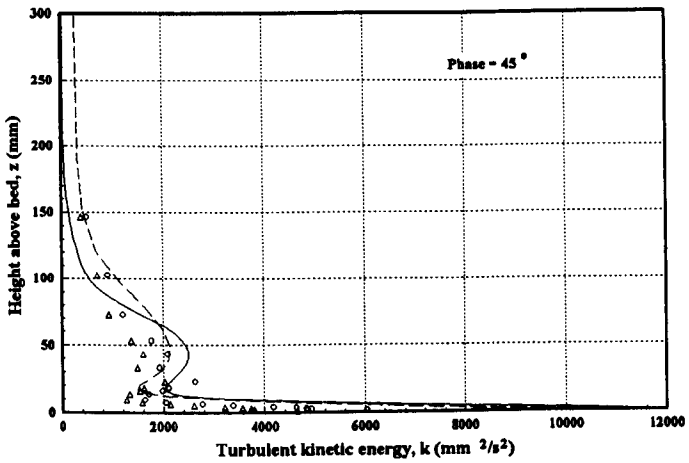

(d)

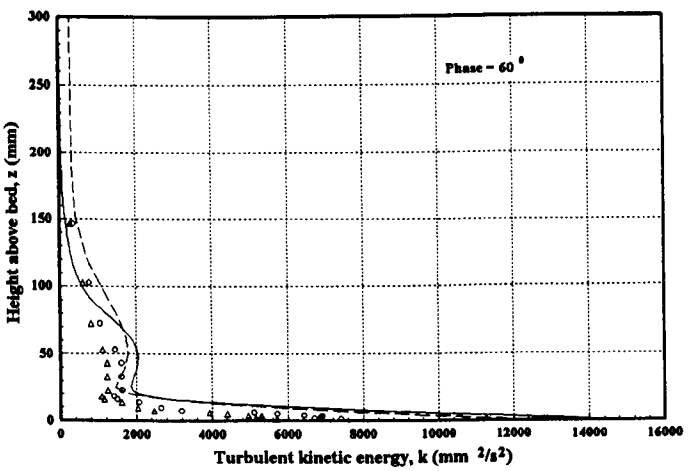

(e)

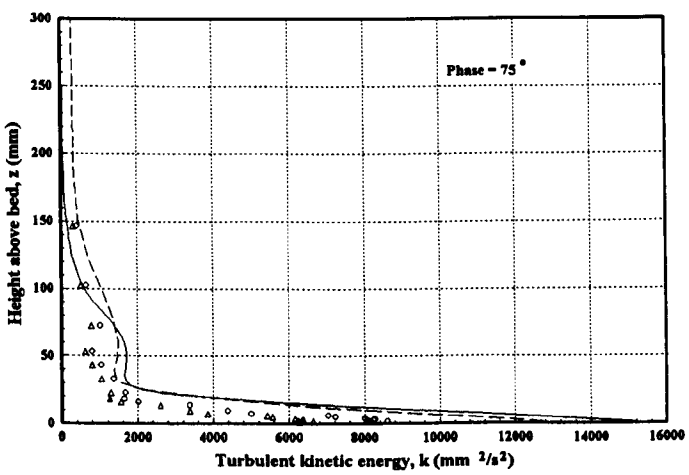

(f)

Figure 6.11(Cont.): Comparison of k values from k-ε model and time-dependent k-model against laboratory data of Jensen *et al.* (1989): O (x 1.3) Δ (x 1.0) test 12, Jensen *et al.*; —— k-ε model; — — k-model.

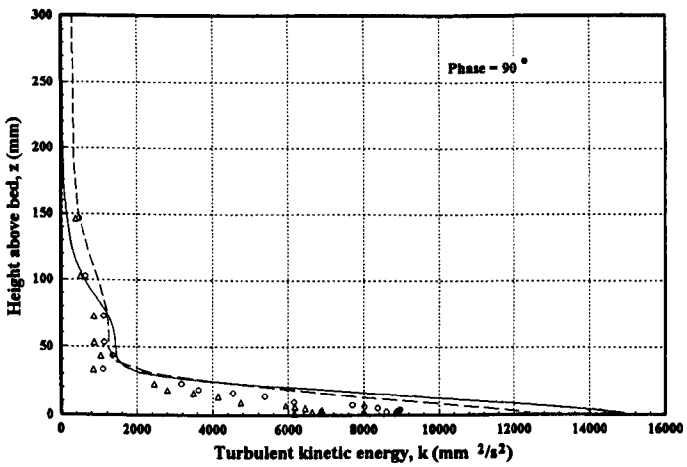

(g)

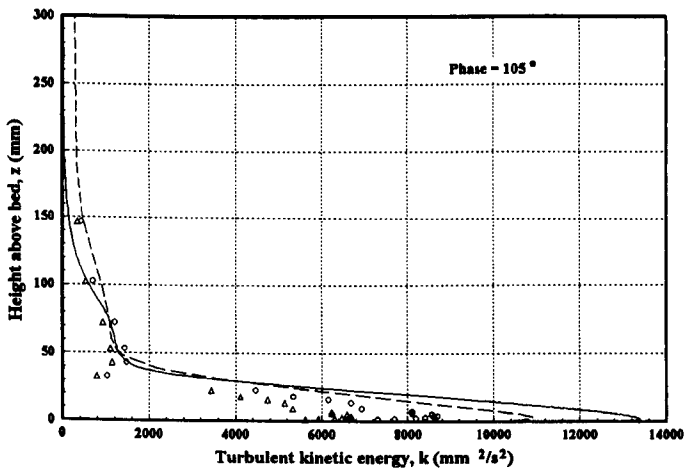

(h)

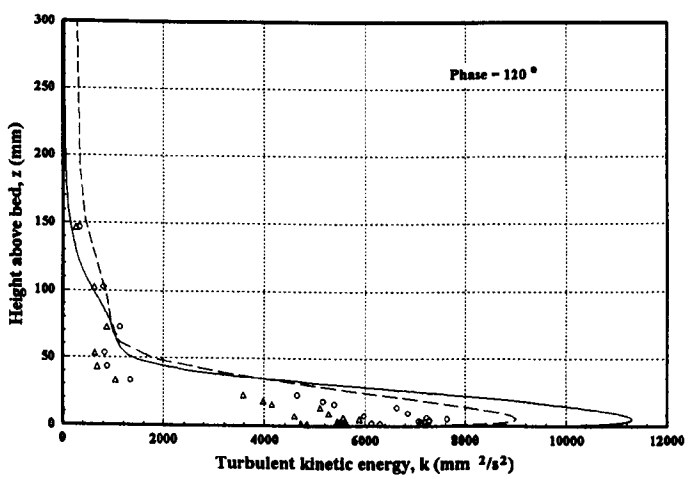

(i)

Figure 6.11(Cont.): Comparison of k values from k-ε model and time-dependent k-model against laboratory data of Jensen *et al.* (1989): O (x 1.3) Δ (x 1.0) test 12, Jensen *et al.*; —— k-ε model; — — k-model.

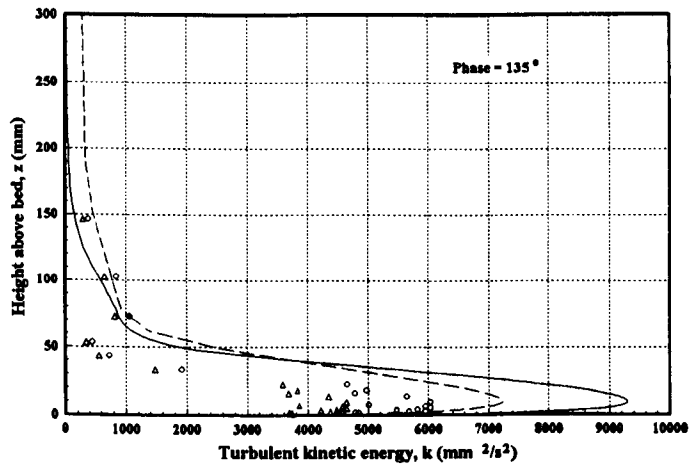

(j)

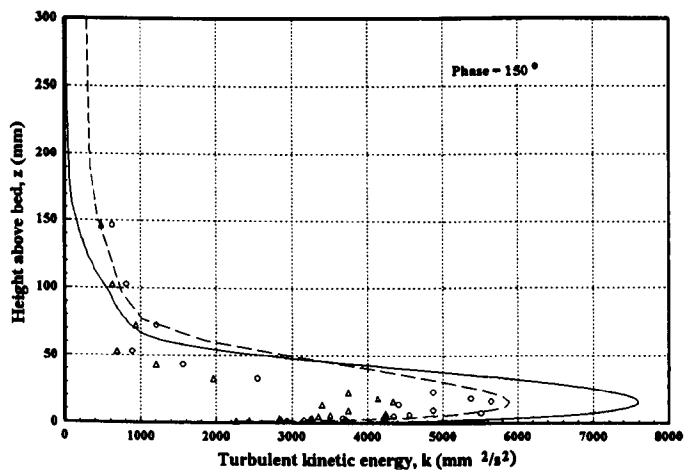

(k)

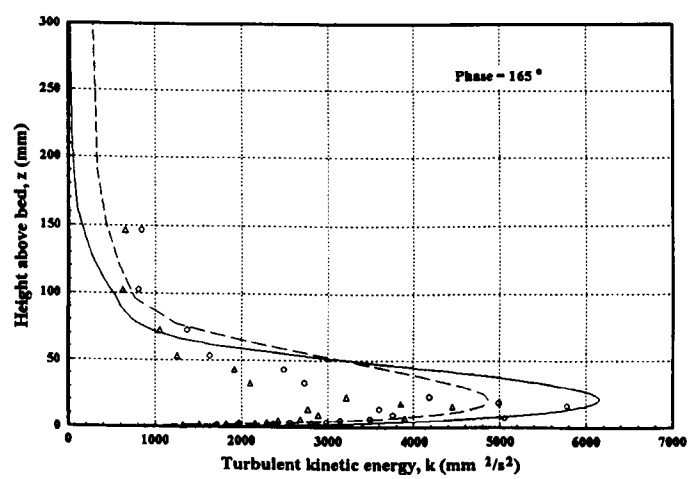

(l)

Figure 6.11(Cont.): Comparison of k values from k-ε model and time-dependent k-model against laboratory data of Jensen *et al.* (1989): O (x 1.3) Δ (x 1.0) test 12, Jensen *et al.*; —— k-ε model; — — k-model.

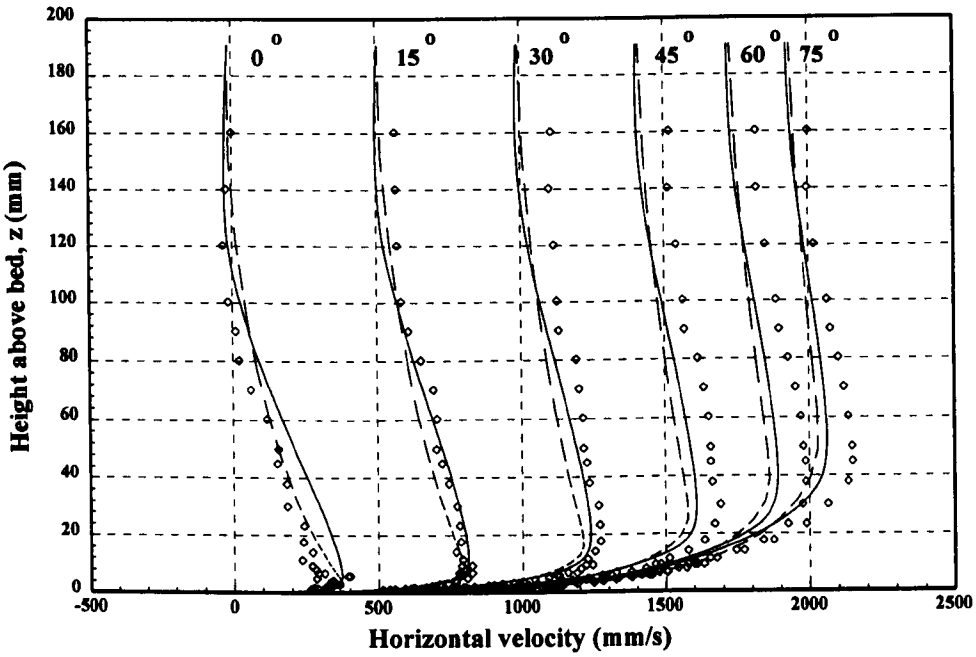

Figure 6.12a: Comparison of k-ε model and time-dependent k-model against laboratory data of Jensen *et al.* (1989): ◊ test 13, Jensen *et al.*; —— k-ε model; — — k-model.

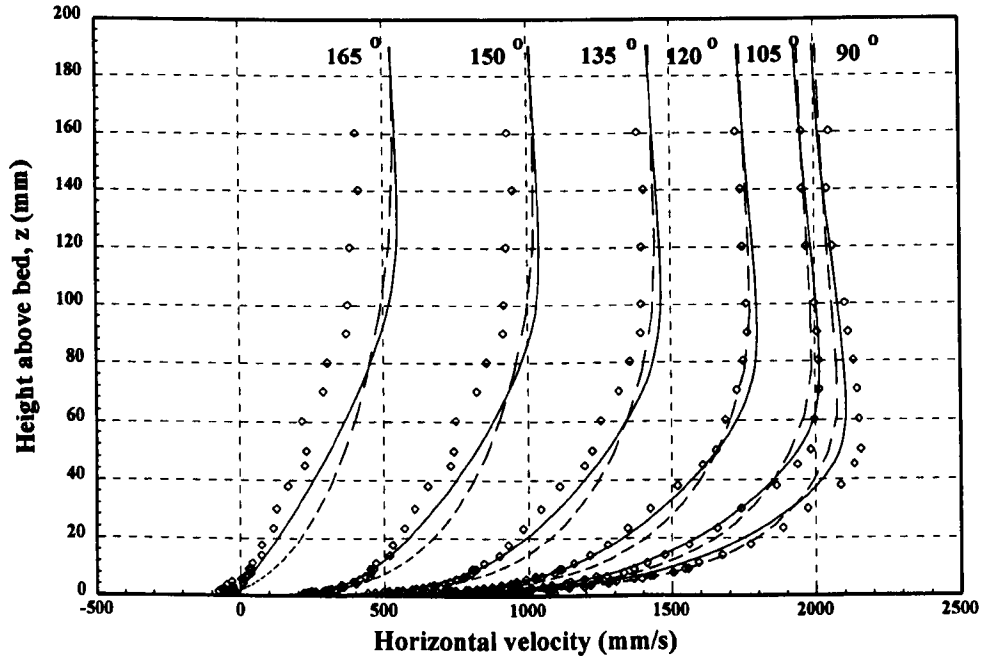

Figure 6.12b: Comparison of k-ε model and time-dependent k-model against laboratory data of Jensen *et al.* (1989): ◊ test 13, Jensen *et al.*; —— k-ε model; — — k-model.

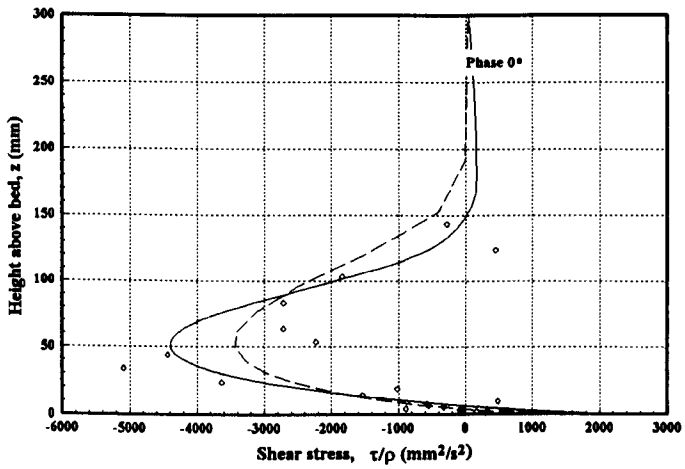

(a)

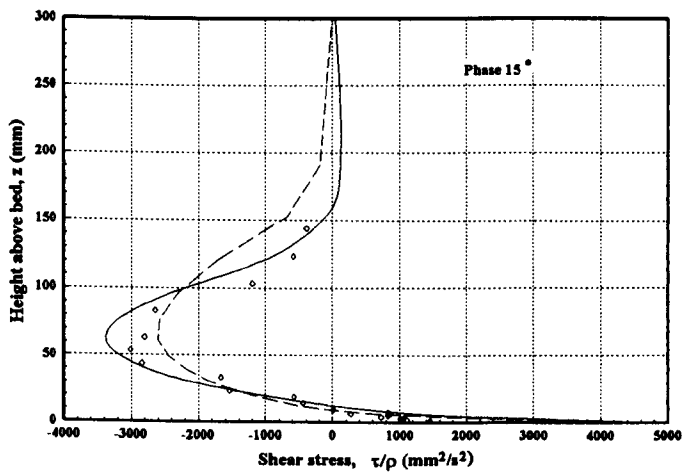

(b)

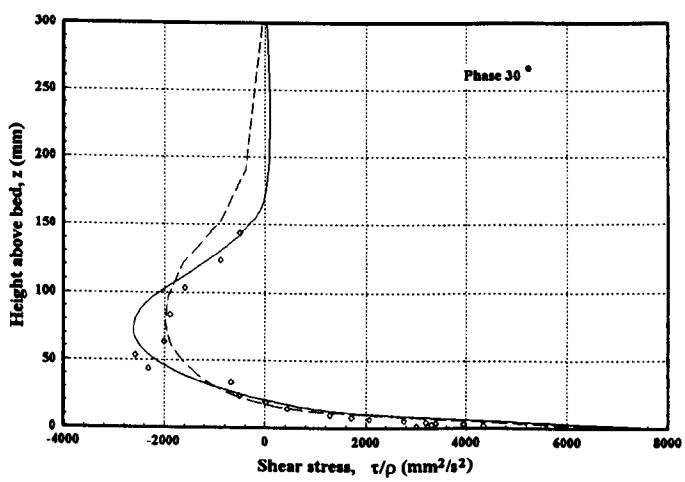

(c)

Figure 6.13: Comparison of shear stress values from k-ε model and time-dependent k-model against laboratory data of Jensen *et al.* (1989): ◊ test 13, Jensen *et al.*; —— k-ε model; — — k-model.

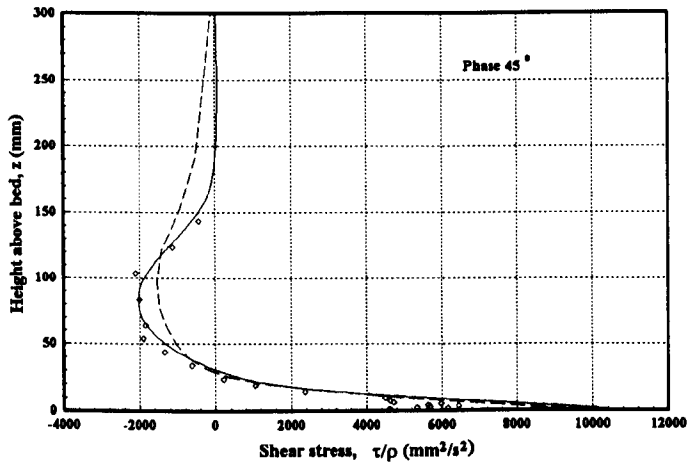

(d)

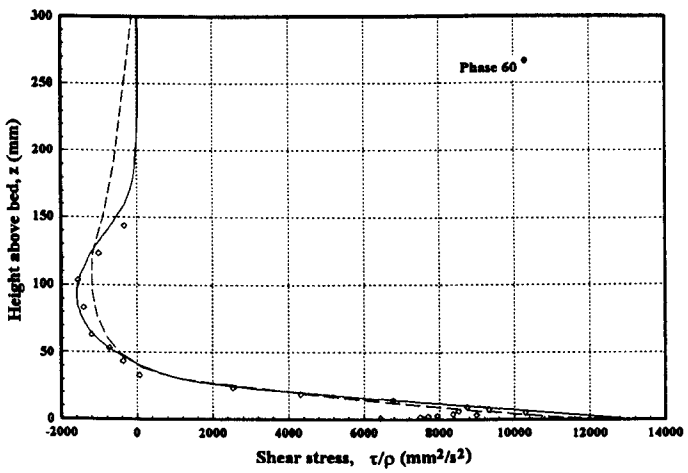

(e)

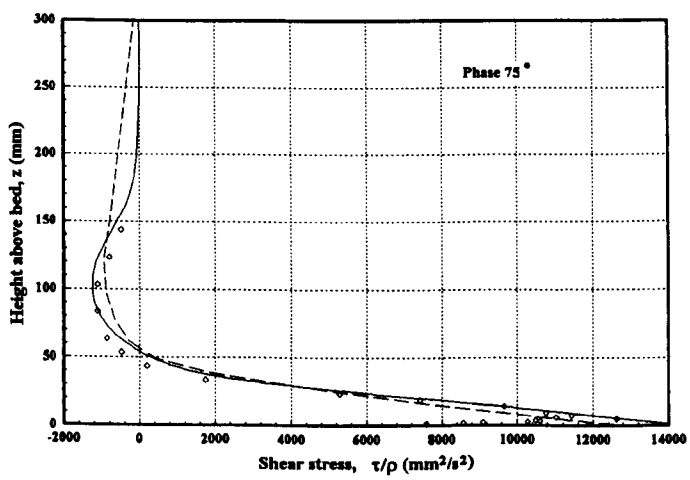

(f)

Figure 6.13(Cont.): Comparison of shear stress values from k-ε model and time-dependent k-model against laboratory data of Jensen *et al.* (1989): ◊ test 13, Jensen *et al.*; —— k-ε model; — — k-model.

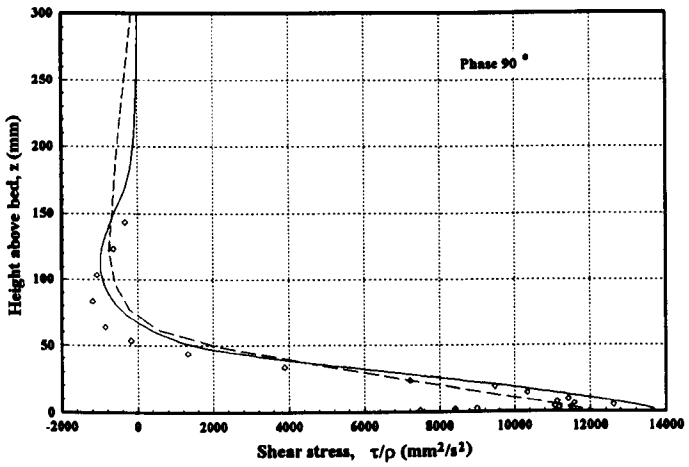

(g)

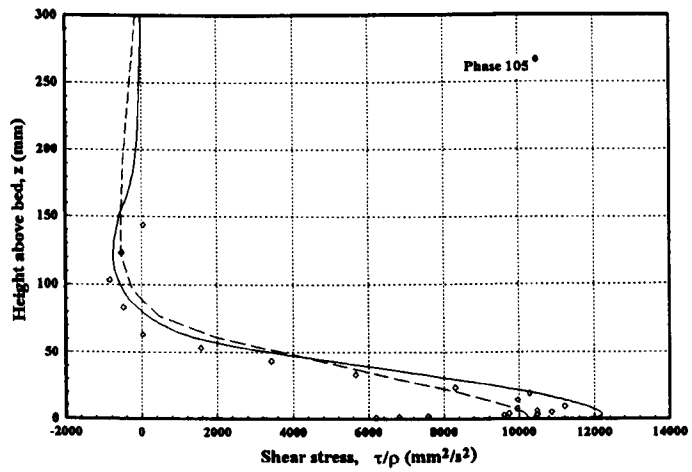

(h)

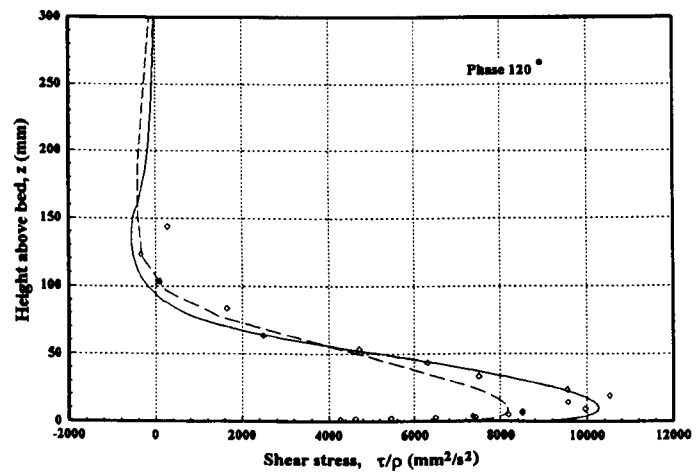

(i)

Figure 6.13(Cont.): Comparison of shear stress values from k-ε model and time-dependent k-model against laboratory data of Jensen *et al.* (1989): ◊ test 13, Jensen *et al.*; —— k-ε model; — — k-model.

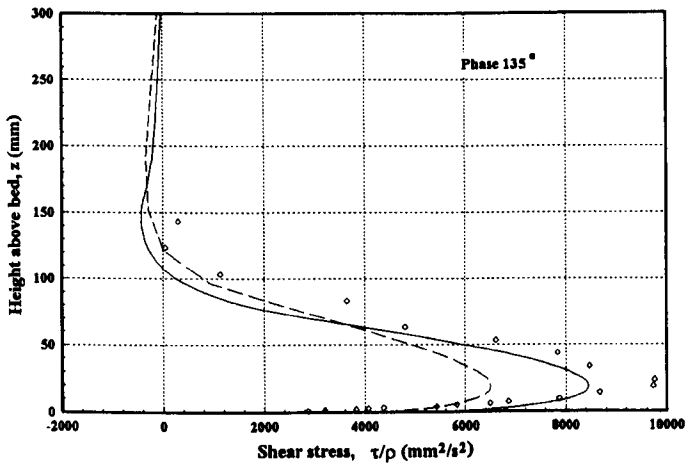

(j)

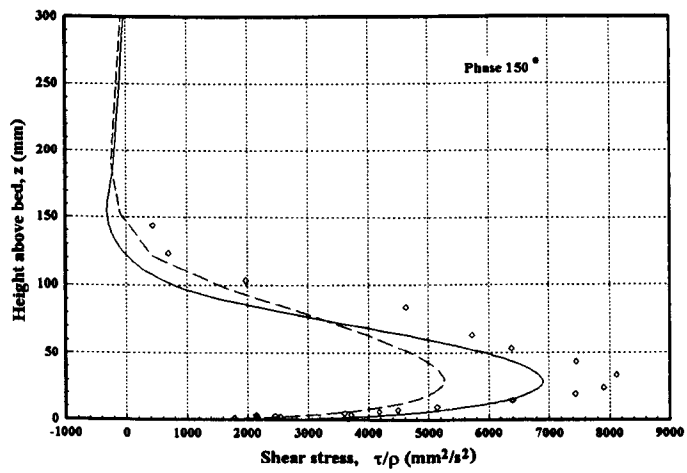

(k)

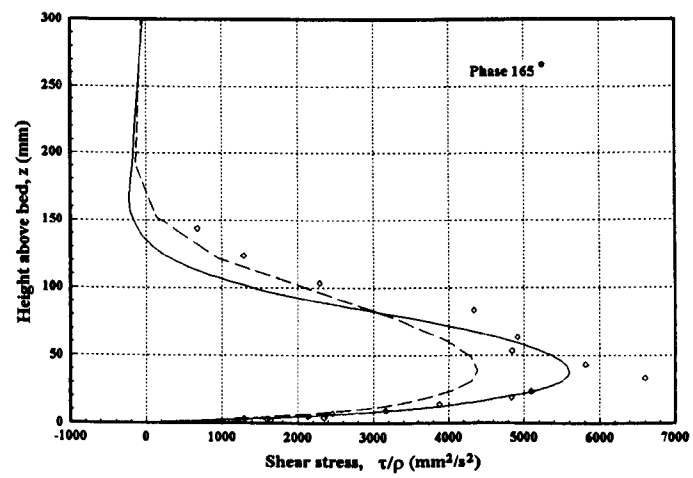

(l)

Figure 6.13(Cont.): Comparison of shear stress values from k-ε model and time-dependent k-model against laboratory data of Jensen *et al.* (1989): ◊ test 13, Jensen *et al.*; —— k-ε model; — — k-model.

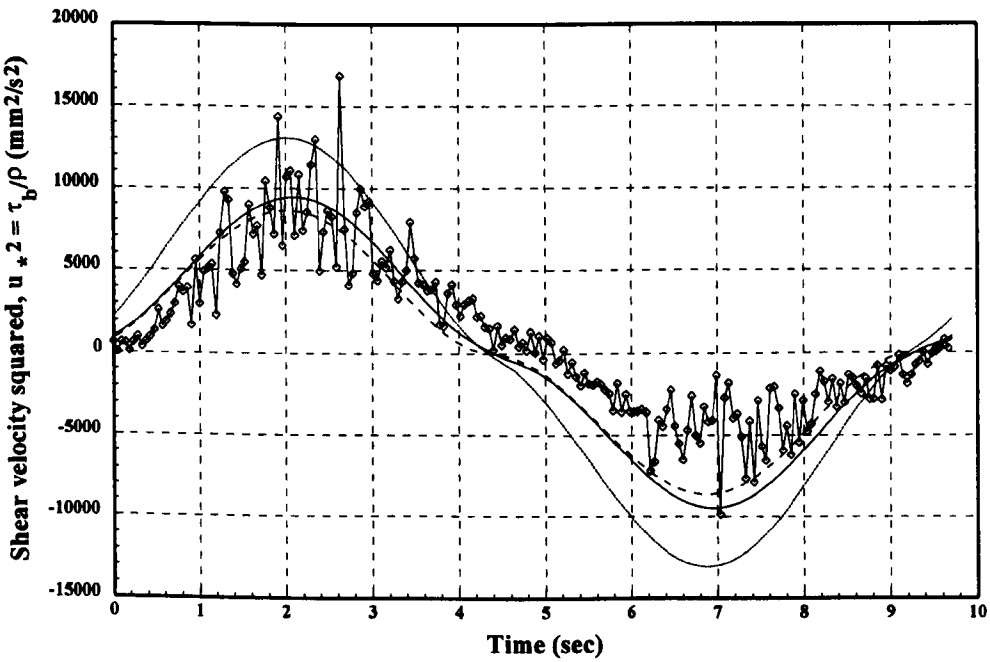

Figure 6.14: Comparison of bed shear stress values from k-ε model and time-dependent k-model against laboratory data of Jensen *et al.* (1989): —◊— test 13, Jensen *et al.*; —— k-ε model; – – – k-model; — — k-model with kinematic (molecular) viscosity included in solution.

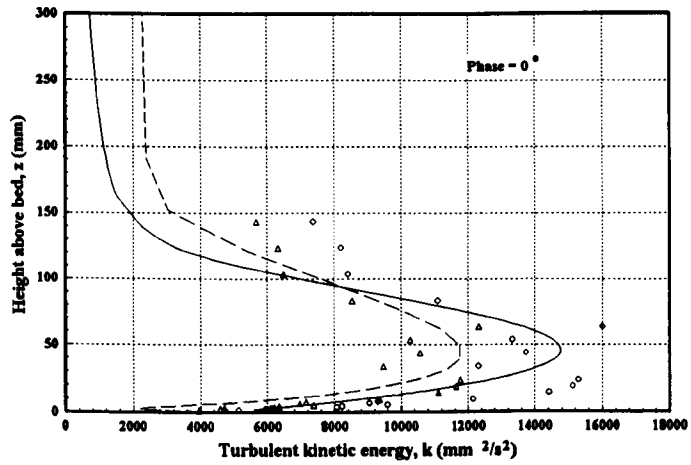

(a)

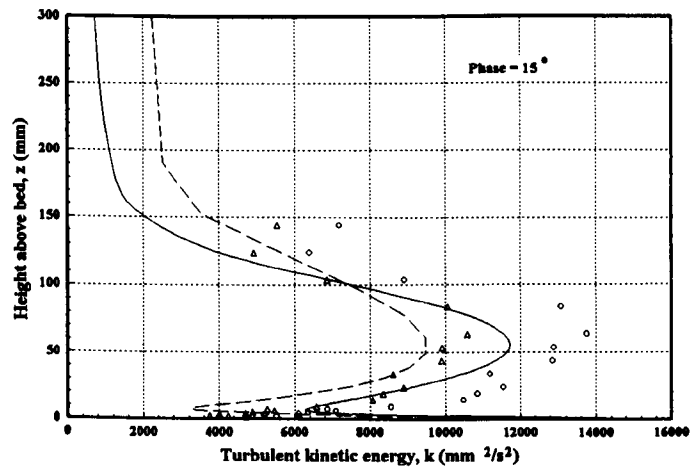

(b)

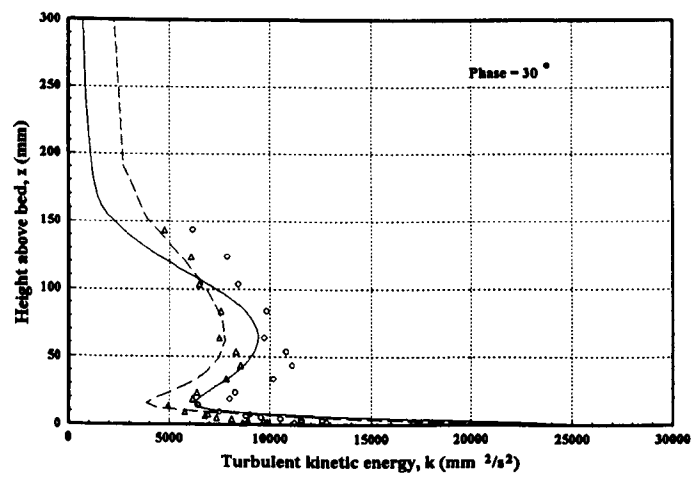

(c)

Figure 6.15: Comparison of turbulent kinetic energy (k) values from k-ε model and time-dependent k-model against laboratory data of Jensen *et al.* (1989): O (x 1.3) Δ (x 1.0) test 13, Jensen *et al.*; —— k-ε model; — — k-model.

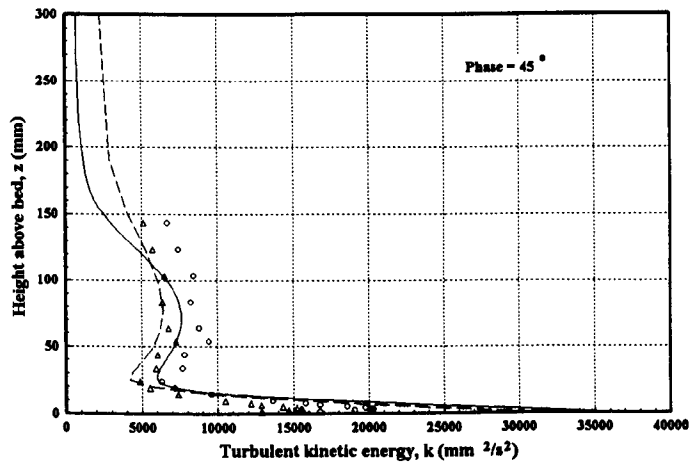

(d)

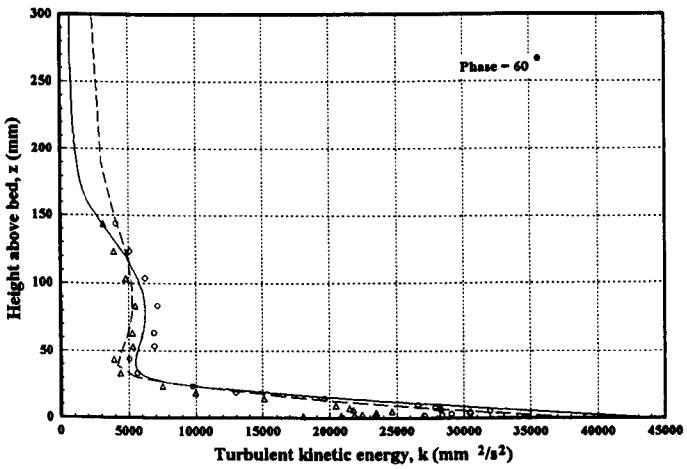

(e)

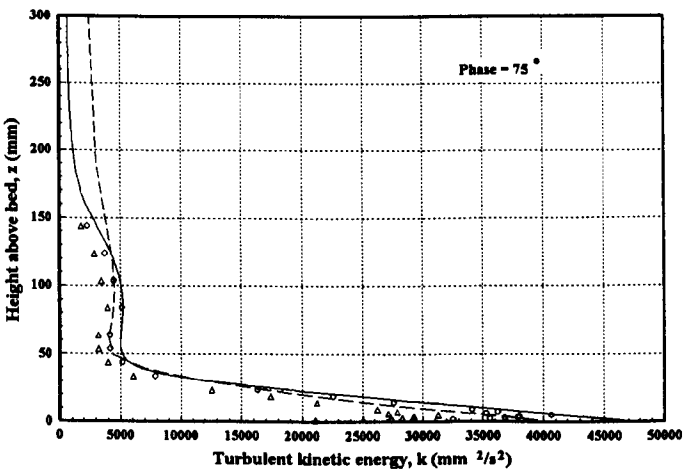

(f)

Figure 6.15(Cont.): Comparison of k values from k-ε model and time-dependent k-model against laboratory data of Jensen *et al.* (1989): O (x 1.3) Δ (x 1.0) test 13, Jensen *et al.*; —— k-ε model; — — k-model.

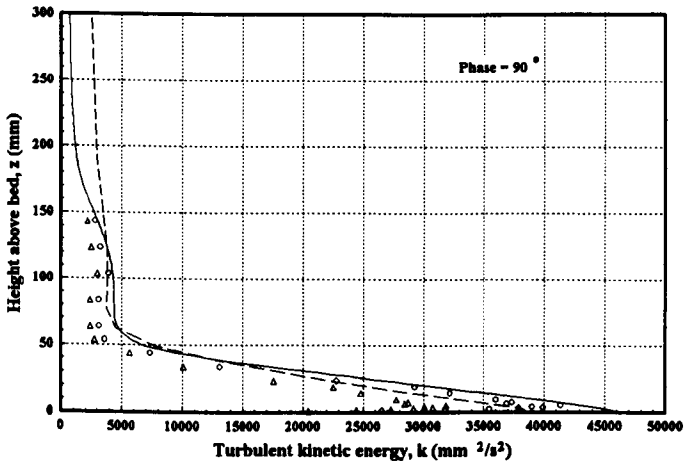

(g)

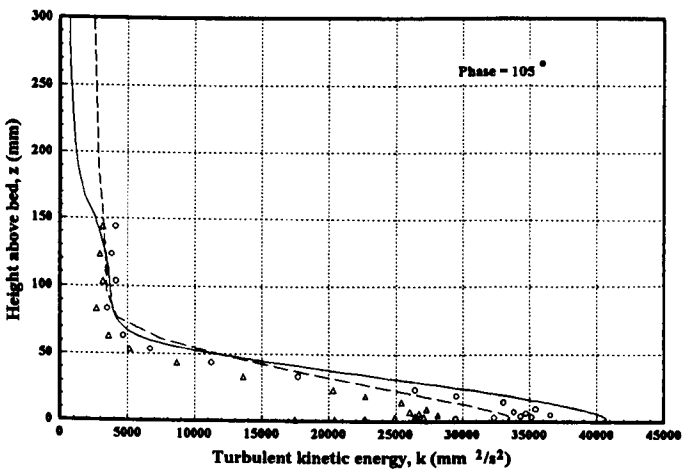

(h)

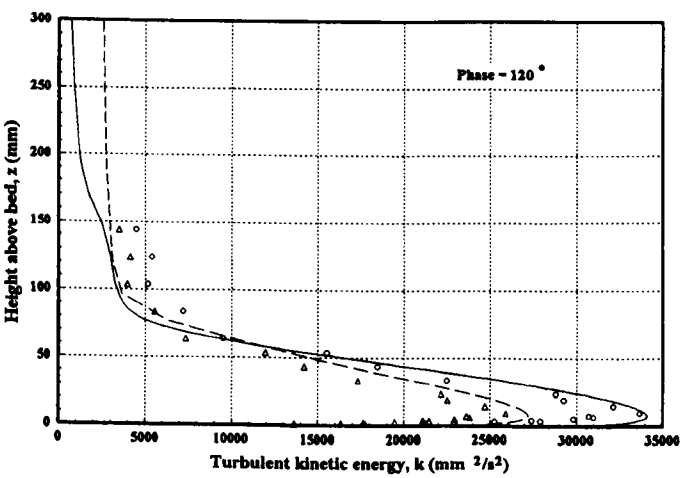

(i)

Figure 6.15(Cont.): Comparison of k values from k-ε model and time-dependent k-model against laboratory data of Jensen *et al.* (1989): O (x 1.3) Δ (x 1.0) test 13, Jensen *et al.*; —— k-ε model; — — k-model.

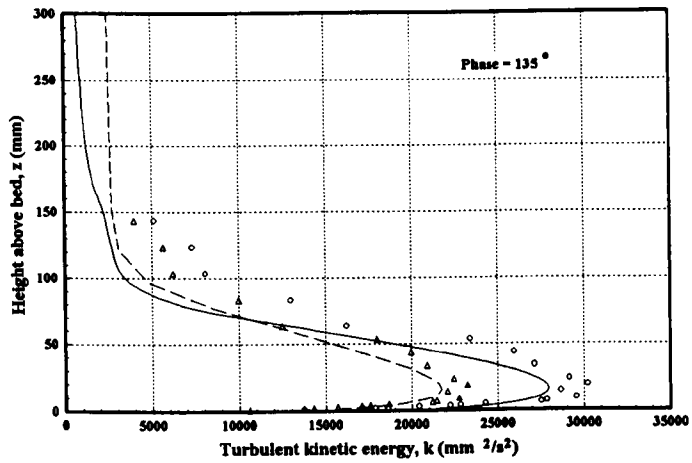

(j)

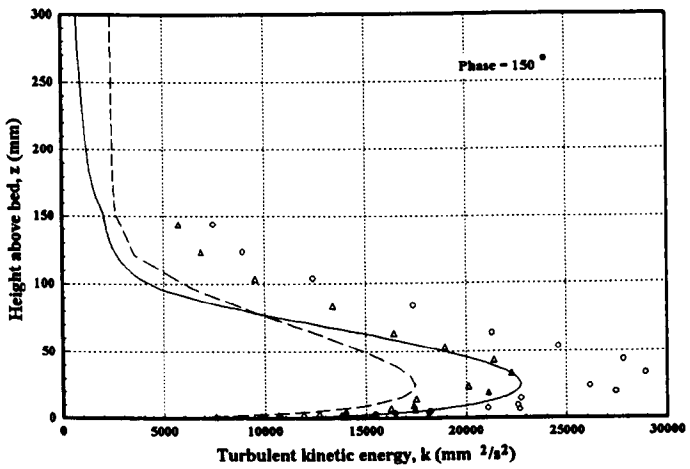

(k)

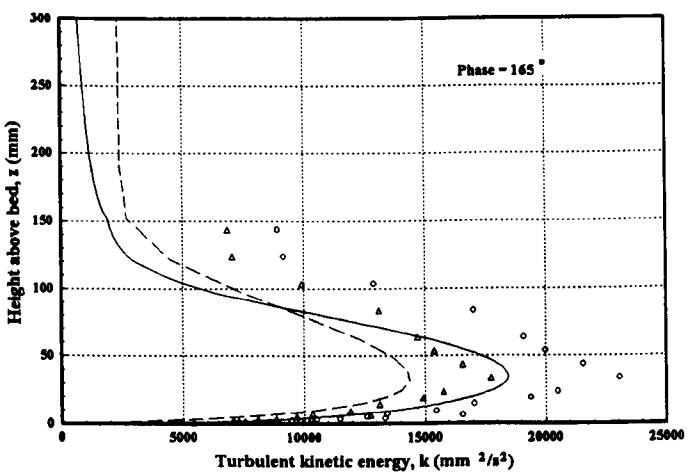

(l)

Figure 6.15(Cont.): Comparison of k values from k-ε model and time-dependent k-model against laboratory data of Jensen *et al.* (1989): O (x 1.3) Δ (x 1.0) test 13, Jensen *et al.*; —— k-ε model; — — k-model.

Chapter 7
Results: Part II

7.1 Manchester Experiments

7.1.1 Introduction

During the late 1970's and early 1980's a comprehensive experimental programme was undertaken at the University of Manchester under the direction of Professors D.M. McDowell and B.A O'Connor. The main objective of the laboratory work was to investigate the interaction occurring in combined wave and current flows, with a view to providing a better description for bed friction and sediment entrainment for use in computer models. Much of the early work has been presented in various sources (see McDowell 1983; Wong 1984; Savell 1986; O'Connor 1987; Taplin 1989).

Initial tests took place in a small scale flume 450 mm deep, 500 mm wide and 22 m in length (see Figures 7.1 and 7.2). This flume was equipped with a wave-absorbing paddle capable of reproducing both mono-frequency and random waves (Ellis *et al.* 1981). Later tests took place in a larger glass-sided flume, 1.2 m deep 1.2 m wide and 30 m in length (O'Connor *et al.* 1988).

	Test Number	
	52	**59**
Nominal mean current (mm/s)	0.0	125.0
Mean velocity at 100 mm (mm/s)	0.0	119.4
Wave period	1.53	1.50
Wave height (mm)	74	72
Amplitude Reynolds No.	7523	7818
Displacement, a (mm)	44.1	43.0
Water temperature, (° C)	18.0	21.0
Kinematic viscosity, ν_L (mm^2/s)	1.066	0.990

Table 7.1: Experimental conditions for tests 52 and 59.

Some of the experimental data remains unpublished, however, two small flume tests have been chosen for comparison with the numerical turbulence models developed during the present research, test 52 , an experiment involving mono-frequency waves alone and test 59, which is for combined waves and current conditions (see Savell 1986). All measurements were undertaken using a two-channel Laser-Doppler anemometer (LDA).

Before embarking on the main experimental programme, a large number of preliminary experiments was carried out. The principle aims were to test the equipment and to establish the validity of the measurements by comparing the results against accepted published work (see Savell 1986). The tests included comparison with results for steady undisturbed flow as well as against Lamb's (1932) analytical solution for laminar flow. (see Chapter 3 and Figure 3.2). The results of these preliminary tests showed the experimental set-up to be performing well.

7.2 Test 52: Waves alone

Test 52 was used to establish the characteristics of the hydrodynamics of the waves alone. Savell (1986) suggests that the results were not totally satisfactory due to problems with the data acquisition software and a possible drift in the LDA calibration resulting in the mean horizontal and vertical velocities being out by up to 10 mm/s. However, any error was confined to the mean velocities only. Test 52 was carried out in the small scale facility and the physical scale is such as to place the flow field into the transitional regime (Re = 7523).

The test was chosen to investigate the effect of transitional flows on model performance as well as the applicability of model type. The models were run with the boundary conditions given in Chapters 2 and 4 and the constants used were as stated in Chapter 4. Applying a high-Reynolds-number model should lead to poor results since the assumption of a fully turbulent regime has not been reached. In such instances, a low-Reynolds-number model or a two-layer k-ε model should be used. This is clearly demonstrated in Figure 7.3 where a comparison between a two-layer k-ε model and a high-Reynolds-number k-ε model and velocity data from test 52 show the latter model to predict too high a level of turbulence in the

flow field. In contrast, the two-layer model shows reasonable agreement with the data. Further, since the free stream velocity is not a pure sinusoid as the laboratory signal contains harmonics, it is possible to improve the simulation by using Fourier analysis to represent the free stream velocity, see Figure 7.4. The distortion of the wave shape is most likely due to reflections from the beach at the end of the flume, additional wave harmonics due to imperfect paddle motion and shallow water effects. Savell (1986) discusses these points in some detail.

The Fourier series representation of the free stream velocity signal is given by the following expression:-

$$u_0(t) = \frac{a_0}{2} + \sum_{k=1}^{n}\left[a_k \cos\left(\frac{2\pi kx}{2n+1}\right) + b_k \sin\left(\frac{2\pi kx}{2n+1}\right)\right] \qquad \textbf{(7.1a)}$$

where a_0 , a_k and b_k are coefficients and are determined by the formulae:-

$$a_0 = \frac{2}{(2n+1)}\sum_{i=0}^{2n} f(x_i) \qquad \textbf{(7.1b)}$$

$$a_k = \frac{2}{(2n+1)}\sum_{i=0}^{2n} f(x_i)\cos\left(\frac{2\pi kx_i}{2n+1}\right), \; k = 0,\ 1,\ 2,\ \ldots\ldots,n \qquad \textbf{(7.1c)}$$

$$b_k = \frac{2}{(2n+1)}\sum_{i=0}^{2n} f(x_i)\sin\left(\frac{2\pi kx_i}{2n+1}\right), \; k = 0,\ 1,\ 2,\ \ldots\ldots,n \qquad \textbf{(7.1d)}$$

and f (x) is the function, that is, the free stream velocity, $u_0(t)$. For further details see Newland (1984).

Comparison of the two-layer model with the Reynolds stress measurements would appear to be less satisfactory, generally showing significant scatter (Figure 7.5). Whilst, overall, the model predicts the main trend, at first sight the agreement with the laboratory data is less convincing. Savell (1986) suggests that a possible reason for this large scatter in the laboratory data may be due, in part, to not taking a sufficiently long measurement period. In addition, the Reynolds stress is a product of two inaccurate measurements (u', w') and must, therefore, be considered as being less reliable. However, it should be remembered that whilst the two-layer model calculates the shear stress as a combination of turbulent eddy viscosity and kinematic (molecular) viscosity, the measured values are only based on the turbulent

fluctuations and not the total shear. This difference is clearly shown in Figure 7.6 where model results are presented for the total shear (molecular viscosity and Reynolds stress) and for the Reynolds stress alone, that is:-

$$\tau_{Total} = \tau_{Viscous} + \tau_{Turbulent} = \rho\nu_L \frac{\partial u}{\partial z} + \rho\overline{u'w'} \qquad (7.2)$$

Accounting for the measurement height in the data but calculating the total shear, the maximum measured 'bed shear velocity' is seen to be approximately four times smaller than that predicted by the model. However, once the influence of molecular viscosity is removed from the model, the comparison between measured and modelled shear stress shows a much more reasonable fit (Figure 7.6). Figure 7.6 also shows the calculated total shear stress at the measurement height compared with the 'true' calculated bed shear velocity, this 'true' bed value is calculated at z_0 = 0.035 mm and the lowest measurement point is at 0.73 mm. Comparison between the total stress values calculated by the model for the true bed value and that corresponding to the lowest measurement point show a phase shift, whilst the actual magnitudes are little altered. The phase lead between the maximum bed shear stress and the maximum free stream velocity is approximately 36°.

A comparison of the two layer model with the measured turbulent kinetic energy profiles shows significant scatter, Figure 7.7. It is difficult to assess whether the overall trend is well predicted by the model since it is not that clear from the laboratory data what the actual trend is. For some of the phases a higher level of turbulence is observed outside the boundary layer, whilst the model shows a decrease. The reduction in the measured values close to the bed is reflected in the model results indicating the effect of the laminar wall layer damping out the turbulence.

7.3 Test 59: Combined waves and current

The general test conditions for test 59 are shown in Table 7.1. Figure 7.8 shows a comparison between a two-layer k-ε model, a high-Reynolds number k-ε model and velocity data from test 59. The two-layer model is unable to reproduce the increase in the wave boundary layer thickness due to the addition of a current (compare with Figure 7.3 for test 52). It is the high-

Reynolds number model which now provides a better description of the laboratory data. Clearly, the interaction of the waves and current increases mixing within the wave boundary layer. The addition of the current has clearly increased the turbulence production. Savell (1986) argues that the adding of the current makes the boundary layer turbulent.

Figure 7.9 shows a comparison of the measured free stream velocity and that calculated by the model. It is observed that the profile is not symmetrical with the wave crest being much sharper than the trough.

Figure 7.10 shows a comparison of the shear stress values calculated by the high-Reynolds number k-ε model against the laboratory data. Whilst there is considerable scatter, the overall agreement appears reasonable, although there appears to be a phase error with one of the data sets (Figure 7.10c). The model predicts a much sharper decrease in the shear stress outside the boundary layer than does the experimental data. Initially, it was thought that this was due to a coding error in the model, but on further examination this was eliminated.

The model assumes that the flow is uniform in the direction of the flow. However, this is not true and the near-bed velocity variation must be changed from Eq. (2.29):-

$$u_0 = u_\infty \sin(\omega t) \qquad \textbf{(2.29)}$$

and represented now by the equation:-

$$u_0 = u_\infty \sin(\omega t - kx) \qquad \textbf{(7.3)}$$

where k (= 2π /L) is the wave number and L is the wavelength.

The result of this change is to lead to the creation of a vertical flow velocity, which is small compared to the orbital velocities. The additional vertical velocity outside the boundary layer, w_∞, decreases through the boundary layer to a value of zero at the bed. The creation of this small vertical velocity leads to a time-average term, $\overline{u_\infty w_\infty}$ which is not exactly ninety degrees out of phase and hence, non-zero. This means that an additional shear stress will be induced, giving rise to a weak circulatory current. It is suggested that it is this phenomenon which is part of the reason why there is a difference in the measured shear velocity outside the boundary layer to that predicted by the model.

Comparison of the turbulent kinetic energy results from the k-ε model and those from test 59 reveal a similar tendency as that shown by the shear stress (Figure 7.11). The model underpredicts the values of the shear stress and turbulent kinetic energy in the upper part of the water column, showing a more rapid reduction than is observed in the experimental data. A zero gradient condition has been applied as the upper boundary condition in the turbulent kinetic energy equation (Eq. 4.41b) which may not be appropriate when a current is applied. Therefore, providing a different boundary condition might also result in an improved fit between the model and measured data. However, initial results applying a non-zero gradient condition proved unsuccessful. Further work is required into both the effect of streaming (as discussed above), as well as the type of upper boundary condition applied in the turbulent kinetic energy equation. The experimental data shows large scatter as in the shear velocity measurements.

7.4 Conclusions

Comparison of a two-layer k-ε model and a high-Reynolds number k-ε model against laboratory experiments conducted at the University Manchester (Savell 1986) show the importance of applying the correct model to the physics. For low Reynolds number flows, it is essential to include the effects of molecular viscosity (Test 52).

The addition of a current to waves has been demonstrated to increase mixing within the wave boundary layer and increase the wave boundary layer thickness. In addition, such increased mixing leads to an increase in turbulence in the boundary layer.

It is suggested that the observed difference in magnitude of the shear stress and turbulent kinetic energy outside the boundary layer between the model and experimental data is partly due to streaming. The present models make no attempt to reproduce this phenomenon and it has not been investigated further. In addition, it is not clear whether the boundary conditions applied for the turbulent kinetic energy equation are sufficient to incorporate the effects of the current.

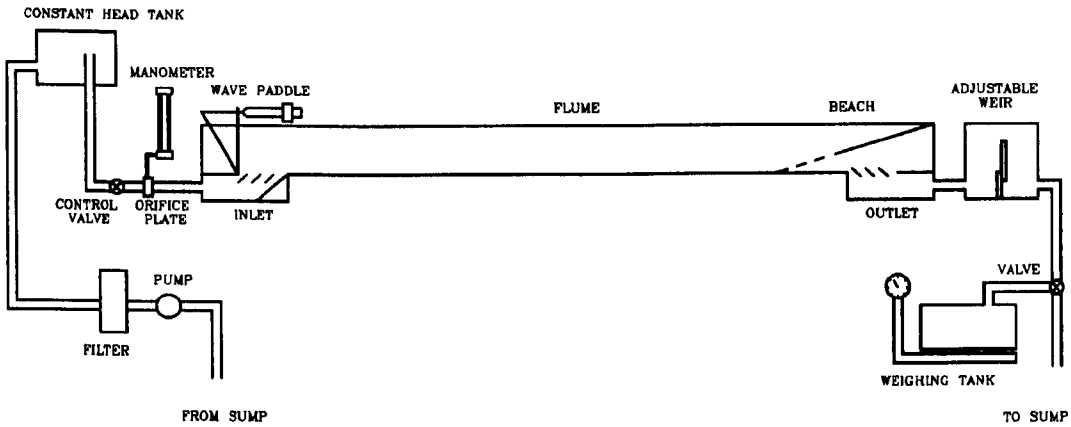

Figure 7.1: Schematic diagram of the wave/current flume at Manchester University. (*After Savell 1986*).

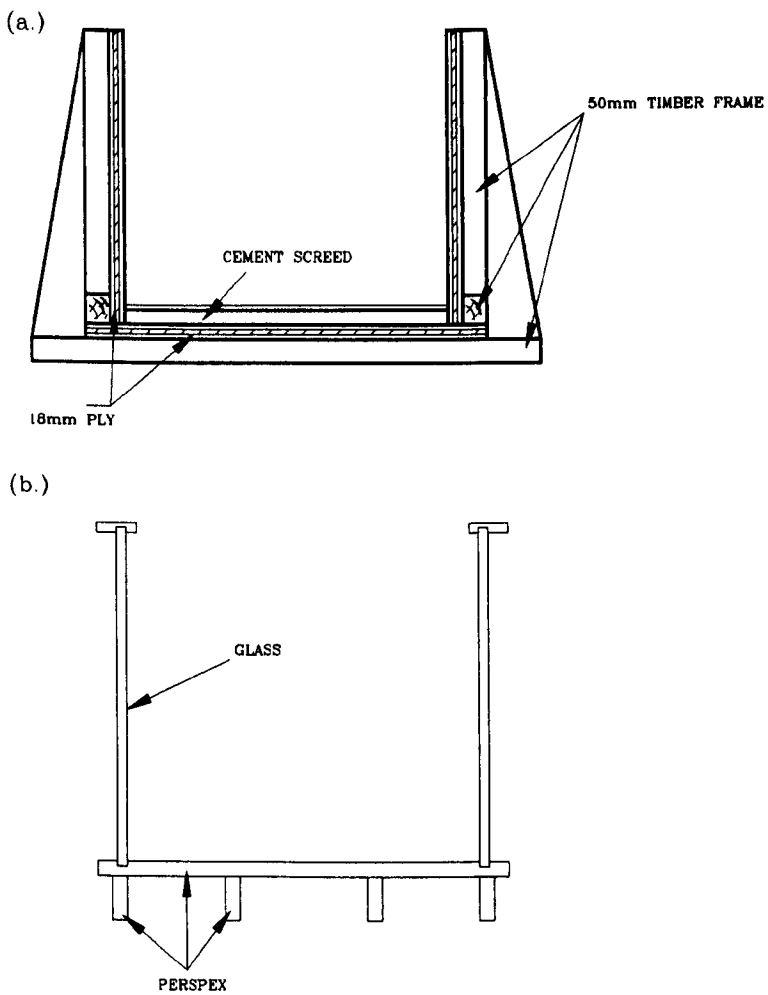

Figure 7.2: Cross-sections of the Manchester flume showing the normal construction (a.) and the construction of the measuring section (b.). Both sections are 500 mm wide and 450 mm deep (internal dimensions). (*After Savell 1986*).

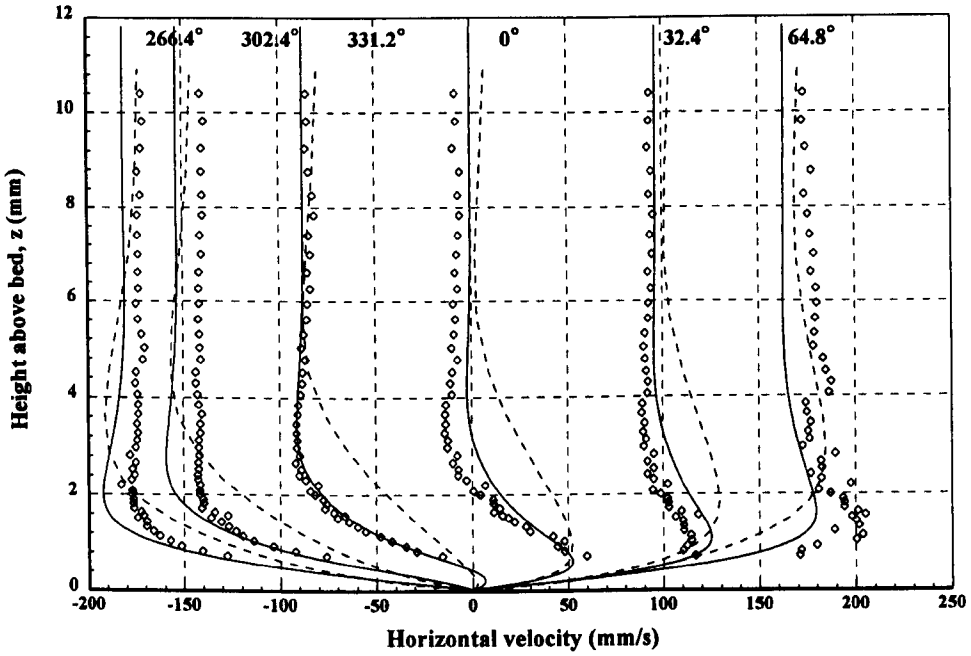

Figure 7.3: Comparison of k-ε model and two-layer k-ε model against Manchester laboratory data (Savell 1986): ◊ test 52, Savell; —— two-layer model; — — k-ε model.

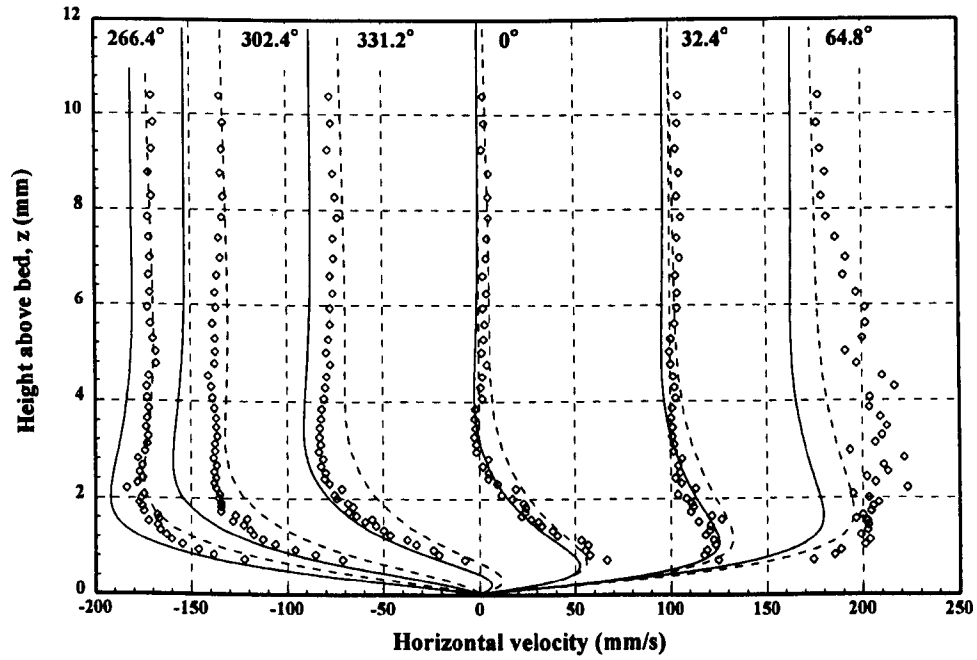

Figure 7.4: Comparison of two-layer k-ε model against Manchester laboratory data (Savell 1986): ◊ test 52, Savell; — — two-layer model (Fourier series, 5 components); —— two-layer model.

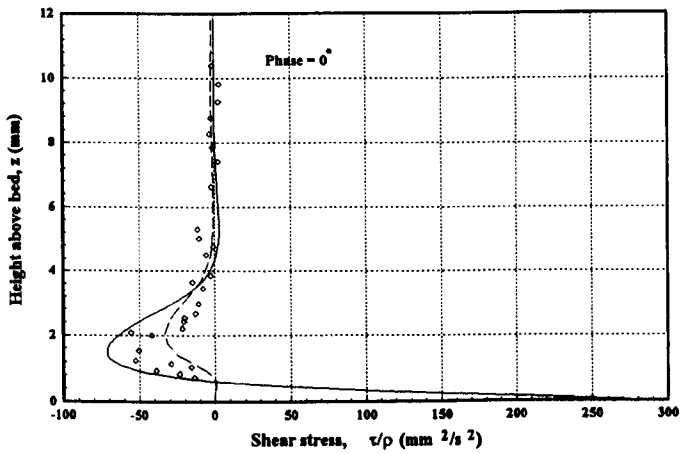

(a)

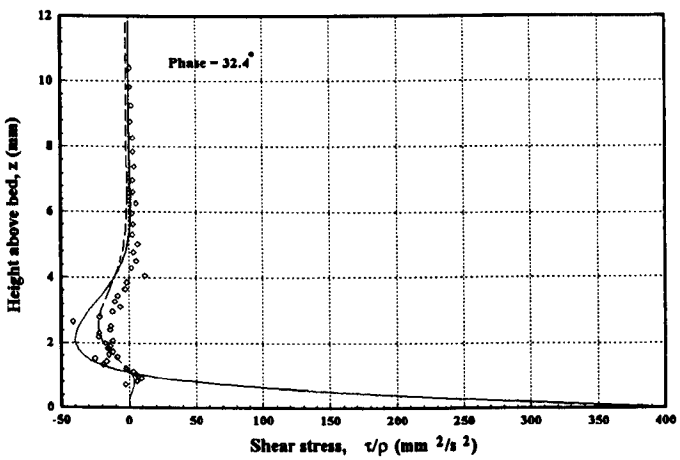

(b)

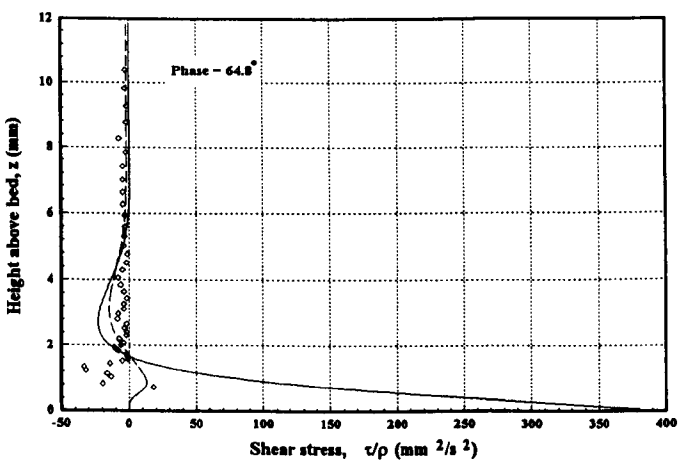

(c)

Figure 7.5: Comparison of shear stress values from two-layer k-ε model (Fourier series, 5 components) against laboratory data of Savell (1986): ◊ test 52, Savell; —— k-ε model (Total stress); — — k-ε model (Reynolds stress).

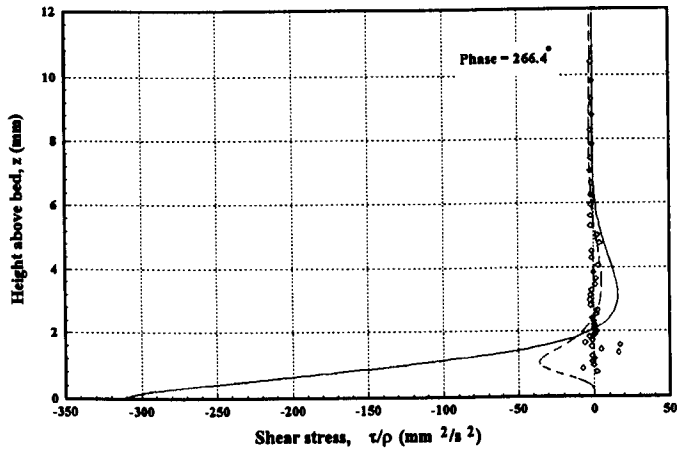

(d)

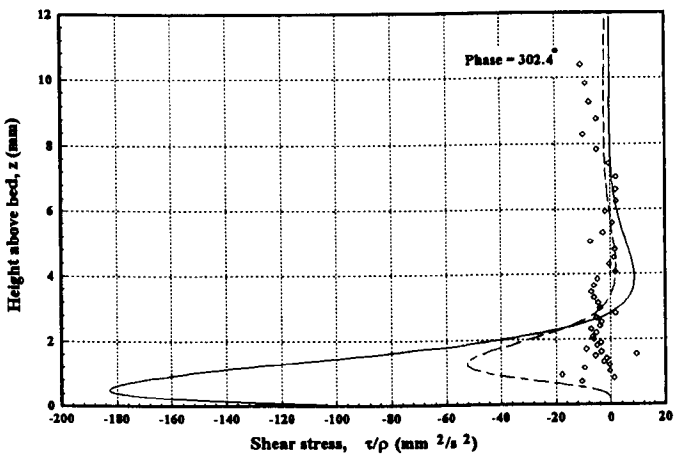

(e)

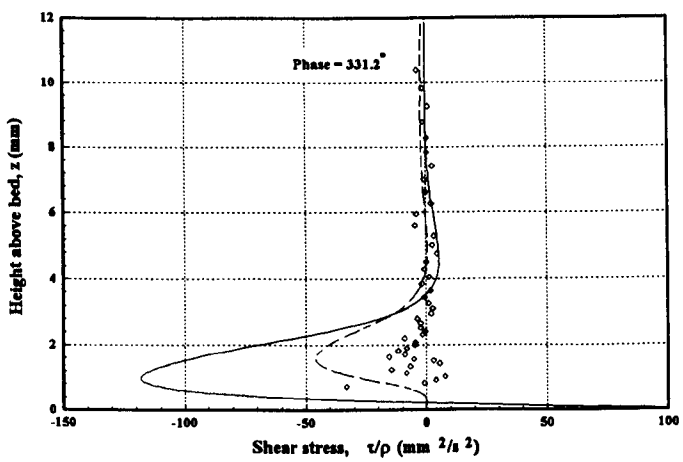

(f)

Figure 7.5(Cont.): Comparison of shear stress values from two-layer model (Fourier series, 5 components) against laboratory data of Savell (1986): ◊ test 52, Savell; —— k-ε model (Total stress); — — k-ε model (Reynolds stress).

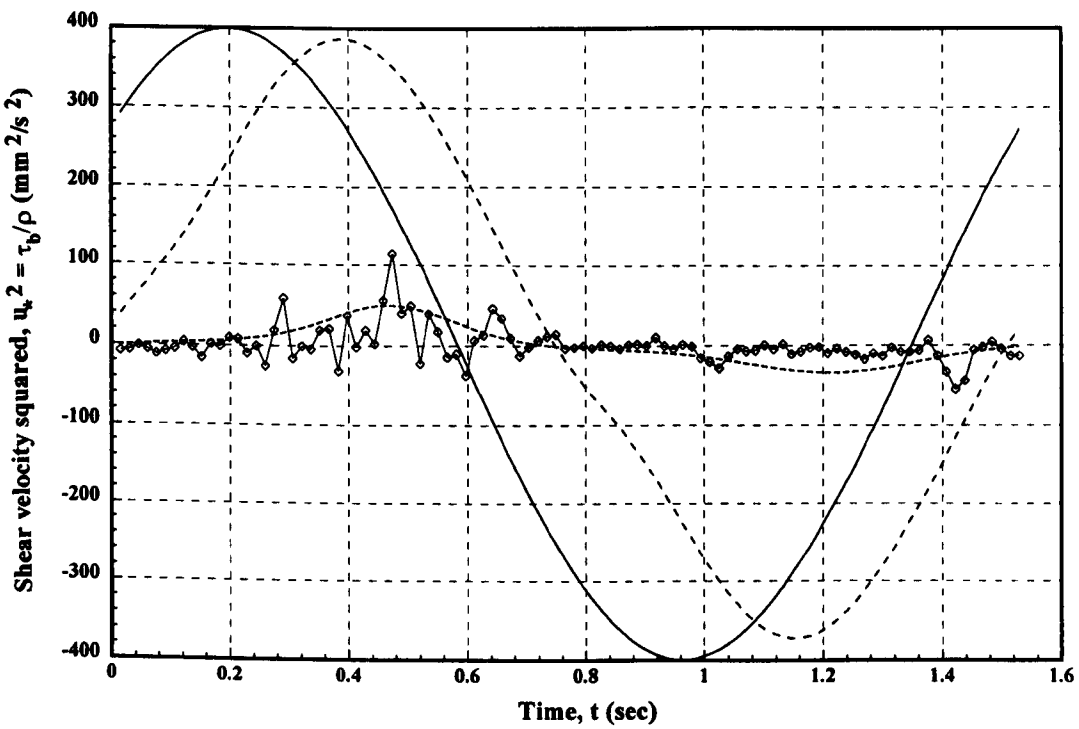

Figure 7.6: Comparison of bed shear stress values: —◊— test 52 (Savell 1986); - - - Reynolds stress (model, corresponding to lowest measurement point); — — total stress (model, corresponding to lowest measurement point); —— actual calculated bed shear stress (corresponding to lowest calculation point in the model).

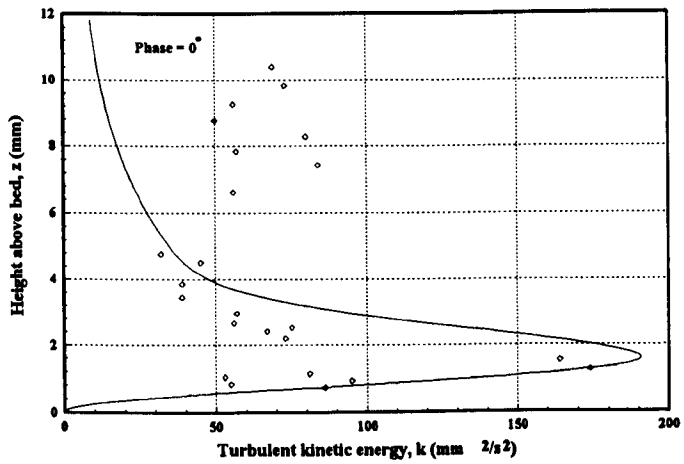

(a)

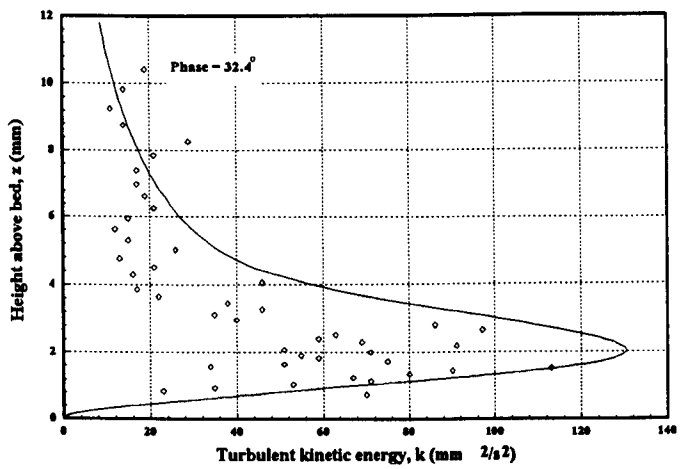

(b)

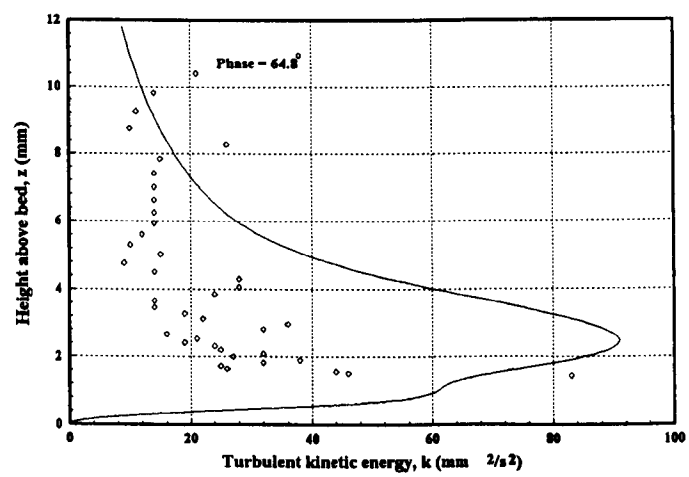

(c)

Figure 7.7: Comparison of turbulent kinetic energy, k, values from two-layer k-ε model (Fourier series, 5 components) against laboratory data of Savell (1986): ◊ test 52; —— k-ε model.

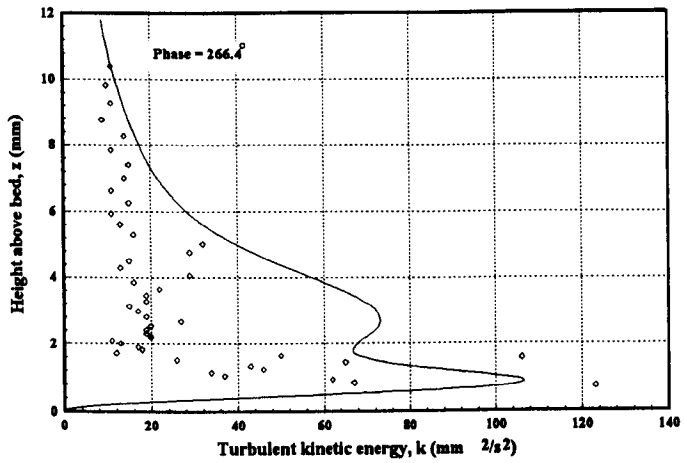

(d)

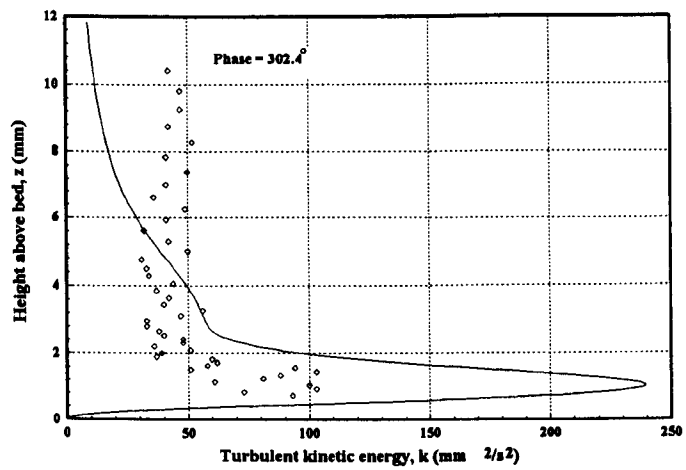

(e)

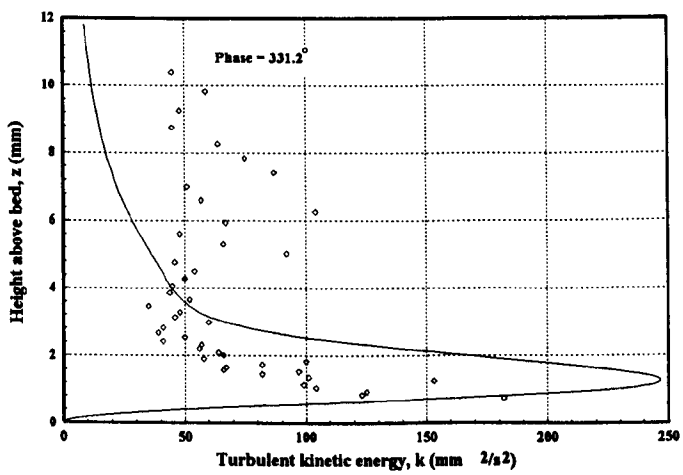

(f)

Figure 7.7(Cont.): Comparison of turbulent kinetic energy, k, values from two-layer k-ε model (Fourier series, 5 components) against laboratory data of Savell (1986): ◊ test 52; —— k-ε model.

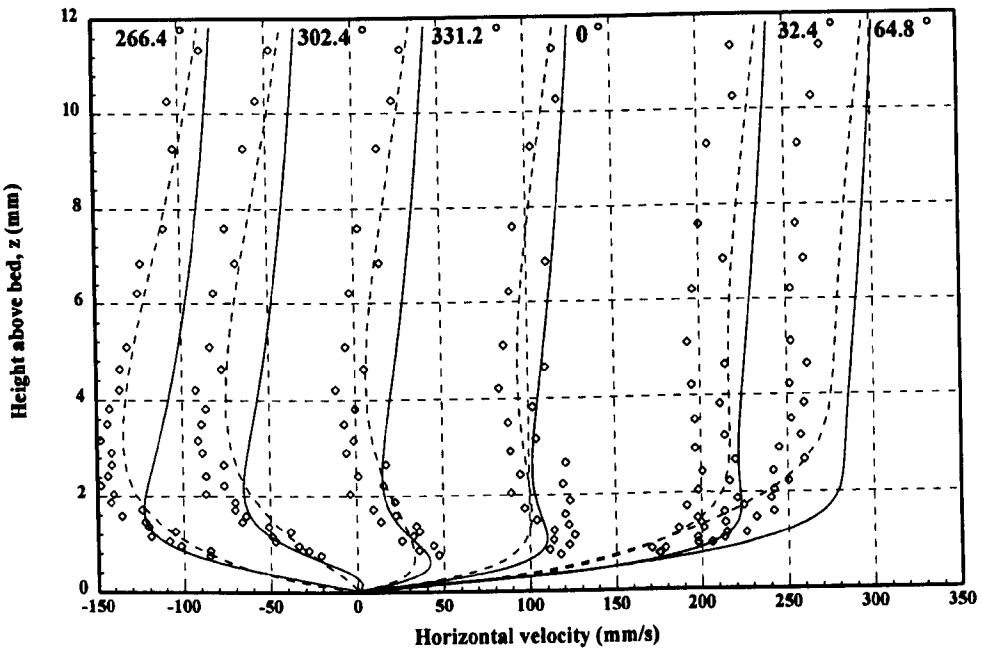

Figure 7.8: Comparison of k-ε model and two-layer k-ε model against Manchester laboratory data (Savell 1986): ◊ test 59, Savell; —— two-layer model; — — k-ε model.

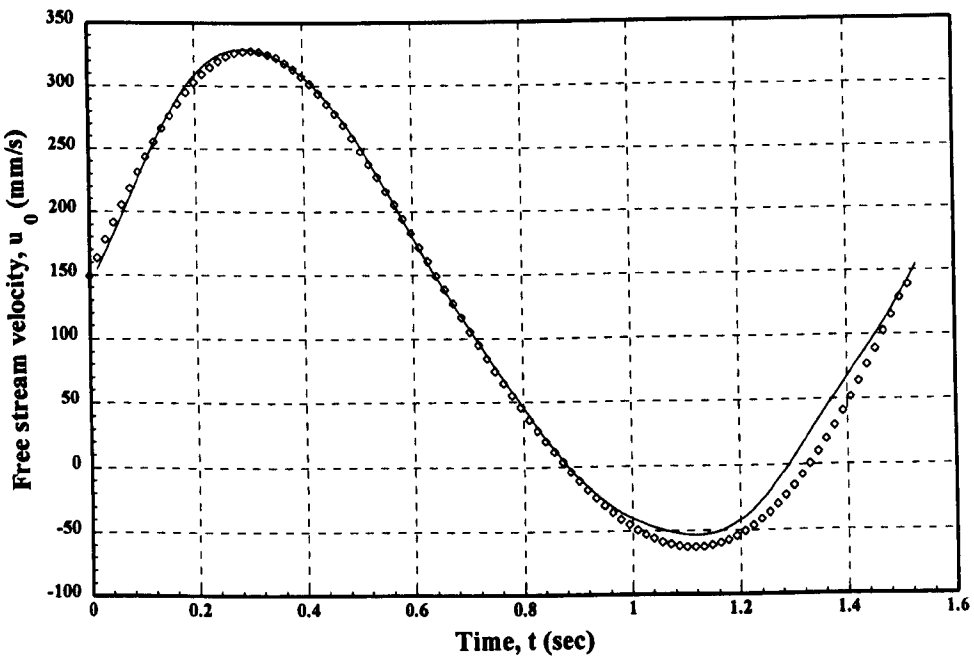

Figure 7.9: Velocity variation with time: ◊ test 59, Savell (1986); — k-ε model.

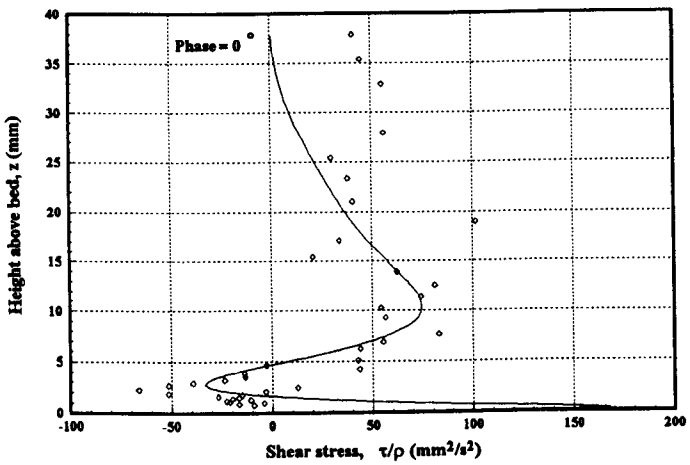

(a)

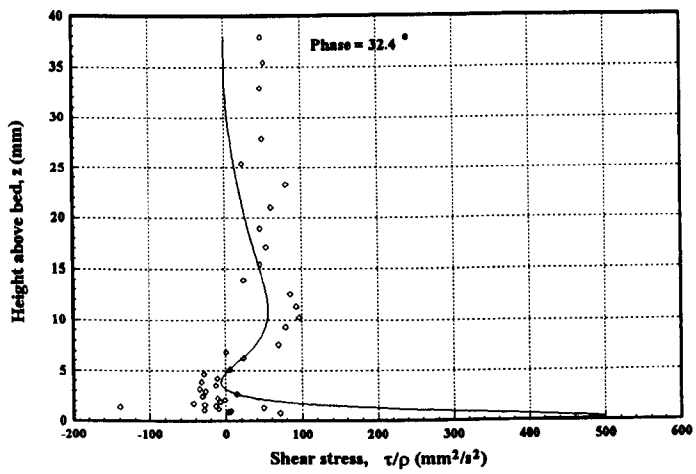

(b)

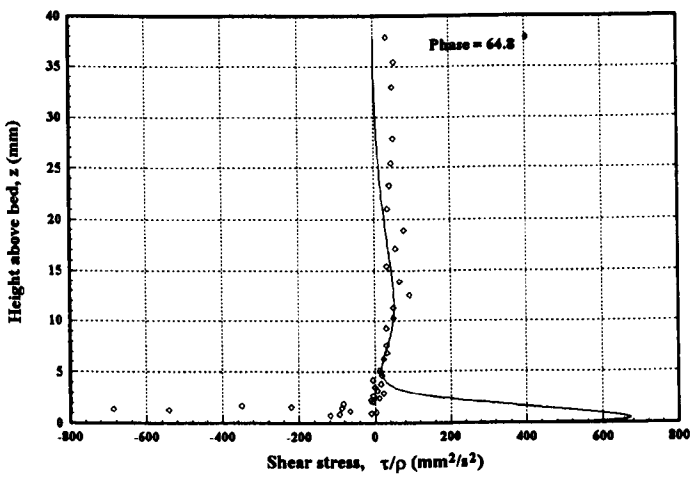

(c)

Figure 7.10: Comparison of shear stress values from k-ε model against laboratory data of Savell (1986): ◊ test 59, Savell; — k-ε model.

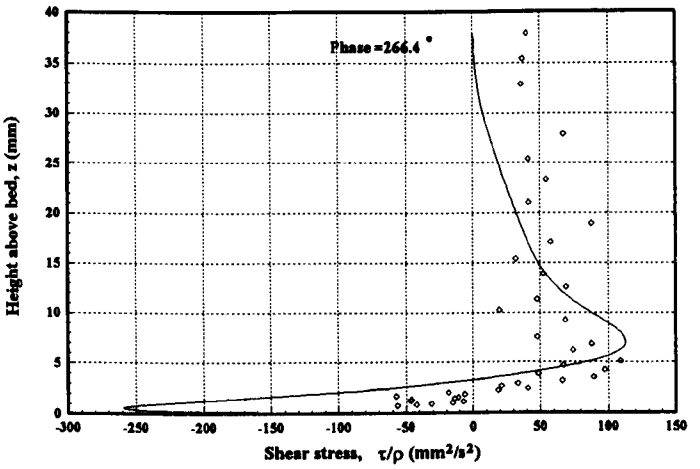

(d)

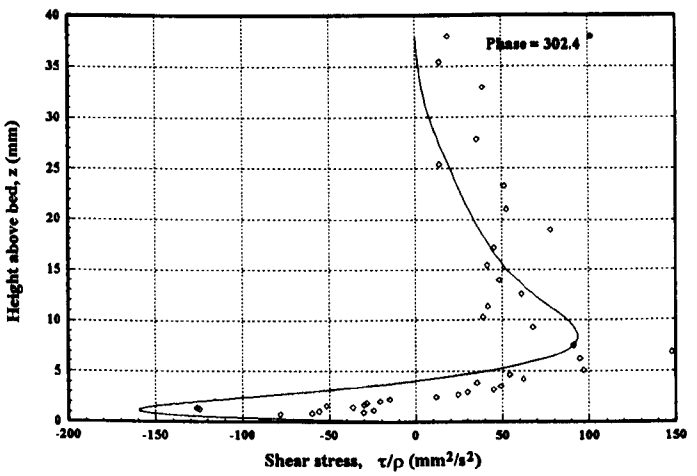

(e)

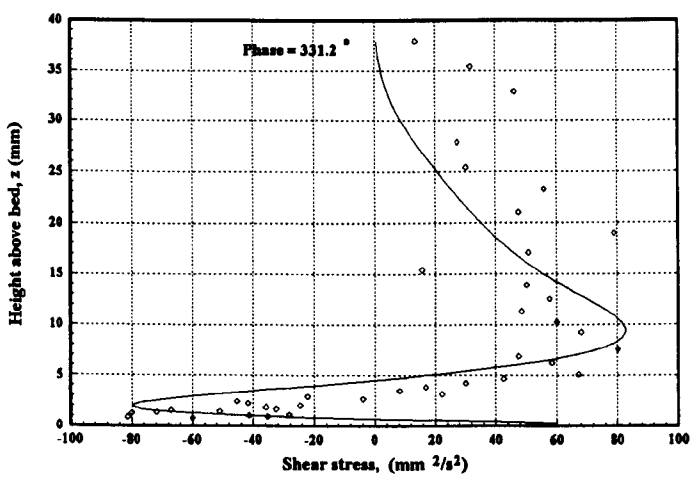

(f)

Figure 7.10(Cont.): Comparison of shear stress values from k-ε model against laboratory data of Savell (1986): ◊ test 59, Savell; — k-ε model.

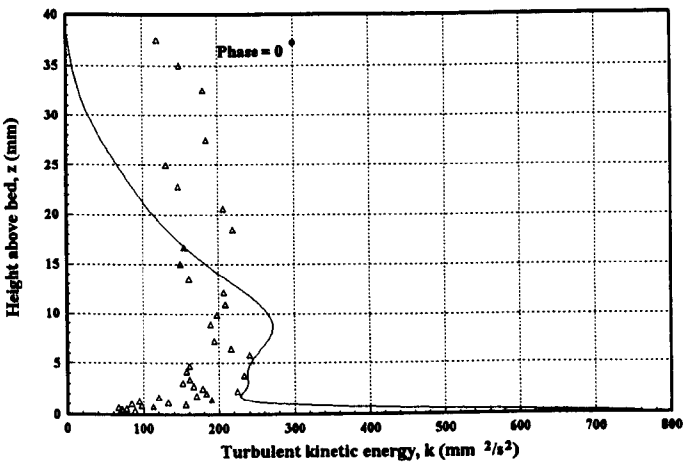

(a)

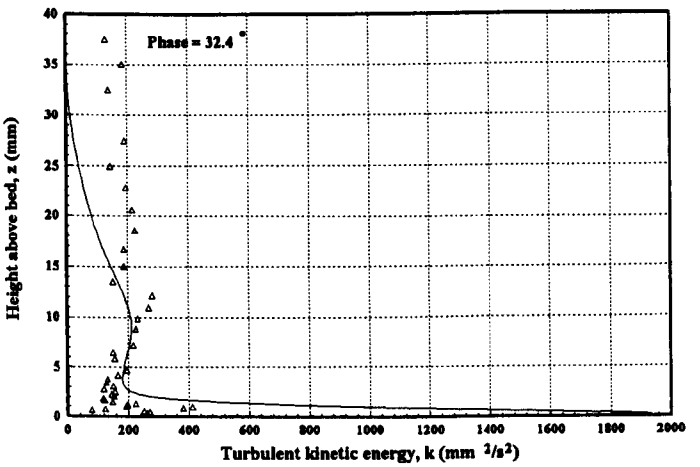

(b)

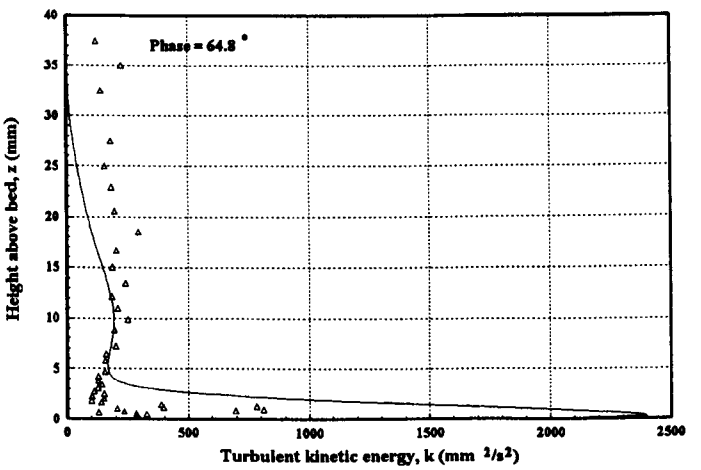

(c)

Figure 7.11: Comparison of turbulent kinetic energy values (k) from k-ε model against laboratory data of Savell (1986): ◊ test 59, Savell; — k-ε model.

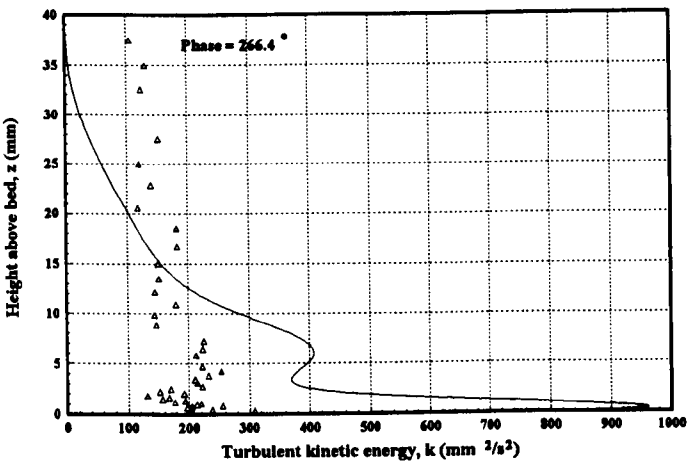

(d)

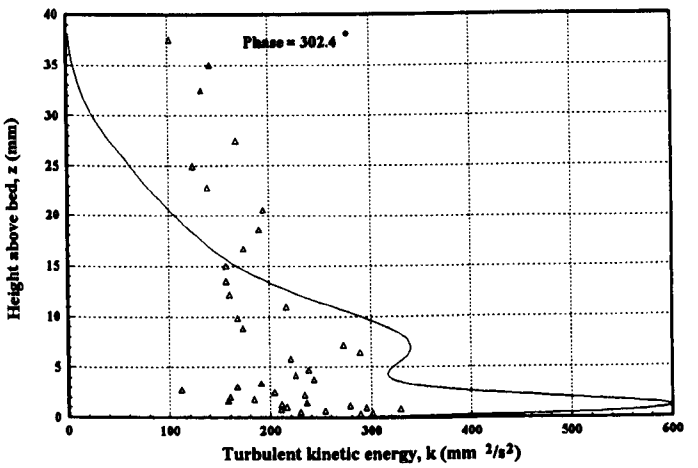

(e)

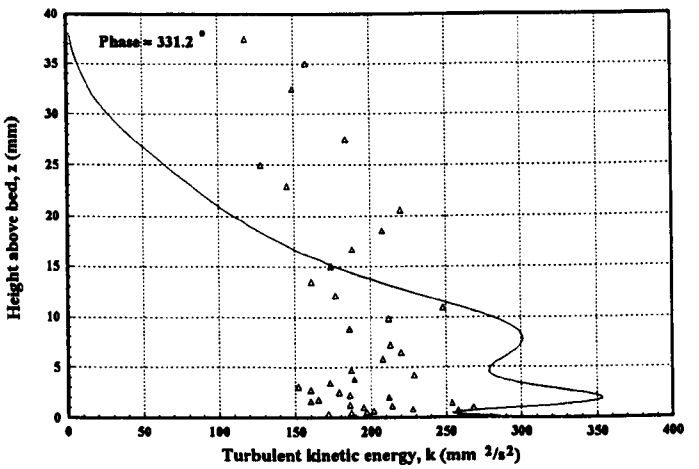

(f)

Figure 7.11(Cont.): Comparison of turbulent kinetic energy values (k) from k-ε model against laboratory data of Savell (1986): ◊ test 59, Savell; — k-ε model.

Chapter 8
Results: Part III

8.1 Random waves without current:

8.1.1 Introduction

This chapter presents the results of the work involving testing the two-equation random wave boundary layer model against the laboratory experiments of Ostrowski (1993). The chapter provides a brief description of the wave flume experiments before going on to describe the results of the comparison between laboratory data and model.

8.1.2 Gdansk flume experiments

Ostrowski (1993) describes in detail a series of experiments carried out in the wave flume at IBW PAN, Poland, see also Kaczmarek and Ostrowski (1995). The wave flume has the dimensions, 0.5m in width, and approximately 20m in length and is equipped with a piston wave-maker. The wave generator is programmable enabling it to generate irregular waves that have statistical target properties. Figure 8.1 shows a flow diagram outlining a typical approach for the preparation of the input signal to the wave maker in order to obtain irregular waves of prescribed characteristics (see also Goda 1985 and Takayama 1990).

The experimental set up involved a bed slope of mean inclination 1:20 with an underwater bar, see Figure 8.2. Measurements of the bed shear stress were carried out with a shear plate located in the bed. The plate is sensitive to small shear forces whilst being resistant to any vertical loading. The plate is buoyant and returns to its equilibrium position once the shearing force is removed. The device was placed in a steel casing with a square hole on top exposing the plate surface to the flow and allowing the shear stresses to act on the plate. The acting stresses cause a displacement in the shear plate which is proportional to the shearing force.

The relationship between plate displacement and the shear stresses was determined using static and dynamic calibration. The calibration allowed for inertia, damping and resonance effects. Further details including a discussion can be found in Ostrowski (1993).

The shear plate was positioned in the bed at a depth of 38.5 cm, between the toe of the slope and the offshore bar, Figure 8.2. Within this zone no wave breaking took place. The active surface of the plate was level with the bed surface. The plate displacement was videoed through the glass wall of the flume at a frequency of 50 frames per second. Processing of this data provided the bed shear stress time series at 0.1 s intervals.

In addition, the free surface elevation was measured using a wave gauge and the horizontal velocity component was measured at several vertical points above the bed. The lowest velocity measurement point was 1.3 cm above the bed and this was assumed to represent the free stream velocity at the top of the boundary layer.

Three tests were performed for three different experimental conditions. The main parameters are given in Table 8.1.

Test Number	H_s (cm)	T_p (s)	k_s (cm)
1	12.5	1.5	0.52
2	18.9	2.0	0.13
3	16.8	1.5	0.23

Table 8.1: Basic test parameters at the measurement section for the three irregular wave tests.

8.1.3 The numerical model

The boundary layer models developed for the present work are capable of reproducing results of a given set of data in two different ways. Firstly, it is possible to drive the model using a Fourier transformation of an actual velocity time-series. Alternatively, if a surface wave spectrum exists for the measured data, this can be decomposed as described in Chapter 4, to give a velocity time-series. The most important difference between the two methods is that

the former reproduces the measured free stream velocity time-series exactly since this is used to drive the numerical model. The latter method, however, generates a velocity time-series which has the same parameters as that measured but does not necessarily provide a signal in the sequence recorded. The latter method has the advantage of allowing the model to be run for an indefinite period and not just for the length of the data set.

Firstly, the high Reynolds number k-ε model was run using a Fourier series of the measured data for the three separate tests; test 1, 2 and 3, respectively. Taking the measured free stream velocity and carrying out harmonic analysis on each of the three signals enabled time-series to be generated that allowed a sufficient number of time steps to be used in order that the turbulence model remained numerically stable. The results of these model runs are shown in Figures 8.3 - 8.16.

Next, the model was run using the measured surface wave height spectrum for test 1. The velocity time-series was generated using the method described in Chapter 4. The results of this analysis are shown in Figures 8.17 - 8.21. For all the model runs, the empirical model constants remained the same and the values of these are given in Section 4.3.6.

8.2 Results

8.2.1 Test 1

Figure 8.3 shows the computed free stream velocity for the first 30 seconds of test 1. The time-series was determined using Fourier analysis and provides the upper boundary condition for the velocity in the model. Deviation from the original signal is negligible with a mean error of only 0.26% between measured and computed values.

Figure 8.4 shows a comparison of the computed bed shear velocity against the measured values. Whilst, overall, the model reproduces the trend of the measured data, there are discrepancies between the two time-series. The model results show a greater level of turbulent fluctuation than do the measured values. This is to be expected since the time-step used in the numerical scheme is $\Delta t = 0.00077$ whereas, the laboratory signal was recorded at $\Delta t = 0.1$. The small time-step in the model is required for numerical stability. It is possible to

'smooth' the computed values by increasing the interval between the time-steps at which the model stores data to the hard drive or, for example, only plotting every fifth value. The experimental shear velocity values were determined using a video camera to record the displacement of the shear plate. The camera operated at 50 frames per second. After the recorded data is processed the bed shear velocity time-series was obtained at 0.1s between sampling intervals. It is evident that the low sampling rate has dampened out much of the turbulent fluctuation in the measured signal. In addition, whilst the main peaks in the measured bed shear stress are reproduced quite well by the model, some of the smaller peaks and troughs are not. It is possible that the experimental free stream velocity signal used to drive the model is not as reliable as assumed.

The discrepancies between the computed and measured shear velocity signals are probably due, in part, to the photographic method used to determine the shear plate displacement. The measured velocity signal certainly suggests that the signal is being 'clipped' at the crests and troughs. Unfortunately Kaczmarek and Ostrowski (1995) provide little information on the calibration of the shear plate and so it is only possible to speculate as to the possible cause of the difference in measured and computed values.

Figures 8.5 and 8.6 show time-series for the turbulent kinetic energy and isotropic dissipation rate at the bed, respectively. It is not possible to compare these results to any experimental values since no such measurements were undertaken.

The plot of the time-series for the bed turbulent kinetic energy suggests that the underlying turbulence level is not constant, implying that, perhaps turbulence is carried over from one wave period to the next. This point will be explored in more detail later in the chapter and in Chapter 11.

The isotropic dissipation rate follows the same pattern as the turbulent kinetic energy but with a greater magnitude. This is to be expected since the isotropic dissipation rate is related to the square of the turbulent kinetic energy through the equation (see Chapter 4):-

$$\nu_t = c_\mu \frac{k^2}{\varepsilon} \qquad \textbf{(4.24)}$$

There is no phase difference between the turbulent kinetic energy and the dissipation rate and this can be deduced from Eq. (4.24).

8.2.2 Test 2

Figure 8.7 shows the computed free stream velocity for the first 30 seconds of test 2. As for test 1, the time-series was determined using Fourier analysis and provides the upper boundary condition for the velocity in the model. Deviation from the original signal shows a mean error of 6.46% between measured and computed values.

A comparison of the measured and computed bed shear velocity results for test 2 are shown in Figure 8.8. Deviation from the measured signal shows a greater discrepancy than was seen for test 1. Whilst the occurrence of peaks and troughs is reflected in the computed data, the magnitude of these values compared with the measured shear velocity values is poor.

As previously, for test 1, the measured values for the shear velocity were determined using a video camera. It is expected that the discrepancies between the measured and computed values should be of a similar order as test 1. However, from a visual inspection, the differences in peak values can be up to the order of 3 times the measured value compared with order 2 for test 1. Clearly, the shear plate dampens out the higher frequency displacements, whilst the model results allow for higher frequency turbulent fluctuations. This is not sufficient to account for all of the difference. Kaczmarek and Ostrowski (1995) make no comment on possible reasons for the poorer fit between the measured results and a time-invariant eddy viscosity model. Test 2 has the largest peak period and significant wave height of the three runs (see Table 8.1) and correspondence between measured and computed shear velocity values is the worst. It is possible that the shear plate damps out more of the turbulence when the peak wave period and significant wave height are increased. No surface wave breaking was present in any of the experiments. Without greater information it is only possible to speculate on possible causes. It is unknown whether the plate surface was artificially roughened or left smooth. Again, this might be a possible cause for disagreement.

Figures 8.9 and 8.10 show the computed bed turbulent kinetic energy and isotropic dissipation rate for test 2, respectively. The observed carry over of turbulence from one half period to another seen in test 1 appears present in the results of test 2. This matter will be discussed later in the chapter.

The isotropic dissipation rate (Figure 8.10) follows the same pattern as the turbulent kinetic energy but with a greater magnitude as for test 1.

Any real quantitative comparison between the computed results for the turbulent kinetic energy and the isotropic dissipation rate and those present during the experiments is not possible since no such measurements were undertaken.

8.2.3 Test 3

Figure 8.11 shows the computed free stream velocity for the first 30 seconds of test 3. The time-series was determined using Fourier analysis and provides the upper boundary condition for the velocity in the model as for the two previous tests. Deviation from the original signal is negligible with only a mean error of only 0.72% between measured and computed values.

Figure 8.12 shows a comparison between the measured bed shear velocity and that computed by the random k-ε boundary layer model. Overall, agreement between the data is reasonable. As in previous tests, the model results show a greater level of turbulent fluctuation than do the measured values due to the time-step used in the numerical scheme.

The discrepancies between the measured bed shear velocity and the computed values are of a similar order to test 1. The model has a tendency to underpredict the measured trough values more than the crest values. Certainly, the models overprediction of some peak values could be due to damping in the shear plate, however, the reason for underprediction is less obvious.

Figures 8.13 and 8.14 show time-series for the turbulent kinetic energy and isotropic dissipation rate at the bed, respectively. As in the other experimental runs, it is not possible to

compare these results to any experimental values since no such measurements were undertaken.

The plot of the time-series for the bed turbulent kinetic energy, again, suggests that the underlying turbulence level in not constant, indicating that, perhaps turbulence is carried over from one wave period to the next in a 'cascade' effect.

8.2.4 Comparison between the k-ε model and a time-invariant eddy viscosity model

Figure 8.15 shows a comparison between the random k-ε model used in the present study, the random time invariant eddy viscosity model of Kaczmarek and Ostrowski (1995) and the measured shear velocity for test 1. Clearly, from a visual inspection of the data, the two models provide very similar results. Both models underpredict many of the observed peak trough values.

Kaczmarek and Ostrowski (1995) use the method of O'Connor *et al.* (1993) to provide the surface boundary condition for the velocity. The hydrodynamic model is based on the two-layer time-invariant eddy viscosity approach of Brevik (1981) for regular waves (see Chapter 3). Values for the representative shear velocity and boundary layer thickness are determined using the momentum integral approach of Fredsøe (1984).

Compared to the high-Reynolds number k-ε turbulence model employed in the present study, the model of Kaczmarek and Ostrowski (1995) is conceptually quite simple although the analytical calculations are less straight forward. The results indicate a similar order of accuracy for the two approaches. The disadvantage of the time-invariant model is that it is incapable of providing a description of the turbulence.

8.3 Turbulent kinetic energy under random waves

As Figures 8.5, 8.9 and 8.13 suggest, the underlying turbulence level grows and decays under random waves. The assumption that has often been made in the past, for example Smith (1977), that the turbulence does not carry over from one half period to the next appears to be

incorrect. To explore this point in more detail, regression analysis was performed on the turbulent kinetic energy profiles of all three experimental runs, to obtain the underlying trend in the data. The results of part of this analysis are shown in Figure 8.16.

Figure 8.16a shows the turbulent kinetic energy profile at the bed for the first 15 seconds of data for test 2. Imposed on the figure, is the result of a 6th order polynomial regression analysis. It is clear from the results, that the underlying turbulence grows and decays. This indicates that the turbulent kinetic energy does in fact get carried over from one half period to the next.

Figure 8.16b shows the bed turbulent kinetic energy for 15 seconds of data for test 3. Again, imposed on the figure is a 6th order polynomial regression fit. Similarly, the underlying level of turbulence is seen to grow and decay with time.

The cascade of turbulence from one half period to the next could have significant implications for sediment transport. Williams (1996) found from the analysis of suspended sediment concentration measurements that there was a correlation between increased concentration values and wave groups. It is hypothesized that this increased concentration is in part due to the carry over of turbulence.

8.4 Spectral approach to generating time-series

Figures 8.17 -8.21 show the results from the two-equation k-ε model run for the conditions of test 1. The velocity time series was derived from the measured surface wave height spectrum, see Figures 8.17 and 8.18. Comparison of the measured and computed spectra for the free stream velocity shows good agreement, see Figure 8.20a.

The shear velocity time-series generated by the model is shown in Figure 8.19. A comparison of the measured and computed bed shear velocity squared, u_{*b}^2 spectra is shown in Figure 8.20b. The correlation is reasonable.

To investigate further the assertion that turbulent kinetic energy is carried over from one wave period to the next, the time-series for k has been plotted with the corresponding surface wave height time-series, Figure 8.21a. Figure 8.21b shows a section of the turbulent kinetic energy time-series displaying the underlying trend calculated using a 6th order polynomial regression fit. As previously, the underlying trend shows a growth in turbulent kinetic energy.

To obtain a more detailed insight into how the turbulent kinetic energy varies with wave period, a single wave from the calculated surface wave height is shown together with the corresponding k profile (Figure 8.21c). It is evident from the figure that the underlying energy level is changing. For a monochromatic wave the turbulent kinetic energy profile is symmetric and there is no carry over of energy from one half period to the next, see Figure 8.21d. Under random waves this is no longer the case and it has been shown that kinetic energy does get carried over from one half-period to the next. Failure to account for this effect in modelling of sediment transport under random waves will result in underprediction in the concentration values. Methods such as those proposed by Smith (1977), assuming each wave can be treated separately for irregular series are, therefore, incorrect, particularly for fine sediment.

8.5 Conclusions

The numerical model has been used to compare three different random wave laboratory tests. Unfortunately, the tests are limited in that full depth profiles were not measured and this has limited the comparison with the model. In addition, it is arguable that, since no turbulent quantities were measured then is it really necessary to use a two-equation model when maybe a more simple zero-equation mixing length model would provide similar answers. Kaczmarek and Ostrowski (1995) applied a simple time-invariant eddy viscosity model to the problem and obtained similar results, to those obtained with a k-ε model. A comparison is shown in Figure 8.15

However, the comparison has been useful in that it has allowed the model to be tested against controlled data and has been shown to give similar results to those measured. Further, whilst the model should not be seen as giving 'the total truth', the model results do enable a

researcher to look at the measured data and perhaps be able to interpret some of the trends more easily as well as highlight possible errors in measurement (as was done in the CSTAB project) in the same way that comparison of a model with data enables the reliability of the particular model to be assessed.

The results of the random k-ε model indicate that turbulence can be carried over from one half wave period to the next, in a cascade effect. The effect appears to be more noticeable under groups of large waves. The implication of this effect is that the previously adopted approach, assuming random waves can be treated individually as monochromatic waves, (see Smith 1977) is flawed. Failure to allow for the persistence of turbulent kinetic energy from one half period to the next will result in the underprediction of sediment suspension, particularly for fine sediment.

The random numerical boundary layer model has been run using an actual time-series as well as with a time-series derived from a surface wave height spectrum. Good agreement with the experimental results of Ostrowski (1993) has been found using both approaches. The numerical model has been shown to perform well, although further testing with more detailed experimental data is recommended.

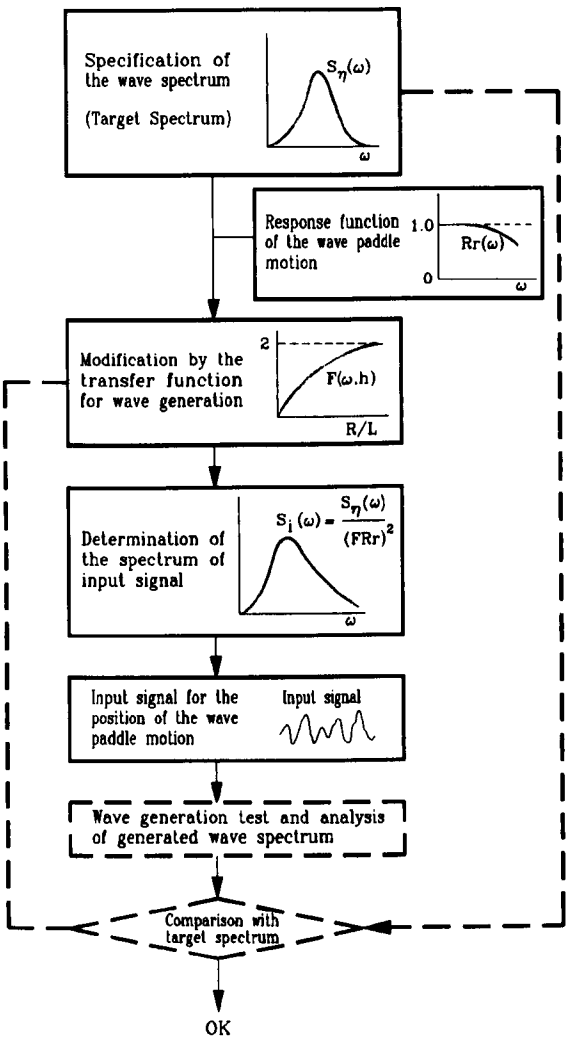

Figure 8.1: Flow diagram for laboratory random wave generation. (*After Takayama 1990*).

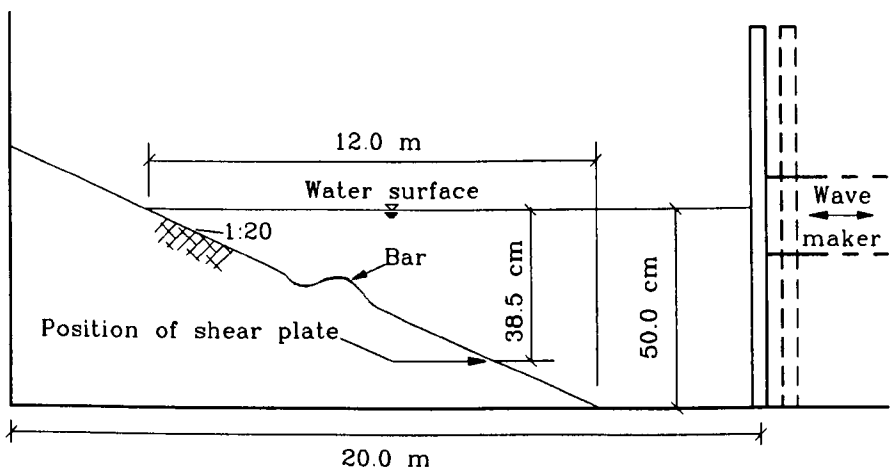

Figure 8.2: Experimental set-up for IBW PAN random wave tests (*After Kaczmarek and Ostrowski 1995*).

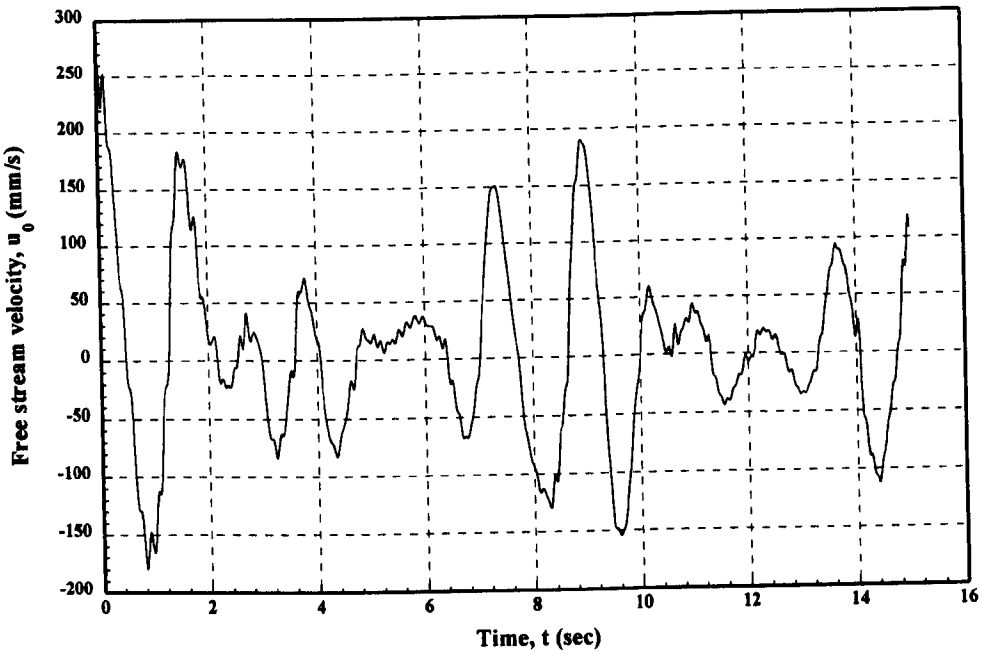

Figure 8.3a: Free stream velocity as given by the k-ε model for test No. 1.

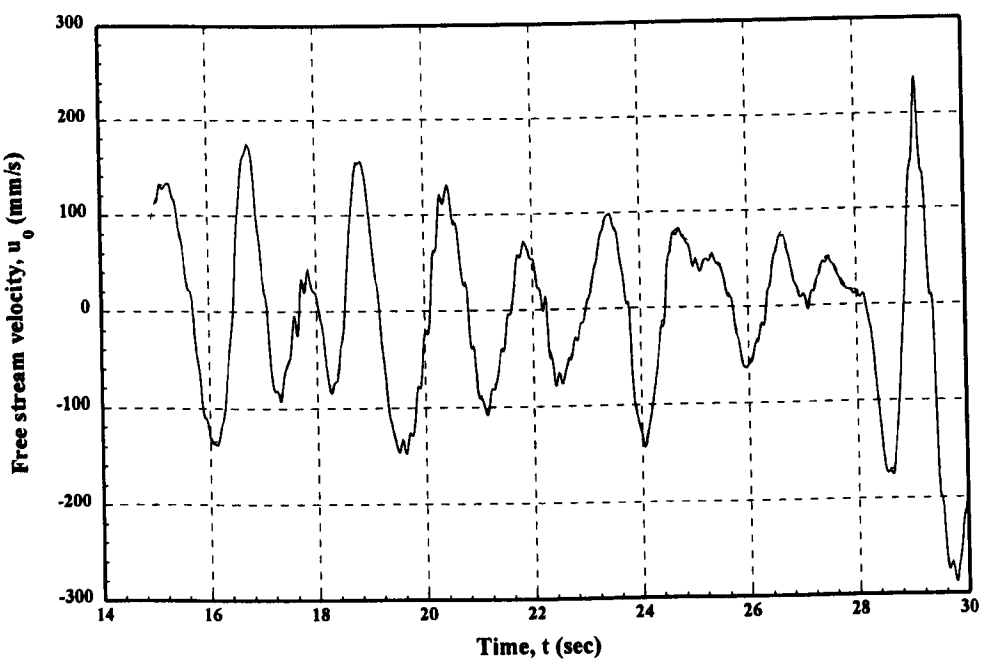

Figure 8.3b: Free stream velocity as given by the k-ε model for test No. 1.

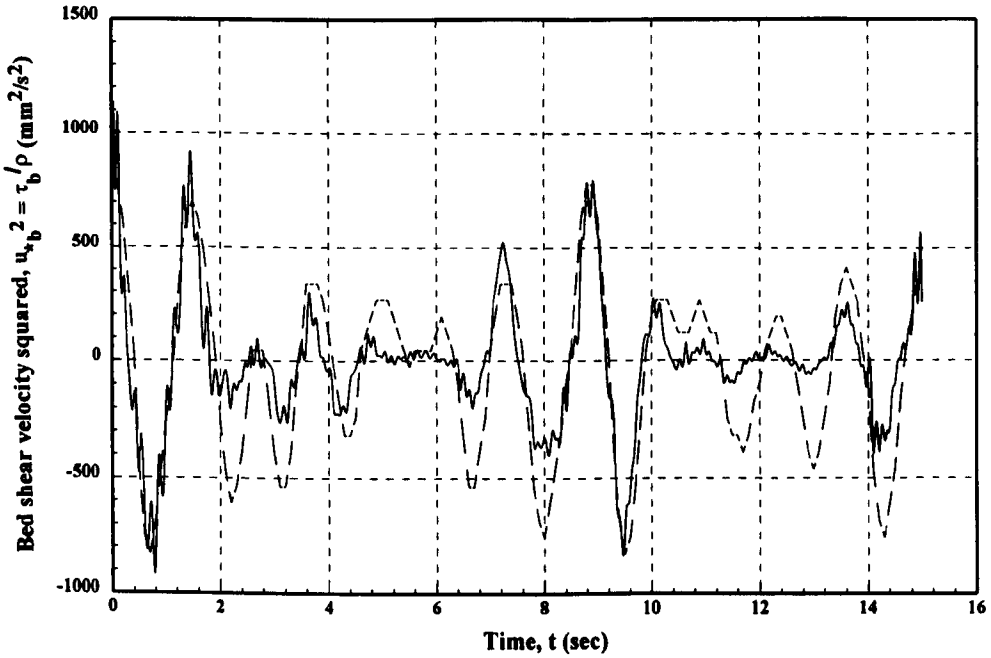

Figure 8.4a: Comparison of bed shear velocity from laboratory data, Kaczmarek and Ostrowski (1995) (– – –) and k-ε model (—) for test No. 1.

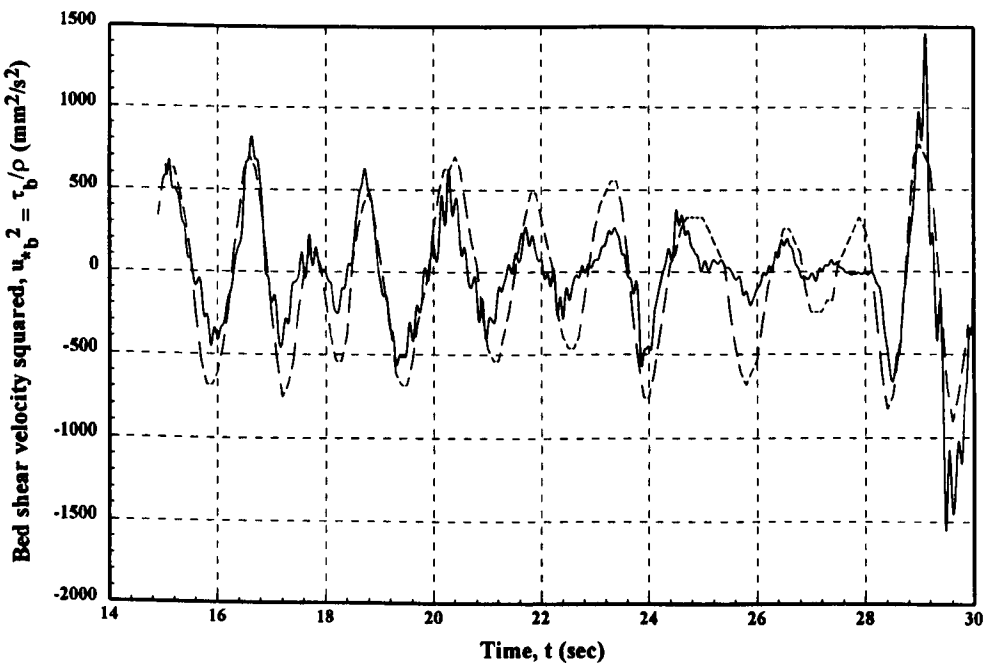

Figure 8.4b: Comparison of bed shear velocity from laboratory data, Kaczmarek and Ostrowski (1995) (– – –) and k-ε model (—) for test No. 1.

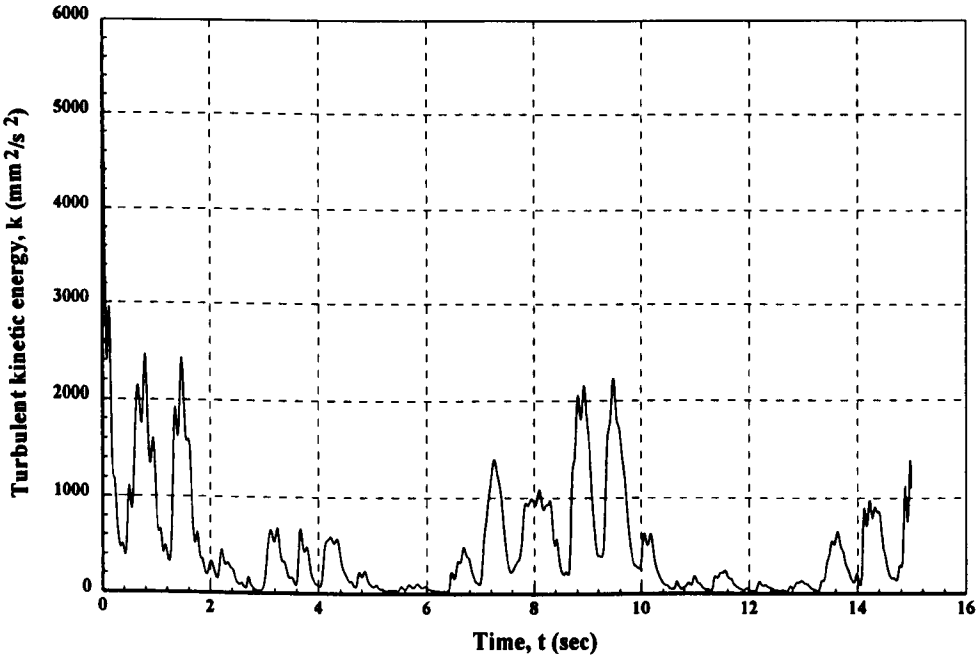

Figure 8.5a: Profile of the turbulent kinetic energy at the bed for conditions matching test No. 1, Kaczmarek and Ostrowski (1995); (—) k-ε model.

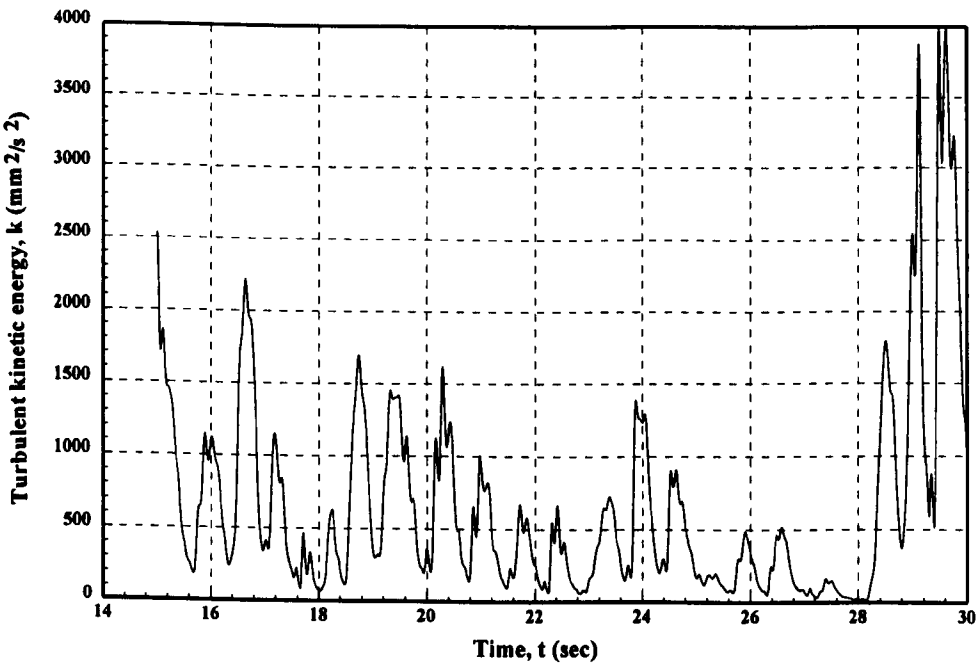

Figure 8.5b: Profile of the turbulent kinetic energy at the bed for conditions matching test No. 1, Kaczmarek and Ostrowski (1995); (—) k-ε model.

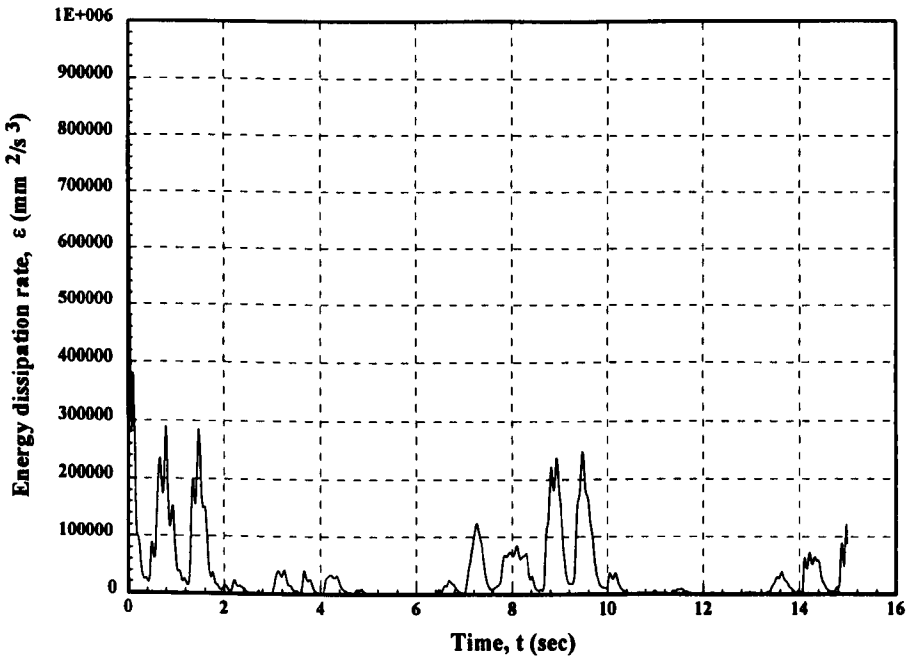

Figure 8.6a: Profile of the isotropic dissipation rate at the bed for conditions matching test No. 1, Kaczmarek and Ostrowski (1995); (—) k-ε model.

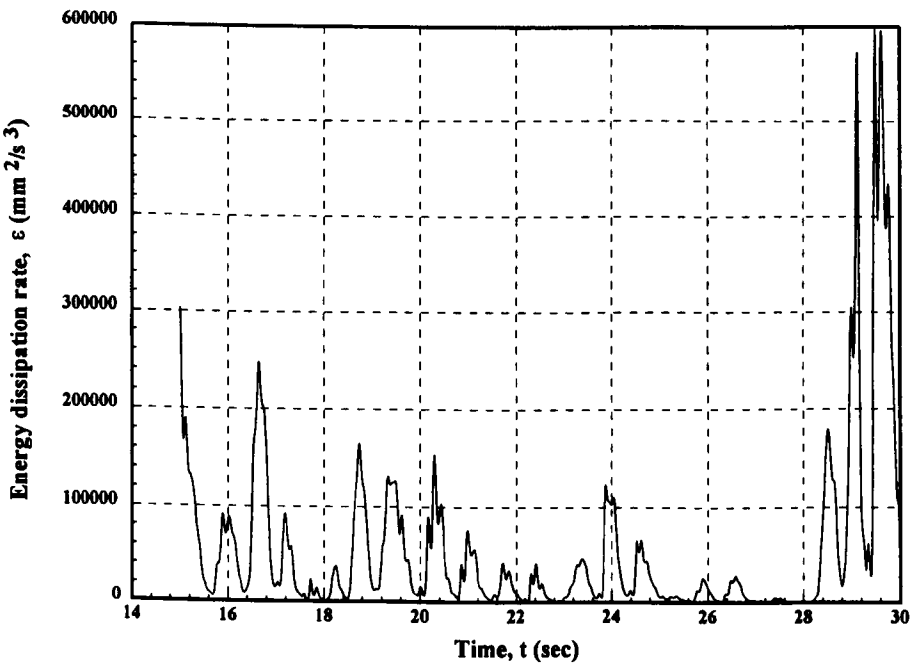

Figure 8.6b: Profile of the isotropic dissipation rate at the bed for conditions matching test No. 1, Kaczmarek and Ostrowski (1995); (—) k-ε model.

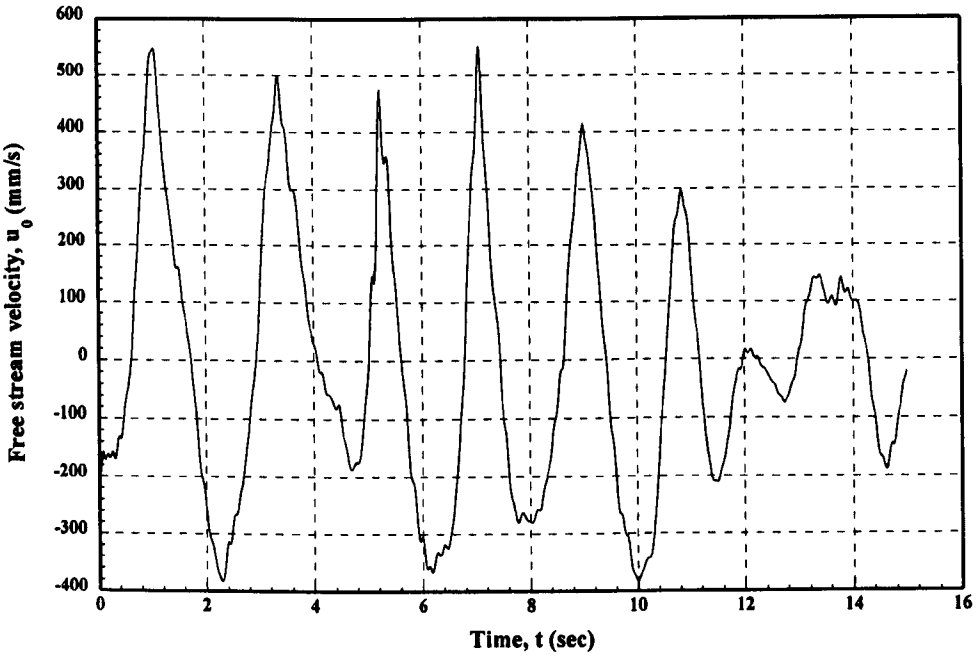

Figure 8.7a: Free stream velocity as given by the k-ε model for test No. 2.

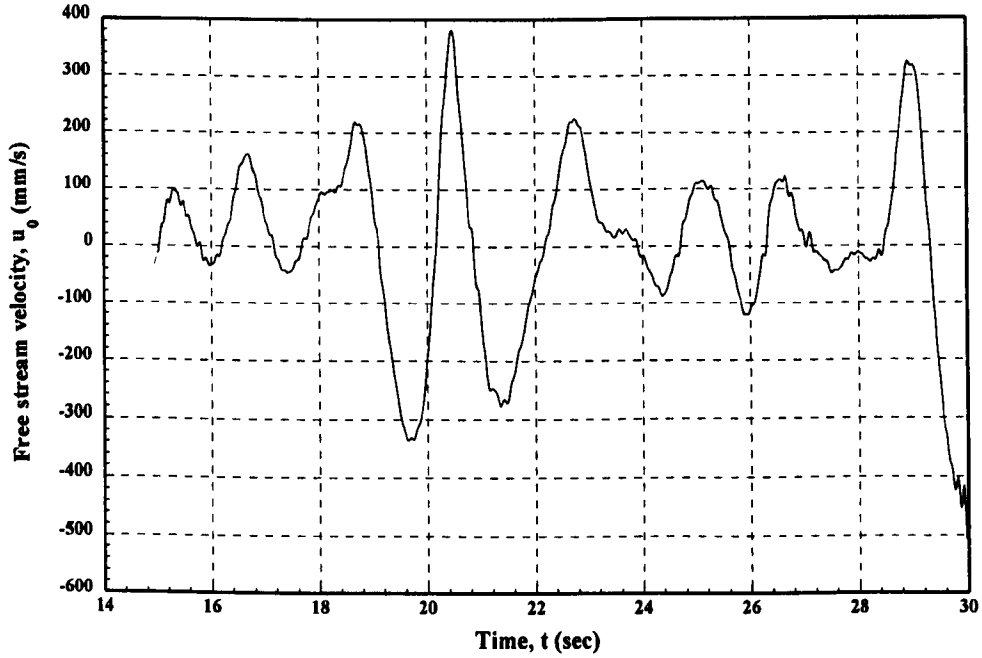

Figure 8.7b: Free stream velocity as given by the k-ε model for test No. 2.

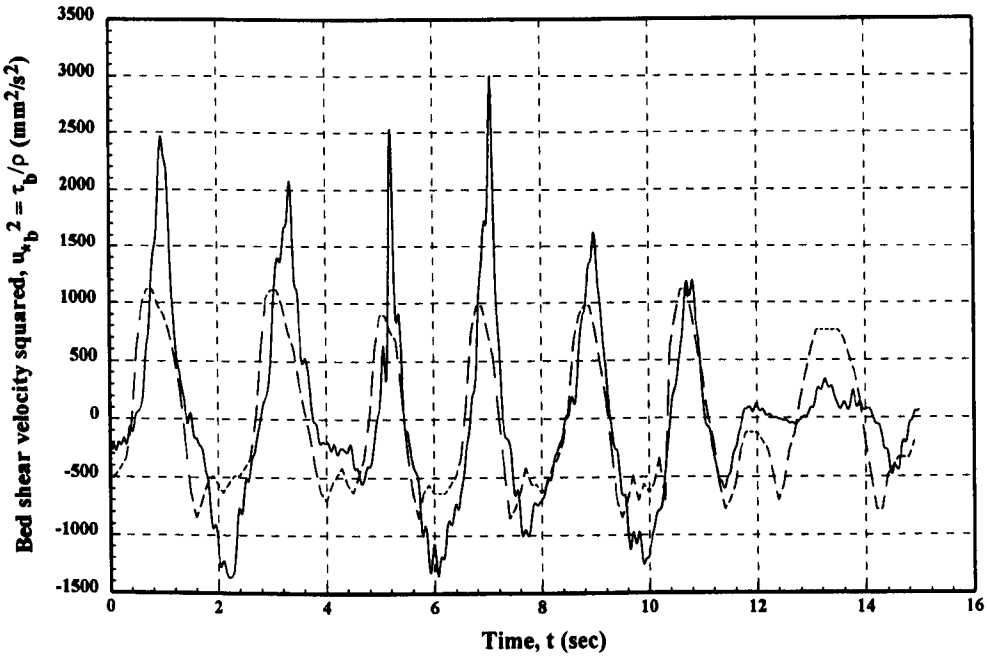

Figure 8.8a: Comparison of bed shear velocity from laboratory data, Kaczmarek and Ostrowski (1995) (– – –) and k-ε model (—) for test No. 2.

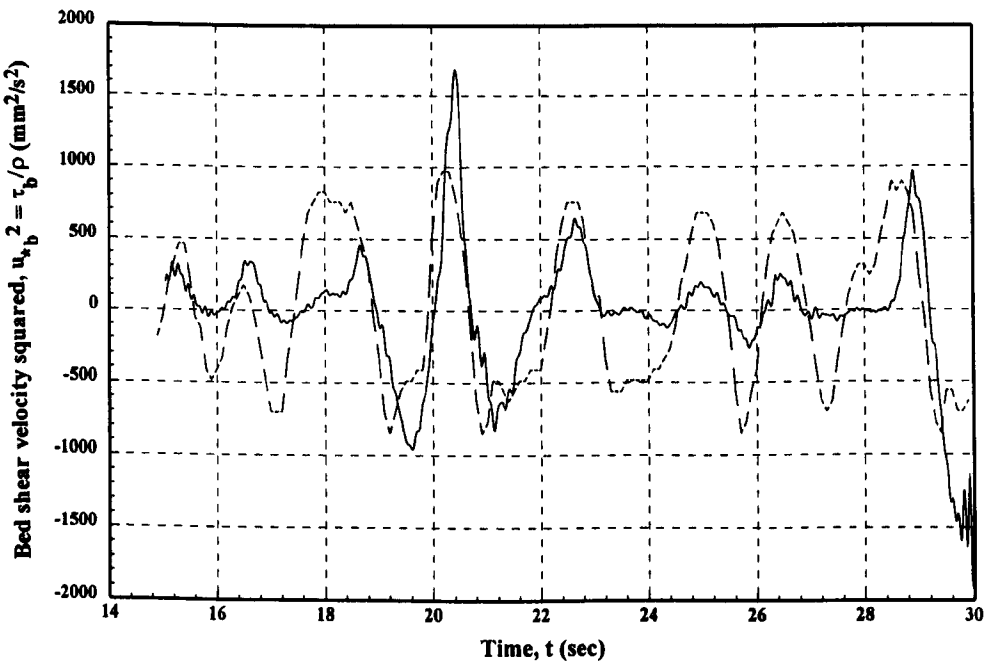

Figure 8.8b: Comparison of bed shear velocity from laboratory data, Kaczmarek and Ostrowski (1995) (– – –) and k-ε model (—) for test No. 2.

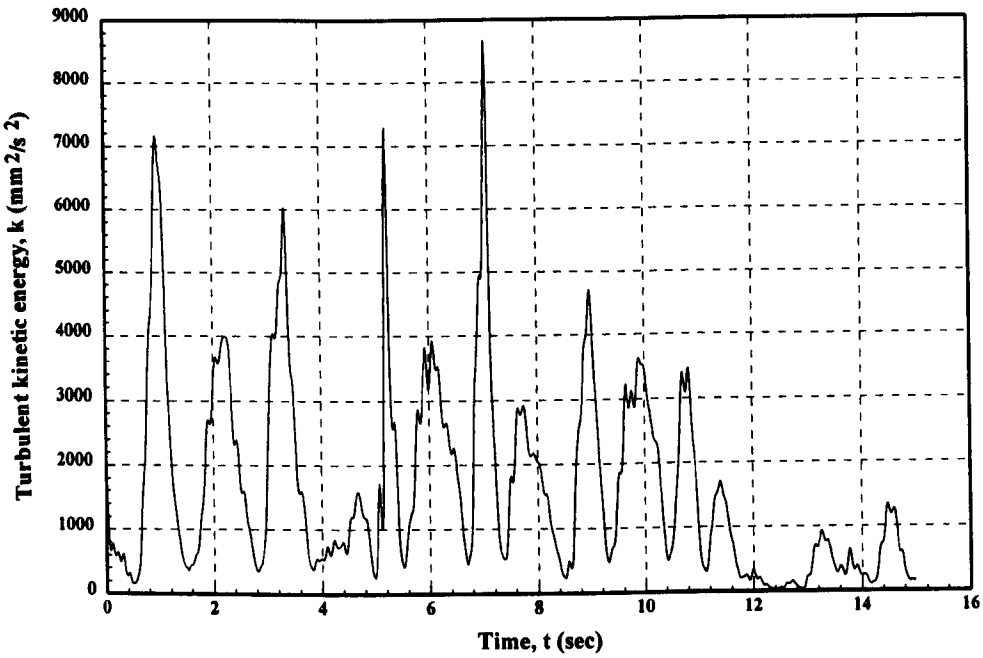

Figure 8.9a: Profile of the turbulent kinetic energy at the bed for conditions matching test No. 2, Kaczmarek and Ostrowski (1995); (—) k-ε model.

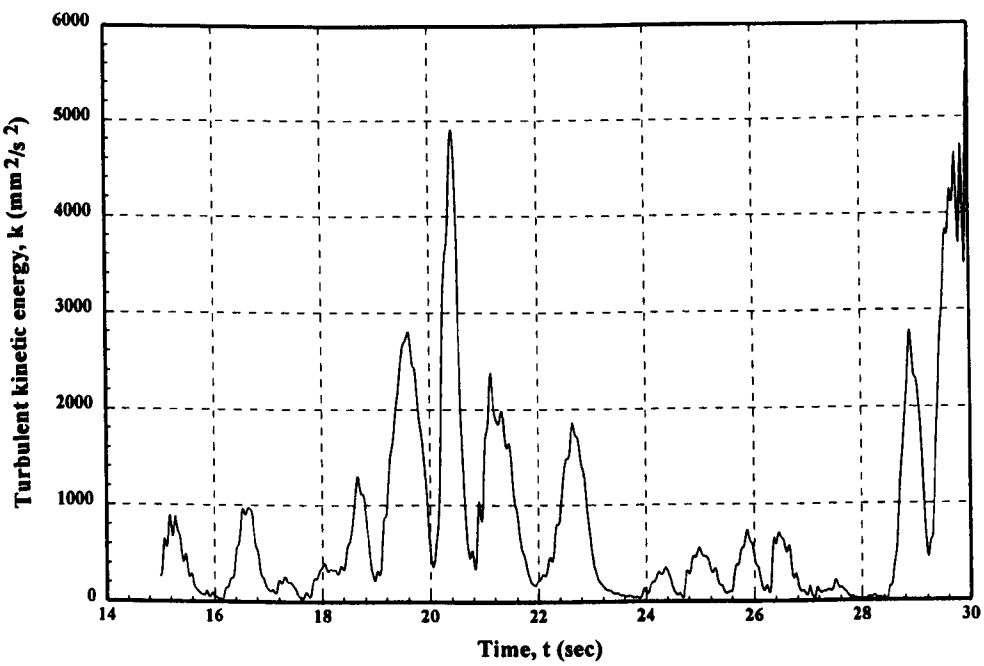

Figure 8.9b: Profile of the turbulent kinetic energy at the bed for conditions matching test No. 2, Kaczmarek and Ostrowski (1995); (—) k-ε model.

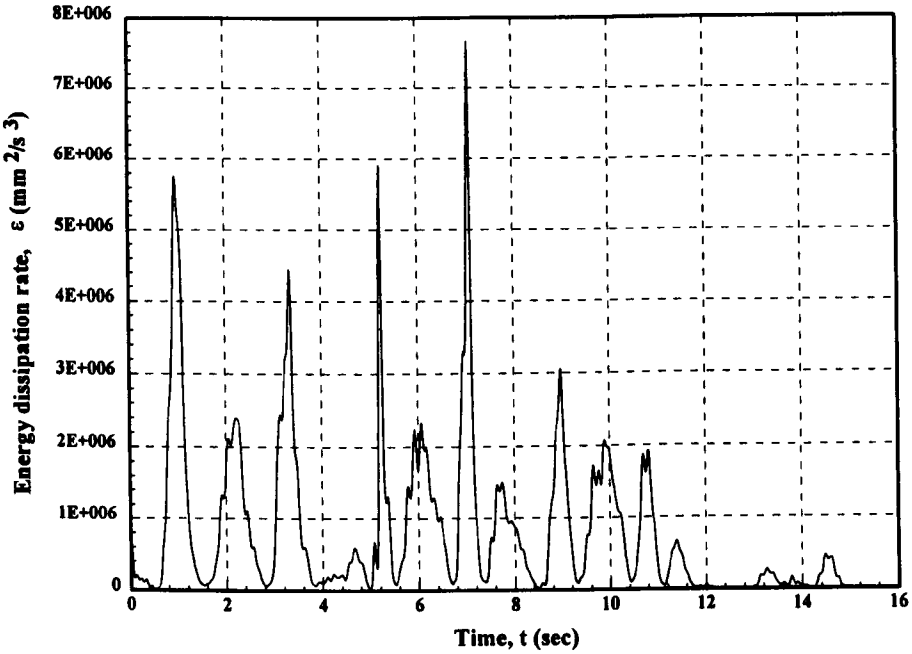

Figure 8.10a: Profile of the isotropic dissipation rate at the bed for conditions matching test No. 2, Kaczmarek and Ostrowski (1995); (—) k-ε model.

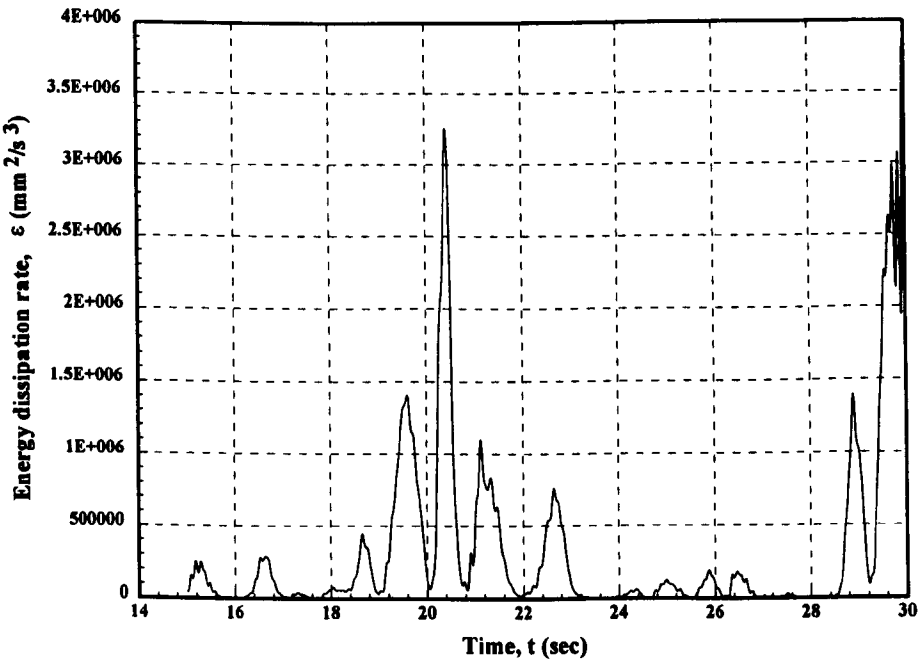

Figure 8.10b: Profile of the isotropic dissipation rate at the bed for conditions matching test No. 2, Kaczmarek and Ostrowski (1995); (—) k-ε model.

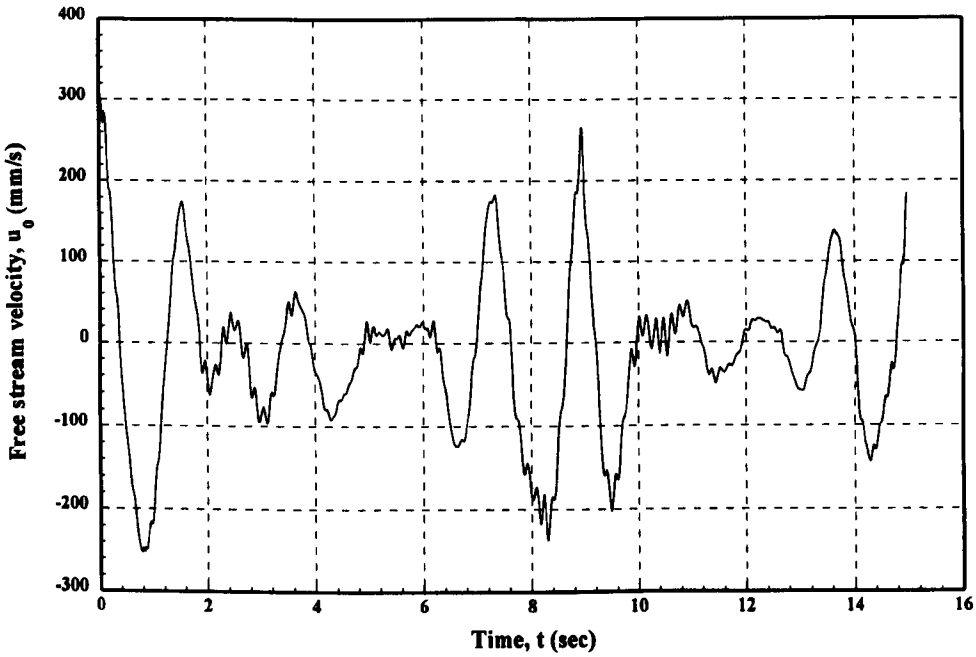

Figure 8.11a: Free stream velocity as given by k-ε model for test No. 3.

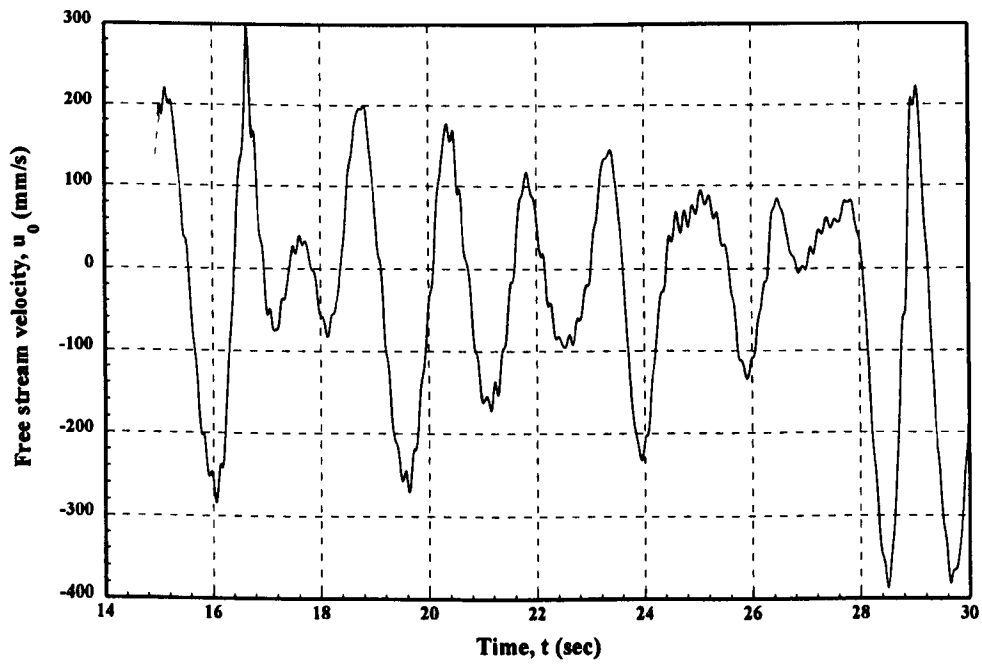

Figure 8.11b: Free stream velocity as given by the k-ε model for test No. 3.

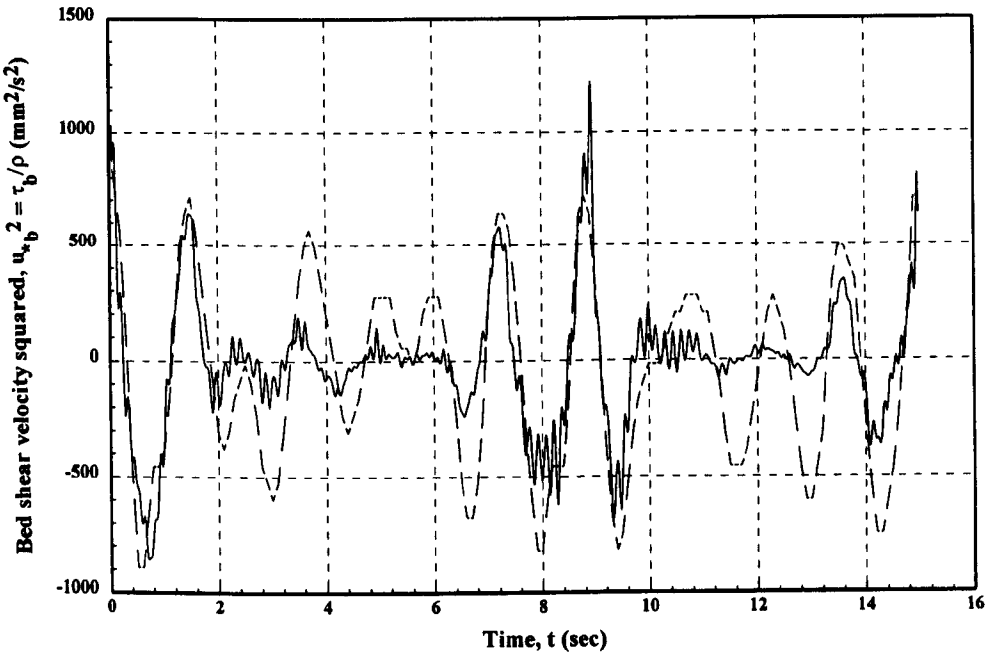

Figure 8.12a: Comparison of bed shear velocity from laboratory data, Kaczmarek and Ostrowski (1995) (– – –) and k-ε model (—) for test No. 3.

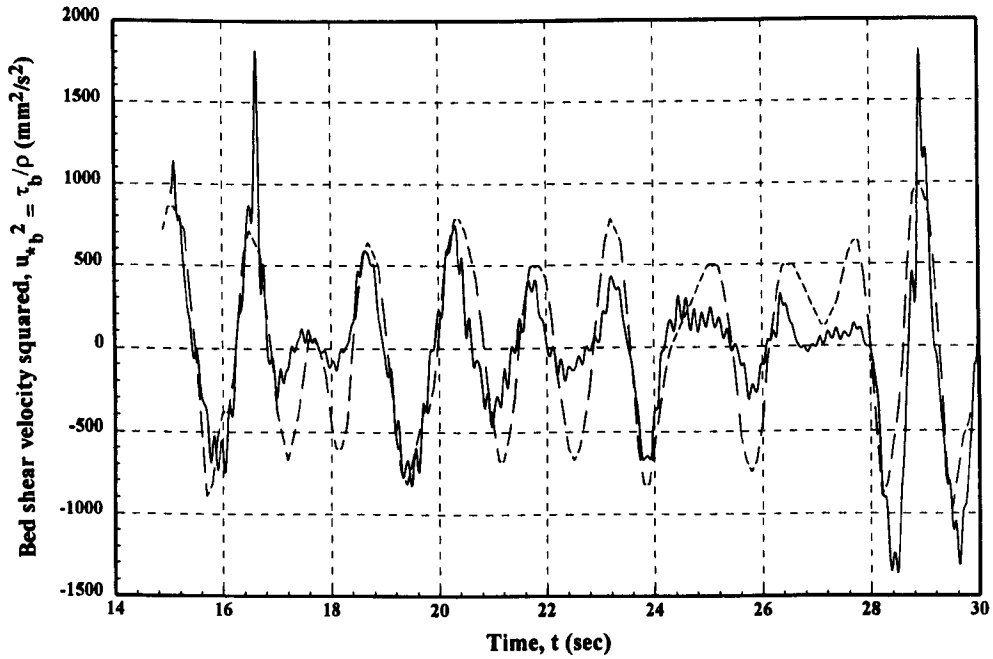

Figure 8.12b: Comparison of bed shear velocity from laboratory data, Kaczmarek and Ostrowski (1995) (– – –) and k-ε model (—) for test No. 3.

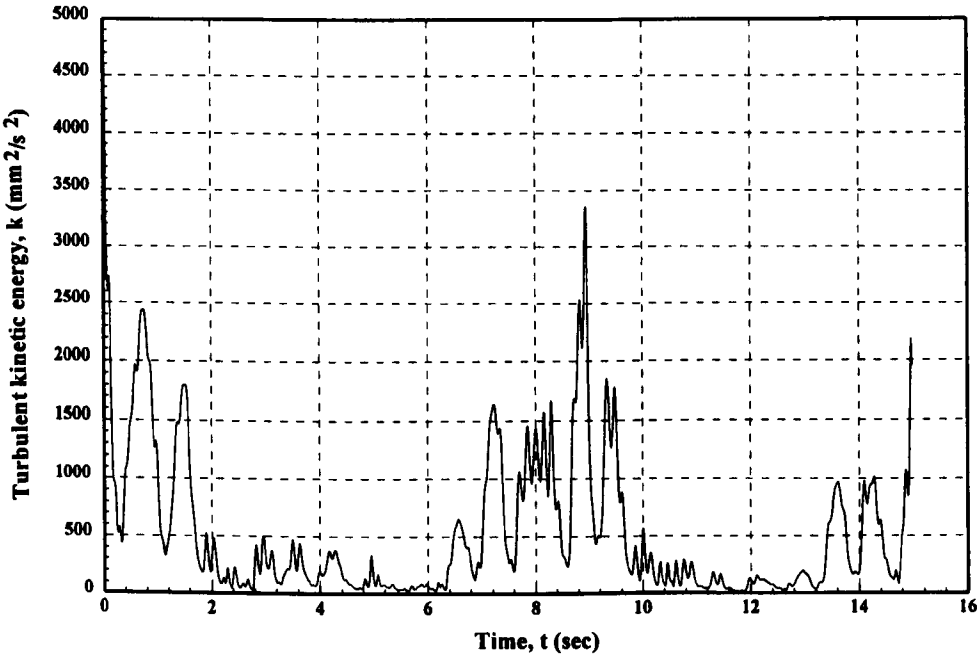

Figure 8.13a: Profile of the turbulent kinetic energy at the bed for conditions matching test No. 3, Kaczmarek and Ostrowski (1995); (—) k-ε model.

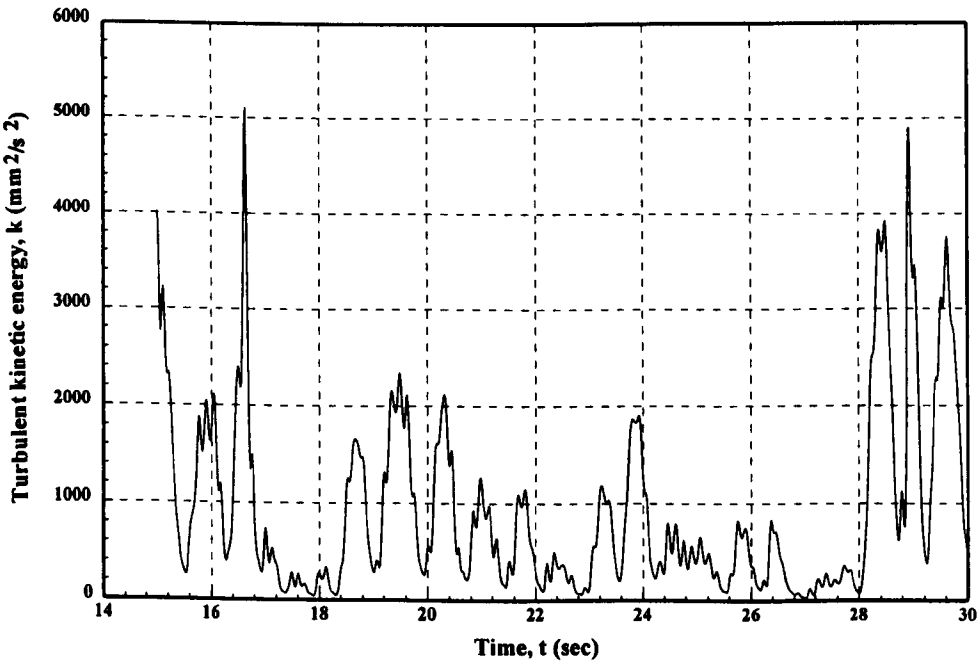

Figure 8.13b: Profile of the turbulent kinetic energy at the bed for conditions matching test No. 3, Kaczmarek and Ostrowski (1995); (—) k-ε model.

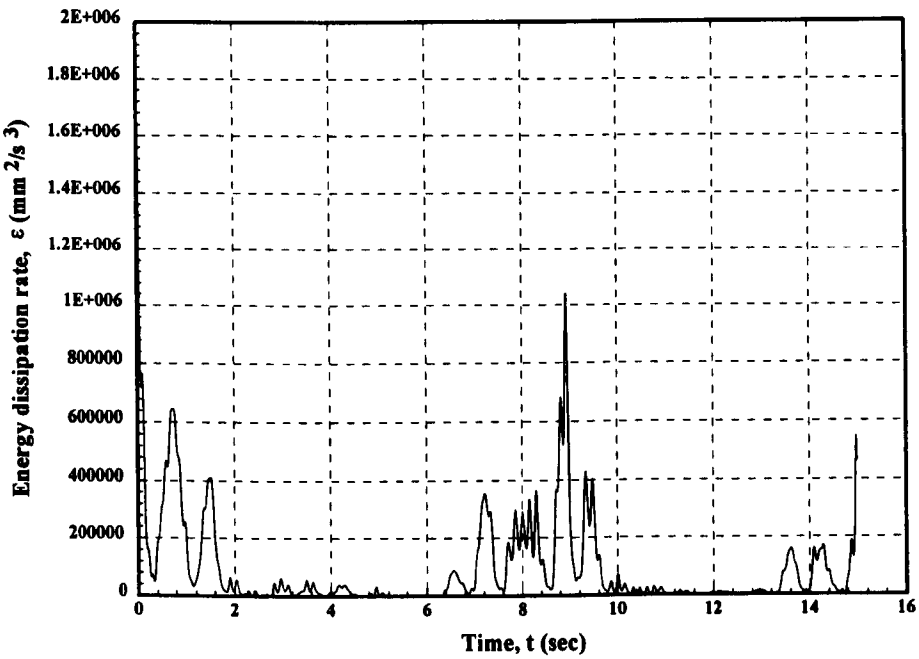

Figure 8.14a: Profile of the isotropic dissipation rate at the bed for conditions matching test No. 3, Kaczmarek and Ostrowski (1995); (—) k-ε model.

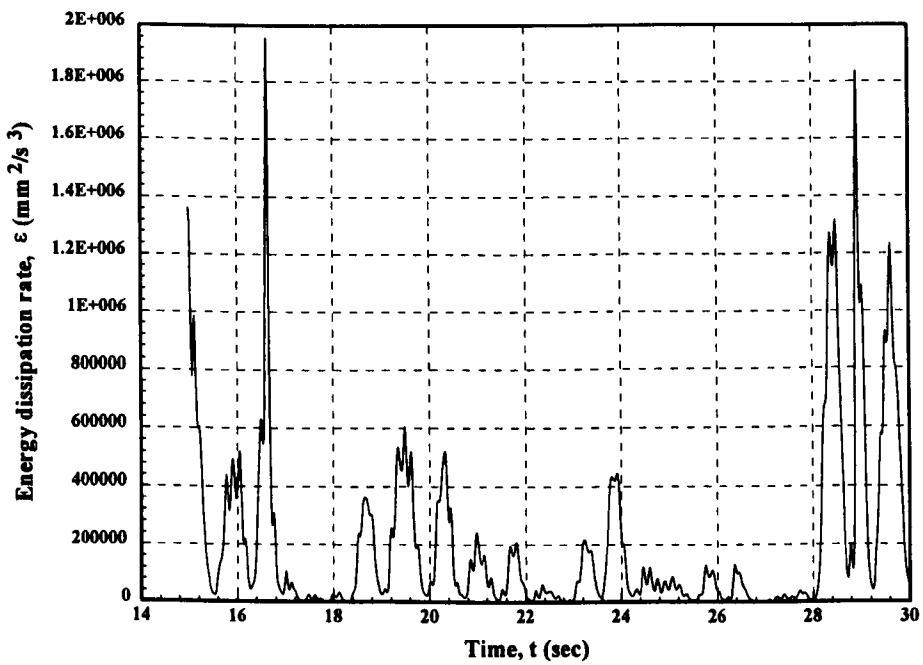

Figure 8.14b: Profile of the isotropic dissipation rate at the bed for conditions matching test No. 3, Kaczmarek and Ostrowski (1995); (—) k-ε model.

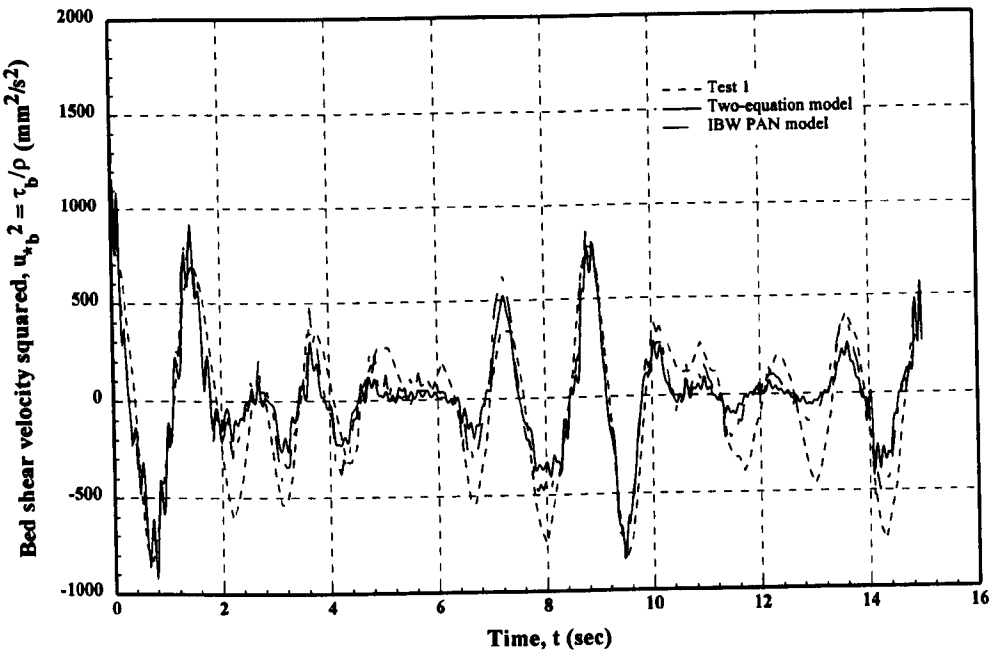

Figure 8.15a: Comparison of two-equation k-ε model and time-invariant eddy viscosity model of Kaczmarek and Ostrowski (1995) against measured bed shear velocity.

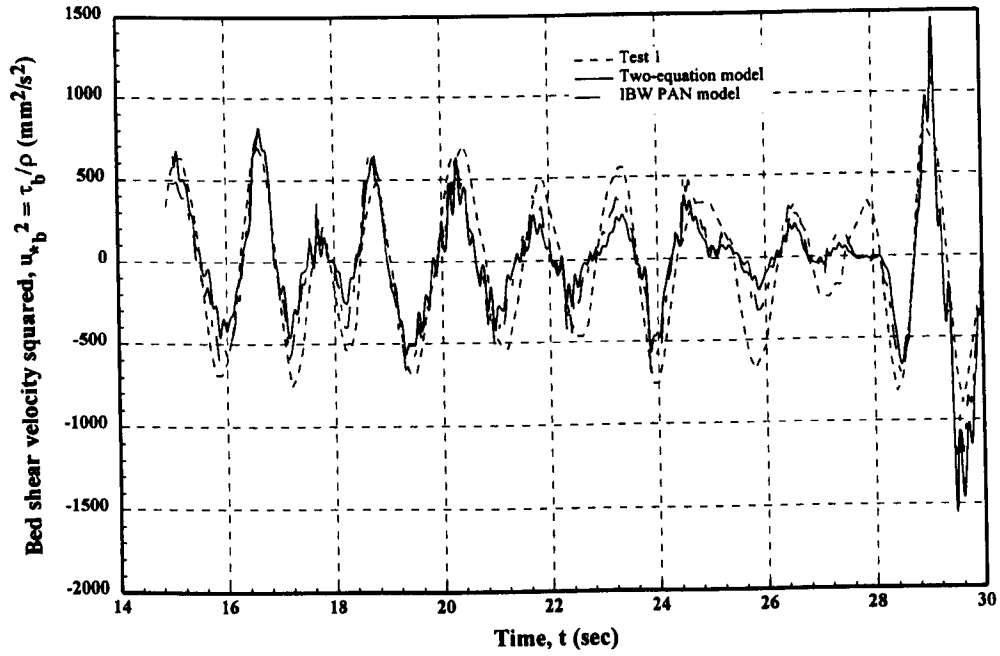

Figure 8.15a: Comparison of two-equation k-ε model and time-invariant eddy viscosity model of Kaczmarek and Ostrowski (1995) against measured bed shear velocity.

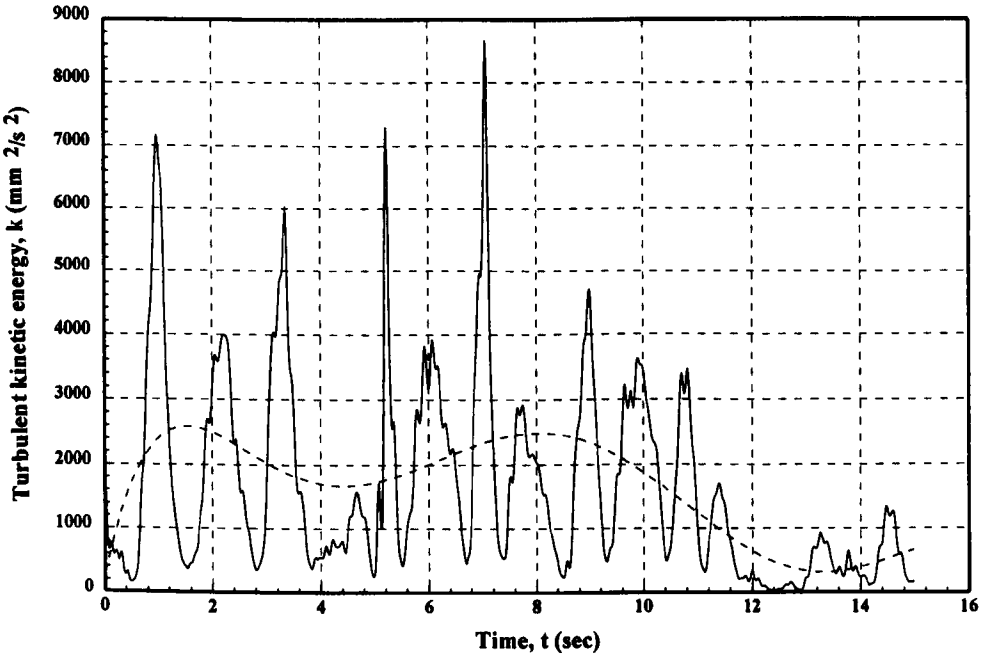

Figure 8.16a: Plot of calculated turbulent kinetic energy, k, together with a 6th order polynomial regression analysis showing the underlying trend of the data, for test 2.

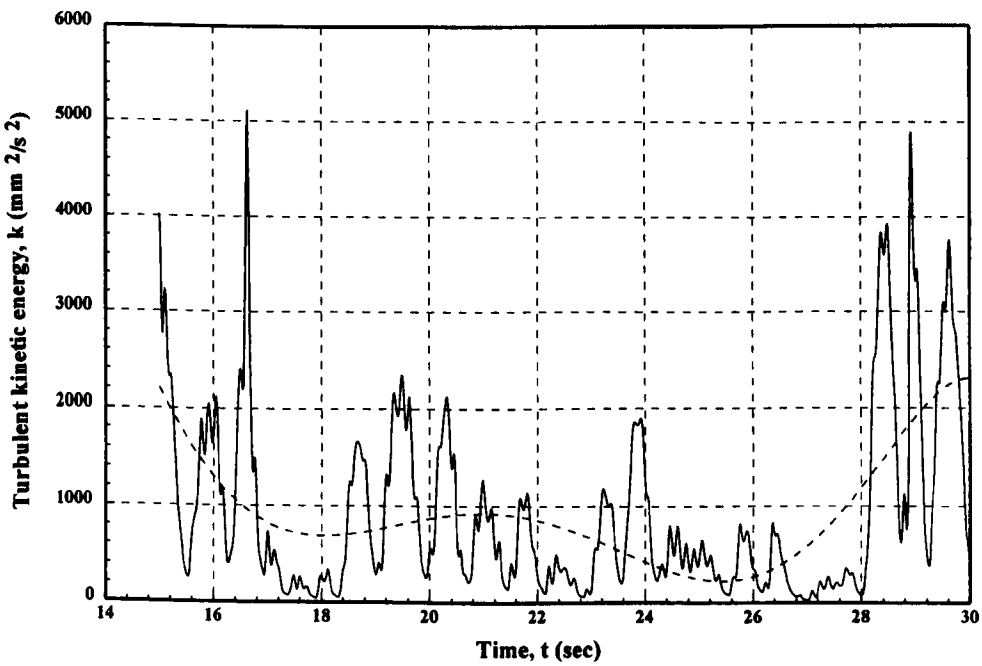

Figure 8.16b: Plot of calculated turbulent kinetic energy, k, together with a 6th order polynomial regression analysis showing the underlying trend of the data, for test 3.

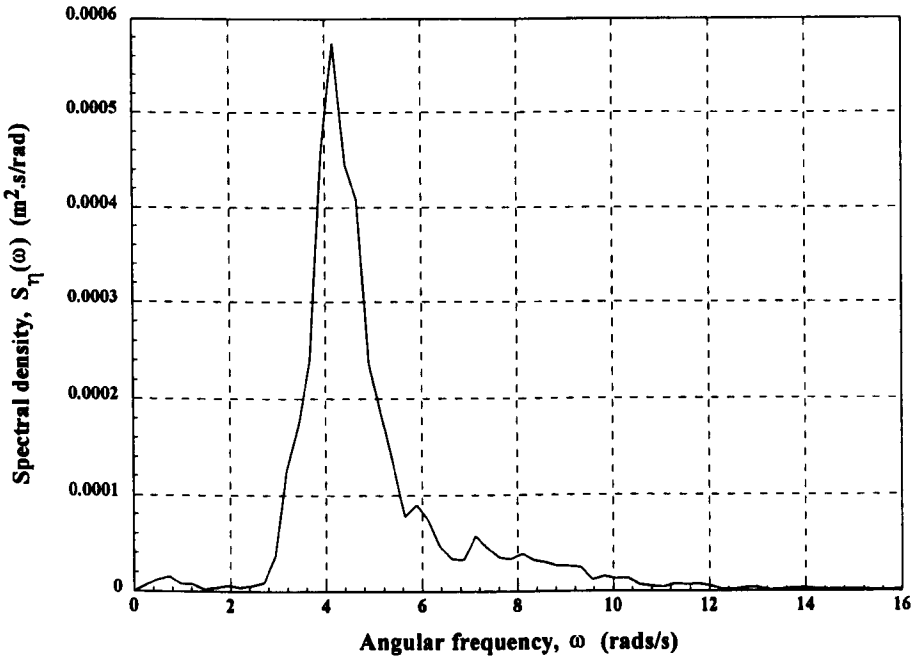

Figure 8.17 Measured surface wave height spectrum for test 1.

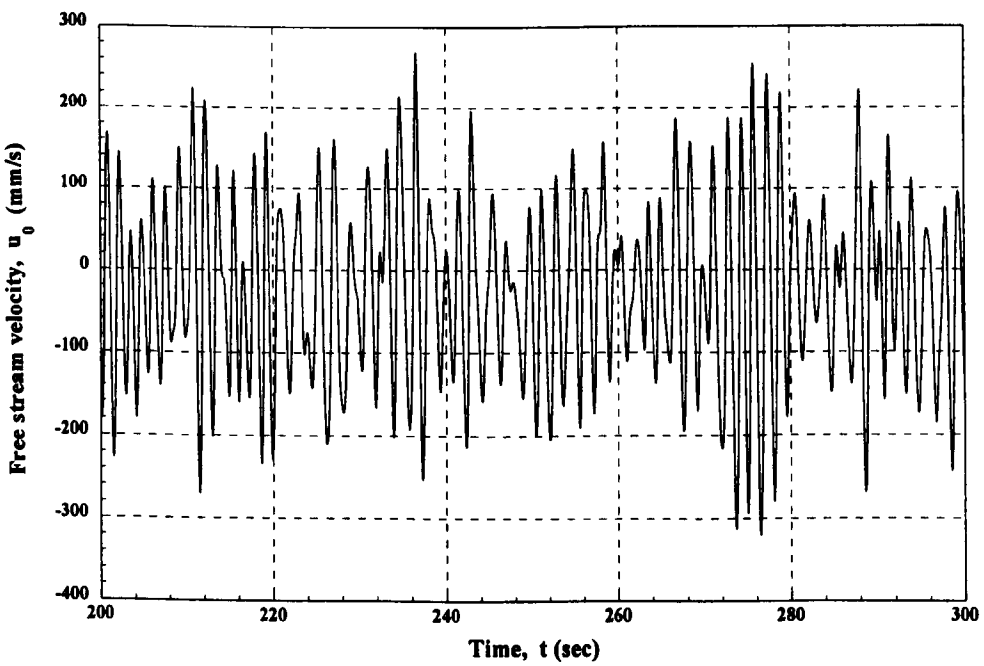

Figure 8.18: Computed free stream velocity for test 1 conditions, determined using spectral approach, see text.

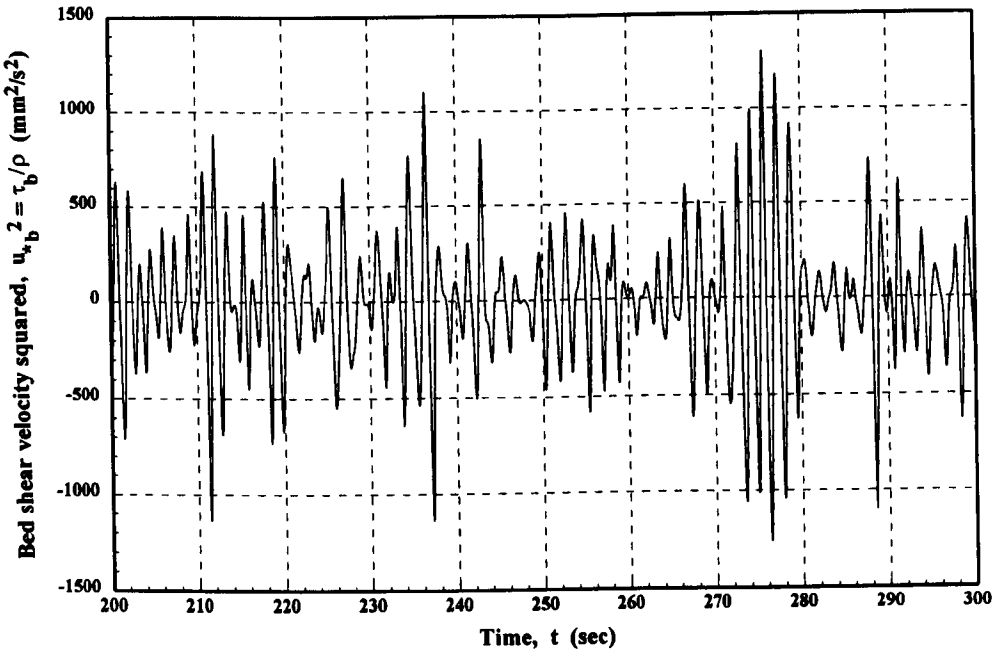

Figure 8.19: Computed shear velocity for test 1 conditions, determined using spectral approach, see text.

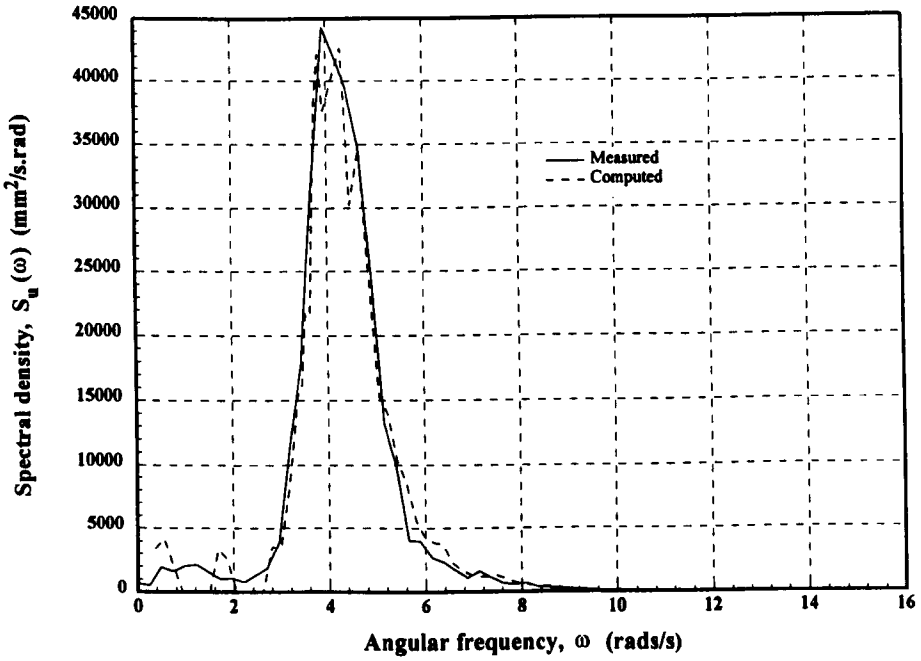

Figure 8.20a: Comparison of free stream velocity spectra for computed and measured free stream velocity for test no.1.

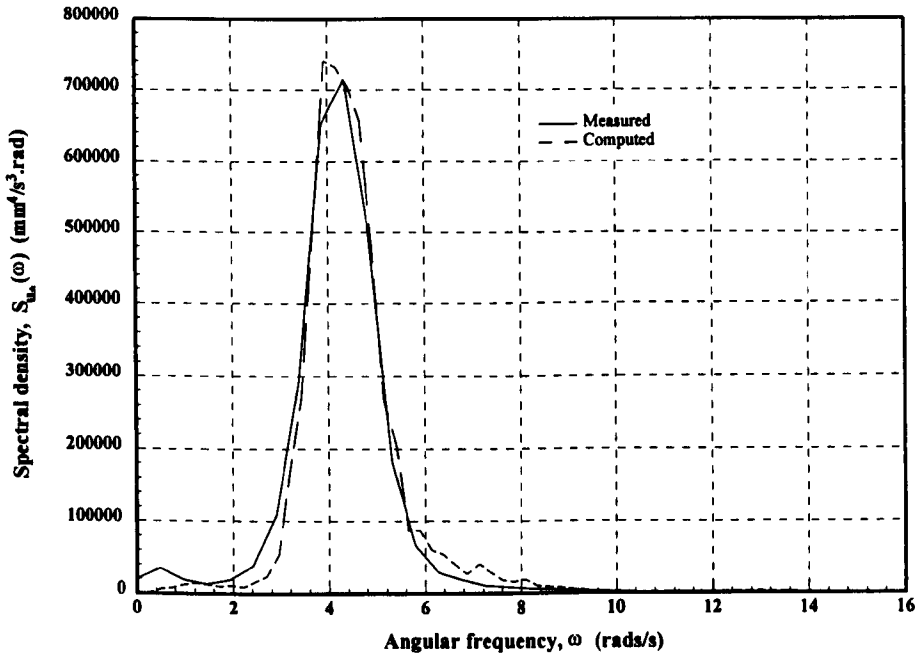

Figure 8.20b: Comparison of bed shear spectra for computed and measured shear stress for test no.1.

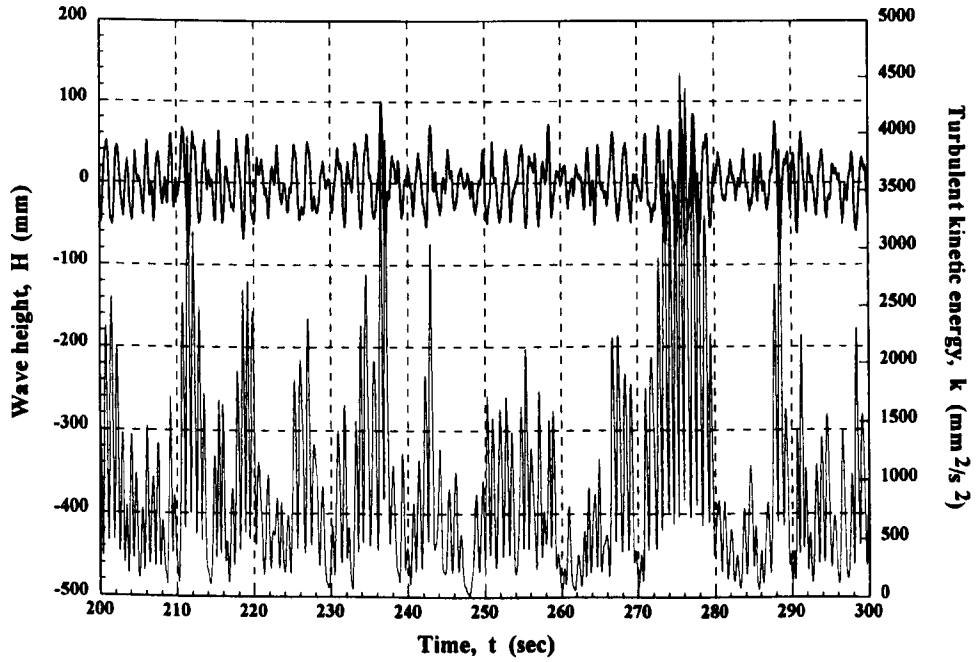

Figure 8.21a: Plot showing the variation of turbulent kinetic energy and wave height with time, for the parameters of test 1.

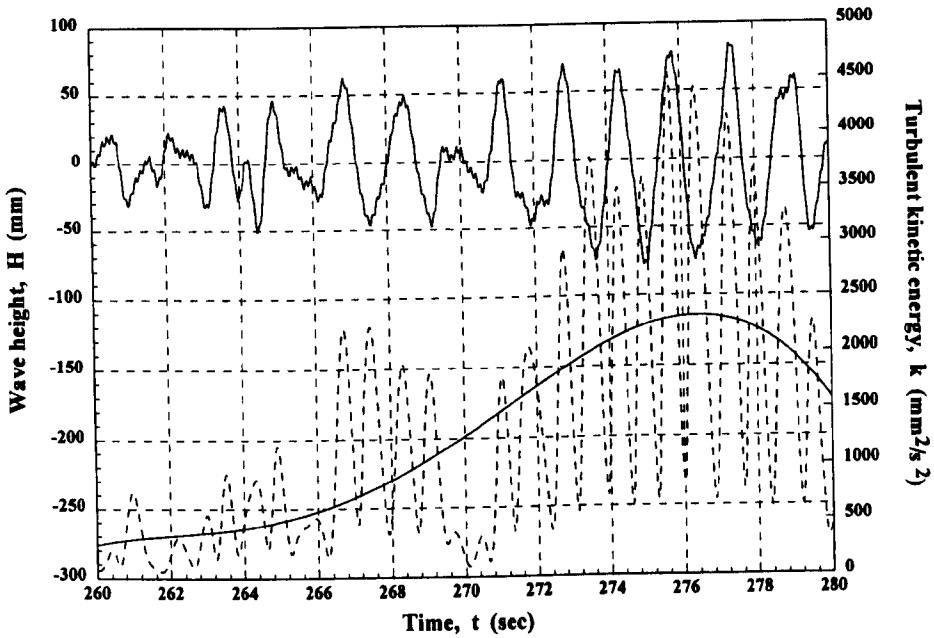

Figure 8.21b: Plot showing the variation of turbulent kinetic energy, k, with wave height. Also shown is the underlying trend of k calculated with a 6th order polynomial.

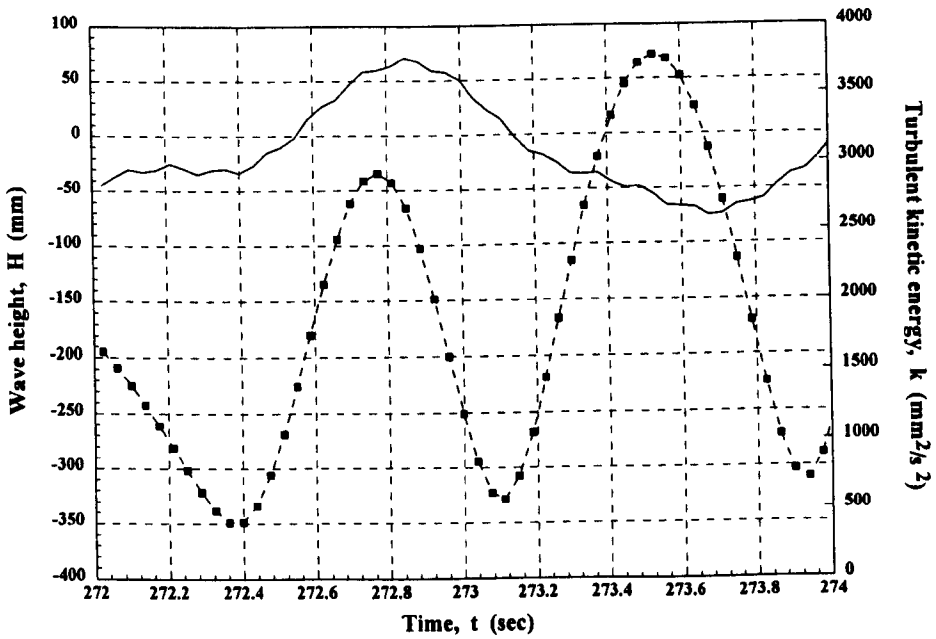

Figure 8.21c: Plot showing the variation of turbulent kinetic energy, k, with wave height for one wave of the random wave time-series.

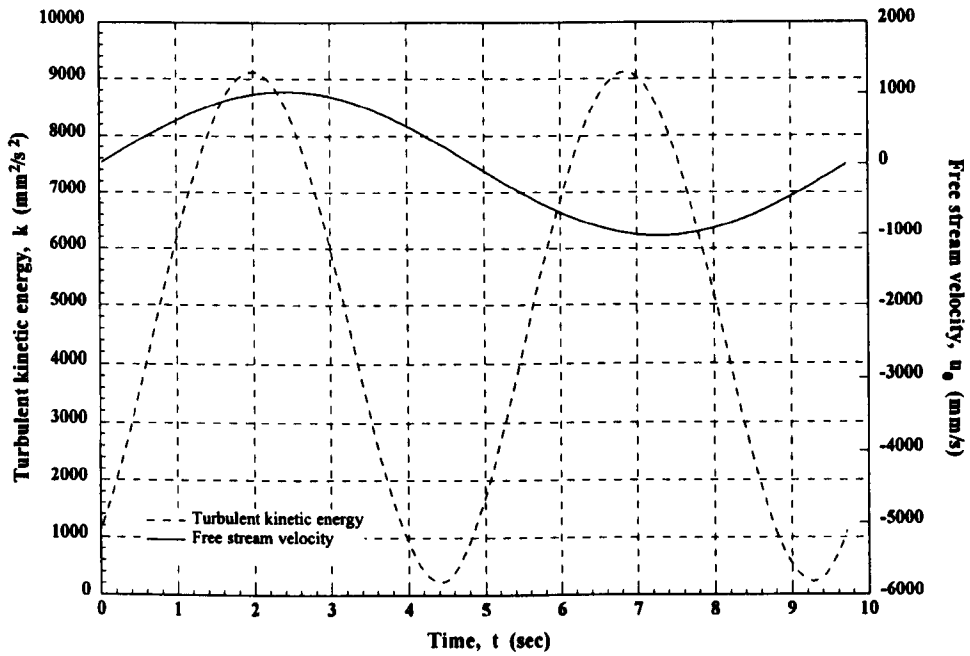

Figure 8.21d: Plot showing a typical turbulent kinetic energy profile at the bed for a monochromatic wave.

Chapter 9
Results: Part IV

9.1 Multi-directional seas

9.1.1 Introduction

In Chapter 9 the two-equation k-ε turbulence model is configured to enable the study of wave boundary layers in multi-directional seas through the use of field data. The field data was collected as part of a European Communities funded research project, CSTAB, (see O'Connor 1996). Up until this point, the turbulence models developed as a part of this thesis have only been tested against laboratory data, although the oscillating tunnel data of Jonsson and Carlsen (1976) and Jensen *et al.* (1989) is of prototype scale. As with all field data, the difficulties of collecting information in such a harsh and uncontrollable environment, require the instrumentation to be robust and, thus, relatively bulky. This hinders measurement in the wave boundary layer due to the small thickness of the layer (typically 0.1 - 0.5 m). The data sets are, therefore, limited in providing information for the near-bed region, with the lowest measurement point 40 cm from the seabed.

9.1.2 Background

The Circulation and Sediment Transport Around Banks (CSTAB) project was designed with the aim of obtaining a greater understanding of coastal hydrodynamic and morphodynamic processes around offshore sandbanks. In addition, the effect of the sandbanks on the adjacent shore was included within the study.

The CSTAB project was partially funded by the European Union and was conducted over a three year period. The project was a continuation and expansion of a previous project 'Circulation and Sediment Transport on Sandbanks in European Shelf Seas' (LSB), both of

which were co-ordinated by Professor B.A. O'Connor, see O'Connor (1992). The main objectives of the CSTAB project were:-

- To measure and model sandbank drag partitioning.
- To measure and model residual circulation and vertical flow structure around sandbanks.
- To determine and model the influence of offshore sandbanks on regional surface and near-bed currents.
- To determine bed shear stresses and directions over the sandbank.
- To study interactions between coherent turbulent structures in the benthic boundary layer with bottom sediments and to determine the incipient threshold *in situ*.
- To measure sediment transport pathways and magnitudes on the sandbank.
- To examine wave interactions with the sandbank and beach.
- To study beach hydrodynamics and interactions with offshore sandbanks.
- To determine sediment transport pathways and magnitudes inshore of the sandbank.
- To study coastal protection afforded by sandbanks in a storm.

The field data used in the present chapter was obtained during part of the offshore fieldwork using the benthic boundary layer rig STABLE II (Sediment Transport And Boundary Layer Equipment), see Humphrey (1987). STABLE II measured the near-bed benthic turbulence using electromagnetic current meters (ECM's). Further, STABLE II measured the suspended sediment concentration using acoustic backscatter (ABS) probes as well as the tides and wind waves using pressures sensors. The STABLE II rig was deployed in approximately 21m of water over coarse sand with mega-ripples at the Northern end of Middelkerke sandbank.

STABLE II was deployed for approximately 60 hours from 25 - 28 February, 1993. During the deployment 58 burst measurements were obtained. Each burst record is of about 20 minutes duration and was recorded every hour.

9.2 Field data

The offshore field work was undertaken by the Proudman Oceanographic Laboratory. The deployment of STABLE II coincided with a moderate storm which generated significant

wave heights (H_s) of approximately 3 m, see Figure 9.1. The location of STABLE II in relation to Middelkerke sandbank and the coastline is shown in Figure 9.2.

The STABLE II rig is a tripod frame capable of deploying a range of instruments, Figure 9.3 (see also Humphrey 1987). For the fieldwork campaign in the CSTAB project the boundary layer rig was equipped with four ECM torroidal open-headed current meters (Valeport series 2000) mounted in two pairs at 80 cm and 40 cm above the seabed. The arrangement of the ECM's was such as to allow each meter to measure two components of the instantaneous near-bed flow in orthogonal vertical planes (x-z, y-z). In addition to these ECM's, were four rotary current meters, located at 91 cm, 73 cm, 55 cm and 37 cm above the seabed on a vertical support at the centre of the rig; two acoustic back-scatter (ABS) suspended sediment probes (operating at 1 MHz and 2.5 MHz) covering the lower 1.2 m of the water column; two pressure transducers at 1.69 m above the seabed (Digiquartze) to measure water levels and wave heights; and a compass together with pitch and roll sensors to record the rig attitude.

The four rotary current meters measured average (1 minute) velocity profiles, eliminating high frequency velocity components and allowing the study of tidal flows. The data was measured at 8 Hz except in the case of the ABS sensors which measured at 4 Hz. The ECM's ABS probes and the wave sensors sampled in burst mode recording for 20 minutes every hour as described above.

9.3 Model results

In order to operate the 1DV k-ε boundary layer model, it is necessary to determine an appropriate value for the bed roughness (z_0) at the field site. The model uses the field data as an input and, therefore, calculates the bed roughness by trial and error. STABLE II measured the velocity at 80 cm and 40 cm above the seabed. The velocity at 80 cm is used to represent the free stream velocity within the turbulence model. The calculated and observed velocities at 40 cm are then compared and z_0 is adjusted until a reasonable match between the velocities at 40 cm is found. The suitability of such a method will be discussed later in the current chapter. The data used in Chapter 9 is for burst 37. Table 9.1 shows general values calculated from the field data (Williams 1997).

Figures 9.4 and 9.6 show the computed velocity profiles at 80 cm above the seabed for the u and v components, respectively. The model uses a Fourier series (800 components for the length of series shown in the figures) to represent the field data at 80 cm. The method is identical to that outlined in Chapter 7 and will not be discussed further. The mean differences between the computed time-series and the measured time-series at 80 cm are 2.05% and 0.693% for the u and v components, respectively. The total record length for burst 37 is approximately 1200 seconds, though in the present work only the first 200 seconds of data are shown.

Burst 37	
Depth, D (m)	20.61
Significant wave height, H_s (m)	2.7913
Peak Period, T_p (s)	7.9814
Mean velocity, $\bar{u}_{40}$ (cm/s)	4.11
Mean velocity, $\bar{v}_{40}$ (cm/s)	34.13
Current speed, S_{40} (cm/s)	39.54
Current direction at 40 cm (degrees)	208.67
Mean velocity, $\bar{u}_{80}$ (cm/s)	4.32
Mean velocity, $\bar{v}_{80}$ (cm/s)	42.4
Current speed, S_{80} (cm/s)	46.61
Current direction at 80 cm (degrees)	211.72

Table 9.1: General parameters for burst 37.

Figures 9.5 and 9.7 show the comparison between the measured and computed velocity components, u and v at 40 cm above the seabed, respectively. The time-series for the horizontal velocity component, u, is well reproduced by the k-ε model although, in places, the model tends to underpredict the peak velocities whilst overpredicting the minimum values (Figure 9.5). The horizontal velocity component, v, shows more variation between the measured and calculated values. In Figure 9.7 the model is seen to overpredict peak velocities whilst underpredicting the minimum velocities in the y-direction.

Comparing both the measured and model velocities at 80 cm and 40 cm above the seabed reveals relatively small variation between the time-series with height (z-direction). The greatest variation is seen in the y-direction (Figures 9.6 and 9.7). This suggests that finding a suitable z_0 value by matching the calculated velocities at 40 cm with the measured values is not that sensitive and ideally more than two measurement points in the vertical would ensure greater accuracy, particularly if one of the points was within the wave boundary layer. The value of z_a, the apparent bed roughness calculated in the present results is $z_a \approx 1.7$ cm. This value is slightly larger than some values suggested for bursts 25, 35 and 39 in earlier work (8 - 14 mm, O'Connor *et al.* 1994). z_a relates to the roughness height in the case of combined waves and current whilst z_0 relates to the bed roughness in the absence of currents. The method of fixing the bed roughness based on velocity profiles at two different points is somewhat questionable. Not only is the method sensitive to the location, with depth, of the two points, but the method of fit must also be doubtful due to the model formulations.

Chapter 6 showed a comparison of three different turbulence models against the data of Jonsson and Carlsen (1976). The three models compared were a simple zero-equation, mixing length model, a one-equation, k model and a two-equation, k-ε model. From the results shown in Figure 6.4 it is clear that the mixing length model fails to provide a good fit to the data outside the near-bed region whilst the higher-order models provide good agreement, overall. To use the output of a model at two different levels, adjusting the mean of the lower level until a fit is obtained, when the model itself appears incapable of providing the correct profile makes the use of such a method suspect. If a model produces a reasonable representation of a measured time-series at one level, but produces a mean error of, say, 20% at the second level, adjusting the model to fit a measured time-series at this second position is clearly going to lead to further errors and, hence, an incorrect estimate of the bed roughness. It is suggested that the differences between the z_a values calculated by O'Connor *et al.* (1994) and the present work are possibly due to errors in the numerical techniques applied, since the O'Connor *et al.* use a zero equation, mixing length model to obtain their results.

Figures 9.8 and 9.9 show the bed shear velocity for the x- and y-directions respectively. Whilst a direct measurement of the bed shear velocity was not made, Williams (1996) has

estimated a mean value of the bed shear velocity for burst 37 using two different methods. Williams determined the shear velocity using the Reynolds stresses (RS) and turbulent kinetic energy (TKE) methods.

Williams (1996) defines the RS method as:-

$$\bar{u}_*^2 = \frac{\tau}{\rho} = \left(\overline{u'w'}^2 + \overline{v'w'}^2\right)^{0.5} \qquad (9.1)$$

and the TKE method by the equation:-

$$\bar{u}_*^2 = \frac{\tau}{\rho} = 0.19(E) \qquad (9.2)$$

and

$$E = \frac{1}{2}\left(\sigma_{xt}^2 + \sigma_{yt}^2 + \sigma_{zt}^2\right) \qquad (9.3)$$

where E is the turbulent kinetic energy and σ_{xt}^2, σ_{yt}^2 and σ_{zt}^2 are turbulent variance values for tidal flow in the absence of waves (see Williams 1996 for further details). The constant of proportionality (0.19) is given by Soulsby (1983).

Burst 37	$\bar{u}_*$ **(cm/s)**	$\bar{u}_*$ **(cm/s)**
	z = 80 cm	**z = 40 cm**
TKE	4.19	2.85
RS	2.87	1.68

Table 9.2: Estimated shear velocity values for burst 37 using the TKE and RS methods. (*After Williams 1996*).

From the model results, the mean bed shear velocity is approximately 4.14 cm/s. Comparing the computed value with the measured values gives differences for the TKE method of between 1.2 - 44.3 % and between 45.3 - 146.4 % for the RS method. Williams (1996) suggests that due to inter-wave period misalignment of the ECM sensors relative to the mean flow streamline and to period asymmetrical near-bed wave-induced flow caused by tidal

current interaction, the TKE method provides more reliable results. The computed mean bed shear velocity would appear, therefore, to be reasonable estimate.

Using the logarithmic profile method provides a third, if less reliable, method for estimating the bed shear velocity. The logarithmic velocity distribution is assumed to be given by the equation:-

$$S = \frac{\bar{u}_*}{\kappa} \ln\left(\frac{z}{z_a}\right) \qquad \textbf{(9.4)}$$

where κ is the von Karman constant; $\bar{u}_*$ is the bed shear velocity; and S is the turbulent mean current speed at a given height z.

Using the logarithmic profile method gives a value for the measured mean bed shear velocity of 4.08 cm/s. The assumption of a logarithmic distribution of mean velocity with height has been shown to be valid for combined wave-current flows by Kemp and Simons (1983). However, changes in bed elevation occurring during the measurement period could not be directly related to the relative sensor positions. Further, variations due to stratification, bed roughness and waves will produce errors in estimates made using the logarithmic profile approach. Nevertheless, the computed value for the mean bed shear velocity appears reasonable, on the basis of the above, and suggests that model values can be viewed with some confidence.

Figure 9.10 shows the calculated turbulent kinetic energy, k, at the seabed as a time-series for the first 200 seconds of the burst record. No measurements of k at the bed exist, so comparison is not possible.

Figure 9.11 shows the calculated turbulent kinetic energy at 40 cm and 80 cm above the seabed. Surprisingly the time-series are quite 'linear'. The results show the turbulence to be decaying quite rapidly from the bed. It is possible that the gradient condition at the upper boundary, $\partial k/\partial z = 0$, employed by the model is inadequate when currents are applied (that is, 80 cm above the seabed) and thus forcing the turbulent kinetic energy profile to conform.

It would, perhaps, be more appropriate if the model could be run at full depth (≈ 21m) which would allow the turbulent kinetic energy profile to adjust more gradually.

Comparison of the monochromatic version of the k-ε model and test 59, from the experiments conducted at Manchester University (see Chapter 7) showed a failure of the model to correctly predict the turbulent kinetic energy outside the boundary level. It has been suggested that this might be due to streaming (mass transport effects) but further work is required to study this. The model values outside the wave boundary layer must, at present, be viewed with caution for conditions including waves and currents.

Figures 9.12 and 9.13 show the corresponding time-series for the isotropic dissipation rate, ε. The values follow a similar trend to those of the kinetic energy, although with greater magnitude. This is to be expected since ε is a function of k to the power of 2.

Figure 9.14 shows the turbulent kinetic energy at the bed together with the results of a regression analysis of the signal, calculated using a 6th order polynomial fit. As was observed in the model results for turbulent kinetic energy obtained for the Gdansk flume data, the underlying turbulence structure grows and decays.

Figure 9.15 shows the velocity profile with depth as predicted by the model. The results show a sequential record for three different instances in time. The results suggest veering in the horizontal velocity from the current direction, as demonstrated by Davies *et al.* (1988). Coriolis effects are not included in the model formulation (Soulsby and Humphrey 1990 observed some veering in their field measurements and attributed the effects to the tidal dynamics). Veering is caused by the generation of very different levels of turbulent kinetic energy in corresponding half wave periods. In the case of co-linear waves and currents, there is a tendency for the mean flow to be retarded more in the half cycle in which the current and the wave velocities are in the same direction than in the half-period in which they are opposed. This results in a veering of the mean flow within the wave-current boundary layer away from the direction in which the waves and current compliment each other. In addition, the effect of the cascade of turbulence caused by the random nature of the waves could well enhance this effect. This point requires further study.

9.4 Conclusions

The model has been run using the horizontal time-series for the measured u and v velocity signals at 80 cm above the seabed. Using a Fourier series, as in Chapter 7, it has been possible to recreate the measured signal, enabling the numerical model to be used to compare the field data and computed results. The results suggest that the random wave boundary layer model is capable of providing a reasonable description of multi-directional sea states.

Results suggest that the method proposed by O'Connor *et al.* (1994) for finding the bed roughness, by calculating the mean velocity at one level and adjusting the parameter, z_0, in the numerical model until the mean velocity corresponds to the mean measured velocity at the same level, is questionable. The method has been found to be highly sensitive to the location above the bed of the measured data, and it has been argued, to the numerical model used.

The computed mean bed shear velocity was found to correspond favourably with those values estimated from the measured data. The computed value of 4.14 cm/s showed good agreement with the measured values obtained using the TKE method (4.19 cm/s) and the logarithmic profile method (4.08 cm/s).

The carry over of turbulent kinetic energy obtained by the numerical model against the random flume data of Ostrowski (1993) was observed in the model results for burst 37. In addition, it is suggested that the cascade of turbulent energy from one half-period to the next might enhance the veering effect observed in wave-current interaction, for example Davies *et al.* (1988).

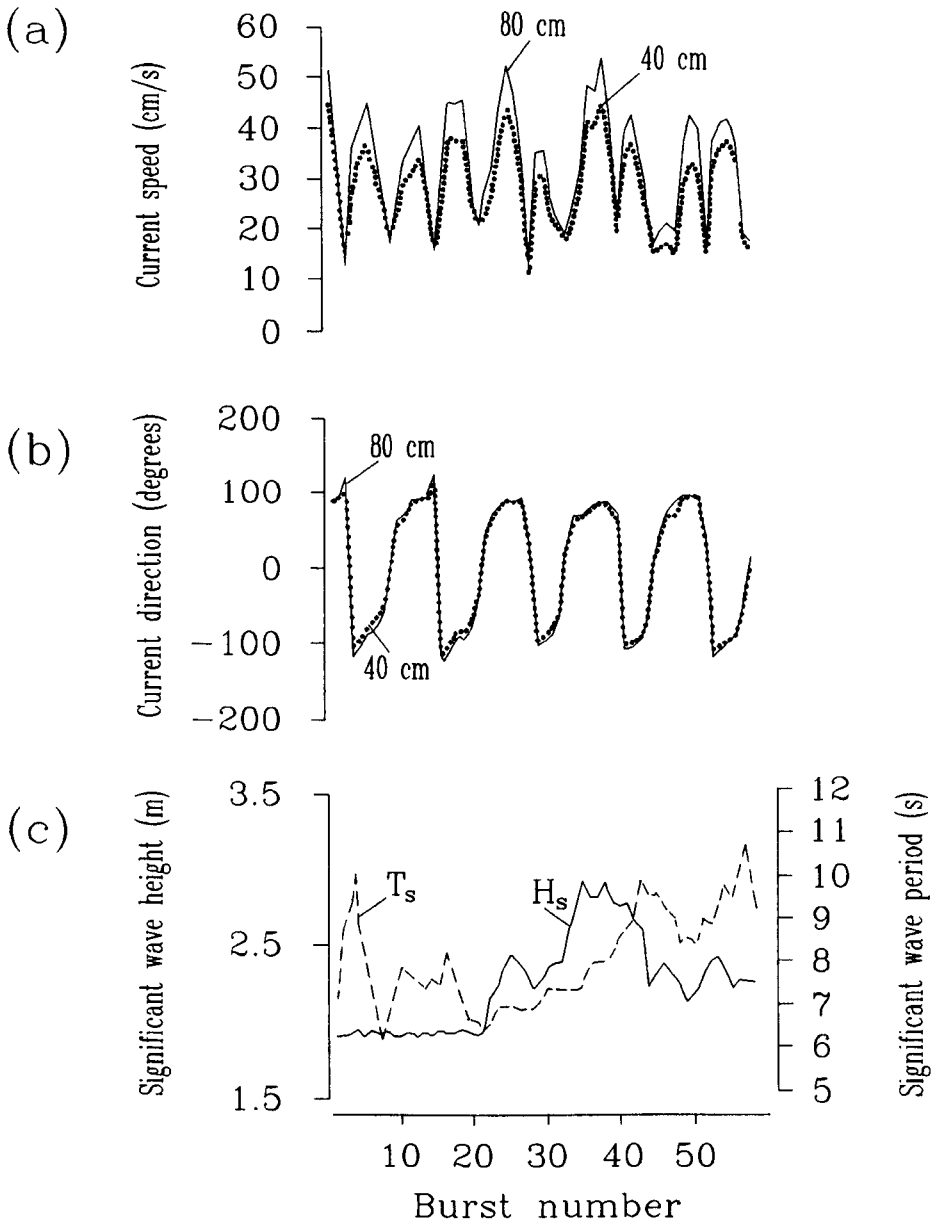

Figure 9.1: STABLE II data, showing average current speed and direction and significant wave height and period. (*AfterWilliams 1996*).

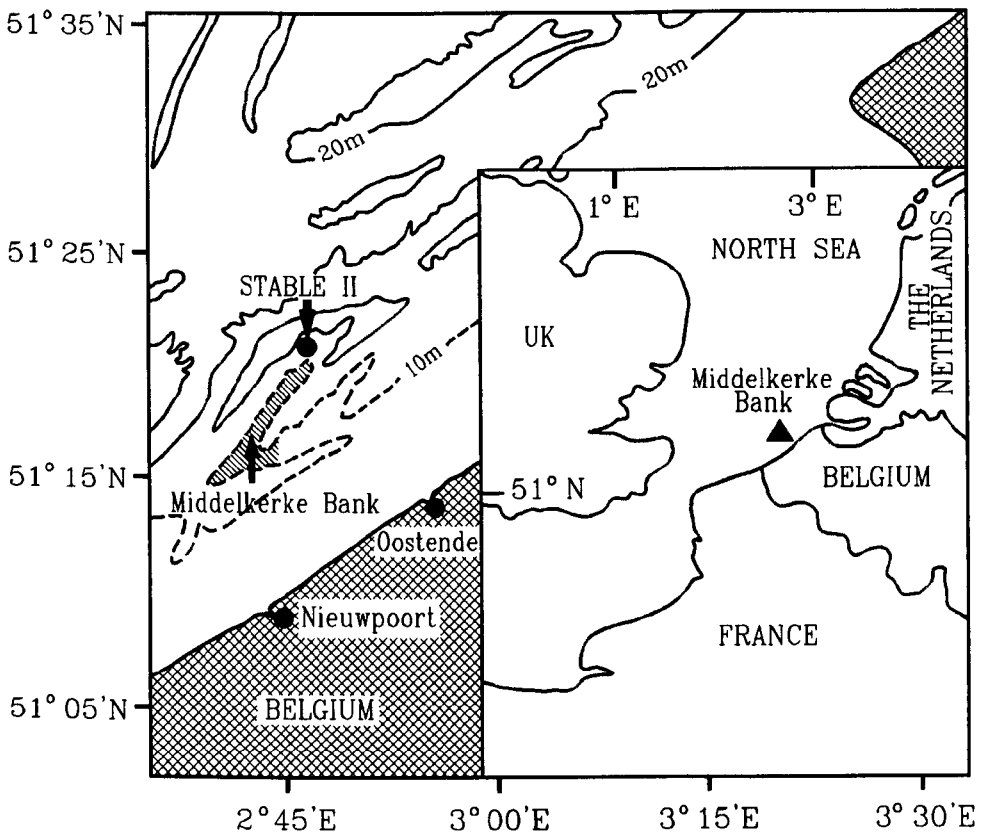

Figure 9.2: Location of STABLE II within CSTAB study area (*After Williams 1996*).

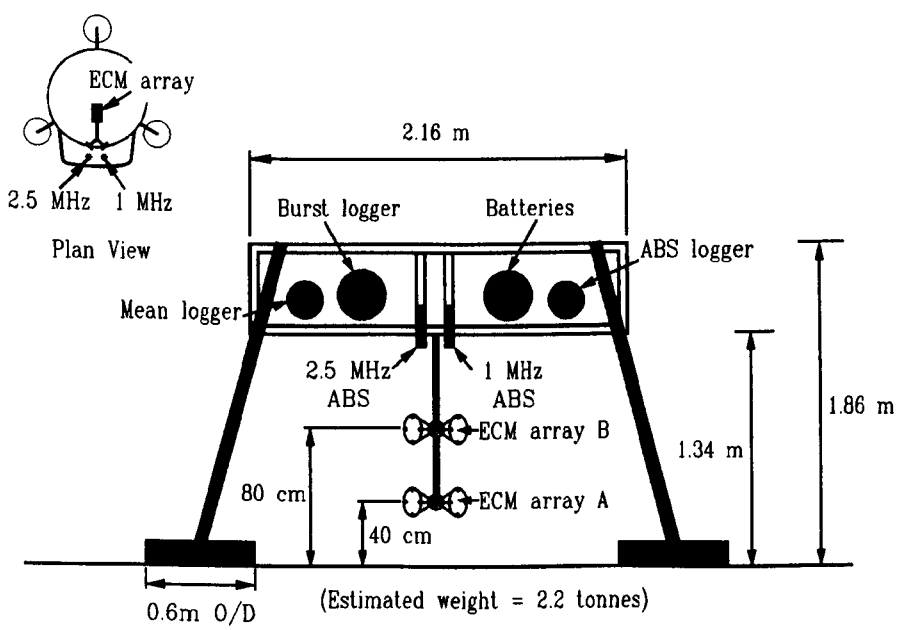

Figure 9.3: STABLE II, benthic boundary layer rig (*After Williams 1996*).

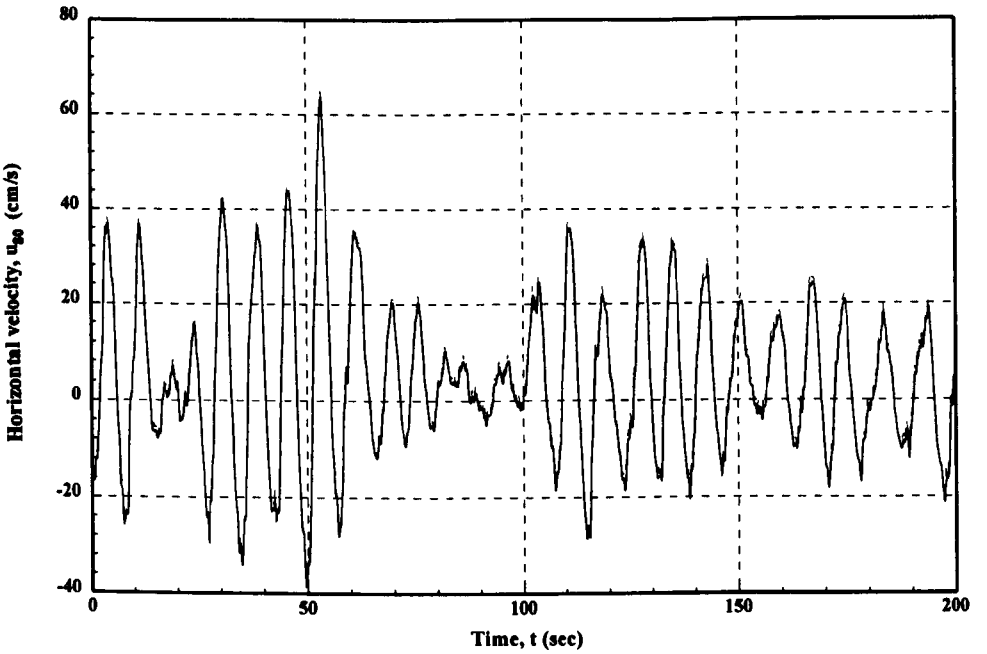

Figure 9.4: Time-series of horizontal velocity component,u at 80 cm above the bed for burst 37. (— = k-ε model).

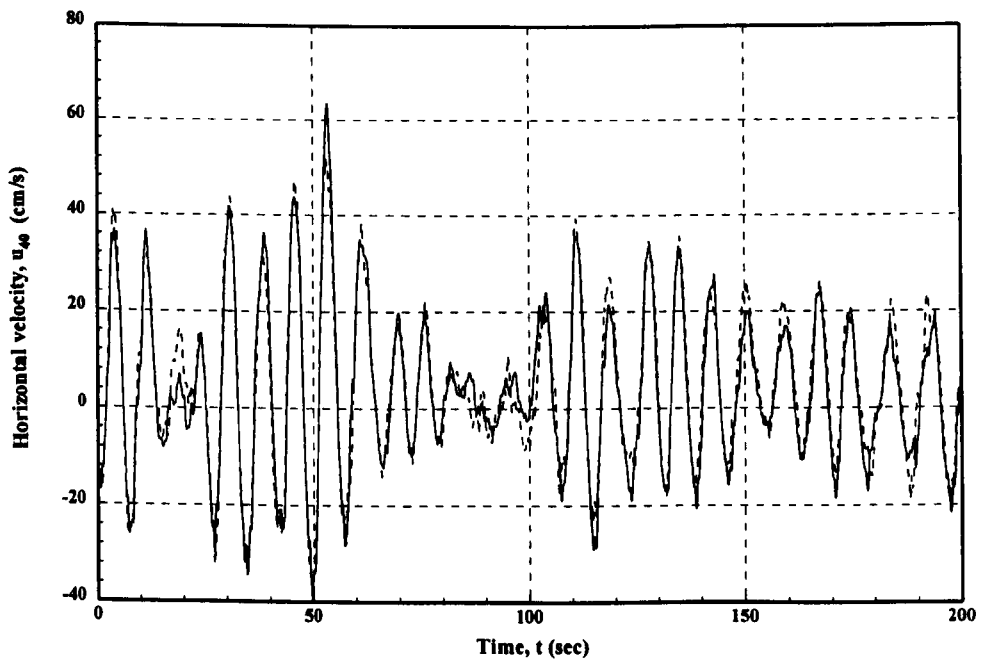

Figure 9.5: Time-series of horizontal velocity component,u at 40 cm above the bed showing comparison between field data (– – burst 37) and k-ε model (—).

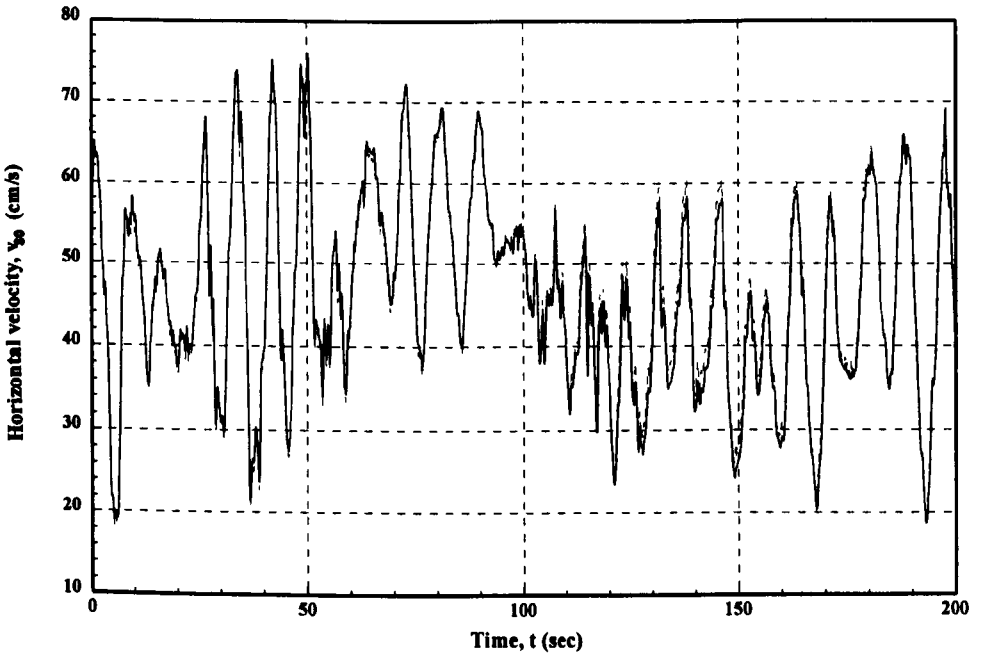

Figure 9.6: Time-series of horizontal velocity component,v, at 80 cm above the bed for burst 37. (— = k-ε model).

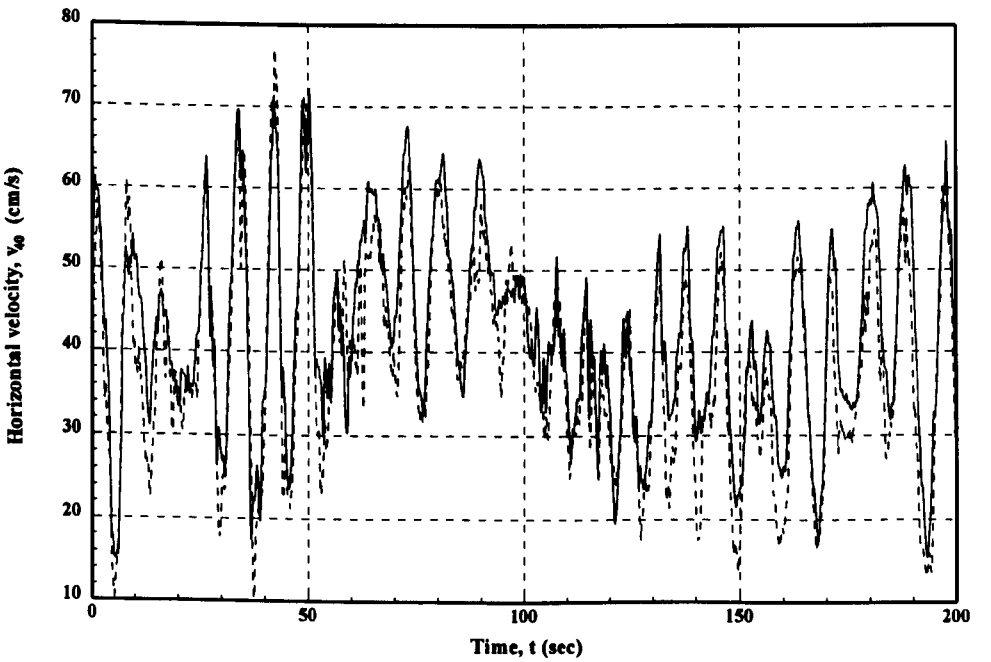

Figure 9.7: Time-series of horizontal velocity component,v at 40 cm above the bed showing comparison between field data (– – burst 37) and k-ε model (—).

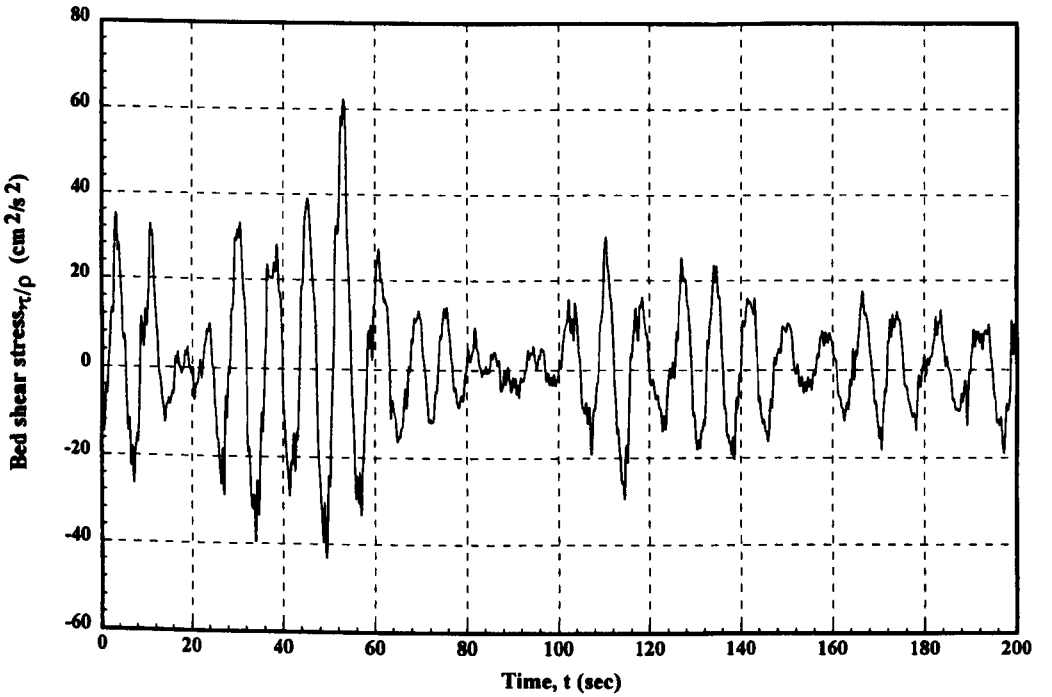

Figure 9.8: Time-series of the bed shear velocity in the x-direction from k-ε model prediction.

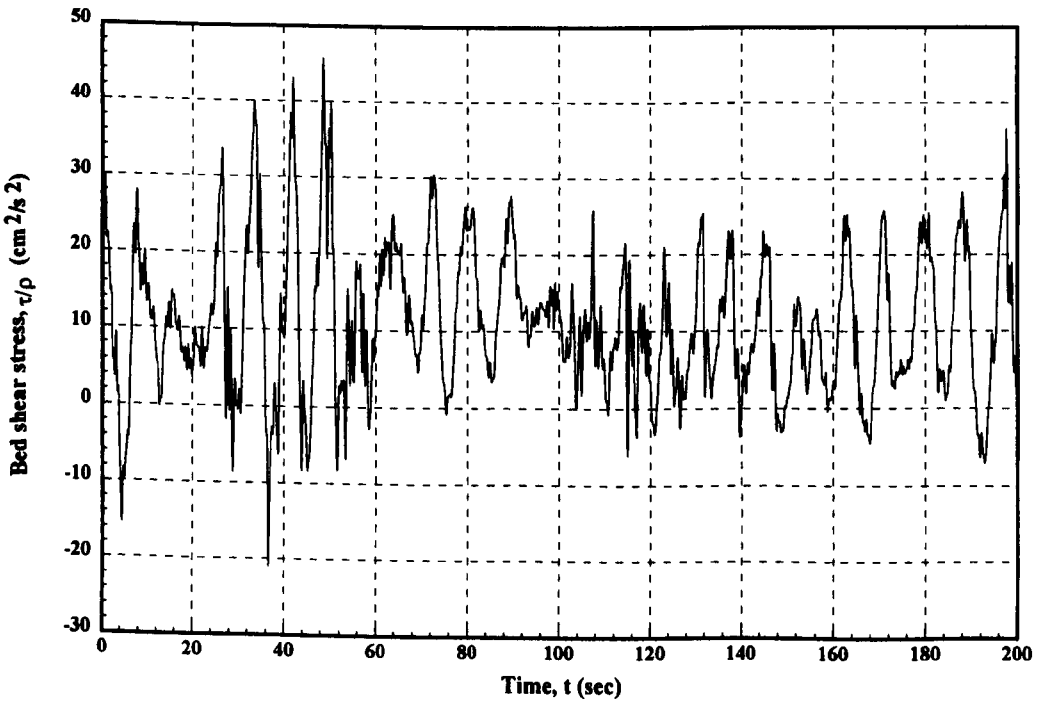

Figure 9.9: Time-series of the bed shear velocity in the y-direction from k-ε model prediction.

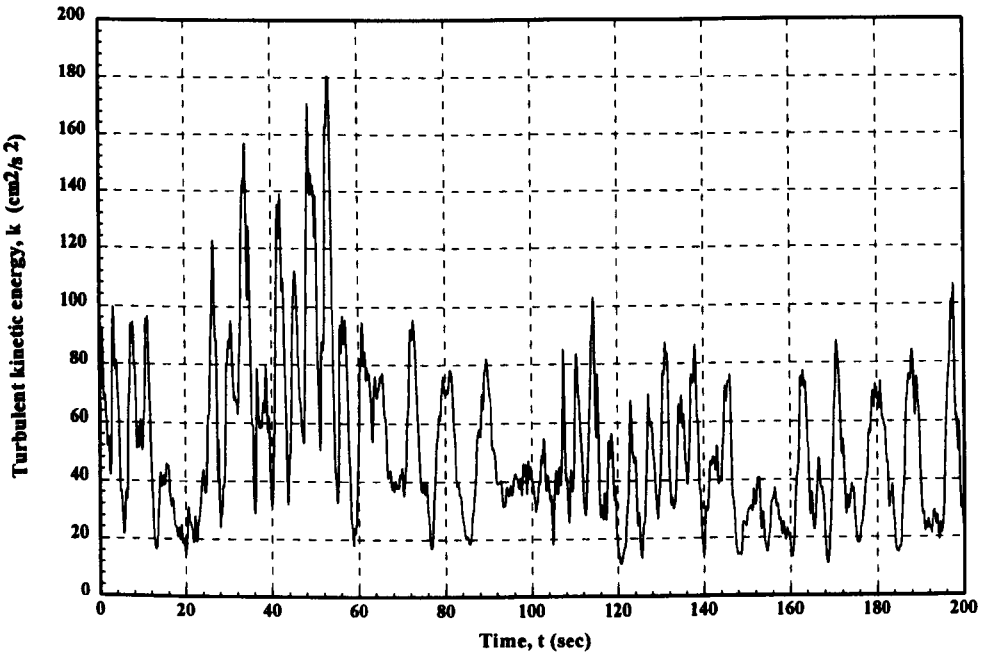

Figure 9.10: Time-series of turbulent kinetic energy at the seabed from k-ε model prediction.

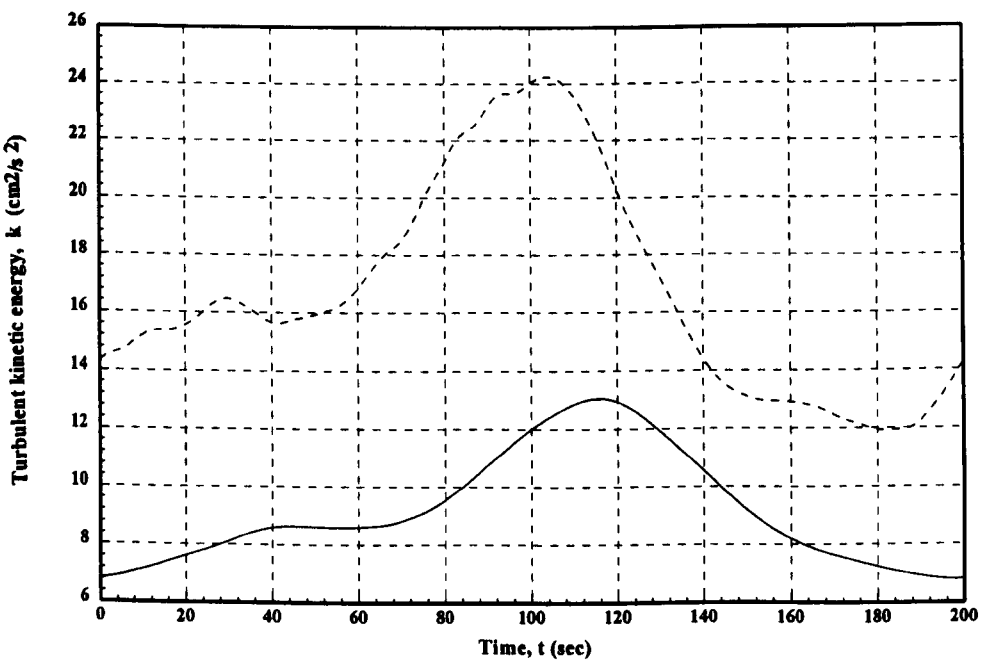

Figure 9.11: Time-series of turbulent kinetic energy as predicted by k-ε model at 40cm (– –) and 80 cm (—) above the seabed.

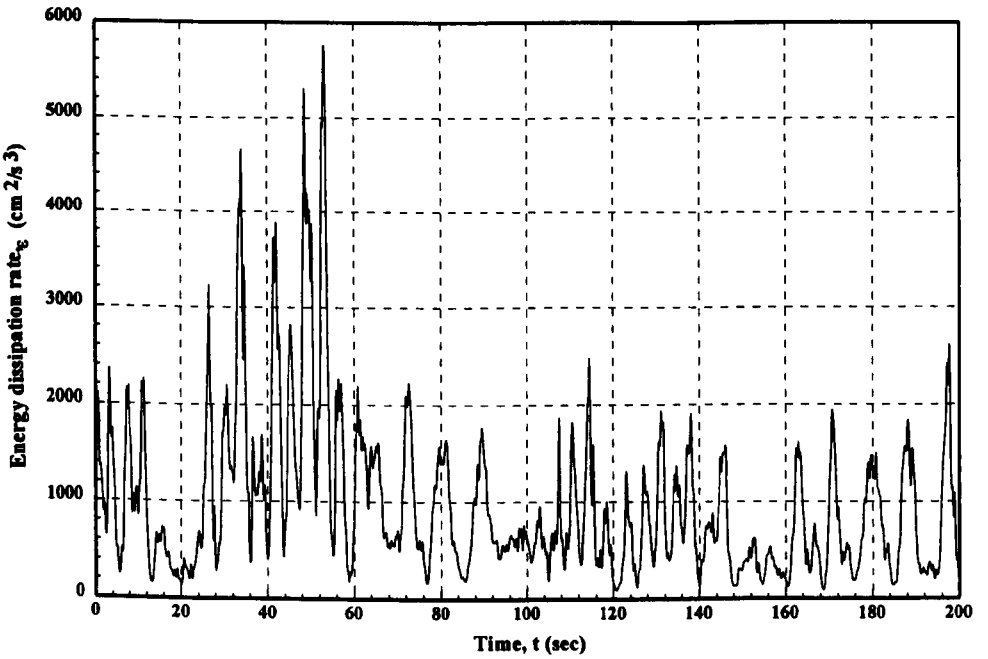

Figure 9.12: Time-series of isotropic dissipation rate at the bed from k-ε model prediction.

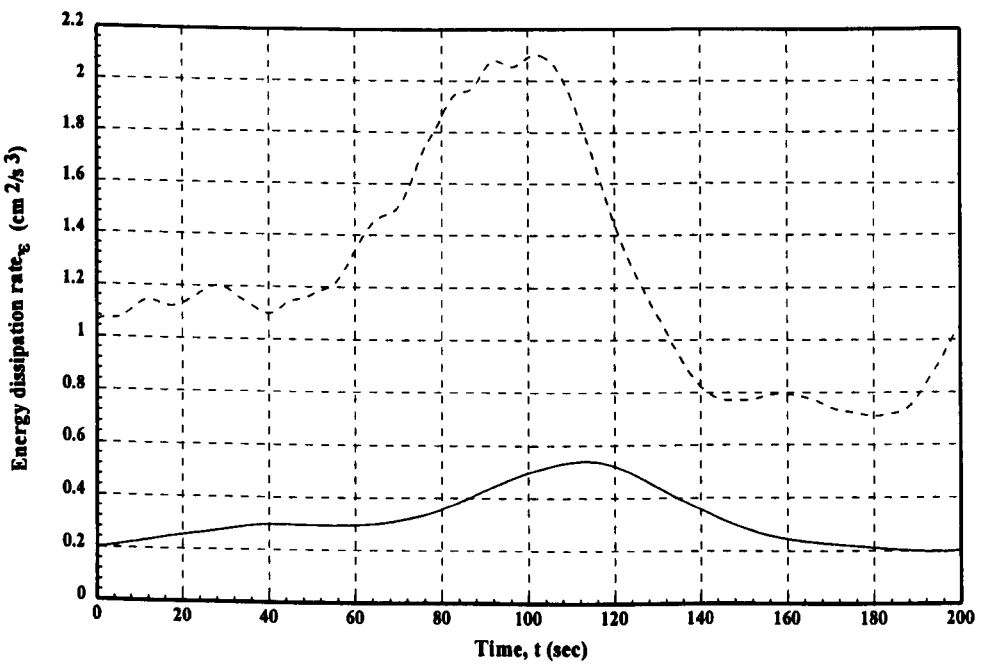

Figure 9.13: Time-series of isotropic dissipation rate as predicted by k-ε model at 40 cm (– –) and 80 cm (—) above the seabed.

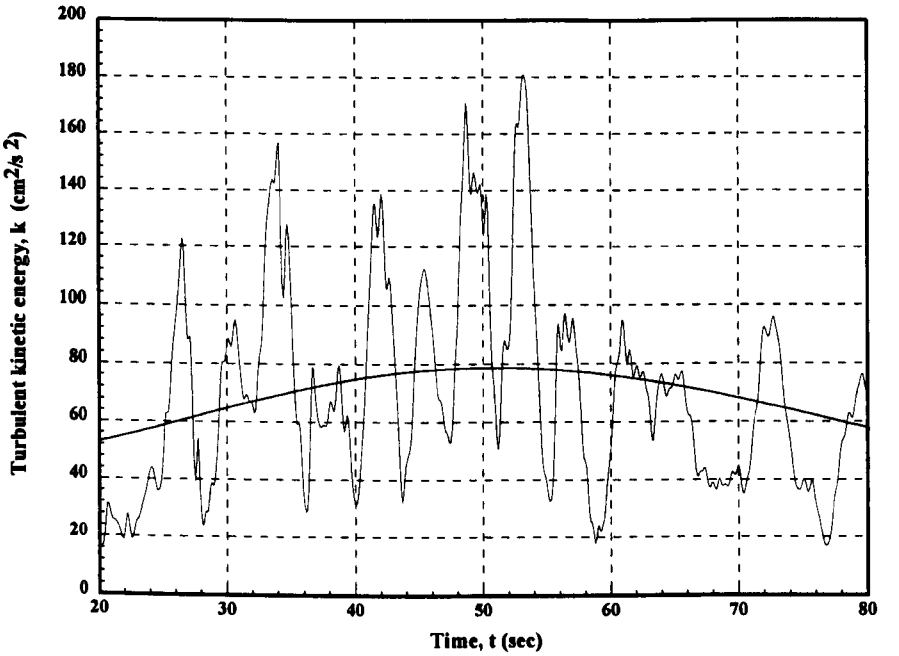

Figure 9.14: Plot showing turbulent kinetic energy at the seabed together with underlying trend calculated using 6th order polynomial regression analysis.

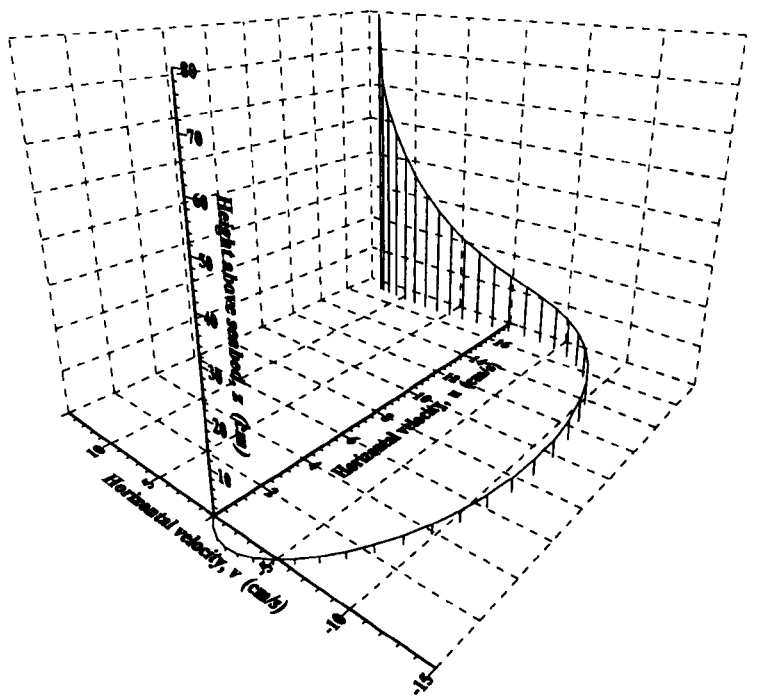

Figure 9.15a: Velocity profile as predicted by k-ε random wave boundary layer model (t ≈ 5.410 s).

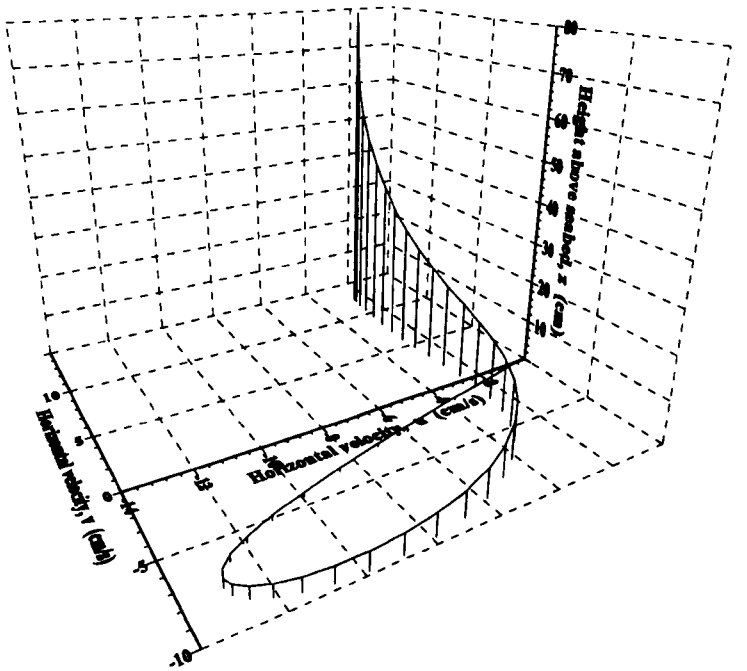

Figure 9.15b: Velocity profile as predicted by k-ε random wave boundary layer model (t ≈ 6.011 s).

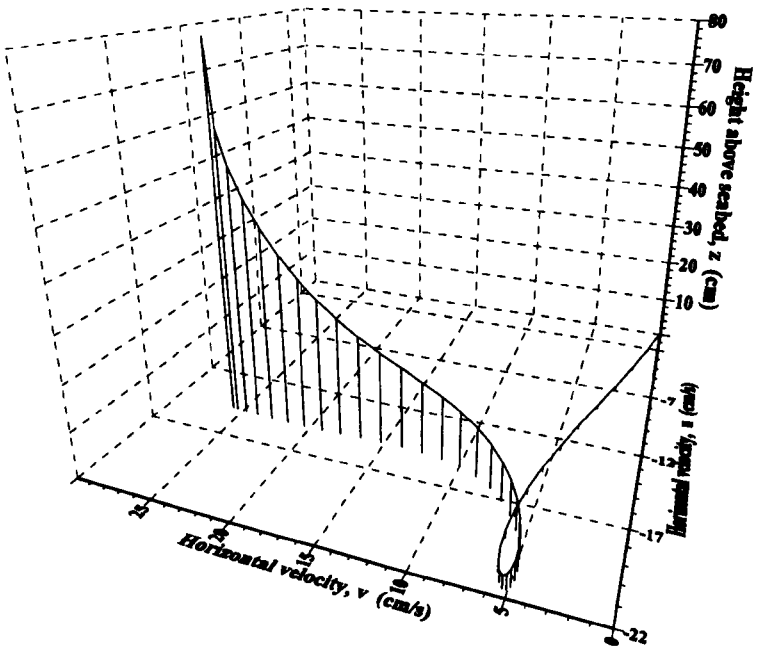

Figure 9.15c: Velocity profile as predicted by k-ε random wave boundary layer model (t ≈ 6.612 s).

Chapter 10
Moveable Bed Model

10.1 Moveable bed roughness

The seabed is generally never flat and is more likely than not to be covered by bedforms which vary in shape and size. These sediment structures can be variations due to bioturbation, ripples, sand waves, bars, or sandbanks. The large structures such as sandbanks, sand waves and bars can have a significant effect on the flow pattern, causing refraction, diffraction or wave breaking. The small scale features such as ripples can have a significant effect on the boundary layer structure and the associated near-bed turbulence.

It is these small scale features that are of interest in the present work and the effect that a changing boundary shape has on the bed boundary layer under regular and random waves.

In coastal shelf seas, wind generated waves are subject to the effects of the seabed. The main effects are due to bed friction, shoaling and wave refraction. An assumption that the flow field is inviscid throughout the depth accounts for the latter two effects. The bed friction is due to the no-slip condition at the seabed. Close to the bed a thin boundary layer is formed where energy dissipation can be significant.

The hydrodynamics of such flows have been discussed and investigated in the earlier chapters of this thesis. The models developed within have enabled these processes to be estimated with a certain amount of confidence. Using such models it is possible to relate the bed shear stress to the near-bed velocity through the use of a friction factor. For fully rough turbulent flows the friction factor is dependent on the relative roughness of the bed alone.

The relative bed roughness is defined as the ratio of the length scale of the near-bed wave orbital velocity to the length scale of the bottom roughness. This assumes that the bed

geometry can be represented by a single length scale. For a flat sediment bed the roughness is assumed to be a function of the grain diameter.

Iwagaki and Kakinuma (1963; 1967) investigated transformation of waves as they approached the shore at several sites off the Japanese coast. Using the measured field data they estimated the bed friction factor and found it to be larger than those that could be expected from a flat bed. Similar findings have been presented by Treloar and Abernethy (1978) for field measurements taken at Botany Bay, Australia. These increased friction factors are due to the presence of bedforms increasing the resistance to the wave motion.

By developing a model to attempt to reproduce the formation of such bedforms for a cohesionless sediment it is intended to try to provide a better description of the bed roughness primarily within the random boundary layer models.

10.2 Friction factor under oscillatory waves over a fixed horizontal bed

10.2.1 Introduction

Early experimental and theoretical work investigated the effect of oscillatory flow over flat beds as well as ripples and artificial roughnesses. Some of these studies included investigating the effect of energy dissipation caused by the bed, for example Bagnold (1946); Jonsson (1963); Carstens *et al.* (1969); Kamphuis (1975) and Lofquist (1981). A brief review of part of this work has been given in Chapter 3.

Over the last few decades the effect of wave height attenuation due to energy dissipation taking place at the seabed has become researched in more detail and to place the present work in context a brief overview will be given.

10.2.2: Friction factor formulae

Lamb (1932) provided an analytical solution to the equations governing laminar oscillatory flow. This has been presented elsewhere within this work (see Chapter 3 and Appendix D). Jonsson (1967) has shown that for laminar boundary layers, the friction factor, f_w, is only dependant on the amplitude Reynolds number such that:-

$$f_w = \frac{2}{\sqrt{Re}} \qquad (10.1)$$

where $Re = u_0 a / \nu$ and where the friction factor, f_w has been defined by the equation:-

$$f_w = 2\left(\frac{u_{*m}}{u_{0m}}\right)^2 \qquad (10.2)$$

and u_{*m} is the maximum shear velocity at the bed and u_{0m} is the maximum near-bed orbital wave motion, Figure 10.1.

Jonsson (1963; 1967) suggested using the integrated momentum equation to obtain an expression with which to evaluate the friction factor. Jonsson assumed a logarithmic velocity profile to extend to the free stream velocity. For rough turbulent flow Jonsson obtained the semi-empirical relationship:-

$$\frac{1}{4\sqrt{f_w}} + \log_{10}\frac{1}{4\sqrt{f_w}} = -0.08 + \log_{10}\frac{a}{k_s} \qquad \frac{a}{k_s} > 1.57 \qquad (10.3)$$

where a is the orbital wave amplitude and k_s is defined as previously and is the Nikuradse equivalent roughness.

Jonsson chose to ignore the phase differences between the maximum shear stress and maximum free steam velocity in deducing this expression.

Similar expressions for wave friction factor were derived by Kajiura (1968) for both smooth turbulent and rough turbulent flow. Kajiura used a drag coefficient, $\hat{C}$, which was equal to half that of Jonsson's friction factor, f_w. For rough turbulent flow Kajiura proposed the equation:-

$$\frac{1}{4.07\sqrt{f_w}} + \log_{10}\frac{1}{4\sqrt{f_w}} = -0.253 + \log_{10}\frac{a}{k_s} \qquad \textbf{(10.4)}$$

Swart (1974) proposed an approximation to Jonsson's expression (Eq. 10.3) that allowed f_w to be calculated directly and is given by the expression:

$$f_w = \exp\left[5.213\left(\frac{a}{k_s}\right)^{-0.194} - 5.977\right] \qquad \textbf{(10.5)}$$

Kamphuis (1975) suggested a slightly different empirical relationship to that of Jonsson (Eq. 10.3) based on the results of experiments carried out in an oscillating water tunnel. The expression was determined as a best fit through the data points and is given by the equation:

$$\frac{1}{4\sqrt{f_w}} + \log_{10}\frac{1}{4\sqrt{f_w}} = -0.35 + \frac{4}{3}\log_{10}\frac{a}{k_s} \qquad \frac{a}{k_s} > 1.57 \qquad \textbf{(10.6)}$$

For the range, $a/k_s \leq 100$, Kamphuis proposed a simple empirical expression for the friction factor.

$$f_w = 0.4\left(\frac{a}{k_s}\right)^{-0.75} \qquad \frac{a}{k_s} \leq 100 \qquad \textbf{(10.7)}$$

In the original paper the power term, 0.75, is missing a minus sign.

Myrhaug (1989) proposed empirical expressions for the friction factor for rough, smooth and transition from smooth to rough turbulent flow. The expressions were similar in form to that of Jonsson (1963; 1967) and Kamphuis (1975). Myrhaug, like Jonsson, disregarded the phase lead of the bed shear stress over the free stream velocity in deriving his expressions. For rough turbulent flow Myrhaug proposed the equation:-

$$\frac{1}{4.07\sqrt{f_w}} + \log_{10}\frac{1}{4\sqrt{f_w}} = 0.256 + \log_{10}\frac{a}{k_s} \qquad \textbf{(10.8)}$$

More recently, You *et al.* (1991) proposed a simplified expression for the wave friction factor based on an approximation of an implicit formula which they also developed. Their simplified formula is given as:-

$$f_w = 0.108\left(\frac{a}{k_s}\right)^{-0.343} \qquad \frac{a}{k_s} \geq 3.5 \qquad \textbf{(10.9)}$$

All these various expressions are plotted in Figure 10.2. Whilst Figure 10.2 shows considerable agreement amongst many of the empirical expressions developed for the wave

friction factor, the figure also shows significant variation. Alternately, it is possible to calculate the wave friction factor using a theoretical approach. The models developed and described within the present work allow the bed shear stress to be determined and hence the wave friction factor (see Figure 10.3).

It should be noted that Jonsson (1963; 1967) proposed that the wave friction factor be considered a constant when the relative roughness, a/k_s is less than unity. Jonsson based his derivation of Eq. (10.3) on the assumption that the physical scale of the bed roughness, k_s is much smaller than the thickness of the wave boundary layer. This is one of the criteria for horizontal uniformity in the boundary layer since any disturbances due to the individual bed roughnesses should be confined to a layer considerably thinner than that of the boundary layer itself.

Based on the experimental data of Bagnold (1946), Kajiura (1968) suggested that a constant value for the wave friction factor of 0.25 should be used for the following relative roughness:-

$$f_w = 0.25 \qquad \frac{a}{k_s} < 1.67 \qquad \textbf{(10.10)}$$

Jonsson (1976a; 1980) proposed that a constant value of 0.30 for the wave friction factor be used when:-

$$f_w = 0.30 \qquad \frac{a}{k_s} < 1.57 \qquad \textbf{(10.11)}$$

As Kajiura (1968), Jonsson based this value on the experimental work of Bagnold (1946).

Grant and Madsen (1982) also suggested that the wave friction factor be considered a constant when a/k_s is less than unity. However, recent measurements by Sleath (1985) over rippled sand beds have given values for the energy dissipation factor, f_e in excess of 0.5 and more recently, Simons *et al.* (1988) measured values of f_e much greater than 1.0.

The assumption that the friction factor remains constant at low values of relative roughness, a/k_s has generally been based on measurements such as those of Bagnold (1946). Kyriacou (1988) found that for 0.7 s waves the wave friction factor continued to increase with

decreasing values of a/k_s (see Figure 10.4). Sleath (1984) suggested that as the relative roughness approaches zero, the wave friction factor varies as:-

$$f_w \propto \left(\frac{a}{k_s}\right)^{-1} \qquad \textbf{(10.12)}$$

Sleath reasoned that Bagnold's experiments showed the friction factor to be constant at small values of a/k_s because it was the energy dissipation that was measured and not the friction force. Since the pressure force dominates the bed friction at low values of a/k_s and does not contribute to the energy dissipation, Sleath argued that such a deviation is not surprising from the trend shown in Figure 10.4.

10.2.3: Energy dissipation factor

The energy dissipation factor, f_e was defined by Jonsson (1967) through the equation:

$$D_E = \frac{2}{3\pi}\rho f_e (a\omega)^3 \qquad \textbf{(10.13)}$$

and

$$D_E = \overline{u_\infty \tau_0} \qquad \textbf{(10.14)}$$

However, different researchers have all used different definitions and terminology and care should be taken in relating them to the definition given above (e.g. see Nielsen 1992).

The wave friction factor and the energy dissipation factor, f_e are related differently depending on which definition is used. However, since experimentally, there is large scatter in the measurements made of both factors over natural sand beds, it is generally assumed that f_w and f_e are equal.

There is quite a large variation in the range of measured f_e values. In the laboratory the values found by Bagnold (1946), Carstens *et al.* (1969), Sleath (1985), Lofquist (1986) and Kyriacou (1988) vary between 0.03 and 15.8 whilst field measurements by Iwagaki and Kakinuma (1963; 1967) and Treloar and Abernethy (1977) have yielded values in the range 0.02 to 2.32.

Finally, the above list of expressions for wave friction factor is not exhaustive. Other expressions not shown are those of Grant and Madsen (1979), who derived an equation based on a linear eddy viscosity model and Nielsen (1992), who proposed an adjustment to Swart's formula (Eq. 10.5).

10.3 Energy dissipation over fixed ripples

Bagnold (1946) and Sleath (1985) measured energy dissipation over beds consisting of fixed artificial ripples. Bagnold oscillated a tray covered with artificial ripples in a tank of still water. Sleath (1985) also oscillated a tray covered in artificial roughness elements (fixed ripples and fins, see Sleath 1985 for further details) in a tank of still water.

Sleath's ripple profiles were sinusoidal in shape with a wavelength of 7.3 cm and ripple height (crest-to-trough) of 1.7 cm. In contrast, Bagnold used a series of circular arcs with a sharp cusp at the crest. Sleath chose a different ripple profile to that of Bagnold because he suggested that the sharp crests of Bagnold's ripples caused vortex formation even at low Reynolds numbers. Sleath wished to investigate a profile that would produce vortices at high Reynolds numbers but which didn't force vortex formation at lower values of Reynolds number.

The purpose of using the data of Sleath and Bagnold in the present work is that this data can be used to attempt to establish a relationship between ripple geometry and the bed roughness due to the bedform.

Various relationships have been suggested for the equivalent roughness due to bedforms. Generally, it has been assumed that the roughness due to the bedforms takes the form:-

$$k_s \propto \Delta \qquad \textbf{(10.15)}$$

where k_s is the Nikuradse equivalent roughness and Δ is the ripple height.

Kajiura (1968) suggested that the Nikuradse equivalent roughness be given by the equation:-

$$k_s = 4\Delta \qquad \textbf{(10.16)}$$

Assuming that the energy dissipation factor is equal to the wave friction factor on the basis that the experimental scatter of one or the other term is significantly large, then it is possible to use an expression for wave friction factor and calculate a corresponding roughness value.

Figure 10.5 shows a plot of the ratio of equivalent roughness to the ripple height as a function of the energy dissipation factor. The roughness value was calculated using the wave friction factor expression of Swart (1974), Eq. (10.5). 80% of the points lie between 1 and 4 ripple heights. Using the wave friction factor expression of Jonsson (1963) gives just over 50% of the points falling between 1 and 3 ripple heights with no points beyond 3 ripple heights. Clearly, how the roughness is determined, that is, which expression is used, will affect what constant of proportionality is chosen.

Alternately, Grant and Madsen (1982) suggested that the equivalent roughness due to bedforms be represented by both their height, Δ, and wavelength, λ, and proposed the relationship:-

$$k_s \propto \frac{\Delta^2}{\lambda} \qquad \textbf{(10.17)}$$

Figure 10.6 shows a plot of relative ripple roughness as a function of energy dissipation factor. As previously, Swart's wave friction factor expression was used to calculate the relative roughness. The data shows a range of values for the constant of proportionality in Eq. (10.17).

In both Figures 10.5 and 10.6 a greater amount of scatter is observed with the data of Sleath (1985). As mentioned earlier in Section 10.3, Sleath's ripples were sinusoidal and enabled him to investigate a profile that would produce vortices at high Reynolds numbers but which didn't force vortex formation at lower values of Reynolds number. Sleath found that the low values of energy dissipation factor (and hence, of k_s/Δ) occurred during the transitional stage from laminar to turbulent flow, when vortex formation was just starting. Sleath (1985) argued that this transitional stage was less apparent in the data of Bagnold because of his sharp crested ripples causing flow separation even at low velocities.

Equilibrium ripples formed under monochromatic waves are sharp crested with slopes of approximately 30°. They therefore resemble more the profiles of Bagnold than of Sleath, though they cannot possess the sharp edge of Bagnold's artificial ripples.

The high-Reynolds number k-ε model was run for the laboratory conditions of Bagnold (1946) and Sleath (1985) and the energy dissipation factor and wave friction factor calculated for each fixed ripple test. The bedform drag was assumed as 4Δ in the model. The results are shown in Figures 10.7 and 10.8. The results are disappointing, with the results of Sleath lying above and below the line x = y (i.e. calculated energy dissipation factor = measured energy dissipation factor) and Bagnold's results lying considerably below the x = y line.

The plot of calculated friction factor against measured energy dissipation factor (Figure 10.8) indicates the relatively small difference between friction factor and energy dissipation factor (compare with Figure 10.7).

The reason for the results of Sleath (1985) falling both above and below the x = y line is that the model over predicts the energy dissipation factors for those measured values calculated during the transitional stage from laminar to turbulent flow. This should be expected since the flow conditions are outside the valid range of the high-Reynolds number k-ε model. For such flow conditions a low-Reynolds number k-ε model or two-layer k-ε model should be applied. However, the reason why all the results of Bagnold and some of the results of Sleath are underpredicted by the k-ε model is less clear. This point will be returned to later in this chapter.

10.4 Energy dissipation over a moveable bed

The fixed bed tests of Bagnold (1946) and Sleath (1985) were used in an attempt to assess the most suitable expression for the form drag of ripples. These tests used a smooth surface for the ripples unlike real sand ripples which have a rough surface. The advantage of the fixed bed tests is that the specific gravity of the sand, s, the grain diameter, d_{50}, and acceleration due to gravity, g, are not present, reducing the problem to just the form drag.

The simultaneous measurement of energy dissipation over moveable sand beds and ripple geometry has only been undertaken by a limited number of researchers. The earliest experiments were conducted by Carstens *et al.* (1969). Carstens *et al.* performed a series of tests in an oscillating water tunnel measuring ripple geometry. In addition, in some of these tests the energy dissipation was also calculated.

The oscillating water tunnel consisted of a test section approximately 3 m in length, 30 cm high and 1.22 m wide. In the central section the floor was depressed to form a container for the sediment. The dimensions of this container were 1.82 m long 1.22 m wide and 10 cm deep (See Carstens *et al.* 1969 for further details).

Carstens *et al.* (1969) used three different sands, the properties of which are given in Table 10.1.

Sand	**Mean grain diameter, d_{50} (mm)**	**Specific gravity, s**
Ottawa (Banding)	0.190	2.66
Glass beads	0.297	2.47
Ottawa (Flint shot)	0.585	2.62

Table 10.1: Properties of the material used in the experiments of Carstens *et al.* (1969).

Carstens *et al.* (1969) performed a series of tests using the three sizes of bed material in what were essentially duplicate tests. For all the experiments the period of oscillation was held relatively constant at approximately 3.6 s, whilst the orbital amplitude of the water motion was varied. A flat bed was an initial condition in all the runs. Carstens *et al.* split their study into four main topics: incipient motion, evolution of a rippled bed, geometry of equilibrium ripples and energy dissipation over rippled beds.

Carstens *et al.* measured the energy dissipation in the oscillating water tunnel by monitoring the air pressure and the water level in the risers of the tunnel. They first calculated the energy dissipation over a smooth bed, by covering over the sediment test section with an aluminium sheet (see Carstens *et al.* 1969 for details). From the series of smooth bed experiments they

fitted a calibration curve through the data giving energy dissipation and amplitude. The calibration curve was then used to provide energy dissipation values to correspond to those values obtained in the rippled bed experiments.

Wikramanayake and Madsen (1991) simplify the method used by Carstens *et al.* for calculating the energy dissipation values. For the smooth bed experiments Wikramanayake and Madsen denote the total energy dissipation in the tunnel by E_{ds}. The total energy dissipation consists of the dissipation due to the curvature of the tunnel and tunnel walls, E_{dt}, and the dissipation due to the smooth bed itself, E_{dsb}. Thus,

$$E_{ds}(a) = E_{dt}(a) + E_{dsb}(a) \qquad \textbf{(10.18)}$$

where a is the near-bed orbital amplitude.

Similarly the total dissipation for a rippled bed, E_{dr}, is given by the equation:-

$$E_{dr}(a) = E_{dt}(a) + E_{drb}(a) \qquad \textbf{(10.19)}$$

where E_{drb} is the dissipation due to the rippled bed.

Subtracting Eq. (10.19) from Eq. (10.18) enables the dissipation due to the rippled bed to be calculated:-

$$E_{drb}(a) = E_{dr}(a) - E_{ds}(a) + E_{dsb}(a) \qquad \textbf{(10.20)}$$

Taking the quantities on the right-hand-side of Eq. (10.20), the first term, E_{dr}, is measured during the rippled bed test, whilst the second term, E_{ds}, is determined from the calibration curve found from the smooth bed tests. The final term was neglected by Carstens *et al.* as well as by other researchers (Nielsen 1983; Sleath 1985; Vongvisessomjai 1987).

Wikramanayake and Madsen (1991) argued that this term could be calculated by using the friction factor for a smooth bed (Figure 10.1) and ignoring this term results in differences of the order of 10%. Wikramanayake and Madsen use this approach to modify the measured

values of Carstens *et al.* (1969) and it is these modified values that have been used in the present work.

The other experimental data sets where simultaneous measurement of energy dissipation over moveable sand beds and ripple geometry have been undertaken are those of Lofquist (1986), Rosengaus (1987) and Mathisen (1989).

Lofquist (1986) measured the energy dissipation in a wave tunnel by means of pressure taps at each end of the tunnel. Using the records obtained from the taps, Lofquist calculated the instantaneous shear stress over the test section. Partitioning the tunnel longitudinally enabled Lofquist to have a smooth bed and sand bed either side of the partition, respectively. This allowed the sidewall effects to be taken into account.

In order that the pressure measurements could be taken, Lofquist found it necessary to limit the number of ripple crests in the tunnel by fixing a rigid sand crest at each end of the tunnel. This constraint affected the ripple wavelength and to avoid distorting the results, Lofquist confined his flow conditions to those that gave ripple lengths identical to those observed with no barriers present. Lofquist performed a few experiments with ripple profiles different to those observed in an unrestrained test section to investigate the effect of distortion on the energy dissipation.

Lofquist also investigated energy dissipation over growing ripples, recording ripple geometry and energy dissipation at various stages of growth. Lofquist (1986) found that to increase the ripple height by 1 cm required 30 to 100 wave periods. These results have not been used in the present work.

Wikramanayake and Madsen (1991) describe, briefly, experiments performed by Rosengaus (1987) and Mathisen (1989) in a wave flume to investigate energy dissipation, measured by recording the change in wave height along the flume. Sidewall effects as well as effects of non-linearity were taken into account by conducting a series of smooth flat bed tests. To this author's knowledge, the experiments of Rosengaus and Mathisen are presently the only such tests where the energy dissipation and bed geometry have been measured simultaneously

under irregular waves. Wikramanayake and Madsen consider the two data sets as one since both researchers used the same experimental equipment.

Figures 10.9 and 10.10 show the calculated energy dissipation factor and wave friction factor against the measured energy dissipation factor, respectively, for the data of Carstens *et al.* (1969), Lofquist (1986), Rosengaus (1987) and Mathisen (1989). As is clearly evident from the figures, the model results underpredict the measured energy dissipation factors by a considerable amount, over 80% in the worst case. A similar trend was observed when the model results were compared with the fixed ripple tests of Bagnold (1946) and Sleath (1985).

It is necessary to ensure that, for the a flat bed, the turbulence models are performing correctly. Friction factors for both the k and k-ε models are plotted in Figure 10.3 alongside the results of Jonsson and Carlsen (1976), Sleath (1987) and Dick and Sleath (1991). These confirm that the models are producing reasonable values. The results of Dick and Sleath (1991) were included since they represent a flat bed but under sheet flow conditions.

Figure 10.11 shows a plot of calculated wave friction factor against measured wave friction factor for the data of Dick and Sleath. Whilst the results show the model to overpredict the wave friction factor values in most cases, a linear fit through the points indicates that the trend is predicted, though not the absolute values. Dick and Sleath (1991) calculated an equivalent bed roughness on the basis of fitting logarithmic curves to their velocity measurements. Their experimentally determined values of friction factor all lie below the fixed bed curve of Jonsson (1963), see Figure 10.3. Dick and Sleath stated that the bed roughness, and hence, the wave friction factor are increased when the bed is mobile. This would seem to create a paradox, which they explain by reasoning that, although the wave friction factor is increased, the value of the ratio of near-bed orbital amplitude to equivalent roughness decreases at a greater rate. By compensating for the moving sediment in the numerical model by representing the equivalent roughness in terms of an equivalent roughness due to the grain as well as due to the moving sediment it is expected the model and measured results should show reasonable correlation.

Therefore, from the above it is argued that for flat beds, the numerical models can be used with some confidence. It is now necessary to return to the problem of the poor model fit against the measured energy dissipation factors over ripples. Based on the above and on the fixed bed experiments of Sleath (1985) it is suggested that the important factor unaccounted for in the k-ε model is the production of vortices over the ripple. For those fixed bed tests of Sleath (1985) where the flow was in transitional stage from laminar to turbulent the model either underpredicted or predicted the measured values. The reason for underprediction has already been discussed in Section 10.3. These experimental runs corresponded to negligible or small vortex production. It is, therefore, hypothesized that to correctly predict the flow over ripples using a 1DV turbulence model (i.e. a point model through the vertical) such as those described and used in the present work, it is necessary to account for vortex action. Use of a modified equivalent roughness, such as 4 x the ripple height, is not sufficient to account for the effect of vortex shedding.

In previous work to investigate sediment transport in steady flows using a two-equation k-ε model, Roisin (1985) showed that it is necessary to modify the dissipation term in the turbulent kinetic energy transport equation. Roisin, following Hino (1963), argued that since a part of the fluid is occupied by solid particles, the effective space available for energy dissipation is reduced. Using the same approach, it is argued that because the vortices, caused by flow separation off the ripples, occupy a proportion of the water column, so they too reduce the effective space available for energy dissipation. Figure 10.12 shows the effect of vortex action over equilibrium ripples. The description and figure are based on the work of Nielsen (1979). Clearly, for a moveable bed, the vortices will contain sediment, but in the fixed ripple experiments of Bagnold (1946) and Sleath (1985) the vortices will contain trapped fluid and no sediment. However, in both cases, the vortices reduce the effective space available for energy dissipation. Therefore, it is proposed that the dissipation term in the k transport equation be modified and expressed as:-

$$(1 - C_{vor})\varepsilon \qquad \textbf{(10.21)}$$

where C_{vor} represents a coefficient for the vortex generation.

It is necessary to derive an expression for C_{vor} so that values can be determined for any possible experimental condition. Intuitively, the coefficient C_{vor} should increase with ripple growth and decrease as the ripple is washed out under increasing flow. It is expected that C_{vor} assumes something of a parabolic shape, though not necessarily that defined by a true parabola.

The data of Carstens *et al.* (1969), Lofquist (1986), Rosengaus (1987) and Mathisen (1989) have been used to investigate the possible form of C_{vor}. The data of Carstens *et al.*, Rosengaus and Mathisen was mostly measured for constant wave periods. Figures 10.14a and 10.14b show the variation of C_{vor} with Shields parameter, θ for Carstens *et al.*, Rosengaus and Mathisen. The figures indicate that the data follows a parabolic shape. However, the figures also show that the parameter C_{vor} varies with grain size. To assess how the data responds to changes in period, some of the data of Lofquist (1986) was selected for analysis. Lofquist performed measurements for a range of periods. Because of the limited number of tests for the same period it has been necessary to assume mean periods for sets of data for periods falling within a given range. The results are shown in Figure 10.14c. Again, the results suggest that C_{vor} follows a parabolic form as well as showing that C_{vor} varies with period.

Generally, the results of the analysis suggest that C_{vor} increases with grain size, as can be observed in Figures 10.14a and 10.14b. Further, Figure 10.14c suggests that the larger the wave period the greater the value of the coefficient C_{vor}. The results show that the spread of the parabolic curve is greater with increasing grain size, corresponding to the increasing energy required to move larger sediment sizes. The effect of sediment mixtures on the value of C_{vor} is unknown.

Attempts made to try and collapse the results down to a single curve have failed. From this analysis C_{vor} was found to be insensitive to the near-bed orbital amplitude. To obtain a better correlation, the Shields parameter, θ, was divided by the critical Shields parameter, θ_c. The critical Shields parameter was determined by the expression:-

$$\theta_c = \frac{0.0666D_* + 0.375}{2.22D_* + 0.938} \qquad \textbf{(10.22)}$$

where D_* is a dimensionless grain size given by the equation:-

$$D_* = \left[\frac{(s-1)g}{\nu_L^2}\right]^{1/3} d_{50} \qquad \textbf{(10.23)}$$

The above expression is based on a comparison with measured data (see Soulsby 1994).

Dividing through by θ_c sets all the data to a common start point, 1. In addition, since C_{vor} must be 0 at this point, since this corresponds to the initiation of sediment motion, and hence a flat bed, it has been assumed that all data fits the point (1,0) in the x-y plane. Results are shown in Figure 10.14d for the data of Carstens *et al.* (1969), Rosengaus (1987) and Mathisen (1989). The figure clearly suggests that a parabolic relationship for C_{vor} exists at least for the initial growth of the ripple. The larger grain sizes suggest perhaps a more linear decay exists as the ripple is washed out. Lack of data and a failure to reduce the available data to a single curve has prevented any definite relationship for C_{vor} being proposed. This has had significant implications on the work described later in this chapter

10.5 Moveable bed models

Grant and Madsen (1982) proposed a moveable bed model based on the laboratory data of Carstens *et al.* (1969) for monochromatic waves. The wave-induced roughness was represented as a combination of form drag around the individual bedforms and a contribution due to the near-bed sediment transport.

$$k_s = 160(s + C_m)d_{50}\left(\sqrt{\theta} - 0.7\sqrt{\theta_c}\right)^2 + 28\frac{\Delta^2}{\lambda} \qquad \textbf{(10.24)}$$

where θ is the Shields parameter; θ_c is the critical Shields parameter for the initiation of sediment motion; and C_m is an added mass coefficient. Grant and Madsen assumed s = 2.65 and $C_m = 0.5$ reducing Eq. (10.24) to:-

$$k_s = 504 d_{50}\left(\sqrt{\theta} - 0.7\sqrt{\theta_c}\right)^2 + 28\frac{\Delta^2}{\lambda} \qquad \textbf{(10.25)}$$

Field studies have shown that the early model of Grant and Madsen (1982) is inappropriate for predicting bed roughnesses under irregular waves since the model uses empirical relationships based on monochromatic waves to relate ripple roughness to ripple geometry. The studies have shown that irregular waves result in shorter and less steep ripples than those formed by monochromatic waves (Dingler and Inman 1976; Nielsen 1981; Madsen *et al.* 1991; Ribberink and Al-Salem 1994).

Vongvisessomjai *et al.* (1987) proposed a theoretical model to represent the profile of a ripple bed under monochromatic waves. The model was based on earlier work of Kennedy and Falcon (1965) where the profile of a rippled bed was characterized by a moving sinusoid of varying height $\Delta(t)$ but constant ripple length. Vongvisessomjai *et al.* modified this approach by allowing the wavelength of the ripple to vary with time. Vongvisessomjai *et al.* suggested that the growth rates of ripple height, $\Delta(t)$ and ripple wavelength, $\lambda(t)$ could be represented by the equations:-

$$\Delta(t) = \Delta_{max}\left\{1 - \exp\left[-B^*\left(\frac{t}{T}\right)\right]\right\} \qquad \textbf{(10.26)}$$

and

$$\lambda(t) = \lambda_{max}\left\{1 - \exp\left[-B^*\left(\frac{t}{T}\right)\right]\right\} \qquad \textbf{(10.27)}$$

where Δ_{max} is the maximum ripple height; λ_{max} is the maximum wavelength of the ripple; B^* is the dimensionless growth of the ripple and T is the wave period.

Based on experimental results used to determine the growth rate of ripples, Vongvisessomjai *et al.* (1987) suggested that B^* could be represented by the expression:-

$$B^* = 1.77 \times 10^{-6} a_*^{1.68} \psi^{-0.394} \qquad \textbf{(10.28)}$$

where a_* is the relative bed smoothness and is given by:-

$$a_* = \frac{a}{d_{50}} \tag{10.29}$$

a is the near-bed orbital amplitude such that $a = u_\infty/\omega$; u_∞ is the near-bed velocity amplitude; ω is the angular frequency; and d_{50} is the median grain diameter.

ψ is the mobility number and is defined as:-

$$\psi = \frac{(a\omega)^2}{(s-1)gd_{50}} \tag{10.30}$$

where s is the specific gravity of the sediment, given by $s = \rho_s/\rho$, where ρ_s is the density of the sediment and ρ is the fluid density.

Both the above approaches are predictive relationships for ripple geometry under monochromatic waves. Madsen *et al.* (1989a) proposed a moveable bed model for spectral waves based on the linearized equation of motion and a simple time-invariant eddy viscosity relationship. They obtained model closure by allowing the solution to reduce, in the limit, to a simple harmonic wave.

Madsen *et al.* (1988a) let the wave motion be described by its directional spectrum which leads to the solution being given by the equation:-

$$u_{nm} = \left(1 - \frac{\ker 2\sqrt{\varsigma_n} + i\,\mathrm{kei}\,2\sqrt{\varsigma_n}}{\ker 2\sqrt{\varsigma_{n0}} + i\,\mathrm{kei}\,2\sqrt{\varsigma_{n0}}}\right) u_{bnm} e^{i\omega_n t} \tag{10.31}$$

where ker and kei denote the zeroth order Kelvin functions; n and m represent summation over frequency and direction; u_b is the near-bed velocity and ς_n is defined as:-

$$\varsigma_n = \frac{z\omega_n}{\kappa u_{*r}} \tag{10.32}$$

where u_{*r} is the representative shear velocity; κ is the von Karman constant; ω_n represents the angular frequencies. ς_{n0} denotes the value of ς_n at $z = z_0 = k_s/30$.

The near-bed velocity u_b is related to the near-bed velocity spectrum $S_{ub}(\omega,\theta)$ by the equation:-

$$u_{bnm} = \sqrt{2S_{ub}(\omega_n,\theta_m)d\theta d\omega} \qquad \textbf{(10.33)}$$

Madsen *et al.* (1988a) simplify the solution by the introduction of representative values for the wave height, H_{rms}, angular frequency, ω_r and near-bed orbital velocity, u_{br}. Madsen *et al.* eventually obtain a solution for the spectral wave energy dissipation in the form:-

$$D_E(\omega,\theta) = \frac{1}{2}\rho f_{wr} u_{br} S_{ub}(\omega,\theta) \qquad \textbf{(10.34)}$$

where f_{wr} is the representative wave friction factor and can be determined using any of the empirical friction factor relationships.

Madsen *et al.* (1989b; 1991) present the results from a series of experiments conducted in a wave flume. The results given in Madsen *et al.* (1989b) are limited by the range of the experiments. Only a single grain size was used (0.2 mm diameter quartz sand) and the wave settings in the flume were confined to conditions just above those that would cause initiation of sediment movement. In Madsen *et al.* (1991) it was attempted to improve on the previous tests by performing experiments with an additional grain size of 0.12 mm diameter and for a wider range of wave conditions.

Madsen *et al.* (1991) concluded that the spectral wave friction factor can be represented by the equation:-

$$f_{wr} = 0.29\left(\frac{\theta'_{mr}}{\theta_c}\right) \quad \text{for} \quad \frac{\theta'_{mr}}{\theta_c} > 1.2 \qquad \textbf{(10.35)}$$

where θ_c is the critical Shields parameter for initiation of sediment motion and θ'_{mr} is the Shields parameter obtained with the maximum bed shear stress, τ'_{bm}, predicted for the representative monochromatic wave and is defined as:-

$$\theta'_{mr} = \frac{\tau'_{bm}}{(s-1)\rho g d_{50}} \qquad \textbf{(10.36)}$$

Madsen *et al.* (1991) suggest that Eq. (10.36) is accurate to within 20%.

The moveable bed roughness for spectral waves is defined by Madsen *et al.* (1991) by the relationship:-

$$\frac{k_s}{A_{br}} = 1.5\left(\frac{\theta'_{mr}}{\theta_c}\right)^{-2.5} \qquad \textbf{(10.37)}$$

where A_{br} is the representative near-bed orbital amplitude. Madsen *et al.* suggest that this relationship is accurate to within 30%.

Madsen *et al.*'s (1988a) approach for determining moveable bed friction factors for spectral waves is quite laborious and the reader is referred to the original paper for further details. Other approaches have been presented by Tolman (1994) and Kaczmarek *et al.* (1995) (see Appendix G). Myrhaug (1995) presented a method to calculate the bed friction under random waves. The approach is similar to Madsen *et al.* (1988a). Myrhaug assumes that for rough turbulent flow the maximum bed shear stress follows the Weibull distribution.

Tolman (1994) developed a moveable bed model based on the hydrodynamic model of Madsen *et al.* (1989) and a modified version of Grant and Madsen's (1982) moveable bed model. Tolman makes a distinction between swell and wind seas in his analysis.

Kaczmarek *et al.* (1995) presented an approach based on the work of Kaczmarek and Ostrowski (1995) and O'Connor *et al.* (1993). Details of the approach are given in Appendix G.

Kaczmarek (1995), Madsen (1995) and You (1996) have investigated the effect of combined waves and currents on moveable bed roughnesses under spectral waves. In the present work currents have been neglected to simplify the analysis.

10.6: The proposed model

In the present approach the method of Vongvisessomjai *et al.* (1987) has been adapted, following a suggestion by Professor B.A. O'Connor, to enable the prediction of field generated ripples, that is ripple geometry under irregular waves.

The proposed model is based on Eqs.(10.26) and (10.27). Replacing the period, T, by the zero-upcrossing period, T_z, leads to the modified equations:-

$$\Delta(t) = \Delta_{max\,n}\left\{1 - \exp\left[-B_n^*\left(\frac{t}{T_{zn}}\right)\right]\right\} \qquad \textbf{(10.38)}$$

and

$$\lambda(t) = \lambda_{max\,n}\left\{1 - \exp\left[-B_n^*\left(\frac{t}{T_{zn}}\right)\right]\right\} \qquad \textbf{(10.39)}$$

where B_n^* is defined as:-

$$B_n^* = 1.77 \times 10^{-6} a_{*n}^{1.68} \psi_n^{-0.394} \qquad \textbf{(10.40a)}$$

and a_{*n} is the relative bed smoothness and is given by:-

$$a_{*n} = \frac{a_n}{d_{50}} \qquad \textbf{(10.40b)}$$

a_n is the near-bed orbital amplitude such that $a_n = u_{\infty n}/\omega_n$; u_∞ is the near-bed velocity amplitude; ω_n is the angular frequency.

ψ_n is the mobility number and is defined as:-

$$\psi_n = \frac{(a_n \omega_n)^2}{(s-1)g d_{50}} \qquad \textbf{(10.40c)}$$

All other terms are defined as previously.

The model allows T_z to vary, so for a given surface wave height time-series, n zero-upcrossing periods can be calculated along with the corresponding wave heights, H_n. n denotes the number of zero-upcrossing periods in the given wave height record. Knowing T_{zn} and H_n allows the maximum near-bed orbital amplitude, a_n, and maximum near-bed orbital velocity, $u_{\infty n}$, to be calculated. From this, it is possible to calculate n values for the maximum possible ripple geometry, $\Delta_{max\,n}$ and $\lambda_{max\,n}$. Using these values and Eqs. (10.38) and (10.39) enables a time-series for the ripple geometry to be generated. For each nth value, the value of t within the exponential term is reset to zero, whilst leaving the actual time-series to run continuously. A ripple will continue to grow in height until the value of the present

$\Delta_{max\,n}$ is reached. If for the n+1 value, the value of $\Delta_{max(n+1)}$ is smaller than $\Delta_{max\,n}$ the ripple height will start to decay. A similar process operates for the ripple length.

The maximum ripple geometry has been assumed to be given by the expressions of Nielsen (1981: 1992). For monochromatic wave conditions, the maximum ripple height and length may be determined using the equations:-

$$\frac{\Delta_{max}}{a} = \begin{cases} 0.275 - 0.022\psi^{0.5} & \text{for } \psi < 156 \\ 0 & \text{for } \psi > 156 \end{cases} \qquad \textbf{(10.41)}$$

and

$$\frac{\lambda_{max}}{a} = 2.2 - 0.345\psi^{0.34} \quad \text{for } 2 < \psi < 230 \qquad \textbf{(10.42)}$$

For irregular waves Nielsen suggests the formulae:-

$$\frac{\Delta_{max}}{a} = 21\psi^{-1.85} \quad \text{for } \psi > 10 \qquad \textbf{(10.43)}$$

and

$$\frac{\lambda_{max}}{a} = \exp\left(\frac{693 - 0.37\ln^8\psi}{1000 + 0.75\ln^7\psi}\right) \qquad \textbf{(10.44)}$$

Figures 10.15, 10.16 and 10.17 show the results of the monochromatic moveable bed model compared against equilibrium ripple data from the experiments of Kennedy and Falcon (1965), Carstens *et al.* (1969), Mogridge and Kamphuis (1973), Lofquist (1978), Nielsen (1979), Du Toit (1980), Lambie (1984), Shibayama (1984), Rosengaus (1987), Mathisen (1989) and Ribberink and Al-Salem (1994). Figure 10.15 shows a comparison of calculated ripple height against measured ripple height, whilst Figure 10.16 shows a comparison of calculated ripple length to measured ripple length. Figure 10.15 shows more scatter than for the ripple length, Figure 10.16. This is to be expected since there is potentially greater error in the measured ripple height since the scale is much smaller than the ripple length, which is typically 5 to 10 times larger than the height.

Figure 10.17 shows a comparison of calculated ripple steepness to the measured values. Figures 10.15 to 10.17 show good comparison with the measured data.

Figure 10.18 shows a typical result of the moveable bed model for monochromatic waves. Figure 10.18a shows the development of the ripple height with time, whilst Figure 10.18b shows the ripple length growth with time. Since the wave conditions are constant the ripple geometry develops until equilibrium is achieved. In the field, the wave conditions are continually changing and it is expected that the bedforms reflect this.

Figures 10.19 to 10.21 show a typical result from the moveable bed model for random waves. The moveable bed model has been run using a JONSWAP spectrum for the parameters shown in the figures. Figures 10.19 and 10.20 show the development of ripple height and length with time. To properly assess the performance of the model requires time-series data of both the surface wave conditions as well as the corresponding bedform geometry. Such data is currently not available. Figure 10.21 shows the variation of equivalent roughness with time based on a bedform drag of 4Δ. Figures 10.19 and 10.20 show the model adjusting the bedform geometry with time, allowing the ripples to grow and decay. The rate of growth of the bedforms is governed by the parameter B^*. The constant used in this relationship is based on experiments performed under monochromatic waves. To test the validity of this parameter is not possible until more detailed experimental data for ripple formation under random waves is available. However, it would seem unlikely that such a constant should be universally valid.

Figure 10.22 shows the development of the ripple height with time together with the corresponding surface wave conditions. The figure suggests that a time lag exists between the surface waves and the response of the bed, though to what extent is not totally clear. The growth and decay of the ripples in response to the waves varies with the size of the waves.

The next stage of testing involved inputting the varying roughnesses into the random boundary layer model and allowing the hydrodynamic model to run for the given time-series. Results of the maximum bed shear stress and hence friction factor were then to be compared with the approach of Madsen *et al.* (1998a). Such an analysis is not yet possible until a satisfactory method for calculating C_{vor} can be found. To attempt to do so at this stage would render any comparison meaningless, since the under prediction of the energy dissipation over

ripples by the model leads to the under prediction in the bed shear stress and hence the friction factor.

10.7 Conclusions

The presence of bedforms has been shown to lead to an increase in the value of the wave friction factor (Iwagaki and Kakinuma 1963; 1967; Treloar and Abernethy 1978). The present chapter has suggested a new approach to predict the moveable bed roughness for such conditions and presented results from the proposed model.

The assumption that the wave friction factor is constant at small values of a/k_s is questionable. Results from the experimental work of Kyriacou (1988) as well as theoretical reasoning of Sleath (1984) have been used to challenge this assumption.

The fixed ripple tests of Bagnold (1946) and Sleath (1985) have been used in an attempt to establish a relationship between ripple geometry and the form drag of the ripple. Based on the relationship given by Eq. (10.15):-

$$k_s \propto \Delta \qquad \textbf{(10.15)}$$

results suggest a constant of proportionality of between 1 and 4. Alternatively, representing the equivalent roughness in terms of the length and height of the ripple, Eq. (10.17):-

$$k_s \propto \frac{\Delta^2}{\lambda} \qquad \textbf{(10.17)}$$

the constant of proportionality is between about 10 and 20.

Comparison of results from the hydrodynamic turbulence model with measured values for the energy dissipation over both fixed and moveable bed ripples show the model to significantly underpredict the energy dissipation. The assumption that allowing for the form drag using approaches such as those given by Eqs. (10.15) and (10.17) has been shown to be incorrect. It has been hypothesized that the underprediction of the energy dissipation by the 1DV turbulence model is due to a failure to compensate for the effect of vortex shedding off the

ripples. In an attempt to correct for this failing, it has been proposed that a correction be applied to the dissipation term in the turbulent kinetic energy transport equation leading to:-

$$(1 - C_{vor})\varepsilon \qquad (10.21)$$

where C_{vor} represents a coefficient for the vortex generation. It is further suggested that C_{vor} follows a parabolic shape, increasing in value as the ripple develops and then decaying as the ripple is washed out. Analysis of the data of Carstens *et al.* (1969), Lofquist (1986), Rosengaus (1987) and Mathisen (1989) confirms this trend. Because of a lack of field and laboratory data recording the development and decay of ripples, it has not yet been possible to develop an equation for C_{vor} which is valid for all cases. C_{vor} was found to increase with increasing grain diameter and wave period.

Results from the moveable bed model presented within appear promising. It has not been possible to confirm whether the rate of growth of the ripples as predicted by the model is correct due to a lack of appropriate experimental data for bedforms developed under random waves. The moveable bed model for random waves uses a novel approach, enabling the ripple geometry to be determined as a continual time-series. Such a method allows the bed roughness to be prescribed as a time-series and thus used in a modified random wave boundary layer model. This permits the boundary layer model to vary its roughness condition and enable investigation of boundary layers over moveable beds.

The present work has been limited by a lack of adequate field and laboratory data. It has been shown that it is possible to develop a model for a moveable bed under random waves that can describe the variation in ripple geometry with time.

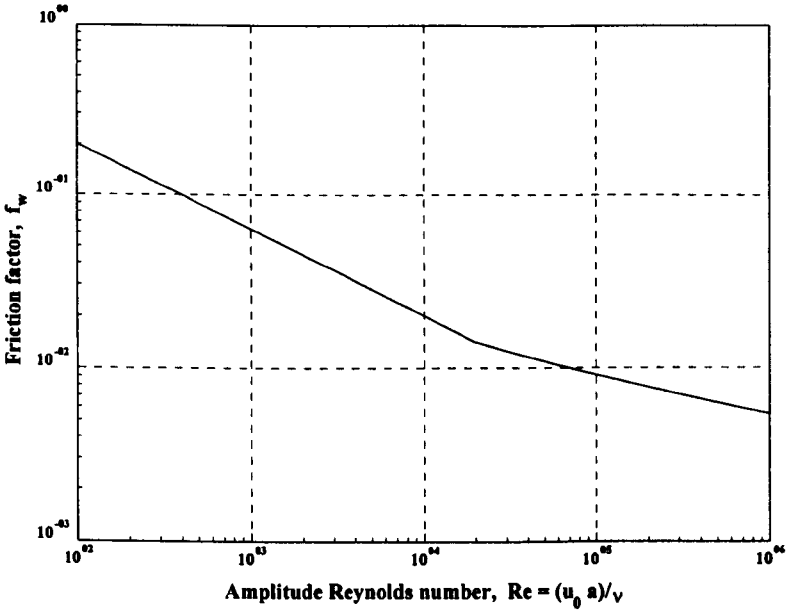

Figure 10.1: Friction factor for laminar and smooth turbulent flow. (*After Jonsson 1966*).

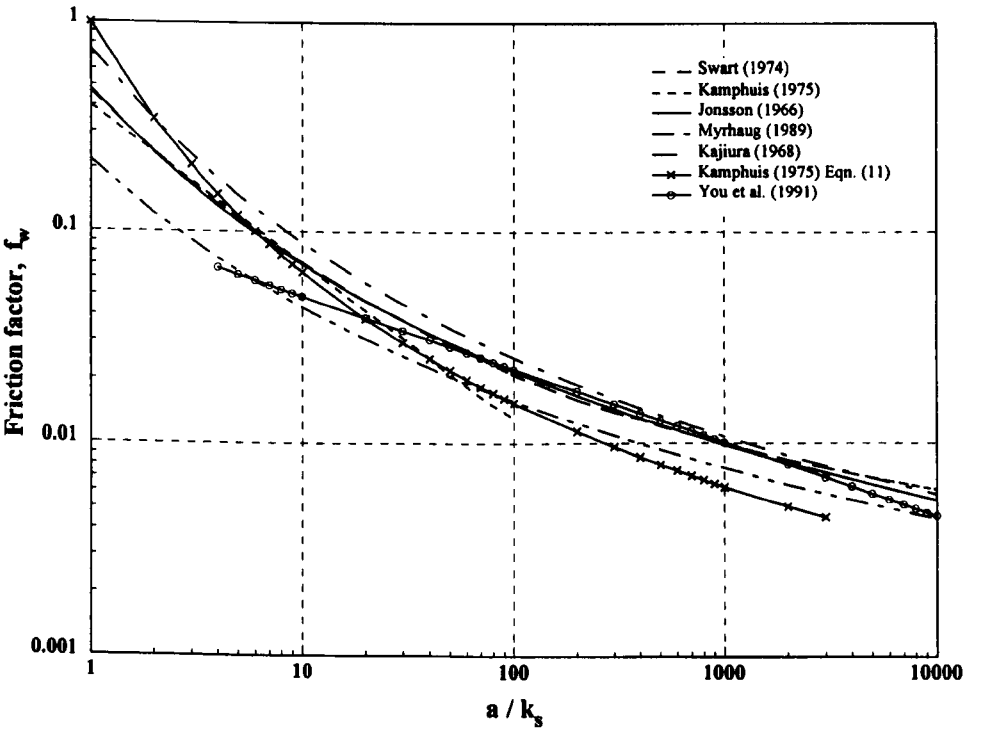

Figure 10.2: Friction factor equations for fully rough turbulent flow.

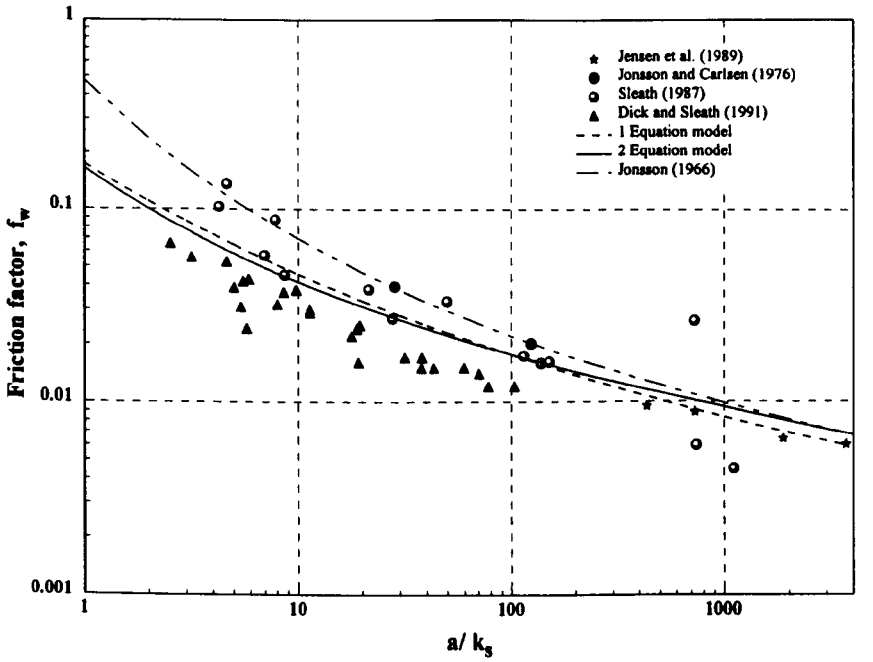

Figure 10.3: Friction factor as given by the k and k-ε models plotted against laboratory data and the friction factor expression of Jonsson (1966).

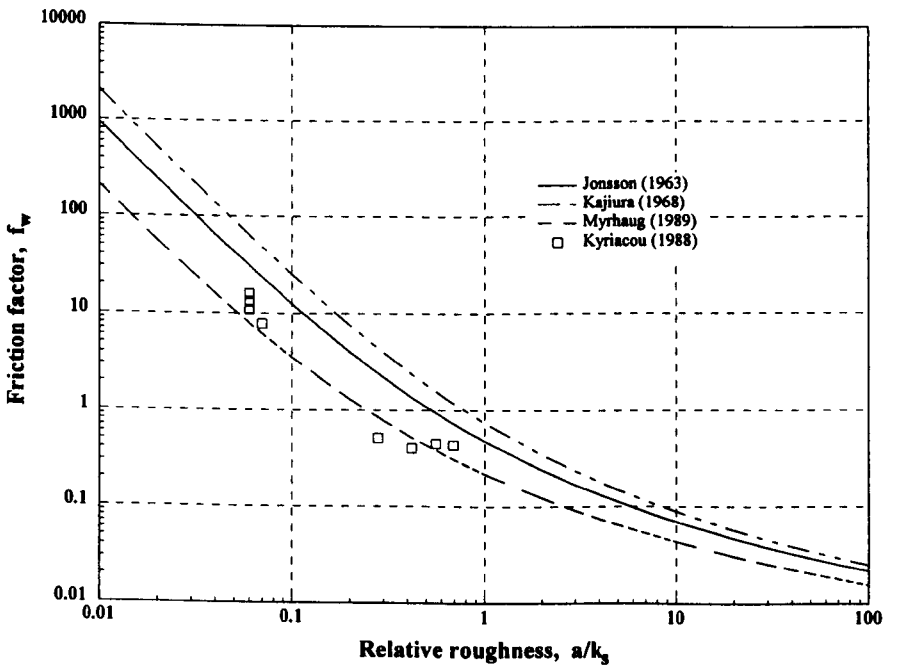

Figure 10.4: Friction factor diagram showing the results of Kyriacou (1988).

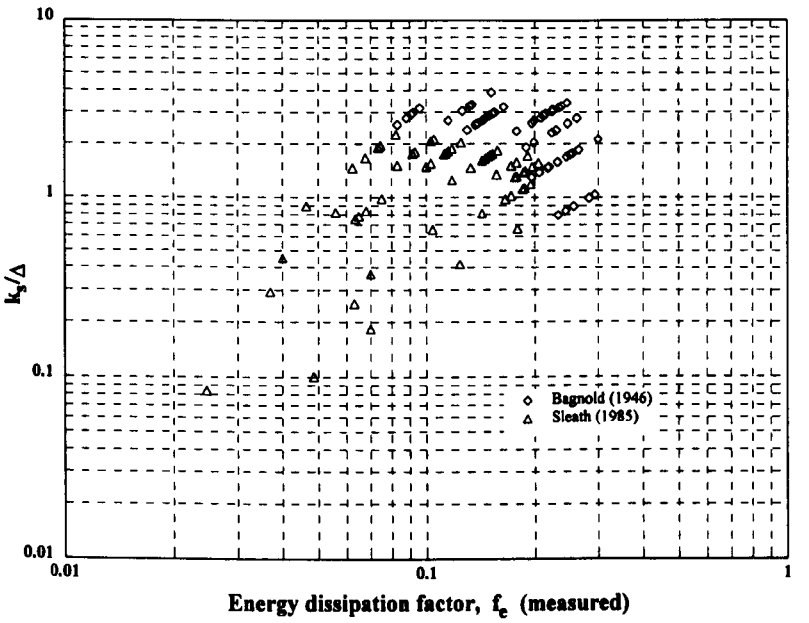

Figure 10.5: The ratio of equivalent roughness to ripple height, k_s/Δ, plotted against the measured energy dissipation factor for the data of Bagnold (1946) and Sleath (1985).

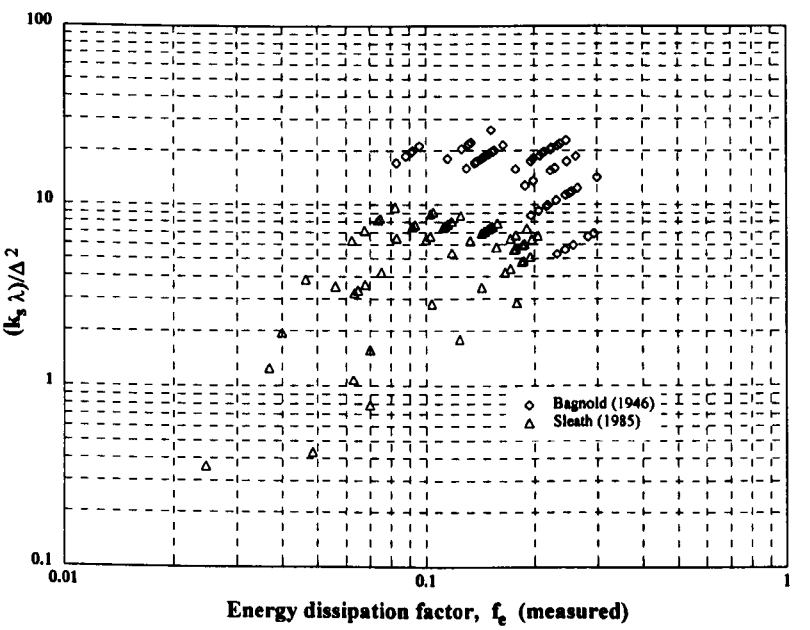

Figure 10.6: The ratio of relative ripple roughness, $(k_s\lambda)/\Delta^2$, plotted against the measured energy dissipation factor for the data of Bagnold (1946) and Sleath (1985).

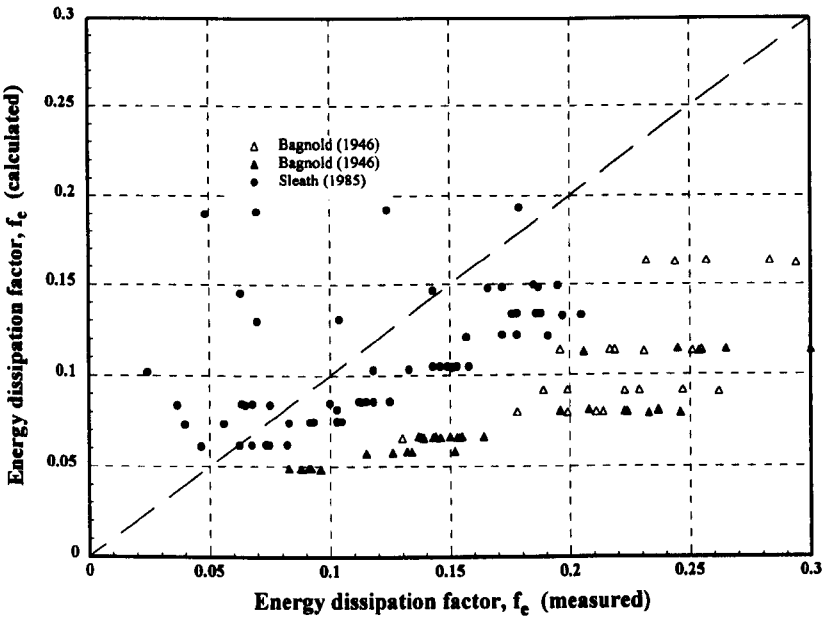

Figure 10.7: Calculated energy dissipation factor against measured energy dissipation factor for the data of Bagnold (1946) and Sleath (1985).

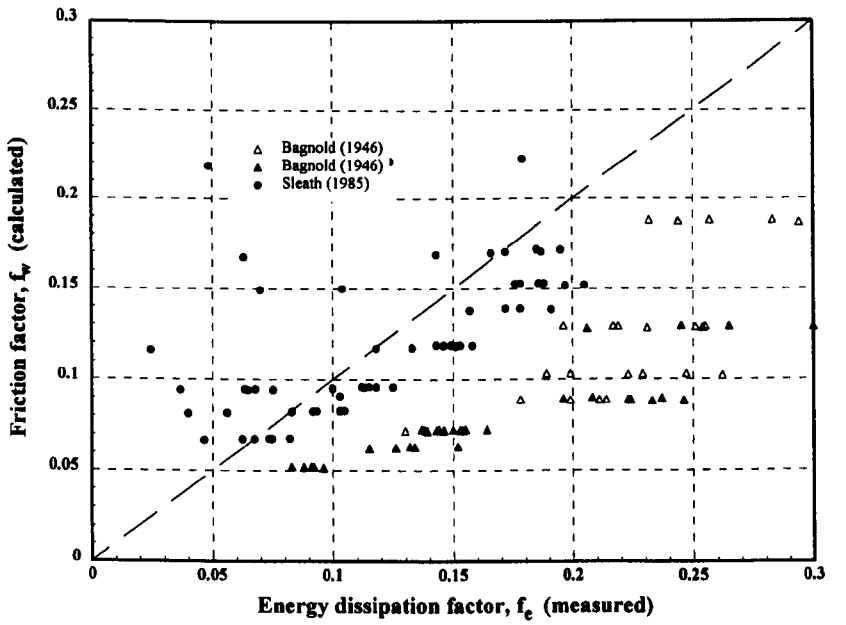

Figure 10.8: Calculated wave friction factor against measured energy dissipation factor for the data of Bagnold (1946) and Sleath (1985).

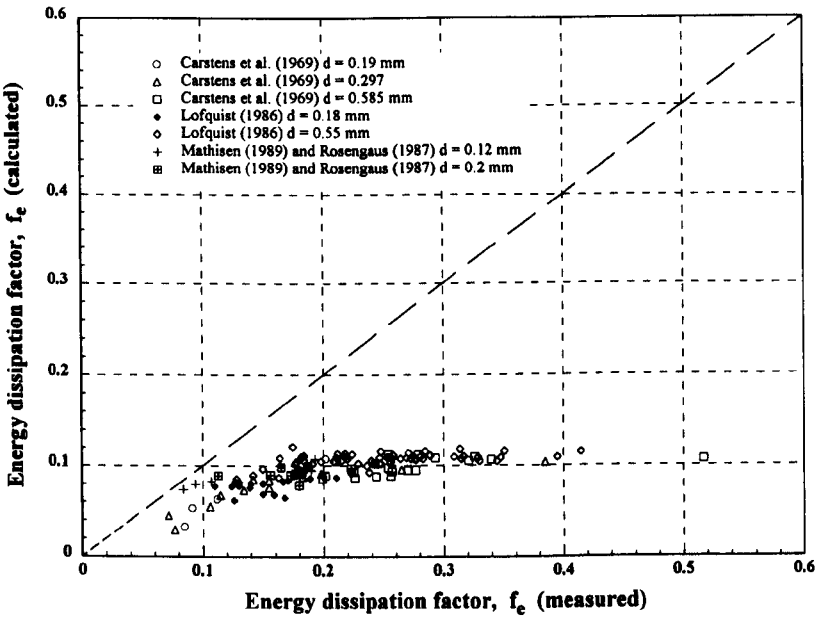

Figure 10.9: Calculated energy dissipation factor against measured energy dissipation factor for the data of Carstens *et al.* (1969), Lofquist (1986), Rosengaus (1987) and Mathisen (1989).

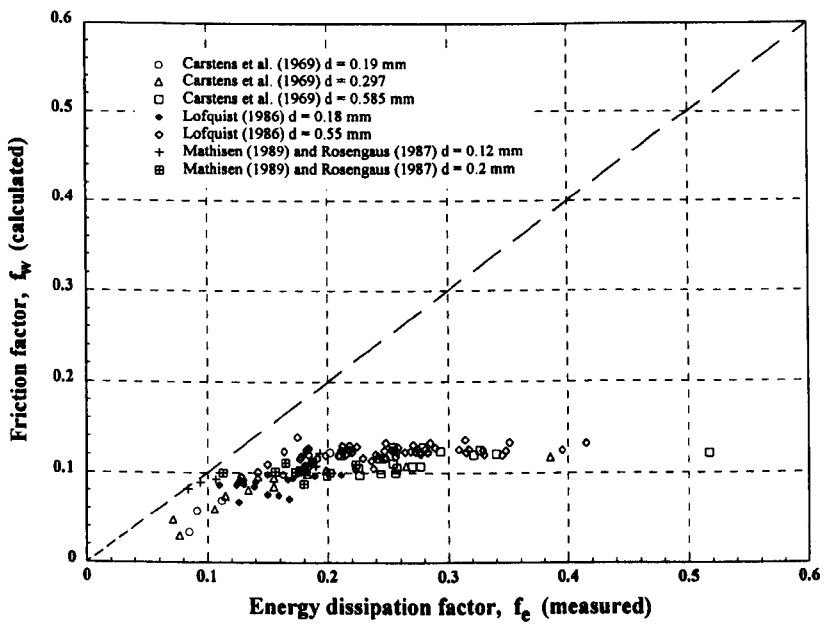

Figure 10.10: Calculated wave friction factor against measured energy dissipation factor for the data of Carstens *et al.* (1969), Lofquist (1986), Rosengaus (1987) and Mathisen (1989).

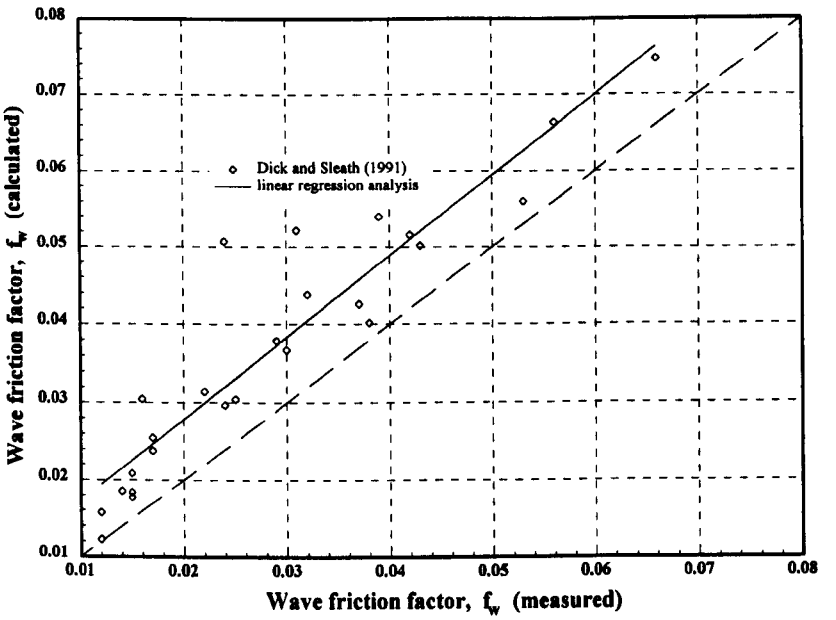

Figure 10.11: Calculated wave friction factor against measured wave friction factor for the data of Dick and Sleath (1991). The linear regression line is given by the equation $y = 6.765 \times 10^{-3} + 1.053x$.

Figure 10.12: Figure 10.12 (shown over page) depicts the process of vortex action over equilibrium ripples and is based on Nielsen (1979).

In Figure 10.12a, the vortices A and B move up into the flow as the flow reverses. A previous vortex, C can be seen to be rotating anti-clockwise above A. The wave phase is shown in the top left-hand corner.

Figure 10.12b shows vortex A moving to the right, whilst the previous vortex, C is decaying and being absorbed into the main flow.

Figure 10.12c shows that as the free stream velocity approaches its maximum value significant erosion occurs on the upstream side of the ripple. Flow separation has yet to begin behind the ripple crest.

In Figure 10.12d the free stream velocity is past its maximum and a new lee side vortex is beginning to form. Erosion is still taking place on the upstream side of the ripple and much of this material is trapped by the vortex.

At flow reversal the vortex is at its maximum intensity and is causing significant erosion at the lower part of the slope. Further erosion is occurring in the ripple trough, helping to maintain the ripple slope. (Figure 10.12e).

The next half wave period sees a the above process repeated symmetrically. (*After Nielsen 1979*).

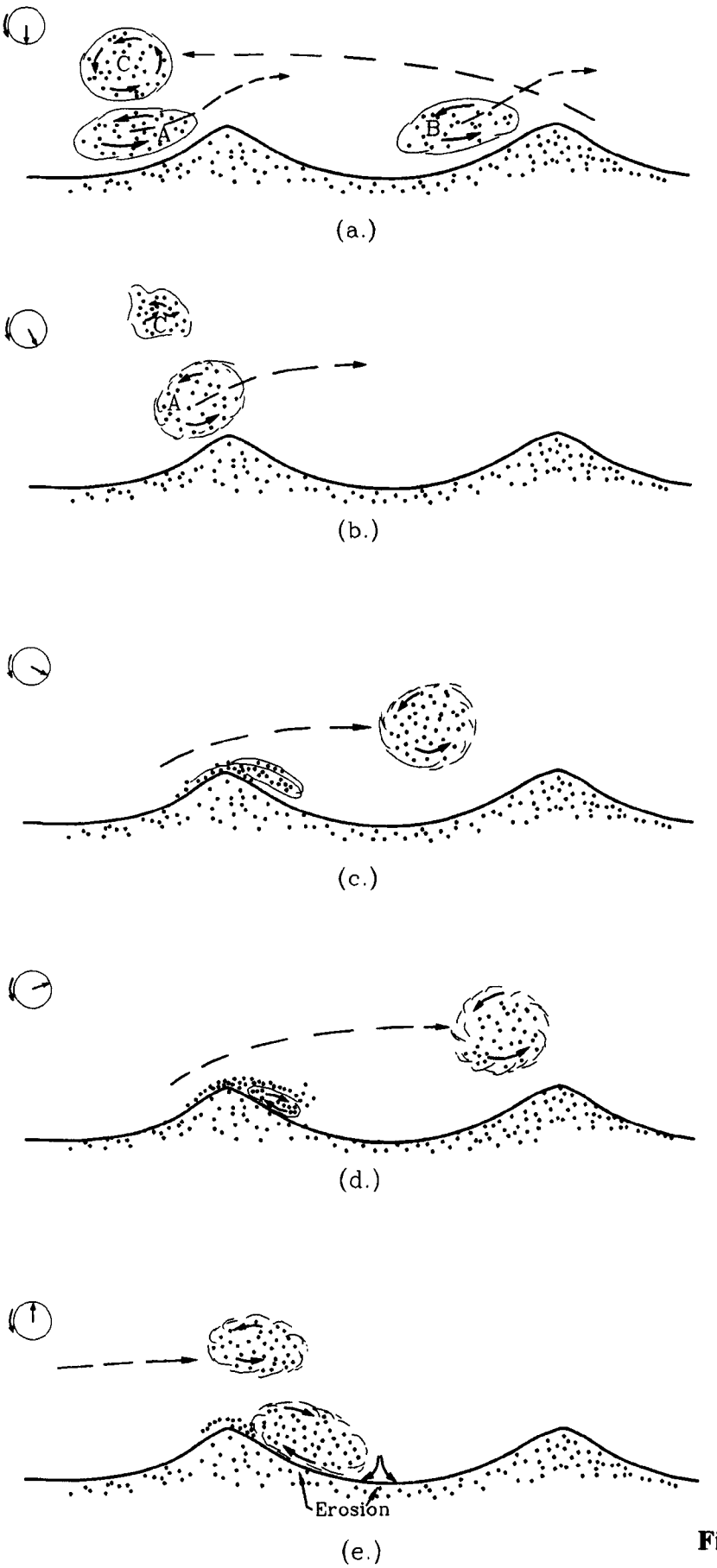

Figure 10.12:

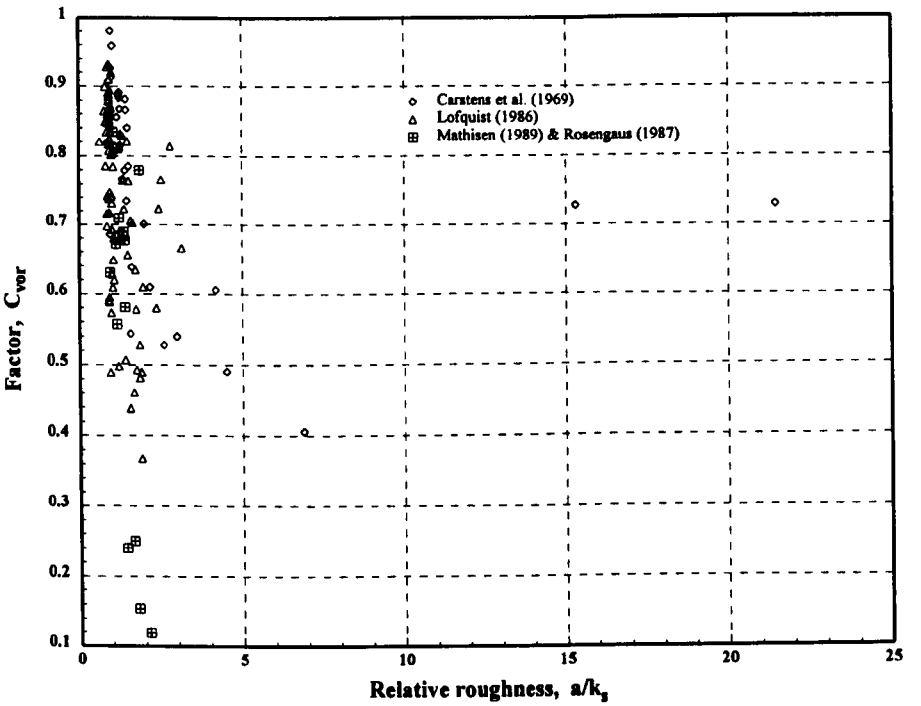

Figure 10.13: Plot of coefficient C_{vor} against relative roughness.

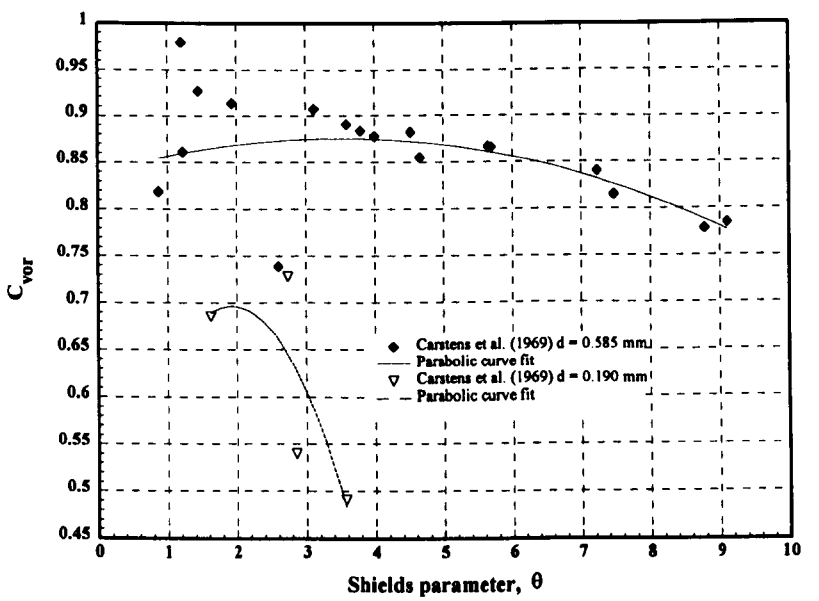

Figure 10.14a: Parabolic curve fit against the data of Carstens *et al.* (1969) to obtain an expression for the proposed coefficient C_{vor}. The regression curves are represented by the equations $y = 0.838 + 0.022x - 0.0031x^2$ and $y = 0.401 + 0.306x - 0.079x^2$ for the grain sizes 0.585 mm and 0.19 mm, respectively.

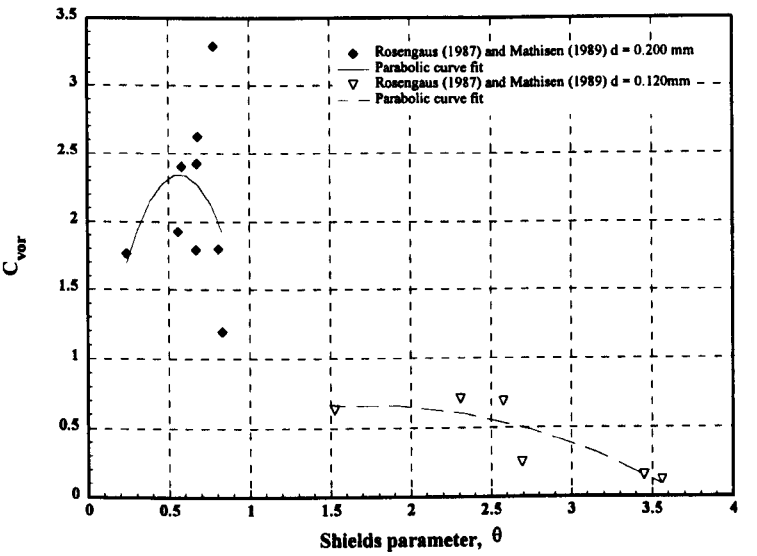

Figure 10.14b: Parabolic curve fit against the data of Rosengaus (1987) and Mathisen (1989) to obtain an expression for the proposed coefficient C_{vor}. The regression curves are represented by the equations $y = 0.387 + 6.879x - 6.033x^2$ and $y = 0.162 + 0.584x - 0.170x^2$ for the grain sizes 0.2 mm and 0.12 mm, respectively.

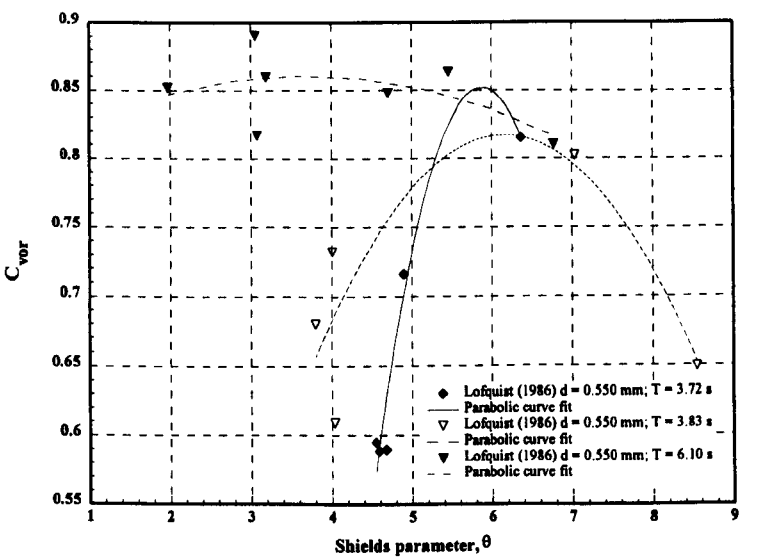

Figure 10.14c: Parabolic curve fit against the data of Lofquist (1986) to obtain an expression for the proposed coefficient C_{vor}. The regression curves are represented by the equations $y = 0.797 + 0.034x - 0.0046x^2$, $y = -0.282 + 0.036x - 0.029x^2$ and $y = -4.524 + 1.827x - 0.155x^2$ for the wave periods 6.1 s, 3.83 s and 3.72 s, respectively.

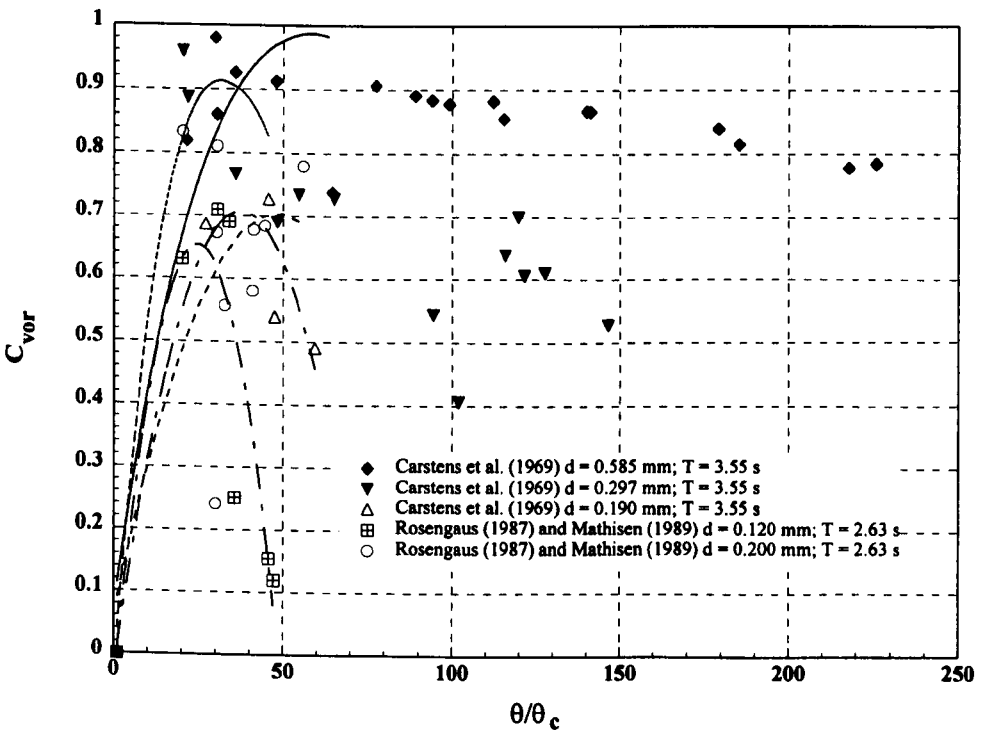

Figure 10.14d: Plot of C_{vor} against θ/θ_c where θ is Shields parameter and θ_c is the critical Shields parameter. The figure suggests that sets of curves exist for C_{vor} for different periods and grain sizes.

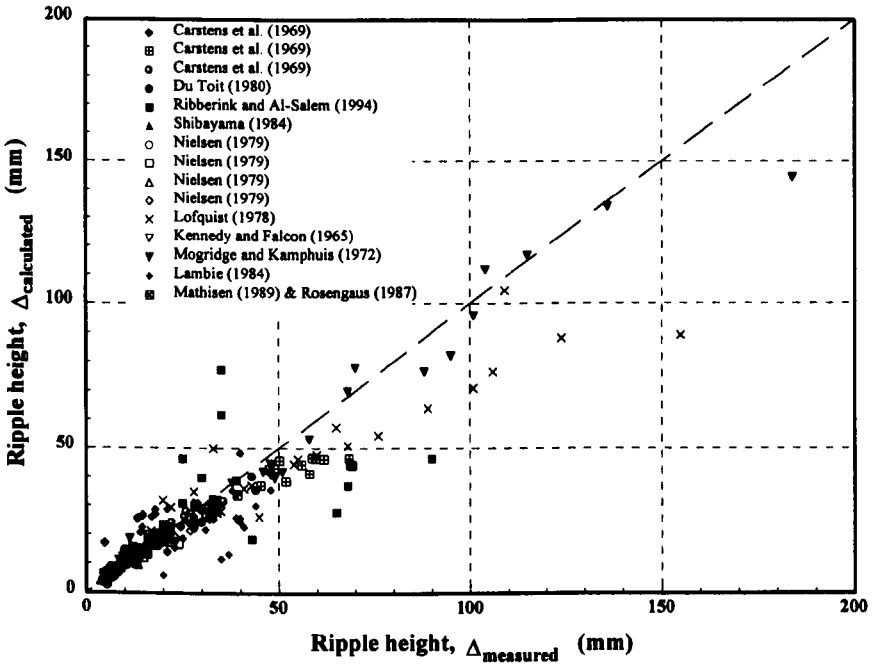

Figure 10.15: Comparison of calculated ripple height against measured ripple height.

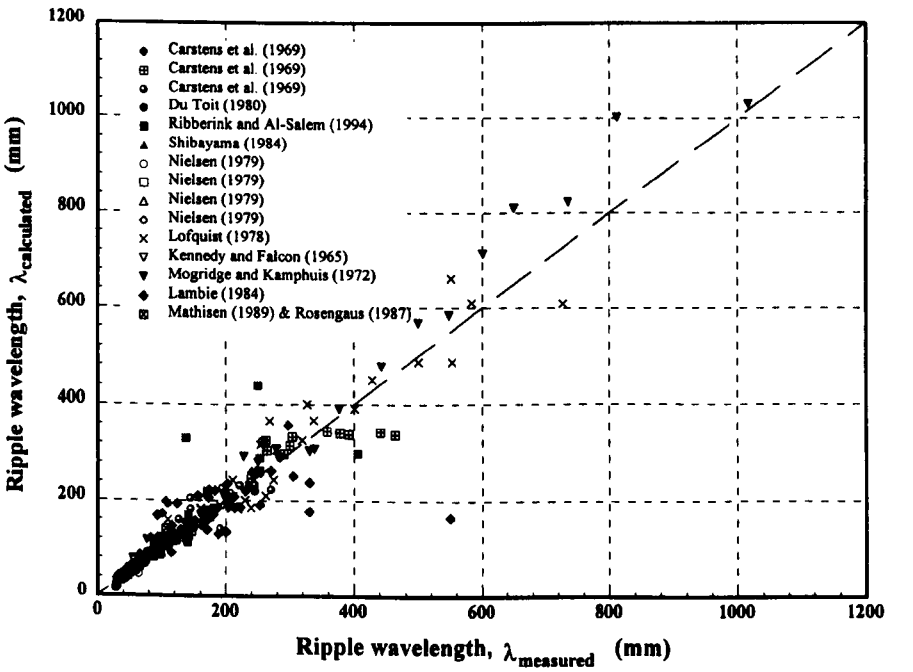

Figure 10.16: Comparison of calculated and measured ripple lengths.

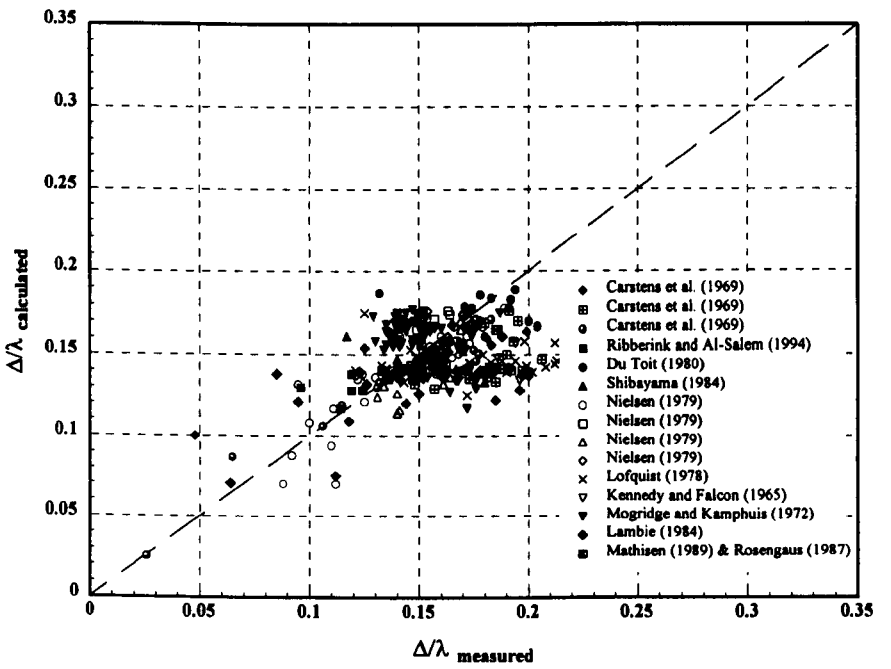

Figure 10.17: Comparison of computed and measured values for ripple steepness.

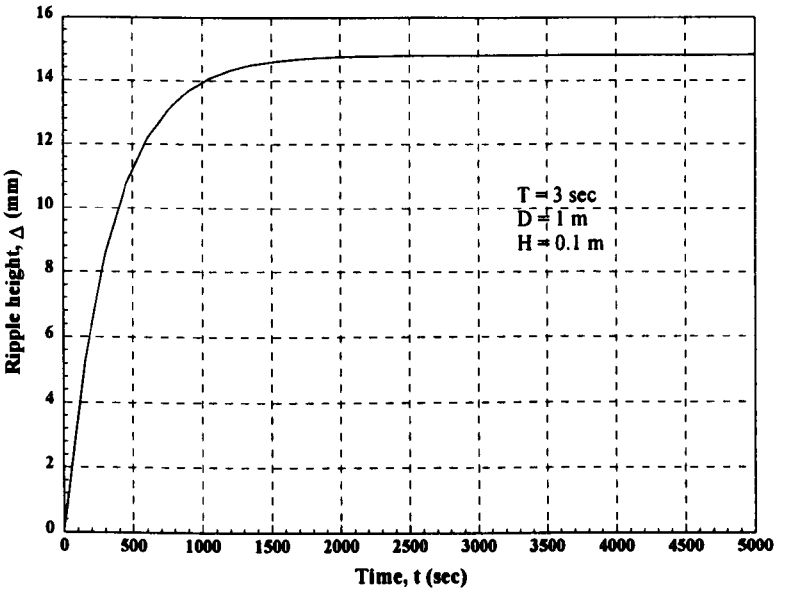

Figure 10.18a: Development of ripple height with time as predicted by moveable bed model for a monochromatic wave.

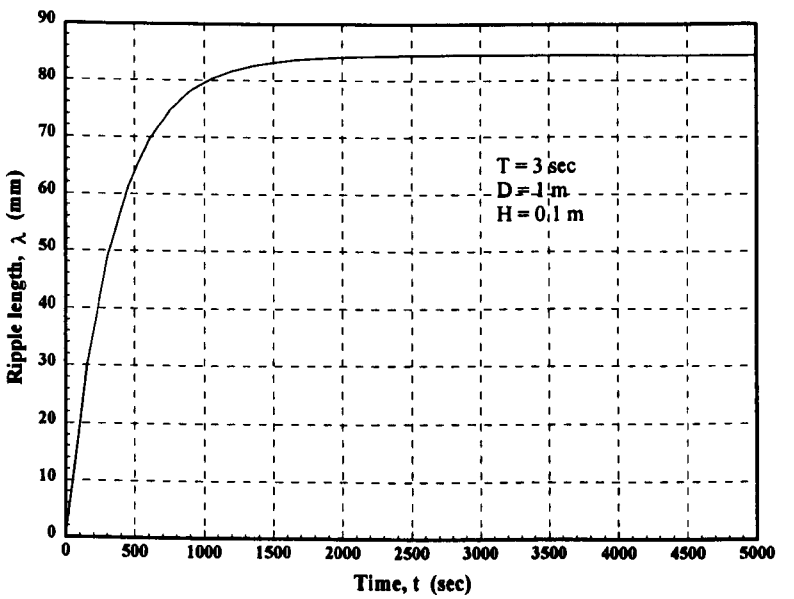

Figure 10.18b: Development of ripple length with time as predicted by moveable bed model for a monochromatic wave.

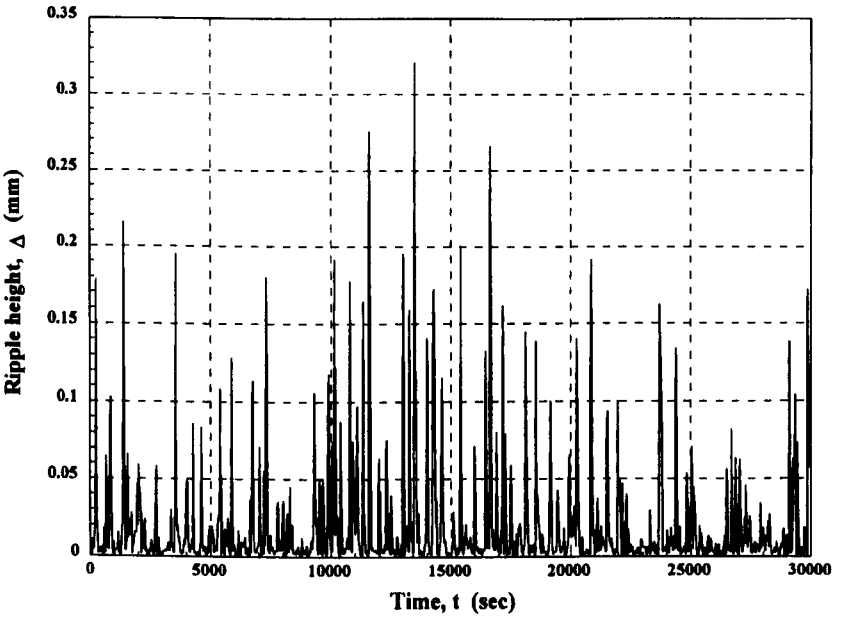

Figure 10.19: Development of ripple height with time as predicted by moveable bed model for a spectral sea defined by a JONSWAP spectrum. (Test parameters: D = 20.0 m; d_{50} = 0.2 mm; T_z = 6 s; H_s = 2 m).

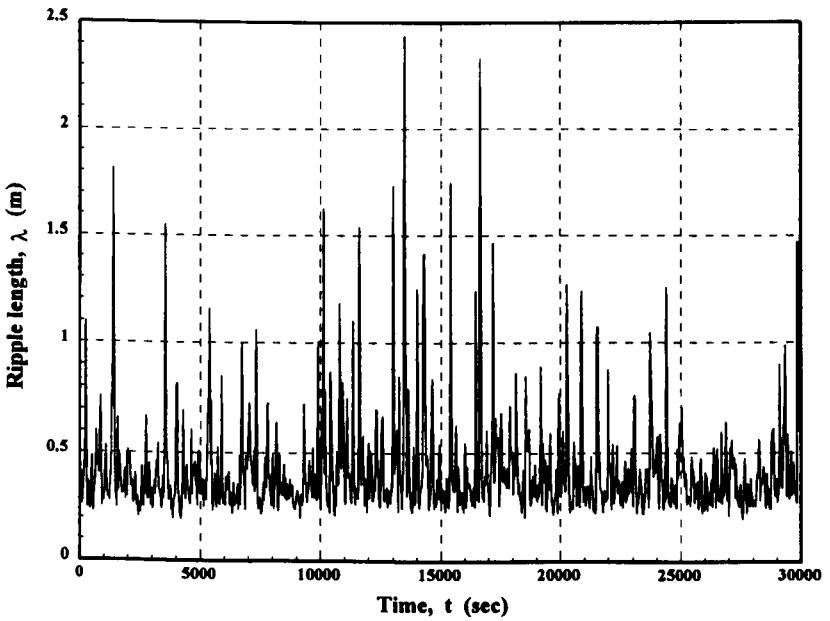

Figure 10.20: Development of ripple length with time as predicted by moveable bed model for a spectral sea defined by a JONSWAP spectrum. (Test parameters: D = 20.0 m; d_{50} = 0.2 mm; T_z = 6 s; H_s = 2 m).

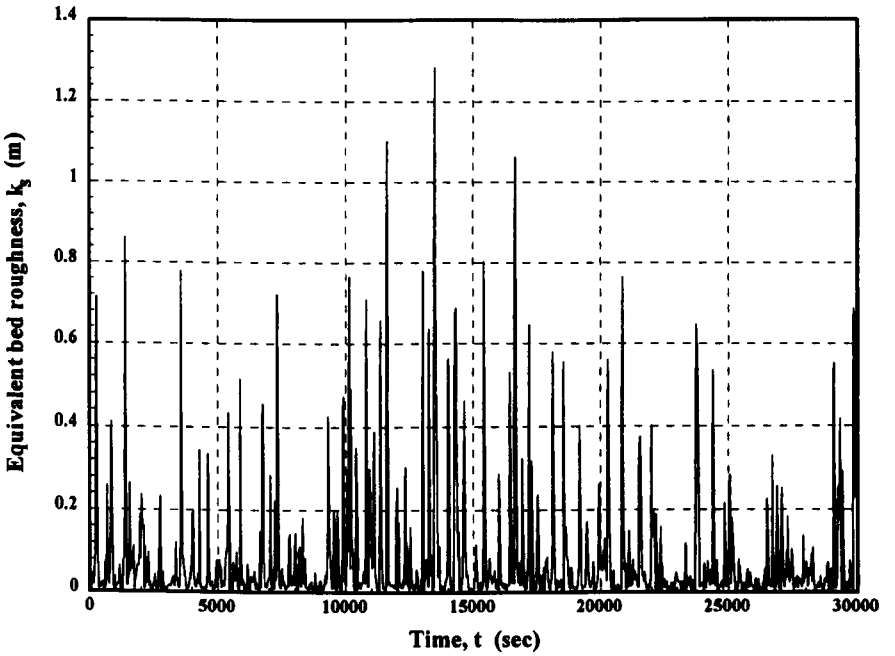

Figure 10.21 Equivalent bed roughness with time as predicted by moveable bed model for a spectral sea defined by a JONSWAP spectrum. (Test parameters: D = 20.0 m; d_{50} = 0.2 mm; T_z = 6 s; H_s = 2 m).

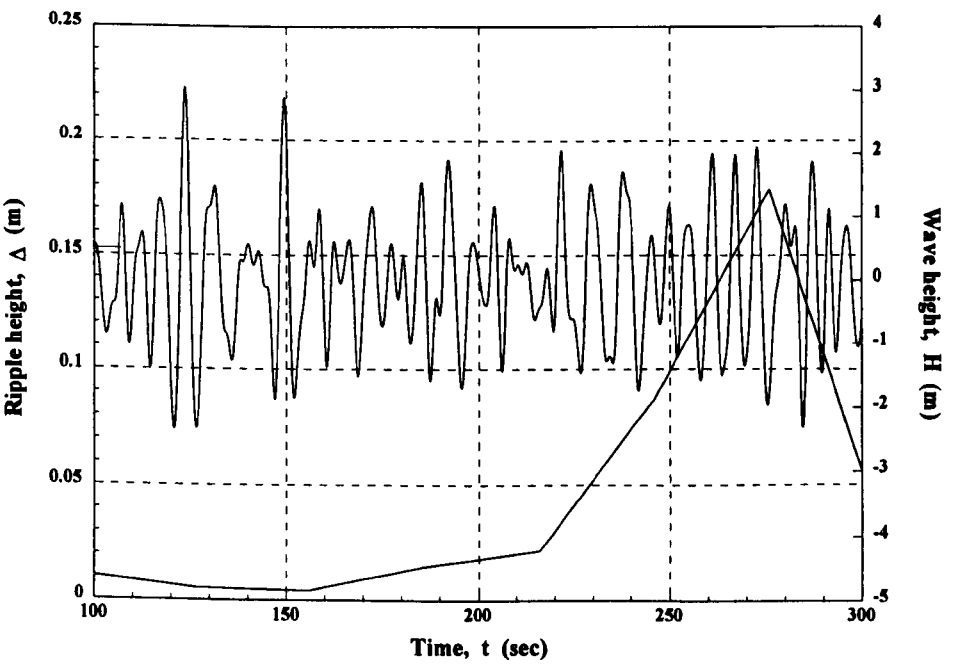

Figure 10.22a: Plot of ripple height development with time together with corresponding surface wave conditions.

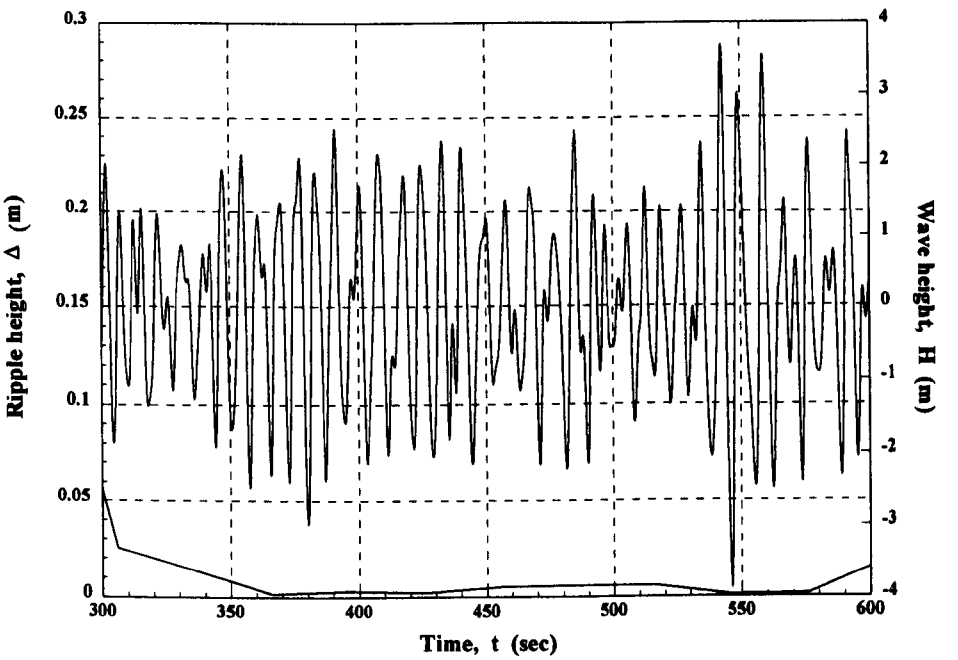

Figure 10.22b: Plot of ripple height development with time together with corresponding surface wave conditions.

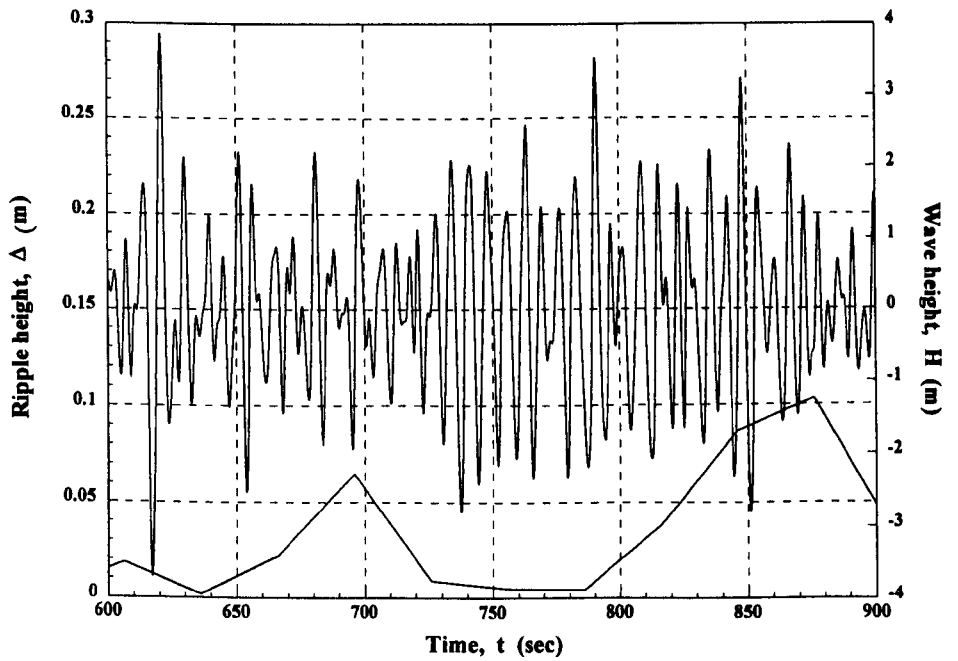

Figure 10.22c: Plot of ripple height development with time together with corresponding surface wave conditions.

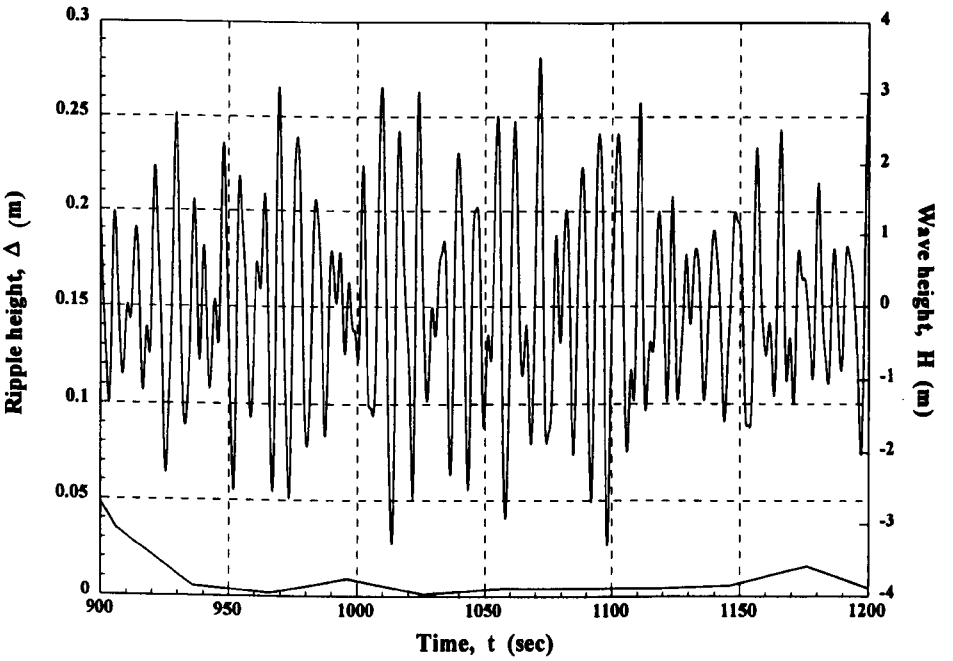

Figure 10.22d: Plot of ripple height development with time together with corresponding surface wave conditions.

Chapter 11
Conclusions and Recommendations

11.1 Introduction

This chapter presents the main conclusions from the work contained within this thesis. Those findings of most significance to modelling random wave boundary layers are highlighted. In addition, recommendations are made for further study.

11.2 Overview of present work

Chapter 3 provided a state-of-the-art overview of wave boundary layer modelling. From the review several key elements were established:

- There is a variety of models available with which to study turbulent wave boundary layers, many of which are simplistic time-invariant eddy viscosity models.

- Time dependence is necessary in order to reproduce fundamental flow mechanisms, for example, the turbulent eddy viscosity varies with time.

- 1st order closure models have been shown to be adequate, whilst 2nd order schemes eliminate the Boussinesq eddy viscosity assumption by providing the ability to model the individual stress terms. However, the cost of such schemes is prohibitive and the level of sophistication has not yet been justified. In addition, the k-ε model has been shown to provide a similar level of accuracy as a 2nd order Reynolds stress approach (Brørs and Eidsvik 1994).

- The choice of model formulation is important and will influence the performance and accuracy of the chosen scheme.

- The one-equation k model has been shown to be the lowest order of closure required to model environmental flows (Smith and Takhar 1977).

- The two-equation k-ε model has been shown to accurately reproduce oscillatory boundary layer flows (Spalart and Baldwin 1987), excluding the near-wall region.

The present study has involved the development of both one- and two-equation turbulence models of varying sophistication. The simplest approach used was a one-equation k model. Several types of two-equation k-ε models were developed, a high-Reynolds number model, a low-Reynolds number model (not used in the present work) and a two-layer k-ε model. The application of a two-layer k-ε model to the problem of studying turbulent wave boundary layers is, to this author's knowledge, unique. The two-layer k-ε scheme uses a standard high-Reynolds number model away from the wall, whilst the near-wall region is modelled using a one-equation k approach.

In addition to the turbulence models, sub-models have been developed enabling the description of most sea-states encountered on the continental shelf, including allowance for the effects of currents on wave spectra and the representation of a directional sea. These sub-models provide boundary conditions for the turbulent wave boundary layer models.

The numerical solution of the partial differential equations was obtained by using finite difference techniques. The numerical scheme applied was the Crank-Nicolson semi-implicit method, Crank and Nicolson (1947). To ensure that there was a sufficient number of calculation points within the boundary layer a logarithmic grid transform was applied to the vertical space.

In order that the turbulence models could be applied to random wave boundary layers it was first necessary to test the numerical schemes against experimental data for monochromatic

waves and monochromatic waves plus current. The experimental data used was at both laboratory and prototype scale, see Chapters 6 and 7. The random wave model was tested against laboratory data and field data. In addition, a novel approach has been proposed, allowing the bed roughness in the random wave model to be prescribed as a time-series, through the development of a moveable bed model.

Prior to testing the proposed boundary layer models against laboratory and field data the accuracy and convergence of the numerical schemes were tested by comparing model results against the analytical solution for laminar flow presented by Lamb (1932). Tests were performed using a range of grid densities, the lowest of which was 20 points through the vertical. For grid densities of 40 and 60 points through the vertical, velocity results for the k and k-ε models show a maximum error of approximately 2%. Similarly, a comparison of shear stress results for the same grid densities shows a maximum error of about 3% from the analytical solution. This work is summarized in Chapter 5 and Appendix D.

The use of the logarithmic grid straining ensures that, even for a grid density of only 20 points through the vertical, the numerical models reproduce the near-wall analytical results well.

The one-equation model (run with both a time-variant and time-invariant mixing length) and k-ε model have been compared with the prototype scale oscillating tunnel data of Jonsson and Carlsen (1976) and Jensen *et al.* (1989). Both models show good agreement, overall, with the experimental data. In addition, the performance of a zero-equation mixing length model has been compared with the higher order models. Both the k and k-ε models out-performed the mixing length model with differences of nearly 20% in some instances.

The results of using both a time-invariant and time-variant description for the mixing length in the k model revealed the importance of choosing the expression for the length scale carefully. The time-variant expression showed a better description of the physics than did the simple time-invariant form of the mixing length.

Results of the model runs against the shear stress data of Jensen *et al.* (1989) suggest that, possibly, even for flows considered to be fully turbulent (amplitude Reynolds number, Re = 6.0×10^6), kinematic (molecular) viscosity may still have some influence during certain phases through the wave cycle. Unfortunately, this cannot be verified experimentally since measurements are not able to be made, currently, at this scale ($\Delta z = 0.0071$ mm in the model).

Comparison of a two-layer k-ε model and a high-Reynolds number k-ε model against laboratory experiments conducted at the University of Manchester shows the importance of including the effects of molecular viscosity for low-Reynolds number flows.

The addition of a current to waves has been demonstrated to increase mixing within the wave boundary layer and increase the wave boundary layer thickness. Further, such increased mixing leads to an increase in turbulence in the boundary layer.

Observed differences in the magnitude of the measured and computed values of shear stress and turbulent kinetic energy outside the boundary layer appear to be due to streaming caused by the presence of second order effects.

The k model was found to be computationally slower than the two-equation k-ε model due to the summation required to obtain the time-varying mixing length. For this reason, the k-ε model was chosen to be adapted to enable the representation of random waves.

The random wave model was first tested against the laboratory experiments of Ostrowski (1993). Ostrowski measured the bed shear stress under long-crested random waves using a shear plate. The computed results compare favourably with those measured.

The random model has been run using an actual time-series as well as a time-series generated from a wave height spectrum. In both cases, the model has been shown to perform well.

In addition to the laboratory data of Ostrowski (1993), the model has been run for a multi-directional sea state using the field data of Williams (1996). The measured velocity time-series at 80 cm above the seabed was used as the upper boundary for the velocity in the

model. Adjusting the bed roughness in the model until the computed and measured mean velocities at a second lower depth matched produced an estimate for the bed roughness, as suggested by O'Connor *et al.* (1994). However, it has been argued that such a method is not sound and is too sensitive to errors in model formulation and to the spatial displacement of the second measurement point from the seabed.

The mean bed shear velocity has been compared with estimated values from the measured data. The results suggest that the random wave model is providing reasonable predictions.

In comparisons of the model against both the random laboratory and field data the turbulent kinetic energy has been shown to carry over energy from one half period to the next. This is an important result, since it changes previously held views that for random waves each wave can be treated individually as a monochromatic wave, for example Smith (1977). It has been demonstrated that this is not true and has significant implications for sediment transport modelling. Such an effect could account for the increase in sediment concentration under wave groups observed in field measurements (Williams 1996).

The presence of bedforms has been shown to cause an increase in the value of the wave friction factor, for example Iwagaki and Kakinuma (1963; 1967); Treloar and Abernethy (1978). In order to provide a better description of the wave boundary layer by the addition of a varying bed roughness, a new movable bed roughness model has been developed.

The development of the moveable bed roughness model was undertaken in a structured manner. Using the fixed ripple experiments of Bagnold (1946) and Sleath (1985) the relationship between ripple geometry and the form drag of the ripple has been investigated. Based on the relationship given by Eq. (10.15):-

$$k_s \approx \Delta \qquad \textbf{(10.15)}$$

results suggest a constant of proportionality of between 1 and 4. Alternatively, representing the equivalent roughness in terms of the length and height of the ripple, Eq. (10.17):-

$$k_s \propto \frac{\Delta^2}{\lambda} \qquad \textbf{(10.17)}$$

the constant of proportionality is between about 10 and 20.

Comparison of results from the hydrodynamic turbulence model with measured values for the energy dissipation over both fixed and moveable bed ripples show the model to significantly underpredict the energy dissipation. The assumption that the effect of ripples can be represented in a point model using relationships for the form drag such as those given by Eqs. (10.15) and (10.17) has been shown to be incorrect. It has been hypothesized that the underprediction of the energy dissipation by the 1DV turbulence model is due to a failure to compensate for the effect of vortex shedding off the ripples. In an attempt to correct for this failing, it has been proposed that a correction be applied to the dissipation term in the turbulent kinetic energy transport equation so that the dissipation term becomes:-

$$(1 - C_{vor})\varepsilon \qquad \textbf{(10.21)}$$

where C_{vor} represents a coefficient for the vortex generation.

C_{vor} has been shown to follow a parabolic shape, increasing in value as the ripple develops and then decaying as the ripple is washed out. Analysis of the data of Carstens *et al.* (1969), Lofquist (1986), Rosengaus (1987) and Mathisen (1989) confirms this trend, though it has not been possible to develop an equation for C_{vor} which is valid for all cases. C_{vor} was found to increase with increasing grain diameter and wave period.

Results from the moveable bed model are promising. It has not been possible to confirm whether the rate of growth of the ripples as predicted by the model is correct due to a lack of appropriate experimental data for bedforms developed under random waves. The moveable bed model for random waves uses a novel approach, enabling the ripple geometry to be determined as a continuous time-series.

Using the calculated values for ripple geometry allows the bed roughness to be prescribed as a time-series and thus used in a modified random wave boundary layer model. This permits

the boundary layer model to vary its roughness condition and enable investigation of boundary layers over moveable beds.

The present work has been limited by a lack of adequate field and laboratory data and, therefore, it has not been possible to find a satisfactory representation of the proposed coefficient C_{vor}. It has been shown that the moveable bed model is capable of describing the variation of ripple geometry and, hence, bed roughness with time, for random waves.

11.3 Recommendations for future work

Results from the present work have highlighted several shortfalls in the aspects of the areas covered.

- Experimental data is required to enable the coefficient C_{vor}. The experiments include the measurement of dissipation rates over both developing and equilibrium ripples as well as recording the corresponding ripple geometry. The tests should cover a range of wave periods and sediment grain sizes. In addition, the effect of sediment mixtures on the value of the coefficient C_{vor} could be investigated.

- Second order effects should be investigated in the boundary layer model, in particular, for combined wave and current conditions. Mass transport effects can be included using a pseudo-spectral approach as suggested by Johns (1977), a simplification based on the assumption of periodicity in space and time together with the continuity equation as suggested by Trowbridge *et al.* (1987) or by solving for two points in space and then using the continuity equation to find the vertical velocity.

- The discrepancies observed in the computed turbulent kinetic energy profiles for the combined wave and current case can be tested against oscillating wave tunnel data since this eliminates any vertical oscillatory velocities. This should

provide a relatively simple check to whether the difference is due to a boundary value problem.

- The random wave model should be adapted to include a sediment transport sub-model thereby enabling the study of sediment transport under random waves. The results should then be compared with experimental studies.

- The effect of bounded long waves could be included in the model to study the effect on bed roughness and sediment transport rates.

- The wave boundary layer model should be adapted to enable the study of turbulent wave boundary layers in the breaker zone. This will require modification in the upper boundary conditions to take account of the turbulent kinetic energy produced in the surface roller in the upper part of the water column.

- Finally, having determined an expression for coefficient C_{vor}, the random boundary layer model should be run with a varying bed roughness and the results compared to the work of Madsen *et al.* (1991).

References

Abbott, M.B. and Basco, D.R. (1989). *Computational Fluid Dynamics: An Introduction for Engineers.* Longman Scientific and Technical, Singapore, 425 pp.

Agrawal, Y.C. and Aubrey, D.G. (1992). Velocity observations above a rippled bed using laser Doppler velocimetry. *J. of Geophys. Res.*, Vol. 97, No. C12, pp. 20,249 - 20,259.

Arthur, S.A. (1949). Variability in direction of wave travel. *Annals New York Acad. Sciences*, Vol. 51, pp. 511 - 522.

Asano, T., Godo, H. and Iwagaki, Y. (1988). Application of low-Reynolds number turbulence model to oscillatory bottom boundary layers. *Coastal Engng. in Japan*, Vol. 30, No. 2, pp. 1 - 9.

Aydin, I. and Shuto, N. (1988). An application of the k-ε model to oscillatory boundary layers. *Coastal Engng. in Japan*, Vol. 30, No. 2, pp. 11 - 24.

Bakker, W.T. (1975). Sand concentration in an oscillatory flow. In: *Coastal Engng.*, Proc. 14th Coastal Engng. Conf., Copenhagan, Denmark, 24 - 28 Jun., 1974, Vol. 2, Chap. 66, ASCE, New York, pp. 1129 - 1148.

Bakker, W.T. and van Doorn, T. (1979). Near-bottom velocities in waves with a current. In: *Coastal Engng.*, Proc. 16th Coastal Engng. Conf., Hamburg, Germany, 27 Aug. - 3 Sept., 1978, Vol. 2, Chap. 82, ASCE, New York, pp. 1394 - 1412.

Bagnold, R.A. (1946). Motion of waves in shallow water. Interaction between waves and sand bottoms. *Proc. Royal Soc.*, Series A, Vol. 187, Royal Soc., London, pp. 1 - 18.

Bretherton, F.P. (1971). The general linearised theory of wave propagation. In: *Mathematical Problems in the Geophysical Sciences*, (ed.) Reid, W.H., Lectures in Applied Maths., No. 13, Vol. 1, Amer. Math. Soc., Washington D.C., pp. 61 - 102.

Bretherton, F.P. and Garrett, C.J.R. (1969). Wavetrains on inhomogoneous moving media. *Proc. Royal Soc.*, Series A, Vol. 302, Royal Soc., London, pp. 529 - 554.

Bijker, E.W. (1967). The increase of bed shear in a current due to wave motion. In: *Coastal Engng.*, Proc. 10th Conf. on Coastal Engng., Tokyo, Japan, Sept., 1966, Vol. 1, Chap. 43, ASCE, New York, pp. 746 - 765.

Blondeaux, P. (1987). Turbulent boundary layer at the bottom of gravity waves. *J. Hydr. Res.*, Vol. 25, No. 4, pp. 447 - 464.

Boczar-Karakiewicz, B. and Chapalain, G. (1990). Wave-induced boundary-layer flow over erodible and rippled beds: a model. In: *Proc. Canadian Coastal Conf.*, Kingston, Ontario, 8 - 11 May, (ed.) Davies, M.H., pp. 489 - 500.

Borgman, L.E. (1969). Ocean wave simulation for engineering design. *J. Waterways and Harbors Div.*, Vol. 95, No. WW4, Nov., ASCE, New York, pp. 557 - 583.

Boussinesq, J. (1877). Essai sur la théorie des eaux courantes. *Mémoires présentés par divers savants à l'Académie des Sciences*, Vol. 23, Paris, 46 pp.

Brevik, I. (1981). Oscillatory rough turbulent boundary layers. *J. Waterway, Port, Coastal and Ocean Div.*, Vol. 107, No. WW3, Aug., ASCE, New York, pp. 175 - 198.

Brørs, B. and Eidsvik, K.J. (1994). Oscillatory boundary layer flows modelled with dynamic Reynolds stress turbulence closure. *Continental Shelf Res.*, Vol. 14, No. 13/14, pp. 1455 - 1475.

Carstens, M.R., Neilson, F.M. and Altinbilek, H.D. (1969). *Bed forms generated in the laboratory under and oscillatory flow: Analytical and experimental study*. Tech. Memo., No. 28, June, US Army Corps of Engrs., CERC, 39 pp.

Cartwright, D.E. and Smith, N.D. (1964). Buoy techniques for obtaining directional wave spectra. *Buoy Technology*, Marine Tech. Soc., Washington, D.C., pp. 112 - 121.

Chapalain, G. and Boczar-Karakiewicz, B. (1992). Modeling of hydrodynamics and sedimentary processes related to unbroken progressive shallow water waves. *J. Coastal Res.*, Vol. 8, No. 2, pp. 419 - 441.

Celik, I. and Rodi, W. (1985). Calculation of wave-induced turbulent flows in estuaries. *Ocean Engng.*, Vol. 12, No. 6, pp. 419 - 542.

Chen, H.C. and Patel, V.C. (1988). Near-wall turbulence models for complex flows including separation. *AIAA Journal*, Vol. 26, pp. 641 - 648.

Chen, H.C. and Patel, V.C. (1989). Evolution of axisymmetric wakes from attached and separated flows. In: *Turbulent Shear Flows 6*, Springer-Verlag, Berlin, pp. 215 - 231.

Chou, P.Y. (1945). On velocity correlations and the solutions of the equations of turbulent fluctuation. *Quart. Applied Maths.*, Vol. III, April, pp. 38 - 54.

Chriss, T.M. and Caldwell, D.R. (1982). Evidence for the influence of form drag on bottom boundary flow. *J. of Geophysical Res.*, Vol. 87, No. C6, pp. 4148 - 4154.

Coté, L.J., Davis, J.O., Marks, W., McGough, R.J., Mehr, E., Pierson, W.J., Ropek, J.F., Stephenson, G. and Vetter, R.C. (1960). The directional spectrum of a wind-generated sea as determined from data obtained by the Stereo Wave Observation Project, *Meteor. Papers*, Vol. 2, No. 6, New York University, 88 pp.

Cousteix, J., Desopper, A. and Houdeville, R. (1979). Structure and development of a turbulent boundary layer in an oscillatory external flow. In: *Turbulent Shear Flows 1*, (eds.) Durst, F., Launder, B.E., Schmidt, F.W. and Whitelaw, J.H., Springer-Verlag, Berlin, pp. 154 - 171.

Crank, J. and Nicolson, P. (1947). A practical method for numerical evaluation of solutions of partial differential equations of the heat-conduction type. *Proc. Cambridge Phil. Soc.*, Vol. 43, Jan., Part 1, pp. 50 - 67.

Davidov, B.I. (1961). On the statistical dynamics of an incompressible turbulent fluid. *Dokl. AN SSSR*, Vol. 136, No. 47.

Davies, A.G. (1986a). A model of oscillatory rough turbulent boundary flow. *Est. and Coastal Shelf Sci.*, Vol. 23, No. 3, pp. 353 - 374.

Davies, A.G. (1986b). A numerical model of the wave boundary layer. *Continental Shelf Res.*, Vol. 6, No. 6, pp. 715 - 739.

Davies, A.G. (1991). Transient effects in wave-current boundary layer flow. *Ocean Engng.*, Vol. 18, No. 1/2, pp. 75 - 100.

Davies, A.G. and Li, Z. (1997). Modelling sediment transport beneath regular symmetrical and asymmetrical waves above a plane bed. *Continental Shelf Res.*, Vol. 17, No. 5, pp. 555 - 582.

Davies, A.G., Soulsby, R.L. and King, H.L. (1988). A numerical model of the combined wave and current bottom boundary layer. *J. Geophys. Res.*, Vol. 93, No. C1, Jan., pp. 491 - 508.

Davies, A.M. and Jones, J.E. (1987). Modelling turbulence in shallow sea regions. In: *Small-scale Turbulence and Mixing in the Ocean*, Proc. 19th Liège Colloq. on Ocean Hydrodynamics, (eds.) Nihoul, J.C.J. and Jamart, B.M., Elsevier, Amsterdam, pp. 63 - 76.

Dean, R.G. (1965). Stream function representation of non-linear ocean waves. *J. Geophys. Res.*, Vol. 70, No. 18, pp. 4561 - 4572.

Deigaard, R., Jacobsen, V. and Bryndum, M.B. (1985). A critical review of bottom boundary layer models with special attention to stability of marine pipelines. In: *Proc. 4th Int. Offshore Mechanics and Artic Engng. Symp.*, (eds.) Chung, J.S., Lunardini, V.J., Chakrabarti, S.K., Wang, Y.S., Sodhi, D.S. and Karal, K., 17 - 21 Feb., Dallas, Texas, Vol. 1, ASME, New York, pp. 542 - 549.

Deigaard, R., Justesen, P. and Fredsøe, J. (1986). *Two-dimensional circulation in the surf zone*. DCAMM Rep. 341, Tech. University of Denmark, Lyngby, 41 pp.

Dick, J.E. and Sleath, J.F.A. (1991). Velocities and concentrations in oscillatory flow over beds of sediment. *J. Fluid Mech.*, Vol. 233, pp. 165 - 196.

Drake, D.E. and Cacchione, D.A. (1985). Seasonal variation in sediment transport on the Russian River shelf, California. *Continental Shelf Res.*, Vol. 4, No. 5, pp. 495 - 514.

Drake, D.E. and Cacchione, D.A. (1986). Field observations of bed shear stress and sediment resuspension on continental shelves, Alaska and California. *Continental Shelf Res.*, Vol. 6, No. 3, pp. 415 - 429.

Du Toit, C.G. (1980). *Velocities Close to a Bed of Sand in Oscillatory Flow*. D. Phil. thesis, University of Cambridge, 183 pp.

Durbin, P.A. (1991). Near-wall turbulence closure modeling without damping functions. In: *Theoretical and Computational Fluid Dynamics*, Vol. 3, pp. 1.

Ellis, G.P., O'Connor, B.A. and McDowell, D.M. (1981). Generation of laboratory waves using a microcomputer. *2nd Int. Conf. on Engng. Software*, Imperial College, London, pp. 899 - 913.

Fredsøe, J. (1984). Turbulent boundary layer in wave-current motion. *J. Hydr. Engng.*, Vol. 110, No. 8, Aug., ASCE, New York, pp. 1103 - 1120.

Fujisawa, N., Rodi, W. and Schönung, B. (1990). Calculation of transitional boundary layers with a two-layer model of turbulence. In: *Proc. 3rd Int. Symp. on Transport Phenomena and Dynamics of Rotating Machinery*, Honolulu, Hawaii, April.

Gibson, M.M. and Launder, B.E. (1978). Ground effects on pressure fluctuations in the atmospheric boundary layer. *J. Fluid Mech.*, Vol. 86, Part 3, pp. 491 - 511.

Goda, Y. (1985). *Random Seas and Design of Maritime Structures*. University of Tokyo Press, Japan, 323 pp.

Goda, Y., Takayama, T. and Suzuki, Y. (1979). Diffraction diagrams for directional random waves. In: *Coastal Engng.*, Proc. 16th Coastal Engng. Conf., Hamburg, Germany, 27 Aug. - 3 Sept., 1978, Vol. 1, Chap. 35, ASCE, New York, pp. 628 - 650.

Grant, W.D. (1977). *Bottom Friction Under Waves in the Presence of a Weak Current: Its Relationship to Coastal Sediment Transport*. Sc.D. thesis, Mass. Inst. Technology, Cambridge, Massachusetts, USA, 275 pp.

Grant, W.D. and Madsen, O.S. (1979). Combined wave and current interaction with a rough bottom. *J. Geophys. Res.*, Vol. 84, No. C4, April, pp. 1797 - 1807.

Grant, W.D. and Madsen, O.S. (1982). Movable bed roughness in unsteady oscillatory flow. *J. of Geophys. Res.*, Vol. 87, No. C1, Jan. 20., pp. 469 - 481.

Grant, W.D. and Madsen, O.S. (1986). The continental-shelf bottom boundary layer. *Ann. Rev. Fluid Mech.*, Vol. 18, pp. 265 - 305.

Gross, T.F., Williams, A.J. and Terray, EA. (1994). Bottom boundary layer spectral dissipation estimates in the presence of wave motions. *Continental Shelf Res.*, Vol. 14, No. 10/11, pp. 1239 - 1256.

Guedes Soares, C. (1984). Representation of double-peaked sea wave spectra. *Ocean Engng.*, Vol. 11, No. 2, pp. 185 - 207.

Hagatun, K. and Eidsvik, K.J. (1986). Oscillating turbulent boundary layer with suspended sediments, *J. Geophys. Res.*, Vol. 91, No. C11, Nov., pp. 13,045 - 13,055.

Harlow, F.H. and Nakayama, P.I. (1967). Turbulence transport equations. *The Physics of Fluids*, Vol. 10, No. 11, Nov., pp. 2323 - 2332.

Harris, J.M., and O'Connor, B.A. (1997). *Use of Two-Layer k-ε Models in Modelling Wave Boundary Layers*. Dept. of Civil Engng., University of Liverpool. (*In preparation*).

Hasselmann, K., Barnett, T.P., Bouws, E., Carlson, H., Cartwright, D.E., Enke, K., Ewing, J.A., Gienapp, H., Hasselmann, D.E., Kruseman, P., Meerburg, A., Müller, P., Olbers, D.E., Richter, K., Sell, W. and Walden, H. (1973). *Measurements of wind-wave growth and swell decay during the joint North Sea wave project (JONSWAP)*. Deutsches Hydrographisches Inst., Reihe A (8^0), No. 12, Hamburg, 95 pp.

Hasselmann, K., Ross, D.B., Müller, P. and Sell, W. (1976). A parametric wave prediction model. *J. Phys. Oceanogr.*, Vol. 6, pp. 200 - 228.

Hedges, T.S. (1981). Some effects of currents on wave spectra. In: *Proc. 1st Indian Conf. in Ocean Engng. I.I.T*, Madras, Vol. 1, pp. 1.30 - 1.35.

Hedges, T.S. (1987). Combinations of waves and currents: an introduction. *Proc. Instn. Civil Engrs.*, Part 1 Design and Construction, Vol. 82, Jun., pp. 567 - 585.

Hedges, T.S., Burrows, R. and Mason, W.G. (1979*). Wave-current interaction and its effect on fluid loading*. Report No. MCE/ 3/79, Dept. Civil Engng., University of Liverpool, 139 pp.

Hedges, T.S., Anastasiou, C. and Gabriel, D. (1985). Interaction of random waves and currents. *J. Waterway, Port, Coastal and Ocean Engng.*, Vol. 111, No. 2, Mar., ASCE, New York, pp. 275 - 288.

Hedges, T.S., Tickell, R.G. and Akrigg, J. (1993). Interaction of short-crested random waves and large-scale currents. *Coastal Engng.*, Vol. 19, pp. 207 - 221.

Hino, M. (1963). Turbulent flow with suspended particles. *J. Hydr. Div.*, Vol. 89, No. HY4, ASCE, New York.

Hino, M., Kashiwayanagi, M., Nakayama, A. and Hara, T. (1983). Experiments on the turbulence statistics and the structure of a reciprocating oscillatory flow. *J. Fluid Mech.*, Vol. 131, pp. 363 - 400.

Hinze, J.O. (1959). *Turbulence. An Introduction to its Mechanism and Theory*. McGraw Hill, New York, 586 pp.

Horikawa, K. and Watanabe, A. (1968). Laboratory study on oscillatory boundary layer flow. *Coastal Engng. in Japan*, Vol. 11, pp. 13 - 28.

Huang, N.E., Chen, D.T., Tung, C.C. and Smith, J.R. (1972). Interaction between steady non-uniform currents and waves with applications for current measurement. *J. Phys. Oceanogr.*, Vol. 2, pp. 420 - 431.

Huang, N.E., Tung, C.C. and Long, S.R. (1990). Wave spectra. In: *The Sea*, (eds.) LeMeheute, B. and Hanes, D.M., Vol. 9, Part A, Chap. 6, Wiley-Interscience, New York, pp. 197 - 237.

Humphery, J.D. (1987). STABLE - an instrument for studying current structure and sediment transport in the benthic boundary layer. In: *5th Int. Conf. on Electronics for Ocean Technology,* 24 - 26th March, Heriot-Watt University, Edinburgh, Institute of Electronic and Radio Engineering, Pub. No. 72, pp 57 - 62.

Hunt, J.C.R. and Maxey, M.R. (1978). Estimating velocities and shear stresses in turbulent flows of liquid metals driven by low frequency electromagnetic fields. In: *MHD - Flows and Turbulence II,* (eds.) Branover, H. and Yakhot, A., Israel University Press pp. 249 - 269.

Huynh-Thanh, S. and Temperville, A. (1991). A numerical model of the rough turbulent boundary layer in combined wave and current interaction. In: *Coastal Engng.*, Proc. 22nd Int. Coastal Eng. Conf., (ed.) Edge, B.L., Delft, The Netherlands, 2 - 6 July, 1990, Vol. 1, Chap. 65, ASCE, New York, pp. 853 - 866.

Huynh-Thanh, S. and Temperville, A. (1991). A numerical model of the rough turbulent boundary layer in combined wave and current interaction. In: *Sand Transport in Rivers, Estuaries and the Sea,* (eds.) Soulsby, R.L. and Bettess, R., EUROMECH 262, 26 - 29 June, 1990, Balkema, Rotterdam, pp. 93 - 100.

Iacovides, H. and Launder, B.E. (1987). The numerical simulation of flow and heat transfer in tubes in orthogonal-mode rotation. In: *Proc. 6th Symp. on Turbulent Shear Flows,* Toulouse, France.

Iwagaki, Y. and Kakinuma, T. (1963). On the bottom friction factor of the Akita coast. *Coastal Engng. in Japan,* Vol. 6, pp. 83 - 91.

Iwagaki, Y. and Kakinuma, T. (1967). On the bottom friction factors off five Japanese coasts. *Coastal Engng. in Japan,* Vol. 10, pp. 13 - 22.

Jacobs, S.J. (1984). Mass transport in a turbulent boundary layer under a progressive water wave. *J. Fluid Mech.*, Vol. 146, pp. 303 - 312.

Jensen, B.L. (1989). *Experimental investigation of turbulent oscillatory boundary layers.* Series Paper 45, Inst. Hydrodyn. and Hydr., Tech. University of Denmark, Lyngby.

Jensen, B.L., Sumer, B.M. and Fredsøe, J. (1989). Turbulent oscillatory boundary layers at high Reynolds numbers. *J. Fluid Mech.*, Vol. 206, pp. 265 - 297.

Johns, B. (Ed.), 1983: Physical oceanography of coastal and shelf seas, Elsevier Oceanography Series, No. 35, Elsevier, Amsterdam, p.470.

Johns, B. (1975). The form of the velocity profile in a turbulent shear wave boundary layer. *J. Geophys. Res.*, Vol. 80, No. 36, Dec., pp. 5109 - 5112.

Johns, B. (1977). Residual flow and boundary shear stress in the turbulent bottom layer beneath waves. *J. Phys. Oceanogr.*, Vol. 7, Sept., pp. 733 - 738.

Jones, W.P. and Launder, B.E. (1972). The prediction of laminarization with a two-equation model of turbulence. *Int. J. Heat Mass Transfer*, Vol. 15, pp. 301 - 314.

Jones, W.P. and Launder, B.E. (1973). The calculation of low-Reynolds-number phenomena with a two-equation model of turbulence. *Int. J. Heat Mass Transfer*, Vol. 16, pp. 1119 - 1130.

Jonsson, I.G. (1963). Measurements in the turbulent wave boundary layer. In: *Proc. 10th Congr. Int. Ass. Hydr. Res. IAHR*, London, Vol. 1, paper 1.12, pp. 85 - 92.

Jonsson, I.G. (1965). On turbulence in open channel flow. Statistical theory applied to micropropeller measurements. *Acta Polytech. Scand.*, Ci 31, 48 pp.

Jonsson, I.G. (1967). Wave boundary layers and friction factors. In: *Coastal Engng.*, Proc. 10th Conf. on Coastal Engng., Tokyo, Japan, Sept., 1966, Vol. 1, Chap. 10, ASCE, New York, pp. 127 - 148.

Jonsson, I.G. (1976). Discussion of: Friction factor under oscillatory waves, by Kamphuis, J.W., *J. Waterways, Harbors and Coastal Engng. Div.*, Vol. 102, ASCE, New York, pp. 108 - 109.

Jonsson, I.G. (1978a). *A New Approach to Oscillatory Rough Turbulent Boundary Layers.* Series Paper 17, Inst. Hydrodyn. and Hydr., Tech. University of Denmark, Lyngby, 79 pp.

Jonsson, I.G. (1978b). Combinations of waves and currents. In: *Stability of Tidal Inlets Theory and Engng.*, (ed.) Brunn, P., Chap. 3.2, Developments in Geotechnical Engng., Elsevier, Amsterdam, The Netherlands, pp. 162 - 203.

Jonsson, I.G. (1980). A new approach to oscillatory rough turbulent boundary layers. *Ocean Engng.*, Vol. 7, No. 1, pp. 109 - 152.

Jonsson, I.G. (1990). Wave-current interactions. In: *The Sea*, (eds.) LeMeheute, B. and Hanes, D.M., Vol. 9, Part A, Chap. 3, Wiley-Interscience, New York, pp. 65 - 120.

Jonsson, I.G. and Carlsen, N.A. (1976). Experimental and theoretical investigations in an oscillatory turbulent boundary layer. *J. Hydr. Res.*, Vol. 14, No. 1, pp. 45 - 60.

Justesen, P. (1988a). *Turbulent Wave Boundary Layers*. Series Paper 43, Inst. Hydrodyn. and Hydr., Tech. University of Denmark, Lyngby, 226 pp.

Justesen, P. (1988b). Prediction of turbulent oscillatory flow over rough beds. *Coastal Engng.*, Vol. 12, pp. 257 - 284.

Justesen, P. (1990). A note on turbulence calculations in the wave boundary layer. *Prog. Rep.*, No. 71, Inst. Hydrodyn. and Hydr. Engng., Tech University of Denmark, Lyngby, pp. 37 - 50.

Justesen, P. (1991). A note on turbulence calculations in the wave boundary layer. *J. Hydr. Res.*, Vol. 29, No. 5, pp. 699 - 711.

Kaczmarek, L.M. (1995). Nonlinear effects of waves and currents on moveable bed roughness and friction. *Archives of Hydro-Engng. and Environmental Mech.*, Vol. 42, No. 1 - 2, pp. 3 - 27.

Kaczmarek, L.M. and Ostrowski, R. (1995). Modelling of bed shear stress under irregular waves. *Archives of Hydro-Engng. and Environmental Mech.*, Vol. 42, No. 1 - 2, pp. 29 - 51.

Kaczmarek, L.M., Harris, J.M. and O'Connor, B.A. (1995). Modelling moveable bed roughness and friction for spectral waves. In: *Coastal Engng. 1994*, Proc. 24th Int. Conf. Coastal Engng., (ed.) Edge, B.L., Kobe, Japan, 23 - 28 Oct., 1994, Vol. 1, Chap. 23, ASCE, New York, pp. 300 - 314.

Kajiura, K. (1964). On the bottom friction in an oscillatory current. *Bul. Earthquake Res. Inst.*, University of Tokyo, Vol. 42, pp. 147 - 174.

Kajiura, K. (1968). A model of the bottom boundary layer in water waves. *Bul. Earthquake Res. Inst.*, University of Tokyo, Vol. 46, pp. 75 - 123.

Kamphuis, J.W. (1975). Friction factor under oscillatory waves. *J. Waterways, Harbors and Coastal Engng.*, Vol. 101, No. WW2, May, ASCE, New York, pp. 135 - 144.

Kemp, P.H. and Simons, R.R. (1982). The interaction between waves and a turbulent current: waves propagating with the current. *J. Fluid Mech.*, Vol. 116, pp. 227 - 250.

Kemp, P.H. and Simons, R.R. (1983). The interaction of waves and a turbulent current: waves propagating against the current. *J. Fluid Mech.*, Vol. 130, pp. 73 - 89.

Kennedy, J.F. and Falcon, M. (1965). *Wave Generated Sediment Ripples*. Report No. 86, Mass. Inst. Tech., Cambridge, Massachusetts, USA.

Kim, J., Moin, P. and Moser, R. (1987). Turbulence statistics in fully developed channel flow at low Reynolds number. *J. of Fluid Mech.*, Vol. 177, pp. 133 - 166.

King, D.B., Powell, J.D. and Seymour, R.J. (1985). A new oscillatory flow tunnel for use in sediment transport experiments. In: *Coastal Engng.*, Proc. 19th Int. Conf. on Coastal Engng., (ed.) Edge, B.L., Houston, Texas, 3 - 7 Sept., 1984, Vol. 2, Chap. 106, ASCE, New York, pp. 1559 - 1570.

King, H.L., Davies, A.G. and Soulsby, R.L. (1985). *A numerical model of the turbulent boundary layer beneath surface waves and tides*. Report No. 196, Inst. Oceanographic Sciences, NERC, 90 pp.

Kitaigordskii, S.A., Krasitskii, V.P. and Zaslavskii, M.M. (1975). On Phillips' theory of equilibrium range in the spectra of wind generated gravity waves. *J. Geophys. Res.*, Vol. 5, pp. 410 - 420.

Kline, S.J., Cartwell, B.J. and Lilley, G.M. (1981). Comparison of computation and experiment. In: *The 1980-81 AFOSR-HTTM-Stanford Conf. on Complex Turbulent Flows*, Vol. 1, Mechanical Engng. Dept., Thermosciences Div., Stanford University, Stanford, California.

Kyriacou, A. (1988). *Wave Height Attenuation in The Presence of a Current*. Ph.D. thesis, University of London, 478 pp.

Lam, C.K.G. and Bremhorst, K. (1981). A modified form of the k-ε model for predicting wall turbulence. *J. Fluids Engng.*, Trans. of ASME, Vol. 103. Sept., pp. 456 - 460.

Lamb, H. (1932). *Hydrodynamics*. 6th edition, Cambridge University Press, Cambridge, UK., 738 pp.

Lambie, J.M. (1984). *An Experimental Study of the Stability of Oscillatory Flow Bed Configurations*. M. S. thesis, Mass. Inst. Tech., Cambridge, Massachusetts, USA.

Lambrakos, K.F. (1985). Tidal boundary layer measurements in the presence of waves. *Ocean Engng.*, Vol. 12, No. 4, pp 271 - 291.

Lambrakos, K.F., Myrhaug, D. and Slaattelid, O.H. (1988). Seabed current boundary layers in wave-plus-current flow conditions. *J. of Waterway, Port, Coastal and Ocean Engng.*, Vol. 114, No. 2, March, ASCE, New York, pp. 161 - 174.

Launder, B.E. and Spalding, D.B. (1974). The numerical computation of turbulent flows. *Computer Methods in Applied Mech. and Engng.*, Vol. 3, pp. 269 - 289.

Lavelle, J.W. and Mofjeld, H.O. (1983). Effects of time-varying viscosity on oscillatory turbulent channel flow. *J. Geophys. Res.*, Vol. 88, No. C12, pp. 7607 - 7616.

Lewis, A.W., Hitching, E., Perrier, G., Asp Hansen, E., Earnshaw, H., Eidsvik, K., Greated, C., Sumer, M. and Temperville, A. (1996). Flow over vortex ripples: Models and experiments. In: *Coastal Dynamics '95*, (eds.) Dally, W.R. and Zeidler, R.B., Gdansk, Poland, 4 - 8 Sept., ASCE, New York, pp. 686 - 697.

Lofquist, K.E.B. (1978). *Sand Ripple Growth in an Oscillatory Flow Water tunnel.* TP-78-5, US Army Corps of Engrs., CERC.

Lofquist, K.E.B. (1981). Measurements of oscillatory drag on sand ripples. In: *Coastal Engng.*, Proc. 17th Int. Conf. Coastal Engng., Sydney, ASCE, New York, pp. 3087 - 3106.

Lofquist, K.E.B. (1986). *Drag on Naturally Rippled Beds Under Oscillatory Flows.* MP-86-13, US Army Corps of Engrs., CERC.

Lundgren, H. (1973). Turbulent currents in the presence of waves. In: *Coastal Engng.*, Proc. 13th Coastal Engng. Conf., Vancouver, B.C., Canada, 10 - 14 July, 1972, Vol. 1, Chap. 33, ASCE, New York, pp. 623 - 634.

Lundgren, H. and Sørensen, T. (1958). A pulsating water tunnel. In: *Coastal Engng.*, Proc. 6th Coastal Engng. Conf., Miami, Florida, 1957, pp. 356 - 358.

Madsen, O.S. (1995). Spectral wave-current boundary layer flows. In: *Coastal Engng. 1994*, Proc. 24th Int. Conf. Coastal Engng., (ed.) Edge, B.L., Kobe, Japan, 23 - 28 Oct., 1994, Vol. 1, Chap. 29, ASCE, New York, pp. 384 - 398.

Madsen, O.S., and Rosengaus, M.M. (1989). Spectral wave attenuation by bottom friction: Experiments. In: *Coastal Engng.*, Proc. 21st Int. Conf. Coastal Engng., (ed.) Edge, B.L., Malaga, Spain, June, 1988, Vol. 1, Chap. 63, ASCE, New York, pp. 849 - 857.

Madsen, O.S., Poon, Y.K. and Graber, H.C. (1989). Spectral wave attenuation by bottom friction: Theory. In: *Coastal Engng.*, Proc. 21st Int. Conf. Coastal Engng., (ed.) Edge, B.L., Malaga, Spain, June, 1988, Vol. 1, Chap. 34, ASCE, New York, pp. 492 - 504.

Madsen, O.S., Mathisen, P.P. and Rosengaus, M.M. (1991). Movable bed friction factors for spectral waves. In: *Coastal Engng.*, Proc. 22nd Int. Conf. Coastal Engng., (ed.) Edge, B.L., Delft, The Netherlands, 2 - 6 July, 1990, Vol. 1, Chap. 32, ASCE, New York, pp. 420 - 429.

Mansour, N.N., Kim, J. and Moin, P. (1987). Near-wall k-ε turbulence modelling. *NASA Tech. Memo.*, TM-89461, Ames Res. Center, Moffett Field, California, 21 pp.

Mathisen, P.P. (1989). *Experimental Study on The Response of Fine Sediments to Wave Agitation and Associated Wave Attenuation.* M.Sc. thesis, Mass. Inst. of Technology, Cambridge, Massachusetts, USA.

McDowell, D.M. (1983). Sediment transport due to waves and currents. In: *Mechanics of Sediment Transport*, Proc. EUROMECH 156, Istanbul, 12 - 14 July, 1982, (eds.) Sumer, B.M. and Müller, A., A.A. Balkema, Rotterdam, pp. 281 - 285.

Mitsuyasu, H., Tasai, F., Suhara, T., Mizuno, S., Ohkusu, M., Honda, T. and Rikiishi, K. (1975). Observations of the directional spectrum of ocean waves using a cloverleaf buoy, *J. Phys. Oceanogr.*, Vol. 5, pp. 750 - 760.

Mogridge, G.R. and Kamphuis, J.W. (1973). Experiments on bed form generation by wave action. In: *Coastal Engng.*, Proc. 13th Coastal Engng. Conf., Vancouver, B.C., Canada, 10 - 14 July, 1972, Vol. 2, Chap. 60, ASCE, New York, pp. 1123 - 1142.

Myrhaug, D. (1982). On a theoretical model of rough turbulent wave boundary layers. *Ocean Engng.*, Vol. 9, No. 6, pp. 547 - 565.

Myrhaug, D. (1989). A rational approach to wave friction coefficients for rough, smooth and transitional turbulent flow. *Coastal Engng.*, Vol. 13, pp. 11 - 21.

Myrhaug, D. (1995). Bottom friction beneath random waves. *Coastal Engng.*, Vol. 24, No. 3-4, March, pp. 259 - 273.

Myrhaug, D., Lambrakos, K.F. and Slaattelid, O.H. (1992). Wave boundary layer in flow measurements near the seabed. *Coastal Engng.*, Vol. 18, pp. 153 - 181.

Nadaoka, K., Kondo, T. and Tanaka, N. (1982). The structure of velocity field within the surf zone revealed by means of laser-Doppler anemometry. *Report of the Port and Harbor Res. Inst.*, Vol. 21, No. 2, pp. 49 - 106. (*In Japanese*).

Nielsen, P. (1979). *Some Basic Concepts of Wave Sediment Transport.* Series Paper 20, Inst. Hydrodyn. and Hydr., Tech. University of Denmark, Lyngby, 160 pp.

Nielsen, P. (1981). Dynamics and geometry of wave generated ripples. *J. Geophys. Res.*, Vol. 86, C7, July 20, pp. 6467 - 6472.

Nielsen, P. (1983). Analytical determination of nearshore wave height variation due to refraction, shoaling and friction. *Coastal Engng.*, Vol. 7, pp. 233 - 251.

Nielsen, P. (1985). *A Short Manual of Coastal Bottom Boundary Layers and Sediment Transport.* Tech. Memo., T.M. 85/1, Public Works Dept. N.S.W., Nov., 56 pp.

Nielsen, P. (1992). *Coastal Bottom Boundary Layers and Sediment Transport.* Advanced Series on Ocean Engng., Vol. 4, World Scientific, Singapore, 324 pp.

Norris, H.L. (1975). *Turbulent Channel Flow With a Moving Wavy Boundary.* Ph.D. thesis, Stanford University, May, 213 pp.

Ockenden, M.C. and Soulsby, R.L. (1994). *Sediment Transport by Currents Plus Irregular Waves.* Report SR 376, Feb., HR Wallingford, 23 pp.

O'Connor, B.A. (1987). Wave-current interactions. In: *Extended Abstracts of EUROMECH 215 Mechanics of Sediment Transport in Fluvial and Marine Environments*, (ed.) Margherita, S., Ligure, Genoa, Italy, 4 pp.

O'Connor, B.A. (ed.) (1996). *CSTAB Handbook and Final Report.*, Vols. I and II, Report Nos. CE/05/96 and CE/06/96, Dept. of Civil Engng., University of Liverpool, pp. 247 - 303.

O'Connor, B.A., Tickell, R.G., Jones, E. and Taplin, M. (1988). Hydrodynamics of random wave current boundary layers. In: *Coastal Impact Modelling*, Vol. 4, Appendix N, Dept. of Civil Engng., University of Liverpool, 23 pp.

O'Connor, B.A., Harris, J.M., Kim, H., Wong, Y.K., Oebius, H. and Williams, J.J. (1993). Bed boundary layers. In: *Coastal Engng. 1992*, Proc. 23rd Int. Conf. Coastal Engng., (ed.) Edge, B.L., Venice, Italy, 4 - 9 Oct., 1992, Vol. 2, Chap. 177, ASCE, New York, pp. 2307 - 2320.

O'Connor, B.A., Kim, H.S. and Williams, J.J. (1994). Hydrodynamics of random wave boundary layers. In: *Coastal Dynamics '94*, Proc. Int. Conf. on the Role of the Large Scale Exps. in Coastal Res., (eds.) -Arcilla, A.S., Stive, M.J.F. and Kraus, N.C., Barcelona, Spain, 21 - 25 Feb., ASCE, New York, pp. 879 - 893.

Ostrowski, R. (1993). *Bottom Friction Induced by Surface Waves and Current With Non-Linear Effects.* Ph.D. thesis, IBW PAN, Gdansk, Poland. (*In Polish*).

Patel, M.H. (1981). An integral method for the oscillating turbulent boundary layer. *The Aeronautical Quart.*, Vol. XXXII, Feb. - Nov., pp. 271 - 298.

Patel, V.C., Rodi, W. and Scheuerer, G. (1985). Turbulence models for near-wall and low Reynolds number flows: A review. *AIAA Journal*, Vol. 23, No. 9, pp. 1308 - 1319.

Pierson, W.J. and Moskowitz, L. (1964). A proposed spectral form for fully developed wind seas based on the similarity theory of S.A. Kitaigordskii. *J. Geophys. Res.*, Vol. 69, No. 24, pp. 5181 - 5190.

Pierson, W.J., Neumann, G. and James, R.W. (1955). Practical methods for observing and forecasting ocean waves by means of wave spectra and statistics. H.O. Pub. No. 603, US Naval Oceanographic Office, 284 pp.

Phillips, O.M. (1958). The equilibrium range in the spectrum of wind-generated waves. *J. Fluid Mech.*, Vol. 4, pp. 246 - 434.

Prandtl, L. (1925). Über die ausgebildete Turbulenz. *ZAMM 5*, pp. 136 - 139.

Reynolds, O. (1894). On the dynamical theory of incompressible viscous fluids and the determination of the criterion. *Phil. Trans. Royal Soc.*, Series A, Vol. 186, Royal Soc., London, pp. 123 - 164.

Ribberink, J.S. and Al-Salem, A.A. (1992). *Time Dependent Sediment Transport Phenomena in Oscillatory Boundary Layer Flow Under Sheet Flow Conditions*. Data report H 840, 20 Part 5, Dec., Delft Hydraulics, The Netherlands.

Ribberink, J.S. and Al-Salem, A.A. (1994). Sediment transport in oscillatory boundary layers in cases of rippled beds and sheet flow. *J. Geophys. Res.*, Vol. 99, No. C6, June, pp. 12,707 - 12,727.

Roach, P.J. (1977). *Computational Fluid Dynamics*. Hermosa, Albuquerque, 446 pp.

Rodi, W. (1980). *Turbulence Models and Their Application in Hydraulics - A State of the Art Review*. IAHR, Delft, The Netherlands, 104 pp.

Rodi, W. (1991). Experience with two-layer models combining the k-ε model with a one-equation model near the wall. In: *29th Aerospace Sciences Meeting*, Reno, Nevada, 7 - 10 Jan., Paper AIAA-91-0216, 12 pp.

Rodi, W. and Scheuerer, G. (1986). Scrutinizing the k-ε turbulence model under adverse pressure gradient conditions. *J. Fluids Engng.*, Trans. ASME, Vol. 108, June, pp. 174 - 179.

Rodi, W., Mansour, N.N. and Michelassi, V. (1993). One-equation near-wall turbulence modeling with the aid of direct simulation data. *J. Fluids Engng.*, Trans. ASME, Vol. 115, June, pp. 196 - 205.

Roisin, J.P. (1985). *Sediment Mixing Processes*. M.Sc. thesis, University of Manchester, 98 pp.

Rosengaus, M. (1987). *Experimental Study on Wave Generated Bedforms and Resulting Wave Attenuation*. Ph.D. thesis, Mass. Inst. of Technology, Cambridge, Massachusetts, USA.

Saffman, P.G. (1970). A model for inhomogeneous turbulent flow. *Proc. Royal Soc.*, Series A, Vol. 317, Royal Soc., London, pp. 417 - 433.

Saffman, P.G. (1974). Model equations for turbulent shear flow. *Studies in Appl. Maths.*, Vol. LIII, No. 1, Mar., pp. 17 - 34.

Sarapkaya, T. and Rajabi, F. (1979). Hydrodynamic drag on bottom-mounted smooth and rough cylinders in periodic flow. In: *Proc. 11th Annual Offshore Technology Conf.*, Houston, Texas, pp. 219 - 226.

Sato, S. (1987). *Oscillatory Boundary Layer Flow and Sand Movement Over Ripples*. Ph.D. thesis, University of Tokyo, 135 pp.

Sato, S., Mimura, N. and Watanabe, A. (1985) Oscillatory boundary layer flow over rippled beds. In: *Coastal Engng.*, Proc. 19th Int. Conf. Coastal Engng., (ed.) Edge, B.L., Houston, Texas, 3 - 7 Sept., 1984, Vol. 3, Chap. 154, ASCE, New York, pp. 2293 - 2309.

Savell, I.A. (1986). *An Experimental Study of Near-Bed Hydrodynamics Under a Combination of Waves and Steady Current and the Effect of this on Sediment Transport*. Ph.D. thesis, University of Manchester, 127 pp.

Sheng, Y.P. (1985). A turbulent model of coastal processes. In: *Coastal Engng.*, Proc. 19th Int. Conf. Coastal Engng., (ed.) Edge, B.L., Houston, Texas, 3 - 7 Sept., 1984, Vol. 3, Chap. 160, ASCE, New York, pp. 2380 - 2396.

Sheng, Y.P. (1987). Modelling turbulent boundary layer dynamics. In: *Coastal Engng.*, Proc. 20th Int. Conf. Coastal Engng., (ed.) Edge, B.L., Taipei, Taiwan, 9 - 14 Nov., 1986, Vol. 2, Chap. 110, ASCE, New York, pp. 1497 - 1508.

Shibayama, T. (1984). *Sediment Transport Mechanism and Two-Dimensional Beach Transformation Due to Waves*. D. Eng. thesis, University of Tokyo, Aug., 159 pp.

Shih, T.H. and Mansour, N.N. (1990). Modelling of near-wall turbulence. In: *Engng. Turbulence Modelling and Experiments*, (eds.) Rodi, W. and Ganic, E.N., Elsevier, The Netherlands, pp. 13 - 22.

Shima, N. (1993). Prediction of turbulent boundary layers with a second-moment closure: Part I - effects of periodic pressure gradient, wall transpiration, and free-stream turbulence. *J. Fluids Engng.*, Trans. of ASME, Vol. 115, Mar., pp. 56 - 63.

Simons, R.R., Kyriacou A., Soulsby, R.L. and Davies, A.G. (1988). Predicting the nearbed turbulent flow in waves and currents. In: *Proc. IAHR, Symp. on Math. Modelling of sediment Transport in the Coastal Zone*, Copenhagen, Denmark, 30 May - 1 Jun., pp. 33 - 47.

Simons, R.R., Grass, A.J., Saleh, W.M. and Tehrani, M.M. (1995). Bottom shear stresses under random waves with a current superimposed. In: *Coastal Engng. 1994*, Proc. 24th Int. Conf. on Coastal Engng., (ed.) Edge, B.L., Kobe, Japan, 23 - 28 Oct., Vol. 1, Chap. 42, ASCE, New York, pp. 565 - 578.

Sleath, J.F.A. (1984). *Sea Bed Mechanics*. John Wiley and Sons, New York, 335 pp.

Sleath, J.F.A. (1985). Energy dissipation in oscillatory flow over rippled beds. *Coastal Engng.*, Vol. 9, pp. 159 - 170.

Sleath, J.F.A. (1987). Turbulent oscillatory flow over rough beds. *J. Fluid Mech.*, Vol. 182, pp. 369 - 409.

Sleath, J.F.A. (1990). Seabed boundary layers. In: *The Sea*, (eds.) LeMeheute, B. and Hanes, D.M., Vol. 9, Part B, Chap. 20, Wiley-Interscience, New York, pp. 693 - 727.

Sleath, J.F.A. (1991a). Velocities and shear stresses in wave-current flows. *J. Geophys. Res.*, Vol. 96, No. C8, pp. 15,237 - 15,244.

Sleath, J.F.A. (1991b). Velocities and bed friction in combined flows. In: *Coastal Engng.*, Proc. 22nd Int. Conf. Coastal Engng., (ed.) Edge, B.L., Delft, The Netherlands, Vol. 1, Chap. 35, ASCE, New York, pp. 450 - 463.

Smith, G.D. (1985). *Numerical Solution of Partial Differential Equations: Finite Difference Methods*. Third edition, Oxford University Press, 337 pp.

Smith, J.D. (1977). Modeling of sediment transport on continental shelves. In: *The Sea: Ideas and Observations on Progress in the Study of the Seas*, (eds.) Goldberg, E.D., McCave, I.N., O'Brien, J.J. and Steele, J.H., Vol. 6, Marine Modelling, Chap. 13, Wiley-Interscience, New York, pp. 539 - 577.

Smith, T.J. and Takhar, H.S. (1977). *The Calculation of Oscillatory Flow in Open Channels Using Mean Turbulence Energy Models.* HHS/77/01, Simon Engng. Laboratories, University of Manchester, 27 pp.

Solomou, D.A. (1987). *Numerical Modelling of Wave/Current Interactions.* M.Sc. Thesis, University of Liverpool, 141 pp.

Soulsby, R.L. (1983). The bottom boundary layer on shelf seas. In: *Physical Oceanography of Coastal and Shelf Seas*, (ed.) Johns, B., Chap. 5, Elsevier Oceanography Series, Elsevier, Amsterdam, pp. 189 - 266.

Soulsby, R.L. (1994). *Manual of Marine Sands.* Report SR 351, Oct., HR Wallingford, 70 pp.

Soulsby, R.L. and Humphery, J.D. (1990). Field observations of wave-current interaction at the sea bed. In: *Water Wave Kinematics,* (eds.) Tørum, A. and Gudmestad, O.T., Proc. of the NATO Advanced Res. Workshop on Water Wave Kinematics, Molde, Norway, 22 - 25 May 1989, Kluwer Academic Publishers, Dordrecht, pp. 413 - 428.

Spalart, P.R. (1988). Direct simulation of a turbulent boundary layer up to $R_\theta = 1410$. *J. of Fluid Mech.*, Vol. 187, pp. 61 - 98.

Spalart, P.R. and Baldwin, B.S. (1987). Direct simulation of a turbulent oscillating boundary layer. *NASA Tech. Memorandum 89460,* NASA, May, Ames Res. Center, Moffett Field, California, 6 pp.

Stokes, G.G. (1851). On the effect of the internal friction of fluids on the motion of pendulums. *Trans. Cambridge Phil. Soc.*, Vol. 9, pp. 8 - 106.

Sumer, B.M., Jensen, B.L. and Fredsøe, J. (1986). Experimental investigation of turbulent oscillatory boundary layer flows. In: *3rd Int. Symposium on Applications of Laser Anemometry to Fluid Mech.*, July 7 -9, Lisbon, Portugal, 6 pp.

Sumer, B.M., Jensen, B.L. and Fredsøe, J. (1987). Turbulence in oscillatory boundary layers, In: *Advances in Turbulence*, (eds.) Comte-Bellot, C. and Mathieu, J., Springer-Verlag, Berlin, pp. 556 - 567.

Supharatid, S., Tanaka, H. and Shuto, N. (1993). Interaction of nonlinear wave and current. In: *Coastal Engng. 1992*, Proc. 23rd Int. Conf. Coastal Engng., (ed.) Edge, B.L., Venice, Italy, 4 - 9 Oct., 1992, Vol. 1, Chap. 50, ASCE, New York, pp. 672 - 683.

Svendsen, I.A. and Jonsson, I.G. (1976). *Hydrodynamics of Coastal Regions*. Tech. University of Denmark, Lyngby, 282 pp.

Swart, D.H. (1974). *Offshore Sediment Transport and Equilibrium Beach Profiles*. Pub. 131, Delft Hydraulics Laboratory, The Netherlands, 302 pp.

Swart, D.H. (1977). Predictive equations regarding coastal transports. In: *Coastal Engng.*, Proc. 15th Coastal Engng. Conf., Honolulu, Hawaii, 11 - 17 July, 1976, Vol. 2, Chap. 66, ASCE, New York, pp. 1113 - 1132

Takayama, T. (1990). Laboratory wave generation. In: *The Sea*, (eds.) LeMeheute, B. and Hanes, D.M., Vol. 9, Part B, Chap. 31, Wiley-Interscience, New York, pp. 1007 - 1032.

Takhar, H.S. and Thomas, T.G. (1991*). Turbulent Mass Transport and Attenuation in Stokes Waves*. Internal Rep., Simon Engng. Laboratories, University of Manchester, 72 pp.

Tanaka, H. (1989). Bottom boundary layer under nonlinear wave motion. *J. Waterway, Port, Coastal and Ocean Eng.*, Vol. 115, No. 1, Jan., ASCE, New York, pp. 40 - 57.

Tanaka, H. and Sana, A. (1994). Numerical study on transition to turbulence in a wave boundary layer. In: *Sediment Transport Mechanisms in Coastal Environments and Rivers*, (eds.) Bélorgey, M., Rajaona, R.D. and Sleath, J.F.A., EUROMECH 310, 13 - 17 Sept., 1993, World Scientific, Singapore, pp. 14 - 25.

Taplin, M.G. (1988). *Hydrodynamics of Wave/Current Flows*. M.Sc. thesis, University of Manchester, 141 pp.

Tickell, R.G. (1985). *Short-Term Wave Statistics*. Lecture notes on ocean waves for engng. design, Dept. of Civil Engng., University of Liverpool, 37 pp.

Tolman, H.L. (1994). Wind waves and moveable-bed bottom friction. *J. Phys. Oceanogr.*, Vol. 24, No. 5, May, pp. 994 - 1009.

Townsend, A.A. (1976). *The Structure of Turbulent Shear Flow*. Second edition, Cambridge University Press, 429 pp.

Treloar, P.D. and Abernethy, C.L. (1978). Determination of a bed friction factor for Botany Bay, Australia. *Coastal Engng.*, Vol. 2, pp. 1 - 20.

Trowbridge, J. and Madsen, O.S. (1984a). Turbulent wave boundary layers 1: Model formulation and first-order solution. *J. Geophys. Res.*, Vol. 89, No. C5, Sept., pp. 7989 - 7997.

Trowbridge, J. and Madsen, O.S. (1984b). Turbulent wave boundary layers 2: Second-order theory and mass transport. *J. Geophys. Res.*, Vol. 89, No. C5, Sept., pp. 7999 - 8007.

Trowbridge, J.H., Kanetkar, C.N. and Wu, N.T. (1987). Numerical simulation of turbulent wave boundary layers. In: *Coastal Engng.*, Proc. 20th Int. Conf. Coastal Engng., (ed.) Edge, B.L., Taipei, Taiwan, 9 - 14 Nov., 1986, Vol. 2, Chap. 119, ASCE, New York, pp. 1623 - 1637.

Utnes, T. (1988). Two-equation (k-ε) turbulence computations by the use of a finite element model. *Int. J. Numerical Methods in Fluids*, Vol. 8, pp. 965 - 975.

Utnes, T. and Eidsvik, K.J. (1995). *Computation of Cyclic Oscillatory Flow Over Ripples.* Report No. R-10-95, Dept. of Structural Engng., University of Trondheim, Norway, Sept. 14, 12 pp.

Vager, B.G. and Kagan, B.A. (1969). The dynamics of the turbulent boundary layer in a tidal current. *Atmosph. and Ocean Physics*, Vol. 5, No. 2, pp. 168 - 179.

Vager, B.G. and Kagan, B.A. (1971). Vertical structure and turbulence in a stratified boundary layer in a tidal flow. *Atmosph. and Ocean Physics*, Vol. 7, pp. 516 - 522.

Van Doorn, T. (1981). *Experimental Investigation Of Near Bottom Velocities In Water Waves Without And With A Current.* Report M1423, Part 1, Delft Hydraulics, The Netherlands.

Van Kesteren, W.G.M. and Bakker, W.T. (1985). Near bottom velocities in waves with a current; analytical and numerical computations. In: *Coastal Engng.*, Proc. 19th Int. Conf. Coastal Engng., (ed.) Edge, B.L., Houston, Texas, 3 - 7 Sept., 1984, Vol. 2, Chap. 79, ASCE, New York, pp. 1161 - 1177.

Vincent, G.E. (1958). Contribution to the study of sediment transport on a horizontal bed due to wave action. In: *Coastal Engng.*, Proc. 6th Coastal Engng. Conf., Miami, Florida, 1957, Chap. 20, ASCE, New York, pp. 326 - 355.

Vongvisessomjai, S. (1984). Oscillatory boundary layer and eddy viscosity, *J. Hydr. Engng.*, Vol. 110, No. 4, April, ASCE, New York, pp. 387 - 404.

Vongvisessomjai, S. (1987). Wave friction factor on sand ripples. In: *Coastal Sediments '87*, Speciality Conf., ASCE, New York, pp. 393 - 407.

Vongvisessomjai, S., Munasinghe, L.C.J. and Gunaratna, P.P. (1987). Transient ripple formation and sediment transport. In: *Coastal Engng.*, Proc. 20th Int. Conf. Coastal Engng., (ed.) Edge, B.L., Taipei, Taiwan, 9 - 14 Nov., 1986, Vol. 2, Chap. 120, ASCE, New York, pp. 1638 - 1652.

Wiberg, P.L. (1995). A theoretical investigation of boundary layer flow and bottom shear stress for smooth, transitional, and rough flow under waves. *J. Geophys. Res.*, Vol. 100, No. C11, Nov. 15, pp. 22,667 - 22,679.

Wikramanayake, P.N. and Madsen, O.S. (1991). *Calculation of Moveable Bed Friction Factors.* Tech. Prog. Report, US Army Corps of Engrs., CERC, 105 pp.

Williams, J.J. (1996). Interactions between currents, waves and sediments. In: *CSTAB Handbook and Final Report*, (ed.) O'Connor, B.A., Vol. II, Chap. 8.1.2, Report No. CE/06/96, Dept. of Civil Engng., University of Liverpool, pp. 247 - 303.

Williams, J.J. (1997). *Personal communication.*

Wong, Y.K. (1984). *A numerical model for the interaction of combined wave and current boundary layers*. M.Sc. thesis, University of Manchester.

Wray, A.A. (1987). Minimal storage time-advancement schemes for spectral methods. *J. Comp. Phys.*

You, Z.J. (1996). Moveable bed roughness and current profiles in the presence of irregular waves with an arbitrary angle to currents. *Ocean Engng.*, Vol. 23, No. 3, pp. 225 - 242.

You, Z.J., Wilkinson, D.L. and Nielsen, P. (1991). Velocity distributions of waves and currents in the combined flow. *Coastal Engng.*, Vol. 15, pp. 525 - 543.

Appendix A

Derivation of The Exact k - Equation

The exact k - equation can be easily derived from the Navier-Stokes and continuity equations, equations (A.1) and (A.2), respectively. (see Harlow and Nakayama 1967; Rodi 1980)

$$\frac{\partial u_i}{\partial t} + u_j \frac{\partial u_i}{\partial x_j} = -\frac{1}{\rho}\frac{\partial p_i}{\partial x_i} + \frac{\partial}{\partial x_j}\left(\nu_t \frac{\partial u_i}{\partial x_j}\right) + g_i \qquad \textbf{(A.1)}$$

$$\frac{\partial u_i}{\partial x_i} = 0 \qquad \textbf{(A.2)}$$

If we assume a Reynolds decompostion (Reynolds 1894) such that u_i is defined by:-

$$u_i = \bar{u}_i + u_i' \qquad \textbf{(A.3)}$$

with $\bar{u}_i$ representing the mean velocity and u_i' the turbulent velocity fluctuation, equation (A.1) becomes

$$\frac{\partial(\bar{u}_i + u_i')}{\partial t} + (\bar{u}_j + u_j')\frac{\partial(\bar{u}_i + u_i')}{\partial x_j} = -\frac{1}{\rho}\frac{\partial(\bar{p}_i + p_i')}{\partial x_i} + \frac{\partial}{\partial x_j}\left(\nu_t \frac{\partial(\bar{u}_i + u_i')}{\partial x_j}\right) + g_i \qquad \textbf{(A.4)}$$

Multiplying equation (A.4) through by the turbulent velocity fluctuation u_i' and expanding gives:-

$$\begin{aligned} &u_i'\frac{\partial \bar{u}_i}{\partial t} + u_i'\frac{\partial u_i'}{\partial t} + u_i'\bar{u}_j\frac{\partial \bar{u}_i}{\partial x_j} + u_i'u_j'\frac{\partial \bar{u}_i}{\partial x_j} + u_i'\bar{u}_j\frac{\partial u_i'}{\partial x_j} + u_i'u_j'\frac{\partial u_i'}{\partial x_j} = \\ &-u_i'\frac{1}{\rho}\frac{\partial \bar{p}_i}{\partial x_i} - u_i'\frac{1}{\rho}\frac{\partial p_i'}{\partial x_i} + u_i'\frac{\partial}{\partial x_j}\left(\nu_t\frac{\partial \bar{u}_i}{\partial x_j}\right) + u_i'\frac{\partial}{\partial x_j}\left(\nu_t\frac{\partial u_i'}{\partial x_j}\right) \end{aligned} \qquad \textbf{(A.5)}$$

However, the definition of the time average of u_i' is zero such that

$$\overline{u_i'} = \lim_{T\to\infty}\frac{1}{T}\int_{t_o}^{t_o+T}(u_i - \bar{u}_i)dt \equiv 0 \qquad \textbf{(A.6)}$$

Where T is a turbulent averaging period, which is long compared to the frequency of the oscillation of the turbulence.

Therefore, time averaging equation (A.5)

$$\overline{u_i'\frac{\partial \bar{u}_i}{\partial t}} + \overline{u_i'\frac{\partial u_i'}{\partial t}} + \overline{u_i'\bar{u}_j\frac{\partial \bar{u}_i}{\partial x_j}} + \overline{u_i'u_j'\frac{\partial \bar{u}_i}{\partial x_j}} + \overline{u_i'\bar{u}_j\frac{\partial u_i'}{\partial x_j}} + \overline{u_i'u_j'\frac{\partial u_i'}{\partial x_j}} =$$
$$-\overline{u_i'\frac{1}{\rho}\frac{\partial \bar{p}_i}{\partial x_i}} - \overline{u_i'\frac{1}{\rho}\frac{\partial p_i'}{\partial x_i}} + \overline{u_i'\frac{\partial}{\partial x_j}\left(\nu_t\frac{\partial \bar{u}_i}{\partial x_j}\right)} + \overline{u_i'\frac{\partial}{\partial x_j}\left(\nu_t\frac{\partial u_i'}{\partial x_j}\right)} \qquad \textbf{(A.7)}$$

gives

$$\overline{u_i'\frac{\partial u_i'}{\partial t}} + \overline{u_i'u_j'}\frac{\partial \bar{u}_i}{\partial x_j} + \overline{u_i'\bar{u}_j\frac{\partial u_i'}{\partial x_j}} + \overline{u_i'u_j'\frac{\partial u_i'}{\partial x_j}} = -\overline{u_i'\frac{1}{\rho}\frac{\partial p_i'}{\partial x_i}} + \overline{u_i'\frac{\partial}{\partial x_j}\left(\nu_t\frac{\partial u_i'}{\partial x_j}\right)} \qquad \textbf{(A.8)}$$

The turbulent kinetic energy k, is defined as:-

$$k = \frac{1}{2}\overline{u_i'u_i'} \qquad \textbf{(A.9)}$$

Therefore equation (A.8) becomes:-

$$\frac{\partial k}{\partial t} + \bar{u}_j\frac{\partial k}{\partial x_j} = -\overline{u_i'\frac{1}{\rho}\frac{\partial p_i'}{\partial x_i}} - \overline{u_i'u_j'}\frac{\partial \bar{u}_i}{\partial x_j} - \overline{u_i'u_j'\frac{\partial u_i'}{\partial x_j}} + \overline{u_i'\frac{\partial}{\partial x_j}\nu_t\frac{\partial u_i'}{\partial x_j}} + \nu_t\overline{\frac{\partial u_i'}{\partial x_j}\frac{\partial u_i'}{\partial x_j}} \qquad \textbf{(A.10)}$$

If we now apply the decomposition rule (equation (A.3)) to the continuity equation , equation (A.2), then:-

$$\frac{\partial u_i}{\partial x_i} = \frac{\partial}{\partial x_i}(\bar{u}_i + u_i') = \frac{\partial \bar{u}_i}{\partial x_i} + \frac{\partial u_i'}{\partial x_i} = 0 \qquad \textbf{(A.11)}$$

Time averaging equation (A.11) leads to

$$\frac{\partial \bar{u}_i}{\partial x_i} = 0 \qquad \textbf{(A.12)}$$

Therefore the mean flow is incompressible. This also means that the turbulent velocity fluctuations are also incompressible (equation (A.11) to equation (A.12)).

$$\frac{\partial u_i'}{\partial x_i} = 0 \qquad \textbf{(A.13)}$$

Through continuity the following equation can be derived.

$$\overline{u_i' u_j' \frac{\partial u_i'}{\partial x_j}} = \frac{1}{2}\frac{\partial}{\partial x_j}\overline{\left(u_i' u_i' u_j'\right)} \tag{A.14}$$

and equation (A.10) becomes

$$\frac{\partial k}{\partial t} + \bar{u}_j \frac{\partial k}{\partial x_j} = -\frac{1}{\rho}\frac{\partial}{\partial x_i}\overline{\left(u_i' p_i'\right)} - \overline{u_i' u_j'}\frac{\partial \bar{u}_i}{\partial x_j} - \frac{1}{2}\frac{\partial}{\partial x_j}\overline{\left(u_i' u_i' u_j'\right)} + \frac{\partial}{\partial x_j}\nu_t \frac{\partial k}{\partial x_j} + \nu_t \overline{\frac{\partial u_i'}{\partial x_j}\frac{\partial u_i'}{\partial x_j}} \tag{A.15}$$

The exact k - equation can therefore be written as:-

$$\frac{\partial k}{\partial t} + \bar{u}_j \frac{\partial k}{\partial x_j} = P_k + T_k + \Pi_k + D_k - \varepsilon \tag{A.16}$$

Where the various terms are defined as follows.

Rate of production:

$$P_k = -\overline{u_i' u_j'}\frac{\partial \bar{u}_i}{\partial x_j} \tag{A.17}$$

Rate of turbulence transport:

$$T_k = -\frac{1}{2}\frac{\partial}{\partial x_j}\overline{\left(u_i' u_i' u_j'\right)} \tag{A.18}$$

Rate of pressure diffusion:

$$\Pi_k = -\frac{1}{\rho}\frac{\partial}{\partial x_i}\overline{\left(u_i' p_i'\right)} \tag{A.19}$$

Rate of viscous diffusion:

$$D_k = \frac{\partial}{\partial x_j}\nu_t \frac{\partial k}{\partial x_j} \tag{A.20}$$

Rate of dissipation:

$$\varepsilon = \nu_t \overline{\frac{\partial u_i'}{\partial x_j}\frac{\partial u_i'}{\partial x_j}} \tag{A.21}$$

Appendix B

Derivation of The Exact ε - Equation

The exact ε - equation can also be derived from the Navier-Stokes and continuity equations, equations (B.1) and (B.2) respectively. (see Chou 1945; Davidov 1961; Harlow and Nakayama 1967)

$$\frac{\partial u_i}{\partial t} + u_j \frac{\partial u_i}{\partial x_j} = -\frac{1}{\rho}\frac{\partial p_i}{\partial x_i} + \frac{\partial}{\partial x_j}\left(\nu_t \frac{\partial u_i}{\partial x_j}\right) + g_i \qquad \textbf{(B.1)}$$

$$\frac{\partial u_i}{\partial x_i} = 0 \qquad \textbf{(B.2)}$$

Again, assuming a Reynolds decomposition (Reynolds 1894) such that u_i is defined by:-

$$u_i = \bar{u}_i + u_i' \qquad \textbf{(B.3)}$$

with $\bar{u}_i$ representing the mean velocity and u_i' the turbulent velocity fluctuation, equation (B.1) becomes

$$\frac{\partial(\bar{u}_i + u_i')}{\partial t} + (\bar{u}_j + u_i')\frac{\partial(\bar{u}_i + u_i')}{\partial x_j} = -\frac{1}{\rho}\frac{\partial(\bar{p}_i + p_i')}{\partial x_i} + \frac{\partial}{\partial x_j}\left(\nu_t \frac{\partial(\bar{u}_i + u_i')}{\partial x_j}\right) + g_i \qquad \textbf{(B.4)}$$

Differentiating equation (B.4) with respect to x_m gives.

$$\frac{\partial}{\partial x_m}\frac{\partial \bar{u}_i}{\partial t}+\frac{\partial}{\partial x_m}\frac{\partial u_i'}{\partial t}+\frac{\partial}{\partial x_m}\bar{u}_j\frac{\partial \bar{u}_i}{\partial x_j}+\bar{u}_j\frac{\partial}{\partial x_m}\frac{\partial \bar{u}_i}{\partial x_j}+\frac{\partial}{\partial x_m}\bar{u}_j\frac{\partial u_i'}{\partial x_j}+$$
$$\bar{u}_j\frac{\partial}{\partial x_m}\frac{\partial u_i'}{\partial x_j}+\frac{\partial}{\partial x_m}u_j'\frac{\partial \bar{u}_i}{\partial x_j}+u_j'\frac{\partial}{\partial x_m}\frac{\partial \bar{u}_i}{\partial x_j}+\frac{\partial}{\partial x_m}u_j'\frac{\partial u_i'}{\partial x_j}+u_j'\frac{\partial}{\partial x_m}\frac{\partial u_i'}{\partial x_j}= \qquad \textbf{(B.5)}$$
$$-\frac{1}{\rho}\frac{\partial}{\partial x_m}\frac{\partial \bar{p}_i}{\partial x_i}-\frac{1}{\rho}\frac{\partial}{\partial x_m}\frac{\partial p_i'}{\partial x_i}+\frac{\partial}{\partial x_m}\frac{\partial}{\partial x_j}\left(\nu_t\frac{\partial \bar{u}_i}{\partial x_j}\right)+\frac{\partial}{\partial x_m}\frac{\partial}{\partial x_j}\left(\nu_t\frac{\partial u_i'}{\partial x_j}\right)$$

If we now multiply through by $\partial u_i'/\partial x_m$ and time-average then:-

$$\overline{\frac{\partial u_i'}{\partial x_m}\frac{\partial}{\partial x_m}\frac{\partial u_i'}{\partial t}}+\overline{\frac{\partial u_i'}{\partial x_m}\frac{\partial}{\partial x_m}\bar{u}_j\frac{\partial u_i'}{\partial x_j}}+\overline{\frac{\partial u_i'}{\partial x_m}\bar{u}_j\frac{\partial}{\partial x_m}\frac{\partial u_i'}{\partial x_j}}+\overline{\frac{\partial u_i'}{\partial x_m}\frac{\partial}{\partial x_m}u_j'\frac{\partial \bar{u}_i}{\partial x_j}}$$
$$+\overline{\frac{\partial u_i'}{\partial x_m}u_j'\frac{\partial}{\partial x_m}\frac{\partial \bar{u}_i}{\partial x_j}}+\overline{\frac{\partial u_i'}{\partial x_m}\frac{\partial}{\partial x_m}u_j'\frac{\partial u_i'}{\partial x_j}}+\overline{\frac{\partial u_i'}{\partial x_m}u_j'\frac{\partial}{\partial x_m}\frac{\partial u_i'}{\partial x_j}}= \qquad \textbf{(B.6)}$$
$$-\frac{1}{\rho}\overline{\frac{\partial u_i'}{\partial x_m}\frac{\partial}{\partial x_m}\frac{\partial p_i'}{\partial x_i}}+\overline{\frac{\partial u_i'}{\partial x_m}\frac{\partial}{\partial x_m}\frac{\partial}{\partial x_j}\left(\nu_t\frac{\partial u_i'}{\partial x_j}\right)}$$

Rearranging gives

$$\frac{\partial}{\partial t}\overline{\frac{\partial u_i'}{\partial x_m}\frac{\partial u_i'}{\partial x_m}}+\overline{\frac{\partial u_i'}{\partial x_j}\frac{\partial u_i'}{\partial x_m}\frac{\partial \bar{u}_j}{\partial x_m}}+\bar{u}_j\frac{\partial}{\partial x_j}\overline{\frac{\partial u_i'}{\partial x_m}\frac{\partial u_i'}{\partial x_m}}+\overline{\frac{\partial u_i'}{\partial x_m}\frac{\partial u_j'}{\partial x_m}\frac{\partial \bar{u}_i}{\partial x_j}}$$
$$+\overline{u_j'\frac{\partial u_i'}{\partial x_m}\frac{\partial^2 \bar{u}_i}{\partial x_j\partial x_m}}+\overline{\frac{\partial u_i'}{\partial x_j}\frac{\partial u_i'}{\partial x_m}\frac{\partial u_j'}{\partial x_m}}+\frac{1}{2}\overline{u_j'\frac{\partial}{\partial x_j}\frac{\partial u_i'}{\partial x_m}\frac{\partial u_i'}{\partial x_m}}= \qquad \textbf{(B.7)}$$
$$-\frac{1}{\rho}\frac{\partial}{\partial x_i}\overline{\frac{\partial p_i'}{\partial x_m}\frac{\partial u_i'}{\partial x_m}}+\frac{\partial}{\partial x_j}\nu_t\frac{\partial}{\partial x_j}\overline{\frac{\partial u_i'}{\partial x_m}\frac{\partial u_i'}{\partial x_m}}+\nu_t\overline{\left(\frac{\partial^2 u_i'}{\partial x_j\partial x_m}\right)^2}$$

Taking the isotropic dissipation rate, ε, as:-

$$\varepsilon=2\nu_t\overline{\frac{\partial u_i'}{\partial x_m}\frac{\partial u_i'}{\partial x_m}} \qquad \textbf{(B.8)}$$

and multiplying equation (B.7) by $2\nu_t$ gives

$$\frac{\partial \varepsilon}{\partial t}+2\nu_t\overline{\frac{\partial u_i'}{\partial x_j}\frac{\partial u_i'}{\partial x_m}\frac{\partial \bar{u}_j}{\partial x_m}}+\bar{u}_j\frac{\partial \varepsilon}{\partial x_j}+2\nu_t\overline{\frac{\partial u_i'}{\partial x_m}\frac{\partial u_j'}{\partial x_m}\frac{\partial \bar{u}_i}{\partial x_j}}+$$
$$2\nu_t\overline{u_j'\frac{\partial u_i'}{\partial x_m}\frac{\partial^2 \bar{u}_i}{\partial x_j\partial x_m}}+2\nu_t\overline{\frac{\partial u_i'}{\partial x_j}\frac{\partial u_i'}{\partial x_m}\frac{\partial u_j'}{\partial x_m}}+\nu_t\overline{u_j'\frac{\partial}{\partial x_j}\frac{\partial u_i'}{\partial x_m}\frac{\partial u_i'}{\partial x_m}} \qquad \textbf{(B.9)}$$
$$=-\frac{2\nu_t}{\rho}\frac{\partial}{\partial x_i}\overline{\frac{\partial p_i'}{\partial x_m}\frac{\partial u_i'}{\partial x_m}}+\frac{\partial}{\partial x_j}\nu_t\frac{\partial \varepsilon}{\partial x_j}+2\nu_t^2\overline{\left(\frac{\partial^2 u_i'}{\partial x_j\partial x_m}\right)^2}$$

Therefore the exact ε - equation becomes:-

$$\frac{\partial \varepsilon}{\partial t} + \bar{u}_j \frac{\partial \varepsilon}{\partial x_j} = P_\varepsilon^1 + P_\varepsilon^2 + P_\varepsilon^3 + P_\varepsilon^4 + T_\varepsilon + \Pi_\varepsilon + D_\varepsilon + \gamma \qquad \textbf{(B.10)}$$

where the terms represent:-

Rate of production by the mean velocity gradient.

$$P_\varepsilon^1 = -2\nu_t \overline{\frac{\partial u_i'}{\partial x_m} \frac{\partial u_j'}{\partial x_m}} \frac{\partial \bar{u}_i}{\partial x_j} \qquad \textbf{(B.11)}$$

Rate of mixed production.

$$P_\varepsilon^2 = -2\nu_t \overline{\frac{\partial u_i'}{\partial x_j} \frac{\partial u_i'}{\partial x_m}} \frac{\partial \bar{u}_j}{\partial x_m} \qquad \textbf{(B.12)}$$

Rate of gradient production.

$$P_\varepsilon^3 = -2\nu_t \overline{u_j' \frac{\partial u_i'}{\partial x_m}} \frac{\partial^2 \bar{u}_i}{\partial x_j \partial x_m} \qquad \textbf{(B.13)}$$

Rate of turbulent production.

$$P_\varepsilon^4 = -2\nu_t \overline{\frac{\partial u_i'}{\partial x_j} \frac{\partial u_i'}{\partial x_m} \frac{\partial u_j'}{\partial x_m}} \qquad \textbf{(B.14)}$$

Rate of turbulent transport.

$$T_\varepsilon = -\nu_t \overline{u_j' \frac{\partial}{\partial x_j} \frac{\partial u_i'}{\partial x_m} \frac{\partial u_i'}{\partial x_m}} \qquad \textbf{(B.15)}$$

Rate of pressure transport.

$$\Pi_\varepsilon = -\frac{2\nu_t}{\rho} \frac{\partial}{\partial x_i} \overline{\frac{\partial p_i'}{\partial x_m} \frac{\partial u_i'}{\partial x_m}} \qquad \textbf{(B.16)}$$

Rate of viscous transport.

$$D_\varepsilon = \frac{\partial}{\partial x_j} \nu_t \frac{\partial \varepsilon}{\partial x_j} \qquad \textbf{(B.17)}$$

Rate of dissipation.

$$\gamma = 2\nu_t^2 \overline{\left(\frac{\partial^2 u_i'}{\partial x_j \partial x_m} \right)^2} \qquad \textbf{(B.18)}$$

Appendix C
Vertical Grid Transformation and Model Discretization

C.1 Vertical grid transformation

C.1.1 Introduction

When working with turbulence models it is necessary to ensure that there is an adequate number of calculation points in space within the boundary layer. This requires that the calculation volume is divided into a large number of points, or a split grid is applied or a varying grid is applied. The first method would be impractical for all but laboratory scale, and even then the number of grid points could be the order of several hundred. The second method will result in numerical diffusion, the severity of which will depend on the scale between the two grid sizes applied. Finally, varying the grid size enables the generation of a fine grid within the boundary layer where the velocity gradients are greatest and gradually increasing grid into the main flow where the flow quantities only vary very slightly.

Allowing the grid spacing to vary can be implemented in real or transformed space. However, operating in transformed space can have certain numerical advantages. For example, in transformed space the interval between each grid point becomes constant, whilst in real space these intervals vary in size. Results are shown for the models run with a logarithmic transform since this was found to be the easiest to adapt for the requirements of varying the bed roughness.

In the model the upper boundary condition is taken as the water surface and not the top of the boundary layer. A fictitious point has, therefore, been introduced above the surface grid point to enable a space centred numerical scheme to be applied. For waves alone this is perhaps

unnecessary but with waves and currents in shallow water the current induced boundary layer will normally occupy the whole water depth, Soulsby (1983).

The following details given below describe the logarithmic transform apllied within the model.

C.1.2 Vertical space transform

Let real space, z, be described by the equation:-

$$z = \left(\frac{D}{z_0}\right)^{\eta} z_0 \qquad \textbf{(C.1)}$$

where D is the water depth; z_0 is the roughness height and η is transformed space in the vertical.

Therefore,

$$\frac{z}{z_0} = \left(\frac{D}{z_0}\right)^{\eta} \qquad \textbf{(C.2)}$$

Taking logs gives:-

$$\ln\left(\frac{z}{z_0}\right) = \eta \ln\left(\frac{D}{z_0}\right) \qquad \textbf{(C.3)}$$

Hence η is given by:-

$$\eta = \frac{1}{\ln\left(\frac{D}{z_0}\right)} \ln\left(\frac{z}{z_0}\right) \qquad \textbf{(C.4)}$$

Allowing C to be given by the following equation:-

$$C = \frac{1}{\ln\left(\frac{D}{z_0}\right)} \qquad \textbf{(C.5)}$$

then

$$\eta = C(\ln z - \ln z_0) \qquad \textbf{(C.6)}$$

Differentiating with respect to z leads to:-

$$\frac{\partial \eta}{\partial z} = \frac{C}{z} = \frac{C}{z_0}\left(\frac{D}{z_0}\right)^{-\eta} \qquad \textbf{(C.7)}$$

Therefore,

$$\frac{\partial}{\partial z} = R\frac{\partial}{\partial \eta} \qquad \text{where} \quad R = \frac{C}{z} \qquad \textbf{(C.8)}$$

This provides the first space transform, but it is also necessary to find the second order transform. Hence,

$$\frac{\partial}{\partial z}\left(\frac{\partial}{\partial z}\right) = \frac{\partial}{\partial z}\left(R\frac{\partial}{\partial \eta}\right) \qquad \textbf{(C.9)}$$

$$\frac{\partial}{\partial z}\left(\frac{\partial}{\partial z}\right) = \frac{\partial}{\partial z}\left(\frac{C}{z}\right)\frac{\partial}{\partial \eta} + \frac{C}{z}\frac{\partial}{\partial z}\left(\frac{\partial}{\partial \eta}\right) \qquad \textbf{(C.10)}$$

But $\frac{\partial}{\partial z} = R\frac{\partial}{\partial \eta}$, therefore, the second order transform may be written as:-

$$\frac{\partial^2}{\partial z^2} = R^2\left(-\frac{1}{C}\frac{\partial}{\partial \eta} + \frac{\partial^2}{\partial \eta^2}\right) \qquad \textbf{(C.11)}$$

C.2 Discretized model equations

C.2.1 Introduction

The development of digital computers has led to a more general use of numerical methods in engineering disciplines, particularly for solving fluid flow problems. However, the solution of non-linear partial differential equations has less well established methodology. Normally when solving such equations, a comparison is made with its linear counterpart and then a method is chosen which works for that particular expression. For instance, the equations for the present work are of the parabolic type and their corresponding linear expression is the diffusion equation of the form:

$$\frac{\partial \tilde{u}}{\partial t} = \frac{\partial}{\partial z}\left(\nu_L \frac{\partial \tilde{u}}{\partial z}\right) \qquad \textbf{(C.12)}$$

Various numerical methods exist for solving this equation. However, only finite difference methods are considered here. Within the finite difference method it is possible to introduce two sub-groups, explicit and implicit methods.

Explicit methods

Explicit methods require the solution at time step t_{n+1} to be found from the previous time step. The unknown values can be determined directly (explicitly) with little computational effort at each time step. The main drawback with such methods is their stability, which often requires the time step to be very small, which in turn increases the solution time and hence cost.

Implicit methods

In implicit methods, the solution at time step t_{n+1} is represented by values at both t_{n+1} and a previous time step, t_n. The partial differential equations can be used to provide a difference equation for each grid point which, in turn, goes to form a system of linear equations. These equations can then be solved using matrix methods. Implicit methods are sometimes considered to be less accurate than their explicit counterparts, however, such techniques allow for much greater numerical stability allowing larger time steps to be used.

The numerical scheme used within the present models is the well known Crank-Nicolson semi-implicit method (Crank and Nicolson 1947). The scheme has the advantage of being unconditionally stable and offers higher-order accuracy (see also Abbott and Basco 1989).

C.2.2 The discretized momentum equation

The momentum equation at a point is given by the expression:

$$\frac{\partial \tilde{u}}{\partial t} = \frac{\partial u_0}{\partial t} + \underbrace{\frac{\partial \nu_t}{\partial z}\frac{\partial \tilde{u}}{\partial z}}_{(1)} + \nu_t \frac{\partial^2 \tilde{u}}{\partial z^2} \qquad \textbf{(C.13)}$$

Term (1) is often neglected as being negligible, however, it is included in the present numerical scheme.

The following finite difference schemes have been used to represent the terms in the momentum equation:

A forward difference scheme:

$$\frac{\partial \tilde{u}}{\partial t} = \frac{\tilde{u}_{i+1}^{k} - \tilde{u}_{i}^{k}}{\Delta t} \qquad \textbf{(C.14)}$$

A central difference scheme:

Remembering that the numerical scheme uses transformed space such that equation (C.8) applies:

$$\frac{\partial}{\partial z} = R\frac{\partial}{\partial \eta} \qquad \text{where} \quad R = \frac{C}{z} \qquad \textbf{(C.8)}$$

Then $\partial\tilde{u}/\partial z$ is represented by the equation:

$$\frac{\partial \tilde{u}}{\partial z} = \theta R\left\{\frac{\tilde{u}_{i+1}^{k+1} - \tilde{u}_{i+1}^{k-1}}{2\Delta\eta}\right\} + (1-\theta)R\left\{\frac{\tilde{u}_{i}^{k+1} - \tilde{u}_{i}^{k-1}}{2\Delta\eta}\right\} \qquad \textbf{(C.15)}$$

The non-linear terms are expressed explicitly, therefore:

$$\frac{\partial \nu_t}{\partial z} = R\left\{\frac{\nu_{ti}^{k+1} - \nu_{ti}^{k-1}}{2\Delta\eta}\right\} \qquad \textbf{(C.16)}$$

Second-order terms are expressed using equation (C.11)

$$\frac{\partial^2}{\partial z^2} = R^2\left(-\frac{1}{C}\frac{\partial}{\partial \eta} + \frac{\partial^2}{\partial \eta^2}\right) \qquad \textbf{(C.11)}$$

Therefore $\partial^2\tilde{u}/\partial z^2$ becomes:

$$\frac{\partial^2 \tilde{u}}{\partial z^2} = R^2\left\{-\frac{1}{C}\left[\theta\left(\frac{\tilde{u}_{i+1}^{k+1} - \tilde{u}_{i+1}^{k-1}}{2\Delta\eta}\right) + (1-\theta)\left(\frac{\tilde{u}_{i}^{k+1} - \tilde{u}_{i}^{k-1}}{2\Delta\eta}\right)\right]\right\} + R^2\left\{\theta\left(\frac{\tilde{u}_{i+1}^{k+1} - 2\tilde{u}_{i+1}^{k} + \tilde{u}_{i+1}^{k-1}}{\Delta\eta^2}\right) + (1-\theta)\left(\frac{\tilde{u}_{i}^{k+1} - 2\tilde{u}_{i}^{k} + \tilde{u}_{i}^{k-1}}{\Delta\eta^2}\right)\right\} \qquad \textbf{(C.17)}$$

The value of θ determines how explicit or how implicit the numerical scheme is such that:-

$\theta = 0$ - Fully explicit scheme

$\theta = 1/2$ - Crank - Nicolson semi - implicit scheme

$\theta = 1$ - Fully implicit scheme

Therefore, the discretized momentum equation can now be written as:-

$$\frac{\tilde{u}_{i+1}^{k}-\tilde{u}_{i}^{k}}{\Delta t}=\frac{\partial u_0}{\partial t}+R^2\left\{\frac{\nu_{ti}^{k+1}-\nu_{ti}^{k-1}}{2\Delta\eta}\right\}\left[\theta\left\{\frac{\tilde{u}_{i+1}^{k+1}-\tilde{u}_{i+1}^{k-1}}{2\Delta\eta}\right\}+(1-\theta)\left\{\frac{\tilde{u}_{i}^{k+1}-\tilde{u}_{i}^{k-1}}{2\Delta\eta}\right\}\right]+\nu_{ti}^{k}R^2\left\{-\frac{1}{C}\left[\theta\left(\frac{\tilde{u}_{i+1}^{k+1}-\tilde{u}_{i+1}^{k-1}}{2\Delta\eta}\right)+(1-\theta)\left(\frac{\tilde{u}_{i}^{k+1}-\tilde{u}_{i}^{k-1}}{2\Delta\eta}\right)\right]\right\}+\nu_{ti}^{k}R^2\left\{\theta\left(\frac{\tilde{u}_{i+1}^{k+1}-2\tilde{u}_{i+1}^{k}+\tilde{u}_{i+1}^{k-1}}{\Delta\eta^2}\right)+(1-\theta)\left(\frac{\tilde{u}_{i}^{k+1}-2\tilde{u}_{i}^{k}+\tilde{u}_{i}^{k-1}}{\Delta\eta^2}\right)\right\} \tag{C.18}$$

Removing common terms gives:-

$$CU1_n=\Delta t\frac{\partial u_0}{\partial t} \tag{C.19}$$

$$CU2_n=\frac{\Delta t\,R^2}{2\Delta\eta}\left(\frac{\nu_{ti}^{k+1}-\nu_{ti}^{k-1}}{2\Delta\eta}\right) \tag{C.20}$$

$$CU3_n=\left(-\frac{1}{C}\right)\frac{\Delta t\,R^2\nu_{ti}^{k}}{2\Delta\eta} \tag{C.21}$$

$$CU4_n=\frac{\Delta t\,R^2\nu_{ti}^{k}}{\Delta\eta^2} \tag{C.22}$$

Equation (C.18) is reduced into implicit and explicit terms in order to form a matrix solution.

The implicit terms can therefore be written as:

$$A_n=-(CU2_n+CU3_n+CU4_n)\,\theta\,\tilde{u}_{i+1}^{k+1} \tag{C.23}$$

$$B_n=(1+2CU4_n\theta)\,\tilde{u}_{i+1}^{k} \tag{C.24}$$

$$C_n=-(CU4_n-CU3_n-CU2_n)\,\theta\,\tilde{u}_{i+1}^{k-1} \tag{C.25}$$

The explicit terms are expressed as:-

$$D_n=(CU2_n+CU3_n+CU4_n)(1-\theta)\tilde{u}_{i}^{k+1}-(2CU4_n(1-\theta)-1)\tilde{u}_{i}^{k}+(CU4_n-CU3_n-CU2_n)(1-\theta)\tilde{u}_{i}^{k-1}+CU1_n \tag{C.26}$$

This leads to a tri-diagonal matrix of the following form:

$$\begin{bmatrix} B_1 & A_1 & 0 & \cdots & \cdots & \cdots & \cdots & 0 \\ C_2 & B_2 & A_2 & \ddots & & & & \vdots \\ 0 & C_3 & B_3 & A_3 & \ddots & & & \vdots \\ \vdots & \ddots & C_4 & B_4 & A_4 & \ddots & & \vdots \\ \vdots & & \ddots & \ddots & \ddots & \ddots & \ddots & \vdots \\ \vdots & & & \ddots & \ddots & \ddots & \ddots & 0 \\ \vdots & & & & \ddots & C_{(n-1)} & B_{(n-1)} & A_{(n-1)} \\ 0 & \cdots & \cdots & \cdots & \cdots & 0 & C_n & B_n \end{bmatrix} \begin{bmatrix} D_1 \\ D_2 \\ D_3 \\ D_4 \\ \vdots \\ \vdots \\ D_{(n-1)} \\ D_n \end{bmatrix} = \begin{bmatrix} W_1 \\ W_2 \\ W_3 \\ W_4 \\ \vdots \\ \vdots \\ W_{(n-1)} \\ W_n \end{bmatrix}$$

where W_n is the solution matrix.

This can be solved using the Thomas algorithm, which is a special case of the Gaussian elimination procedure (see Roach 1977, Appendix A; Abbott and Basco 1990, p 117 - 124). Boundary conditions are described in Chapter 2.

The discretized momentum equation in the y direction is given by:-

$$\frac{\partial \tilde{v}}{\partial t} = \frac{\partial v_0}{\partial t} + \frac{\partial \nu_t}{\partial z}\frac{\partial \tilde{v}}{\partial z} + \nu_t \frac{\partial^2 \tilde{v}}{\partial z^2} \qquad \textbf{(C.27)}$$

This is of similar form to Eq. (C.13) and hence discretization follows the same format as outlined above and will not be discussed further.

C.2.3 The discretized turbulent kinetic energy equation

The modelled turbulent kinetic energy transport equation can be written as:

$$\frac{\partial k}{\partial t} = \frac{\partial}{\partial z}\left[\left(\frac{\nu_t}{\sigma_k}\right)\frac{\partial k}{\partial z}\right] + \nu_t\left[\frac{\partial \tilde{u}}{\partial z}\right]^2 - \varepsilon \qquad \textbf{(C.28)}$$

If the model is used all the way to the wall without the use of wall functions then it is usual to include the molecular viscosity in addition to the turbulent eddy viscosity term. Therefore equation (C.28) becomes:-

$$\frac{\partial k}{\partial t} = \frac{\partial}{\partial z}\left[\left(\frac{\nu_t}{\sigma_k} + \nu_L\right)\frac{\partial k}{\partial z}\right] + \left(\nu_t + \nu_L\right)\left[\frac{\partial \tilde{u}}{\partial z}\right]^2 - \varepsilon \qquad \textbf{(C.29)}$$

As with the momentum equation, non-linear terms are modelled explicitly.

$$\frac{k_{i+1}^{k}-k_{i}^{k}}{\Delta t}=\frac{R^{2}}{\sigma_{k}}\left\{\frac{\nu_{ti}^{k+1}-\nu_{ti}^{k-1}}{2\Delta\eta}\right\}\left[\theta\left\{\frac{k_{i+1}^{k+1}-k_{i+1}^{k-1}}{2\Delta\eta}\right\}+(1-\theta)\left\{\frac{k_{i}^{k+1}-k_{i}^{k-1}}{2\Delta\eta}\right\}\right]+$$
$$\frac{\nu_{ti}^{k}R^{2}}{\sigma_{k}}\left\{-\frac{1}{C}\left[\theta\left(\frac{k_{i+1}^{k+1}-k_{i+1}^{k-1}}{2\Delta\eta}\right)+(1-\theta)\left(\frac{k_{i}^{k+1}-k_{i}^{k-1}}{2\Delta\eta}\right)\right]\right\}+$$
$$\frac{\nu_{ti}^{k}R^{2}}{\sigma_{k}}\left\{\theta\left(\frac{k_{i+1}^{k+1}-2k_{i+1}^{k}+k_{i+1}^{k-1}}{\Delta\eta^{2}}\right)+(1-\theta)\left(\frac{k_{i}^{k+1}-2k_{i}^{k}+k_{i}^{k-1}}{\Delta\eta^{2}}\right)\right\}+ \quad \textbf{(C.30)}$$
$$\nu_{ti}^{k}\left\{R\left[\theta\left(\frac{\tilde{u}_{i+1}^{k+1}-\tilde{u}_{i+1}^{k-1}}{2\Delta\eta}\right)+(1-\theta)\left(\frac{\tilde{u}_{i}^{k+1}-\tilde{u}_{i}^{k-1}}{2\Delta\eta}\right)\right]\right\}^{2}-\varepsilon_{i}^{k}$$

Removing common terms gives:

$$CK1_{n}=\frac{\Delta tR^{2}}{\sigma_{k}}\frac{1}{2\Delta\eta}\left\{\frac{\nu_{ti}^{k+1}-\nu_{ti}^{k-1}}{2\Delta\eta}\right\} \quad \textbf{(C.31)}$$

$$CK2_{n}=\left(-\frac{1}{C}\right)\frac{\Delta t\nu_{ti}^{k}}{\sigma_{k}}\frac{R^{2}}{2\Delta\eta} \quad \textbf{(C.32)}$$

$$CK3_{n}=\frac{\Delta t\nu_{ti}^{k}}{\sigma_{k}}\frac{R^{2}}{\Delta\eta^{2}} \quad \textbf{(C.33)}$$

$$CK4_{n}=\Delta t\nu_{ti}^{k}\left\{R\left[\theta\left(\frac{\tilde{u}_{i+1}^{k+1}-\tilde{u}_{i+1}^{k-1}}{2\Delta\eta}\right)+(1-\theta)\left(\frac{\tilde{u}_{i}^{k+1}-\tilde{u}_{i}^{k-1}}{2\Delta\eta}\right)\right]\right\}^{2} \quad \textbf{(C.34)}$$

$$CK5_{n}=\Delta t\varepsilon_{i}^{k} \quad \textbf{(C.35)}$$

Equation (C.30) is reduced into implicit and explicit terms in order to form a matrix solution.

The implicit terms can therefore be written as:

$$A_{n}=-(CK1_{n}+CK2_{n}+CK3_{n})\,\theta\,k_{i+1}^{k+1} \quad \textbf{(C.36)}$$

$$B_{n}=(1+2CK3_{n}\theta)\,k_{i+1}^{k} \quad \textbf{(C.37)}$$

$$C_{n}=-(CK3_{n}-CK2_{n}-CK1_{n})\,\theta\,k_{i+1}^{k-1} \quad \textbf{(C.38)}$$

The explicit terms are expressed as:-

$$D_{n}=(CK1_{n}+CK2_{n}+CK3_{n})(1-\theta)k_{i}^{k+1}$$
$$-(2CK3_{n}(1-\theta)-1)k_{i}^{k} \quad \textbf{(C.39)}$$
$$+(CK3_{n}-CK2_{n}-CK1_{n})(1-\theta)k_{i}^{k-1}+CK4_{n}-CK5_{n}$$

This leads to a tri-diagonal matrix of the form shown above. Boundary conditions are given in Chapter 4.

C.2.4 The discretized isotropic dissipation rate equation

The modelled isotropic dissipation rate transport equation can be written as:

$$\frac{\partial \varepsilon}{\partial t} = \frac{\partial}{\partial z}\left[\left(\frac{\nu_{ti}^{\,k}}{\sigma_\varepsilon}\right)\frac{\partial \varepsilon}{\partial z}\right] + \frac{c_{\varepsilon 1}\nu_{ti}^{\,k}\varepsilon_i^k}{k_i^k}\left[\frac{\partial \tilde{u}}{\partial z}\right]^2 - c_{\varepsilon 2}\frac{\varepsilon_i^{k^2}}{k_i^k} \tag{C.40}$$

As previously, non-linear terms are modelled explicitly.

$$\begin{aligned}\frac{\varepsilon_{i+1}^k - \varepsilon_i^k}{\Delta t} = {} & \frac{R^2}{\sigma_\varepsilon}\left\{\frac{\nu_{ti}^{\,k+1} - \nu_{ti}^{\,k-1}}{2\Delta\eta}\right\}\left[\theta\left\{\frac{\varepsilon_{i+1}^{k+1} - \varepsilon_{i+1}^{k-1}}{2\Delta\eta}\right\} + (1-\theta)\left\{\frac{\varepsilon_i^{k+1} - \varepsilon_i^{k-1}}{2\Delta\eta}\right\}\right] + \\ & \frac{\nu_{ti}^{\,k}R^2}{\sigma_\varepsilon}\left\{-\frac{1}{C}\left[\theta\left(\frac{\varepsilon_{i+1}^{k+1} - k_{i+1}^{k-1}}{2\Delta\eta}\right) + (1-\theta)\left(\frac{\varepsilon_i^{k+1} - k_i^{k-1}}{2\Delta\eta}\right)\right]\right\} + \\ & \frac{\nu_{ti}^{\,k}R^2}{\sigma_\varepsilon}\left\{\theta\left(\frac{\varepsilon_{i+1}^{k+1} - 2\varepsilon_{i+1}^{k} + \varepsilon_{i+1}^{k-1}}{\Delta\eta^2}\right) + (1-\theta)\left(\frac{\varepsilon_i^{k+1} - 2\varepsilon_i^{k} + \varepsilon_i^{k-1}}{\Delta\eta^2}\right)\right\} + \\ & \nu_{ti}^{\,k}\frac{c_{\varepsilon 1}\varepsilon_i^k}{k_i^k}\left\{R\left[\theta\left(\frac{\tilde{u}_{i+1}^{k+1} - \tilde{u}_{i+1}^{k-1}}{2\Delta\eta}\right) + (1-\theta)\left(\frac{\tilde{u}_i^{k+1} - \tilde{u}_i^{k-1}}{2\Delta\eta}\right)\right]\right\}^2 - c_{\varepsilon 2}\frac{\varepsilon_i^{k^2}}{k_i^k}\end{aligned} \tag{C.41}$$

Removing common terms gives:

$$C\varepsilon 1_n = \frac{\Delta t R^2}{\sigma_\varepsilon}\frac{1}{2\Delta\eta}\left\{\frac{\nu_{ti}^{\,k+1} - \nu_{ti}^{\,k-1}}{2\Delta\eta}\right\} \tag{C.42}$$

$$C\varepsilon 2_n = \left(-\frac{1}{C}\right)\frac{\Delta t \nu_{ti}^{\,k}}{\sigma_\varepsilon}\frac{R^2}{2\Delta\eta} \tag{C.43}$$

$$C\varepsilon 3_n = \frac{\Delta t \nu_{ti}^{\,k}}{\sigma_\varepsilon}\frac{R^2}{\Delta\eta^2} \tag{C.44}$$

$$CK4_n = \Delta t \nu_{ti}^{\,k}\frac{c_{1\varepsilon}\varepsilon_i^k}{k_i^k}\left\{R\left[\theta\left(\frac{\tilde{u}_{i+1}^{k+1} - \tilde{u}_{i+1}^{k-1}}{2\Delta\eta}\right) + (1-\theta)\left(\frac{\tilde{u}_i^{k+1} - \tilde{u}_i^{k-1}}{2\Delta\eta}\right)\right]\right\}^2 \tag{C.45}$$

$$CK5_n = \Delta t c_{2\varepsilon}\frac{\varepsilon_i^{k^2}}{k_i^k} \tag{C.46}$$

However, Eq. (C.46) is normally modelled as:

$$CK5_n = \Delta t c_{2\varepsilon}\frac{\varepsilon_i^k \cdot \varepsilon_{i+1}^k}{\left(\theta k_{i+1}^k + (1-\theta)k_i^k\right)} \tag{C.46a}$$

Equation (C.41) is reduced into implicit and explicit terms in order to form a matrix solution.

The implicit terms can therefore be written as:

$$A_n = -\left(C\varepsilon 1_n + C\varepsilon 2_n + C\varepsilon 3_n\right)\theta\ \varepsilon_{i+1}^{k+1} \tag{C.47}$$

$$B_n = (1 + 2C\varepsilon 3_n\theta)\ \varepsilon_{i+1}^{k} \tag{C.48}$$

$$C_n = -\left(C\varepsilon 3_n - C\varepsilon 2_n - C\varepsilon 1_n\right)\theta\ \varepsilon_{i+1}^{k-1} \tag{C.49}$$

The explicit terms are expressed as:-

$$\begin{aligned} D_n = &\left(C\varepsilon 1_n + C\varepsilon 2_n + C\varepsilon 3_n\right)(1-\theta)\varepsilon_i^{k+1} \\ &-\left(2C\varepsilon 3_n(1-\theta) - 1\right)\varepsilon_i^{k} \\ &+\left(C\varepsilon 3_n - C\varepsilon 2_n - C\varepsilon 1_n\right)(1-\theta)\varepsilon_i^{k-1} + C\varepsilon 4_n - C\varepsilon 5_n \end{aligned} \tag{C.50}$$

This leads to a tri-diagonal matrix of the form shown previously. Boundary conditions are given in Chapter 4.

Appendix D
Numerical Stability and Convergence

D.1 Introduction

The numerical schemes used in the present study are described in detail in Appendix C. The non-linear equations used to describe the physics require numerical solution and this requires the introduction of an 'approximation technique'. The finite difference method has been chosen here for solving the partial differential equations and whilst such methods generally provide solutions which are as accurate as required such methods do contain truncation errors. Therefore, it is important to assess the performance of the numerical scheme employed to ensure that it is efficient and also that it is as accurate as the problem warrants.

The accuracy of numerical schemes of this type can usually be improved by either adjusting the density of the numerical grid points or by the inclusion of 'correction terms' in the approximations of the derivatives. The latter, method will not be discussed further (see e.g. Smith (1985)). To enable the numerical scheme to be tested, the analytical solution of Lamb (1932) has been used. However, it is worth noting that, whilst usually of little significance, even analytical solutions only provide approximate answers since all arithmetical work involves rounding errors.

D.2 Numerical convergence

To test the convergence of the numerical scheme used, the k- and k-ε models have been run with a constant viscosity and the solutions compared with the analytical solution of Lamb (1932). Lamb's analytical solution for waves over a flat bed is given by the following equation:

$$u = u_\infty\left(\sin(\omega t) - e^{-\beta z}\sin(\omega t - \beta z)\right) \qquad \textbf{(D.1)}$$

where β is a height scale and is given by the equation:

$$\beta = \sqrt{\frac{\omega}{2\nu_L}} \qquad \textbf{(D.2)}$$

In addition, the shear stress can be obtained by differentiating Eq. (D.1) with respect to z. The resulting equation is:

$$\frac{\tau}{\rho} = \sqrt{2}\nu_L\beta u_\infty e^{-\beta z}\sin\left(\omega t - \beta z + \frac{\pi}{4}\right) \qquad \textbf{(D.3)}$$

The numerical scheme operates in a transformed space (see Appendix C) but real time. The transformed space uses a logarithmic straining which ensures a fine mesh spacing close to the wall where the profile gradients are greatest. In addition, working in transformed space enables a relatively small number of grid points to be used. The models generally operate with between 40 and 60 vertical points. Working in transformed time would enable smaller time steps to be used per wave period, however, working in non-dimensional time makes the development of the random boundary layer model unnecessarily complicated and so real time is used for all cases. The model boundary conditions are as given in Chapters 2 and 4 and the grid system is of the form shown in Figure 5.1.

For the purpose of the tests, the numerical models have been run with three different space grid sizes; with 60, 40 and 20 points through the vertical. The solutions have then been compared with the analytical results from Lamb's equations. This has been done for both the k- and k-ε models and the results are shown in Figures D1 - D4.

Figures D1 and D2 show the results for the k-ε model against the analytical solution for velocity and shear stress respectively. The results for the calculated velocity show little

variation with the analytical solution when using either the 60 and 40 grid densities. Even though the lower grid density of 20 points in the vertical fails to fully reproduce the analytical solution, near the wall (≤ 2 mm) the comparison is still good. This is due to the varying grid applied in the model ensuring a sufficient number of points close to the wall. From the comparison of the model solution for the lowest grid density with Lamb's solution there is a clear variation of accuracy through time (see Figures D1a, f, g and l). Clearly the effect of flow reversal has a significant effect on the performance of the numerical model, and which is particularly noticeable for low grid densities.

To quantify the performance of both models, both depth mean values and root-mean-square deviation values were calculated for both models, for each phase, and for each grid density. The results of this analysis are shown in Tables D1 - D4. The depth mean values are considered to be unreliable since the effect of flow reversal requires averaging quantities which are of varying sign. This is overcome by using root-mean-square deviation values. For the comparison with Lamb's analytical solution for velocity, the root-mean-square deviation suggests a worst error of less than 1 % for both k and k-ε models with a grid density of 60 points in space. This worst error increases to approximately 2 % and 5.2 % for grid densities of 40 and 20 points, respectively. The error is seen to vary with phase (see Tables D1 and D3).

Comparison of the calculated shear stress from the k-ε model compared with the analytical solution shows a similar performance as seen with the velocity profiles. However, the lowest grid density of 20 points through the vertical shows a poorer agreement with the analytical results through the wave cycle for the shear stress than was seen in the velocity solution.

From the root-mean-square deviation analysis, the greatest error in the k-ε model results appears to be approximately 1.4 % (0.7 %) for a grid density of 60 points and 3.0 % (1.5 %) and 9.6 % (3.6 %) for grid densities of 40 and 20 points, respectively. The values in brackets correspond to the errors for the k model. The k model appears to out perform the k-ε model in the prediction of shear stress. (see Tables D2 and D4).

Results from the k model, shown in Figures D3 and D4 show similar results to those observed with the k-ε model, although the root-mean-square deviation analysis indicates that the k model provides better agreement with the analytical solution for shear stress.

D.3 Conclusion

From the results of the comparison between Lamb's analytical solution and the k and k-ε models, the numerical finite difference schemes are performing well. The accuracy of the numerical schemes and their application to the non-linear equations used to model the wave boundary layer has been verified. In addition, whilst the lowest grid density tested fails to fully reproduce the analytical solution, close to the wall the results show good agreement due to the vertical grid straining applied in the numerical models (see Appendix C). However, for the number of vertical points normally applied in model solutions (between 40 and 60 vertical points) it has been demonstrated using root-mean-square deviations that the number of vertical grid points are sufficient to ensure numerical errors are small (2.0 % for velocity calculations and 3.0 % for shear stress results using a grid density of 40 points in space).

Model (No. of nodes)	Percentage Error, %											
	0°	30°	60°	90°	120°	150°	180°	210°	240°	270°	300°	330°
k-ε (60)	0.868	0.214	0.319	0.359	0.378	0.369	0.636	0.493	0.500	0.527	0.586	0.788
k (60)	0.868	0.214	0.319	0.359	0.378	0.369	0.636	0.493	0.500	0.527	0.586	0.788
k-ε (40)	0.886	0.674	0.838	0.914	0.974	1.068	0.586	0.948	1.016	1.079	1.177	1.479
k (40)	0.886	0.674	0.838	0.914	0.974	1.068	0.586	0.948	1.016	1.079	1.177	1.479
k-ε (20)	1.022	2.000	2.343	2.528	2.713	3.121	0.365	2.257	2.510	2.682	2.904	3.507
k (20)	1.021	2.000	2.343	2.528	2.713	3.121	0.365	2.257	2.510	2.682	2.904	3.507

Table D1: Percentage error between computed and measured depth-averaged values of the velocity. Results are shown for different phases through the wave period and for k-ε and k models run with different vertical grid densities.

Model (No. of nodes)	Percentage Error, %											
	0°	30°	60°	90°	120°	150°	180°	210°	240°	270°	300°	330°
k-ε (60)	2.121	1.658	1.428	1.206	0.775	14.247	2.167	1.681	1.452	1.233	0.819	13.354
k (60)	1.547	1.213	1.052	0.892	0.580	10.335	1.594	1.241	1.076	0.919	0.624	9.445
k-ε (40)	4.773	3.722	3.219	2.726	1.775	31.154	4.821	3.751	3.243	2.573	1.821	30.246
k (40)	3.482	2.731	2.371	2.018	1.335	22.370	3.529	2.760	2.396	2.045	1.380	21.469
k-ε (20)	13.872	10.869	9.433	8.034	5.348	87.487	13.922	10.900	9.459	8.063	5.396	86.525
k (20)	8.709	6.905	6.042	5.200	3.580	52.460	8.758	6.935	6.067	5.228	3.626	51.522

Table D2: Percentage error between computed and measured depth-averaged values of the shear stress, τ/ρ. Results are shown for different phases through the wave period and for k-ε and k models run with different vertical grid densities.

Model (No. of nodes)	Percentage Error, %											
	0°	30°	60°	90°	120°	150°	180°	210°	240°	270°	300°	330°
k-ε (60)	0.347	0.997	0.773	0.616	0.494	0.373	0.555	0.780	0.536	0.382	0.211	0.093
k (60)	0.347	0.997	0.773	0.616	0.494	0.373	0.555	0.780	0.536	0.382	0.211	0.093
k-ε (40)	0.204	2.076	1.571	1.226	0.928	0.549	0.681	1.860	1.337	0.996	0.649	0.088
k (40)	0.204	2.076	1.571	1.226	0.928	0.549	0.681	1.860	1.337	0.996	0.649	0.088
k-ε (20)	0.517	5.221	3.868	2.990	2.201	1.126	1.352	5.008	3.643	2.768	1.932	0.682
k (20)	0.517	5.221	3.868	2.990	2.201	1.126	1.352	5.008	3.643	2.768	1.932	0.682

Table D3: Percentage error between computed and measured root-mean-square deviation values, σ of the velocity. Results are shown for different phases through the wave period and for k-ε and k models run with different vertical grid densities.

Model (No. of nodes)	Percentage Error, %											
	0°	30°	60°	90°	120°	150°	180°	210°	240°	270°	300°	330°
k-ε (60)	1.354	1.128	0.925	0.658	0.099	1.192	1.378	1.150	0.949	0.689	0.160	1.195
k (60)	0.676	0.532	0.414	0.264	0.020	0.678	0.700	0.554	0.437	0.296	0.040	0.682
k-ε (40)	3.022	2.523	2.078	1.492	0.274	2.663	3.047	2.546	2.102	1.524	0.335	2.665
k (40)	1.499	1.180	0.921	0.598	0.003	1.515	1.523	1.203	0.944	0.629	0.058	1.518
k-ε (20)	9.563	8.161	6.869	5.131	1.373	8.212	9.589	8.185	6.894	5.164	1.436	8.209
k (20)	3.560	2.820	2.229	1.506	0.207	3.712	3.585	2.842	2.252	1.538	0.269	3.714

Table D4: Percentage error between computed and measured root-mean-square deviation values, σ of the shear stress, τ/ρ. Results are shown for different phases through the wave period and for k-ε and k models run with different vertical grid densities.

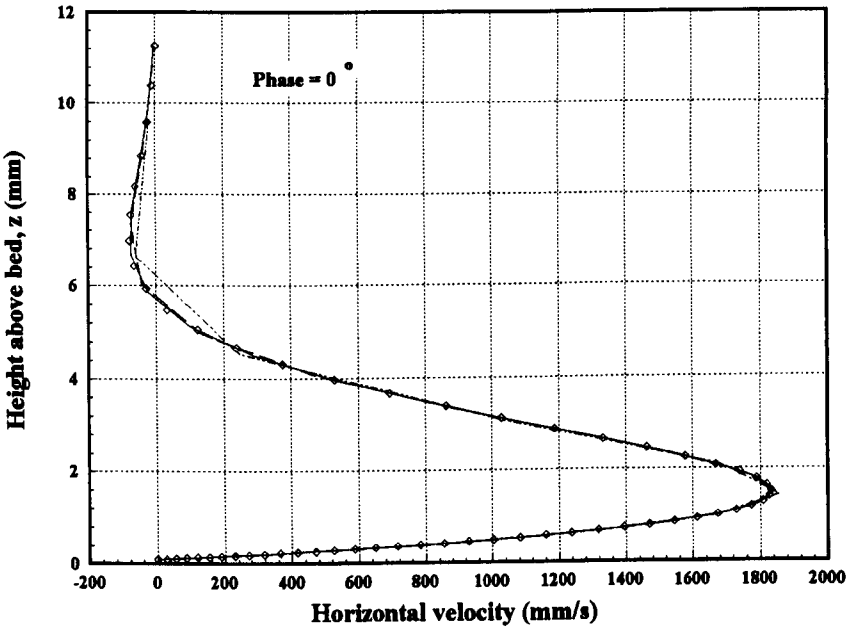

(a)

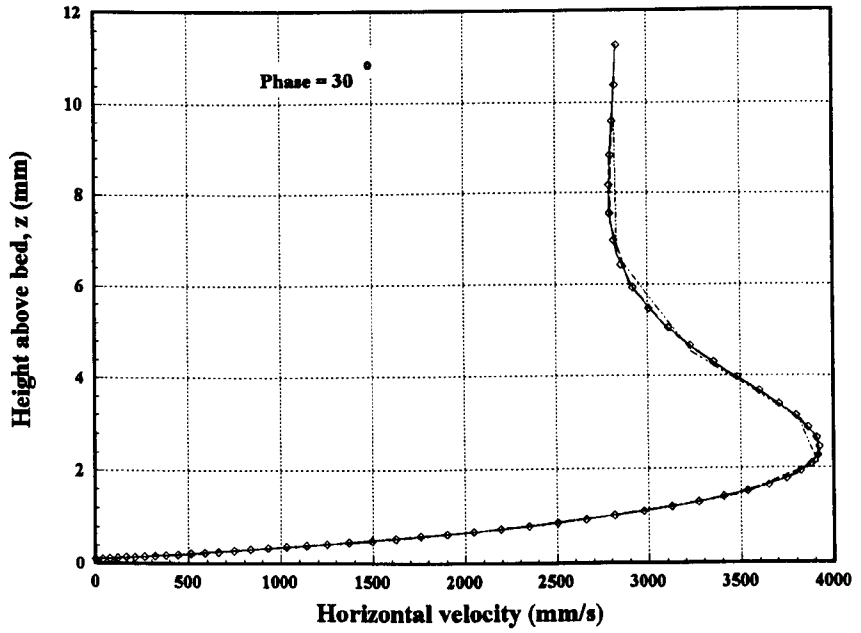

(b)

Figure D1: Comparison of Lamb's analytical solution against results from the k-ε model for different numbers of vertcial nodes: ◊ Lamb; — k-ε model (60 nodes); – – – k-ε model (40 nodes); — – – — k-ε model (20 nodes).

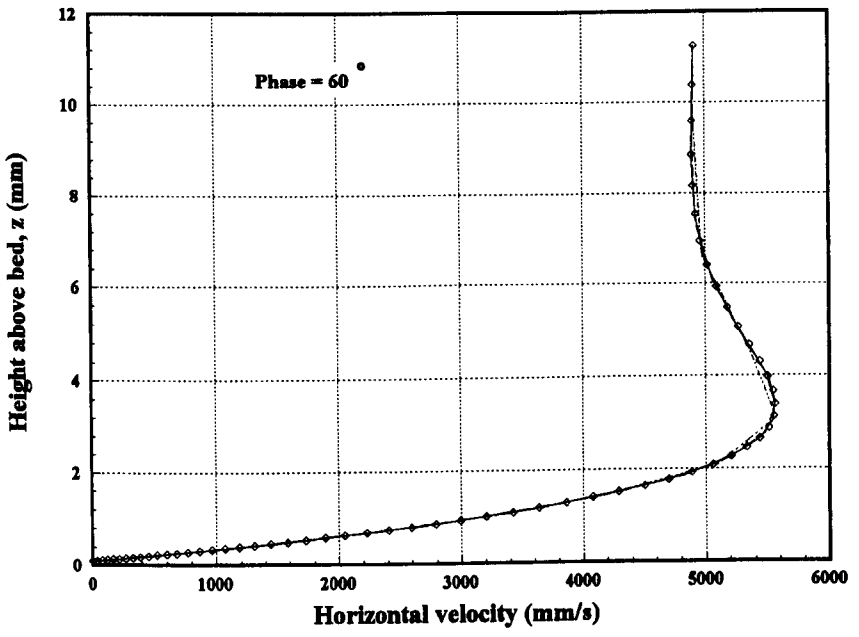

(c)

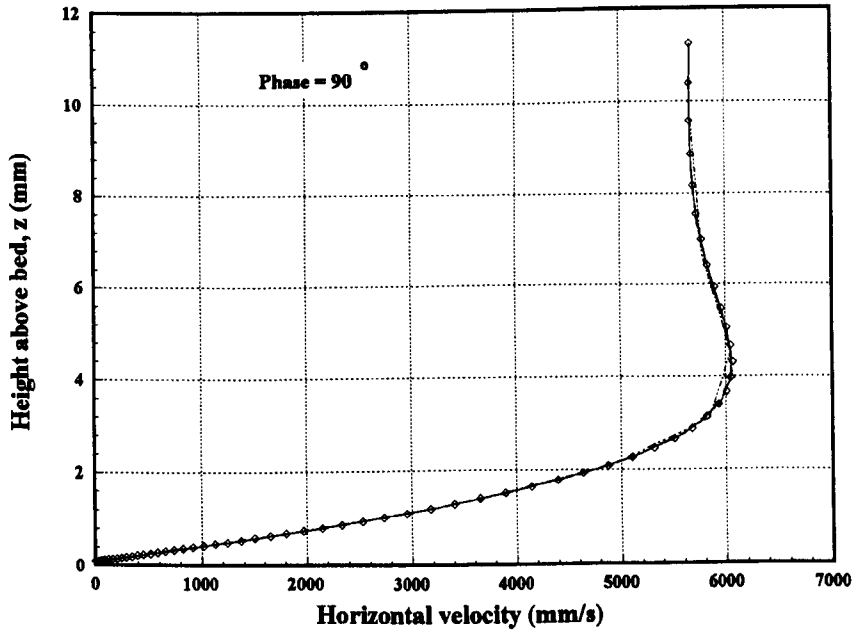

(d)

Figure D1(Cont.): Comparison of Lamb's analytical solution against results from the k-ε model for different numbers of vertcial nodes: ◊ Lamb; — k-ε model (60 nodes); – – – k-ε model (40 nodes); — – – — k-ε model (20 nodes).

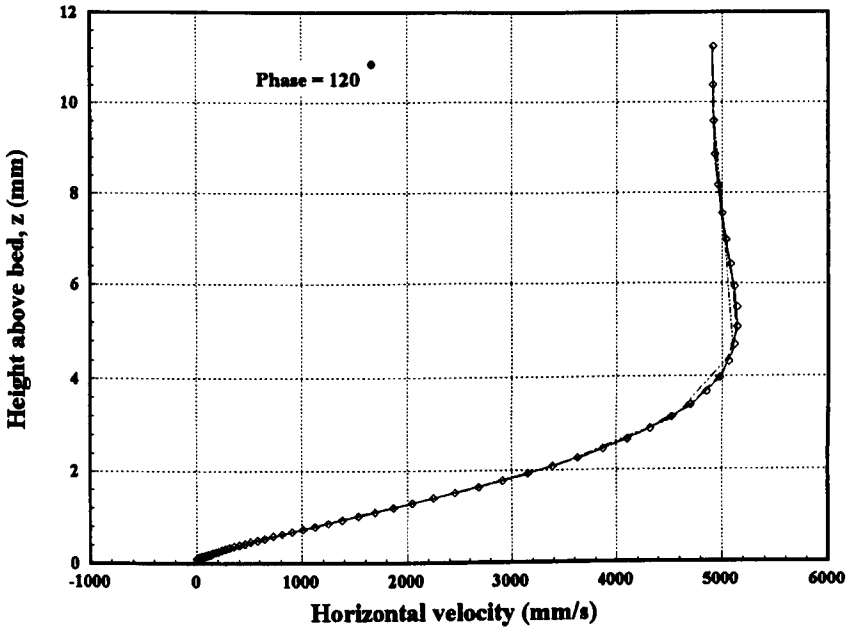

(e)

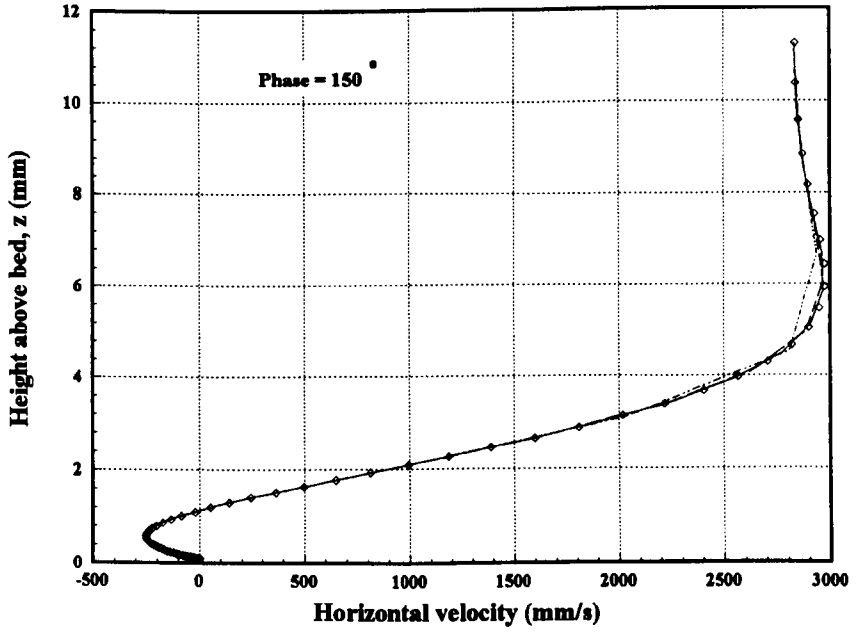

(f)

Figure D1(Cont): Comparison of Lamb's analytical solution against results from the k-ε model for different numbers of vertcial nodes: ◊ Lamb; — k-ε model (60 nodes); – – – k-ε model (40 nodes); — – – — k-ε model (20 nodes).

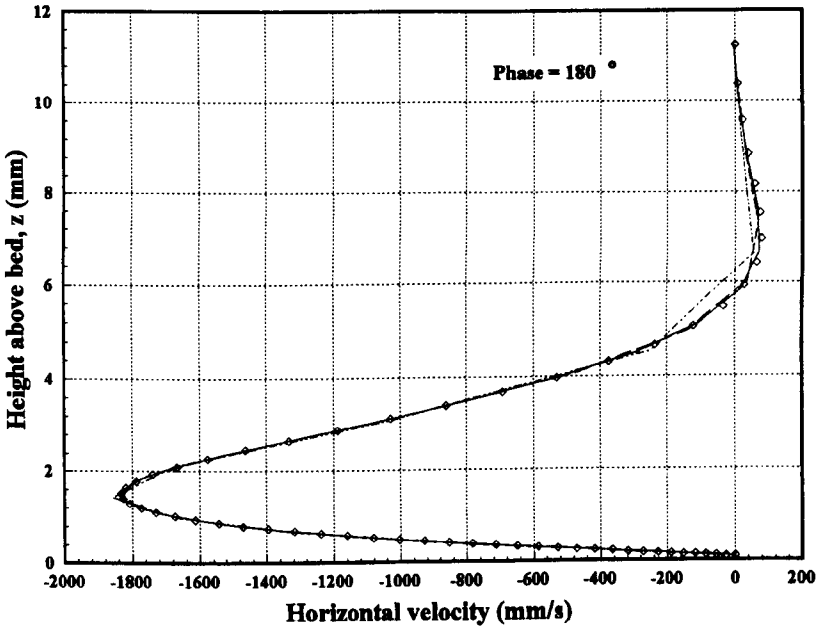

(g)

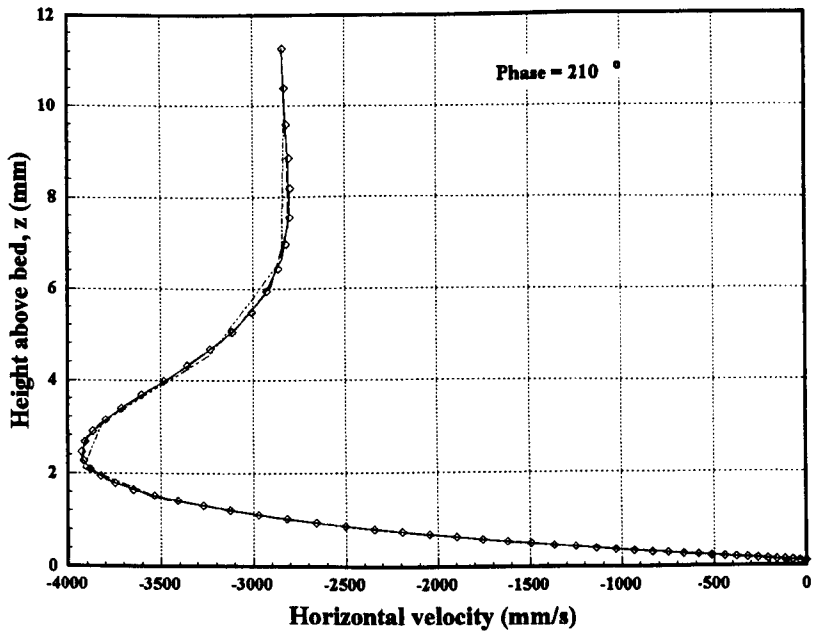

(h)

Figure D1(Cont): Comparison of Lamb's analytical solution against results from the k-ε model for different numbers of vertcial nodes: ◊ Lamb; — k-ε model (60 nodes); – – – k-ε model (40 nodes); — – – — k-ε model (20 nodes).

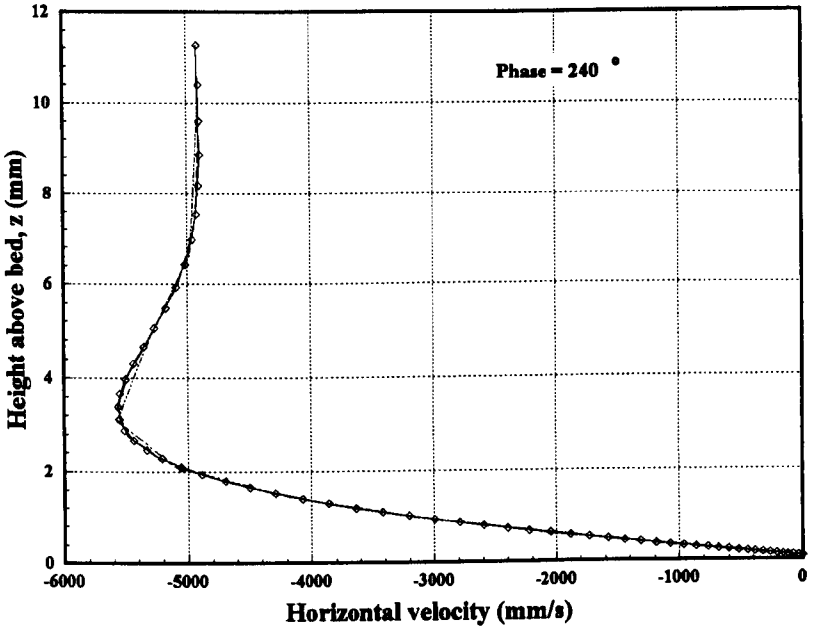

(i)

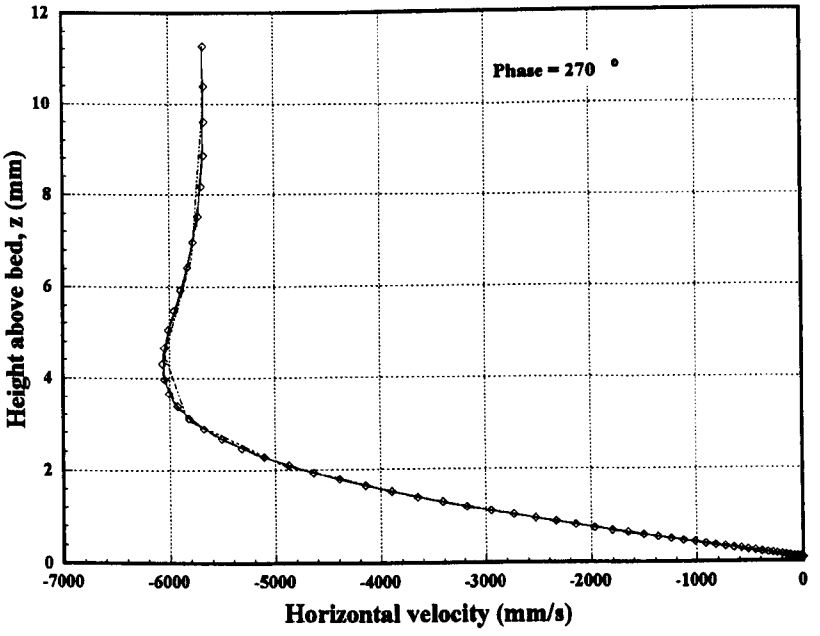

(j)

Figure D1(Cont.): Comparison of Lamb's analytical solution against results from the k-ε model for different numbers of vertcial nodes: ◊ Lamb; — k-ε model (60 nodes); – – – k-ε model (40 nodes); — – – — k-ε model (20 nodes).

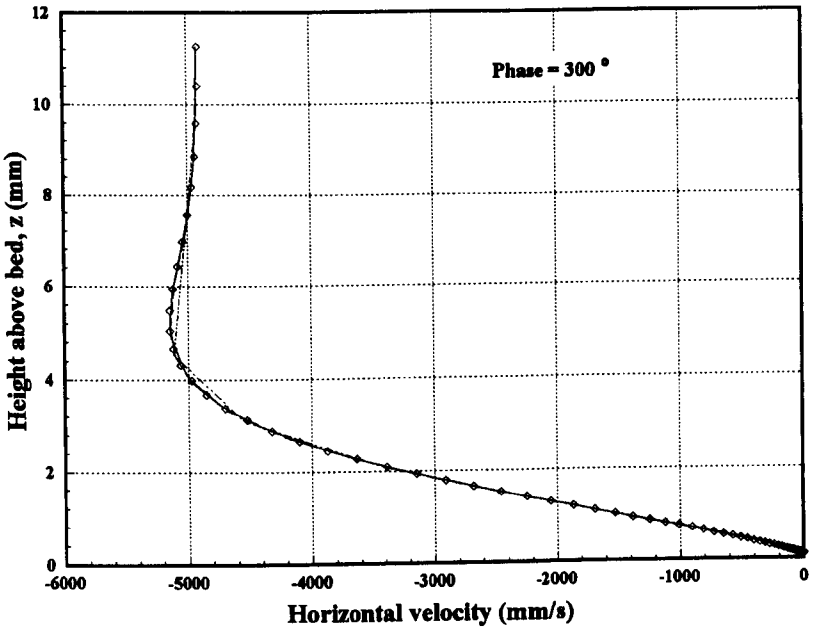

(k)

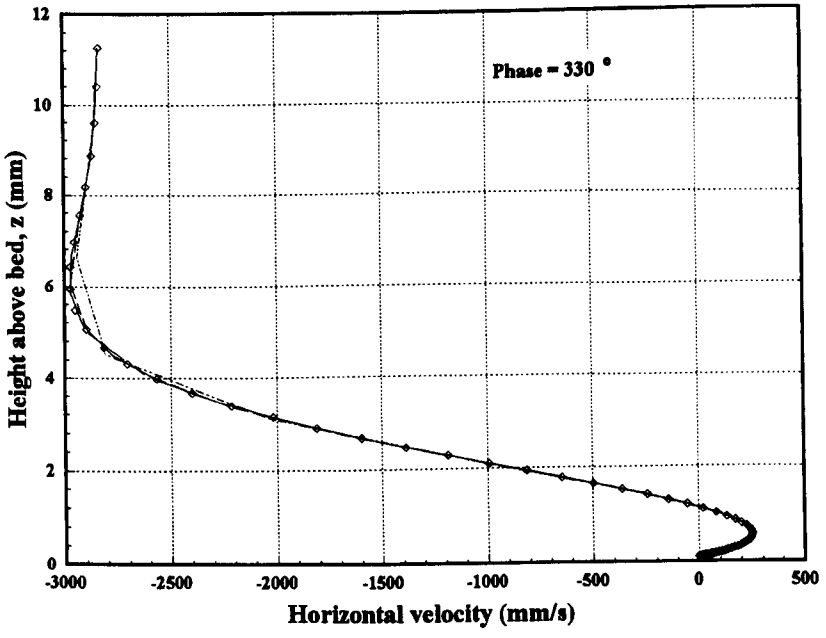

(l)

Figure D1(Cont.): Comparison of Lamb's analytical solution against results from the k-ε model for different numbers of vertcial nodes: ◊ Lamb; — k-ε model (60 nodes); – – – k-ε model (40 nodes); — – – — k-ε model (20 nodes).

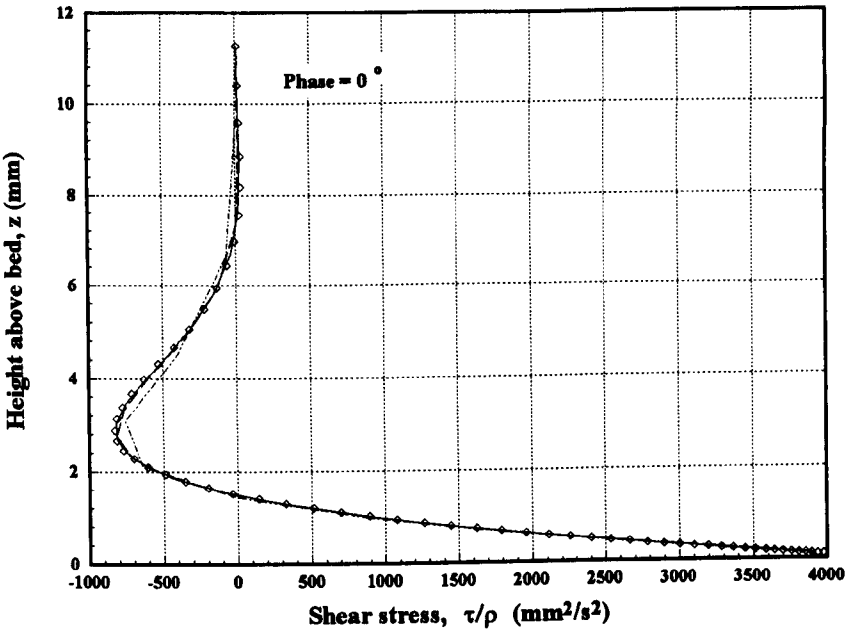

(a)

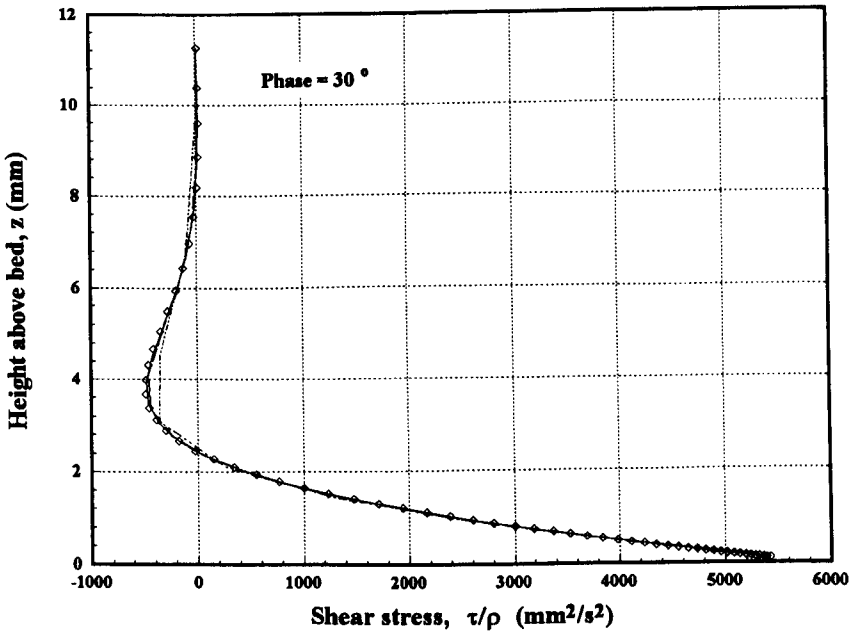

(b)

Figure D2: Comparison of Lamb's analytical solution against results from the k-ε model for different numbers of vertcial nodes: ◊ Lamb; — k-ε model (60 nodes); – – – k-ε model (40 nodes); — – – — k-ε model (20 nodes).

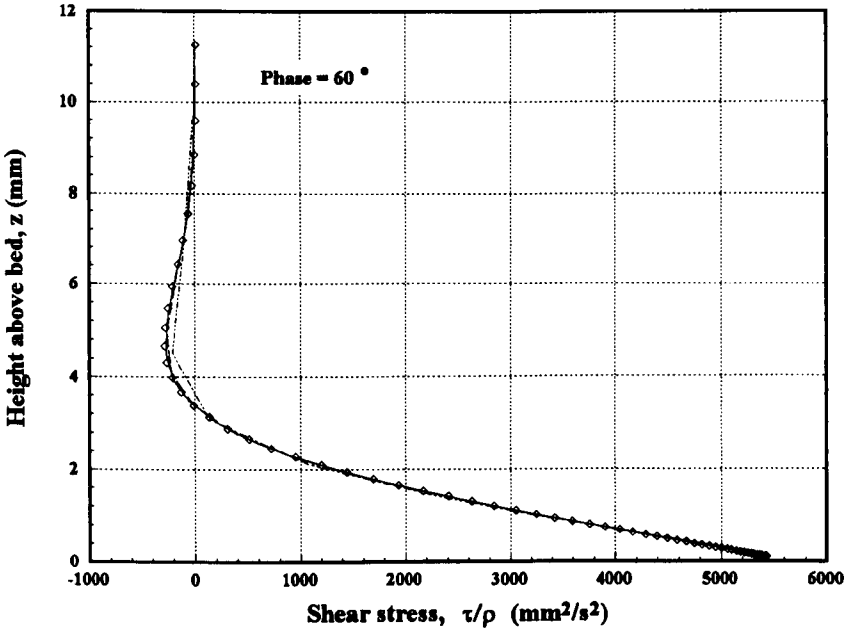

(c)

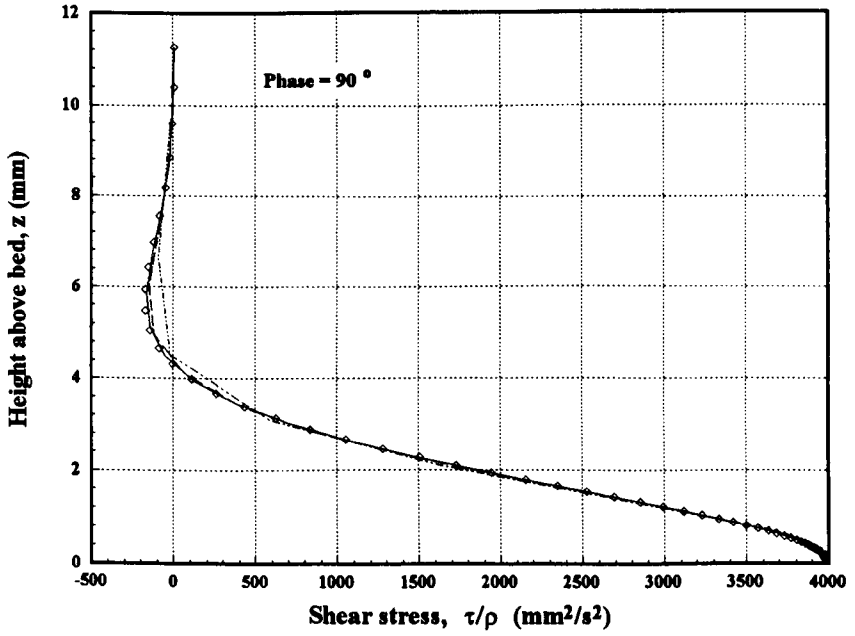

(d)

Figure D2(Cont.): Comparison of Lamb's analytical solution against results from the k-ε model for different numbers of vertcial nodes: ◊ Lamb; — k-ε model (60 nodes); – – – k-ε model (40 nodes); — – – — k-ε model (20 nodes).

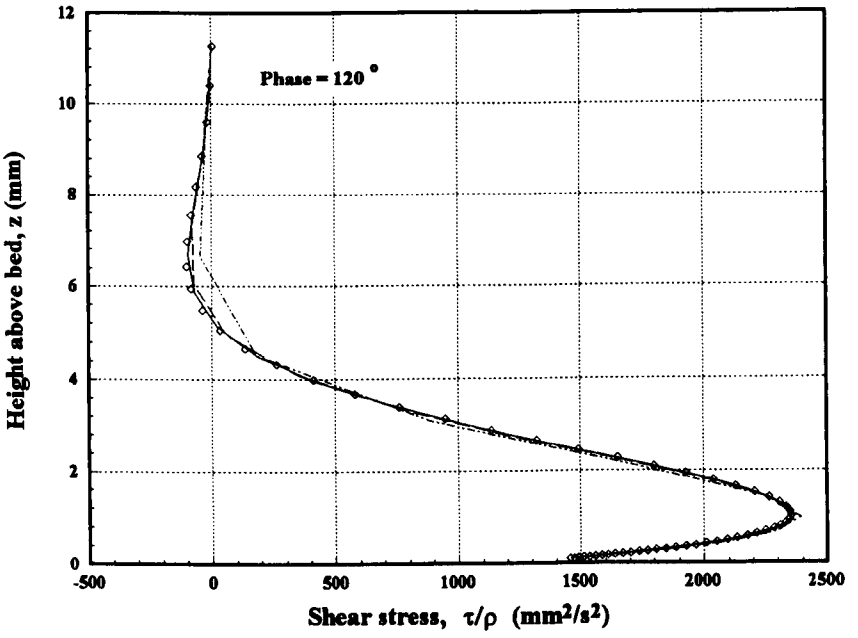

(e)

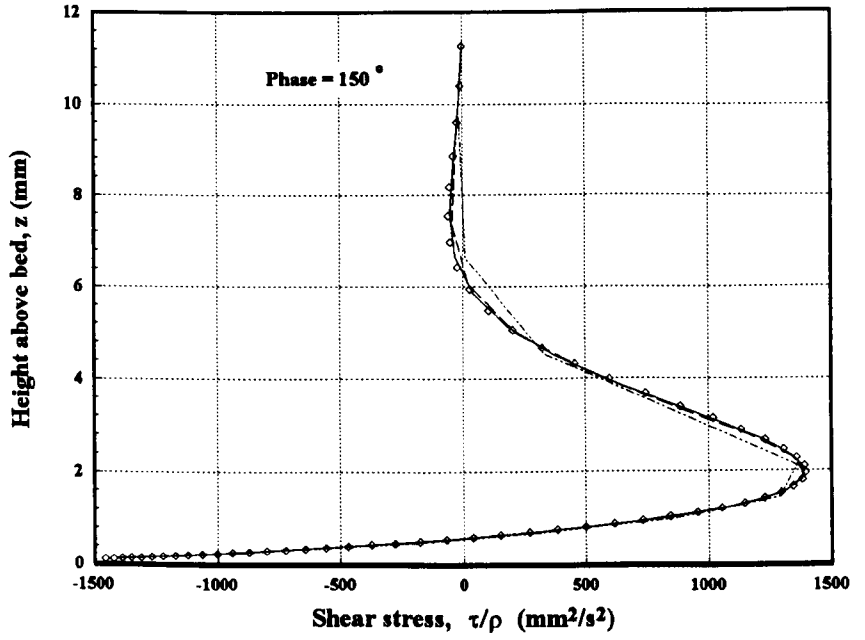

(f)

Figure D2(Cont.): Comparison of Lamb's analytical solution against results from the k-ε model for different numbers of vertcial nodes: ◊ Lamb; — k-ε model (60 nodes); – – – k-ε model (40 nodes); — – – — k-ε model (20 nodes).

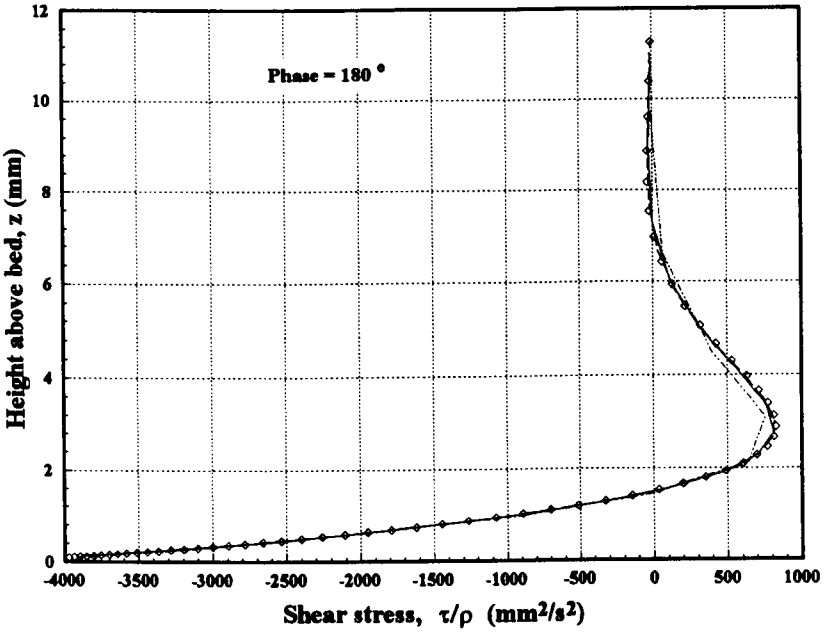

(g)

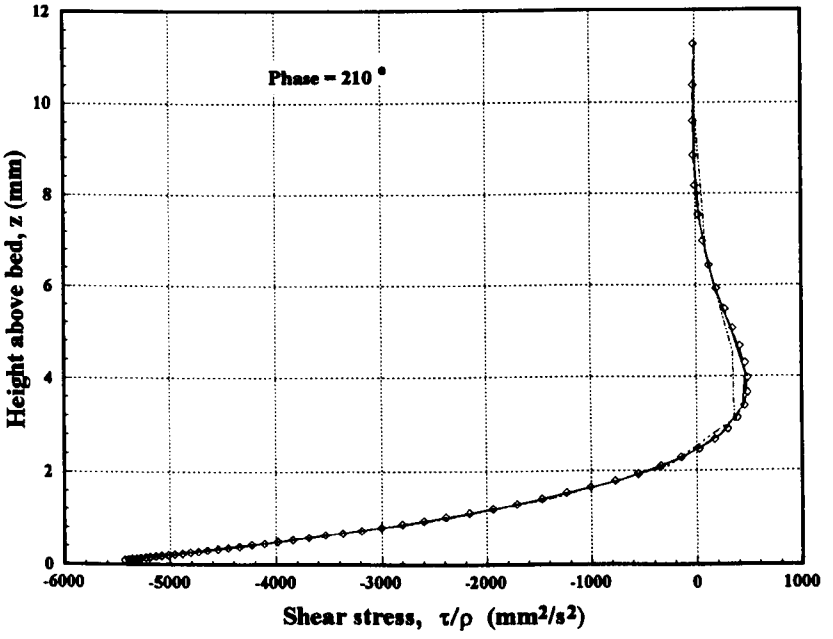

(h)

Figure D2(Cont.): Comparison of Lamb's analytical solution against results from the k-ε model for different numbers of vertcial nodes: ◊ Lamb; — k-ε model (60 nodes); – – – k-ε model (40 nodes); — – – — k-ε model (20 nodes).

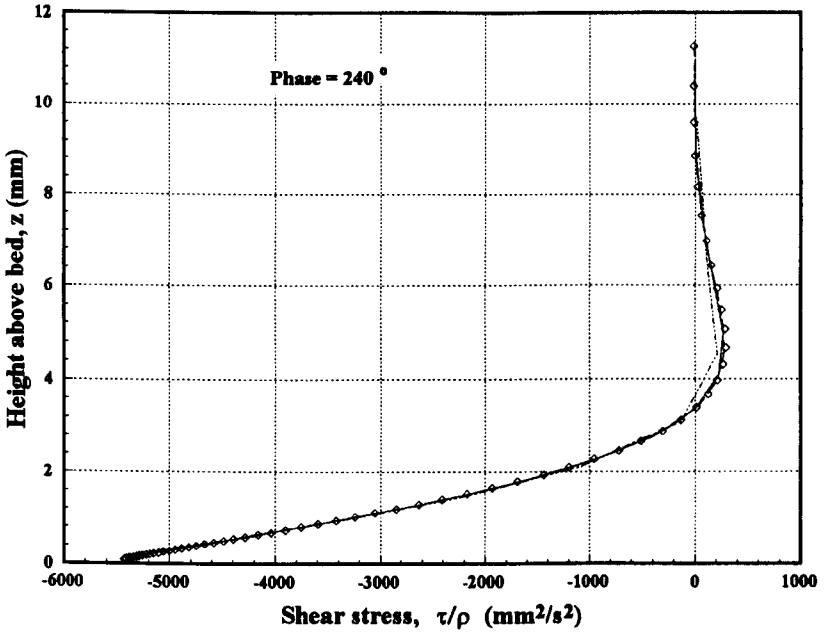

(i)

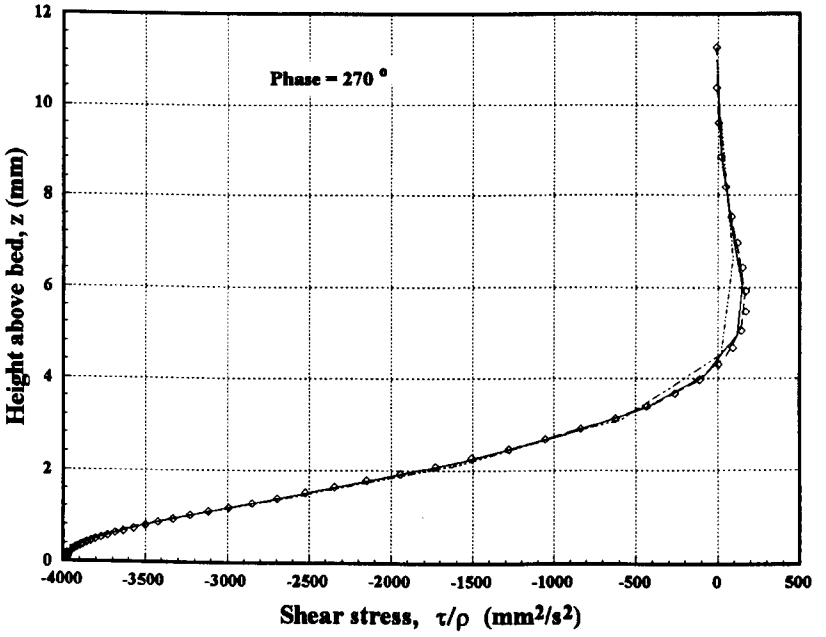

(j)

Figure D2(Cont.): Comparison of Lamb's analytical solution against results from the k-ε model for different numbers of vertcial nodes: ◊ Lamb; — k-ε model (60 nodes); – – – k-ε model (40 nodes); — – – — k-ε model (20 nodes).

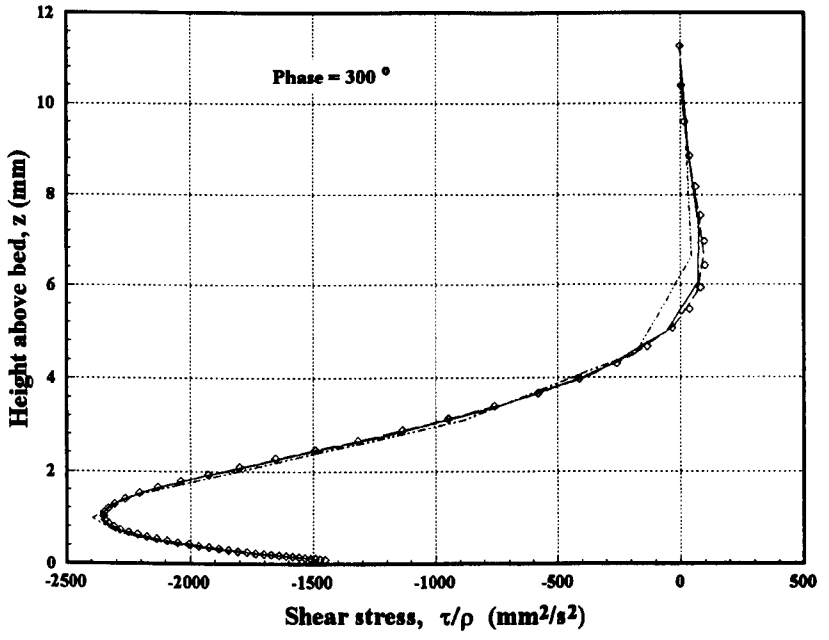

(k)

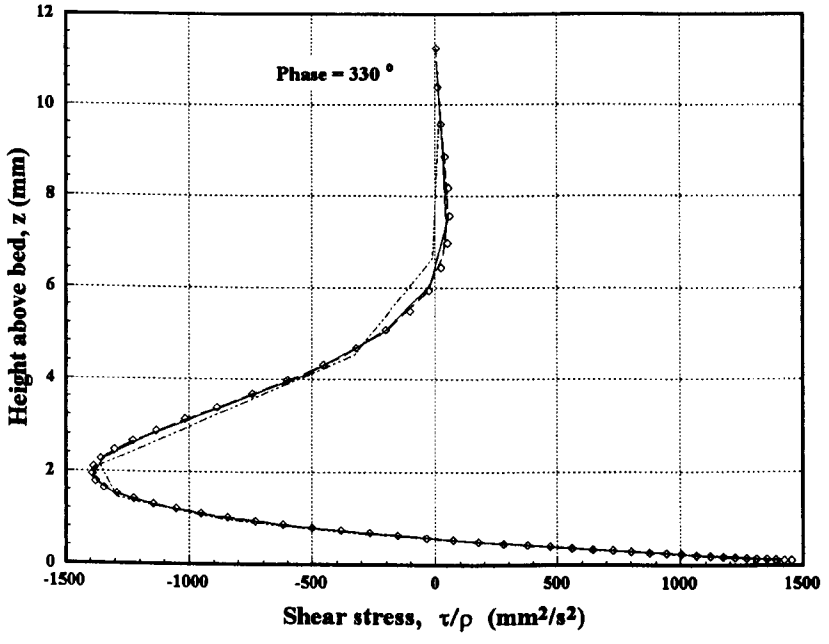

(l)

Figure D2(Cont.): Comparison of Lamb's analytical solution against results from the k-ε model for different numbers of vertcial nodes: ◊ Lamb; — k-ε model (60 nodes); – – – k-ε model (40 nodes); — – – — k-ε model (20 nodes).

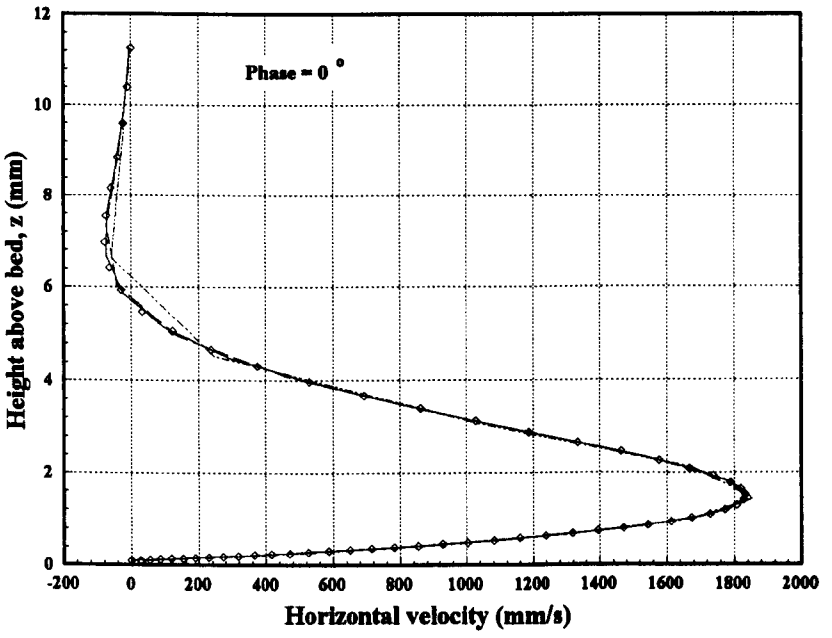

(a)

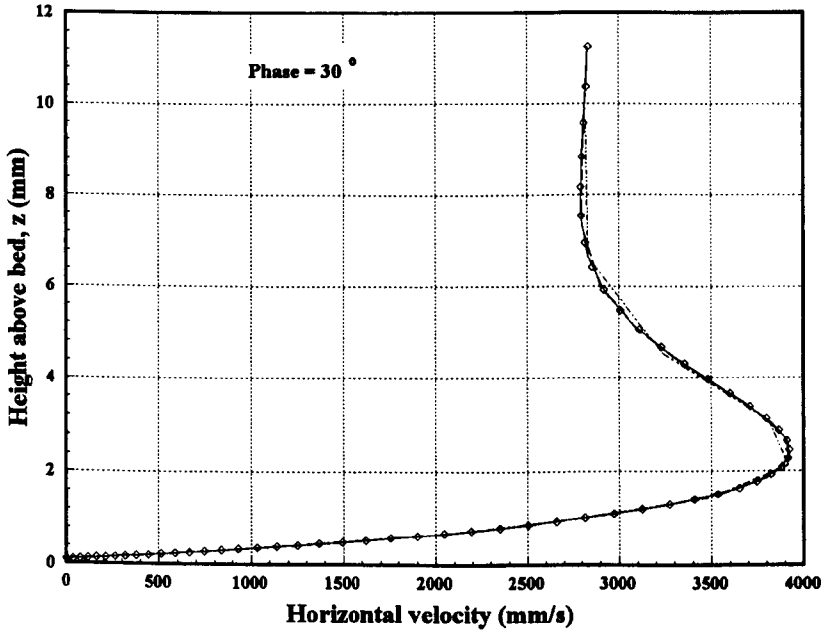

(b)

Figure D3: Comparison of Lamb's analytical solution against results from the k model for different numbers of vertcial nodes: ◊ Lamb; — k model (60 nodes); - - - k model (40 nodes); — - - — k model (20 nodes).

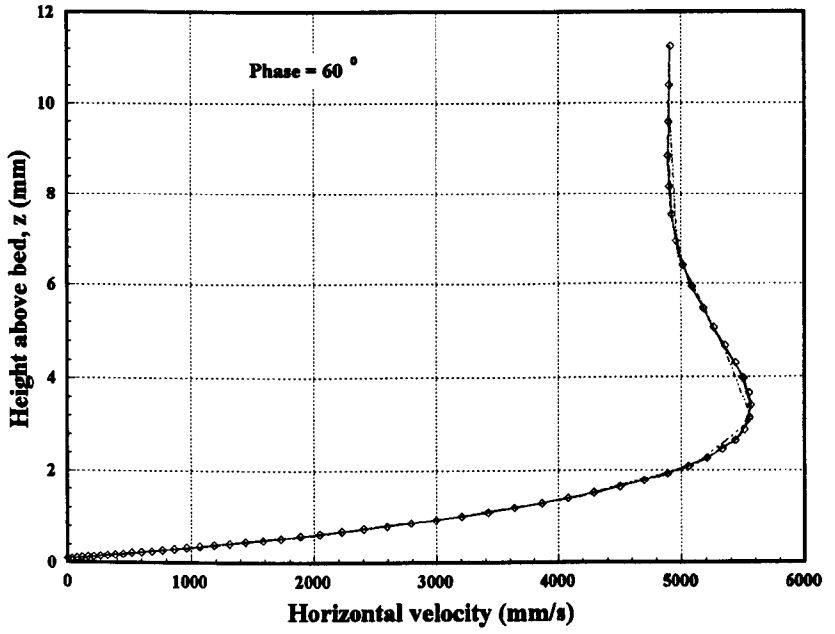

(c)

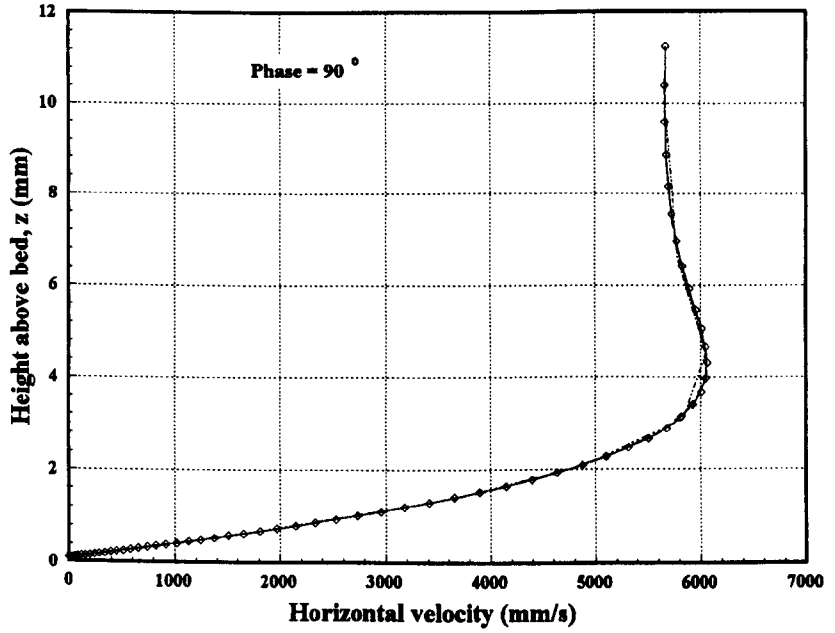

(d)

Figure D3(Cont.): Comparison of Lamb's analytical solution against results from the kmodel for different numbers of vertcial nodes: ◊ Lamb; — k model (60 nodes); – – – k model (40 nodes); — – – — k model (20 nodes).

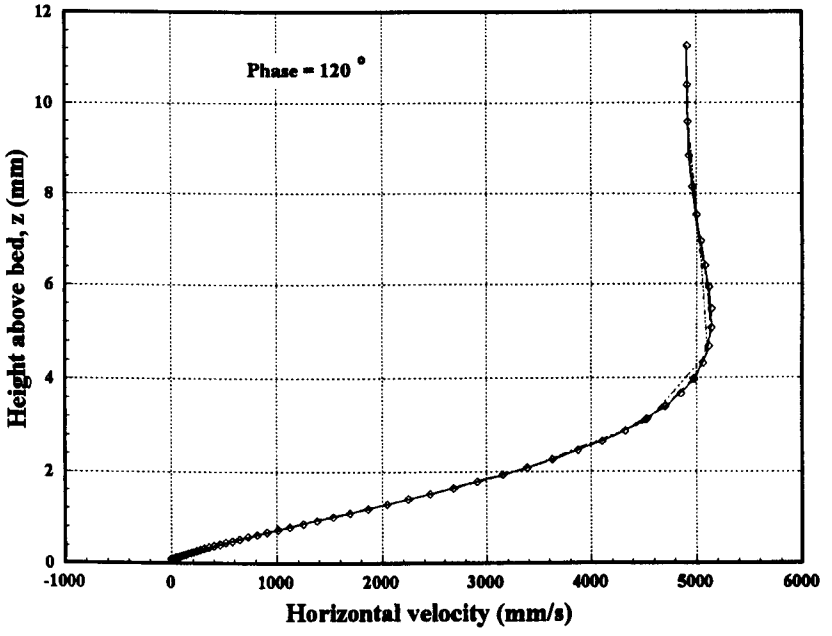

(e)

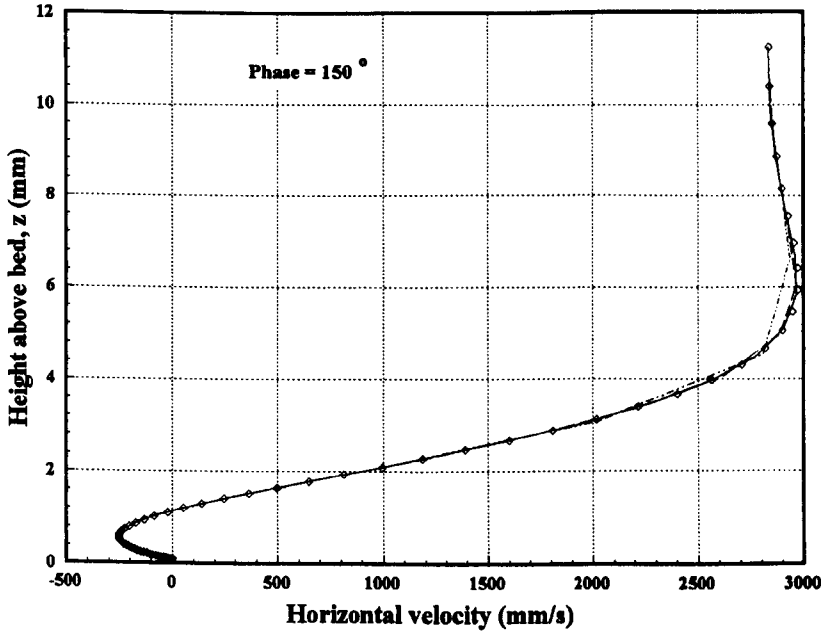

(f)

Figure D3(Cont.): Comparison of Lamb's analytical solution against results from the k model for different numbers of vertcial nodes: ◊ Lamb; — k model (60 nodes); – – – k model (40 nodes); — – – — k model (20 nodes).

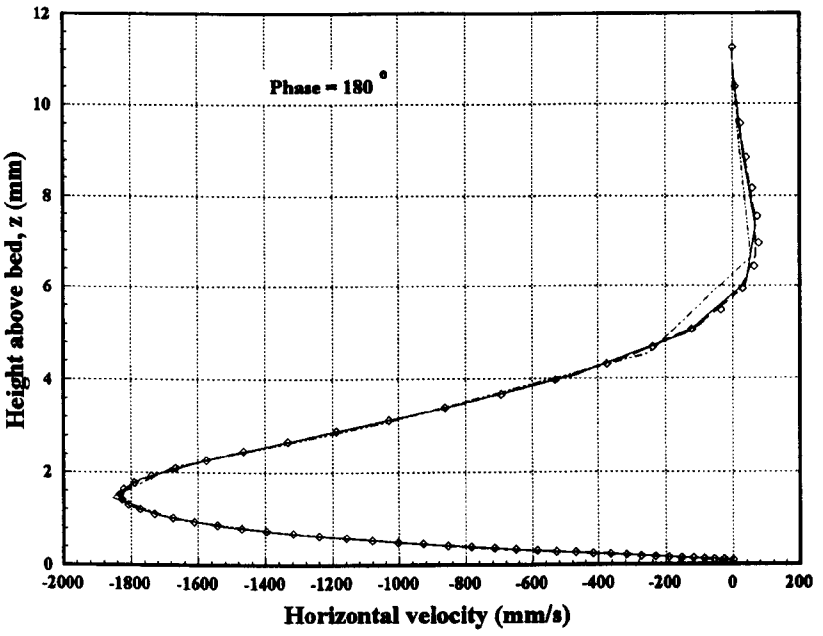

(g)

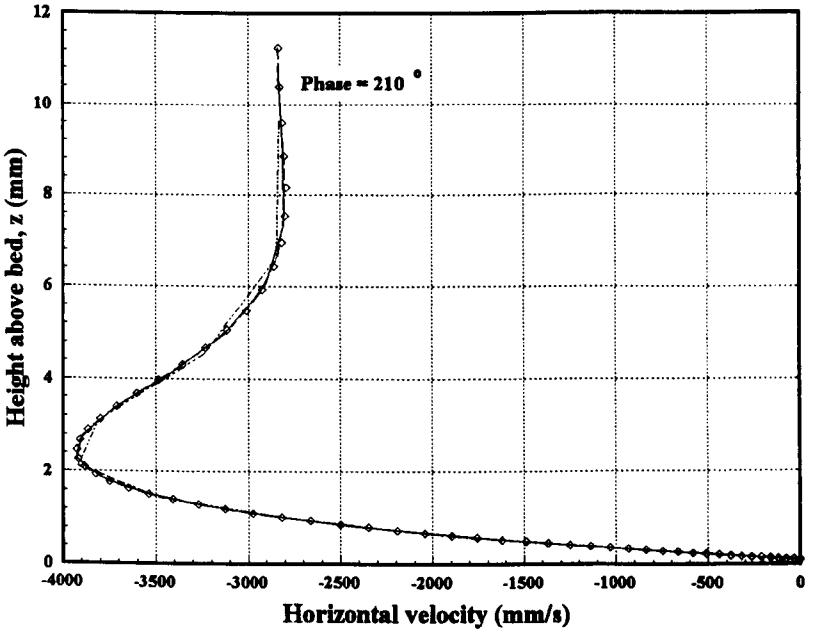

(h)

Figure D3(Cont.): Comparison of Lamb's analytical solution against results from the k model for different numbers of vertcial nodes: ◊ Lamb; — k model (60 nodes); – – – k model (40 nodes); — – – — k model (20 nodes).

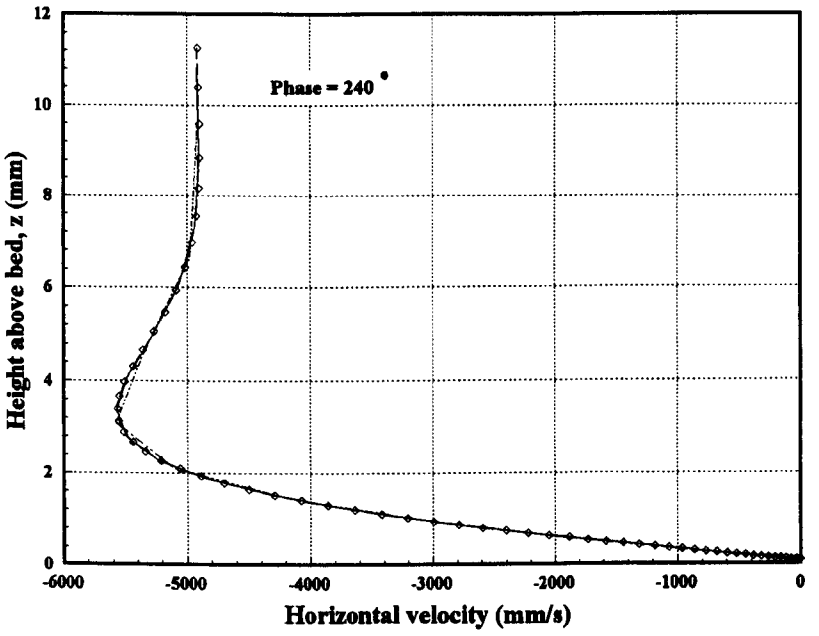

(i)

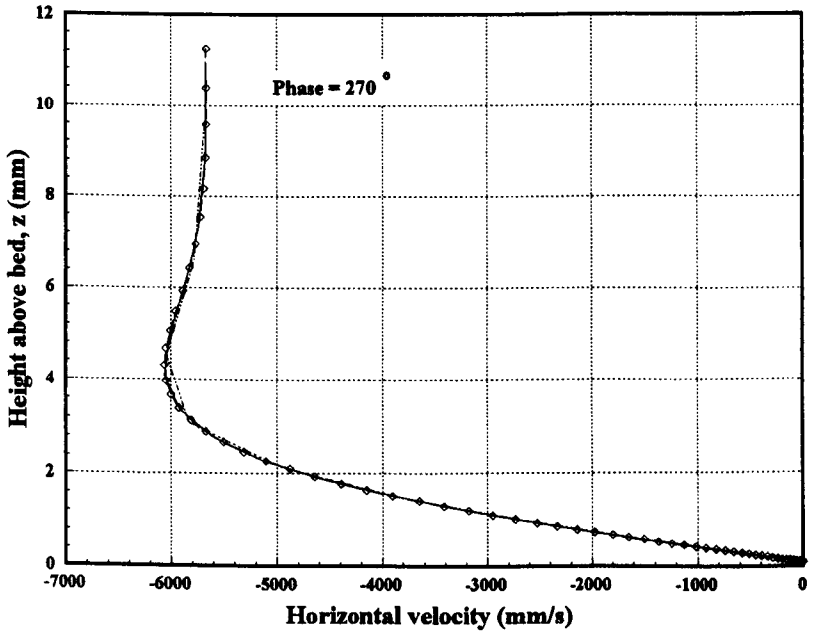

(j)

Figure D3(Cont.): Comparison of Lamb's analytical solution against results from the k model for different numbers of vertcial nodes: ◊ Lamb; — k model (60 nodes); – – – k model (40 nodes); — – – — k model (20 nodes).

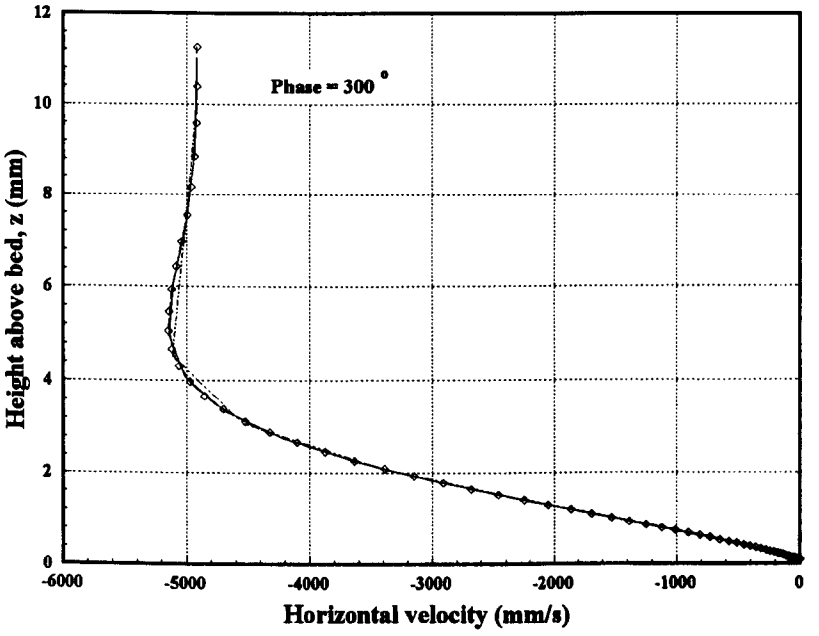

(k)

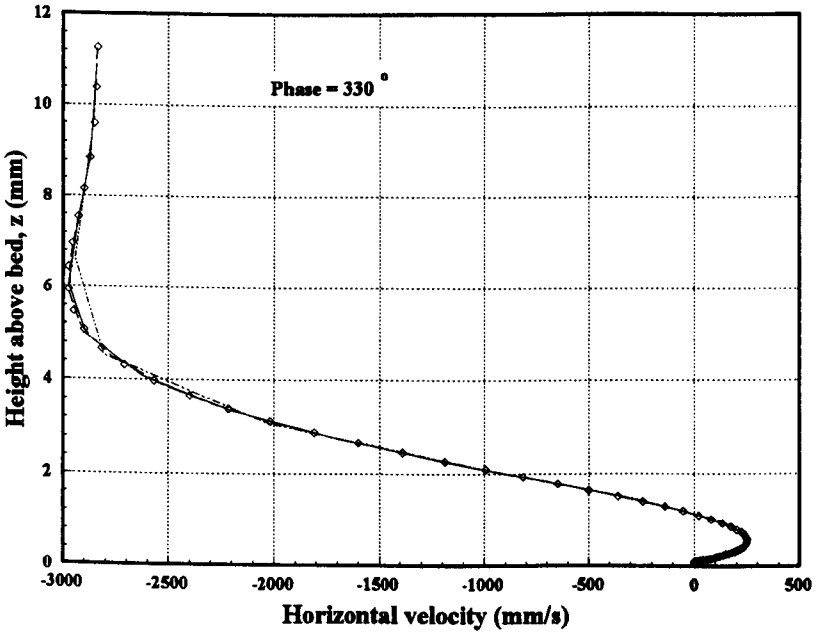

(l)

Figure D3(Cont.): Comparison of Lamb's analytical solution against results from the k model for different numbers of vertcial nodes: ◊ Lamb; — k model (60 nodes); – – – k model (40 nodes); — – – — k model (20 nodes).

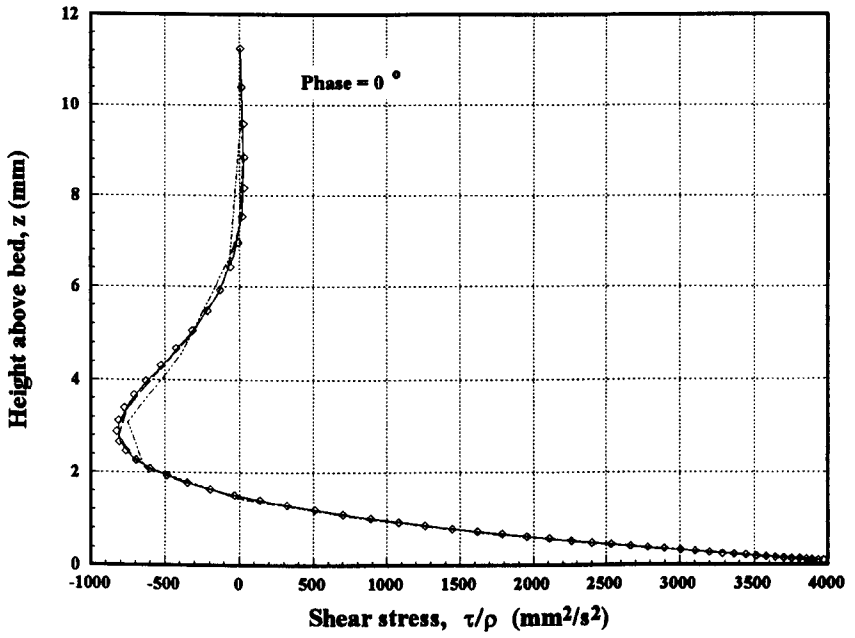

(a)

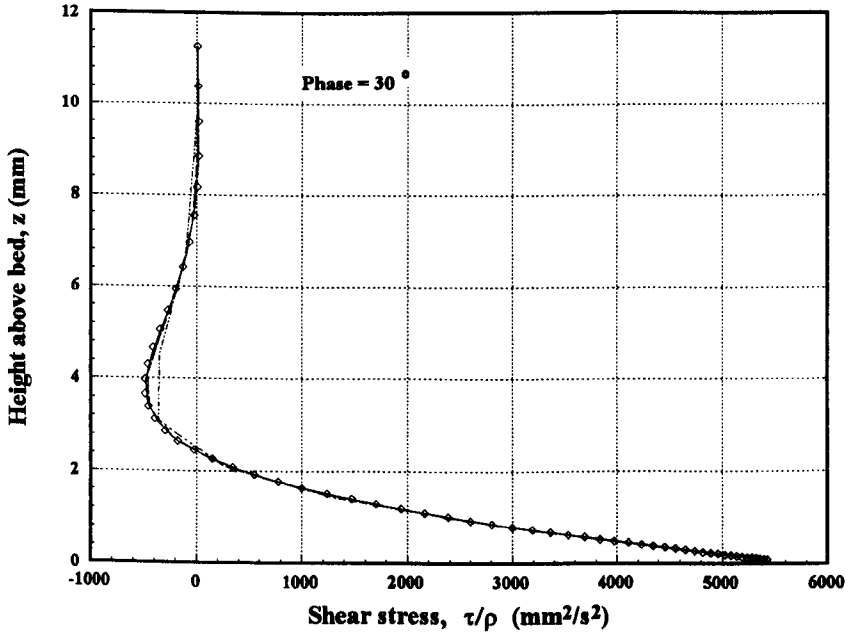

(b)

Figure D4: Comparison of Lamb's analytical solution against results from the k model for different numbers of vertcial nodes: ◊ Lamb; — k model (60 nodes); - - - k model (40 nodes); — - - — k model (20 nodes).

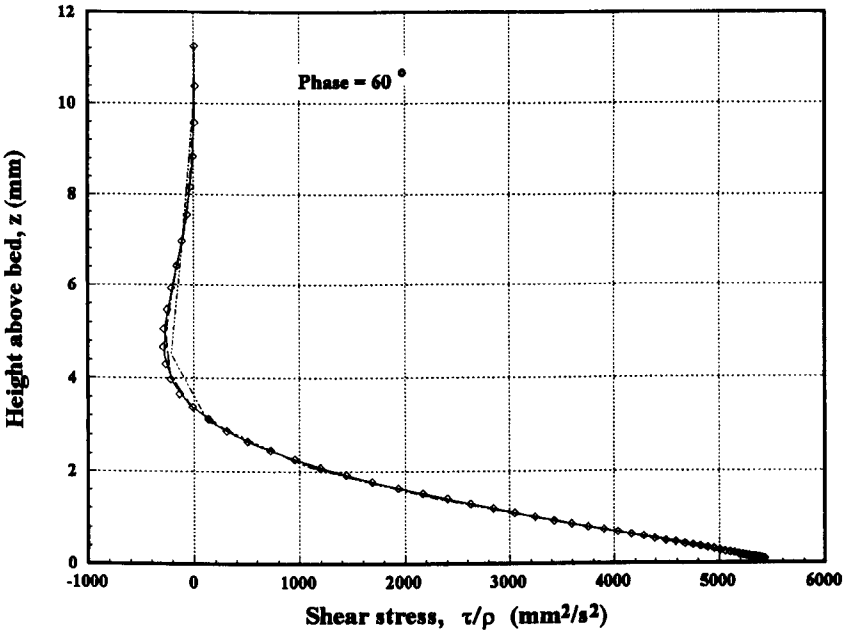

(c)

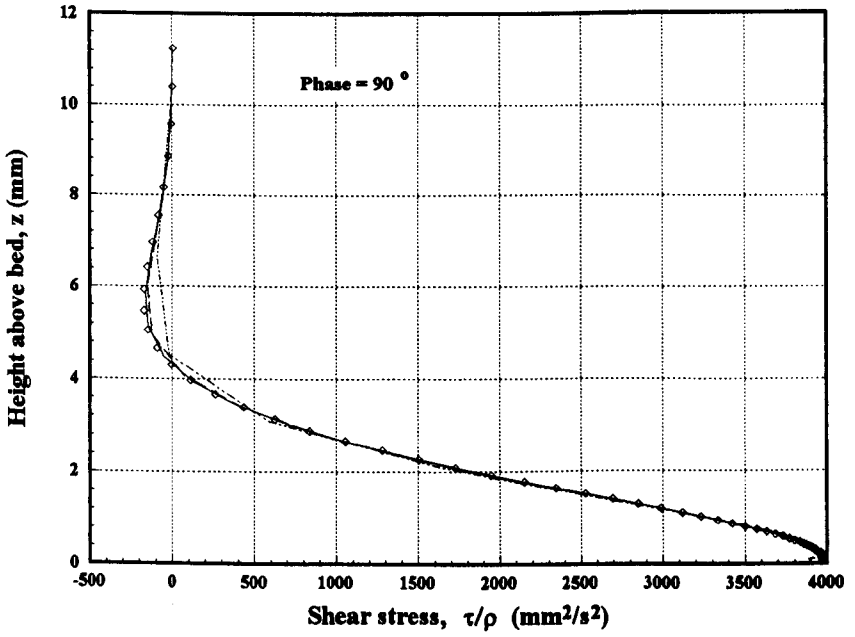

(d)

Figure D4(Cont.): Comparison of Lamb's analytical solution against results from the k model for different numbers of vertcial nodes: ◊ Lamb; — k model (60 nodes); – – – k model (40 nodes); — – – — k model (20 nodes).

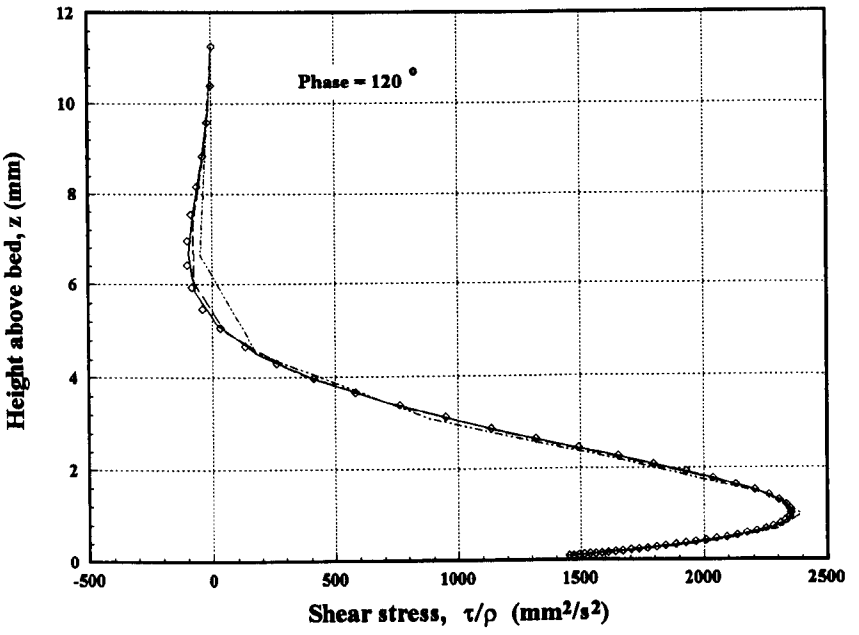

(e)

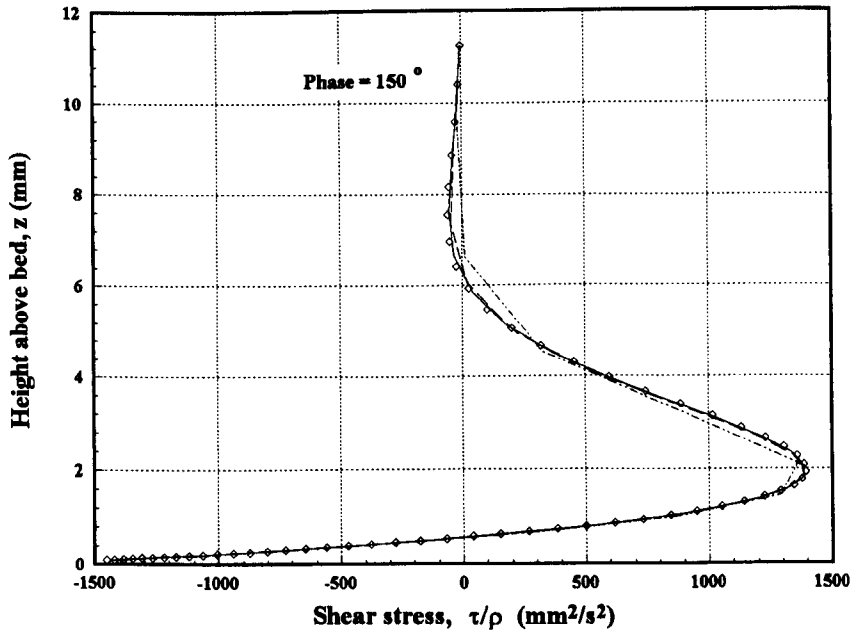

(f)

Figure D4(Cont.): Comparison of Lamb's analytical solution against results from the k model for different numbers of vertcial nodes: ◊ Lamb; — k model (60 nodes); – – – k model (40 nodes); — – – — k model (20 nodes).

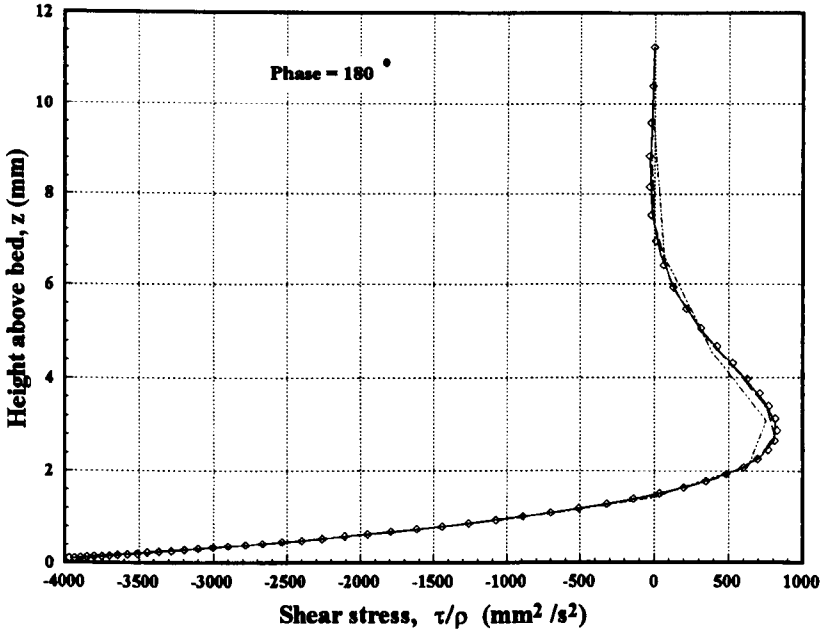

(g)

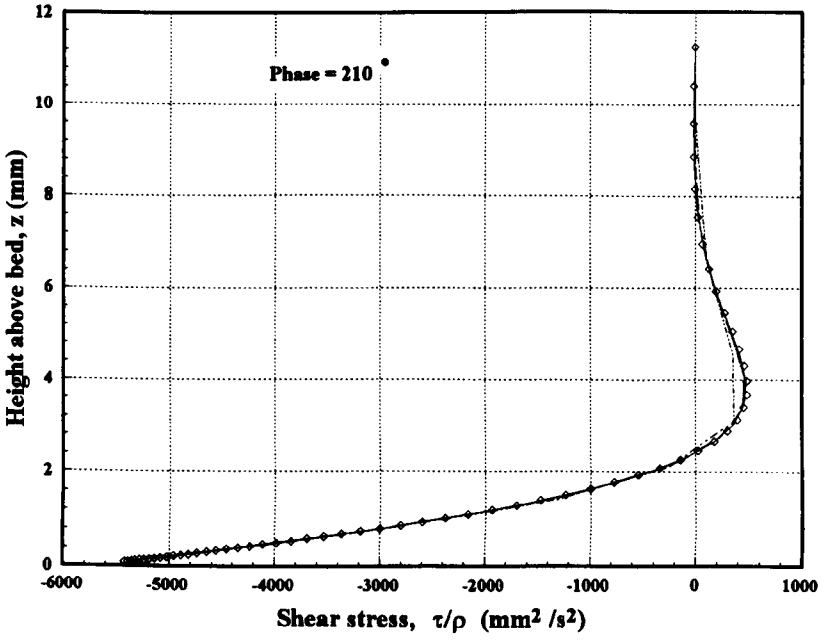

(h)

Figure D4(Cont.): Comparison of Lamb's analytical solution against results from the k model for different numbers of vertcial nodes: ◊ Lamb; — k model (60 nodes); – – – k model (40 nodes); — – – — k model (20 nodes).

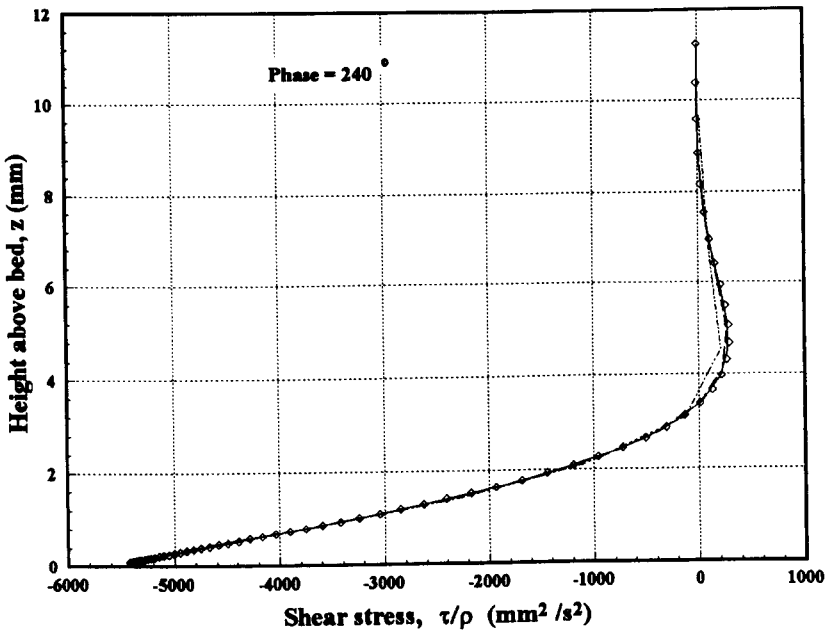

(i)

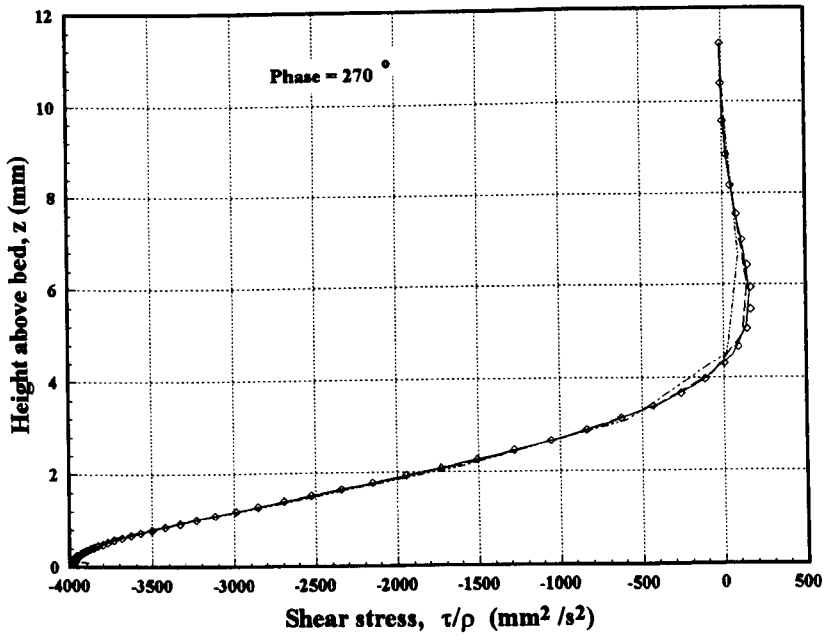

(j)

Figure D4(Cont.): Comparison of Lamb's analytical solution against results from the k model for different numbers of vertcial nodes: ◊ Lamb; — k model (60 nodes); – – – k model (40 nodes); — – – — k model (20 nodes).

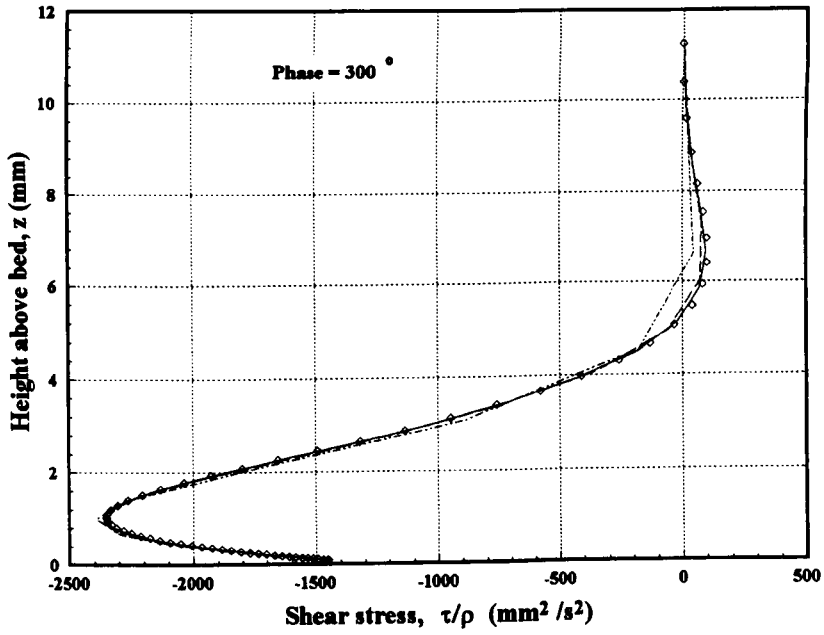

(k)

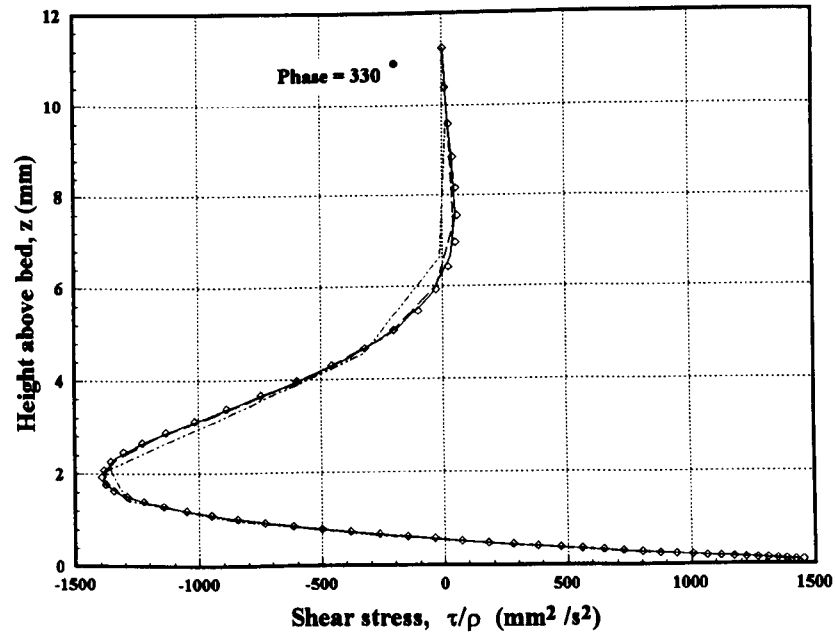

(l)

Figure D4(Cont.): Comparison of Lamb's analytical solution against results from the k model for different numbers of vertcial nodes: ◊ Lamb; — k model (60 nodes); – – – k model (40 nodes); — – – — k model (20 nodes).

Appendix E

Tables of Results For The Hydrodynamic Models

Height above bed (mm)	Horizontal velocity, u (mm/s)		
	30°	60°	270°
0.767	0.000	0.000	0.000
0.887	33.308	38.145	-35.301
1.026	69.351	79.554	-73.717
1.187	108.170	124.280	-115.304
1.373	149.776	172.345	-160.086
1.588	194.154	223.734	-208.052
1.837	241.256	278.397	-259.158
2.124	291.003	336.252	-313.330
2.457	343.286	397.183	-370.464
2.843	397.966	461.044	-430.433
3.288	454.876	527.665	-493.088
3.803	513.824	596.855	-558.268
4.400	574.591	668.405	-625.798
5.089	636.937	742.093	-695.500
5.887	700.599	817.688	-767.191
6.809	765.291	894.948	-840.688
7.876	830.698	973.629	-915.812
9.111	896.473	1053.480	-992.385
10.539	962.219	1134.239	-1070.232
12.191	1027.471	1215.638	-1149.182
14.101	1091.658	1297.389	-1229.062
16.311	1154.027	1379.182	-1309.695
18.868	1213.507	1460.670	-1390.898
21.825	1268.425	1541.447	-1472.470
25.246	1315.913	1621.022	-1554.186
29.202	1351.041	1698.763	-1635.782
33.779	1368.399	1773.810	-1716.938
39.073	1369.069	1844.884	-1797.246
45.197	1359.246	1909.908	-1876.165
52.281	1343.522	1965.117	-1952.937
60.475	1324.078	2003.364	-2026.434
69.953	1301.851	2017.112	-2094.834
80.916	1277.245	2011.333	-2154.896
93.598	1250.454	1995.903	-2200.239
108.268	1221.609	1975.991	-2220.802
125.237	1190.871	1953.654	-2218.277
144.865	1158.536	1929.935	-2205.282
167.569	1125.210	1905.827	-2189.428
193.832	1092.240	1882.908	-2174.276
224.212	1066.351	1866.230	-2163.930
300.000	1051.836	1857.596	-2158.856

Table E1a: Computed velocity values from the k-model (time-variant) for the data of Jonsson and Carlsen (1976).

Height above bed (mm)	Horizontal velocity, u (mm/s)		
	300°	330°	360°
0.767	0.000	0.000	0.000
0.887	-24.231	-2.505	22.269
1.026	-50.751	-5.866	46.122
1.187	-79.612	-10.221	71.569
1.373	-110.838	-15.690	98.603
1.588	-144.426	-22.369	127.193
1.837	-180.351	-30.326	157.282
2.124	-218.564	-39.608	188.780
2.457	-259.001	-50.245	221.563
2.843	-301.582	-62.261	255.460
3.288	-346.221	-75.682	290.246
3.803	-392.826	-90.535	325.622
4.400	-441.304	-106.854	361.186
5.089	-491.566	-124.680	396.379
5.887	-543.527	-144.062	430.392
6.809	-597.108	-165.053	462.002
7.876	-652.239	-187.712	489.380
9.111	-708.856	-212.102	510.142
10.539	-766.902	-238.288	522.376
12.191	-826.326	-266.336	526.135
14.101	-887.082	-296.311	523.118
16.311	-949.123	-328.277	515.167
18.868	-1012.403	-362.292	503.549
21.825	-1076.868	-398.409	489.000
25.246	-1142.452	-436.670	471.906
29.202	-1209.074	-477.107	452.450
33.779	-1276.625	-519.731	430.702
39.073	-1344.958	-564.531	406.664
45.197	-1413.869	-611.465	380.304
52.281	-1483.078	-660.448	351.575
60.475	-1552.187	-711.340	320.433
69.953	-1620.619	-763.918	286.854
80.916	-1687.507	-817.846	250.855
93.598	-1751.474	-872.616	212.516
108.268	-1810.153	-927.445	172.026
125.237	-1859.089	-981.073	129.740
144.865	-1889.666	-1031.337	86.296
167.569	-1897.172	-1074.224	42.830
193.832	-1892.836	-1102.698	1.384
224.212	-1887.743	-1112.036	-28.350
300.000	-1885.034	-1114.009	-42.740

Table E1b: Computed velocity values from the k-model (time-variant) for the data of Jonsson and Carlsen (1976).

Height above bed (mm)	Shear stress , τ/ρ (mm^2/s^2)		
	30°	60°	270°
0.767	26368.713	35737.355	-31456.229
0.887	27078.213	36763.512	-32399.779
1.026	26885.018	36644.930	-32388.539
1.187	26664.553	36509.227	-32374.816
1.373	26413.258	36354.000	-32357.971
1.588	26127.102	36176.484	-32337.166
1.837	25801.594	35973.496	-32311.311
2.124	25431.701	35741.371	-32279.008
2.457	25011.809	35475.902	-32238.498
2.843	24535.650	35172.262	-32187.582
3.288	23996.268	34824.930	-32123.543
3.803	23385.951	34427.574	-32043.045
4.400	22696.199	33972.992	-31942.027
5.089	21917.689	33452.973	-31815.564
5.887	21040.268	32858.195	-31657.732
6.809	20052.990	32178.123	-31461.426
7.876	18944.201	31400.865	-31218.180
9.111	17701.736	30513.080	-30917.955
10.539	16313.258	29499.889	-30548.916
12.191	14766.874	28344.809	-30097.182
14.101	13052.229	27029.771	-29546.586
16.311	11162.503	25535.238	-28878.426
18.868	9098.506	23840.508	-28071.246
21.825	6878.849	21924.316	-27100.688
25.246	4574.946	19765.955	-25939.432
29.202	2432.685	17347.309	-24557.352
33.779	781.705	14656.623	-22922.018
39.073	-426.716	11696.118	-20999.781
45.197	-1358.687	8499.914	-18757.912
52.281	-2131.710	5190.302	-16168.690
60.475	-2820.350	2262.668	-13217.479
69.953	-3455.172	314.432	-9920.633
80.916	-4036.719	-899.310	-6369.630
93.598	-4545.492	-1690.053	-2962.198
108.268	-4945.625	-2242.285	-657.641
125.237	-5184.793	-2628.809	566.281
144.865	-5191.306	-2839.990	1153.953
167.569	-4868.219	-2813.624	1354.270
193.832	-3848.127	-2321.803	1187.934
224.212	-2755.907	-1707.691	898.420
300.000	-780.786	-496.337	263.141

Table E2a: Computed shear stress values from the k-model (time-variant) for the data of Jonsson and Carlsen (1976).

Height above bed (mm)	Shear stress, τ/ρ (mm^2/s^2)		
	30°	60°	270°
0.767	-15842.716	-701.569	10678.547
0.887	-16362.664	-808.937	10903.168
1.026	-16461.984	-987.725	10686.693
1.187	-16573.584	-1186.097	10440.257
1.373	-16698.578	-1405.729	10160.170
1.588	-16838.037	-1648.395	9842.399
1.837	-16992.961	-1915.921	9482.552
2.124	-17164.225	-2210.153	9075.880
2.457	-17352.541	-2532.942	8617.306
2.843	-17558.393	-2886.133	8101.475
3.288	-17781.955	-3271.534	7522.871
3.803	-18023.021	-3690.857	6876.042
4.400	-18280.883	-4145.634	6156.035
5.089	-18554.203	-4637.118	5359.340
5.887	-18840.879	-5166.151	4486.158
6.809	-19137.854	-5733.016	3546.420
7.876	-19440.932	-6337.261	2573.954
9.111	-19744.533	-6977.489	1636.895
10.539	-20041.455	-7651.120	793.125
12.191	-20322.563	-8354.106	39.538
14.101	-20576.473	-9080.616	-653.493
16.311	-20789.197	-9822.656	-1314.638
18.868	-20943.762	-10569.667	-1968.642
21.825	-21019.801	-11308.058	-2633.409
25.246	-20993.164	-12020.705	-3319.268
29.202	-20835.545	-12686.417	-4029.817
33.779	-20514.184	-13279.392	-4762.608
39.073	-19991.750	-13768.686	-5509.191
45.197	-19226.514	-14117.760	-6254.612
52.281	-18173.053	-14284.207	-6976.517
60.475	-16783.945	-14219.798	-7644.0269
69.953	-15013.203	-13871.142	-8216.578
80.916	-12823.156	-13181.459	-8642.990
93.598	-10198.881	-12094.396	-8861.204
108.268	-7182.527	-10561.861	-8799.433
125.237	-3975.057	-8560.680	-8380.054
144.865	-1418.688	-6131.785	-7528.626
167.569	-106.164	-3507.861	-6199.560
193.832	334.776	-1388.576	-4075.418
224.212	369.927	-476.648	-2401.338
300.000	117.916	-73.580	-581.519

Table E2b: Computed shear stress values from the k-model (time-variant) for the data of Jonsson and Carlsen (1976).

Height above bed (mm)	Horizontal velocity, u (mm/s)		
	30°	60°	270°
0.767	0.000	0.000	0.000
0.887	52.024	61.927	-59.718
1.026	107.555	127.940	-123.303
1.187	163.277	193.783	-186.445
1.373	219.338	259.614	-249.278
1.588	275.859	325.565	-311.924
1.837	332.939	391.749	-374.489
2.124	390.666	458.269	-437.074
2.457	449.116	525.221	-499.774
2.843	508.360	592.697	-562.685
3.288	568.459	660.785	-625.902
3.803	629.468	729.579	-689.525
4.400	691.431	799.169	-753.656
5.089	754.371	869.653	-818.407
5.887	818.284	941.129	-883.896
6.809	883.112	1013.698	-950.249
7.876	948.711	1087.465	-1017.605
9.111	1014.786	1162.530	-1086.110
10.539	1080.774	1238.989	-1155.922
12.191	1145.656	1316.920	-1227.210
14.101	1207.637	1396.370	-1300.148
16.311	1263.806	1477.324	-1374.917
18.868	1310.299	1559.653	-1451.693
21.825	1344.048	1643.022	-1530.638
25.246	1365.157	1726.694	-1611.879
29.202	1376.362	1809.158	-1695.468
33.779	1380.525	1887.371	-1781.313
39.073	1379.433	1955.572	-1869.051
45.197	1373.872	2005.533	-1957.768
52.281	1363.964	2033.174	-2045.424
60.475	1349.439	2043.347	-2127.555
69.953	1329.825	2042.436	-2195.070
80.916	1304.592	2033.772	-2236.079
93.598	1273.292	2018.432	-2250.380
108.268	1235.733	1996.579	-2247.893
125.237	1192.265	1968.263	-2235.012
144.865	1144.353	1933.956	-2214.199
167.569	1095.814	1895.207	-2186.992
193.832	1054.905	1855.874	-2155.960
224.212	1031.837	1823.815	-2126.529
300.000	1024.387	1807.487	-2107.950

Table E3a: Computed velocity results from the k-ε model for the data of Jonsson and Carlsen (1976).

Height above bed (mm)	Horizontal velocity, u (mm/s)		
	300°	330°	360°
0.767	0.000	0.000	0.000
0.887	-44.323	-13.199	33.979
1.026	-91.421	-27.195	70.135
1.187	-137.824	-40.489	106.593
1.373	-183.623	-53.200	143.376
1.588	-228.910	-65.483	180.428
1.837	-273.785	-77.495	217.606
2.124	-318.345	-89.388	254.655
2.457	-362.695	-101.306	291.177
2.843	-406.942	-113.382	326.602
3.288	-451.200	-125.748	360.173
3.803	-495.586	-138.534	391.004
4.400	-540.229	-151.872	418.222
5.089	-585.263	-165.896	441.197
5.887	-630.835	-180.753	459.730
6.809	-677.101	-196.594	474.059
7.876	-724.230	-213.586	484.694
9.111	-772.404	-231.911	492.208
10.539	-821.820	-251.765	497.092
12.191	-872.689	-273.365	499.697
14.101	-925.240	-296.945	500.226
16.311	-979.714	-322.763	498.740
18.868	-1036.370	-351.097	495.180
21.825	-1095.476	-382.245	489.369
25.246	-1157.309	-416.526	481.028
29.202	-1222.141	-454.276	469.782
33.779	-1290.227	-495.840	455.169
39.073	-1361.774	-541.561	436.662
45.197	-1436.888	-591.765	413.692
52.281	-1515.480	-646.724	385.685
60.475	-1597.073	-706.603	352.107
69.953	-1680.408	-771.347	312.531
80.916	-1762.537	-840.481	266.729
93.598	-1836.759	-912.662	214.832
108.268	-1890.041	-984.675	157.632
125.237	-1912.342	-1049.163	97.237
144.865	-1911.803	-1092.310	38.577
167.569	-1898.769	-1106.471	-8.001
193.832	-1878.766	-1102.286	-30.709
224.212	-1857.087	-1091.164	-34.615
300.000	-1841.908	-1081.836	-32.533

Table E3b: Computed velocity results from the k-ε model for the data of Jonsson and Carlsen (1976).

Height above bed (mm)	Shear stress, τ/ρ (mm^2/s^2)		
	30°	60°	270°
0.767	23818.414	35047.703	-33564.813
0.887	21285.043	31298.496	-29956.631
1.026	21857.920	32353.672	-31112.758
1.187	21702.582	32292.016	-31166.879
1.373	21510.684	32202.078	-31207.250
1.588	21279.629	32082.836	-31234.684
1.837	21005.988	31932.490	-31249.400
2.124	20685.498	31748.469	-31251.053
2.457	20313.021	31527.410	-31238.709
2.843	19882.492	31265.098	-31210.813
3.288	19386.838	30956.379	-31165.113
3.803	18817.891	30595.059	-31098.564
4.400	18166.295	30173.760	-31007.209
5.089	17421.438	29683.764	-30886.016
5.887	16571.430	29114.814	-30728.693
6.809	15603.202	28454.906	-30527.465
7.876	14502.892	27690.035	-30272.785
9.111	13256.830	26803.932	-29953.029
10.539	11853.966	25777.779	-29554.111
12.191	10291.825	24589.969	-29059.061
14.101	8591.221	23215.934	-28447.523
16.311	6825.939	21628.191	-27695.225
18.868	5140.578	19796.928	-26773.406
21.825	3667.105	17691.717	-25648.258
25.246	2411.918	15286.095	-24280.498
29.202	1307.444	12570.309	-22625.268
33.779	291.529	9592.494	-20632.861
39.073	-676.970	6578.290	-18251.330
45.197	-1617.901	3993.500	-15433.753
52.281	-2531.114	2053.787	-12159.898
60.475	-3398.171	566.063	-8519.451
69.953	-4183.110	-638.210	-4980.019
80.916	-4832.158	-1637.272	-2317.679
93.598	-5273.238	-2451.465	-524.400
108.268	-5416.847	-3057.057	726.547
125.237	-5161.777	-3398.766	1575.160
144.865	-4415.551	-3402.518	2071.546
167.569	-3170.717	-2996.380	2201.236
193.832	-1736.240	-2179.734	1924.886
224.212	-703.528	-1190.829	1271.549
300.000	-138.823	-304.227	366.274

Table E4a: Computed shear stress values from the k-ε model for the data of Jonsson and Carlsen (1976).

Height above bed (mm)	Shear stress, τ/ρ (mm^2/s^2)		
	300°	330°	360°
0.767	-19656.244	-3321.431	9262.465
0.887	-17524.857	-2958.189	8263.898
1.026	-18365.738	-3323.686	8324.335
1.187	-18525.789	-3533.469	8118.658
1.373	-18688.615	-3756.483	7876.322
1.588	-18856.434	-3995.426	7594.589
1.837	-19031.137	-4252.998	7270.626
2.124	-19214.295	-4531.760	6902.024
2.457	-19407.133	-4834.118	6487.646
2.843	-19610.504	-5162.329	6028.925
3.288	-19824.836	-5518.491	5531.427
3.803	-20050.061	-5904.511	5005.628
4.400	-20285.514	-6322.041	4465.069
5.089	-20529.813	-6772.389	3921.389
5.887	-20780.699	-7256.396	3379.636
6.809	-21034.842	-7774.283	2837.686
7.876	-21287.602	-8325.450	2288.745
9.111	-21532.742	-8908.245	1723.797
10.539	-21762.078	-9519.674	1133.092
12.191	-21965.070	-10155.049	507.142
14.101	-22128.322	-10807.580	-162.471
16.311	-22235.016	-11467.881	-882.366
18.868	-22264.232	-12123.385	-1656.578
21.825	-22190.191	-12757.660	-2485.633
25.246	-21981.395	-13349.603	-3365.369
29.202	-21599.711	-13872.503	-4285.507
33.779	-20999.465	-14292.975	-5227.987
39.073	-20126.697	-14569.774	-6165.167
45.197	-18918.941	-14652.569	-7058.071
52.281	-17306.264	-14480.823	-7854.898
60.475	-15215.369	-13983.189	-8490.099
69.953	-12581.678	-13078.290	-8884.354
80.916	-9389.293	-11679.025	-8945.974
93.598	-5842.589	-9706.341	-8574.842
108.268	-2754.114	-7136.721	-7672.081
125.237	-746.910	-4200.170	-6167.040
144.865	478.096	-1746.479	-4119.046
167.569	1127.965	-281.461	-2029.289
193.832	1289.752	426.142	-662.929
224.212	1001.066	537.544	-44.035
300.000	313.020	192.250	41.058

Table E4b: Computed shear stress values from the k-ε model for the data of Jonsson and Carlsen (1976).

Height above bed (mm)	Horizontal velocity, u (mm/s)			
	0°	15°	30°	45°
0.028	0.000	0.000	0.000	0.000
0.035	7.451	13.170	18.210	22.113
0.044	16.535	29.144	40.221	48.785
0.055	27.280	47.794	65.724	79.556
0.069	39.813	69.235	94.814	114.500
0.087	54.198	93.481	127.453	153.544
0.109	70.428	120.437	163.483	196.481
0.137	88.417	149.925	202.651	243.012
0.171	108.020	181.707	244.654	292.782
0.215	129.050	215.521	289.167	345.422
0.269	151.303	251.105	335.877	400.577
0.338	174.567	288.210	384.487	457.913
0.423	198.631	326.603	434.727	517.129
0.531	223.272	366.067	486.349	577.949
0.666	248.240	406.392	539.122	640.123
0.835	273.226	447.369	592.828	703.420
1.047	297.806	488.782	647.255	767.622
1.313	321.320	530.397	702.195	832.524
1.646	342.648	571.945	757.431	897.925
2.064	359.862	613.100	812.735	963.625
2.588	370.603	653.438	867.851	1029.417
3.246	374.220	692.344	922.482	1095.076
4.070	372.209	728.825	976.258	1160.350
5.104	366.225	761.021	1028.687	1224.939
6.400	357.233	785.072	1079.058	1288.464
8.0251	345.668	796.063	1126.223	1350.422
10.063	331.669	795.284	1168.060	1410.085
12.619	315.215	787.459	1199.796	1466.306
15.824	296.207	775.348	1213.414	1517.041
19.844	274.508	760.040	1210.864	1557.957
24.884	249.979	741.894	1199.932	1578.579
31.204	222.513	720.982	1184.467	1577.383
39.129	192.078	697.279	1165.764	1565.409
49.067	158.780	670.773	1144.244	1548.470
61.529	122.961	641.563	1120.087	1528.364
77.156	85.381	609.998	1093.507	1505.715
96.753	47.595	576.939	1064.979	1480.956
121.326	12.832	544.317	1035.590	1454.788
152.141	-10.733	516.089	1007.419	1428.518
190.782	-13.263	506.796	993.033	1411.809
300.000	-11.184	506.208	989.217	1405.046

Table E5a: Computed horizontal velocity values from the k model for test 13 from the experiments of Jensen *et al.* (1989).

Height above bed (mm)	Horizontal velocity, u (mm/s)			
	60°	75°	90°	105°
0.028	0.000	0.000	0.000	0.000
0.035	24.570	25.382	24.451	21.786
0.044	54.174	55.957	53.924	48.087
0.055	88.252	91.133	87.864	78.460
0.069	126.866	130.966	126.334	112.983
0.087	169.920	175.356	169.241	151.587
0.109	217.181	224.060	216.354	194.073
0.137	268.319	276.738	267.346	240.146
0.171	322.950	332.998	321.834	289.459
0.215	380.678	392.435	379.428	341.654
0.269	441.120	454.660	439.751	396.388
0.338	503.922	519.313	502.457	453.346
0.423	568.762	586.069	567.234	512.248
0.531	635.350	654.635	633.803	572.844
0.666	703.423	724.751	701.917	634.917
0.835	772.743	796.179	771.356	698.273
1.047	843.092	868.709	841.923	762.743
1.313	914.268	942.147	913.442	828.178
1.646	986.079	1016.316	985.755	894.447
2.064	1058.345	1091.051	1058.720	961.437
2.588	1130.883	1166.197	1132.207	1029.048
3.246	1203.512	1241.601	1206.094	1097.195
4.070	1276.035	1317.108	1280.265	1165.800
5.104	1348.232	1392.553	1354.602	1234.793
6.400	1419.846	1467.753	1428.978	1304.102
8.0251	1490.555	1542.486	1503.250	1373.650
10.063	1559.940	1616.477	1577.238	1443.341
12.619	1627.413	1689.359	1650.713	1513.048
15.824	1692.101	1760.621	1723.353	1582.587
19.844	1752.571	1829.505	1794.700	1651.685
24.884	1806.181	1894.797	1864.053	1719.918
31.204	1846.797	1954.333	1930.280	1786.611
39.129	1861.139	2003.851	1991.355	1850.626
49.067	1854.321	2030.424	2043.401	1909.879
61.529	1839.010	2028.745	2074.501	1960.328
77.156	1819.863	2014.659	2074.898	1989.142
96.753	1798.260	1996.120	2061.134	1987.628
121.326	1774.957	1975.369	2042.986	1973.365
152.141	1750.947	1953.560	2023.280	1955.849
190.782	1733.962	1937.349	2008.311	1942.330
300.000	1725.310	1928.019	1999.204	1933.953

Table E5b: Computed horizontal velocity values from the k model for test 13 from the experiments of Jensen *et al.* (1989).

Height above bed (mm)	Horizontal velocity, u (mm/s)			
	120°	135°	150°	165°
0.028	0.000	0.000	0.000	0.000
0.035	17.495	11.803	5.118	-1.706
0.044	38.681	26.180	11.437	-3.765
0.055	63.283	43.054	19.032	-6.197
0.069	91.402	62.556	28.049	-9.020
0.087	123.014	84.723	38.594	-12.221
0.109	157.972	109.488	50.716	-15.743
0.137	196.037	136.699	64.399	-19.461
0.171	236.919	166.148	79.568	-23.173
0.215	280.315	197.606	96.109	-26.598
0.269	325.933	230.854	113.902	-29.407
0.338	373.509	265.693	132.836	-31.271
0.423	422.810	301.953	152.823	-31.929
0.531	473.633	339.495	173.806	-31.217
0.666	525.803	378.201	195.750	-29.062
0.835	579.168	417.978	218.644	-25.446
1.047	633.599	458.752	242.497	-20.367
1.313	688.984	500.464	267.335	-13.811
1.646	745.230	543.076	293.201	-5.745
2.064	802.264	586.565	320.151	3.889
2.588	860.024	630.927	348.256	15.170
3.246	918.468	676.174	377.600	28.198
4.070	977.565	722.331	408.275	43.087
5.104	1037.295	769.441	440.383	59.961
6.400	1097.646	817.554	474.033	78.953
8.0251	1158.605	866.725	509.330	100.196
10.063	1220.156	917.009	546.380	123.820
12.619	1282.259	968.445	585.272	149.943
15.824	1344.842	1021.050	626.076	178.667
19.844	1407.770	1074.790	668.823	210.062
24.884	1470.803	1129.559	713.487	244.152
31.204	1533.534	1185.126	759.948	280.889
39.129	1595.269	1241.058	807.940	320.112
49.067	1654.780	1296.577	856.950	361.486
61.529	1709.727	1350.244	906.037	404.363
77.156	1755.365	1399.224	953.392	447.542
96.753	1776.456	1436.903	995.376	488.625
121.326	1770.712	1447.000	1021.426	522.359
152.141	1756.112	1437.634	1021.608	535.301
190.782	1744.183	1427.560	1014.097	531.837
300.000	1736.756	1421.160	1008.802	527.881

Table E5c: Computed horizontal velocity values from the k model for test 13 from the experiments of Jensen *et al.* (1989).

Height above bed (mm)	Shear stress, τ/ρ (mm^2/s^2)			
	0°	15°	30°	45°
0.028	2139.939	4776.186	7757.344	10487.705
0.035	2124.967	4729.227	7666.495	10353.118
0.044	2129.651	4765.878	7745.446	10474.383
0.055	2113.348	4746.211	7722.953	10450.316
0.069	2093.480	4723.047	7697.307	10423.616
0.087	2069.624	4696.193	7668.480	10394.402
0.109	2041.222	4665.149	7635.997	10362.263
0.137	2007.458	4628.997	7598.888	10326.271
0.171	1967.192	4586.427	7555.802	10285.155
0.215	1918.964	4535.832	7505.143	10237.445
0.269	1861.030	4475.368	7445.125	10181.550
0.338	1791.381	4402.947	7373.756	10115.709
0.423	1707.721	4316.176	7288.743	10037.905
0.531	1607.417	4212.266	7187.391	9945.745
0.666	1487.451	4087.944	7066.487	9836.344
0.835	1344.387	3939.363	6922.193	9706.204
1.047	1174.415	3762.029	6749.935	9551.092
1.313	973.777	3550.734	6544.289	9365.905
1.646	741.616	3299.527	6298.872	9144.523
2.064	492.296	3001.724	6006.236	8879.645
2.588	254.838	2650.015	5657.797	8562.620
3.246	32.022	2236.781	5243.815	8183.295
4.070	-187.835	1754.936	4753.503	7729.875
5.104	-414.346	1202.087	4175.365	7188.887
6.400	-657.371	641.385	3497.995	6545.306
8.0251	-924.860	188.586	2712.344	5783.034
10.063	-1221.608	-186.681	1812.054	4886.066
12.619	-1548.803	-522.490	884.388	3841.497
15.824	-1903.174	-846.140	203.908	2645.044
19.844	-2275.530	-1175.596	-289.289	1329.880
24.884	-2648.760	-1514.862	-682.519	349.930
31.204	-2995.468	-1855.620	-1028.008	-262.378
39.129	-3275.623	-2176.973	-1349.004	-688.107
49.067	-3434.867	-2443.251	-1638.770	-1015.439
61.529	-3404.698	-2601.296	-1868.200	-1280.104
77.156	-3106.803	-2579.576	-1987.954	-1468.263
96.753	-2469.949	-2294.140	-1930.212	-1536.062
121.326	-1454.618	-1689.019	-1631.582	-1426.922
152.141	-414.476	-694.720	-881.327	-930.946
190.782	-8.527	-194.676	-384.576	-529.523
300.000	31.622	-8.817	-57.407	-103.915

Table E6a: Computed shear stress values from the k model for test 13 from the experiments of Jensen *et al.* (1989).

Height above bed (mm)	Shear stress, τ/ρ (mm^2/s^2)			
	60°	75°	90°	105°
0.028	12399.458	13073.532	12336.197	10306.342
0.035	12233.253	12896.727	12173.370	10179.199
0.044	12386.308	13063.063	12331.105	10308.691
0.055	12362.471	13041.576	12314.084	10297.877
0.069	12336.648	13018.848	12296.609	10287.380
0.087	12309.117	12995.319	12279.294	10277.967
0.109	12279.589	12970.881	12262.243	10269.990
0.137	12247.268	12944.939	12245.127	10263.423
0.171	12211.049	12916.637	12227.389	10258.043
0.215	12169.696	12885.038	12208.442	10253.637
0.269	12121.906	12849.206	12187.759	10250.091
0.338	12066.272	12808.169	12164.848	10247.402
0.423	12001.188	12760.831	12139.180	10245.614
0.531	11924.735	12705.872	12110.101	10244.746
0.666	11834.566	12641.637	12076.733	10244.716
0.835	11727.788	12566.028	12037.896	10245.271
1.047	11600.838	12476.395	11991.980	10245.902
1.313	11449.344	12369.396	11936.863	10245.742
1.646	11267.960	12240.831	11869.730	10243.437
2.064	11050.183	12085.468	11786.904	10236.971
2.588	10788.134	11896.791	11683.606	10223.451
3.246	10472.322	11666.730	11553.674	10198.821
4.070	10091.394	11385.346	11389.200	10157.503
5.104	9631.885	11040.466	11180.125	10091.946
6.400	9078.026	10617.310	10913.737	9992.094
8.0251	8411.683	10098.120	10574.138	9844.729
10.063	7612.573	9461.898	10141.672	9632.744
12.619	6659.092	8684.388	9592.433	9334.359
15.824	5530.343	7738.604	8897.981	8922.363
19.844	4212.580	6596.577	8025.634	8363.588
24.884	2700.279	5233.415	6939.985	7618.996
31.204	1121.499	3647.574	5606.779	6645.188
39.129	131.728	1816.690	4015.143	5398.667
49.067	-438.842	430.487	2121.703	3861.484
61.529	-796.151	-277.634	545.671	1980.111
77.156	-1037.802	-659.719	-218.591	454.830
96.753	-1178.456	-869.093	-583.160	-244.582
121.326	-1184.775	-951.099	-738.205	-535.084
152.141	-878.661	-775.740	-655.943	-535.080
190.782	-600.672	-602.349	-557.344	-488.934
300.000	-137.159	-152.344	-151.544	-140.095

Table E6b: Computed shear stress values from the k model for test 13 from the experiments of Jensen *et al.* (1989).

Height above bed (mm)	Shear stress, τ/ρ (mm^2/s^2)			
	120°	135°	150°	165°
0.028	7382.856	4175.661	1399.230	-367.546
0.035	7304.084	4144.386	1399.162	-363.012
0.044	7393.273	4192.657	1418.555	-353.274
0.055	7389.709	4196.466	1428.798	-339.410
0.069	7387.143	4201.825	1441.158	-322.333
0.087	7386.455	4209.624	1456.301	-301.458
0.109	7388.251	4220.680	1475.047	-276.163
0.137	7392.832	4235.633	1498.283	-245.826
0.171	7400.332	4254.987	1526.883	-209.861
0.215	7410.903	4279.244	1561.703	-167.738
0.269	7424.831	4309.034	1603.653	-118.945
0.338	7442.558	4345.167	1653.783	-62.867
0.423	7464.653	4388.633	1713.318	1.362
0.531	7491.756	4440.567	1783.658	74.916
0.666	7524.517	4502.205	1866.348	159.262
0.835	7563.547	4574.844	1963.044	256.152
1.047	7609.347	4659.790	2075.471	367.622
1.313	7662.228	4758.286	2205.368	495.957
1.646	7722.197	4871.420	2354.412	643.609
2.064	7788.807	4999.993	2524.119	813.085
2.588	7860.953	5144.337	2715.698	1006.790
3.246	7936.604	5304.072	2929.863	1226.833
4.070	8012.456	5477.790	3166.568	1474.762
5.104	8083.482	5662.642	3424.664	1751.223
6.400	8142.384	5853.817	3701.444	2055.524
8.0251	8178.908	6043.886	3992.053	2385.087
10.063	8179.033	6221.995	4288.739	2734.755
12.619	8124.039	6372.896	4579.920	3095.955
15.824	7989.490	6475.824	4849.045	3455.671
19.844	7744.244	6503.258	5073.265	3795.220
24.884	7349.702	6419.694	5221.963	4088.822
31.204	6759.793	6180.720	5255.318	4302.033
39.129	5922.733	5733.002	5123.277	4390.247
49.067	4786.555	5016.577	4765.818	4297.814
61.529	3329.070	3974.184	4116.367	3959.090
77.156	1514.342	2570.543	3120.376	3305.028
96.753	237.430	928.232	1718.977	2288.088
121.326	-301.825	10.494	427.756	957.408
152.141	-414.029	-277.357	-99.596	133.371
190.782	-412.577	-333.949	-248.186	-140.017
300.000	-123.210	-104.283	-84.293	-61.523

Table E6c: Computed shear stress values from the k model for test 13 from the experiments of Jensen *et al.* (1989).

Height above bed (mm)	Turbulent kinetic energy, k (mm^2/s^2)			
	0°	15°	30°	45°
0.028	0.000	0.000	0.000	0.000
0.035	9827.792	17578.586	24991.914	30322.330
0.044	9883.145	17674.477	25123.443	30478.664
0.055	10001.237	17873.205	25391.033	30793.645
0.069	10186.102	18177.568	25795.652	31267.055
0.087	10432.870	18576.475	26320.666	31878.803
0.109	10726.969	19045.404	26933.559	32591.520
0.137	11045.729	19550.215	27591.520	33357.297
0.171	11361.872	20052.852	28248.771	34125.988
0.215	11647.516	20516.850	28863.049	34852.301
0.269	11877.331	20911.043	29399.627	35499.988
0.338	12030.187	21211.041	29832.598	36043.020
0.423	12089.345	21398.818	30144.029	36464.484
0.531	12041.704	21461.232	30321.945	36754.242
0.666	11876.630	21388.117	30357.943	36906.281
0.835	11584.803	21170.451	30244.934	36916.207
1.047	11157.371	20798.840	29975.250	36779.145
1.313	10585.622	20262.422	29539.193	36488.090
1.646	9861.410	19548.219	28924.012	36032.695
2.064	8978.810	18641.000	28113.234	35398.313
2.588	7938.045	17523.727	27086.385	34565.371
3.246	6754.331	16178.913	25819.117	33508.945
4.070	5478.407	14591.446	24283.924	32198.635
5.104	4246.004	12754.324	22451.770	30598.871
6.400	3379.079	10680.666	20295.354	28669.947
8.0251	3262.898	8431.041	17795.471	26370.309
10.063	3790.101	6180.394	14953.858	23661.148
12.619	4625.741	4404.991	11821.219	20515.508
15.824	5580.363	3857.454	8564.347	16936.852
19.844	6566.250	4329.061	5649.559	13000.305
24.884	7523.288	5161.858	4220.709	8950.111
31.204	8386.895	6040.141	4369.946	5519.352
39.129	9074.842	6829.957	5048.038	4208.566
49.067	9481.713	7434.105	5728.497	4430.773
61.529	9479.411	7747.212	6219.048	4938.683
77.156	8927.949	7647.196	6397.579	5281.797
96.753	7708.672	7007.497	6147.379	5292.098
121.326	5812.074	5741.854	5365.041	4860.601
152.141	3522.932	3891.955	4013.704	3927.898
190.782	2506.297	2695.712	2889.083	3008.567
300.000	2248.312	2261.090	2323.399	2413.409

Table E7a: Computed turbulent kinetic energy values from the k model for test 13 from the experiments of Jensen *et al.* (1989).

Height above bed (mm)	Turbulent kinetic energy, k (mm^2/s^2)			
	60°	75°	90°	105°
0.028	0.000	0.000	0.000	0.000
0.035	32268.807	3515.022	30296.213	24792.016
0.044	32435.291	3533.633	30456.459	24930.100
0.055	32770.195	3575.023	30780.957	25214.131
0.069	33273.418	3642.059	31271.234	25648.537
0.087	33924.219	3734.184	31908.967	26220.303
0.109	34684.129	3846.217	32658.545	26900.561
0.137	35504.086	3968.076	33473.867	27650.225
0.171	36333.117	4085.707	34306.750	28427.490
0.215	37125.676	4182.927	35114.156	29194.557
0.269	37845.938	4243.486	35862.527	29921.902
0.338	38468.949	4252.713	36529.031	30589.748
0.423	38979.457	4198.500	37100.543	31187.355
0.531	39369.520	4071.831	37571.359	31711.135
0.666	39635.738	3867.364	37940.605	32162.320
0.835	39776.688	3584.824	38209.723	32544.750
1.047	39790.777	3232.556	38380.395	32862.949
1.313	39674.508	2835.719	38452.859	33120.570
1.646	39421.160	2453.139	38424.563	33319.086
2.064	39019.715	2199.504	38289.043	33456.695
2.588	38454.008	2216.628	38034.938	33527.262
3.246	37701.961	2546.846	37645.047	33519.281
4.070	36735.000	3116.832	37095.418	33414.738
5.104	35517.605	3846.201	36354.426	33187.902
6.400	34007.230	4687.662	35381.973	32804.078
8.0251	32154.809	5614.866	34128.949	32218.365
10.063	29906.406	6607.527	32537.244	31374.682
12.619	27206.967	7642.147	30540.893	30205.346
15.824	24008.004	8686.009	28069.291	28631.850
19.844	20283.242	9692.544	25054.402	26567.871
24.884	16061.867	10597.412	21445.736	23926.598
31.204	11507.333	11315.438	17242.109	20636.504
39.129	7089.769	11739.279	12565.786	16675.291
49.067	4423.995	11741.581	7812.450	12149.499
61.529	4055.111	11184.080	4507.651	7452.601
77.156	4343.773	9941.006	3756.176	4205.821
96.753	4508.938	7955.582	3844.204	3428.941
121.326	4328.094	5378.235	3818.871	3373.000
152.141	3720.785	3042.278	3457.605	3179.681
190.782	3033.568	2404.966	2982.474	2882.015
300.000	2499.771	2284.741	2557.820	2576.405

Table E7b: Computed turbulent kinetic energy values from the k model for test 13 from the experiments of Jensen *et al.* (1989).

Height above bed (mm)	Turbulent kinetic energy, k (mm^2/s^2)			
	120°	135°	150°	165°
0.028	0.000	0.000	0.000	0.000
0.035	17025.520	8920.859	2704.104	458.051
0.044	17128.352	8981.017	2724.586	460.358
0.055	17345.605	9113.736	2773.303	466.216
0.069	17685.127	9329.143	2858.524	477.292
0.087	18141.391	9629.745	2987.384	495.734
0.109	18695.660	10009.117	3164.397	524.279
0.137	19319.684	10453.022	3390.412	566.405
0.171	19981.510	10942.706	3662.640	626.574
0.215	20651.275	11459.023	3975.888	710.497
0.269	21305.244	11985.924	4324.472	825.193
0.338	21927.549	12512.443	4703.987	978.510
0.423	22510.025	13033.180	5112.381	1178.058
0.531	23050.857	13547.698	5550.231	1430.140
0.666	23552.766	14059.372	6020.438	1739.378
0.835	24021.176	14574.078	6527.588	2109.165
1.047	24462.590	15098.935	7077.212	2542.374
1.313	24883.193	15641.155	7675.020	3041.854
1.646	25287.674	16207.017	8326.160	3610.518
2.064	25678.160	16800.873	9034.488	4251.074
2.588	26053.156	17424.166	9801.809	4965.514
3.246	26406.449	18074.355	10627.036	5754.383
4.070	26725.885	18743.748	11505.237	6615.878
5.104	26992.000	19418.156	12426.490	7544.754
6.400	27176.529	20075.402	13374.538	8531.009
8.0251	27240.813	20683.658	14325.179	9558.341
10.063	27134.236	21199.674	15244.429	10602.344
12.619	26792.906	21566.973	16086.468	11628.452
15.824	26138.947	21714.299	16791.508	12589.665
19.844	25081.086	21554.668	17283.852	13424.188
24.884	23517.764	20985.850	17470.627	14053.261
31.204	21345.145	19893.744	17242.205	14379.786
39.129	18474.979	18161.578	16476.145	14288.968
49.067	14874.064	15691.245	15048.487	13653.432
61.529	10658.871	12452.424	12860.971	12348.163
77.156	6296.457	8601.160	9906.538	10288.034
96.753	3642.033	4838.989	6419.261	7522.911
121.326	3065.761	3064.366	3568.210	4490.917
152.141	2917.379	2706.180	2604.521	2698.729
190.782	2754.812	2619.604	2496.189	2411.990
300.000	2556.002	2504.084	2431.749	2352.841

Table E7c: Computed turbulent kinetic energy values from the k model for test 13 from the experiments of Jensen *et al.* (1989).

Height above bed (mm)	Horizontal velocity, u (mm/s)			
	0°	15°	30°	45°
0.028	0.000	0.000	0.000	0.000
0.035	12.069	24.929	40.014	54.069
0.044	26.884	54.847	86.688	115.556
0.055	44.380	87.944	135.127	176.472
0.069	64.109	122.189	182.332	233.863
0.087	85.310	156.292	227.558	287.873
0.109	107.269	189.871	271.155	339.472
0.137	129.535	223.029	313.702	389.575
0.171	151.895	256.020	355.723	438.876
0.215	174.253	289.112	397.628	487.882
0.269	196.521	322.538	439.735	536.956
0.338	218.550	356.494	482.282	586.364
0.423	240.079	391.138	525.456	636.304
0.531	260.710	426.595	569.406	686.926
0.666	279.921	462.961	614.257	738.354
0.835	297.156	500.289	660.119	790.693
1.047	311.969	538.575	707.093	844.044
1.313	324.167	577.704	755.278	898.506
1.646	333.834	617.348	804.764	954.187
2.064	341.236	656.783	855.629	1011.204
2.588	346.687	694.575	907.905	1069.684
3.246	350.452	728.359	961.518	1129.759
4.070	352.698	755.402	1016.131	1191.553
5.104	353.476	774.378	1070.773	1255.143
6.400	352.715	786.223	1123.033	1320.463
8.025	350.203	792.783	1167.917	1387.058
10.063	345.568	795.476	1199.314	1453.409
12.619	338.258	794.988	1216.423	1515.160
15.824	327.512	791.397	1223.558	1562.673
19.844	312.361	784.294	1224.278	1588.137
24.884	291.671	772.866	1219.975	1596.865
31.204	264.237	755.969	1210.584	1595.935
39.129	228.947	732.237	1195.209	1587.977
49.067	184.999	700.288	1172.533	1572.963
61.529	132.248	659.087	1141.232	1549.863
77.156	72.120	608.702	1100.600	1517.701
96.753	11.277	552.699	1052.080	1476.757
121.326	-22.505	507.454	1004.118	1431.779
152.141	-19.966	499.852	985.736	1404.820
190.782	-5.728	511.054	992.976	1407.199
300.000	0.692	517.976	999.957	1413.796

Table E8a: Computed horizontal velocity values from the k-ε model for test 13 from the experiments of Jensen *et al.* (1989).

Height above bed (mm)	Horizontal velocity, u (mm/s)			
	60°	75°	90°	105°
0.028	0.000	0.000	0.000	0.000
0.035	64.434	69.220	24.451	21.786
0.044	136.409	145.894	53.924	48.087
0.055	205.712	218.802	87.864	78.460
0.069	269.855	285.790	126.334	112.983
0.087	329.704	348.071	169.241	151.587
0.109	386.640	407.209	216.354	194.073
0.137	441.780	464.402	267.346	240.146
0.171	495.925	520.493	321.834	289.459
0.215	549.634	576.059	379.428	341.654
0.269	603.300	631.499	439.751	396.388
0.338	657.200	687.090	502.457	453.346
0.423	711.535	743.030	567.234	512.248
0.531	766.455	799.459	633.803	572.844
0.666	822.076	856.486	701.917	634.917
0.835	878.497	914.198	771.356	698.273
1.047	935.809	972.674	841.923	762.743
1.313	994.105	1031.998	913.442	828.178
1.646	1053.485	1092.259	985.755	894.447
2.064	1114.065	1153.565	1058.720	961.437
2.588	1175.977	1216.043	1132.207	1029.048
3.246	1239.375	1279.849	1206.094	1097.195
4.070	1304.432	1345.165	1280.265	1165.800
5.104	1371.339	1412.207	1354.602	1234.793
6.400	1440.286	1481.219	1428.978	1304.102
8.025	1511.424	1552.467	1503.250	1373.650
10.063	1584.763	1626.214	1577.238	1443.341
12.619	1659.896	1702.659	1650.713	1513.048
15.824	1735.181	1781.767	1723.353	1582.587
19.844	1805.180	1862.788	1794.700	1651.685
24.884	1856.024	1942.644	1864.053	1719.918
31.204	1878.055	2010.707	1930.280	1786.611
39.129	1881.424	2046.524	1991.355	1850.626
49.067	1874.339	2053.792	2043.401	1909.879
61.529	1858.662	2046.496	2074.501	1960.328
77.156	1833.988	2029.010	2074.898	1989.142
96.753	1800.190	2001.966	2061.134	1987.628
121.326	1760.220	1967.366	2042.986	1973.365
152.141	1728.521	1934.523	2023.280	1955.849
190.782	1725.512	1926.249	2008.311	1942.330
300.000	1731.289	1930.799	1999.204	1933.953

Table E8b: Computed horizontal velocity values from the k-ε model for test 13 from the experiments of Jensen *et al.* (1989).

Height above bed (mm)	Horizontal velocity, u (mm/s)			
	120°	135°	150°	165°
0.028	0.000	0.000	0.000	0.000
0.035	17.495	11.803	5.118	-1.706
0.044	38.681	26.180	11.437	-3.765
0.055	63.283	43.054	19.032	-6.197
0.069	91.402	62.556	28.049	-9.020
0.087	123.014	84.723	38.594	-12.221
0.109	157.972	109.488	50.716	-15.743
0.137	196.037	136.699	64.399	-19.461
0.171	236.919	166.148	79.568	-23.173
0.215	280.315	197.606	96.109	-26.598
0.269	325.933	230.854	113.902	-29.407
0.338	373.509	265.693	132.836	-31.271
0.423	422.810	301.953	152.823	-31.929
0.531	473.633	339.495	173.806	-31.217
0.666	525.803	378.201	195.750	-29.062
0.835	579.168	417.978	218.644	-25.446
1.047	633.599	458.752	242.497	-20.367
1.313	688.984	500.464	267.335	-13.811
1.646	745.230	543.076	293.201	-5.745
2.064	802.264	586.566	320.151	3.889
2.588	860.024	630.927	348.256	15.170
3.246	918.468	676.174	377.600	28.198
4.070	977.565	722.331	408.275	43.087
5.104	1037.295	769.441	440.383	59.961
6.400	1097.646	817.554	474.033	78.953
8.025	1158.605	866.725	509.330	100.196
10.063	1220.156	917.009	546.380	123.819
12.619	1282.259	968.445	585.272	149.943
15.824	1344.842	1021.050	626.076	178.667
19.844	1407.770	1074.790	668.823	210.062
24.884	1470.803	1129.559	713.487	244.152
31.204	1533.534	1185.126	759.948	280.889
39.129	1595.269	1241.058	807.939	320.112
49.067	1654.780	1296.577	856.950	361.485
61.529	1709.727	1350.244	906.037	404.363
77.156	1755.365	1399.224	953.392	447.542
96.753	1776.456	1436.903	995.376	488.625
121.326	1770.712	1447.000	1021.426	522.359
152.141	1756.112	1437.634	1021.608	535.301
190.782	1744.183	1427.560	1014.097	531.837
300.000	1736.756	1421.160	1008.802	527.881

Table E8c: Computed horizontal velocity values from the k-ε model for test 13 from the experiments of Jensen *et al.* (1989).

Height above bed (mm)	Shear stress, τ/ρ (mm^2/s^2)			
	0°	15°	30°	45°
0.028	21.261	107.256	297.963	568.038
0.035	18.883	94.091	257.389	484.062
0.044	88.693	425.558	1105.765	1973.805
0.055	227.530	985.708	2301.585	3795.142
0.069	433.245	1620.387	3408.775	5285.478
0.087	671.448	2180.705	4255.571	6348.675
0.109	898.222	2617.226	4866.723	7093.490
0.137	1086.718	2940.017	5304.669	7622.628
0.171	1229.602	3172.794	5619.271	8004.035
0.215	1329.474	3336.103	5843.985	8280.206
0.269	1391.493	3444.526	6000.380	8477.884
0.338	1420.333	3507.567	6102.203	8614.150
0.423	1419.563	3530.919	6158.021	8699.956
0.531	1392.026	3517.416	6172.809	8742.131
0.666	1340.487	3467.623	6148.875	8744.533
0.835	1267.944	3380.166	6086.354	8708.686
1.047	1177.188	3251.884	5983.444	8634.102
1.313	1070.027	3077.965	5836.442	8518.393
1.646	946.906	2852.409	5639.644	8357.234
2.064	806.819	2569.980	5385.099	8144.189
2.588	647.172	2232.624	5062.260	7870.408
3.246	463.719	1861.430	4657.563	7524.202
4.070	250.756	1493.850	4154.314	7090.445
5.104	1.517	1148.788	3535.360	6549.792
6.400	-291.223	817.057	2802.197	5877.688
8.0251	-634.218	482.565	2034.911	5043.536
10.063	-1032.240	129.453	1370.982	4015.572
12.619	-1485.733	-255.898	819.062	2820.945
15.824	-1987.394	-681.836	320.154	1717.026
19.844	-2517.683	-1148.524	-164.900	902.068
24.884	-3039.792	-1644.357	-656.206	250.831
31.204	-3495.508	-2140.849	-1152.464	-323.322
39.129	-3803.942	-2585.821	-1628.662	-848.051
49.067	-3863.591	-2895.869	-2031.360	-1309.959
61.529	-3554.682	-2950.537	-2270.860	-1655.021
77.156	-2739.689	-2588.598	-2213.562	-1785.258
96.753	-1327.303	-1644.382	-1696.863	-1557.495
121.326	-266.937	-487.964	-692.054	-831.353
152.141	116.542	23.688	-71.7214	-161.898
190.782	103.467	89.424	68.606	42.268
300.000	18.248	19.753	19.974	18.878

Table E9a: Computed shear stress values from the k-ε model for test 13 from the experiments of Jensen *et al.* (1989).

Height above bed (mm)	Shear stress, τ/ρ (mm^2/s^2)			
	60°	75°	90°	105°
0.028	829.400	972.566	930.483	720.982
0.035	700.112	817.340	782.729	610.344
0.044	2745.997	3148.414	3032.237	2435.053
0.055	5028.943	5646.531	5466.379	4532.627
0.069	6774.110	7504.065	7288.083	6169.792
0.087	7978.901	8771.363	8535.643	7314.148
0.109	8813.110	9646.366	9399.846	8114.880
0.137	9404.963	10268.371	10016.850	8690.767
0.171	9833.685	10721.507	10469.360	9116.689
0.215	10147.593	11056.726	10807.692	9438.999
0.269	10376.919	11305.951	11063.559	9687.246
0.338	10541.121	11489.911	11257.751	9881.033
0.423	10652.946	11622.433	11404.364	10033.873
0.531	10720.710	11712.845	11513.180	10155.387
0.666	10749.602	11767.353	11591.030	10252.587
0.835	10742.409	11789.823	11642.591	10330.619
1.047	10699.913	11782.212	11670.820	10393.191
1.313	10621.046	11744.764	11677.183	10442.793
1.646	10502.896	11676.045	11661.702	10480.758
2.064	10340.575	11572.849	11622.890	10507.212
2.588	10126.959	11429.958	11557.543	10520.895
3.246	9852.303	11239.796	11460.414	10518.857
4.070	9503.698	10991.908	11323.730	10496.019
5.104	9064.364	10672.283	11136.534	10444.536
6.400	8512.713	10262.444	10883.798	10352.970
8.0251	7821.147	9738.295	10545.280	10205.166
10.063	6954.495	9068.642	10094.053	9978.814
12.619	5867.963	8213.321	9494.645	9643.595
15.824	4509.489	7120.648	8700.734	9158.855
19.844	2910.045	5723.726	7652.248	8470.758
24.884	1521.937	3960.150	6271.289	7508.796
31.204	596.824	2076.491	4464.981	6181.292
39.129	-103.807	817.961	2335.986	4376.806
49.067	-669.004	-0.638	847.693	2170.690
61.529	-1105.709	-585.852	-19.557	677.502
77.156	-1364.000	-962.183	-565.794	-131.176
96.753	-1334.177	-1083.481	-824.366	-557.243
121.326	-880.290	-848.104	-759.248	-636.122
152.141	-241.530	-304.667	-345.321	-360.149
190.782	12.794	-17.106	-45.177	-69.735
300.000	16.495	12.940	8.444	3.335

Table E9b: Computed shear stress values from the k-ε model for test 13 from the experiments of Jensen *et al.* (1989).

Height above bed (mm)	Shear stress, τ/ρ (mm^2/s^2)			
	120°	135°	150°	165°
0.028	437.861	194.707	59.522	-5.705
0.035	374.846	169.126	52.389	-3.353
0.044	1572.332	755.769	251.997	-3.902
0.055	3113.428	1644.261	614.462	3.748
0.069	4424.834	2518.321	1041.825	16.117
0.087	5383.698	3215.194	1427.505	32.479
0.109	6069.044	3735.372	1735.818	53.086
0.137	6568.206	4123.404	1975.013	78.568
0.171	6941.734	4419.273	2163.141	109.797
0.215	7228.670	4651.421	2316.005	147.853
0.269	7454.465	4839.322	2445.461	194.029
0.338	7636.300	4996.544	2560.242	249.839
0.423	7786.252	5132.908	2666.963	317.021
0.531	7913.164	5255.850	2770.864	397.536
0.666	8023.742	5371.255	2876.308	493.550
0.835	8123.211	5483.963	2987.089	607.379
1.047	8215.690	5598.058	3106.615	741.408
1.313	8304.385	5717.020	3238.011	897.955
1.646	8391.654	5843.764	3384.145	1079.078
2.064	8478.953	5980.596	3547.599	1286.351
2.588	8566.683	6129.083	3730.572	1520.611
3.246	8653.916	6289.822	3934.695	1781.761
4.070	8737.995	6462.096	4160.746	2068.685
5.104	8813.964	6643.379	4408.234	2379.322
6.400	8873.786	6828.649	4674.799	2710.865
8.0251	8905.309	7009.452	4955.378	3059.816
10.063	8890.892	7172.643	5241.079	3421.488
12.619	8805.620	7298.720	5517.657	3788.484
15.824	8615.024	7359.651	5763.499	4148.020
19.844	8272.221	7316.083	5946.987	4478.395
24.884	7714.401	7113.878	6023.100	4745.155
31.204	6858.492	6679.977	5929.186	4897.064
39.129	5594.990	5917.350	5580.053	4861.526
49.067	3799.043	4694.971	4863.164	4538.862
61.529	1657.131	2877.089	3635.103	3793.523
77.156	380.378	1008.277	1804.798	2476.796
96.753	-265.463	68.873	439.862	868.648
121.326	-492.667	-331.983	-149.035	53.956
152.141	-349.529	-316.670	-265.506	-198.360
190.782	-89.444	-103.220	-110.309	-110.370
300.000	-1.994	-7.145	-11.752	-15.517

Table E9c: Computed shear stress values from the k-ε model for test 13 from the experiments of Jensen *et al.* (1989).

Height above bed (mm)	Turbulent kinetic energy, k (mm^2/s^2)			
	0°	15°	30°	45°
0.028	0.000	0.000	0.000	0.000
0.035	1846.064	3854.125	6126.098	8028.566
0.044	3853.615	7820.594	12142.031	15662.020
0.055	5788.181	11267.305	16985.547	21522.818
0.069	7456.775	13961.721	20556.475	25708.869
0.087	8791.045	15979.028	23142.676	28692.148
0.109	9814.817	17473.248	25027.949	30852.539
0.137	10579.747	18575.195	26411.736	32437.949
0.171	11134.012	19378.445	27425.617	33606.664
0.215	11514.623	19947.250	28156.738	34462.121
0.269	11747.854	20325.398	28663.805	35073.863
0.338	11851.271	20542.457	28986.771	35489.590
0.423	11835.508	20617.727	29152.559	35742.145
0.531	11705.519	20562.652	29178.473	35853.609
0.666	11461.391	20382.236	29074.229	35837.770
0.835	11099.008	20075.807	28843.137	35701.598
1.047	10610.969	19637.344	28482.715	35446.082
1.313	9988.688	19055.465	27984.904	35066.574
1.646	9227.702	18313.186	27335.938	34552.832
2.064	8340.306	17387.564	26515.906	33888.695
2.588	7380.608	16249.702	25498.008	33051.465
3.246	6473.591	14866.406	24247.502	32010.908
4.070	5793.494	13207.747	22720.465	30727.854
5.104	5449.446	11273.197	20862.955	29152.354
6.400	5416.771	9166.836	18612.814	27221.414
8.0251	5609.801	7229.695	15912.613	24856.855
10.063	5960.143	5955.830	12765.476	21965.627
12.619	6432.527	5468.295	9430.047	18452.727
15.824	7012.988	5504.570	6743.356	14291.048
19.844	7693.030	5828.185	5454.562	9823.992
24.884	8451.812	6322.116	5202.662	6400.111
31.204	9232.876	6921.640	5429.747	5014.691
39.129	9914.117	7549.780	5860.458	4828.628
49.067	10275.692	8065.061	6333.605	5067.488
61.529	9980.000	8218.113	6653.052	5373.351
77.156	8597.841	7634.917	6515.622	5452.132
96.753	5828.438	5906.756	5519.690	4932.767
121.326	2680.214	3130.567	3421.326	3477.330
152.141	1364.868	1413.307	1515.821	1639.426
190.782	819.033	801.614	791.510	791.473
300.000	461.540	460.676	459.218	457.570

Table E10a: Computed turbulent kinetic energy values from the k-ε model for test 13 from the experiments of Jensen *et al.* (1989).

Height above bed (mm)	Turbulent kinetic energy, k (mm^2/s^2)			
	60°	75°	90°	105°
0.028	0.000	0.000	0.000	0.000
0.035	8984.090	576.959	8682.512	7201.216
0.044	17402.295	1237.594	16854.604	14141.025
0.055	23735.623	1947.875	23038.871	19566.584
0.069	28204.734	2652.155	27423.848	23501.641
0.087	31374.197	3290.364	30547.910	26347.281
0.109	33668.840	3823.340	32822.203	28444.295
0.137	35358.824	4238.570	34510.035	30020.516
0.171	36614.871	4540.400	35778.688	31224.037
0.215	37548.277	4739.935	36737.898	32153.580
0.269	38234.133	4850.096	37462.340	32877.359
0.338	38724.461	4884.777	38004.430	33444.117
0.423	39055.754	4860.217	38401.664	33889.555
0.531	39253.402	4797.183	38680.992	34240.199
0.666	39334.398	4722.245	38861.434	34515.719
0.835	39308.930	4665.885	38955.699	34730.355
1.047	39181.332	4656.470	38971.125	34893.758
1.313	38950.543	4713.078	38910.152	35011.406
1.646	38610.195	4842.641	38770.453	35084.703
2.064	38148.414	5043.103	38544.750	35110.801
2.588	37547.230	5309.103	38220.309	35082.141
3.246	36781.715	5636.399	37778.121	34985.691
4.070	35818.656	6024.015	37191.676	34801.836
5.104	34614.762	6474.801	36425.266	34502.797
6.400	33114.289	6995.142	35431.695	34050.496
8.0251	31245.949	7594.007	34149.234	33393.688
10.063	28919.307	8280.934	32497.672	32464.094
12.619	26021.521	9061.932	30373.447	31171.412
15.824	22419.260	9931.822	27644.422	29397.006
19.844	17988.014	10861.506	24147.604	26986.848
24.884	12780.397	11779.905	19705.773	23746.906
31.204	7740.261	12553.593	14245.684	19456.789
39.129	5024.456	12971.428	8423.400	13985.324
49.067	4363.212	12743.000	4858.986	7949.927
61.529	4412.398	11517.366	3899.519	4317.084
77.156	4529.903	8952.927	3804.686	3380.317
96.753	4299.496	5094.126	3697.484	3181.425
121.326	3340.871	2270.166	3087.982	2784.346
152.141	1744.461	1381.138	1801.899	1801.067
190.782	801.432	838.922	818.614	838.354
300.000	456.178	461.574	455.410	455.463

Table E10b: Computed turbulent kinetic energy values from the k-ε model for test 13 from the experiments of Jensen *et al.* (1989).

Height above bed (mm)	Turbulent kinetic energy, k (mm^2/s^2)			
	120°	135°	150°	165°
0.028	0.000	0.000	0.000	0.000
0.035	24950.174	15373.476	6998.667	2440.562
0.044	25249.211	15564.864	7093.100	2486.353
0.055	25711.391	15877.607	7261.370	2576.789
0.069	26269.723	16271.966	7489.546	2709.815
0.087	26870.357	16713.420	7763.636	2881.021
0.109	27473.822	17174.871	8071.274	3084.692
0.137	28054.154	17637.473	8403.095	3315.334
0.171	28596.691	18090.145	8753.336	3568.738
0.215	29095.398	18528.283	9119.664	3842.339
0.269	29550.346	18952.227	9502.526	4135.107
0.338	29965.607	19365.785	9904.351	4447.263
0.423	30347.633	19774.998	10328.783	4780.024
0.531	30704.023	20187.127	10780.078	5135.419
0.666	31042.592	20609.832	11262.649	5516.190
0.835	31370.656	21050.531	11780.773	5925.761
1.047	31694.438	21515.852	12338.405	6368.238
1.313	32018.504	22011.168	12939.059	6848.440
1.646	32345.236	22540.184	13585.698	7371.915
2.064	32674.215	23104.500	14280.603	7944.906
2.588	33001.508	23703.146	15025.123	8574.229
3.246	33318.801	24331.975	15819.273	9266.964
4.070	33612.227	24982.828	16661.080	10029.874
5.104	33860.871	25642.352	17545.557	10868.398
6.400	34034.695	26290.262	18463.172	11785.062
8.0251	34091.738	26896.895	19397.592	12777.117
10.063	33974.273	27419.689	20322.447	13833.245
12.619	33603.641	27798.338	21196.773	14929.108
15.824	32873.352	27948.123	21958.693	16021.521
19.844	31640.225	27751.063	22516.920	17040.854
24.884	29713.787	27044.588	22739.584	17881.139
31.204	26846.377	25608.307	22440.334	18387.240
39.129	22735.400	23152.768	21362.877	18339.176
49.067	17094.918	19329.754	19170.379	17436.439
61.529	10156.010	13867.957	15471.539	15297.270
77.156	4993.268	7387.656	10094.772	11544.547
96.753	3439.456	3687.747	4746.610	6362.447
121.326	3025.059	2738.824	2665.615	2913.162
152.141	2392.630	2204.327	2027.994	1901.724
190.782	1327.925	1325.613	1301.996	1263.096
300.000	718.251	723.170	727.252	729.407

Table E10c: Computed turbulent kinetic energy values from the k-ε model for test 13 from the experiments of Jensen *et al.* (1989).

Appendix F

Tables of Results For The Moveable Bed Model

Run No.	Wave period, T (sec)	Amplitude, 2a (cm)	Water Temperature (°C)	Δ/λ	Δ (cm)	λ (cm)
85	3.611	18.0086	17.222	0.181	2.09	11.59
96A	3.584	23.7490	25.278	0.161	2.45	15.18
106A	3.542	36.3220	26.222	0.134	1.46	10.89
111A	3.533	47.3964	24.833	0.125	1.33	10.56
112B	3.533	62.6618	23.889	0.048	0.48	10.03
114A	3.551	16.3576	24.444	0.199	2.07	10.41

s = 2.66; grain diameter = 0.190 mm.

Table F1: Wave tunnel data for regular waves from Carstens *et al.* (1969) for smallest grain diameter.

Run No.	Wave period, T (sec)	Amplitude, 2a (cm)	Water Temperature (°C)	Δ/λ	Δ (cm)	λ (cm)
21	3.557	17.831	26.11	0.171	1.82	10.63
22	3.555	23.978	24.44	0.175	2.22	12.71
23	3.549	27.330	23.89	0.176	2.55	14.52
24	3.551	30.734	25.00	0.179	2.59	14.46
25	3.552	41.707	22.78	0.170	3.29	19.39
26	3.551	46.787	22.78	0.162	3.58	22.13
27	3.528	52.222	22.78	0.132	3.23	24.50
29B	3.544	64.770	22.78	0.115	3.10	27.03
30B	3.522	71.196	22.22	0.106	2.14	20.11
31B	3.521	89.002	22.22	0.026	0.49	19.10
32B	3.534	78.105	21.94	0.065	1.43	21.98
36	3.553	56.159	22.78	0.131	3.21	24.50
51	3.579	16.002	23.89	0.183	1.90	10.37
52	3.434	17.272	23.89	0.157	1.71	10.90
53	3.309	14.707	23.33	0.176	1.55	8.82
54	3.681	19.050	22.78	0.175	2.07	11.82
55	3.790	15.519	24.17	0.170	1.78	10.45

s = 2.47; grain diameter = 0.297 mm.

Table F2: Wave tunnel data for regular waves from Carstens *et al.* (1969) for mid grain diameter.

Run No.	Wave period, T (sec)	Amplitude, 2a (cm)	Water Temperature (°C)	Δ/λ	Δ (cm)	λ (cm)
63	3.568	20.2184	25.833	0.191	2.78	14.63
64	3.552	24.0284	25.556	0.195	3.26	16.67
65A	3.543	27.5336	24.444	0.186	3.36	18.08
66	3.554	32.1310	24.722	0.193	3.94	20.36
67	3.540	37.0840	23.889	0.190	4.54	23.87
68	3.568	39.2938	25.000	0.206	5.19	25.16
69	3.556	44.7040	24.444	0.200	5.81	29.02
70	3.543	48.3870	25.000	0.185	4.76	25.74
71	3.530	49.5300	25.000	0.185	4.88	26.38
72	3.532	53.2892	25.000	0.187	5.60	29.95
73	3.547	58.1660	22.222	0.192	5.03	26.21
74	3.560	61.5950	22.778	0.197	5.97	30.36
75	3.554	65.3542	22.778	0.150	5.88	39.14
76	3.531	70.3580	22.778	0.181	6.83	37.79
77	3.545	74.8538	22.778	0.173	6.18	35.74
78	3.474	78.4352	22.778	0.148	6.87	46.33
79	3.555	84.7090	23.333	0.157	6.93	44.11
80A	3.540	24.8920	22.778	0.180	3.13	17.37

s = 2.62; grain diameter = 0.585 mm.

Table F3: Wave tunnel data for regular waves from Carstens *et al.* (1969) for largest grain diameter.

Wave period, T (sec)	Amplitude, a (cm)	Water Temperature (°C)	Δ/λ	Δ (cm)	λ (cm)
1.07	2.08	18.3	0.170	0.51	3.0
1.95	3.88	18.3	0.171	0.82	4.8
1.95	5.39	18.3	0.196	1.1	5.6
2.34	5.78	18.3	0.182	1.0	5.5

s = 2.65; grain diameter = 0.095 mm.

Table F4: Wave flume data for regular waves from Kennedy and Falcon (1965).

Wave period, T (sec)	Amplitude, a (cm)	Water Temperature (°C)	Δ/λ	Δ (cm)	λ (cm)
1.39	4.99	23.9	0.159	1.0	6.3
1.57	5.33	23.9	0.167	1.2	7.2
1.57	6.47	23.9	0.186	1.6	8.6
1.39	4.79	23.9	0.194	1.2	6.2
1.57	4.26	23.9	0.220	1.3	5.9
1.39	3.24	23.9	0.152	0.7	4.6

s = 2.65; grain diameter = 0.32 mm.

Table F5: Wave flume data for regular waves from Kennedy and Falcon (1965).

Wave period, T (sec)	Amplitude, a (cm)	Water Temperature (°C)	Δ/λ	Δ (cm)	λ (cm)
8.05	77.6	17.8	0.164	7.0	42.7
2.51	9.41	17.2	0.163	2.1	12.9
4.03	15.7	17.2	0.168	3.3	19.7
4.03	15.6	17.8	0.170	3.4	20.0
4.03	25.8	17.8	0.171	4.8	28.1
5.66	21.8	17.8	0.169	4.8	28.4
5.66	29.4	17.8	0.154	5.8	37.7
4.03	32.0	17.8	0.151	5.1	33.8
8.05	36.0	17.8	0.153	6.8	44.3
8.05	42.8	17.8	0.176	8.8	50.0
8.05	51.9	17.8	0.173	9.5	54.8
10.05	53.7	17.8	0.168	10.1	60.1
12.06	60.9	17.8	0.160	10.4	65.0
12.06	66.8	17.8	0.156	11.5	73.5
14.06	75.4	18.3	0.167	13.6	81.2
14.06	93.0	18.3	0.181	18.4	101.7
4.03	13.5	17.8	0.174	3.0	17.2
4.03	21.1	17.8	0.152	3.8	25.0
4.03	29.7	17.8	0.139	4.6	33.0
4.03	38.0	17.8	0.176	4.9	27.8
4.03	43.9	17.8	0.172	3.9	22.7

s = 2.65; grain diameter = 0.36 mm.

Table F6: Wave tunnel data for regular waves from Mogridge and Kamphuis (1972).

Wave period, T (sec)	Amplitude, a (cm)	Water Temperature (°C)	Δ/λ	Δ (cm)	λ (cm)
1.09	2.50	13.6	0.173	0.57	3.3
1.08	2.69	13.3	0.139	0.50	3.6
1.08	3.00	14.4	0.143	0.53	3.7
1.08	3.22	14.4	0.160	0.64	4.0
1.08	3.40	13.3	0.155	0.65	4.2
1.08	3.66	13.3	0.138	0.66	4.8
1.09	3.13	13.8	0.139	0.61	4.4
1.08	2.91	7.5	0.142	0.51	3.6
1.09	3.27	5.8	0.142	0.61	4.3
1.08	2.93	7.2	0.139	0.53	3.8
1.08	2.74	4.7	0.129	0.44	3.4
1.08	3.30	4.4	0.144	0.62	4.3
1.08	3.00	5.6	0.150	0.54	3.6
1.06	3.98	8.1	0.141	0.69	4.9
1.09	4.03	5.8	0.142	0.75	5.3
1.09	4.17	7.8	0.138	0.69	5.0
1.08	3.51	5.3	0.136	0.61	4.5
1.09	4.28	5.8	0.134	0.67	5.0
1.09	3.90	16.7	0.130	0.65	5.0
1.00	2.62	18.1	0.150	0.48	3.2
1.00	2.25	18.9	0.147	0.44	3.0
1.00	2.83	19.2	0.135	0.54	4.0
1.00	3.61	19.4	0.138	0.62	4.5
1.01	3.14	17.8	0.140	0.56	4.0
1.00	3.30	18.6	0.137	0.56	4.1
1.01	2.89	18.9	0.146	0.54	3.7
1.00	3.24	19.2	0.136	0.57	4.2
1.00	3.66	19.2	0.135	0.62	4.6
1.26	3.07	18.9	0.149	0.67	4.5
1.25	4.00	19.2	0.135	0.70	5.2
1.26	3.57	18.6	0.144	0.69	4.8
1.26	3.81	18.3	0.157	0.80	5.1
1.26	2.92	18.6	0.151	0.53	3.5
1.26	3.05	18.6	0.140	0.59	4.2
1.26	2.97	18.6	0.144	0.59	4.1
2.51	5.57	19.2	0.174	1.15	6.6
2.51	8.78	19.2	0.147	1.13	7.7
2.51	5.88	19.2	0.187	1.31	7.0
2.51	5.55	17.8	0.152	1.00	6.6

s = 2.65; grain diameter = 0.36 mm.

Table F6(Cont): Wave tunnel data for regular waves from Mogridge and Kamphuis (1972).

Wave period, T (sec)	Amplitude, a (cm)	Water Temperature (°C)	Δ/λ	Δ (cm)	λ (cm)
2.03	5.47	19.2	0.148	0.95	6.4
2.02	4.91	21.9	0.139	0.85	6.1
1.09	3.19	21.9	0.153	0.58	3.8
1.09	2.80	21.7	0.153	0.52	3.4
1.09	3.76	21.9	0.152	0.70	4.6
1.09	3.88	22.2	0.150	0.75	5.0
1.09	3.48	22.5	0.151	0.65	4.3
1.08	4.04	21.7	0.147	0.72	4.9
1.09	3.11	21.7	0.157	0.58	3.7
1.09	2.69	21.7	0.140	0.49	3.5
1.09	3.89	21.7	0.140	0.67	4.8

s = 2.65; grain diameter = 0.36 mm.

Table F6(Cont): Wave tunnel data for regular waves from Mogridge and Kamphuis (1972).

Test No.	Wave period, T (sec)	Amplitude, a (cm)	Δ/λ	Δ (cm)	λ (cm)
11	3.97	6.0	0.132	1.0	7.6
84	3.91	6.5	0.178	1.6	9.0
87	4.73	8.5	0.183	2.2	12.0
90	4.98	11.0	0.171	2.8	16.4

s = 2.65; grain diameter = 0.41 mm; D = 0.48 m.

Table F7: Oscillating tray tank data from Du Toit (1980).

Test No.	Wave period, T (sec)	Amplitude, a (cm)	Δ/λ	Δ (cm)	λ (cm)
96	5.37	12.2	0.174	3.0	17.2
97	4.22	9.6	0.191	2.2	11.5
98	3.21	10.1	0.204	2.8	13.7
99	4.87	19.5	0.170	4.3	25.3
100	3.18	14.1	0.157	3.3	21.0
101	5.75	8.1	0.194	2.1	10.8
102	4.62	8.5	0.192	1.9	9.9
103	4.65	16.6	0.180	4.4	24.5
104	3.80	10.8	0.200	3.0	15.0

s = 2.65; grain diameter = 0.41 mm; D = 0.48 m.

Table F8: Wave tunnel data for regular waves from Du Toit (1980).

Run No.	Wave period, T (sec)	Wave height, h (cm)	Δ/λ	Δ (cm)	λ (cm)
1	0.84	5.8	0.117	0.35	3.0
2	1.05	6.5	0.140	0.60	4.3
3	1.20	8.3	0.148	0.80	5.4
4	1.00	6.0	0.158	0.60	3.8
5	1.20	7.6	0.180	0.90	5.0
6	1.30	6.0	0.158	0.90	5.7
7	1.10	6.5	0.150	0.60	4.0

s = 2.7; grain diameter = 0.2 mm; D = 16.0 cm.

Table F9: Wave flume data for regular waves from Shibayama (1984).

Wave period, T (sec)	Amplitude, a (cm)	Water Temperature (°C)	Δ/λ	Δ (cm)	λ (cm)
5.76	11.0	65.2	0.125	1.45	11.6
5.76	39.0	60.2	0.064	3.50	55.0
5.98	14.5	64.0	0.145	1.80	12.4
2.30	8.0	62.2	0.184	1.40	7.6
5.51	20.25	69.0	0.085	1.80	21.2
5.51	21.0	65.0	0.135	2.10	15.6
4.49	13.0	65.0	0.143	2.00	14.0
3.14	10.5	64.4	0.143	1.50	10.5
2.90	8.5	59.6	0.191	2.10	11.0
2.90	10.5	59.6	0.123	1.30	10.6
2.90	19.5	67.2	0.308	2.00	6.5
2.30	7.75	52.3	0.182	1.20	6.6
2.30	11.25	54.0	0.150	1.20	8.0
2.30	9.0	52.4	0.160	1.20	7.5
4.49	17.5	65.0	0.150	2.7	18.0
3.14	14.5	60.0	0.277	2.3	8.3
5.76	59.5	57.0	fb	fb	fb
5.76	65.0	57.0	fb	fb	fb
7.48	80.5	48.4	fb	fb	fb

s = 2.65; grain diameter = 0.09 mm; fb = flat bed

Table F10: Wave tunnel data for regular waves from Lambie (1984).

Wave period, T (sec)	Amplitude, a (cm)	Water Temperature (°C)	Δ/λ	Δ (cm)	λ (cm)
4.69	19.75	56.5	0.159	2.9	18.2
4.69	19.75	56.0	0.143	3.3	23.0
2.80	6.75	59.0	0.183	2.1	11.5
2.80	10.25	50.0	0.184	2.3	12.5
2.72	11.75	60.5	0.167	2.2	13.2
3.85	21.75	64.5	0.126	3.2	25.3
3.83	19.25	60.5	0.197	4.0	20.3
3.83	16.75	58.7	0.178	3.3	18.5
3.83	13.90	63.5	0.172	2.8	16.3
3.85	10.15	60.0	0.157	1.8	11.5
5.93	15.50	65.0	0.163	2.8	17.2
3.85	25.50	62.5	0.185	4.1	22.2
3.88	24.00	70.0	0.196	4.0	20.4
5.28	39.40	68.5	0.118	3.9	33.0
5.28	36.00	64.2	0.144	4.4	30.5
5.28	28.00	64.2	0.141	3.8	27.0
5.28	26.30	67.1	0.200	4.8	24.0
5.28	17.70	69.7	0.168	3.4	20.2
5.28	9.75	75.5	0.165	3.1	18.8
5.28	9.15	63.0	0.149	1.4	9.4
5.28	12.6	63.0	0.183	1.7	9.3
5.28	11.5	63.0	0.188	2.6	13.8
7.22	37.75	21.9	0.135	4.0	29.7
4.59	21.00	22.0	0.162	2.8	17.3
4.69	40.50	51.0	0.112	3.7	33.0
2.80	15.00	64.5	0.147	2.5	17.0
2.80	18.75	59.5	0.095	1.9	20.0

$s = 2.65$; grain diameter = 0.15 mm.

Table F11: Wave tunnel data for regular waves from Lambie (1984).

Wave period, T (sec)	Amplitude, a (cm)	Δ/λ	Δ (cm)	λ (cm)
2.98	11.4	0.143	2.0	14.0
3.27	11.4	0.121	1.7	14.0
2.71	11.4	0.135	1.8	13.3
2.74	9.27	0.140	1.6	11.4
5.51	18.3	0.133	2.8	21.0
7.57	27.5	0.123	3.3	26.8

s = 2.65; grain diameter = 0.18 mm.

Table F12: Wave tunnel data for regular waves from Lofquist (1978).

Wave period, T (sec)	Amplitude, a (cm)	Δ/λ	Δ (cm)	λ (cm)
8.27	45.8	0.213	15.5	72.7
8.06	45.9	0.212	12.4	58.4
11.22	49.7	0.198	10.9	55.1
6.54	36.7	0.183	10.1	55.3
5.32	36.7	0.208	8.9	42.8
4.25	36.7	0.190	7.6	40.1
4.16	23.0	0.194	5.4	27.9
5.24	30.1	0.199	6.5	32.7
8.06	36.7	0.212	10.6	50.1
3.41	19.3	0.173	4.3	24.9
2.82	13.9	0.146	3.5	23.9
3.06	15.1	0.153	3.5	22.9
2.71	13.8	0.154	3.2	20.8
2.77	14.3	0.179	3.4	19.0
4.46	24.5	0.188	6.0	31.9
2.27	11.9	0.257	2.8	10.9
4.33	23.8	0.217	5.5	25.4
3.43	18.3	0.150	4.1	27.4
4.46	27.6	0.202	6.8	33.7
2.25	27.6	0.172	4.5	26.2
2.71	13.7	0.156	3.4	21.8
3.31	13.8	0.138	2.2	16.0
4.65	13.7	0.125	2.0	16.0

s = 2.65; grain diameter = 0.55 mm.

Table F13: Wave tunnel data for regular waves from Lofquist (1978).

Wave period, T (sec)	Amplitude, a (cm)	Δ/λ	Δ (cm)	λ (cm)
2.63	4.61	0.185	1.2	6.5
2.63	6.44	0.160	1.3	8.1
2.63	8.00	0.136	1.2	8.8
2.63	9.39	0.141	1.3	9.2
2.63	10.30	0.133	1.2	9.0
2.63	7.16	0.146	1.3	8.9

s = 2.65; grain diameter = 0.12 mm.

Table F14: Wave flume data for regular waves from Rosengaus (1987) and Mathisen (1989).

Wave period, T (sec)	Amplitude, a (cm)	Δ/λ	Δ (cm)	λ (cm)
2.63	9.08	0.162	1.6	9.9
2.63	5.55	0.176	1.3	7.4
2.63	7.23	0.169	1.5	8.9
2.63	12.05	0.151	1.6	10.6
2.17	6.07	0.151	1.3	8.6
3.10	9.16	0.157	1.6	10.2
2.40	6.43	0.161	1.4	8.7
2.63	9.27	0.156	1.7	10.9
2.63	9.01	0.158	1.6	10.1

s = 2.65; grain diameter = 0.2 mm.

Table F15: Wave flume data for regular waves from Rosengaus (1987) and Mathisen (1989).

Appendix G
Publications Related to Present Study

Paper 1
"Bed Boundary Layers"

O'Connor, B.A., Harris, J.M., Kim, H., Wong, Y.K., Oebius, H. and Williams, J.J. (1993). Bed boundary layers. In: Coastal Engng. 1992, Proc. 23rd Int. Conf. Coastal Engng., (ed.) Edge, B.L., Venice, Italy, 4 - 9 Oct., 1992, Vol. 2, Chap. 177, ASCE, New York, pp. 2307 - 2320.

Bed Boundary Layers

B.A. O'Connor[1], J.M. Harris[1], H. Kim[1],
Y. K. Wong[1], H.U. Oebius[2], and J.J. Williams[3].

ABSTRACT

The paper describes the development and application to laboratory and North Sea field data of a series of random wave and current computer models of bed boundary layer flows and associated suspended sediment concentrations. The EC-funded (MAST 1) work is part of a larger project, which also includes the laboratory testing of a new seabed shear stress meter (SSM) and the field collection of nearbed data using a special boundary layer rig (STABLE). Both two-dimensional (2DV) and one-dimensional (1DV) hydrodynamic models are described based on a mixing length closure but including simulation techniques to enable the inclusion of both long and short-crested random waves and steady currents. A 1DV suspended sediment model is also described with realistic boundary conditions to enable the simulation of vortex entrainment from seabed ripples. Application of the various models to the SSM and STABLE data shows realistic results.

1. INTRODUCTION

The present paper is concerned with the computer simulation of water and sediment movements over rippled seabeds in random wave and current conditions appropriate to the North Sea. It reports on one element of a larger multi-disciplinary research programme involving engineers, oceanographers and geologists, who are studying the formation of nearshore sandbanks and their role in providing protection to adjacent coastlines.

---

1. Department of Civil Engineering, University of Liverpool, L69 3BX, England.

2. Versuchsanstalt für Wasserbau und Schiffbau, Berlin, Germany.

3. Proudman Oceanographic Laboratory, Bidston Observatory, L34 7RA, England.

The research involves the field and laboratory testing of equipment to measure near-bed waves and currents and the associated sediment transport rates. In particular, staff from VWS, Berlin, have tested an improved seabed shear plate (SSM) to enable the direct measurement of seabed shear stress in waves and currents, Oebius (1992). Staff from the NERC's Proudman Oceanographic Laboratory have used a large bed boundary layer rig (STABLE) to provide field information on near-bed turbulence, waves, currents and sediment movements at the Brown Ridge Sandwave Site in the North Sea, Williams (1991). In addition, staff from the Department of Civil Engineering at Liverpool University have developed a series of hydrodynamic and sediment transport computer models to help with the interpretation of the data collected by both the SSM and STABLE rigs.

2. MODEL WORK

Four models have been developed: a two-dimensional (x, z) full-depth rough-turbulent hydrodynamic model (2DV) to study advective (mass-transport) effects on vertical mixing; a two-dimensional (x, z) bed boundary layer hydrodynamic model of wave-induced flow over bed ripples to assist with vortex entrainment ideas (2DV); a one-dimensional, rough-turbulent hydrodynamic model (1DV) to simulate wave-current interactions at arbitrary intersection angles in directional random waves; and an associated one-dimensional suspended sediment model (1DV) to study vertical sediment distributions in directional random waves and hence the effect of wave groupiness.

2.1. 2DV Hydrodynamic Model

The model solves simplified forms of the horizontal momentum and mass continuity equations for multi-frequency waves using a mixing length closure. The model equations are given as:-

$$\rho\partial u/\partial t + \rho u\partial u/\partial x + \rho w\partial u/\partial z + \partial p/\partial x = \partial \tau_{xz}/\partial z \qquad (1a)$$

$$\partial u/\partial x + \partial w/\partial z = 0 \qquad (1b)$$

where u and w are the phase-point-average turbulent-mean flow velocities in the horizontal (x) and vertical (z) cartesian co-ordinate directions, respectively; p is pressure; ρ is the fluid density; and τ_{xz} is the horizontal component of the Reynolds stresses.

The wave-induced boundary layer is assumed to be thin and the motion outside it is assumed to be irrotational so that the pressure gradient in equation (1a) can be approximated by the equation:-

$$-\partial p/\partial x = \rho \partial u_\infty/\partial t + \rho u_\infty \, \partial u_\infty/\partial x \qquad (2a)$$

$$\text{with} \quad u_\infty = \bar{u}_\infty + \sum_{i=1}^{m} u_i \cos(i\omega t - ikx + \phi_i) \qquad (2b)$$

where u_∞ is the wave-induced orbital velocity at the sea surface (mean water level); $\bar{u}_\infty$ is a wave-period-averaged steady velocity component; u_i are velocity amplitudes of the m Fourier frequency components making up the wave signal; ω is the wave frequency (= $2\pi/T$, T is the wave period); and k is the wave number (= $2\pi/L$, L is the wave length).

The Reynolds stress (τ_{xz}) is approximated by a simple mixing length expression ($\rho\kappa\partial u/\partial z$), where $\nu_t = \kappa^2 z^2 \partial u/\partial z$ and κ is Von Karman's constant (0.40).

The set of equations is solved using an implicit Crank-Nicolson finite difference technique on a space-staggered grid using zero velocity at the seabed ($z=z_o$), a zero velocity gradient at the water surface and repeating conditions for lateral boundaries, Kim (1993).

2.2. 1DV Hydrodynamic Model

The 1DV model also solves simplified flow equations using a mixing length closure. The model works for arbitrary-angled wave and current flows and uses simulation techniques involving surface wave spectra to produce appropriate model boundary conditions. The equations used in the model are given in tensor form as:-

$$\rho \partial u_i/\partial t - \partial p/\partial x_i = \partial \tau_{xzi}/\partial z \qquad (3a)$$

$$\partial p/\partial x_i = -\rho \partial u_{\delta i}/\partial t + \rho g \partial H/\partial x_i \qquad (3b)$$

$$\tau_{xzi} = -\rho \nu_t \partial u_i/\partial z; \quad \nu_t = \ell^2 \partial V/\partial z; \quad V = \sqrt{(u^2 + v^2)} \qquad (3c)$$

u_i (=u,v) are the cartesian velocity components in the horizontal (x) and lateral (y) co-ordinate directions respectively; x_i are the co-ordinates x, y respectively; g is the acceleration due to gravity; $\partial H/\partial x_i$ is the mean water surface slope; ℓ is a mixing length (=κz) and $u_{\delta i}$ are the u, v components at the top of the wave boundary layer, respectively.

Equation 3 can be solved in terms of a shear velocity (p_*, $\tau_{xz} = \rho p_*^2$) - see Bakker (1974), Wong (1984) for the case of co-linear waves and currents. Alternatively, the vertical co-ordinate (z) can be transformed by a power law and the transformed equations solved directly for u_i.

Both approaches have been used in the MAST 1 work. However the transformed co-ordinate approach is simpler to use for directional wave simulations. In this lattermost case the surface boundary conditions for the variation of velocity (U_T) with time is obtained from simulation techniques, see for example, Ellis et al (1981).

$$U_T = \sum_{m=1}^{M} \sum_{n=1}^{N} \left[\frac{2\pi f_m}{\sinh (k_m h)} \right] F \qquad (4a)$$

$$F = a_{m,n} \cos (2\pi f_m t + \phi_m) \cos\theta_n \qquad (4b)$$

where f_m is the wave frequency ($=1/T_m$, T_m is the wave period); ϕ_m are random phase angles in the range 0 - 2π; k_m is the wave number; h is the water depth; t is time; and $a_{m,n}$ is a wave amplitude obtained by integration of the directional wave energy spectrum. Thus:-

$$a_{m,n} = \sqrt{(2\, S(f_m, \theta_m)\, \Delta f_m . \Delta\theta_n)} \qquad (5a)$$

$$S(f_m, \theta_m) = S(f_m).\ G\ (f_m, \theta_n) \qquad (5b)$$

$$G(f_m, \theta_n) = G_0 \cos^{2s}(\theta_n/2) \qquad (5c)$$

$$G_0 = 2^{2s-1} . \Gamma^2\ (s + 1)/(\pi . \Gamma(2s+1)) \qquad (5d)$$

where G_0 is a constant dependent upon parameter s, which varies with peak spectral frequency and has a typical value of 20, Goda (1985); Γ is the Gamma function; θ_n is a wave direction in the range $\pm$ 90° of the dominant wave direction; $S(f_m, \theta_n)$ is any directional surface wave energy spectrum; $S(f_m)$ is a surface wave energy frequency spectrum; $G(f_m, \theta_n)$ is a spectral wave energy spreading function. $\Delta\theta_n$ is the band width of the n-th directional wave angle obtained by dividing the range of wave angles ($\pm$90°) into n equal intervals and Δf_m is the bandwidth of the m-th frequency interval obtained from the co-cumulative energy spectrum by using equal energy bands, see Ellis et al (1981).

A zero-velocity bed boundary condition is used (u=w=0) at $z=z_0$. The value of z_0 can be adjusted in random wave simulations using Madsen's (1990) approach, if desired.

2.3. 1DV Sediment model

In order to study the vertical distribution of suspended sediment over a rippled seabed, a one-dimensional sediment model has been used. The model equations used are:-

$$\partial c/\partial t + (\bar{w} - w_f)\partial c/\partial z = \partial(\epsilon_s \partial c/\partial z)/\partial z \qquad (6)$$

where c is the phase-point-averaged turbulent-mean suspended sediment concentration; $\tilde{w}$ is the vertical wave induced fluid velocity; w_f is the effective vertical sediment diffusion coefficient.

Previous work has generally ignored the effect of $\tilde{w}$, and has determined ϵ_s during the wave cycle from the hydrodynamic shear stress determined by a 1DV-type model, see for example, Davies (1990). Such an approach does not include all the major processes contributing to vertical mixing, see for example, O'Connor (1991). The inclusion of extra mixing has usually been done in the past by taking a wave-period-average view of vertical sediment distributions and then using the sediment distribution itself to determine effective mixing coefficients see for example, Van Rijn (1989), In the MAST 1 work, a different approach has been used. Sediment is released into the water column at two discrete times during the wave period (at t = T/16 and 9T/16 for a mono-wave) at a height of between one and two ripple heights above the mean bed level, as suggested by the 2DV model tests for a rippled bed, see O'Connor et al (1992). Shear-induced entrainment is also allowed during the wave period as dictated by the 1DV hydrodynamic bed shear stress, see Figure 1. Additional mixing due to mass-transport is allowed by using the 2DV "flat"-bed hydrodynamic model (see Section 2.1) to provide the ϵ_s values.

Solution of equation (6) is achieved by a number of intermediate steps. Firstly, a transformed vertical co-ordinate is used in order to resolve the large near-bed concentration gradients. The same approach was used for the 1DV hydrodynamic equations. Secondly, a split operator finite difference approach is used to introduce the vortex entrainment concentrations into the water column at a height of $1.5 \cdot \Delta_r$ above the mean bed level (z = 0). Thirdly, the new equations are then solved sequentially using appropriate boundary conditions between the water surface (mean see level) and the sea bed $z-z_o$; the co-ordinate origin being located half a ripple height above a ripple trough.

The necessary equations are given below:-

$$\partial c/\partial t - w_f \, \partial c/\partial z = \partial \, (\epsilon_s \, \partial c/\partial z)/\partial z \qquad (7a)$$

$$\partial c/\partial t + \tilde{w}\partial c/\partial z = S(t) \qquad (7b)$$

$$S(t) = M_v/(\Delta_r T_v), \text{ for } \Delta_r \le z \le 2\Delta r, \text{ and} \qquad (7c)$$

$$^{5T}/_{16} \le t \le {}^{3T}/_{8}, \text{ or } {}^{13T}/_{16} \le t \le {}^{7T}/_{8}$$

$$M_v = \int_o^{T/2} E_v \, dt \qquad (7d)$$

$$E_v = (1-\alpha)E_t ; \; E_t = A\,\Phi^{1.5} ; \; T_v = T/16 \qquad (7e)$$

$$\Phi = \tau_b(t)/((\rho_s-\rho)\; g\; D_{50}) \qquad (7f)$$

Where $\tau_b(t)$ is the bed ($z = 0$) shear stress from the 1DV model; ρ_s is the sediment density; g is the acceleration due to gravity; D_{50} is the 50% finer grain size of the bed sediment; A, α are model constants determined by field/laboratory tests.

Equation 7a is solved by an implicit finite difference method while equation 7b is solved as a second step using the method of characteristics. The model uses a zero flux condition ($\epsilon_s\, \partial c/\partial z = -w_f c$) at the water surface and a surface entrainment condition at the seabed ($\epsilon_s \partial c/\partial z = \alpha E_t$ at $z=z_o$). Values of ϵ_s are obtained from the 2DV hydrodynamic model.

3. MODEL APPLICATIONS

3.1. 1DV Hydrodynamic Model Tests

The ability of the 1DV model to reproduce conditions in mono-frequency waves was demonstrated using the oscillating tunnel data of Jonsson and Carlsen (1975), see Wong (1984). In addition, data from the VWS flume tests, Oebius (1992) were reproduced using a suitable plate roughness ($2D_{50}$) and scale factor, see Figure 2.

The ability of the Bakker version of the 1DV model to reproduce velocities near the top of the wave boundary layer (10 mm above the bed) with multi-frequency (3 components) waves, and waves and currents was demonstrated by using the small-scale flume data of Savell (1986), see Figures 3,4. Good agreement is apparent for maximum amplitude and phase. The velocity model's ability to reproduce long-crested random waves was tested for conditions approximated to those at the Brown Ridge Site ($h = 30m$; $z_o = 0.01$ m. Wave conditions we: assumed to be described by a Pierson-Moskowitz (PM) spectrum with significant wave height of $H_s = 2.5m$ (wind speed = 11 m/s) and a peak energy period of $T_m = 8.1$ s. The PM spectrum was simulated by 60 frequency components and the velocity time series used to drive the model.

The accuracy of the simulation process can be judged by Figure 5, which shows a compassion between the PM spectrum and the model spectrum obtained by subjecting the model surface elevation time series to a Fast Fourier Transform (FFT) analysis.

Typical bed shear stresses and orbital velocities from the model at the top of the wave boundary layer are shown in Figure 6 for a typical 64s time interval. The random nature of the results is clearly seen as is also the phase shift over the depth of the boundary layer.

Figure 7 shows the root-mean-square (rms) and significant amplitudes of the wave-induced orbital velocities from a direct analysis of model time series for conditions at the Brown Ridge Site. These significant values can be directly compared with the results from the 1DV model operated with representative mono-frequency wave heights and wave periods -the 'design-wave' approach. Figure 8 shows the results for the mono-wave simulations using H_s, T_{max} and H_s, T_z. It is clear that the best comparison with the random wave model is obtained with H_s, T_{max} and not with the more traditional H_s, T_z combination.

The 1DV model was next used to investigate the effect of short-crested seas. The Brown Ridge model with its PM spectrum was re-run with a Goda spreading function, equation 5, s = 20. Figure 9 shows the u, v velocity components for a short length of record while Figure 10 shows the corresponding instantaneous wave direction vectors. The groupy nature of the wave signal is clearly seen as is also the lateral scattering effect of the short-crested sea. Such lateral movements will add significantly to the dispersal of both sediment and pollutant within the water volume. Similar results to the 1DV model have also been found with the STABLE data, see O'Connor et al (1992).

In order to examine the 1DV model's ability to reproduce the correct magnitude and phase of velocities within the boundary layer, use was made of S4 current meter data collected during the STABLE deployment at the Brown Ridge Site, see Williams (1991) Field velocities for a 22 second period at 800mm above the seabed were used as the upper boundary condition in the model. Figure 11 shows the comparison of field results at 800mm and 400mm with model results at 70mm. It is clear that the model reproduces the main features of the field results.

3.2. 1DV SEDIMENT MODEL APPLICATIONS

The ability of the 1DV model to reproduce suspended sediment concentrations during a wave period was tested using laboratory data of Bosman (1982). Figure 12 shows quite a good comparison considering the difficulty in obtaining such laboratory data.

The need for the inclusion of extra mixing in 1DV models is illustrated by the wave-period-average results of Figure 14. Both the 2DV and 1DV hydrodynamic models were used for conditions appropriate to Bosman's (1984) laboratory studies,

and the wave-period-average mixing coefficient (ϵ_s) determined by period-averaging. The 1DV sediment model was then used with vortex and shear-induced entrainment to reproduce wave-period-average concentrations, Figure 13. It is clear that the extra mixing inherent in the 2DV model is essential for correct simulation of sediment profiles.

Finally, the long-crested 1DV random wave model was used to simulate suspended sediment conditions at the Brown Ridge Site, see Figure 14. The influence of groupiness in the wave and shear records is clearly seen to influence suspended sediment concentrations with the larger groups having the greatest effects. Unfortunately, no comparable field data was obtained from the STABLE deployment and consequently, more field data is needed to test model ideas further.

4. CONCLUSIONS

A range of 1DV and 2DV bed boundary layer models have been developed to assist with interpretation of field data obtained from the Brown Ridge Sandwave Site in the Southern North Sea. Comparison of model results with mono-and multi-frequency laboratory data for both velocities and shear stresses shows good results. Realistic model simulations were also obtained for both long and short-crested random wave conditions when compared with measured field data. Use of the long-crested 1DV hydrodynamic model also demonstrates the importance of using the correct wave period when using the mono-frequency "design wave" approach to predict seabed velocities and shear stresses.

An 1DV suspended sediment model was also developed with new boundary conditions which attempted to reproduce the influence of both vortex and shear-induced entrainment. Good comparisons were obtained with laboratory data. The importance of including enhanced mixing due to mass-transport currents in 1DV model simulations was also demonstrated as was the influence of wave groupiness on sediment concentrations at the Brown Ridge Field Site.

5. ACKNOWLEDGEMENTS

The authors are grateful for financial assistance from the Commission of the European Directorate General for Science, Research and Development under Contract No. MAST - 0036(C).

References

Bakker, W.T., (1974). Sand Concentration in an Oscillatory Flow. Proc. 14th Coastal Eng. Conf. ASCE, pp 1129-1148.

Bosman, J.J., (1982). Concentration Measurements under Oscillatory Water Motion. Delft Hydraulics Laboratory/TOW Report on Model Investigation M1695 Part II. Delft.

Bosman, J.J. (1984). Design and Specification of OPCON, on Optical Instrument for Instantaneous Sediment Concentration Measurements. Report on Investigation R716, Part VI, Delft Hydraulics Laboratory.

Davies, A.G., (1990). Modelling the Vertical Distribution of Suspended Sediment in Combined Wave-Current Flow. Proc. 5th Int. Conf. on the Physics of Estuaries and Coastal Seas. (In Press).

Ellis, G.P., O'Connor, B.A. and McDowell, D.M., (1981). Generation of Laboratory Waves using a Microcomputer. 2nd Int. Conf. on Engineering Software, Imperial College, London, pp 899-913.

Goda. Y., (1985). Random Seas and Design of Maritime Structures. University of Tokyo Press, 323 pp.

Jonsson, I.G. and Carlsen, N.A., (1975). Experimental and Theoretical Investigations in an Osillatory Turbulent Boundary Layer. J. Hydr. Res., Vol. 14, No. 1, pp 45-60.

Kim, H., (1993). A Three Dimensional Sediment Transport Model. Ph.D. Thesis, Dept. of Civil Engineering, University of Liverpool (in preparation).

Madsen, O.S., Mathison, P.P. and Rosengaus, M.M., (1990). Moveable Bed Friction Factors for Spectral Waves. Proc. 22nd Coastal Eng. Conf., ASCE, pp 420-429.

O'Connor, B.A., (1991). Suspended Sediment Transport in the Coastal Zone, Keynote Lecture, IAHR Symposium, Florence, 2-5 September, 1991, pp 17-63.

O'Connor, B.A., Williams, J.J., Oebius, H.U. and Sarmento A., (1992). Circulation and Sediment Transport on Sand Banks in European Shelf Seas. Final Report to DGXII, EC MAST Programme. Dept. of Civil Engineering, University of Liverpool.

Oebius, H.U., (1992). Circulation and Sediment Transport on Sand-Banks in European Shelf Seas. Part: Development of a Shear Stress Meter. Report No. 1208/92, VWS, Berlin, 100pp.

Savell, I.A., (1986). An Experimental Study of Near-Bed Hydrodynamics of Waves and Steady Current and the Effect of this on Sediment Transport. Ph.D. Thesis. Dept. of Civil Engineering, University of Manchester.

Williams, J.J., (1991). Wave, Current and Sediment Interaction Study. POL Cruise Report No. 13, RRS Challenge 87, 4-20 Dec. 1991, 30pp

Wong, Y.K., (1984). A Numerical Model for the Interaction of Combined Wave and Current Boundary Layers. M.Sc. Thesis, Dept. of Civil Engineering, University of Manchester.

Van Rijn, L.C., (1989). Handbook Sediment Transport by Currents and Waves. Delft Hydraulics, Report H461.

Figures

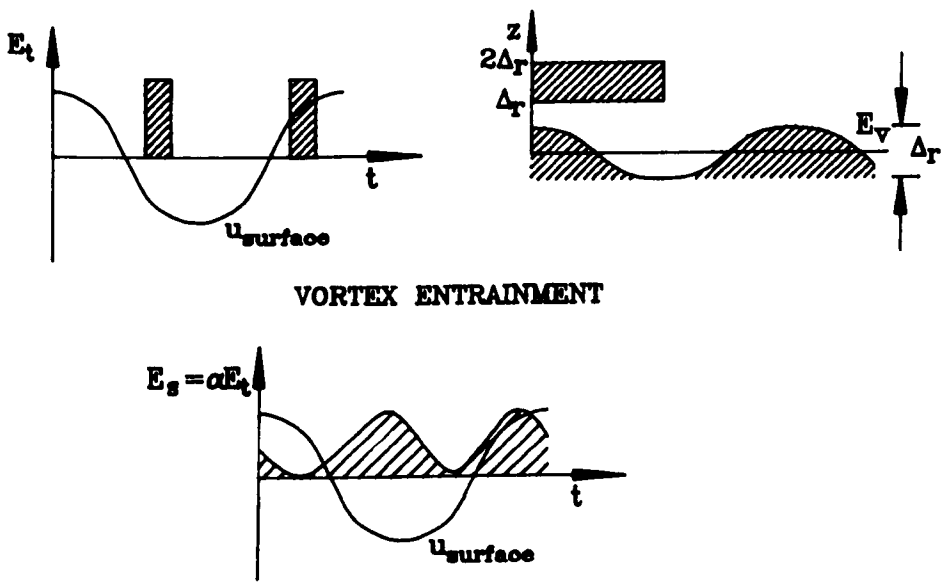

FIGURE 1

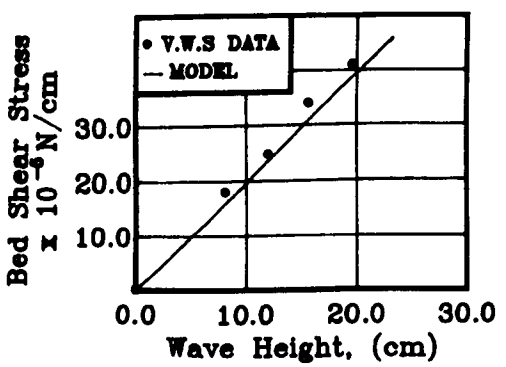

FIGURE 2

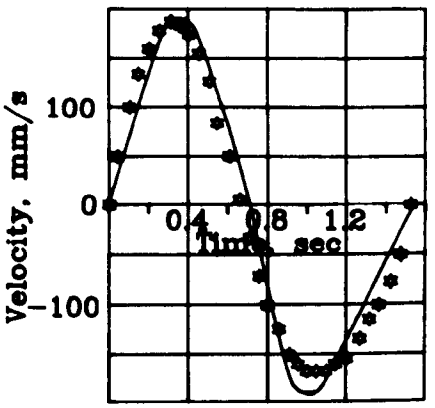

FIGURE 3

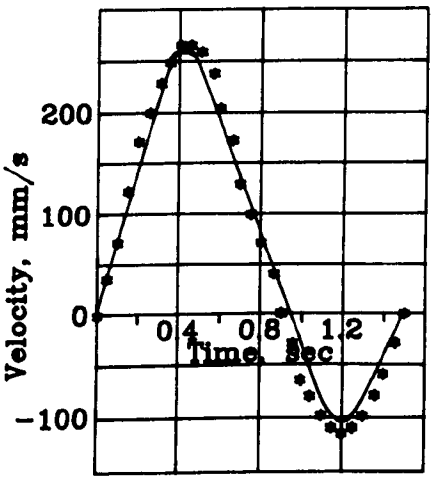

FIGURE 4

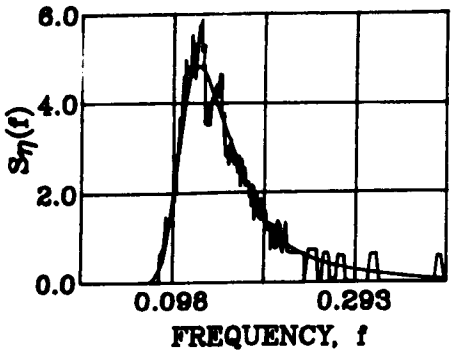

FIGURE 5

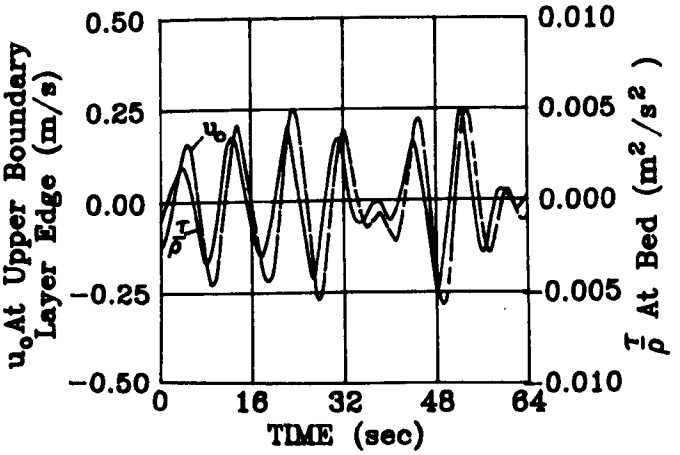

FIGURE 6

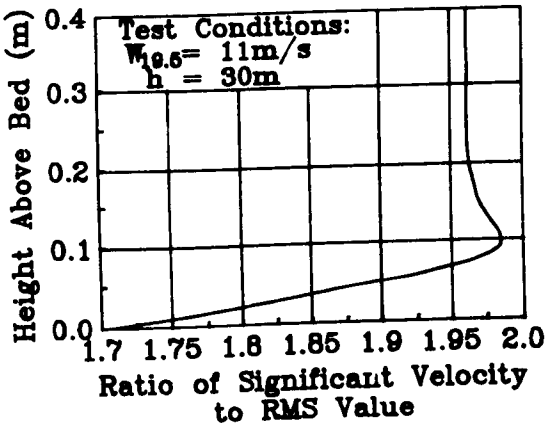

FIGURE 7

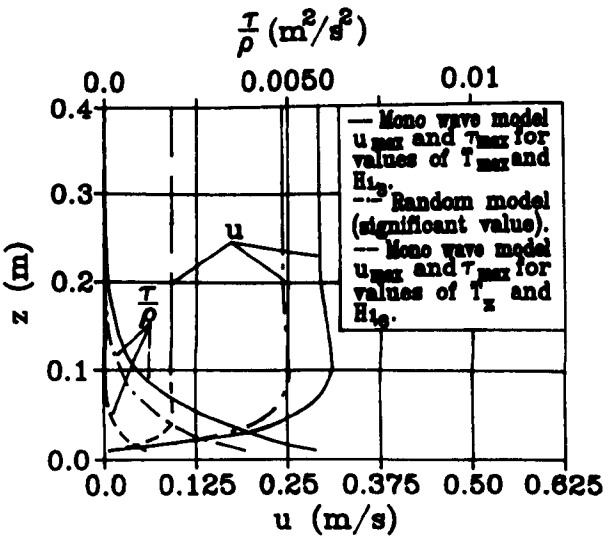

FIGURE 8

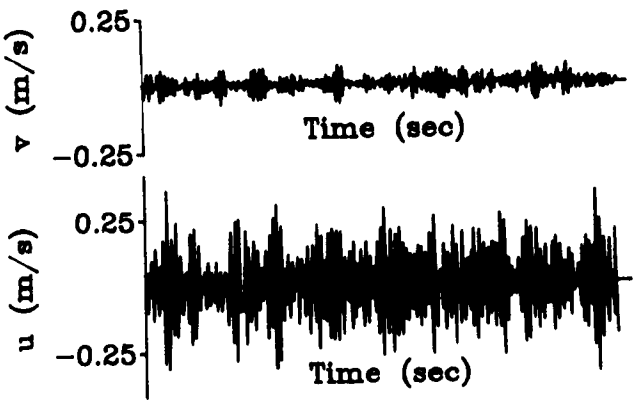

FIGURE 9

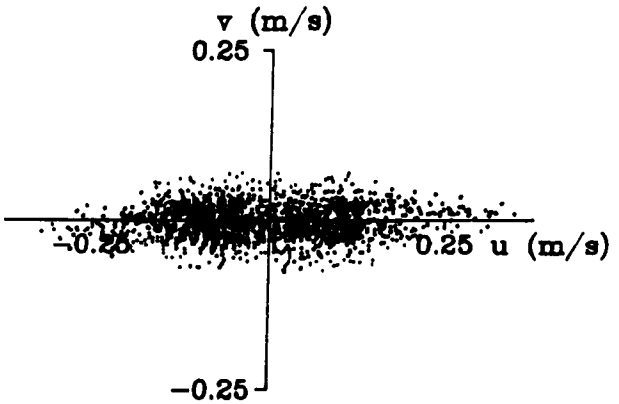

FIGURE 10

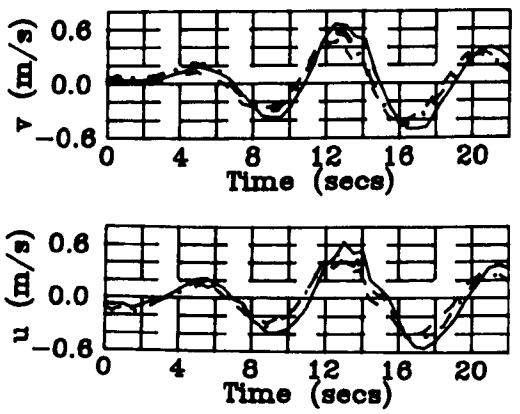

LEGEND:
Model/Field ——
(at 80cm above bed).
Field — —
(at 40cm above bed).
Model — - —
(at 7cm above bed).

FIGURE 11

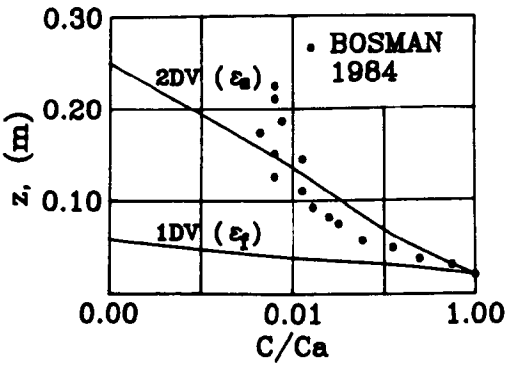

FIGURE 13

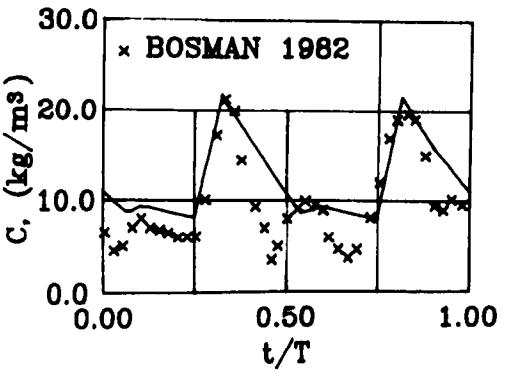

FIGURE 12

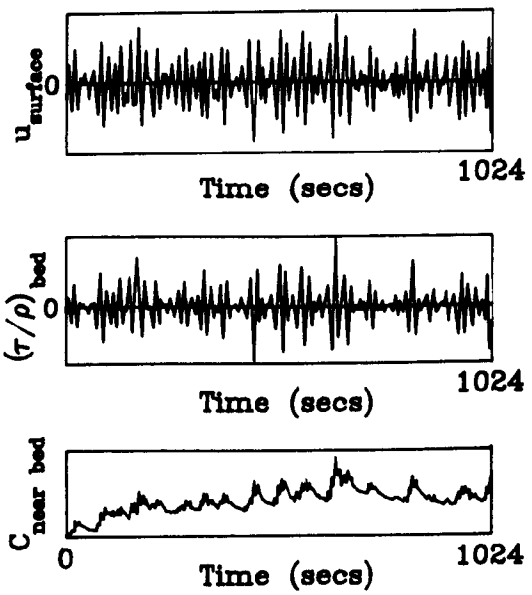
$u_{surface}$
0
Time (secs)
1024
$(\tau/\rho)_{bed}$
0
Time (secs)
1024
$C_{near\ bed}$
0
Time (secs)
1024

FIGURE 14

Paper 2
"Modelling Moveable Bed Roughness and Friction for Spectral Waves"

Kaczmarek, L.M., Harris, J.M. and O'Connor, B.A. (1995). Modelling moveable bed roughness and friction for spectral waves. In: Coastal Engng. 1994, Proc. 24th Int. Conf. Coastal Engng., (ed.) Edge, B.L., Kobe, Japan, 23 - 28 Oct., 1994, Vol. 1, Chap. 23, ASCE, New York, pp. 300 - 314.

Modelling Moveable Bed Roughness and Friction for Spectral Waves

Kaczmarek, L.M.[1], Harris, J.M.[2], O'Connor, B.A.[2]

Abstract

The present paper is concerned with the simulation of turbulent boundary layer dynamics over a moveable seabed in random waves. A new theoretical approach for the evaluation of moveable bed roughness in spectral waves based on the grain-grain interaction idea is presented and tested against data from the laboratory and field. The new approach is combined with the methodology which assumes that the spectral wave condition can be represented by a monochromatic representative wave. Good results have been obtained, although further testing against data gathered in the North Sea is required.

1. Introduction

For a moveable sandy bed, one may distinguish three general seabed conditions due to the action of surface gravity waves: a flat bed, rippled bed and sheet flow. If we consider the latter condition, the need to study sediment transport under wave-induced sheet flow conditions is necessary in the understanding of beach profile changes in the surf zone. The understanding of nearbed sediment dynamics is also of great importance for the mathematical description of cross-shore sediment transport.

To understand the effect of changing bed roughness by the hydrodynamic forces requires knowledge of the dynamic behaviour of sand grains in the collision-dominated, high concentration nearbed region. At high shear stresses and sediment transport intensities, the nearbed sediment transport appears to take place in a layer with a thickness that is large compared to the grain size. It is therefore not possible to properly describe flow in this layer by conventional engineering models which assume that bed load transport occurs in a layer that has a thickness of the order of one or two grain diameters.

1 Polish Academy of Sciences, Institute of Hydro-Engineering, IBW PAN, 7 Koscierska, 80-953, Gdansk, Poland.

2. Department of Civil Engineering, University of Liverpool, Brownlow St., P.O. Box 147, Liverpool L69 3BX. UK.

The present paper is concerned with developing an iterative procedure for the estimation of the effective bed roughness for a monochromatic wave, as characterised by the roughness parameter k_s , and extending this to the case of a spectral sea. The nearbed sediment dynamics are modelled in two regions with continuous profiles of stress and velocity. Namely (i) a granular fluid region and (ii) a wall bounded turbulent fluid shear region.

In sheet flow conditions it is assumed that the external drag produced by the boundary layer flow is related to the particle interactions within the sub-bed layer and hence to the effective roughness at the boundary.

2. The sheet flow model

2.1 Formulation of the problem

A typical velocity distribution with depth of a rough bed is supposed to be characterised (Kaczmarek & O'Connor 1993a,b) by a sub-bottom flow and a main or outer flow, as shown in Figure 1.

The velocity distribution is supposed to be continuous. Its intersection with the nominal bottom is the apparent slip velocity u_b . The downward extension of the velocity distribution in the outer zone of the main flow yields a fictitious slip velocity, u_o at the nominal bed, which is necessarily larger than u_b because of the supposed asymptotic transition in the buffer layer between the sub-bed flow and the fully turbulent flow in the turbulent-fluid shear region.

The velocity distribution in the roughness layer depends on the type of geometric roughness pattern and the bed permeability. There must be some transition between both parts of the velocity distribution bridged by the buffer zone. However, for present purposes it is assumed that the velocity distribution in the turbulent-fluid shear region can be determined by parameters dependent on the geometric roughness properties of the bed and the outer flow parameters, such as the free-stream orbital velocity. It is proposed to extend the sub-bed granular-fluid flow region to the matching point with the velocity distribution in the turbulent-fluid shear region. Thus, shear stress velocities in the two layers are set equal at the theoretical bed level, as it is shown in Figure 1, point A.

The sub-bed flow region has a high sediment concentration. For sheet flow conditions in this layer, chaotic collisions of grains are the predominant mechanism. In this case water does not really transfer shear stresses at all. The dynamic state of such a mixture is characterised by stresses σ_{ij} which are the sum of dynamic σ^*_{ij} and plastic σ°_{ij} stresses.

The first problem, therefore, is to determine the velocity profile distribution in the upper turbulent layer, which means determining the effective roughness height of

the bed k_s as well as the lower grain-fluid flow. The intersection of these two profiles will determine point A (See Figure 1).

2.2 Mathematical description of flow in the turbulent upper region

It is assumed that flow in the upper layer is governed by the simplified equation of motion:

$$\frac{\partial u}{\partial t} = \frac{\partial U}{\partial t} + \frac{1}{\rho}\frac{\partial \tau}{\partial z} \tag{2.1}$$

in which u(z,t) is, in general, a combined wave-period-averaged "steady" current and wave velocity and U(t) is the free-stream wave velocity at the top of the wave boundary layer.

The present work uses an eddy viscosity model, which is an extension of Kajiura's (1968) and Brevik's (1981) model. Thus the eddy viscosity over the flow depth is assumed to be given by the equations.

$$\nu_t(z) = \kappa u_{f\max} z \qquad \text{for} \quad \frac{k_s}{30} \le z \le \frac{\delta_m}{4} + \frac{k_s}{30} \tag{2.2}$$

$$\nu_t(z) = \kappa u_{f\max}\left(\frac{\delta_m}{4} + \frac{k_s}{30}\right) \quad \text{for} \quad \frac{\delta_m}{4} + \frac{k_s}{30} < z \le 2\delta_m + \frac{k_s}{30} \tag{2.3}$$

in which κ is von Karmen's constant; u_{fmax} is the maximum value of bed shear velocity ($u_f(\omega t)$) during the wave period that is max [$u_f(\omega t)$]; δ_m is the maximum value of δ_1 and δ_2 , that is, max (δ_1 , δ_2) where δ_1 and δ_2 are the boundary layer thickness at the moments corresponding to maximum and minimum velocity (of the combined wave and current flow) at the top of the turbulent boundary layer.

The quantities u_{fmax} , δ_m are determined from the solution of the integral equation derived from equation (2.1) as used by Fredsøe (1984):

$$\frac{\tau(\delta)}{\rho} - \frac{\tau_o}{\rho} = -\int_{\frac{k_s}{30}}^{\delta+\frac{k_s}{30}} \frac{\partial}{\partial t}(U-u)dz \tag{2.4}$$

Fredsøe (1984) assumed a logarithmic velocity profile in the boundary layer

$$\frac{u}{u_f} = \frac{1}{\kappa}\ln\frac{30z}{k_s} \tag{2.5}$$

The solution of equation (2.4) using Fredsøe's (1984) approach enables the value of u_{fmax} to be determined, if k_s is specified. Equation (2.1) can then be solved to provide the velocity distribution in the wave boundary layer.

2.3 Mathematical description of the flow in the granular-fluid region

Particle interactions in the shear-grain-fluid flow are assumed to produce two distinct types of behaviour. The Coulomb friction between particles gives rise to rate-independent stresses (of the plastic type) and the particle collisions give rise to stresses that are rate-dependent (of the viscous type). We assume the co-existence of both types of behaviour and the stress tensor is divided into two parts.

$$\sigma_{ij} = \sigma^{0}_{ij} + \sigma^{*}_{ij} \tag{2.6}$$

Where σ^{0}_{ij} is the plastic stress and σ^{*}_{ij} is the viscous stress.

For two-dimensional deformation in the rectangular Cartesian co-ordinates x' and z' the Coulomb yield criterion is satisfied by employing the following stress relations:

$$\sigma^{0}_{x'x'} = -\sigma'(1 + \sin\varphi\cos 2\psi) \tag{2.7}$$

$$\sigma^{0}_{z'z'} = -\sigma'(1 - \sin\varphi\cos 2\psi) \tag{2.8}$$

$$\sigma^{0}_{x'z'} = -\sigma'\sin\varphi\cos 2\psi \tag{2.9}$$

Where φ is the quasi-static angle of internal friction, while ψ , denoting the angle between the major principal stress and the x'-axis is equal to:

$$\psi = \frac{\pi}{4} - \frac{\varphi}{2} \tag{2.10}$$

For the average normal stress:

$$\sigma' = -\left(\frac{\sigma^{0}_{x'x'} + \sigma^{0}_{z'z'}}{2}\right) \tag{2.11}$$

we employ the following approximate expression (Sayed and Savage 1983).

$$\sigma' = \alpha^{0}\left(\frac{c - c_0}{c_m - c}\right) \tag{2.12}$$

where α^0 is a constant and c_0 and c_m are the solid concentrations corresponding to fluidity and closest packing respectively.

The viscous part of the stress tensor according to Sayed and Savage (1983) is assumed to have the following form:

$$\sigma^{*}_{x'x'} = \sigma^{*}_{z'z'} = -(\mu_0 + \mu_2)\left(\frac{\partial u}{\partial z'}\right)^2 \tag{2.13}$$

$$\sigma^{*}_{x'z'} = \sigma^{*}_{z'x'} = \mu_1 \left|\frac{\partial u}{\partial z'}\right| \frac{\partial u}{\partial z'} \tag{2.14}$$

in which the viscous stress coefficients μ_0 , μ_1 and μ_2 are functions of the solids concentration c:

$$\frac{\mu_1}{\rho_s d^2} = \frac{0.03}{(c_m - c)^{1.5}} \tag{2.15}$$

$$\frac{\mu_0 + \mu_2}{\rho_s d^2} = \frac{0.02}{(c_m - c)^{1.75}} \tag{2.16}$$

Considering steady fully developed two-dimensional shear-grain-flow, the balance of linear momentum according to Kaczmarek & O'Connor (1993a,b) yields:

$$\alpha^0 \left[\frac{c - c_0}{c_m - c}\right] \sin\varphi \sin 2\psi + \mu_1 \left[\frac{\partial u}{\partial z'}\right]^2 = \rho u_f^2 \tag{2.17}$$

$$\alpha^0 \left[\frac{c - c_0}{c_m - c}\right] (1 - \sin\varphi \cos 2\psi) + (\mu_0 + \mu_2) \left[\frac{\partial u}{\partial z'}\right]^2 = \left[\frac{\mu_0 + \mu_2}{\mu_1}\right]_{c=c_0} \rho u_f^2 + (\rho_s - \rho) g \int_0^{z'} c\,dz \tag{2.18}$$

where ρ is the density of the fluid.

Eliminating $(\partial u/\partial z')$ from equations (2.16) and (2.17) allows the calculation of the profiles of the sub-bed sediment concentration c and velocity u in relation to known maximum shear stress ($\rho\, u^2_{f\,max}$) at the theoretical bed level (z'=0).

In Kaczmarek & O'Connor (1993a,b) equation (2.18) was solved for c as a function of depth (z') by using an iteration method in conjunction with numerical integration. Integration started at the theoretical bed level (z'=0) with $c=c_0$. Proceeding downwards at each step the iteration method was used to evaluate c. The integration was stopped when c was equal to c_{ms}. For the calculations the following numerical values were recommended for the various sand beds.

$$\frac{\alpha^0}{\rho_s g d} = 1 \; ; \; c_0 = 0.32 \; ; \; c_m = 0.53 \; ; \; c_{ms} = 0.50 \; ; \; \varphi = 24.4^\circ$$

3. Results for monochromatic waves

3.1 Plane bed

The above procedure was used to compare computations for the model with the experimental results of Horikawa *et al.* (1982). The conditions for Horikawa *et al.*'s test 1 were used for the model calculations: d = 0.2mm, $s = \rho_s/\rho = 2.66$, $\varphi = 24.4°$, T = 3.64s and U = 127 cm/s. A value of $k_s = 7.3$mm was found for the roughness parameter.

Having obtained the roughness parameter it is then easy to obtain the instantaneous profiles both in the turbulent layer and the sub-bottom flow zone without reference to empirical formulas of any kind. Knowing u_f and solving equations 2.17 and 2.18 the velocity and concentration distributions at any time inside the entire sub-bottom layer can be found.

The results are shown in Figure 2. A reasonable agreement is obtained between the model and the laboratory data.

The model was then run for a range of conditions including those outside its range of application. The results of these tests are shown in Figure 3. The calculations were obtained using the simplified iteration procedure to determine k_s by introducing a simple logarithmic distribution (2.5) instead of the numerical solution of equation (2.1). Such a simplification makes the calculations much more efficient. It is seen that the roughness parameter, k_s , decreases with increasing dimensionless bed shear stress θ_{max} and k_s is seen to attain its greatest value for small dimensionless shear stresses where $\theta \approx 1$ (the transition from plane bed to ripples).

The trend shown in the present results, that is, that the roughness parameter increases drastically with decreasing dimensionless maximum shear stress, is similar to that shown by Nielsen (1992). Nielsen (1992) showed that the hydraulic roughness for equilibrium ripple formations is of the order $100d_{50}$ to $1000d_{50}$. However, for artificial flat beds where measurements were taken before ripples had time to form Nielsen (1992) found that the hydraulic roughness decreased with decreasing grain roughness Shields parameter.

Next, calculations were carried out for a moveable sandy bed (d = 0.2mm, s = 2.66, $\varphi = 24.4°$) with a variety of wave heights with a mean water depth of 5.0m. The wave period was kept constant at T = 3.6s. The maximum shear stresses were calculated on the basis of equation (2.4) and using the simplified iteration procedure to determine k_s . The results of the analysis of friction for wave-induced sheet flow, shown in Figure 4, suggest that the present approach restricted to the sheet flow regime may be extended to lower flow regimes and on the basis of analogy used to investigate lower flow conditions involving bed ripples.

3.2 Rippled bed

Calculations for a rippled bed were performed for two different sediment sizes (0.2mm and 0.12mm diameter quartz sands). The calculations were carried out in two steps. Firstly, the values of the bed roughness k_s were obtained using the proposed iterative scheme. Then, the friction factors were calculated on the basis of an adjusted version of the semi-empirical formula of Jonsson and Carlsen (1976) in order to include the effects of the vortices formed in the lee of the roughness element crest due to turbulent mixing.

The theoretical results are shown in Figure 5. Presented alongside these results are the experimental results over a moveable bed reported by Madsen *et al.* (1990). The values of wave friction factor f_w are plotted against the representative value of a fluid-sediment interaction parameter, defined as:

$$S_r = \frac{\theta'}{\theta_c} \tag{3.1}$$

in which the skin Shields parameter is defined for a monochromatic wave as:

$$\theta' = \frac{u'^2_{f\,max}}{(s-1)gd} \tag{3.2}$$

The agreement between theoretical and experimental results appears quite reasonable. It therefore appears that the sheet flow model can be used to investigate rippled bed conditions.

If the model can be used to investigate rippled bed conditions then it might also be possible to extend the analogy to include spectral wave conditions.

4 Spectral sheet flow model

4.1 Introduction

In the real world the Sea's motion is a random process. To describe a real sea it is usual to use spectral methods. However, it is possible to simplify the process by using appropriate representative values for the spectral components (See O'Connor *et al.* 1992).

The effect of random waves on bed roughness needs to be studied, since it is known that the bed friction changes between mono-frequency and random wave conditions. It is hypothesized by Madsen *et al* (1990) that the larger waves in a spectral simulation shave off the sharp ripple crests thereby causing the observed reduction in dissipation and friction factors for spectral waves. In an attempt to explain this reduction of spectral wave friction factors a new theoretical approach for predictive evaluation of moveable bed roughness for spectral waves is

proposed. The new approach is based on the methodology which assumes that the spectral wave condition can be represented by a monochromatic wave and is combined with the theoretical grain-grain interaction ideas.

4.2 Modified iterative method

Following on from the iterative method used for monochromatic waves, a modified iterative procedure to evaluate the moveable bed roughness under spectral waves is proposed as shown in Figure 6.

Representative values are used in the calculation routine for the free stream velocity and the angular frequency. Previously for monochromatic waves, the maximum value of shear stress was the maximum value of shear stress during a wave period. For spectral waves the maximum value of the random shear stress time series is used:

$$\tau_{max} = \frac{3\tau_{rms}}{\sqrt{2}} = 3\sigma_{\tau} \qquad (4.1)$$

The choice of this maximum value of the random shear stress time series was checked using the simple Rayleigh Method as well as a through running a more sophisticated one dimensional through depth (1DV) k-ε boundary layer model.

4.3 Spectral shear stress

Using the Rayleigh method, it is possible to quickly determine a value for the shear stress for a random time series. Assuming a Rayleigh distribution then:

$$\frac{\tau_{max}}{\tau_{rms}} = \left[\ln(N)\right]^{\frac{1}{2}} = R \qquad (4.2)$$

T_z /sec	10	10	10
Time /min	10	20	40
N	60	120	240
R	2.02	2.18	2.34

The assumed value of R is:

$$3/\sqrt{2} = 2.12$$

The 1DV k-ε boundary layer model provides a method to directly simulate a random from shear stress from a known random velocity field. The method is based on the previous work of O'Connor *et al.* (1992) where a zero equation mixing length model was used to simulate a random sea.

The two equation k-ε model uses the standard equations to represent the momentum, the turbulent energy, k and the dissipation rate , ε.

Momentum:

$$\frac{\partial u}{\partial t} = \frac{\partial u_f}{\partial t} + \frac{\partial}{\partial z}\left(\nu_t \frac{\partial u}{\partial z}\right) \tag{4.3}$$

Turbulent Energy, k:

$$\frac{\partial k}{\partial t} = \frac{\partial}{\partial z}\left(\frac{\nu_t}{\sigma_k}\frac{\partial k}{\partial z}\right) + \nu_t\left(\frac{\partial u}{\partial z}\right)^2 - \varepsilon \tag{4.4}$$

Dissipation Rate, ε:

$$\frac{\partial \varepsilon}{\partial t} = \frac{\partial}{\partial z}\left(\frac{\nu_t}{\sigma_\varepsilon}\frac{\partial \varepsilon}{\partial z}\right) + c_{1\varepsilon}\frac{\varepsilon}{k}\nu_t\left(\frac{\partial u}{\partial z}\right)^2 - c_{2\varepsilon}\frac{\varepsilon^2}{k} \tag{4.5}$$

Turbulent Eddy Viscosity, ν_t:

$$\nu_t = c_l \frac{k^2}{\varepsilon} \tag{4.6}$$

The upper boundary condition for the k-ε model is given by :-

$$u_o(t) = \sqrt{\frac{2M_{oc}}{N}}\sum_{n=1}^{N}\left(\frac{\omega_n}{\sinh(k_n d)}\right)\cos(-\omega_n t + \delta_n) \tag{4.7}$$

Results from the model appear to indicate that the shear stress time series is not necessarily Rayleigh in its distribution. A typical model value for R was 2.6.

5. Results

5.1 Spectral bed roughness

The ability of the present iteration procedure, shown in Figure 6 to evaluate moveable bed roughness, k_s, under spectral waves was checked for a sandy bed: s = ρ_S/ρ = 2.66 φ = 24.4° with different grain size and various wave conditions. The results of the computations plotted in Figure 7 are for both irregular and regular waves.

In an attempt to explain the reduction of spectral wave friction factors the present theoretical approach was compared with Madsen *et al.* (1990) laboratory data. The results are shown in Figure 5 with the previous results for a monochromatic

wave. The parameters are defined as before except that for spectral waves as the skin Shields parameter is given by:

$$\theta' = \frac{u_{fr}'^2}{(s-1)gd} = \frac{\tau'_{rms}}{\rho(s-1)gd} \tag{5.1}$$

The calculation of the friction factors were carried out in two steps. First, the values of the bed roughness k_s were obtained using the modified iterative scheme (Figure 6) with Fredsøe's (1984) model used to determine the bed shear stress, τ_{rms} . Then the friction factors were calculated on the basis of adjusted the semi-empirical formula of Jonsson & Carlsen (1976) , as for monochromatic waves, in order to include the contribution of vortex formation in the lee of the roughness crests on the shear stress. Here, Jonsson & Carlsen's (1976) formulae were proposed for the calculations of both the friction factors and the dimensionless skin shear stresses.

Similarly as for monochromatic waves, the calculations were performed for two different sediments (0.2mm and 0.12mm diameter quartz sands). Again the agreement between theoretical and experimental results appears quite satisfactory.

6. Conclusions

The sheet flow model appears to produce reasonable results for the conditions tested. However further testing is required.

The use of the model for a range of flow conditions and grain sizes produces a trend of large bed roughnesses at low flow regimes. According to this trend it is suggested that the sheet flow model provides a simple method, or rather an analogy, for the investigation of rippled bed conditions.

Using τ_{rms} to represent mono-frequency waves and τ_{max} to represent spectral waves produces a reasonable agreement with laboratory data.

The simple model results for k_s / d may be of use in preliminary engineering estimates although further testing is required. The present findings can be summarized for both the plane and rippled bed by the equation:

$$\tau_{rms1,2} = F_{1,2}\left[U_{rms}, T_p, k_s = f\left(\frac{3\tau_{rms1}}{\sqrt{2}}, s, d\right)\right] \tag{6.1}$$

The subscripts 1 and 2 refer to the plane and rippled bed respectively.

The function f is described by the proposed iterative procedure and may be represented by the approximating formula:

$$\log\left[\frac{k_s}{d}\right] = -1.05\ \log\left[\theta_{rms}\right] + 4.00 \qquad (6.2)$$

where the Shields parameter is calculated using Fredsøe's (1984) model.

The above approximation differs from that given for monochromatic waves due to the largest waves causing a reduction in the roughness parameter.

To calculate the function F in the case of a plane bed, Fredsøe's (1984) model is recommended ($F_1 \rightarrow \tau_{rms}$). For the rippled bed case, the empirical formula of Kamphuis (1975) or semi-empirical formula of Jonsson & Carlsen (1976) have been used ($F_1 \rightarrow \tau_{rms}$) in order to include the effects of the vortices formed in the lee of the roughness crest on the turbulent mixing.

Based on experimental data, it was found that the representative period equals the peak period. It appears as though the proposed method of predicting bed roughness in spectral waves by using ideas derived for sheet-flow modelling and a representative design wave is capable of providing realistic values for effective bed roughness height. Further work is in progress on the application of the model to additional North Sea data.

7. References

Brevik, I. (1981). 'Oscillatory rough turbulent boundary layers.' J. Waterways, Port, Coastal and Ocean Eng. Div., ASCE, Vol. 107, No.WW3, pp175-188.

Fredsøe, J. (1984). 'The turbulent boundary layer in combined wave and current motion.' J. Hydraulic Eng., ASCE, Vol. 110, No. HY8, pp1103-1120

Horikawa, K., Watanabe, A. and Katori, S. (1982). 'Sediment transport under sheet flow condition.' Proc. 18th Int. Conf. on Coastal Eng., ASCE, Cape Town, South Africa, pp1335-1352.

Jonsson, I.G. and Carlsen, N.A. (1976). 'Experimental and theoretical investigations in an oscillating turbulent boundary layer.' J. Hydr. Res., Vol. 14, No. 1, pp45-59.

Kaczmarek, L.M. and O'Connor, B.A. (1993a). 'A new theoretical approach for predictive evaluation of wavy roughness on a moveable-flat bed.' Part I, Report No. CE/14/93, Department of Civil Engineering, University of Liverpool, 31pp.

Kaczmarek, L.M. and O'Connor, B.A. (1993b). 'A new theoretical approach for predictive evaluation of wavy roughness on a moveable-rippled bed.' Part II, Report No. CE/15/93, Department of Civil Engineering, University of Liverpool, 29pp.

Kamphuis, J.W. (1975). 'Friction factor under oscillatory waves.' J. Waterways, Port, Coastal and Ocean Eng. Div., ASCE, Vol. 101, No. WW2, pp135-144.

Kajiura, K. (1968). 'A model of the bottom boundary layer in water waves.' Bull. Earthq. Res. Inst., Univ. Tokyo, Vol. 46, pp75-123.

Madsen, O.S., Mathison, P.P. and Rosengaus, M.M. (1990). 'Moveable bed friction factors for spectral waves.' Proc. 22nd Int. Conf. on Coastal Eng., ASCE, pp420-429.

Nielsen, P. (1992). 'Coastal bottom boundary layers and sediment transport'. Advanced Series on Ocean Engineering, Vol. 4, World Scientific, Singapore, 324pp.

O'Connor, B.A., Harris, J.M., Kim, H., Wong, Y.K., Oebius, H.U. and Williams, J.J. (1992). 'Bed boundary layers.' Proc. 23rd Int. Conf. on Coastal Eng., ASCE, pp2307-2320.

Savage, S.B. (1984). 'The mechanics of rapid granular flows.' Advances in Applied Mechanics, Vol. 24, pp289-367.

Sayed, M. and Savage, S.B. (1983). 'Rapid gravity flow of cohesionless granular materials down inclined chutes.' J. Applied Mathematics and Physics (ZAMP), Vol.34, pp84-100.

Figures

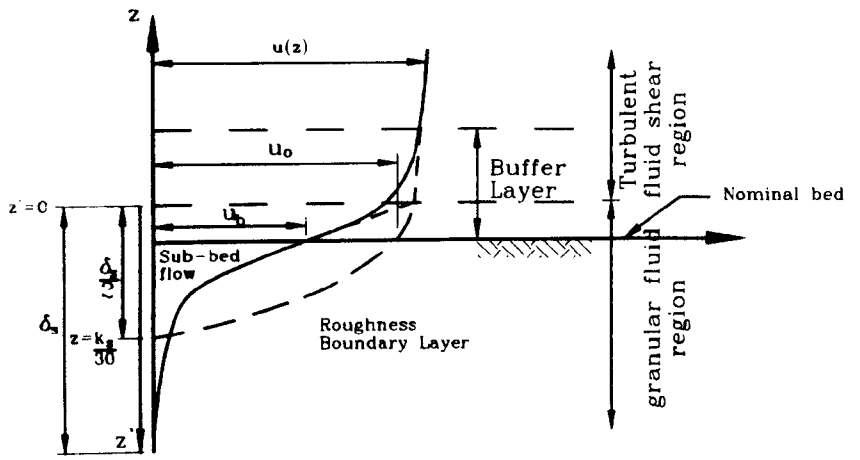

Figure 1: Definition sketch of turbulent flow over a moveable bed.

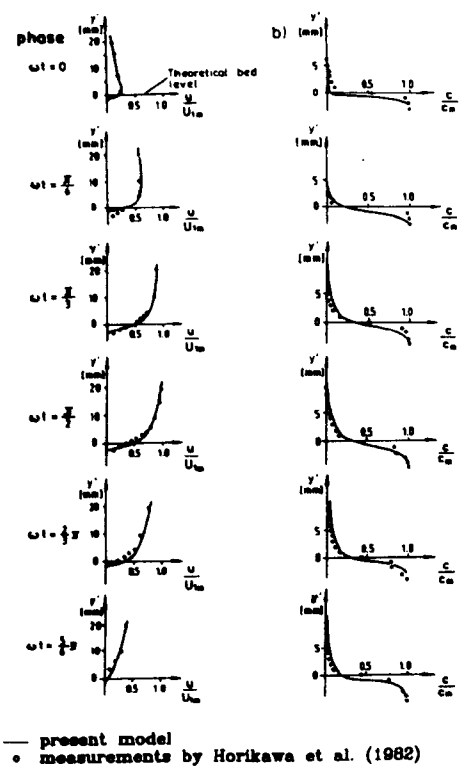

Figure 2: Theoretical and experimental distributions of velocity (a) and concentration (b) below and above the bed.

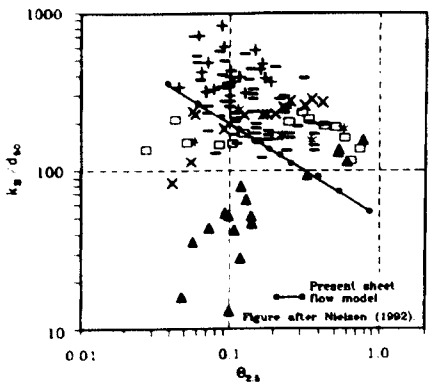

Figure 3: Nikuradse sand roughness by present theory along with results of Nielsen .

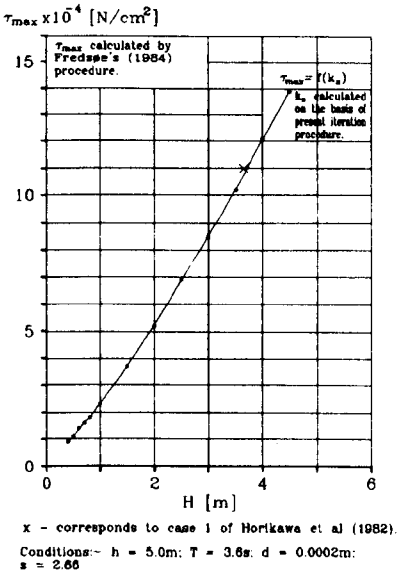

Figure 4: Calculation of maximum shear stresses

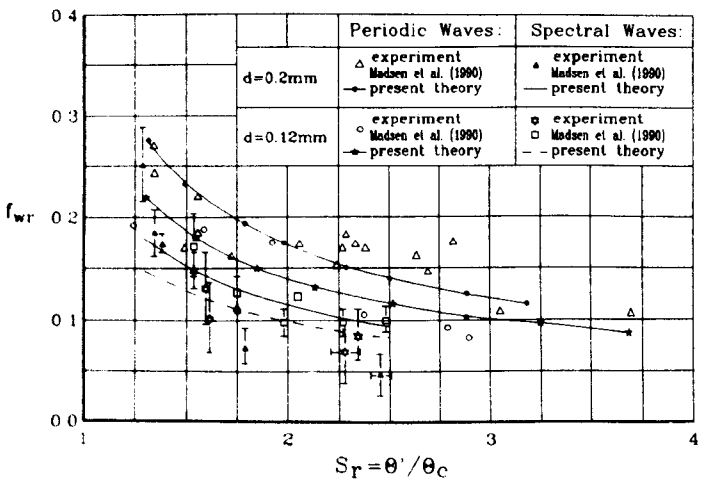

Figure 5: Moveable bed friction factors.

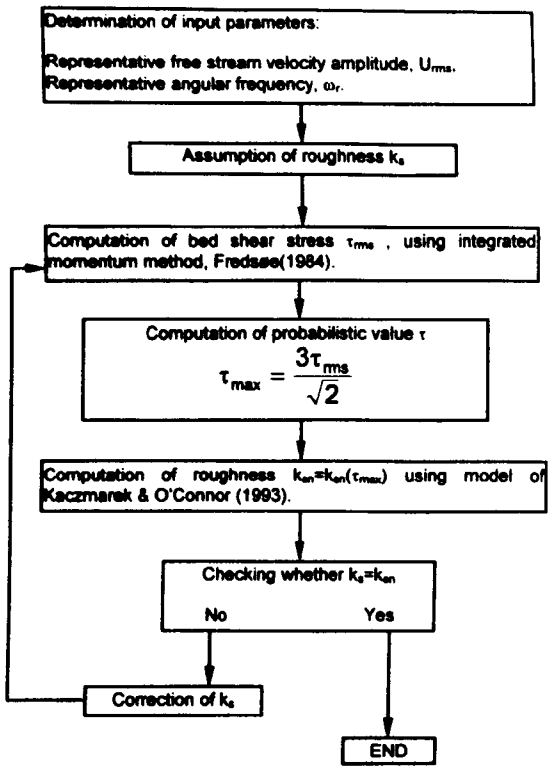

Figure 6: **Modified iteration scheme for spectral waves.**

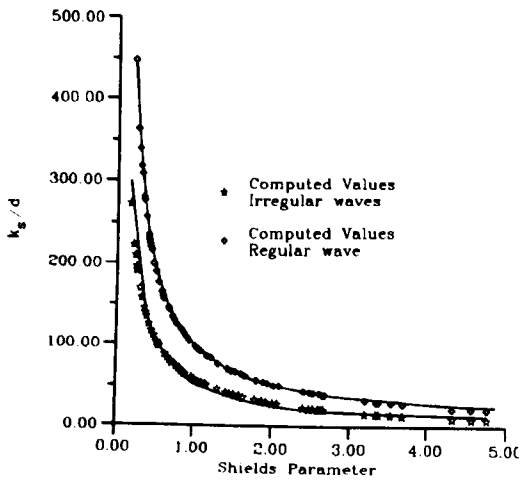

Figure 7: **Results of sheet flow model for regular and random waves.**